



HAL
open science

Méthode de dimensionnement en codesign basée sur une approche semi-probabiliste mettant en jeu la fabrication, le tolérancement et l'analyse statique d'assemblages aéronautiques

Gabriele Capasso

► To cite this version:

Gabriele Capasso. Méthode de dimensionnement en codesign basée sur une approche semi-probabiliste mettant en jeu la fabrication, le tolérancement et l'analyse statique d'assemblages aéronautiques. Matériaux. Université Paul Sabatier - Toulouse III, 2023. Français. NNT : 2023TOU30143 . tel-04354296

HAL Id: tel-04354296

<https://theses.hal.science/tel-04354296>

Submitted on 19 Dec 2023

HAL is a multi-disciplinary open access archive for the deposit and dissemination of scientific research documents, whether they are published or not. The documents may come from teaching and research institutions in France or abroad, or from public or private research centers.

L'archive ouverte pluridisciplinaire **HAL**, est destinée au dépôt et à la diffusion de documents scientifiques de niveau recherche, publiés ou non, émanant des établissements d'enseignement et de recherche français ou étrangers, des laboratoires publics ou privés.



THÈSE

En vue de l'obtention du
DOCTORAT DE L'UNIVERSITE DE TOULOUSE
Délivré par l'Université Toulouse 3 – Paul Sabatier

Présentée et soutenue par
Gabriele CAPASSO

Le 28 juin 2023

**Méthode de dimensionnement en codesign basée sur une
approche semi-probabiliste mettant en jeu la fabrication, le
tolérancement et l'analyse statique d'assemblages aéronautiques**

Ecole doctorale : **MEGEP - Mécanique, Energétique, Génie civil, Procédés**

Spécialité : **Génie mécanique, mécanique des matériaux**

Unité de recherche :
ICA – Institut Clément Ader

Thèse dirigée par
Christian GOGU et Christian BES

Jury

M. Julien BAROTH, Université de Grenoble, Rapporteur

M. Jean-Marc BOURINET, SIGMA Clermont, Rapporteur

Mme Nathalie BARTOLI, ONERA, Présidente

M. Rodolphe LE RICHE, CNRS LIMOS, Examineur

M. Christian GOGU, ISAE-SUPAERO, Directeur de thèse

M. Jean-Philippe NAVARRO, Airbus, Invité

M. Martin KEMPENEERS, Airbus, Invité

M. Laurent RISSE, Airbus, Invité

Abstract

In aircraft design, engineers need to prove the structural integrity of airframe components and assemblies, in spite of the uncertainties associated to all the physical parameters affecting the structural performances, and potentially affecting the safety of the aircraft. Classical static sizing of aeronautical structures introduces scenarios associated to low probability events to deal with the input uncertainties: by piling-up of low probability events, deterministic static strength assessments generally reflect scenarios beyond what needs to be reasonably considered. Except for the loads and material properties (for which clear guidelines are given in the regulations), for a number of parameters, these deterministic values are defined by engineering judgment or by worst cases, and can lead to suboptimal performances (e.g. weight, manufacturing costs).

The main goal of this PhD is to challenge the classical approaches and integrate the uncertainties associated to material properties, manufacturing and assembly process in the structural design and sizing of aeronautical assemblies in order to improve their performances. A semi-probabilistic framework is proposed to extend current aeronautical certification requirements (on loads and material properties) to other phenomena affecting structural performances. The basic idea is to control the probability that representative deterministic values (used in a deterministic design process) over-estimate the structural performances of the real structure: this facilitates the integration of the proposed semi-probabilistic co-design framework in the current way of working (specifically in deterministic sizing). On one hand, the proposed framework can identify the structural consequences of the input variabilities, thus defining new improved deterministic quantities to be adopted in the design phase. On the other hand, this framework can be used to determine new constraints, called tolerances, on the geometric input variability to ensure (in probabilistic terms) specific structural performances.

The implementation of probabilistic analyses generally involves repeated simulations of often computationally expensive numerical models. To ease the computational burden, a sampling strategy is proposed to better exploit the information in a given database and, thus, reduce the number of required simulations to achieve a targeted accuracy. With the same objective in mind, an adaptive machine learning algorithm is proposed to replace the full model with a cheap surrogate model that is adaptively enriched: the algorithm allows to reduce the number of the needed full model simulations by balancing the uncertainties associated to the surrogate model and to the sampled population. Particular attention is given to the scalability of the surrogate model for high number of inputs, which constitutes a challenge for most of machine learning techniques.

The common application thread of the whole project is given by Airbus Hole2Hole project, aiming at simplifying the aeronautical assembly process by using pre-drilled components. New variabilities, associated to geometrical positioning of the manufac-

tured holes, arise from this application. Considering worst cases scenarios would make the Hole2Hole not affordable in terms of weight. The proposed framework allows to significantly improve the sizing assumptions and thus the structural weight, while relaxing the tolerance plans defining the constraints on the input variability.

Keywords: codesign, semi-probabilistic framework, high-dimensional reliability, aeronautical assemblies, machine learning, sampling methods

Résumé

Dans la conception des avions, les ingénieurs doivent prouver l'intégrité structurale des composants et des assemblages de la cellule, malgré les incertitudes associées à tous les paramètres physiques qui peuvent affecter les performances structurales, et potentiellement nuire à la sécurité de l'avion. Dans l'approche classique de dimensionnement statique, on introduit des scénarios associés à des événements rares pour traiter les incertitudes d'entrée : en cumulant ces événements rares, le dimensionnement classique peut mener à des scénarios qui vont au delà de ce qui serait raisonnable à considérer. À l'exception des charges et des propriétés des matériaux (pour lesquelles des directives claires sont fournies dans la réglementation), la plupart du temps, pour d'autres paramètres, ces valeurs déterministes sont définies par jugement d'ingénieur ou en considérant le pire cas, et peuvent conduire à des performances sous-optimales (par exemple, en termes de poids et coûts de fabrication).

L'objectif principal de cette thèse est d'aller au-delà de ces approches classiques et d'intégrer les incertitudes liées aux propriétés des matériaux, à la fabrication et au processus d'assemblage dans la conception et le dimensionnement des assemblages aéronautiques afin d'améliorer leurs performances. Un cadre semi-probabiliste est proposé pour étendre les exigences actuelles de certification aéronautique (sur les charges et les propriétés des matériaux) à d'autres phénomènes affectant les performances structurales. L'idée de base est de contrôler la probabilité que les valeurs déterministes représentatives (utilisées dans un processus de conception déterministe) surestiment les performances structurelles d'une structure réelle donnée : cela facilite l'intégration du cadre semi-probabiliste de codesign proposé dans la manière actuelle de travailler dans l'industrie (en particulier en termes de dimensionnement déterministe). D'une part, le cadre proposé permet d'identifier les conséquences structurales des variabilités d'entrée, définissant ainsi des nouvelles quantités déterministes (améliorées) à adopter en phase de conception. D'autre part, ce cadre peut être utilisé pour déterminer des nouvelles contraintes, dites tolérances, sur la variabilité des entrées géométriques pour assurer (en termes statistiques) des performances structurales spécifiques.

La mise en œuvre d'analyses probabilistes implique généralement des simulations répétées de modèles numériques, souvent coûteux du point de vue des temps de calcul. Pour réduire ces coûts numériques, une stratégie d'échantillonnage est proposée pour réduire le nombre de simulations nécessaires pour atteindre une précision ciblée, en exploitant mieux l'information disponible. Dans le même but, un algorithme d'apprentissage automatique avec enrichissement adaptatif est proposé pour remplacer le modèle complet par un modèle de substitution beaucoup moins coûteux : cet algorithme permet d'équilibrer les incertitudes associées au modèle de substitution et celles associées à l'échantillonnage. Une attention particulière est accordée à la capacité du modèle de sub-

stitution à gérer un nombre élevé d'entrées, ce qui constitue un défi pour la plupart des techniques d'apprentissage automatique.

Le fil conducteur applicatif de l'ensemble de la thèse est donné par le projet Hole2Hole d'Airbus, visant à simplifier le processus d'assemblage aéronautique en utilisant des composants pré-percés. Des nouvelles variabilités, associées aux erreurs de positionnement géométrique des trous fabriqués, sont introduites par cette application. Si on considérait les scénarios des pires cas, le Hole2Hole ne serait pas abordable en termes de poids. Le cadre méthodologique proposé permet d'améliorer significativement les hypothèses de dimensionnement et donc le poids structurel, tout en élargissant les plans de tolérance qui définissent les contraintes sur la variabilité des propriétés géométriques.

Mots clés: codesign, cadre semi-probabiliste, fiabilité en hautes dimensionnes, assemblages aéronautiques, apprentissage automatique, méthodes d'échantillonnage

Contents

1	Introduction	19
1.1	General context	19
1.2	Dealing with uncertainties: a general overview	21
1.3	Industrial context	22
1.4	Hole2Hole (H2H) Project	24
1.5	Challenges of UQ&M on structural applications	28
1.6	Structure of the present study	30
2	State of the art on probabilistic frameworks applications in aeronautical and civil engineering	33
2.1	UQ&M applications: a goal-oriented classification	34
2.2	Current legislation requirements	35
2.2.1	Civil engineering legislation	35
2.2.2	Aeronautical industry regulations	36
2.3	Structural testing	38
2.3.1	Civil applications	39
2.3.2	Aeronautical applications	40
2.4	Reliability assessment	42
2.4.1	Civil applications	45
2.4.2	Aeronautical applications	46
2.5	Safety factors	48
2.5.1	Civil applications	50
2.5.2	Aeronautical applications	52
2.6	Conclusion	54
3	Deterministic Exploration of Input Variability	57
3.1	Introduction	57
3.2	Challenges arising from numerical investigations on H2H	58
3.3	Modal description	62
3.3.1	Principal Components Analysis	63
3.3.2	Partial Least Squares	64
3.3.3	Application on H2H: coupon 1x2	66
3.3.4	Application on H2H: coupon 1x5	68
3.3.4.1	PCA on outputs	68
3.3.4.2	PCA on inputs-outputs	69
3.3.4.3	PLS regression between inputs and reduced outputs	72

3.3.4.4	PLS regression between inputs and original outputs . . .	72
3.3.5	Application on H2H: coupon 3x5	74
3.3.6	Implications on further statistical analyses	78
3.4	Screening	79
3.4.1	Metamodel-based Screening	81
3.4.2	Physics separation	82
3.4.3	Spectral Co-clustering	83
3.4.4	Application to H2H: coupon 1x2	85
3.4.5	Application to H2H: coupon 1x5	85
3.5	Conclusion	86
4	Semi-probabilistic Approach for Aircraft Components Design	89
4.1	Introduction	89
4.2	Definition of the OverLoad (<i>OL</i>)	90
4.3	Classification of random inputs for aircraft components sizing	93
4.4	Semi-probabilistic approach: a double-declination formalization	95
4.5	Quantile Analysis	98
4.5.1	Wilks' method	99
4.5.2	Declination for semi-probabilistic approach	101
4.6	H2H application	103
4.6.1	General setting	103
4.6.2	Coupon 1x2	107
4.6.2.1	Effect of mathematical framework	107
4.6.2.2	Effect of industrial choices	112
4.6.3	Coupon 1x5	115
4.6.4	Coupon 3x5	117
4.7	Conclusion	119
5	Sampling Methods for Reliability Analysis	121
5.1	Introduction	121
5.2	Background on relevant sampling-based methods	123
5.2.1	Monte Carlo (MC) Simulation	123
5.2.2	Importance Sampling (IS)	124
5.2.3	Separable Monte Carlo (SMC)	124
5.3	ImpSMC approach	126
5.3.1	Probability of failure estimation	127
5.3.2	Variance estimation on \widehat{P}_f	127
5.3.3	Mirror formulation	131
5.3.4	On the equivalence of <i>S</i> -based and <i>R</i> -based variance estimator	132
5.3.5	Necessary conditions for variance estimator validity	134
5.3.5.1	First proof: $\phi_1 \geq 0$	136
5.3.5.2	Second proof: $\phi_2 \geq 0$	136
5.3.5.3	Third proof: $\xi_{12} \geq 0$	136
5.3.6	Variance estimator potential	136
5.4	Numerical results	137
5.4.1	Composite plate test case	138

5.4.2	Truss test case	145
5.4.2.1	Effect of variation of $\sigma(R)$	146
5.4.2.2	Effect of failure probability target	151
5.5	Discussion of results	152
5.6	Conclusion	155
6	High-dimensional Adaptive Learning for Reliability Analysis	159
6.1	Introduction	159
6.2	Mathematical Framework	161
6.2.1	Monte Carlo (MC) Simulation	161
6.2.2	Kriging - Partial Least Square (KPLS)	161
6.2.2.1	Kriging	162
6.2.2.2	Partial Least Square	163
6.2.2.3	KPLS	164
6.2.3	Kriging-based adaptive learning techniques for reliability	165
6.2.4	Variance decomposition	166
6.2.4.1	Ill-conditioned covariance matrix	168
6.2.4.2	Simulate large amounts of data	169
6.3	Adaptive Variance-based Kriging Partial Least Square (Vb-KPLS)	170
6.3.1	Exploration criteria	170
6.3.2	Stopping criteria	171
6.3.3	Proposed Variance-based (<i>Vb</i>) algorithm	173
6.4	Numerical results	175
6.4.1	40-dimensional linear problem	175
6.4.2	100-dimensional linear problem	178
6.4.3	53-dimensional truss example	179
6.4.4	53-dimensional heat conduction problem	180
6.5	Improvement with SMC	183
6.5.1	Application to the truss example	185
6.5.2	Application to Hole2Hole	187
6.6	Discussion of results	191
6.7	Conclusion	192
7	Codesign Framework for Aircraft Assembly Design	195
7.1	Introduction	195
7.2	Formulations background	198
7.2.1	Reliability-Based Design Optimization	198
7.2.2	Multi-objective optimization	199
7.3	Semi-probabilistic codesign framework	201
7.3.1	Definition of main random variables	202
7.3.2	Definition of design variables	204
7.3.3	Definition of main costs	206
7.3.4	Introduction of semi-probabilistic constraints	210
7.3.5	Sensitivities of the main quantities	214
7.3.6	Problem statement	216
7.3.7	Preliminary analysis	217

7.3.8	Numerical tools	218
7.4	Applications on built-in stresses	219
7.4.1	Built-in stress examples: wing root joint	221
7.4.1.1	Mathematical formulation	222
7.4.1.2	Results for <i>current practice</i>	225
7.4.1.3	Results for codesign framework with fixed top-level requirement	229
7.4.1.4	Results for full codesign framework (with smart top-level requirement re-definition)	232
7.4.2	Built-in stress results: spar2cover	237
7.5	Applications on H2H	240
7.5.1	H2H: coupon 1x2	246
7.5.1.1	Study of the Pareto front	246
7.5.1.2	Study of the optimal tolerance variables v_i	250
7.5.1.3	Study of the optimal top-level requirement v_{assy}	253
7.5.2	H2H: coupon 1x5	255
7.5.3	H2H: coupon 3x5	259
7.6	Discussion of results	262
7.7	Conclusion	265
	Appendices	295
	A Overload output distributions for H2H: coupon 1x2	297
	B Additional material on ImpSMC	299
B.1	Proof of Eq. 5.19	299
B.2	Experimental variance validation on truss test case	300
	C Additional material on codesign tolerance optimization	303
C.1	Additional formulations of codesign framework	303
C.2	Additional results on H2H applications	304
C.2.1	Coupon 1x5	304
C.2.2	Coupon 3x5	306

List of Figures

1.1	Example of uncertainties linked to structural design (Source: [Larsen and Raju, 2016])	20
1.2	General framework for <i>Uncertainty Quantification & Management</i> (UQ&M): a simplified scheme	22
1.3	Assembly levels in aircrafts (Source [Diet, 2021])	23
1.4	Current practice for aeronautical assembly routine	24
1.5	Aeronautical assembly routine in H2H perspective	25
1.6	Oversize definition	25
1.7	Role of oversize of absorbing the variability of hole misalignments on H2H assembly (illustration not at scale)	26
1.8	Illustration of the effect of oversize and misalignments on H2H load transfer	27
2.1	Definition of general safety factors FS according to CS-25	38
2.2	Pyramid of tests (Source: [Rouchon, 1990])	41
2.3	Reliability: general illustration	44
2.4	Probabilistic analysis concept from FAA (Source: [Long and Narciso, 1999])	48
2.5	Illustration of the principle of design by safety factors (aeronautical nota- tion is used)	50
2.6	Distribution of reliability indexes β before and after code calibration (Source: [Sørensen, 2002])	52
3.1	Illustration of uni-axial loaded Single Lap Shear bolted joint assembly (bolting pattern: 2x5)	59
3.2	Illustration of geometrical misalignment definition	60
3.3	Evolution of the number of input variables as function of the bolting patterns	62
3.4	Illustration of main failure modes for bolted joint assemblies (mixed failure mode not reported)	63
3.5	Schematic diagram of the first component in PLS analysis on coupon 1x2	67
3.6	Spy matrix plot of the four modes obtained for all output responses through PCA for coupon 1x5 (threshold 0.05)	69
3.7	Spy matrix plots of the modes obtained for all output responses through PCA for coupon 1x5 (threshold 0.05)	70
3.8	First four modes obtained through PCA for coupon 1x5	70
3.9	Convergence plot for the first four modes obtained through PCA for coupon 1x5	71
3.10	First four modes obtained through PLS on reduced outputs (from PCA) for coupon 1x5	73

3.11	Graphical representation of coefficient matrix obtained through PLS on reduced outputs (from PCA) for coupon 1x5	73
3.12	First four modes obtained through PLS for coupon 1x5	73
3.13	Graphical representation of coefficient matrix obtained through PLS for coupon 1x5	75
3.14	Convergence plots for the first four modes obtained through PLS for coupon 1x5	75
3.15	Graphical representation of coefficient matrix obtained through PLS for coupon 3x5	76
3.16	Coefficients of transferred bearing load forces retrieved through PLS expressed as function of the relative longitudinal misalignments on different bolt locations for coupon 3x5	77
3.17	Illustration of the benefits of adding transversal misalignment samples in presence of a tolerance acceptance criterion	79
3.18	Graphical synthesis of sensitivity analysis methods (Source: [Iooss and Lemaître, 2015])	80
3.19	Example of physics separation for a 200-dimensional problem	84
3.20	Screening spy matrix plot for H2H coupon 1x2	85
3.21	Example of physics separation on H2H coupon 1x5	86
3.22	Effects of the dimensionality reduction on different bolting patterns . . .	88
4.1	Effect of oversize and misalignments on H2H load transfer	91
4.2	Schematic representation of three design approaches	97
4.3	Minimum number of samples according to Wilks' formula (confidence $\beta = 0.95$)	100
4.4	Schematic representation of stack chains associated with manufacturing processes	104
4.5	General setting options for OL analysis on H2H	105
4.6	Comparison of performances for OL quantile estimation on the H2H 1x2 coupon (via semi-probabilistic approach) with Wilks and bootstrap enrichment for different ranks: values of OL quantile estimation ($\alpha = 0.9$) . . .	109
4.7	Box-plots of quantile estimations for two decision criteria and three quantile levels in function of Wilks' rank	110
4.8	Comparison between Wilks and Monte Carlo estimations at three different quantile levels	111
4.9	Convergence of quantile estimations for two decision criteria and three quantile levels as a function of the number of simulations	112
4.10	Coupon 1x2: Overload results for 90th percentile for different decision criteria, stack chains and tolerance acceptance criteria (input distribution: uniform)	113
4.11	Coupon 1x2: Overload results for 90th percentile for different decision criteria, stack chains and tolerance acceptance criteria (input distribution: triangular)	114
4.12	Coupon 1x2: Overload results for 90th percentile for different decision criteria, stack chains and tolerance acceptance criteria (input distribution: normal)	115

4.13	Coupon 1x5: Overload results for 90th percentile for different decision criteria, stack chains and tolerance acceptance criteria (input distribution: uniform)	115
4.14	Coupon 1x5: Overload results for 90th percentile for different decision criteria, stack chains and tolerance acceptance criteria (input distribution: triangular)	116
4.15	Coupon 1x5: Overload results for 90th percentile for different decision criteria, stack chains and tolerance acceptance criteria (input distribution: normal)	116
4.16	Coupon 3x5: Overload results for 90th percentile for different decision criteria, stack chains and tolerance acceptance criteria (input distribution: uniform)	117
4.17	Coupon 3x5: Overload results for 90th percentile for different decision criteria, stack chains and tolerance acceptance criteria (input distribution: triangular)	118
4.18	Coupon 3x5: Overload results for 90th percentile for different decision criteria, stack chains and tolerance acceptance criteria (input distribution: normal)	118
5.1	Cross-ply test case: illustration (Source: [Smarslok et al., 2010, Chaudhuri and Haftka, 2013])	139
5.2	Composite plate test case: outputs distributions in $LRVF$	139
5.3	Composite plate test case: outputs distributions in $HRVF$	140
5.4	Composite plate test case: experimental validation of both variance estimators	140
5.5	Composite plate test case: $coV(\widehat{P}_f)$ contour plots on two LSF formulations	144
5.6	Composite plate test case: effect of LSF formulation on variance reduction of \widehat{P}_f estimation as a function of number of samples N of S and M of R .	144
5.7	Truss test case: illustration (Source: [Lelievre, 2018])	145
5.8	Truss nominal case: coV contour plot	147
5.9	Truss test case: effect of $\sigma(R)/\sigma(S)$ on coV contour plot	149
5.10	Truss test case: effect of $\sigma(R)/\sigma(S)$ on variance reduction in function of number of samples N of S and M of R (fixed $\sigma(S) = 6.47 \times 10^{-3}$)	150
5.11	Minimum N and M to obtain $coV = 0.05$ in function of $\sigma(R)/\sigma(S)$	150
5.12	Truss test case: effect of $\sigma(R)/\sigma(S)$ on needed number of samples N of S and M of R to achieve $cov(P_f) = 0.05$ at given M/N ratios	151
5.13	Truss test case: effect of P_f target on $coV(P_f)$ contour plot	152
5.14	Truss test case: effect of P_f on variance reduction in function of number of samples N of S and M of R	153
5.15	Minimum N and M to obtain $coV = 0.05$ in function of P_f target	153
5.16	Truss test case: effect of P_f target on needed number of samples N of S and M of R to achieve $cov(P_f) = 0.05$ at given M/N ratios	154
6.1	Proposed algorithm flowchart	174
6.2	40-dimensional linear problem: variance decomposition results across iterations with different adaptive approaches (4 components in KPLS setting)	177
6.3	Truss test case: illustration (Source: [Lelievre, 2018])	180
6.4	Heat conduction problem: domain definition and output sample distribution	181

7.1	Assembly levels in aircrafts (Source [Diet, 2021])	196
7.2	Example of conflict of costs in tolerance allocation (Source [Cheikh and McGoldrick, 1988])	197
7.3	Illustration of geometrical features for H2H problem (one hole considered)	202
7.4	Illustration of the association of tolerance bounds \mathbf{v} to H2H geometrical features at component level (one hole considered)	205
7.5	Capability to distinguish acceptable from unacceptable assemblies which must be ensured by the <i>tolerance acceptance criterion</i> , in presence of a physical obstacle: two H2H examples with a limited oversize	206
7.6	Illustration of the steps followed in the implementation of the tolerance plans	208
7.7	Possible outcomes of the application of the top-level requirement check on the distribution of the tolerance model output	210
7.8	Illustration of the benefits of adding transversal misalignment samples in presence of a tolerance acceptance criterion $\sqrt{dX_1^2 + dY_1^2} \leq v_{assy}$	215
7.9	Built-in stress arising from gaps closure in fastener installation [Kempeneers, 2018]	220
7.10	Illustration of wing components (Source: [Venkatesan et al., 2021])	220
7.11	Gap closure on wing root joint (fastener between wing cover and cruciform not represented)	221
7.12	Representation of reference systems on wing root joint example (the arrows directions indicate the positive sign of the different geometrical features)	222
7.13	Wing root joint example: results of optimization with <i>current practice</i>	227
7.14	Wing root joint example: <i>PoE</i> results post-optimization with <i>current practice</i> for two reference quantiles on strength R	227
7.15	Wing root joint example: representation of results from optimization with <i>current practice</i> at fixed sizing gap G_{REF} and budget \bar{c}_2	228
7.16	Wing root joint example: representation of results from optimization with codesign framework at fixed top-level requirement v_{assy} and sizing gap G_{REF}	230
7.17	Wing root joint example: evolution of results from optimization with codesign framework with respect to the sizing gap G_{REF} for two top-level requirements v_{assy}	231
7.18	Wing root joint example: evolution of results from optimization with codesign framework with respect to the sizing gap G_{REF} for two fixed budgets \bar{c}_2	233
7.19	Wing root joint example: results of optimization with <i>full codesign framework</i>	234
7.20	Wing root joint example: representation of results from optimization with full codesign framework at fixed \bar{c}_2 and sizing gap G_{REF}	235
7.21	Wing root joint example: comparison of optimization results with different formulations of the <i>full codesign framework</i> and <i>current practice</i>	236
7.22	Illustration of the spar2cover junction test case	237
7.23	Example of liquid shim application	238
7.24	Spar2cover example: results of optimization with full codesign framework	239
7.25	Schematic representation of stack chains associated with manufacturing processes	240
7.26	H2H coupon 1x2: obtained Pareto fronts for different overload limits OL , regrouped per stack chain	247
7.27	H2H coupon 1x2: zoom on optimization results for stack chain 4, as a function of cost c_2	249

7.28	H2H coupon 1x2: optimal v_i with full codesign framework on different stack chains at fixed budgets \bar{c}_2	250
7.29	H2H coupon 1x2: optimal v_i with full codesign framework on different budgets \bar{c}_2 regrouped per stack chain	252
7.30	H2H coupon 1x2: optimal v_{assy} with full codesign framework on different stack chains at fixed budgets \bar{c}_2	254
7.31	H2H coupon 1x2: optimal v_{assy} with full codesign framework on different budgets \bar{c}_2 regrouped per stack chain	255
7.32	H2H coupon 1x5: obtained Pareto fronts for different overloads OL , regrouped per stack chain	256
7.33	H2H coupon 1x5: optimal v_i with full codesign framework on different stack chains at fixed budgets \bar{c}_2	257
7.34	H2H coupon 1x5: optimal v_{assy} with full codesign framework on different stack chains at fixed budgets \bar{c}_2	259
7.35	H2H coupon 3x5: obtained Pareto fronts for different overloads OL , regrouped per stack chain	260
7.36	H2H coupon 3x5: optimal v_i with full codesign framework on different stack chains at fixed budgets \bar{c}_2	261
7.37	H2H coupon 3x5: optimal v_{assy} with full codesign framework on different stack chains at fixed budgets \bar{c}_2	262
A.1	Overload output PDFs for different stack chains and tolerance acceptance criteria (individual distribution: uniform)	297
A.2	Overload output PDFs for different stack chains and tolerance acceptance criteria (individual distribution: triangular)	298
A.3	Overload output PDFs for different stack chains and tolerance acceptance criteria (individual distribution: normal)	298
B.1	Truss test case: experimental validation of both variance estimators	301
C.1	H2H coupon 1x5: optimal v_i with full codesign framework on different budgets \bar{c}_2 regrouped per stack chain	305
C.2	H2H coupon 1x5: optimal v_{assy} with full codesign framework on different budgets \bar{c}_2 regrouped per stack chain	306
C.3	H2H coupon 3x5: optimal v_i with full codesign framework on different budgets \bar{c}_2 regrouped per stack chain	307
C.4	H2H coupon 3x5: optimal v_{assy} with full codesign framework on different budgets \bar{c}_2 regrouped per stack chain	308

List of Tables

3.1	Original list of input variables on H2H problem for different bolting patterns	61
3.2	Final list (after dimensionality reduction) of input variables on H2H problem for different bolting patterns	87
5.1	Main outcomes of variance estimator	137
5.2	Cross-ply test case: random variables	138
5.3	Composite plate test case: output statistical parameters for <i>LRVF</i> and <i>HRVF</i> formulations	140
5.4	Composite plate: main results for <i>LRVF</i> from Eq. 5.45a (values issued from 100 repetitions of each reliability algorithm)	141
5.5	Composite plate: main results for <i>HRVF</i> from Eq. 5.45b (values issued from 100 repetitions of each reliability algorithm)	141
5.6	Composite plate test case: extrapolation parameters for two <i>LSF</i> formulations at different M/N sample ratios ($N = 100$, R -based variance estimator is adopted)	142
5.7	Truss test case: random variables	146
5.8	Truss test case: main reliability results from different simulation algorithms (values issued from 100 repetitions of each reliability algorithm)	146
5.9	Truss test case: configurations for study on $\sigma(R)/\sigma(S)$ effect (fixed statistical parameters of S : mean $\bar{S} = \bar{V}_1 = 0.079$, standard deviation $\sigma(S) = \sigma(V_1) = 6.47 \times 10^{-3}$ and coefficient of variation $coV(S) = coV(V_1) = 0.082$)	147
5.10	Truss test case: reference results for study on $\sigma(R)/\sigma(S)$ effect (100 simulations considered, targeted $coV(\widehat{P}_f) = 0.05$)	148
5.11	Truss test case: configurations and reference results for study on P_f effect (100 simulations considered, targeted $coV(\widehat{P}_f) = 0.05$, fixed statistical parameters of S : mean $\bar{S} = \bar{V}_1 = 0.079$, standard deviation $\sigma(S) = \sigma(V_1) = 6.47 \times 10^{-3}$ and coefficient of variation $coV(S) = coV(V_1) = 0.082$)	151
6.1	Main results for 40-dimensional linear problem (reference MC: $P_f = 2.00 \times 10^{-3}$). Note that the number in parentheses provide the coV of the values provided in the respective cells.	176
6.2	Main results for 100-dimensional linear problem (reference MC: $P_f = 1.66 \times 10^{-3}$). Note that the number in parentheses provide the coV of the values provided in the respective cells.	179
6.3	Truss test case: random variables	179

6.4	Main results for 53-dimensional truss problem (reference MC: $P_f = 2.00 \times 10^{-3}$). Note that the number in parentheses provide the <i>coV</i> of the values provided in the respective cells.	180
6.5	Main results for 53-dimensional heat conduction problem (reference MC: $P_f = 4.75 \times 10^{-2}$). Note that the number in parentheses provide the <i>coV</i> of the values provided in the respective cells.	182
6.6	Main results for 53-dimensional truss problem with $\bar{R} = 0.105$ (reference MC: $P_f = 1.76 \times 10^{-2}$). Note that the number in parentheses provide the <i>coV</i> of the values provided in the respective cells.	186
6.7	Main results for 53-dimensional truss problem with $\bar{R} = 0.095$ (reference MC: $P_f = 9.70 \times 10^{-2}$). Note that the number in parentheses provide the <i>coV</i> of the values provided in the respective cells.	186
6.8	Application of Vb-KPLS+SMC on H2H coupons (*: only relative longitudinal misalignments are considered)	190
7.1	Notations and definitions used for the applications of the <i>full codesign framework</i> on H2H problem, with Stack Chain 1 (<i>datum plate</i>)	242
7.2	Notations and definitions used for the applications of the <i>full codesign framework</i> on H2H problem, with Stack Chain 4, 5, 6 (<i>datum first hole</i>)	243
B.1	Truss test case: configurations used for validation purpose	300

Chapter 1

Introduction

The present dissertation covers the activities of a Cifre PhD research project, born from the collaboration between Airbus Operations SAS and Institut Clément Ader (convention Cifre n° 2019/1564).

1.1 General context

In aircraft design, multiple disciplines are involved, like structural mechanics, thermodynamics, automatics, electronics, flight physics, material science, among others. These are not totally detached, but can interact with each other. The focus of the entire work presented in this manuscript is centered around the design of aeronautical structures. This is interfaced with several other disciplines, for example:

- *material science*, to evaluate the resistance of structural components;
- *aerodynamics* and *flight physics*, to define the loads applied on the structure;
- *manufacturing*, affecting the properties of the structure;
- *tolerancing activities*, which manage the geometrical variability of real structural components.

In the specific case of structural design, we need to deal with several sources of uncertainties which may have an impact on structural performances. Typical examples of sources of uncertainties involved in structural design can be given by the material mechanical properties, applied loads, temperatures, geometrical variability of manufactured parts, among others. In Fig. 1.1 we list other examples of possible sources of uncertainties, reported in the work in [Larsen and Raju, 2016]. In the chart in Fig. 1.1, the variability of input parameters can lead to a statistical dispersion of the structural response (e.g. stress) and structural resistance (e.g. strength), associated to several phenomena - known as *failure modes* - which can make the structure collapse. The statistical results can lead to cases (interference region), where the applied solicitations can exceed the structural strength. Consequently, the statistical variability of design parameters can affect the safety of the aircraft structure.

To guarantee the safety of aeronautical structures, the manufacturers need to take into account and demonstrate the reliability and the robustness of the engineering solutions, in spite of the uncertainties linked to the statistical variability of the input parameters. The

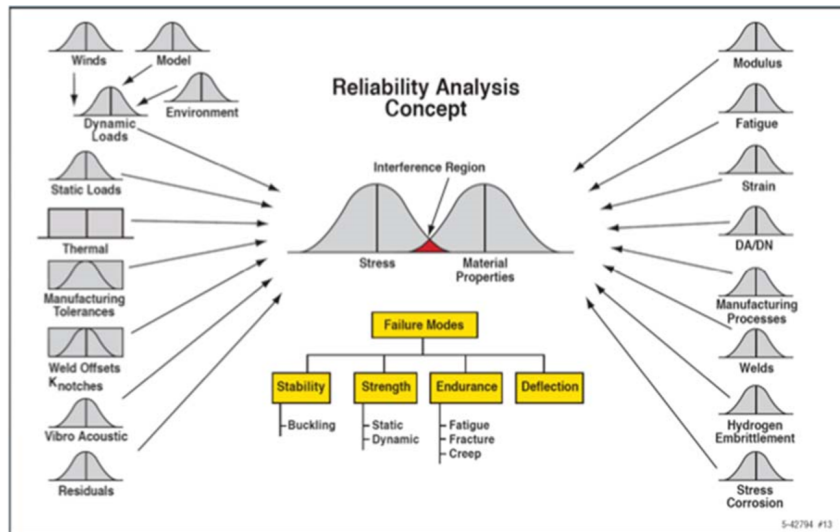


Figure 1.1: Example of uncertainties linked to structural design (Source: [Larsen and Raju, 2016])

aeronautical certification authorities define *standards* to ensure the design of airplanes is safe enough. In particular, the *EASA* specifies *certification requirements* that all aircrafts intended to fly in Europe need to satisfy. Meeting such requirements is mandatory to obtain the *Certificate of Airworthiness*, corresponding to the permission to operate.

When seeking to comply with these certification requirements, designers traditionally cope with uncertainties of input design parameters within the deterministic design framework itself: the statistical variability is implicitly treated via the adoption of deterministic quantities corresponding to detrimental low probability events. In particular, according to the specific property, different choices of these deterministic quantities can be done: specific quantiles of the random properties (if explicitly prescribed by the certification requirements, e.g. A-basis or B-basis values for material allowables), worst cases or other deterministic quantities dictated by past experience. In particular, the *worst case scenario* approach is common practice (though not explicitly prescribed by current certification requirements) for a number of complex phenomena with a large variability. The assumptions set in traditional deterministic design may lead to scenarios beyond what is actually needed, leading to sub-optimal performances in terms of weight and/or manufacturing costs.

The main industrial need treated in this PhD project is the formalization of a general statistical framework to compute and justify the scenarios to adopt in the design phase: this framework is of industrial interest because the management of the uncertainties has the potential to improve the sizing assumptions typically used in classical design approaches. From a process standpoint, this framework may allow to support the engineering judgment choices (generally done on a case-by-case basis) of which scenario to adopt for sizing, thus passing to a general formal process. From a performance standpoint, the quantification and the management of the input uncertainties can allow gains in terms of weight and reductions of manufacturing costs.

In this PhD project we propose a formal framework to establish a consistent approach to define the scenarios used in classical design phase, by means of integrating the prob-

abilistic description of the different sources of uncertainties in the design of aeronautical structures. A particular attention will be given to the compliance with current certification requirements: we will define a formal framework to take into account the input uncertainties as an *extension* of the current certification requirements. The study will also involve multiple disciplines: in particular, we will analyze the interfaces between structural analyses, manufacturing process and tolerancing activities. The common thread of the whole manuscript will be given by the application on an actual industrial project at Airbus. In the following sections we will provide an overview of the main topics and challenges addressed in the present work.

1.2 Dealing with uncertainties: a general overview

The *Uncertainty Quantification & Management* (UQ&M) constitutes a general framework to manage the statistical variability of system performances [De Rocquigny et al., 2008]. A simplified scheme of the UQ&M general framework is provided in Fig. 1.2. This is based on the logical concatenation of different ingredients, which need to be defined prior to the analysis itself:

- *Input variables definition*: the choice of the input involved in the design process and affecting final performances;
- *Input uncertainties description*: the probabilistic modelings defining the variability of the different inputs (e.g. the associated distributions);
- *Input variables classification*: the distinction between uncertain input parameters X and deterministic inputs d , referred to as *scenarios*;
- *Output identification*: the key-phenomena Z representing the specific performances which we need to monitor;
- *Model*: the representation of the behavior of a given system, linking all inputs X, d to the outputs Z , via a specific function G : this can be either a physical or a numerical model, complete or simplified or also a surrogate model (i.e. via machine learning techniques);
- *Output uncertainty measure*: the *quantity of interest* which allows to evaluate the output performances from a statistical point of view: typical examples may be given by specific quantiles of the random outputs, mean values, probability of exceeding deterministic values, among others;
- *Decision criteria*: the principle defining whether the output uncertainty measure is acceptable or not, consistently with the precise scope of the UQ&M analysis;
- *Feedback process*: this consists in the redefinition of the input uncertainties description and/or the input variables classification, i.e. artificially fixing at deterministic values (thus scenarios) some of the variables which would be random by nature;

- *Deterministic format*: the representation of the results of the probabilistic analysis in form of a collection of deterministic quantities, allowing the automatic management of uncertainties also in the classical deterministic design, for example via tables of multiplicative coefficients to adjust analytical models, extreme boundaries of the output variability, among others.

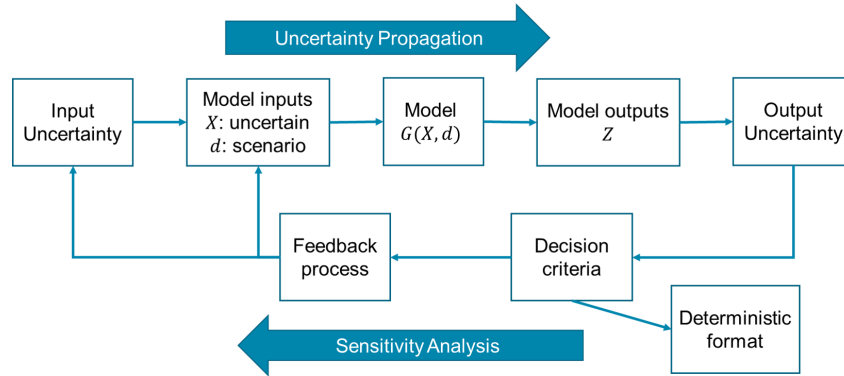


Figure 1.2: General framework for *Uncertainty Quantification & Management (UQ&M)*: a simplified scheme

All these ingredients are interconnected as shown in Fig. 1.2. In particular, two main directions can be recognized:

1. *Uncertainty Propagation*: Starting from an input statistical dispersion, certain variables are fixed (i.e. defined as *scenarios* d) while others are kept free to vary (uncertain variables X). These are introduced in a model G that determines the outputs Z , the uncertainties of which are quantified in a statistical framework;
2. *Sensitivity Analysis*: Starting from the output uncertainties, a decision criterion is established, so that it can allow to intervene in a feedback loop on input definitions (i.e. their statistical distributions), on the input classification (i.e. to re-define the distinction between random and scenario variables) and also to present results in a deterministic format (e. g. tables providing specific quantiles or corrective coefficients to introduce in the deterministic structural sizing).

The UQ&M framework described in this section constitutes a general process which needs to be adapted for the specific applications. In the following we will present a general overview of the industrial context in which this PhD is carried out, in order to illustrate the challenges and the expected benefits of UQ&M on a concrete use case of industrial interest.

1.3 Industrial context

The aeronautical assembly process generally involves several *layers* (or *levels*): in a top-down decomposition, we generally recognize the aircraft level, the section, the work-package, the assembly and the elementary parts, as illustrated in the example in Fig. 1.3.

The single elements involved in the assembly are referred indifferently as *parts*, *structural components* or *contributors*. In the general process decomposition, the assembly (in its broadest sense) at one level becomes then a part in the superior level.

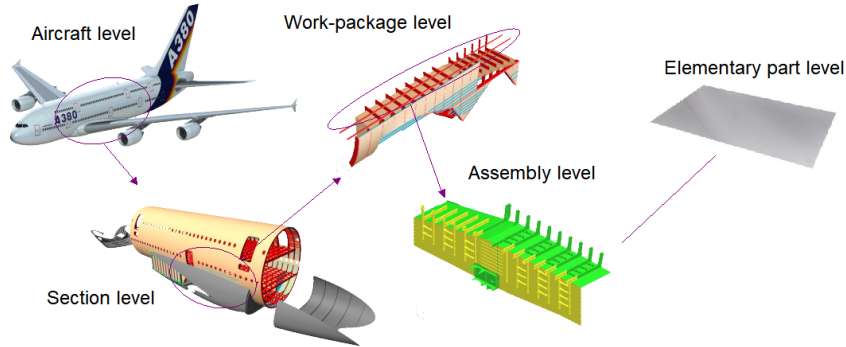


Figure 1.3: Assembly levels in aircrafts (Source [Diet, 2021])

The geometrical features of the real manufactured components can differ from the theoretical values (referred to also as *nominal values*), possibly leading to difficulties in assembling the different parts together. To ensure that all pieces can be assembled also in presence of uncertainties on the geometric features, specific requirements are defined at the highest level (referred to as *top-level requirements*): these latter are then cascaded to each interface at the lower levels, defining specific limits, called *tolerances*, which constitute constraints on the variability of the geometric features of each component. The tolerances allow to be sure that each elementary part can be connected to the other elementary parts. The process to assign specific tolerances at component level from a top-level requirement is generally called *tolerance cascade* or *tolerance allocation*.

The connections between structural components can be done by welding or, more commonly, via the introduction of fasteners, including bolts and rivets. When introducing bolts to connect two components, it is common to refer to the obtained assembly as *bolted joint assembly*. Note that the connections via fasteners can be either permanent or non-permanent: the latter category does not imply that the connections are *provisional*, but that they can be disassembled without destroying them (e.g. using screws and nuts).

Current practices for aeronautical structural assemblies based on fastener connections (which are illustrated in Fig. 1.4) prescribe a succession of precise steps which strongly integrate manufacturing and assembly processes. In general, the holes are drilled during the assembly phase itself. The steps generally followed can be summarized as follows:

1. The parts to assemble are placed in the expected final positions;
2. Reference holes are drilled on the superposed parts;
3. The parts are detached;
4. The reference holes are cleaned on separated elements;
5. The parts are re-positioned together;
6. Provisional fasteners are installed on the superposed structural parts;
7. All other holes are drilled on the superposed parts;
8. At this point, elements are detached, cleaned and re-positioned;
9. Sealant is applied between parts;
10. Provisional fasteners are installed on the superposed structural parts;

11. The holes are cleaned and finished in place (*reaming* phase);
12. Provisional fasteners are progressively removed and replaced by final (not necessarily permanent) fasteners.

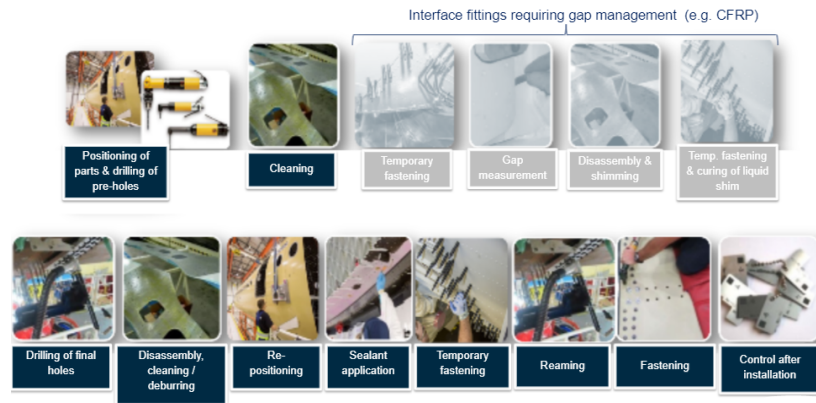


Figure 1.4: Current practice for aeronautical assembly routine

This complex procedure does not introduce significant geometric errors in manufacturing and assembly chain: all holes from two connected parts are always perfectly aligned. On the other hand, this process implies a significant amounts of work, time and money. We may identify, therefore, a specific industrial need: to simplify the overall procedure to assemble bolted joint structures. This constitutes the main purpose of the *Hole2Hole* project, described in the following section.

1.4 Hole2Hole (H2H) Project

The *Hole2Hole* (H2H) project is an Airbus initiative aiming at simplifying the overall assembly process. The base idea is to transfer part of the drilling process in the manufacturing step, in order to move it out from the assembly line. Practically speaking, it is sought to make use of pre-drilled parts: therefore, as the holes are manufactured before entering in the assembly line, all steps related to the drilling, cleaning and reaming on the holes are removed from the process (in the assembly line). The simplified procedure is illustrated in Fig. 1.5.

The H2H has the potential to significantly simplify the assembly routine. However, it has also consequences on logistic planning, current way of working and structural performances. In this work we will focus on structural performances which are mainly linked to *hole misalignments* and *hole oversize*.

As the parts are produced individually and entirely out of the assembly line, the positions of the holes can differ from the theoretical nominal locations. When superposing the parts in the assembly line, we can have holes which are not perfectly aligned between them. These *hole misalignments* can constitute already a problem for assembling the parts, as we might not be able to insert the bolt inside the holes.

In order to ensure the capability to assemble the parts, we need to account for the variability of the *hole misalignment*. Strictly speaking, we need to be sure that even in presence of misaligned holes, the bolts can fit inside the holes so that the assembly can

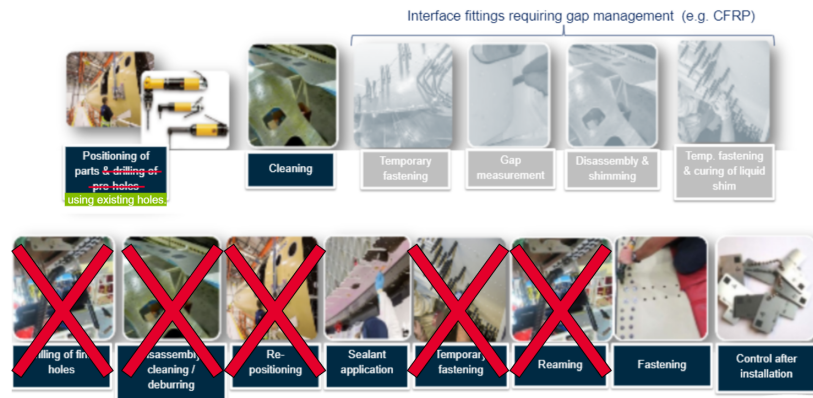


Figure 1.5: Aeronautical assembly routine in H2H perspective

be built. In particular, it was chosen to make use of the concept of *oversize*, illustrated in Fig. 1.6. Note that in classical assemblies with perfectly aligned holes, the diameter of the hole is also slightly larger than the bolt, such to allow to insert this latter inside the hole: this differences of diameters (between hole and bolt) is generally referred to as *fit clearance*. The *oversize* is an extension of the concept of *fit clearance*, defined as an additional increase of the hole diameter. Note that in Fig. 1.6, we represent both *fit clearance* and *oversize* as radius to simplify the illustration: but in fact, these are defined as additional increases of *diameters*.

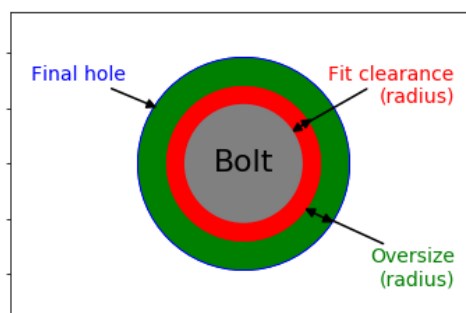


Figure 1.6: Oversize definition

In Fig. 1.7, we illustrate the effect of the *oversize* on the assembly capability of the H2H assemblies. Without *oversize*, the hole misalignments could prevent inserting the bolts inside the holes. Instead, thanks to the *oversize*, the assembly of the structure can be carried even in presence of hole misalignments, up to a certain limit.

However, the added value of the *oversize* (depicted in Fig. 1.7) can be effective only on the configurations with "reasonable" hole misalignments (i.e. not exceeding some threshold). In fact, the *oversize* itself constitutes a new *top-level requirement*: the hole misalignments will then be considered as new geometric features at component level, the variability of which must be regulated by specific tolerances. The hole misalignments will be "reasonable" if their tolerance limits are consistent with (i.e. cascaded from) the *oversize*. Note that the tolerances on hole misalignments constitute a new concept

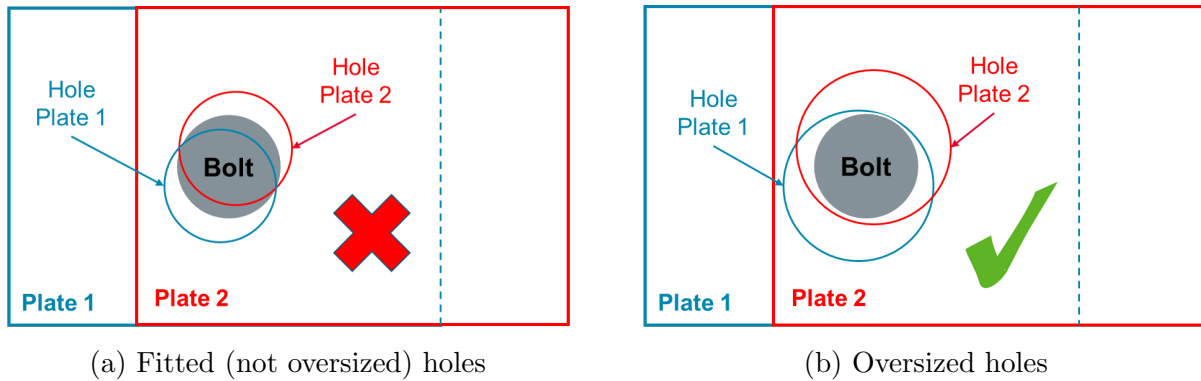


Figure 1.7: Role of oversize of absorbing the variability of hole misalignments on H2H assembly (illustration not at scale)

introduced by the H2H framework.

Up to this point, it could seem that the H2H project simplifies the assembly process, while implying only a change in tolerances activities to account for the additional tolerances related to hole oversize. However, we did not address, until now, the impact on the structural performances. To explain a possible outcome on structural performances, we consider the example illustrated in Fig. 1.8, related to a coupon with only two plates (in blue) and two bolts (in green), subjected to a traction force (orange arrows).

The classical situation is depicted in Fig. 1.8a, where all holes are fitted (i.e. only minimal fit clearance without additional oversize) and perfectly aligned: when pulling the structure in traction, all bolts get in contact at the same time from the opposite sides in the two plates (as the bolts touch the upper plate on the left and the bottom plate on the right). Note that a bolt will contribute to support a part of the total load if it touches the plate on the opposite side with respect to the loading direction: this means that on the upper plate (pulled to the right), the contacts must be on the left side, while for the bottom plate (pulled to the left) on the right side. For fitted and perfectly aligned holes, both bolts thus contribute to support the applied loads: consequently, the loads will be redistributed equally among the bolts (i.e. each bolt supports half of the applied load).

In the case with oversize (i.e. with classical fit clearance plus additional oversize) and perfectly aligned holes (in Fig. 1.8b), the situation does not change. The only difference with respect to the nominal case (in Fig. 1.8a) will be given by the fact that the plates need to be pulled slightly more to achieve the first contact. In this case, each bolt will also support half of the total applied load.

When we introduce both oversize and misalignments, we can obtain in a worst-case scenario the situation depicted in Fig. 1.8c. In this case, only the bolt on the right is in contact with the correct sides of the plates. The left bolt will not contribute to the load transfer: therefore, the right bolt would carry the total load all alone, which would correspond to the double of the amount it would transfer without H2H (as in Fig. 1.8a). This condition where one bolt needs to carry the total applied load all by itself effectively constitutes the *worst case scenario*.

The adoption of *worst case scenarios* is frequent (though not being the general rule) in the classical deterministic sizing of aeronautical structures, to account for the variability of a number of phenomena affecting structural performances. However, suppose that we

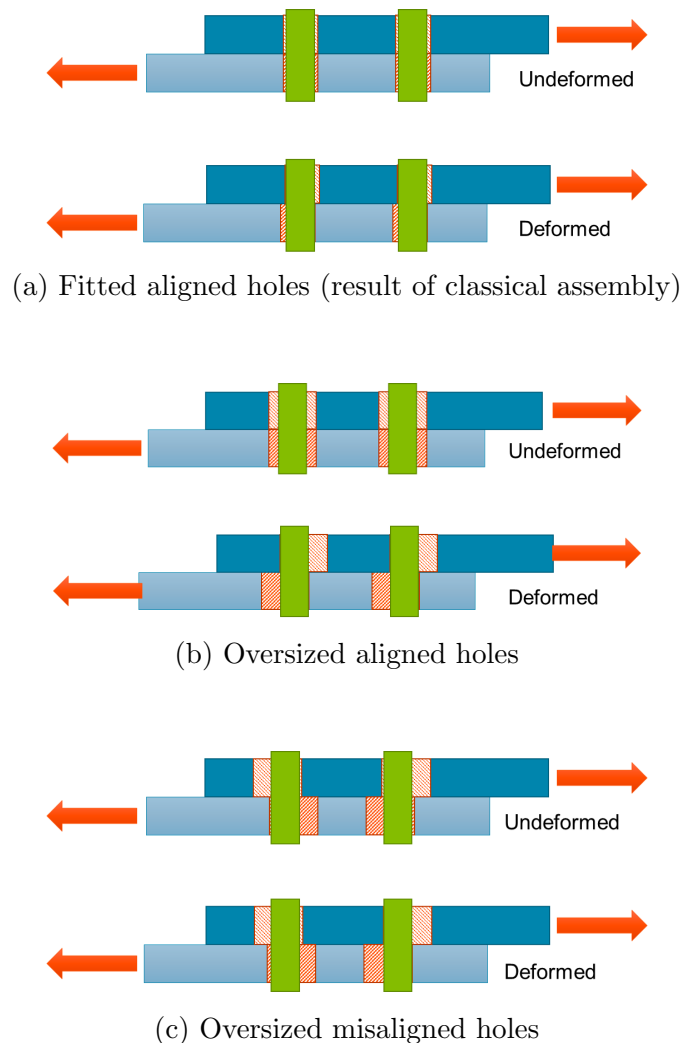


Figure 1.8: Illustration of the effect of oversize and misalignments on H2H load transfer

apply this logic to the H2H framework for a coupon with two bolts, where the sizing of the bolts is more critical than the sizing of the plates: this would imply that each bolt should be sized to resist to a load which is the double of the load considered with a classical assembly process. As a first approximation, this means that each bolt would be twice as thick, thus twice as heavy. If we extend this conclusion to bolted joint assemblies with 20 bolts, the worst-case scenario, even though unlikely, would still be that only one bolt out of the 20 is in full contact with the two plates, thus carries the full load to be transferred. Thus, the weight of the bolts would be increased roughly by a factor 20. Therefore, considering only the *worst case scenario* for the structural sizing would make the H2H framework totally unaffordable.

The knowledge of the uncertainties linked to the input parameters becomes fundamental in order to evaluate the structural performances of the assembly conceived within the H2H framework. A new framework explicitly taking these uncertainties into account has the potential to mitigate the potential over-conservatism of the assumptions associated with a literal application of the *worst case scenario* approach on the H2H example. In the next section, we will present some challenges and investigate the expected benefits

of introducing the UQ&M framework in the structural design, using the H2H project as a common thread application.

1.5 Challenges of UQ&M on structural applications

In the previous sections we described the general UQ&M framework and the industrial application which constitutes the common thread of the entire work, namely the Hole2Hole (H2H) project. In this section, we define the expected added value of the integration of UQ&M in the activities of the aeronautical structural team. We will continue to use as common thread the H2H application. This will help us to illustrate the motivations and the challenges addressed by the present work.

The main interest for considering the probabilistic description of the phenomena is to challenge the sizing assumptions typically used in classical structural design. Indeed, such assumptions can lead to consider scenarios which go beyond what is actually needed. As observed in the previous section, the worst cases are far too penalizing for H2H framework, making it unaffordable in terms of structural weight. The mitigation of the *worst case scenario* approach can be achieved by integrating the statistical description of the uncertain input parameters in the structural sizing process. The first challenge will therefore be given by the formalization of a probabilistic framework, *suitable* for applications on aeronautical structures. But what does *suitable* mean?

First of all, we remind that complying with certification requirements (coming from EASA in Europe) is mandatory to prove the *airworthiness* of aircraft. Also in the example of the H2H project, we need to prove a certain level of safety, to allow the H2H framework itself to be implemented on actual flying aircrafts. However, the current certification requirements do not consider probabilistic design principles, but rather define guidelines for the *classical deterministic design* of aeronautical structures: this means that every UQ&M framework which could be proposed will not be exactly coincident with the current certification requirements. Our first challenge will be the definition of a *general probabilistic framework* which *extends* some of the EASA standards, in a "non-disruptive" manner, i.e. *integrating* rather than *totally replacing* the current way of working, based on deterministic sizing.

The challenge of formalizing a *suitable* probabilistic framework can be summarized in the following question:

1. *Can we conceive a general probabilistic framework able to extend current certification requirements and which can be easily integrated in the classical deterministic structural design?*

If we think of the application on the H2H example, the proposed framework should define coefficients to adjust the nominal quantities of the loads transferred by each bolt, such as to *integrate* in the classical deterministic sizing process. These coefficients, referred to as "safety factors" (in a large sense), are generally intended in aeronautical industry to absorb the uncertainties (mainly linked to random phenomena, lack of knowledge of complex structural responses, modeling errors) at all level of the analysis chain and hence on the computed nominal performances. Practically speaking, instead of considering the amount of force which would be carried by each bolt in the classical assembly process, the

designers will consider an amplified load by a " *partial safety coefficient*" when passing to the application of H2H: one main role of the proposed framework would be the definition of this new deterministic quantity for H2H. Our purpose is to identify a *general* process which provides deterministic quantities consistent with current requirements, which the designers should use in the deterministic sizing process. Moreover, when considering input geometric parameters, we will need to introduce the concept of *tolerances*, intended as constraints of the variability of geometric features: therefore, the deterministic quantities (to be used in structural sizing) will be linked to specific input variabilities and/or tolerance limits (when introducing geometrical variabilities), typically dealt within *tolerancing activities*. Therefore, the challenge 1 also indirectly rises three other questions:

- 1a. *Which measures of the uncertainty of the output can allow to extend the current certification requirements, for general applications on aeronautical structures?*
- 1b. *How can/should the designers use the outcomes of the proposed probabilistic framework?*
- 1c. *How can we manage the interfaces between different disciplines involved in the structural design in the proposed probabilistic framework?*

Once the framework is formalized, we will be able to evaluate the structural performances from a statistical point of view. This framework should therefore be able to address two other questions, following two different perspectives:

2. *What is the effect of the variability of the uncertain input parameters on structural performances of some typical aeronautical structures?*
3. *Which input variabilities can guarantee a specific structural performance?*

In the H2H example, the first question will address the challenge of reducing the potential over-conservatism of the worst case (i.e. the concentration of the whole applied load on a single bolt), by considering the probabilities of occurrence of the misalignments realizations: this will therefore lead to determine *new* "partial safety coefficients", based on the formalized probabilistic framework. Instead, the second question will focus on re-defining the geometric tolerances in H2H, so that the effect on the structural performances can be taken into account. At a more general level, the industrial challenge associated to questions 2-3 is to establish a framework to support the engineering judgment for the definition of the assumptions to be used in the classical structural design process.

The questions 2-3 actually lead to other investigations, related to the identification of the most influential inputs (the variability of which affect most the structural performances), but also the design choices which allow to mitigate the effects on the structural performances.

The last challenge addressed in the present work is given by the actual implementation of the proposed UQ&M framework. A number of approaches involved in the UQ&M analyses make use of repeated samples, thus requiring large numbers of numerical simulations. In the example of the H2H, we use finite element analyses which can take several hours to run (on the most complex models). Making a compromise between accuracy and computational burden becomes fundamental to deal with UQ&M analyses: on one

hand, it can be addressed through the development of new sampling techniques able to reduce the number of samples required to achieve a targeted accuracy; on the other hand, the initial model can be simplified to a surrogate model, that is adaptively trained via machine learning techniques. Both of these approaches will be explored and further developed in this work. Moreover, for complex H2H structures (with high number of bolts), we can have a high number of inputs, related to the hole misalignments: as the input dimensionality can constitute a non-trivial challenge for a number of machine learning techniques, it will be necessary to develop methods which are scalable for high number of inputs. The so-called *high input dimensionality* does not concern only the H2H case, but can be found on a large number of industrial applications. This last challenge will be summarized in the following question:

4. *Which UQ&M methods allow to make an acceptable compromise between computational burden and accuracy, while ensuring the scalability for high number of inputs?*

1.6 Structure of the present study

In this section we present the global structuring of the manuscript allowing us to provide some answers to the previous questions, of which the order was reorganized to better reflect the chronological order in which they will be addressed in the manuscript chapters:

1. *What is the effect of the variability of the uncertain input parameters on structural performances of some typical aeronautical structures?*
2. *Can we conceive a general probabilistic framework able to extend current certification requirements and which can be easily integrated in the classical deterministic structural design?*
3. *Which UQ&M methods allow to make an acceptable compromise between computational burden and accuracy, while ensuring the scalability for high number of inputs?*
4. *Which input variabilities can guarantee a specific structural performance?*

In Chapter 2, a review of applications of probabilistic frameworks in aeronautical engineering is presented. A continuous comparison with civil engineering is reported to highlight similarities and differences between the two fields.

In Chapter 3, question 1 is treated from a deterministic perspective on the H2H application, considering the input variability domain but without introducing the exact statistical description (i.e. assuming general uniform distributions for all the inputs). In particular, we will explore the effects of the inputs on the output response variability, in order to simplify the interpretation of a given problem. This simplification will consist in the reduction of the number of inputs and will be dealt with a double perspective: on one hand, we will identify patterns of the input variables which better describe the effects on the outputs; on the other hand, we will filter the inputs by ignoring the least influential on the output response variability. The outcomes of this chapter on the H2H application will be used to support the interpretation of the results of all successive chapters.

In Chapter 4, a probabilistic approach is proposed to give a first answer to question 2. This includes a framework to determine deterministic values to adopt in design phase, based on a probabilistic environment. The framework will be called *semi-probabilistic* as it will integrate deterministic and probabilistic quantities at the same time. A double perspective is presented to (1) define structural deterministic performances from fixed input variability and (2) retrieve optimal input variability from a given deterministic stress requirement. The first declination will be analyzed in detail in Chapter 4, answering to the question 1 from a statistical point of view.

Chapters 5 and 6 focus on the reduction of the computational burden implied by reliability analyses, both addressing the challenge raised in question 3. The former introduces a sampling method to estimate a probability of exceeding a fixed threshold. In Chapter 6, the reduction of the computational burden is addressed with a scalable machine learning technique, able to estimate reliability outcomes on problems with a high number of inputs.

In Chapter 7 we conceive a framework to optimize the input tolerances to answer to the last question. The perspective introduced in Chapter 4 is re-adapted to develop a dictionary to translate the stress requirements into allowed tolerances. The methods presented and discussed in Chapter 5 (related to the sampling methods) and Chapter 6 (related to the machine learning assisted reliability algorithm) are used to evaluate the stress reliability constraint in the associated optimization process.

Finally, we report the conclusions of the present work in Chapter 8, together with the ways-forward for future activities in the associated academic and industrial research areas.

Chapter 2

State of the art on probabilistic frameworks applications in aeronautical and civil engineering

In the previous chapter we presented the general context of probabilistic design, highlighting the opportunities for aeronautical industry. The base goal of this dissertation is to take into account the variability of input design parameters, in order to switch from the classical worst-case scenario approach to a probabilistic framework, in an attempt to extend some particular requirements of the aeronautical legislation to a more general framework. In this chapter, we present a brief state of the art of the probabilistic framework applications to structural design in the aeronautical industry, comparing them to the ones related to civil engineering field. This study has as main objective to retrieve the differences between those two fields, trying to identify the root reasons behind these differences. Knowing the strengths and weaknesses of the methods currently used for structural design in aeronautical industry would constitute a starting point for us to propose and work on several improvements, which will be discussed in the following chapters.

We will start the general discussion by classifying the different applications of the UQ&M framework (presented in Section 1.2) according to the objectives pursued by the analyses themselves, in Section 2.1. Then, we discuss the current legislation and certification requirements valid in Europe, for civil and aeronautical engineering fields, in Section 2.2: these first two sections will help us to highlight common threads to evaluate, in a critical way, the differences between those two fields. In the successive sections, we report a brief overview of the applications in aeronautical and civil engineering, related to structural testing (in Section 2.3), reliability assessments (in Section 2.4) and the determination of safety factors (in Section 2.5): in each section, we will introduce the different topics and then compare the applications in civil and aeronautical industry, focusing on the directions of the research at a global level. Finally, the conclusions of the comparison between civil and aeronautical engineering are discussed in Section 2.6.

2.1 UQ&M applications: a goal-oriented classification

In the general framework of UQ&M, De Rocquigny et al. [De Rocquigny et al., 2008] classified the different applications according to the objectives which are pursued. In particular, four main classes of objectives (referred in [De Rocquigny et al., 2008] as *goals*) of UQ&M analyses were distinguished:

- Goal U (Understand): To understand the influence or rank importance of input variabilities on output uncertainties. In this category we may retrieve all the analyses devoted to identify the most important sources of variability, in order to simplify the interpretation of a given problem (e.g. reduce the number of variables in a model), facilitate the identification of eventual issues, conceive the best-suited countermeasures and/or to prioritize research investigation only where needed.
- Goal A (Accredit): To give credit to a model or a method of measurement, i.e. to reach an acceptable quality level for its use. In this category, we may include the calibrations of sensors, the hyper-parameters tuning in numerical models, fitting statistical distributions, or validating the degree of conservativeness of particular assumptions.
- Goal S (Select): To evaluate different choices of maintenance policy, operation or design of the system, in order to optimize a specific output performance. All applications of design optimization (based on a probabilistic framework) can cover this goal.
- Goal C (Comply): To demonstrate compliance of the system with an explicit criterion imposed by current legislation, in order to guarantee at least a minimum required level of safety. The concept of *compliance with current rules* plays a fundamental role in the product certification (when required by the law), including all the tests and analyses devoted to evaluating the probability of exceeding safety threshold, the occurrence of the most probable failure event, the degree of conservativeness of the model used.

The choice of the goal which is addressed by a specific application of probabilistic frameworks affects also the choice of the specific performance indicators (thus, also the method to evaluate them) and the feedback process to re-intervene on the inputs to guarantee or improve the output performances.

Typically the performance indicators, referred in UQ&M framework as *quantities of interest*, are defined by statistical measures of the variability of the output. Typical examples can include:

- the probability of the system of exceeding a safety threshold;
- the expectation (i.e. mean value) of the output;
- the coefficient of variation of the output;
- specific quantiles associated to the output;
- the contribution of each input to the variance of the output.

The list is not exhaustive and must be interpreted in a critical way. The quantity of interest is evaluated within a *decision criterion*, which typically states whether a design is acceptable or not. Typical examples may include:

- 'the probability of exceeding a safety threshold must be lower than $10^{-xx}\%$ ';
- 'the coefficient of variation of the output of a structural test cannot overcome 3%';
- 'the 99th percentile should not exceed 1.3 times the mean value of the output';
- 'to neglect a variable X, it should contribute to less than 1% of the output variance'.

Stemming from the outcomes of the decision criterion, some actions may be undertaken to meet the requirements imposed by the decision criterion. According to the specific goal addressed by a given UQ&M analysis, the actions to be taken (in the *feedback process*) can be different. Here we give some examples of feedback actions for each goal:

- Goal U: fixing some uncertain input variables which have low (with respect to the decision criterion) effect on the output variability, simplify a numerical model while maintaining acceptable accuracy;
- Goal A: placing better the sensors to accredit an experimental procedure, use more precise sensors, tuning hyper-parameters in a numerical model to be more consistent with physical testing evidences;
- Goal S: switch between different design solutions to enhance performances;
- Goal C: adjusting the design choices (in input) so that the acceptance criteria (e.g. provided by the regulations) can be satisfied.

Both output uncertainty measures and feedback process are therefore linked to each other and to the purpose of a specific UQ&M analysis. However, they are strictly linked to the decision criteria as well.

In the rest of this chapter, we will identify the main goal of each category of applications. Note that it is not compulsory that a given application fits only inside one single category of goals: for example, a probabilistic-based optimization procedure - which should fit in goal S (select) - can cover the goal C (comply) as well if a probabilistic-based certification requirement is introduced among the constraints.

2.2 Current legislation requirements

The requirements imposed by current legislation and certification standards hugely affect the evolution of the specific engineering fields. The central focus of this section is to briefly present the main features of current European standards related to civil (EN Eurocodes) and aeronautical (EASA norms) engineering.

2.2.1 Civil engineering legislation

EN Eurocodes define the standards used in civil engineering in Europe. The structure of Eurocodes is summarized below:

- EN 1990 Eurocode 0: Basis of structural design
- EN 1991 Eurocode 1: Actions on structures
- EN 1992 Eurocode 2: Design of concrete structures
- EN 1993 Eurocode 3: Design of steel structures
- EN 1994 Eurocode 4: Design of composite steel and concrete structures
- EN 1995 Eurocode 5: Design of timber structures
- EN 1996 Eurocode 6: Design of masonry structures
- EN 1997 Eurocode 7: Geotechnical design
- EN 1998 Eurocode 8: Design of structures for earthquake resistance
- EN 1999 Eurocode 9: Design of aluminium structures

Except EN 1990, each Eurocode is divided into several parts which treat specific aspects of the subject. In EN Eurocodes relating to materials, a Part 1-1 reports general rules for the design of buildings and other civil engineering structures, and a Part 1-2 covers fire design. EN 1992, 1993, 1994, 1995 and 1998 contain a Part 2 covering design of bridges: these must be applied in combination with the corresponding general Parts (Parts 1).

In particular, in EN 1990, some key-points can be outlined:

- partial safety factors defined on material resistance and applied loads;
- worst-case scenario considered only if statistical description of certain components are not available;
- load combination factors specified for each load configuration;
- reliability management considered as main requirement in design;
- reliability target well specified, according to the use and risk associated to each structure;
- different limit states (ultimate and serviceability conditions) must be verified;
- design associated with structural tests also previewed.

Generally, in EN 1991 - 1999 some freedoms are left to National Annexes, where different calibrations of load combination factors or partial safety factors can be defined. Moreover, if not specifically pointed out in EN 1991 - 1999 or in National Annex, the general rules of EN 1990 must be applied.

2.2.2 Aeronautical industry regulations

EASA norms cover all requirements of aircrafts and aerodromes in Europe. A distinction must be made on the basis of binding power and specific topics between the several rules:

- *Basic Regulation*: binding, collects all the mandatory requirements to certify an aeronautical structure;
- *Implementing Rules (IR)*: binding, adopted to specify safety level, uniform conformity and compliance;
- *Acceptable Means of Compliance (AMC)*: non-binding, report the means to achieve Basic Regulation and IR requirements;
- *Certification Specifications (CS)*: non-binding, collect technical standards to meet essential requirements;

- *Special Conditions (SC)*: non-binding, adopted for cases where regulation is not appropriate;
- *Guidance Material (GM)*: non-binding, contain interpretation material on how to meet all requirements in other rules.

Focusing on technical standards, CS are then divided in different categories according to the specific subjects. The reference for our work is CS 25 Amendment 27 [Easa, 2009], reporting the standards to follow to prove the initial airworthiness of large airplanes. Subparts C (Structure) and D (Design) and Appendix K (Interaction of systems and structure) are of particular interest for static strength demonstration. We report here the main concepts of some articles of interest of the CS 25:

- From *CS 25.301*: Strength requirements are specified in terms of limit loads (the maximum loads to be expected in service) and ultimate loads (limit loads multiplied by prescribed safety factors);
- From *CS 25.303*: Unless otherwise specified, a factor of safety of 1.5 must be applied to the prescribed limit load;
- From *CS 25.305*: The structure must be able to support ultimate loads without failure for at least 3 seconds;
- From *CS 25.307*: To prove structural performances, structural analysis may be used only if the structure conforms to that for which experience has shown this method to be reliable;
- From *CS 25.613*: Material strength properties are defined in statistical framework, classified into two classes, namely A- basis (1st or 99th percentile with 95% confidence) and B-basis (10th or 90th percentile with 95% confidence) to be adopted respectively in non-redundant and redundant structures;
- From *CS 25.619*: The factor of safety prescribed in CS 25.303 must be multiplied by the highest pertinent special factor of safety prescribed in CS 25.621 through CS 25.625 for each part of the structure whose strength is uncertain, likely to deteriorate in service before normal replacement or subject to appreciable variability because of uncertainties in manufacturing processes or inspection methods;
- From *K 25.2*: Specific safety factors are defined (cf. Fig. 2.1) for interactions of systems and structures, both at the time of occurrence (as function of the probability of occurrence P_j of the failure mode j per flight hour) and for continuation of flight (as function of the probability Q_j of being in failure j , related to a duration T_j , i.e. $Q_j = P_j \times T_j$).

Apart from the interaction phenomena between structures and systems (in CS 25 Appendix K), regulations requirements provide precise guidelines on how to deal with the input variability only for material properties and loads. Current practices in structural sizing of aircraft components involve, however, additional safety factors for manufacturing

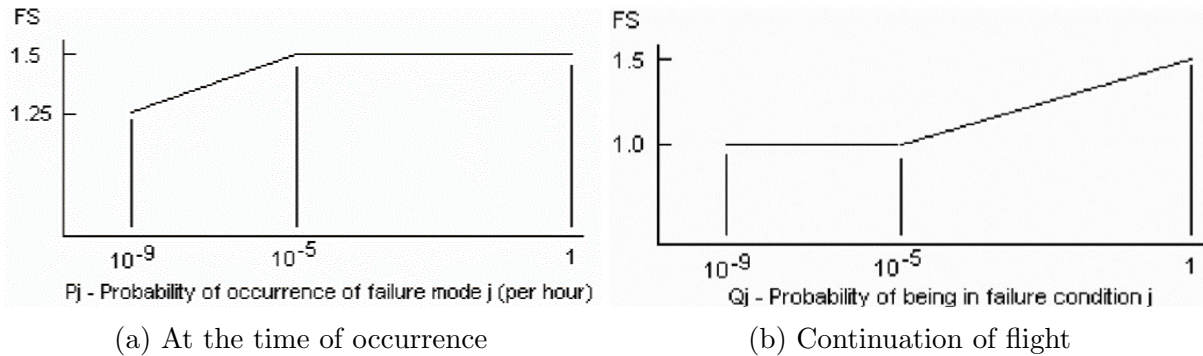


Figure 2.1: Definition of general safety factors FS according to CS-25

uncertainties (see *CS 25.619*) or the adoption of quantities corresponding to low probability events (included worst case scenarios) for a number of other phenomena affecting structural performances. This may lead to take into account scenarios beyond what needs to be reasonably considered.

Meeting all requirements previewed by the certification is mandatory to prove the *Airworthiness*, i.e. the permission for an aircraft to operate.

Overall, comparing the civil and aeronautical regulations, reliability analysis appear not as tightly integrated as for civil engineering. Applications are restricted to a limited number of cases. This is reflected also in aeronautical industry, still strictly linked to legislative guidelines. Moreover, copyright-related issues make availability of industrial data even more complicated. Finally, it is worth noting that most of the aeronautical applications presented in this review are part of pure academic research efforts.

2.3 Structural testing

The first application example of probabilistic frameworks which will be treated in the present review regards the use of structural tests. Generally, they are mainly used to calibrate and validate numerical models, or, alternatively, to certify a structural design. Using the general *UQ&M* classification presented in Section 2.1, the *A* (accredit) and *C* (comply) goals constitute the main interests for structural tests.

Classifying all categories of structural tests is not an easy task, but several attempts have been made. Rackwitz and Schrupp [Rackwitz and Schrupp, 1985] proposed a distinction between pre-investigations (providing prior informations based on observations in past experience), prototype-testing, proof testing and statistical quality control (related to in-service failures). A wider classification was presented by Hall and Tsai [Hall and Tsai, 1989]. In particular, eleven distinctive features were listed, based on:

- *objective*: strength or serviceability verification, or pure research;
- *use*: resistance, load effect or mixed safety;
- *system level*: material, element, member or system;
- *simulation plausibility*: unrealistic, actual loads or combination;
- *presence of time-dependent effects*
- *destructivity*: non-destructive, damaging or destructive;
- *sample couverture*: one, all or sampling;

- *prior statistical knowledge*: complete, partial or none;
- *correlation of components*
- *gross errors treatment*: known, suspected or neglected;
- *measurements*: test load only or completed with non-test informations.

It sounds obvious that the relation between structural tests and reliability assessment is tightly linked.

In the following, the reader will find a list of civil and aeronautical applications. In particular, we classified the applications in both fields per objective. This will help to associate the different applications with a specific goal in the general UQ&M framework, as described in Section 2.1.

2.3.1 Civil applications

The industrial applications of structural tests on civil structures can be distinguished into two categories, with two different purposes:

- *Proof load tests*

The main purpose is to ascertain that a given full scale structure can sustain specific loads [Lin and Nowak, 1984, Olaszek et al., 2016, Vavruš et al., 2019, Lantsoght et al., 2018]. As in general the civil structures are not replicated, the risk of deteriorating the construction itself through full scale proof load tests is another issue investigated in literature [Faber et al., 2000, Val and Stewart, 2002, Lam et al., 2003].

- *Diagnostic load test*

This category includes the collection of in-situ in-service measurements [Guerra-Santin and Tweed, Cantero et al., 2019] (involving traffic data, fatigue behavior and corrosion effects): these are incorporated in a probabilistic framework to update the prior knowledge on the structural behavior (in order to update the analytical and numerical models used in design phase) and to monitor the health of a structure [Song et al., 2017, Fujino et al., 2019, Ostachowicz et al., 2019, Shan et al., 2020, Riggio and Dilmaghani, 2020], in order to preview maintenance interventions. Several research works also investigate the capabilities of the health monitoring systems used in civil engineering [Park et al., 2000, Yang et al., 2008, Li et al., 2020, Bado and Casas, 2021].

This distinction was originally provided by Lantsoght et al. [Lantsoght et al., 2017] to classify the load tests on bridges. Here such classification is extended to general civil structures. From the perspective of UQ&M general framework, the proof load tests cover the goal C (comply), while the diagnostic load tests cover the goal A (accredit).

The link between current legislation and proof load testing is analyzed in [Lantsoght et al., 2018]. The authors stress out that the Eurocodes define target loads (i.e. the load that the structure should be able to withstand during the test) and analysis of measurements for the proof load tests of buildings, but not for bridges. Some tests are even forbidden, in order not to deteriorate the structure itself (as it is not replicated).

Note that we did not include, in the list, the use of structural tests on components to validate (or investigate) the characteristic mechanical properties. In fact, the use, in general, of standardized components reduces needs for huge campaigns of structural

tests. Large scale structural tests campaigns are not even considered for complete structures, as they are not to be replicated. There are, however, some specific examples of applications of structural tests on components available in the literature with very specific research purposes: for example, to demonstrate the conservativeness of national standards [Burgan et al., 2000, Zhou and Young, 2005], evaluate enhancements of classical material properties [Yoo and Yoon, 2015, Zingg et al., 2016, Malecot et al., 2019, Remennikov and Kaewunruen, 2020], investigate new materials [Song et al., 2006, Keller et al., 2008, Abirami et al., 2019], improve the numerical modeling of complex dynamic structural responses [Boudaud et al., 2015, Kumar et al., 2020, Alam et al., 2021] or for research on specific corrosion phenomena [Melchers, 2005, Alfano et al., 2006, Guo et al., 2019, Huang et al., 2020].

The data coming from structural tests can be also exploited in the other applications which will be presented in the following sections: we have examples of the use of structural test data for reliability assessments [Faber et al., 2000, Papadimitriou et al., 2001, Lam et al., 2003, Venter and Scotti, 2012, Frangopol et al., 2019, Zhang et al., 2019c] and calibrations of safety factors [Val and Stewart, 2002]. The explanation of these notions and the exploration of the related applications for civil engineering are reported in Sections 2.4-2.5.

2.3.2 Aeronautical applications

Structural tests play an essential role in the aeronautical industry. In Fig. 2.2 the pyramid of structural tests is depicted. Number of tests can increase exponentially as new designs are conceived. In some cases involving well-mastered architectures, certification authorities allow to prove initial airworthiness requirements (i.e. the permission for the first commercial flight) through numerical investigation.

Still, structural tests maintain a primary role in certification processes. The reason must be searched in the customization of components: contrary to civil engineering, *ad hoc* structures are continuously introduced, leading to unavoidable verification tests at every level of the pyramid (see Fig. 2.2).

Large scale campaigns are daily routine for aeronautic components. Structural tests generally involve the simulation of actual loads present in aircraft service life. Two load levels are distinguished in CSs:

- *Limit load*: level actually reached once in aircraft lifetime (probability of occurrence of 10^{-5} per flight hour);
- *Ultimate load*: level that should never be encountered during service life (related to previous one through a safety factor defined in CSs).

Certification tests aim at guaranteeing that the whole structure can resist to (1) limit loads without plastic deformations - which would possibly affect airworthiness continuation - and to (2) ultimate loads during 3 s before the appearance of the first fracture.

The extraction of material properties in a statistical framework (from physical testing) is described in MIL-17 Handbook [Neal and Vangel, 1990]. It notably provides a precise definition of material properties quantiles:

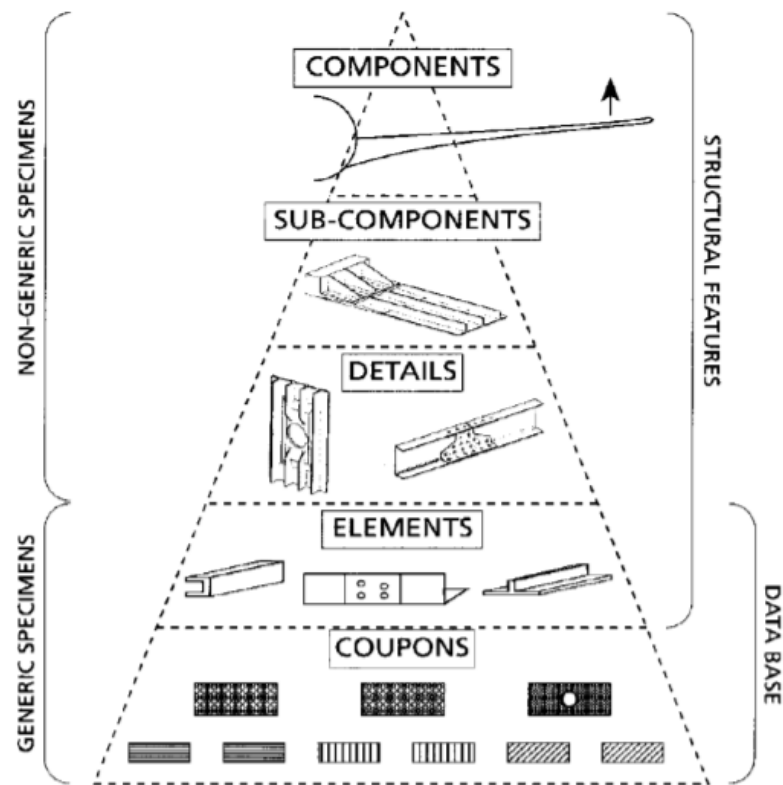


Figure 2.2: Pyramid of tests (Source: [Rouchon, 1990])

- *A-basis* constitute the reference values which are outperformed by the 99% (with the estimation associated to a confidence level of 95%) of a population;
- *B-basis* constitute the reference values which are outperformed by the 90% (confidence level 95%) of a population.

For properties which improve the design when they exhibit high values (e.g. maximum material resistance), respectively the 1st and 10th percentile should be considered for A and B values. For other properties which improve the design when their value gets smaller (e.g. material density), the 99th and 90th percentile are retained. The use of these values are regulated, in Europe, by the CS 25.613 for static strength justification.

Overall, the applications of structural tests in aeronautical engineering cover three main axes:

- *Certification purpose*

This constitutes the classical use of physical tests in aeronautical engineering. The upper-mentioned rules to demonstrate static strength in aircraft design are generally applied through physical testing, even though certification authorities accept more and more frequently virtual investigations. In the general UQ&M framework, the certification covers the goal C (comply), as it is intended to prove that the EASA requirements are met.

- *Validation purpose*

In this category we find all the tests performed to identify material properties of structural components, which are regulated in Europe by EASA standards. Moreover, given the growing interest in virtual modeling to substitute physical tests, there is a natural interest for the validation of complex numerical models. Common examples are given by the validation of high-complexity phenomena, such as bird strike [Kermanidis et al., 2005, Airoidi and Cacchione, 2006, Lavoie et al., 2007, Guida et al., 2008, Heimbs, 2011, Orlando et al., 2018, Belkhelfa and Boukraa, 2020], drop impacts [Wiggenraad et al., 2005, Jackson and Fasanella, 2005, Gransden and Alderliesten, 2017, Perfetto et al., 2018], landing phenomena [Daniels, 1996, Esposito et al., 2014], lightening [Apra et al., 2008, Meyer et al., 2008, Muot et al., 2020], coupling effects between aerodynamics and structure (known as *aeroelasticity*) [Madsen et al., 2010, Keye, 2011, Snyder et al., 2013], among the others. In the general UQ&M framework, the validation purpose addresses the goal A (accredit).

- *Health monitoring purpose*

These include all tests performed during the service life of an aircraft. They are inserted in a probabilistic framework to take into account the evolution of existing damages [Zhang et al., 2010, Molent and Haddad, 2020], corrosion effects [Mangalgiri, 2019, Li et al., 2021], monitor possible hazards linked to the actual use of the aircrafts [Oehling and Barry, 2019, Zhou et al., 2020], inspections [Manco et al., 2021] and to estimate the residual life of aircraft structures [Zhang et al., 2022b]. In this category we retrieve essentially non-destructive testings [Towsyfyan et al., 2020, Shao et al., 2022]. These applications mainly address goals A (accredit), intended as the collection of the data to refine the adopted models, and C (comply), to ensure that the aircraft is still allowed to keep flying.

Overall, structural tests in aeronautical industry assume a prominent role. Perhaps, given the continuous customization of pieces, structural tests are unavoidable and regulations intervene to manage the statistical treatment of the tests data (e.g. CS 25.613 for material properties). The growing interest towards numerical models is justified by the need to reduce the large number of physical tests. In any case, in aeronautical industry design context, structural tests constitute - and probably will continue to be - a fundamental piece of the whole puzzle.

2.4 Reliability assessment

The reliability assessment in a structure is another important example of applications of *UQ&M* framework. The concept of *reliability* is strictly related to the concept of *failure* of a general system (which can be a structure, as in our case).

We may define the *failure*, in a large sense, as the condition of trespassing a safety limit (or threshold). From a mathematical point of view, we can formalize the notion of *failure* by introducing a performance function, called *Limit State Function* (or LSF), as the quantity which tells us whether we are in unsafe or safe conditions (i.e. whether we trespassed or not the given safety threshold). The LSF is generally formulated so that the information about failure is provided through the sign of the LSF quantity itself. The limit state function is often denoted by g and, for a number of structural applications,

can simply be described by the difference between structural capacity (or strength or resistance R) and imposed stress S :

$$g = R - S \begin{cases} \leq 0 & \text{failure} \\ > 0 & \text{no failure} \end{cases} \quad (2.1)$$

The limit condition $g = 0$ represents the border between safe and unsafe domain: this limit is often denoted as *Limit State Surface* (LSS) or simply *limit state*. In the simple case of LSF described by a strength R and a stress S , the LSS contains all conditions with $R = S$.

At this point, we can formalize the reliability in two ways, linked to each other: (1) as the probability of being in safe condition (i.e. the probability of not having failures); (2) as the margin between the average operational condition and the most probable condition leading to a failure. The first, very common in system reliability engineering [Rausand and Høyland, 2003], will be expressed through a *reliability level* $R = 1 - P_f$, related to the *failure probability* P_f , which represents the probability of being in an unsafe condition. The second concept is described by a specific *reliability index*, denoted in literature as β , and represents an indicator of the position of the LSS.

Note that the *reliability* is not linked to the *severity* (i.e. the consequences) of a failure: within this perspective, the collapse of a whole system (e.g. an aircraft engine burning) and minor inconveniences (e.g. a light not working) would be put on the same plan and analyzed (potentially) with the same methods. The differences in the related reliability assessments will be given by the choice of which *reliability target* needs to be ensured. Joining *reliability* and *severity*, we obtain the concept of *risk*: it is this latter the principle which dictates the reliability target to be ensured. For example, considering the resistance to fire, the demanded reliability level will not be the same for a tank of water or for a tank for gasoline, due to the different associated *risk*. The concept of reliability can be summarized, according to Lemaire [Lemaire, 2013], by the sentence: ”*reliability consists of the probabilities plus the decision*”. This *decision* lies in the selected criteria that lead us to say that a system fails (i.e. the *failure modes*), the way of measuring the failure rates (thus, the reliability) and the associated maximum target that must not be overcome.

Following from the definition of the limit state function in 2.1, we can also define the probability of falling in the unsafe condition (or *failure domain*) as the failure probability P_f , which can be formalized as follows:

$$P_f = P(g(\mathbf{X}) < 0) = \int \mathbf{1}_{g(\mathbf{X}) < 0} f_g(\mathbf{X}) d\mathbf{X} = \int_{R(X) < S(X)} f_{R,S}(\mathbf{X}) d\mathbf{X} \quad (2.2)$$

where \mathbf{X} represents a general input random vector which may affect either R , S or both.

The other main reliability metric mentioned earlier is the *reliability index* β . One of the most common reliability indexes is the Hasofer-Lind index β_{HL} [Hasofer and Lind, 1974]: this is defined as the minimum euclidean distance (L^2 norm) between the origin of a centered Gaussian normed space and the limit state surface. In Fig. 2.3, the transformation from original space to centered Gaussian normed space is illustrated. The operator T , responsible for this transformation, is known as *iso-probabilistic transformation*.

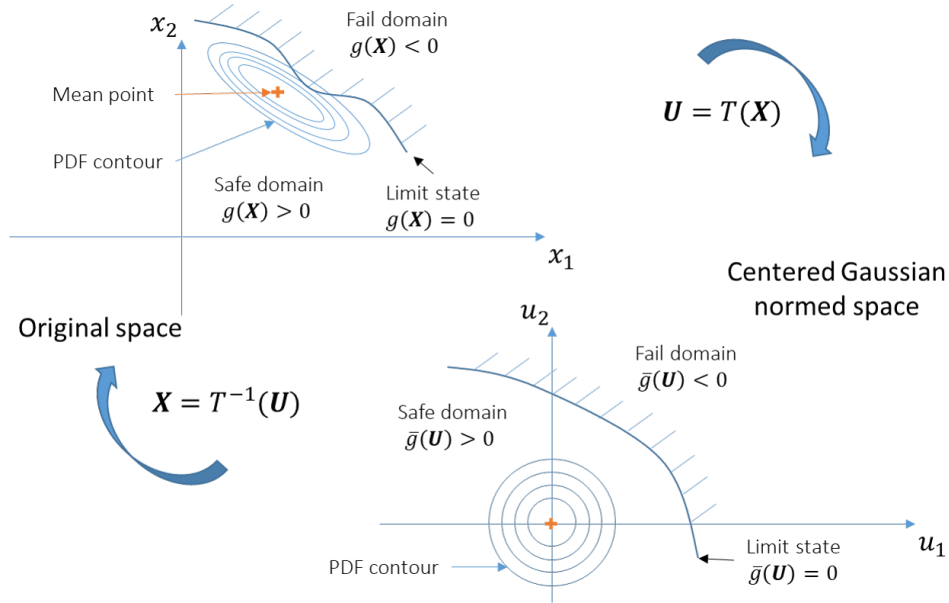


Figure 2.3: Reliability: general illustration

By using the visual representation in Fig. 2.3, the reliability index β_{HL} can be defined as the solution of the following optimization problem:

$$\begin{cases} \beta_{HL} = \min_{\mathbf{U}} \sqrt{\mathbf{U}^T \mathbf{U}} \\ \text{subject to: } g(\mathbf{X}) = g(T^{-1}(\mathbf{U})) = \bar{g}(\mathbf{U}) = 0 \end{cases} \quad (2.3)$$

Where \mathbf{X} is the input vector variable (affecting the LSF g) represented in the physical (original) space, \mathbf{U} the same input vector but transformed on the centered Gaussian space and $\bar{g} = g \circ T^{-1}$ represents the limit state function in the centered Gaussian space (i.e. the composition between the original limit state function g and the inverse of the iso-probabilistic transformation T). The minimum value of the objective function in Eq. 2.3 represents the Hasofer-Lind reliability index β_{HL} . The nearest point to the origin of the centered Gaussian normed space (the coordinates of which are individuated by the optimal \mathbf{U}_{opt}) is known as *design point* or *Most Probable Failure Point (MPFP)*.

Depending on the applications, the probability of failure P_f can be preferred to the reliability index β to define the reliability level of a structure, or vice versa. Typically the civil engineering domain often uses reliability indexes.

The two measures of reliability performance, P_f and β , are obviously tightly linked. Methods such as FORM or SORM allow, based on the approximation of the shape of the limit state surface, to estimate an approximation of P_f . Otherwise, P_f can be computed by sampling based methods for example by Monte Carlo simulations [Lemaire, 2013, Hammersley, 2013, Gogu, 2021]. A deeper analysis of the methods to evaluate P_f on structural applications is reported in Chapters 5 and 6.

Referring to the general $UQ\mathcal{E}M$ framework in [De Rocquigny et al., 2008], structural reliability assessments can involve all four goals listed in Section 2.1:

- Goal U (Understand): identification of the main factors affecting the failure probability or the reliability index of a complex structure;

- Goal A (Accredit): evaluation of the reliability of existing designs or detection systems (to validate the quality of measurements data);
- Goal C (Comply): verification of the compliance with current certification requirements provided by the law, for both existing (i.e. coupled with goal A) and new designs;
- Goal S (Select): in design phase, reliability assessments can be introduced to verify the compliance with current certification requirements imposed either by the law (i.e. coupled with goal C) either by industrial needs prescribed by the customer, stakeholders or the final user.

In the specific case of the goal S, it is common to preview an optimization framework including the reliability assessment as a constraint. Such framework is referred in the literature as *Reliability-Based Design Optimization* (RBDO) [Enevoldsen and Sørensen, 1994].

In the literature, a number of other references on methods [Whittaker and Besuner, 1969, Alfredo and Wilson, 1975, Rackwitz and Flessler, 1978, Manohar and Gupta, 2003, Rausand and Høyland, Qiu et al., 2013], industrial applications [Thoft-Christensen et al., 1998, Faber, 2000, Nikolaidis et al., 2007, Sundararajan, 2012, Thoft-Christensen and Murotsu, 2012] and software implementations [Pellissetti and Schuëller, 2006] of reliability concepts can be found. It is worth noticing that such applications are not limited to civil or aeronautical engineering, but includes also automotive and ship industry [Nikolaidis et al., 2007], among others.

2.4.1 Civil applications

In the civil engineering context, the application of reliability assessments is previewed by the legislative requirements (specifically the Eurocodes in Europe). In this section, we classify the civil applications according to the main categories of phenomena which are taken into account in the literature: in particular, we focus on seismic activity, wind effects and long-terms effects.

Seismic activity was always considered as a main actor in the reliability assessments of every civil structure. Statistical treatment of earthquakes becomes indispensable for this purpose. One of the first formalizations of the seismic structural reliability in a probabilistic framework was provided by Esteva and Villaverde [Esteva and Villaverde, 1973] and dates back to 1973. Current applications cover both evaluations of seismic reliability of already existing structures [Jalayer et al., 2010, Huang et al., 2015, Iervolino et al., 2018] and completely new designs [Cai and Lin, 1998, Mishra et al., 2013, Tuken et al., 2017, Kolathayar et al., 2018], within an RBDO framework. All of these works are strictly connected with the guidelines provided by national and international standards (e.g. the Eurocodes in Europe). Moreover, given the different seismic activities in distinct regions, most of the analyses are focused on national realities, from Canada [Ghobarah and EL-ATTAR, 1998] to Iran [Pourzeynali and Hosseinneshad, 2009], from Italy [Jalayer et al., 2011] to Indonesia [Mase, 2018].

Another important phenomenon analyzed in reliability assessments is the effect of the wind. Most applications of reliability studies on wind effects are focused on buildings (both tall [Caracoglia, 2014, Bernardini et al., 2012, Zhang et al., 2008, Gibbons et al.,] and low buildings [Davenport, 1983, Jin et al., 1999]) and long bridges [Ge et al., 2000, Pourzeynali and Datta, 2002, Baldomir et al., 2013, Dong et al., 2021]. For both buildings and bridges, the safety is the main purpose. However, for the former we may have also

evaluations (and/or reliability constraints) on the *serviceability* [Rojiani and Wen, 1981, Bashor and Kareem, 2007], defined by EN 1990 as the requirement that "the structure during its intended life will remain fit for the use for which it is required, with the appropriate degrees of reliability and in an economic way". As for seismic effects, new designs taking into account wind effects can be introduced in an RBDO framework [Kusano et al., 2014, Spence and Giofrè, 2012].

Another topic of interest regards the guarantee of maintaining a certain level of safety during long periods of time, thus focusing on long-term effects, mainly fatigue [Pourzeynali and Datta, 2005, Krejsa, 2013, Heng et al., 2019, Jia et al., 2020, Fu et al., 2020, Luo et al., 2021], corrosion [Melchers, 2005, Val, 2007, Cascini et al., 2014, Nguyen and Nguyen, 2020, Bojórquez et al., 2021] and combination of both [Mokhtari and Melchers, 2020, Shittu et al., 2020, Xu et al., 2022]. These applications are linked to the concept of time-dependent (or time-variant) reliability [Wang et al., 2021a], based on the perspective that the reliability of a given structure can change when the environmental conditions and the effect of loading history evolve in time. The Eurocodes themselves provide different reliability targets that constructors must demonstrate in the short- (e.g. present and 1 year) and long-terms (e.g. 25/50 years). Note that the applications on long-term effects are not totally disconnected with seismic and wind loadings, as these latter may affect (or be affected by) the previous history of loadings and solicitations [Fu et al., 2020, Bojórquez et al., 2021]. In the conception of new designs, the applications of RBDO frameworks focus on the concept of life-cycle cost [Frangopol and Maute, 2003, Ellingwood and Lee, 2016, Frangopol and Kim, 2019, Xin et al., 2021, Frangopol and Kim, 2022], intended as the cost implied by the construction and maintenance all across the targeted lifetime [Frangopol, 2011].

All the applications described in this section are in close relation with the guidelines provided by current legislation requirements. The proper definition of target reliabilities in national (and international) standards encourages the research to explore new methods, tools and applications in the civil engineering field.

2.4.2 Aeronautical applications

The application of structural reliability concepts spurred a growing interest in the last two decades in aeronautical *research*. The reader can find some literature reviews on methods and applications of aircraft structural Risk and Reliability ($R\&R$) analysis on airframe [Tong, 2001, Long and Narciso, 1999] and aircraft gas turbine engines [Kappas, 2002], as well as computational challenges [Ghiocel and Wang, 2005].

Research efforts mainly focused on the demonstration of the usefulness of probabilistic methods to improve the design of aeronautical and aerospace structures [Wang et al., 2019a], thus covering the goal A (Accredit) in the general UQ&M framework [De Rocquigny et al., 2008]. These may include the definitions of embedded statistical methods [Huang and Lin, 2005, Pradlwarter et al., 2005, Wu et al., 2011], dedicated softwares - such as the "Nonlinear Evaluation of Stochastic Structures Under Stress" (NESSUS/FEM) [Cruse et al., 1988], dedicated routines in ASTROS [Luo and Grandhi, 1997], the "Probabilistic Design of Damage Tolerant Composite Structures" (ProDeCompoS) [Ushakov et al., 2002] and the Python library OpenTURNS [Baudin et al., 2017] - and the reliability of detecting flaws during inspection [Lincoln, 1985, Zhang et al., 2010, Ignatovich and Bouraou, 2013, Woch, 2014, Lin et al., 2018] to properly redefine maintenance plans. The applications at academic

research level aim at analyzing several phenomena, like fatigue [Ghiocel and Tuegel, 2004, Huang et al., 2012, Song et al., 2021, Choi et al., 2021], dynamic loadings [Su and Jin, 2019, Wang and Liu, 2020], combined effects of aerodynamics and structural response [Allen and Maute, 2005, Othman et al., 2019, Wansaseub et al., 2020]. The main purpose is to push towards probabilistic designs to reduce the potential over-conservatism in classical deterministic design [Enrico et al., 2019].

The actual industrial applications of structural reliability concepts in aeronautical context are still limited. In 2002, Zang et al. [Zang et al., 2002] tried to outline needs and opportunities for uncertainty-based design approaches in aeronautical industry. In particular, several barriers were highlighted:

1. industry is reluctant to abandon traditional design methods;
2. benefits of probabilistic approaches are not widely demonstrated in literature;
3. designing a structure or a system when dealing with uncertainties is a far more complex and computationally expensive task than the deterministic counterpart;
4. statistical description of structural imperfections is economically expensive, time consuming and highly dependent on specific configuration, material and manufacturing processes;
5. statistical process control activity is significantly lacking in aerodynamics;
6. there are no effective approaches for characterizing modeling uncertainties, especially for nonlinear problems;
7. current RBDO methods imply a computational burden too significant to be incorporated in high fidelity analysis tools;
8. researchers and analysts are not trained enough on statistics and reliability assessments.

However, this report was not updated with recent advancements in probabilistic approaches and evidences of opportunities for such design methods, since it is dated from 2002. All the applications reported in the present paper demonstrate the collapse of reasons 2, 5, 6, 7. Some barriers, like 3 and 4, will still be true in the short term: however, as this research field is very active, it is reasonable to suppose that such difficulties will be soon minimized. Large efforts are also undertaken in industrial contexts too, in order to cope with organizational - 1 in the list - and training issues - 8 in the list.

Focusing on the last barrier in the list from [Zang et al., 2002], we need also to underline the fact that the reliability analyses are well integrated in the design and verification of aircraft avionic systems [Enrico et al., 2019]. Therefore, the transition from classical deterministic to reliability-based structural designs is not impossible from the capabilities standpoint, as the technical skills are already there, although used, for now, in different departments.

Another obstacle to the development at industrial scale of reliability-based design methods and applications is currently given by the availability of data. We report the example from Huang et al. [Huang and Lin, 2005], who aimed at creating a procedure to systematically compute failure probability of aircraft composite structures subject to accidental damage. A large database needed to be collected: in particular, they sought informations about material category, damage type, aircraft location, detection method and damage cause. Unfortunately, database construction was seen as a nontrivial issue. The authors used two different sources to construct the database: FAA's (*Federal*

Aviation Administration) Service Difficulty Reporting System (SDRS) and data collected in [Gary and Riskalla, 1997] via survey from a U.S. Naval Aviation depot and on-site inspections of several commercial airline maintenance facilities. However, these were incomplete (SDRS database in particular), since damages below maximum acceptable limits were not usually reported, leading to representation of only large flaws, not the overall distributions. An alternative could be found in aircraft operators logbooks of maintenance actions, where all interventions are usually recorded: unfortunately, their availability could not be taken for granted, for confidentiality issues.

Finally, also the FAA itself proposed a probabilistic method for the sizing of composite aircrafts (confront the official document DOT/FAA/AR-99/2 [Long and Narciso, 1999]), twenty years ago. This considers a separate statistical analysis of the phenomena affecting loads and structural strength, and distinct failure modes are analyzed separately, as shown in the flowchart in Fig. 2.4. However, there is no clear definition yet of a target reliability that manufacturers need to demonstrate to the authorities, in order to guarantee the initial airworthiness of new aircrafts. Moreover, the demonstration of aircrafts static strength is still based on the certification tests and the concept of safety factors, which will be the main focus of the next section.

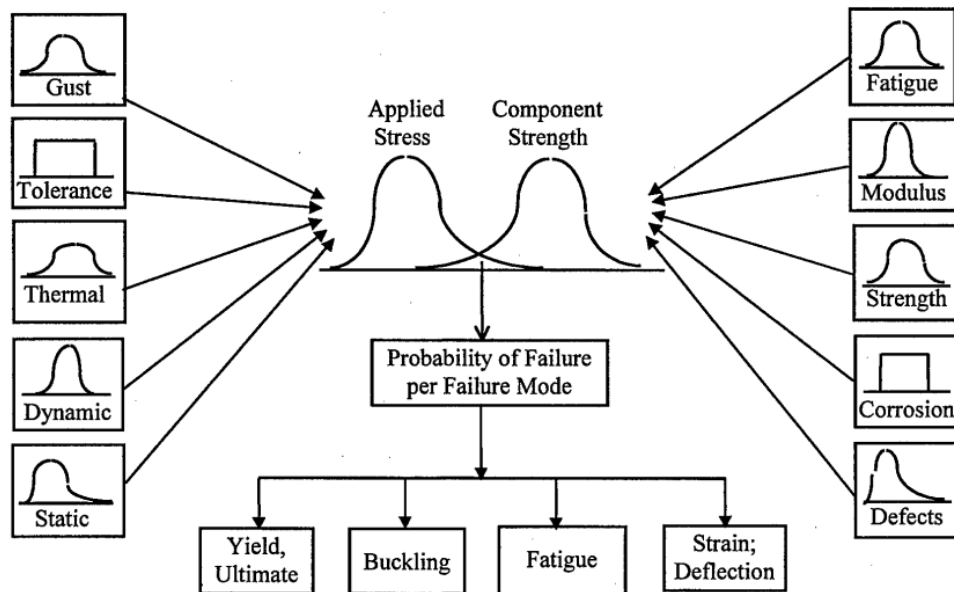


Figure 2.4: Probabilistic analysis concept from FAA (Source: [Long and Narciso, 1999])

2.5 Safety factors

In the previous sections we analyzed two main aspects (namely structural tests and reliability assessments) of probabilistic frameworks to validate a structural design. In this section we are going to explore how the design itself is generally done, within the perspective of controlling the variability of the performances of a given structure.

Above all in the initial stages of design, the sizing of structural components does not explicitly deal with the effects of the whole statistical variability of all the input random parameters involved. The design will be focused on *nominal* quantities. Note that the

concept of "nominal" is not equivalent to "mean": nominal values can be defined either as specific quantiles, means or worst-case scenarios of a given quantity (e.g. load, material property, geometric features, etc.). The uncertainties associated to these parameters (which are apparently left behind, when considering just nominal values) are actually implicitly considered through some other deterministic quantities, called *safety factors*.

From a generic point of view, the concept of *safety factors* is introduced to guarantee a certain margin on the computed nominal performances, in terms of both solicitations (i.e. applied loads) and capacity (i.e. structural strength) of a given structure. These margins are intended to compensate eventual errors in the adopted models, lack of knowledge on complex phenomena, under-conservative assumptions raised to simplify the structural analyses, human errors, unanticipated operational conditions.

From a mathematical point of view, these safety factors consist usually in sets of multiplicative coefficients γ which are used to adjust the nominal loads and structural resistance (or strength). The safety factors will lead to consider in design phase amplified nominal loads and reduced material strengths. The simplest expression used to verify the safety in deterministic design phase can be formulated as:

$$\phi_R R \geq \gamma_S S \quad \text{with} \quad \phi_R \leq 1, \gamma_S \geq 1 \quad (2.4)$$

Where R represents the material strength, S the load, γ_S the safety factor related to the load and ϕ_R is a safety factor related to the strength. These expressions can be enriched with combination of multiple loads (with associated combination factors) and multiple failure modes.

In civil engineering applications, the upper-mentioned factors in Eq. 2.4 are denoted as *partial safety factors* and are always greater than unity: for the strength the reciprocal $\gamma_R = 1/\phi_R$ is adopted in Eurocodes.

In aeronautical and aerospace applications, we refer to ϕ_R as *Knock-down Factors* (KdF, lower than unity) and to γ_R, γ_S simply as *Safety Factors* (SF). Note that several distinct KdFs/SFs can be cumulated (as product of different KdFs/SFs) to take into account the cumulative effect of, for example, manufacturing procedures, thermal treatments of materials, errors in the installation and/or in the assembly line.

The general principle of the design via safety factors is illustrated in Fig. 2.5, where we adopt the aeronautical notation. From the distributions of stress S and strength R , two nominal quantities are identified, leading to the definition of respectively R_{nom} and S_{nom} . These are then modified via the introduction of the SF γ_S and the KdF ϕ_R . Finally, a margin of safety (typically called *reserve factor* in aeronautics) is computed to verify that the condition in Eq. 2.4 is actually satisfied.

Now, these safety factors are actually used in deterministic design, according to the principle shown in Eq. 2.4 and in Fig. 2.5. So why including them among the applications of probabilistic-based frameworks? Actually, the purpose of the introduction of safety factors is to absorb the effects of the input variability on the structural outcomes, i.e. to ensure that the variabilities which could prevent the safety of the structure itself are taken into account within the deterministic design framework. This guarantee comes from how we determine these safety factors. Therefore, the probabilistic concepts are not applied in the final usage of the safety factors (i.e. in the deterministic design, as in Eq. 2.4), but *may* rather intervene on the computation of the safety factors themselves. Note, however, that the safety factors may not necessarily be determined via a probabilistic framework.

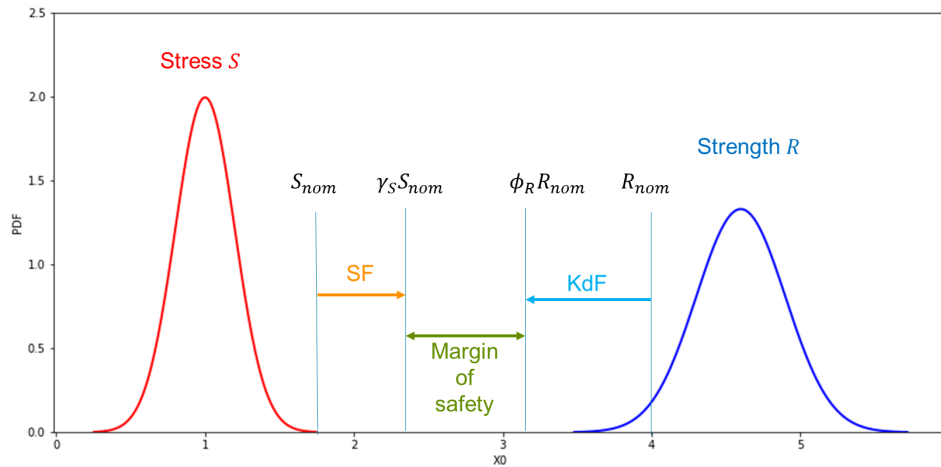


Figure 2.5: Illustration of the principle of design by safety factors (aeronautical notation is used)

In the following of this section, we deal with the modalities on how these safety factors are determined in civil and aeronautical applications, the reason behind the different choices and what challenges affect these two fields.

2.5.1 Civil applications

The determination of partial safety factors is often referred as ”*calibration of partial safety factors*” in the civil engineering field. This concept is based on reliability evaluations and was originally introduced in the civil domain. It is generally performed for a given class of structures, materials or loads in such a way that the reliability index of the structure gets as close as possible to a fixed target.

Another denomination of the ”*calibration of partial safety factors*” is the *code calibration*. The reason for this naming lies in the fact that the related studies do not aim at ensuring a fixed reliability level to a single product (e.g. a single bridge, building, silo, etc.), but rather to propose new national standards, often called *building codes* (from which the name *code calibration*).

Code calibration can be performed by judgment, fitting, optimization or a combination of these [Thoft-Christensen and Baker, 1982, Madsen et al., 2006]. Focusing on the optimization procedure, the following steps are generally performed [Sørensen et al., 1994, Faber and Sørensen, 2002]:

1. *Definition of the scope of the code*: the class of structures to be considered;
2. *Definition of the code objective*: target reliability indexes or probabilities of failure in different failure modes;
3. *Definition of code format*: how many partial safety factors and load combination factors to be used, dependencies between load partial safety factors and material or between material partial safety factors and load type, how to use the partial safety factors in the design equations, rules for load combinations;
4. *Identification of typical failure modes and of stochastic model*: limit state equations and design equations are formulated and specific stochastic models for the

- parameters in the limit state equations are selected;
5. *Definition of a measure of closeness*: a function describing how similar are the obtained reliability indexes to the target values;
 6. *Determination of the optimal partial safety factors for the chosen code format*: optimization procedure;
 7. *Verification*: validity of the optimal safety factors and reliability assessment of the obtained structures.

The design method stemming from a probabilistic-based determination of *partial safety factors* is often referred in the literature related to civil engineering as *Load Resistance Factor Design* (LRFD).

The introduction of a target reliability level, typically defined through a reliability index β , allows to impose a certain safety on the obtained design. Numerical values can vary in function of the susceptibility of the particular structure and the eventual consequences of the specific failure. Varying reliability targets among different failure modes is strictly due to the interest in increasing reliability requirements of the most catastrophic ones.

Another aspect to emphasize in the upper-described algorithm regards the definition of a measure of closeness. It consists in a simple relation quantifying the differences between a general vector of reliability indexes β_i with respect to target values $\bar{\beta}_i$. Each failure mode i will be considered with a different relevance, by the use of appropriate weight factors W_i . Measure of closeness can be formalized in a general form as:

$$M(\beta_i; \bar{\beta}_i, W_i) = \sum_i W_i f(\beta_i; \bar{\beta}_i) \quad (2.5)$$

An example of Eq. 2.5 can be given by:

$$M(\beta_i; \bar{\beta}_i, W_i) = \sum_i W_i (\beta_i - \bar{\beta}_i)^2$$

A common objective in this research field is to uniform reliability indexes for several failure modes, hence fixing the same target $\bar{\beta}_i = \bar{\beta}$. Already in 1971, Lind [Lind, 1971] showed how a partial safety factor format could be calibrated to achieve nearly constant reliability within the framework of a member-by-member design theory.

The applications in civil engineering can address critical evaluations of current national standards [Ghosn and Moses, 1986, Vrouwenvelder and Siemes, 1987, Trezos and Thomos, 2002, Dymiotis, 2002, Beck and Souza Jr, 2010], comparisons between different national standards [Gulvanessian and Holický, 2002, Sørensen et al., 2005] and/or with European standards [Gulvanessian and Holický, 2002, Beck and Souza Jr, 2010]. Furthermore, the redefinition of safety factors through statistical-based calibration can concern all categories of structures: from steel [Leander et al., 2014, Nadolski et al., 2019] to wood constructions [Folz and Foschi, 1989, Ellingwood and Rosowsky, 1991, Ellingwood, 1997, Sørensen et al., 2005], from bridges [Leander, 2018] to off-shore structures [Yoon et al., 2014, Nadim et al., 2015]. The probabilistic-based calibration of safety factors is allowed, in civil engineering, by the large amount (and the continuous update) of publicly available data: these include informations on climatic conditions, geothermic data, seismic and hydrological risks, among others.

We report here an example of application from Sorensen [Sørensen, 2002], who performed a calibration of partial safety factors of a number of sample structures. The list of examined structures included: simply supported beams of reinforced concrete, steel and glued laminated timber, short columns of concrete, steel and glued laminated timber, a central loaded footing (foundation) on sand and clay and a concrete gravity wall. The calibration was intended to obtain the same average reliability index furnished by Danish codes, but minimizing the scatter of the reliability levels among all the structures considered. In particular, safety factors were determined by considering the cumulative effect of consequences of failure, type of failure, uncertainty associated to the material mechanical properties and in the computational models. Results confirmed a previous study by Sorensen et al. [Sørensen et al., 2001], and constituted a proposal for new set of partial safety factors for the Danish National Annex. The final distribution of the reliability indexes is reported in Fig. 2.6.

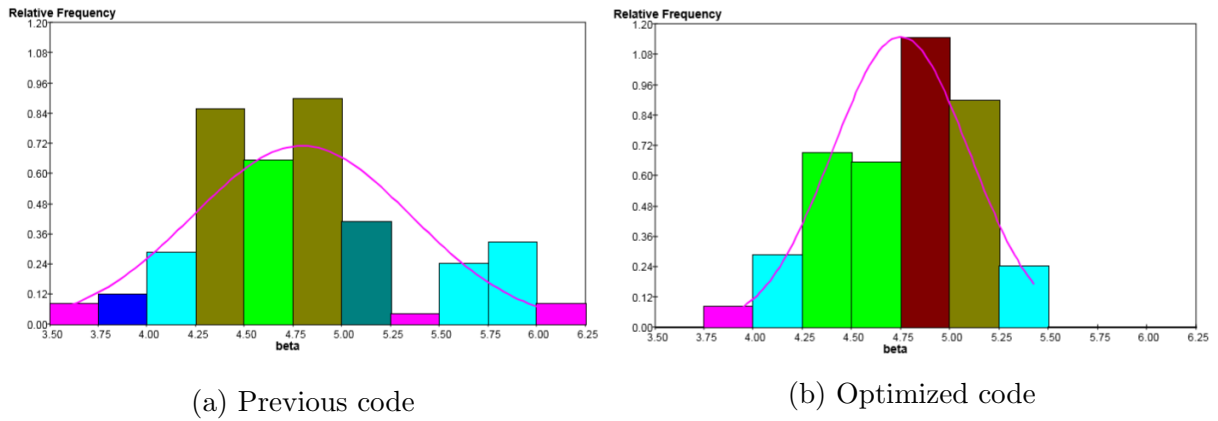


Figure 2.6: Distribution of reliability indexes β before and after code calibration (Source: [Sørensen, 2002])

Finally, the choice of a particular target reliability index, constituting one main starting point in the safety factors calibration, is not trivial. The discussion is still open and eventually will evolve with time [Faber and Sørensen, 2003]. Looking at the outcomes from the most recent works on the subject [Nadolski et al., 2019], a number of effects still need to be studied and the discussion about the calibration of safety factors is all but closed. On top of that, standard codes can still change with time, encouraging further research efforts on this field.

2.5.2 Aeronautical applications

Actual aeronautical applications of safety factors calibrations based on a probabilistic framework are still at birth. Traditionally, in the aeronautical field, multiple safety factors were used. They are currently partly defined by FARs and CS, respectively in US and Europe, and partly by the manufacturers themselves depending on their experience. Therefore, conversely to the current threads of civil engineering applications, the safety factors in aeronautics are not entirely based on probabilistic analyses.

As an example of safety factors not based on probabilistic considerations, we report the case of the link between limit load LL and ultimate load UL in absence of inter-

actions between structures and system: in fact, in presence of interactions between the structure and systems, this safety factor is actually adjusted according to the probability of occurrence of the system failure (see CS 25 Appendix K). As a reminder, the LL is defined as the maximum load arriving at most once in an aircraft life (see CS 25.301). The UL is an amplification of LL representing also the load that the structure must prove to be able to withstand for 3 seconds in certification physical tests (see CS 25.305). These two quantities are linked via the relation $UL = 1.5 \times LL$ (see CS 25.301-303). The first adoption in 1934 of this classical safety factor, equal to 1.5, comes from an analogy with the mechanical properties of aluminum [Mangurian, 1957]. In fact, the ratio between the ultimate strength (i.e. the rupture limit) and the yield strength (i.e. the maximum solicitation before the appearing of plastic deformations) is around 1.5 for the aluminum. On the other hand, each aircraft should be able to withstand limit loads without detrimental permanent deformations (linked then to the yield strength of the structure) and sustain ultimate load without collapsing (thus linked to the rupture limit). Given the extended use of aluminum in aviation, it was chosen to assign a level of 1.5 for the safety factor linking these two reference load levels [Mangurian, 1957, Wang et al., 2019a].

The first to assess the issue related to the choice of the safety factor 1.5 (traditionally used in aeronautics) seems to be Mangurian [Mangurian, 1957]. He pointed out a list of phenomena for which the combination of this 1.5 safety factor with the concept of *limit load* led to over-conservative design. Therefore, lower safety factors would be sufficient to guarantee a rational level of safety, allowing to reduce the over-conservatism in the structural sizing. He raised the hypothesis that, because of the overwhelming fear of degrading safety, it was however unrealistic to expect any incentive for change from the military or civil authorities [Mangurian, 1957]. Note that this work dates back to 1957.

50 years later, Elishakoff and Chamis [Elishakoff and Chamis, 2001] investigated the relation between safety factors and reliability. From their analyses, they concluded that these two concepts could peacefully coexist, even if their nature is different: safety factors are allocated, in aeronautical context, in an *ad hoc* manner, dictated by past experience and driven by the idea that "*if nothing never happened, nothing will happen in the future*" [Elishakoff and Chamis, 2001]; on the opposite side, reliability-based approaches can offer a unified mathematical framework for calculating safety levels and associated safety factors. In order to link these two perspectives an ingredient was still missing: this is, in fact, the determination of precise reliability targets that need to be ensured. Without the general context of reliability, the safety factor will remain, according to [Elishakoff and Chamis, 2001], as "*the factor of "experience" but still the factor of "theoretical ignorance"*".

Several more recent research efforts aimed at concealing the safety factors with reliability concepts [Qu and Haftka, 2004, Acar et al., 2007, Degenhardt et al., 2010, Wang et al., 2013, Schillo et al., 2017, Wang et al., 2019a]. However, for an actual application at industrial level, it is mandatory to create a link between each proposed probabilistic framework and the current certification requirements.

On the other hand, this link needs to be addressed also by the other protagonists, i.e. the regulation authorities defining the certification requirements themselves. As shown by Bristow [Bristow and Irving, 2007] in 2007, safety factors in aeronautical industry did not change since their original adoption [Mangurian, 1957]. In [Bristow and Irving, 2007] one can find a summary of safety factors defined in JARs (i.e. the previous certification

requirements in Europe, before the EASA standards) until 2007 and applied to civil aircraft designs: by comparison with current legislation, no substantial difference can be outlined. The evidences on the improvements allowed by reliability-based definitions of safety factors suggest that the conditions will be probably mature in a not-so-long term to motivate the dialog between aeronautical industry and certification authorities to move towards this direction.

2.6 Conclusion

In this chapter we presented a brief state of the art of the applications of probabilistic frameworks in civil and aeronautical engineering fields. Throughout the chapter we compared the directions of research and industry in these two fields, focusing on three main classes of applications: structural tests, reliability assessments and safety factors. The common thread of this comparison was identified in the legislative certification requirements imposed by the related standards in Europe (Eurocodes for civil engineering, EASA standards for aeronautics).

The applications of structural tests are more spread in aeronautical engineering, with respect to civil engineering. The main reasons can be identified in the continuous customization of components in aeronautics (compared to the wide spread use of standardized components in civil engineering) and the certification constraints. Focusing on these latter, we may observe that Certification Specification (CS) requirements properly define load levels and standard procedures to certify aircrafts. On the other hand, Eurocodes showed some lacks in the proper definition of proof load tests. Moreover, the fact that full scale civil structures are often not to be replicated reduces the possibilities to perform destructive tests, compared to the aeronautical field.

Concerning the applications of reliability assessments, we observe continuous advances in civil engineering: these are supported by the logic defined by the national (and international) standards, which impose reliability targets to be justified on each design. Such targets are also differentiated according to the category of structures, the main phenomena affecting the safety, and separating short or long-term requirements. In parallel, actual industrial applications of reliability-based design methods are slowed in aeronautics mainly by the certification requirements, which do not fix a precise reliability target (for structures) and still demand for a demonstration of the design via the concept of safety factors. Several contributions in the literature aimed at moving aeronautical industry towards probabilistic design approaches. However, the missing link appears to be a tighter interaction between industry and regulation authorities on this topic, allowing to converge towards new standard requirements, in particular, the definition of a target reliability level.

The last category of applications of probabilistic frameworks includes the determination of safety factors (SF). We highlighted the fact that in civil engineering the SFs are generally determined via probabilistic analyses, while in aeronautics SFs are mainly defined by engineering judgment and based on past experience. This difference is due, once again, to the different requirements imposed by certification authorities. We also put in evidence the different evolution rates of legislative standards, which evolve faster in civil engineering.

To summarize the outcomes of this critical review, the applications of probabilistic frameworks in the two analyzed engineering fields (civil and aeronautics) are tightly linked to the respective standard requirements. In order to develop new structural design methods based on probabilistic frameworks, we must conciliate the proposed approaches with current certification requirements to make them applicable to aeronautical structures.

In the following chapters, we will propose a new sizing approach, based on a probabilistic framework and capable to align with current certification requirements. The common thread of all successive chapters will be given by the applications on Hole2Hole project, presented in Section 1.4.

The proposed sizing approach will be presented in two different declinations in Chapter 4 and 7. Before, we will explore the application problem in Chapter 3, aiming at understanding the global relationships between the different quantities in input and the output structural performances.

Chapter 3

Deterministic Exploration of Input Variability

3.1 Introduction

In the previous chapters, we highlighted the interest in recent years in the application of probabilistic analyses in different fields, with a particular focus on the expected gains in the design of aeronautical structures. We reported the main concepts of the *Uncertainty Quantification & Management* (UQ&M) framework (in Chapter 1) and the distinction between different objectives pursued by UQ&M (in Chapter 2). In this chapter, we focus on the goal U (Understand) of the UQ&M framework, consisting in understanding the influence of the variability of the inputs on the variability of the output response.

The common thread of the present dissertation, given by the Hole2Hole project (presented in Chapter 1) constitutes the main application of this chapter. As a reminder, this project aims at simplifying the assembly routine of aeronautical structural elements by drilling the individual parts prior to the entrance in the assembly line. This leads, on one hand, to a dissociation between the manufacturing and the assembly routines, simplifying this latter. On the other hand, some geometric imperfections are introduced: therefore, the associated consequences on the load redistribution of the obtained assemblies need to be evaluated. This chapter constitutes a first step to understand and simplify the H2H problem, in order to facilitate the interpretation of the results issued from the analyses of the following chapters, but also to be able to identify the relevant countermeasures to improve the structural performances.

Most applications of UQ&M require a large number of evaluations of numerical simulations. Furthermore, real-world applications make use of increasingly complex simulation models. The open question is how to balance computational burden and results precision. Therefore, two main challenges arise:

1. how to reduce the number of simulations required to provide sufficient accuracy;
2. how to reduce the complexity of the full model (e.g. via a surrogate model) while minimizing the detriment in terms of precision.

Both goals are made more difficult when dealing with problems characterized by high number of inputs: more simulations are generally required to fully explore a wider input

domain and the construction of a surrogate model becomes more challenging as input dimension increases. Therefore, this chapter aims at exploring various approaches to reduce the input dimensionality of the H2H application problem.

The challenges arising from the amount of input variables on H2H numerical exploration is described in Section 3.2. All successive sections present the general method and the application of input dimensionality reduction on H2H coupons.

This input dimensionality reduction is performed by following three axes:

1. Retrieve relations between inputs that better explain the effects on the response;
2. Remove inputs which only marginally affect the response;
3. Separate effects of inputs that can be superposed.

The first axis is pursued by defining specific patterns of the input variables. In particular, this consists in the identification of the principal modes, defined as linear combinations of the original inputs, which constitute the most informative features that explain the variability of the output response. In the context of H2H framework the modal description is used to redefine the misalignments variables, with a double goal in mind: (1) we need the fewest but more informative input variables; (2) retrieving the most important features (which affect the output response) may facilitate the interpretation of the statistical results presented in the following chapters. The methods used for this modal description and the related applications to H2H constitute the main content of Section 3.3.

The second and the third purposes are pursued via screening techniques, which are part of the larger framework of the sensitivity analysis [Iooss and Lemaître, 2015]. The methods and the applications to two coupons of H2H configurations are reported and discussed in Section 3.4.

Finally, in Section 3.5 the conclusions of the study reported in this chapter are analyzed, highlighting the main consequences of the presented results on the successive statistical analyses of the next chapters.

3.2 Challenges arising from numerical investigations on H2H

Within the H2H framework, the Single Lap Shear (SLS) uni-axial loaded bolted joint assembly (illustrated in Fig. 3.1) was selected here as application problem. This is characterized by the assembly of two plates, connected by a fixed number of bolts. In particular, we clamp an extremity of the first plate (situated on the left in Fig. 3.1) on the left plane perpendicular to X axis, while applying a load F_{app} parallel to X axis and applied on the center of the right face of the second plate. We differentiate the coupons via the *bolting pattern*, which represents the mapping of the bolts in a given assembly. We denote the bolting pattern via the notation $N_X \times N_Y$: here N_X represents the number of rows of bolts in the longitudinal axis (i.e. parallel to the direction of the applied load), while N_Y is the number of rows of bolts in the transversal axis (i.e. perpendicular to the direction of the applied load).

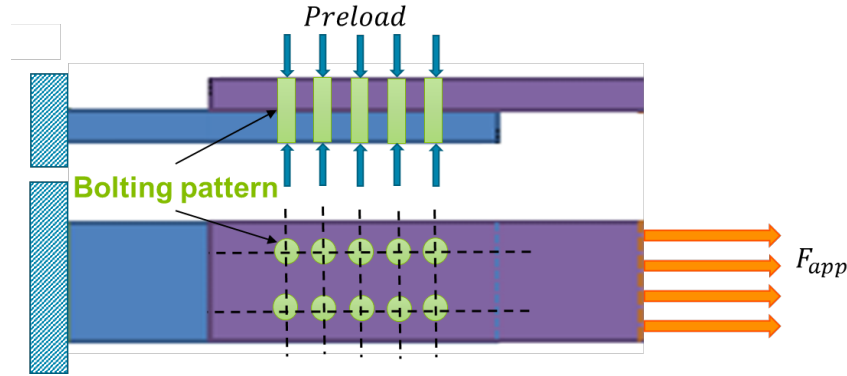


Figure 3.1: Illustration of uni-axial loaded Single Lap Shear bolted joint assembly (bolting pattern: 2x5)

Part of the analyses can be performed via physical testing while other can rely on simulation-assisted exploration.

The present work focuses on simulation-assisted exploration, while physical experiments are used within H2H project in a statistical framework to validate and accredit the numerical model: in the UQ&M framework described in Section 1.2, physical tests of H2H project pursue the goal A (Accredit).

The exploration assisted by the numerical model can be associated in UQ&M framework to the goal U (Understand): in fact, the main objective of this exploration is to understand and rank the different effects on the output response issued from the different inputs.

Focusing on the input variables of the H2H virtual model, one can retrieve:

- Elastic behavior material properties (for both plates and fasteners);
- Plastic behavior material properties (for both plates and fasteners);
- Allowable material limits (for both plates and fasteners);
- Friction (between all surfaces);
- Preload on fasteners to enforce the contacts between each fastener and each plate, and the contact between the two plates;
- Oversize (additional clearance between hole and fastener);
- Misalignment (vector between theoretical and actual hole center positions);
- Load level;
- Bolting pattern;
- Fastener geometry;
- Nominal hole diameter;
- Plate thickness.

We illustrate in Fig. 3.2 the mathematical definition of the misalignments: in particular, we denote by X the longitudinal component (i.e. parallel to the application of the external load) and by Y the transversal component of the vector connecting the theoretical center of the hole (i.e. the nominal and ideal position) and the actual position of the drilled hole. We also make use of the notation X_{ij} (respectively Y_{ij}) to denote the longitudinal (respectively transversal) component of the misalignment vector, related to the j -th hole on the i -th plate.

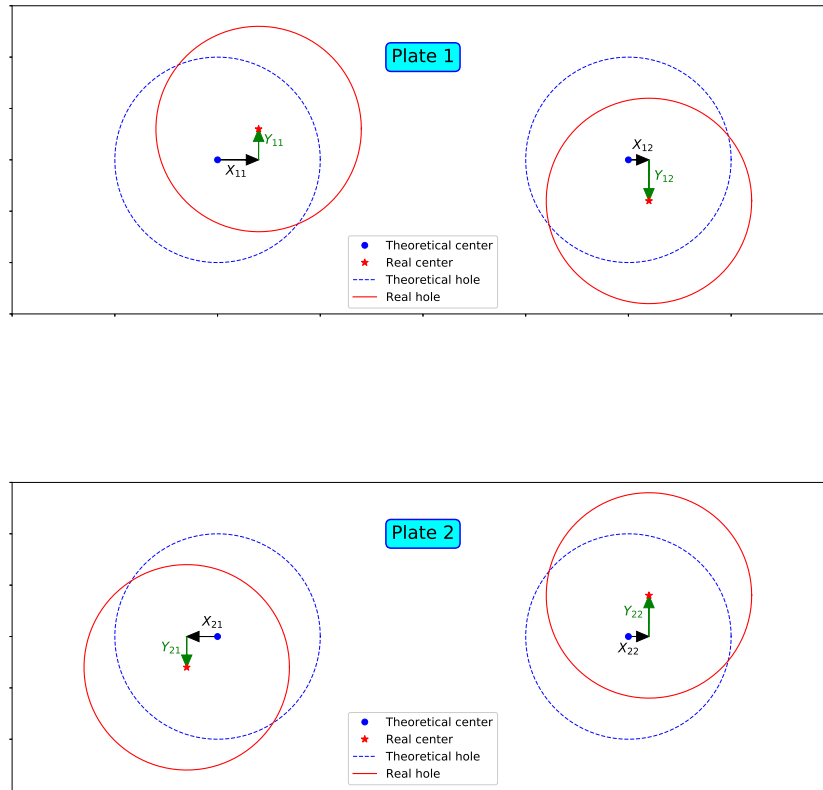


Figure 3.2: Illustration of geometrical misalignment definition

We can cluster the upper-mentioned variables according to their variability and their controllability:

- *Design choices*: material choices, fastener geometry definition, bolting pattern, nominal hole diameter, load level;
- *Random variables*: elastic and plastic behavior material properties, allowable material limits, friction properties, preload, oversize, misalignments, plate thickness.

The design choices can be considered (and consequently treated) as scenarii following the UQ&M framework presented in Section 1.2. Some of the upper-mentioned random variables actually involve small variabilities, due to the precision in manufacturing processes:

- Oversize;
- Plate thickness.

Other random variables are considered at their nominal level because of their limited effect over the variation of the transmitted loads, assumed by engineering judgment:

- Friction between fastener head and plate;
- Friction between fastener nut and plate.

These parameters are kept in the finite element model to ensure numerical stability. Moreover, in the present work we chose to focus on behavior of the material in the

linear elastic domain, so the plastic behavior material properties are not included in our analysis. This is done in order to work with models with lower computational burden. The extension to nonlinear models of the relation between stress and strain is left as perspective.

To sum up, the list of uncertain variables treated in the upcoming UQ&M analysis in the context of H2H is reduced to:

- Elastic behavior material properties (for both plates and fasteners);
- Allowable material limits (for both plates and fasteners);
- Friction (between plates);
- Preload on fasteners;
- Misalignments.

The ensemble of scenarii and design choices are listed below:

- Material choices;
- Fastener geometry;
- Bolting pattern;
- Nominal hole diameter (d) and plate thickness (t), resumed in their ratio t/d;
- Oversize;
- Load level.

Summarizing these considerations, Table 3.1 provides a general overview of the evolution of input dimensionality for different bolting patterns. Note that having for SLS coupons two plates, we always have only one friction coefficient, intervening on the interface between the two plates. In the table, we report "1/2" friction coefficient per plate. We illustrate the evolution of the total number of input variables in Fig. 3.3.

Random variable	Per bolt	Per plate	1x2	1x3	1x5	2x3	2x5	3x5
Misalignments	4		8	12	20	24	40	60
Friction coefficients		1/2	1	1	1	1	1	1
Preloads	1		2	3	5	6	10	15
Plate Young moduli		1	2	2	2	2	2	2
Bolt Young moduli	1		2	3	5	6	10	15
Plate bearing strengths		1	2	2	2	2	2	2
Bolt shear strengths	1		2	3	5	6	10	15
Total	7	5/2	19	26	40	47	75	110

Table 3.1: Original list of input variables on H2H problem for different bolting patterns

In UQ&M framework, the output responses to consider are chosen according to the phenomena which better characterize the overall system performances. For SLS bolted joint assemblies, four failure modes (illustrated in Fig. 3.4), distinguished via engineering judgment and supported by physical testing, are often considered:

- *Net section failure mode*: stress in the plate section between holes exceeds plate material limits (typically ultimate tensile strength).
- *Bearing failure mode*: hole stress overcomes allowable material limits, thus leading to a failure on the plate due to excessive plastic deformation around the hole (typical of joints with plates having low ratio thickness/diameter - namely t/d);

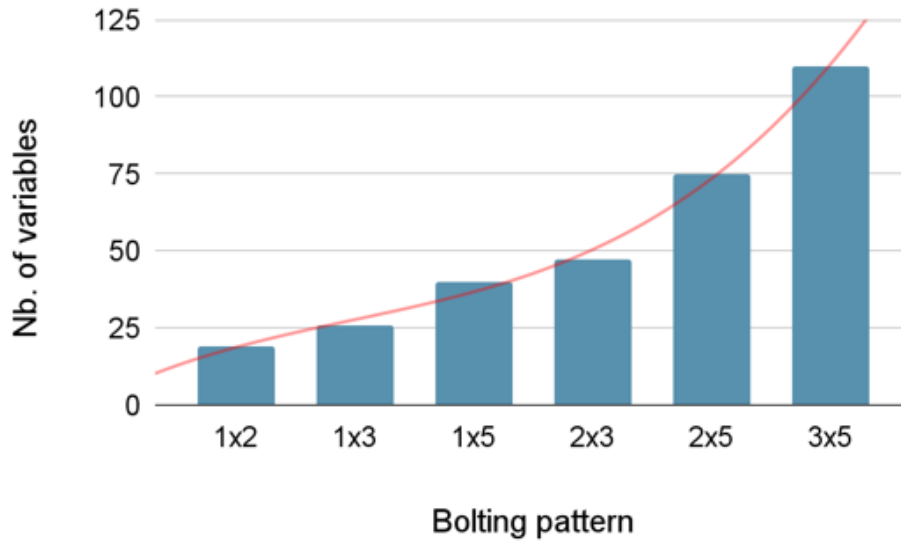


Figure 3.3: Evolution of the number of input variables as function of the bolting patterns

- *Bolt shear failure mode*: shear stress on fastener exceeds capabilities, leading to bolts failure (typical for high t/d);
- *Mixed failure mode*: interaction between bearing and bolt shear failure modes (for intermediate t/d).

In all our work we focus on titanium coupons with $t/d = 0.25$, where bearing failure is the main mode of failure.

3.3 Modal description

This part describes the procedure used to deduce simplified coordinates in the input space, able to appropriately characterize the relationship between input and output. In many applications, it is possible to define certain linear combinations (or modes) of input variables that can explain most of the behavior of a model. The upper-mentioned coordinates represent in fact the principal modes of the original variables.

This approach is interesting as the number of modes can be largely inferior to the number of original variables. This is used in the H2H framework to smartly re-define the input misalignments, which constitute the main contribution to the increase in input dimensionality with the increase of bolting pattern complexity. Moreover, the identification of the principal modes can support the engineering judgment to provide the best-suited countermeasures to ease the consequences of the variability of the input misalignments on the global structural performances.

In order to deduce such modes, two approaches are considered: Principal Components Analysis (PCA) [Jolliffe, 2002, Abdi and Williams, 2010, Bro and Smilde, 2014] and Partial Least Square (PLS) [Vinzi et al., 2010, Mehmood et al., 2012].

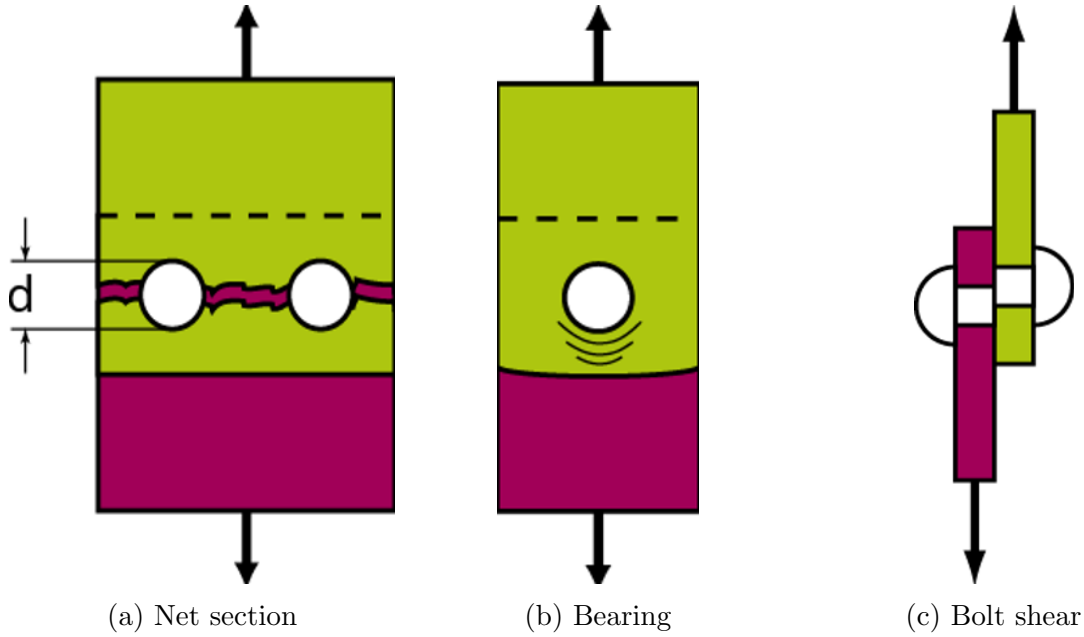


Figure 3.4: Illustration of main failure modes for bolted joint assemblies (mixed failure mode not reported)

3.3.1 Principal Components Analysis

The Principal Components Analysis (PCA) is a common unsupervised machine learning method used to identify patterns of original data that can explain the related variability [Abdi and Williams, 2010, Bro and Smilde, 2014, Vidal et al., 2016]. The main focus is the explanation of the variance of a data matrix X , the rows of which represent different samples.

The PCA allows to transform the data from a high-dimensional original input space to a reduced space of dimension equal to the number of components which are retained.

This transformation is done iteratively by repeated *deflation steps* [Vidal et al., 2016], which correspond to iterative modifications of the original matrix X and are represented by the notation $X_{(i)}$ (related to the i -th deflation step). The directions which induce the upper-mentioned transformation (also referred as *projection*) of the space are given by specific components $w_{(k)}$, where $k = 1, \dots, M$ with M representing the number of components.

The k -th transformation of the sample $X_{(i)}$ due to the k -th component $w_{(k)}$ can be expressed either as a score $t_{k(i)} = X_{(i)}w_{(k)}$ on the transformed coordinates or as the product $\xi_{k(i)} = (X_{(i)}w_{(k)})w_{(k)}^T$ on the original coordinates. The score $t_{k(i)}$ represents the projection of the deflated $X_{(i)}$ induced by the component $w_{(k)}$. On the other hand $\xi_{k(i)}$ represents the k -th component of the reconstruction of $X_{(i)}$ in the original space via PCA.

The first component is obtained as the unitary vector w maximizing the squared covariance of the score t_1 , formalized as follows:

$$w_{(1)} = \operatorname{argmax}_{\|w\|=1} w^T X^T X w$$

Which admits an analytical solution. For the successive components, we update the data matrix by taking into account the transformations on the original input space related

to the previously computed components as follows:

$$X_k = X - \sum_{i=1}^k X w_{(i)} w_{(i)}^T$$

Then the successive components will be obtained by solving the following optimization problem:

$$w_{(k)} = \operatorname{argmax}_{\|w\|=1} w^T X_k^T X_k w$$

This constitutes the k -th eigenvector of the matrix $X^T X$. The related eigenvalues are given by [Jolliffe, 2002]:

$$\lambda_{(k)} = \sum_i t_{k(i)}^2 = \sum_i (X_{(i)} w_{(k)})^2$$

Note that the sum of the $\lambda_{(k)}$ is an index measuring the variance fraction (over the total variance of original data) which is explained by the PCA model. We iteratively add new principal components until we have a sufficiently high level of the *explained variance ratio* (e.g. typically 99%). The total number of components will be denoted as h .

The projection matrix W , defining the projection from the original coordinates (i.e. in the original high-dimensional space) to the reduced lower-dimensional space is given by $W = [w_{(1)}, \dots, w_{(h)}]$.

At first, we use PCA to understand the relations between outputs, comparing the outcomes with an exploratory analysis, if possible, or with engineering considerations.

In a second step, we try to adapt PCA to find a relation between inputs and outputs, conflating both in the same data matrix X : in the H2H application, this would mean stacking per columns both input misalignments and output bearing forces.

It is worth noticing that for PCA there is no distinction between inputs and outputs, as they are all considered as *data*. In fact, PCA is an unsupervised method that cannot be used for regression. This is the main limitation of PCA.

Another alternative use of PCA to overcome this difficulty can be given by the Principal Component Regression (PCR) [Jolliffe, 1982, Bair et al., 2006]: this consists in applying the PCA on a matrix data X containing only the inputs and then introducing a linear regression to understand the connection between reduced inputs and outputs. However, being in our context all input variables considered as independent, the PCA step would not provide useful results: in fact, the dimensionality reduction would not take into account the relation itself between inputs and outputs, leaving all the burden of the identification of such relation to the linear regression itself; moreover, this application of the PCA (in the framework of the PCR) could lead to lose important features and thus important effects of the input variables. This alternative use of the PCA can not be pursued in the applications on the H2H problem.

3.3.2 Partial Least Squares

The Partial Least Squares (PLS) method [Vinzi et al., 2010, Mehmood et al., 2012, Benitez et al., 2020] is a supervised learning technique which presents some similarities with PCA. The main

purpose of PLS is to identify patterns of the input variables that best explain the relationship between inputs X and outputs y . In particular, a linear relation is sought, in the form:

$$y = X\tilde{B} + \tilde{B}_0$$

The matrix B represents the coefficient matrix of the PLS approximation, while B_0 constitutes the intercept. Conversely to PCA, there is a clear distinction between the roles of inputs X and outputs y . On the other hand, the main algorithm is very close to the one presented for PCA.

In analogy with PCA, a score $t_{k(i)} = X_{(i)}w_{(k)}$ on the transformed coordinates is defined for input variables. The first component is obtained as the unitary vector w maximizing the squared crossed covariance between the score t_1 and the output y , formalized as follows:

$$w_{(1)} = \operatorname{argmax}_{\|w\|=1} w^T X^T y^T y X w$$

At this point, we update both input and output matrix by taking into account the transformations on the original input space related to the previously computed components on the input variables [Wang et al., 2003]. The updates of X and y will be defined as:

$$\begin{aligned} X_1 &= X - Xw_{(1)}p_{(1)} \\ y_1 &= y - c_1 t_{(1)} \end{aligned}$$

Where $p_{(1)}$ represents the local linear regression coefficients vector between X and $t_{(1)}$, and c_1 is the scalar local linear regression coefficient between y and $t_{(1)}$. This procedure, often referred as *deflation step*, is then extended for the successive components and updates [Vinzi et al., 2010]. The components $w_{(k)}$ will be obtained by solving the following optimization problem:

$$w_{(k)} = \operatorname{argmax}_{\|w\|=1} w^T X_k^T y_k^T y_k X_k w$$

Where:

$$\begin{aligned} X_k &= X - \sum_{i=1}^k Xw_{(i)}p_{(i)} \\ y_k &= y - \sum_{i=1}^k c_i t_{(i)} \end{aligned}$$

In matrix form, we can express the score $t_{(j)}$ as function of the previous deflation steps of X :

$$t_{(j)} = X_{j-1}w_{(j)} = Xw_{(j)}^*$$

We can define, at this point, a matrix W_* representing the projection of the input variables onto a reduced dimensional space. The matrix W_* will be obtained by [Manne, 1987a]:

$$W_* = W(P^T W)^{-1}$$

Where $W = [w_{(1)}, \dots, w_{(h)}]$ and $P = [p_{(1)}^T, \dots, p_{(h)}^T]$. If we want to represent the modes, we analyze the matrix W_* , i.e. the projection of the original input space onto the reduced-order space of the principal components. In this matrix, each i -th column represents the projection of the original space on the i -th component.

In parallel, we compute the loading matrix $Q = [q_{(1)}^T, \dots, q_{(h)}^T]$, where each $q_{(i)}$ is obtained via the product $q_{(i)} = y^T t_{k(i)}$. If y is 1-dimensional, each $q_{(i)}$ will be a scalar and Q will be a vector. Finally, the coefficient matrix \tilde{B} and the intercept \tilde{B}_0 are obtained by:

$$\tilde{B} = W_* Q \quad \tilde{B}_0 = q_{(1)} - p_{(1)}^T \tilde{B}$$

These terms give the linear relation between inputs X and outputs y . The approximation via PLS \hat{y} related to the true output y will be given by:

$$\hat{y} = X \tilde{B} + \tilde{B}_0$$

For the generation of a surrogate model, it is common practice to split the data set into two non-overlapping subsets: the model is trained on a *training set*, while the rest of the dataset is used as a *testing set* to evaluate the performance of the approximation. To evaluate the accuracy of the PLS model, we will make use of the R^2 score. This is defined as:

$$R^2 = 1 - \frac{\sum_i^N [(\hat{y}_i - y_i)^2]}{\sum_i^N [(y_i - \bar{y})^2]}$$

Where N is the number of samples, y_i represent the real outputs (which we want to approximate), \bar{y} is the mean of all y_i , and \hat{y}_i are the approximations via PLS of the R^2 score generally tends to increase, in PLS, when more components are added. Therefore, in the following analyses, will fix the number of components as the minimum which provides a sufficiently large R^2 score on the available testing dataset.

3.3.3 Application on H2H: coupon 1x2

We consider a Design of Experiments (DoE) of 200 points with misalignments expressed in terms of absolute deviations from theoretical positions (as in Fig. 3.2).

The first point to analyze is the relationship between outputs. These are constituted by the ordered vector of:

- Bearing force on the first hole of the first plate
- Bearing force on the second hole of the first plate
- Bearing force on the first hole of the second plate
- Bearing force on the second hole of the second plate

By performing a PCA on these four ordered bearing loads, we found that a single component can explain 99.7% of the overall variance of the four ordered outputs. The component to take into account can be represented by the vector:

$$w_{(1)} = [0.5, -0.5, -0.5, 0.5]$$

This can be actually interpreted physically by considering two phenomena: in each plate the sum of the transmitted loads should be equal to the total load which is applied;

moreover, at each section, the balance of efforts should be zero to be in an equilibrium condition.

A second step is needed to retrieve the patterns of inputs that affect the responses. In this case, PCA with mixed inputs and outputs gives the same results than PLS regression between inputs and outputs due to the fact that the amount of variance due to the outputs is similar to the one due to the inputs (allowing PCA to provide an approximation as accurate as the one provided by PLS). This is actually more an exception than a rule: generally to find relations between inputs and outputs it is preferable to rely on supervised techniques, such as PLS.

The outputs will be indexed as for the previous analysis, while the inputs are expressed in cartesian coordinates: X_{ij} represents the longitudinal deviation, parallel to applied load vector, related to the j -th hole of the i -th plate; on the other hand, Y_{ij} represent the analogue on the transverse deviation, orthogonal to the applied load vector. The inputs are ordered as follows:

- Deviation x of the first hole of first plate X_{11}
- Deviation x of the second hole of the first plate X_{12}
- Deviation x of the first hole of second plate X_{21}
- Deviation x of the second hole of the second plate X_{22}
- Deviation y of the first hole of first plate Y_{11}
- Deviation y of the second hole of the first plate Y_{12}
- Deviation y of the first hole of second plate Y_{21}
- Deviation y of the second hole of the second plate Y_{22}

Considering PLS notation, we found that a single component could achieve a precision of $R^2 = 0.996$. It can be represented by the vector:

$$w_* = [0.5, -0.5, -0.5, 0.5, 0, 0, 0, 0]$$

Graphically, it can be illustrated on the simple plot in Fig. 3.5. The information that we can extract is the fact that transversal misalignments have no effects on the bearing loads at any location. On the other hand, the only important contribution is given by the relative displacements on the longitudinal axis, with the two holes in phase opposition.

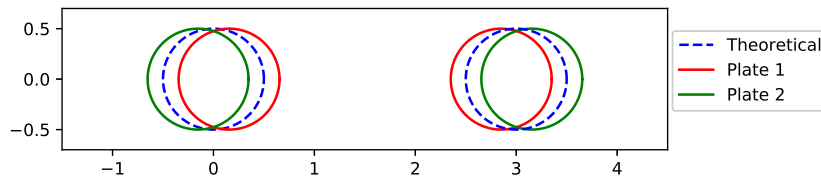


Figure 3.5: Schematic diagram of the first component in PLS analysis on coupon 1x2

We can re-interpret these conclusions as the possibility to concentrate the whole variability on the holes of one plate: this can be done if a previous simple UQ&M analysis is done to understand the PDF of the concentrated misalignment variable (for a difference of two statistical variables, the resulting PDF will be simply given by the convolution of the two original PDFs). Moreover, one can think of splitting the relative misalignment in two halves and assigning each half deviation to the two plates.

3.3.4 Application on H2H: coupon 1x5

In this part, we seek to determine on a coupon with bolting pattern 1x5 the patterns of inputs allowing to explain the impact on the output responses, i.e. determining the relevant input modes. Originally, 20 inputs related to the longitudinal and transversal misalignments on the 10 holes are defined: consistently with the notation introduced in Fig. 3.2, we define the X_{ij}, Y_{ij} related to each plate i (so $i = 1, 2$) and the hole j ($j = 1, \dots, 5$). The output responses which are retained are the bearing load magnitudes at every hole of the structure, denoted as $S_{i,j}$. To improve the readability, in the following illustrations of the present chapter we add a P before the index i related to the plate and F before the index j related to the hole (i.e. fastener) location.

During the analysis of the obtained outputs, we encountered some difficulties related to the modal description. In particular, both PCA and PLS being linear approximations, the points with unloaded locations can constitute a huge obstacle for the regression analysis (as the response would go to zero on several locations at a large number of exploration points in the DoE). Therefore, to enforce the contacts, we introduced (specifically for the analyses of this section) an input force which was far superior to the nominal allowed values predicted by the Airbus stress analysis tool ISAMI (*Improved Structural Analysis through Multidisciplinary Integration*) [Grihon et al., 2009, Grihon, 2018] on the reference configuration (in particular, we tripled the limit force value coming from ISAMI for $t/d = 0.25$). In practice, this choice simplifies the description of the relationship between low bearing loads and input misalignments, improving the overall knowledge of the global behavior of the system. For linear materials, this load level would correspond in fact to the load which would be coherent for an equivalent structure with triple ratio t/d : therefore, as the t/d only affects the structural strength and the failure mechanism, the obtained surrogate models are numerically consistent for coupons with high t/d levels. However, the conclusions can be also applied to the assemblies with thinner plates (i.e. lower t/d) if keeping the assumption of linear elastic materials.

In the analyses presented in this section, we use a DoE with 900 points.

3.3.4.1 PCA on outputs

In a first step, we apply PCA exclusively to the output bearing forces $S_{i,j}$ of the H2H coupon 1x5. We found that we can express the whole variability (99.8% of the whole variance) through 4 principal components (i.e. 4 PCA modes). This can be justified as for the coupon 1x2: in every plate, the sum of transmitted loads should be equal to the applied load (reduced by the amount of force transmitted by friction), reducing to 4 main responses per plate; on the other hand, at every section, the free-body diagram should give a null sum of forces, making it possible to deduce the load transmitted on the second plate based on the load transmitted by the first one. The former is issued from the principle of forces equilibrium at *plate* level, while the latter stems from the principle of the forces equilibrium at *bolt* level.

In order to graphically illustrate the contributions of the different outputs on the principal components, we make use of a representation by pixels of the components matrix W . In particular, we build a matrix with all the retained components $w_{(k)}$, where the rows represent the components and each column is related to a different variable (in this case each bearing output): therefore, what will be represented is the matrix W^T .

To distinguish the relevant from secondary effects, we impose a threshold of 5% of the maximum absolute value in the matrix W^T : for the values of W^T below this limit, we associate an adjusted value equal to 0; for the values above, we associate a 1. The choice of the value 5% for the threshold is an assumption of our analysis. The resulting application of this threshold onto the upper-mentioned matrix W^T will be graphically represented via a *spy* matrix, i.e. a pixelated plot reporting as white pixels the zeros and as black pixels the ones. The result will be a sort of a QR code, with the original variables in the columns and the modes in the rows.

Results are shown in form of a spy matrix plot in Fig. 3.6, reporting in the rows the components and in the columns the outputs. The first five outputs are the bearing forced $S_{1,j}$, related to the holes of the first plate, while the last five are the $S_{2,j}$, associated to the holes of the second plate.

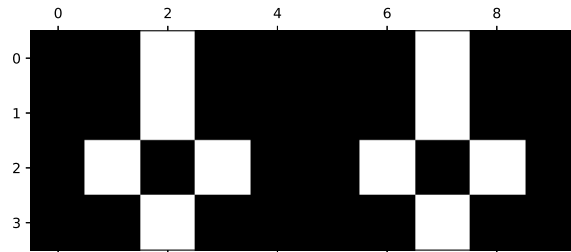


Figure 3.6: Spy matrix plot of the four modes obtained for all output responses through PCA for coupon 1x5 (threshold 0.05)

The force equilibrium at bolts level can be graphically illustrated by the fact that we can superpose the left and the right half (associated to respectively the bearing forces B_{1j} on the first plate and B_{2j} on the second plate) of the plot in Fig. 3.6. Therefore, for a coupon 1x5, four outputs are sufficient to describe the outcomes of the structure.

3.3.4.2 PCA on inputs-outputs

At this point, we apply PCA to the ensemble of input misalignments X_{ij}, Y_{ij} and output bearing forces S_{ij} of the H2H coupon with bolting pattern 1x5. For this application, the data matrix is obtained by stacking horizontally the columns of inputs and outputs:

$$X = [X_{1j}, X_{2j}, Y_{1j}, Y_{2j}, S_{1j}, S_{2j}]$$

As a reminder, before starting any PCA, scaling is needed to center and normalize the relative dimensions between data and assign the same variance to every variable.

We applied the same PCA training procedure depicted in Section 3.3.1 and the graphical representation illustrated in Section 3.3.4.1. In Fig. 3.7a we report the spy matrix plot, where the rows represent the different components and in the columns we report the original variables, namely the input misalignments and the output bearing forces, stacked per columns.

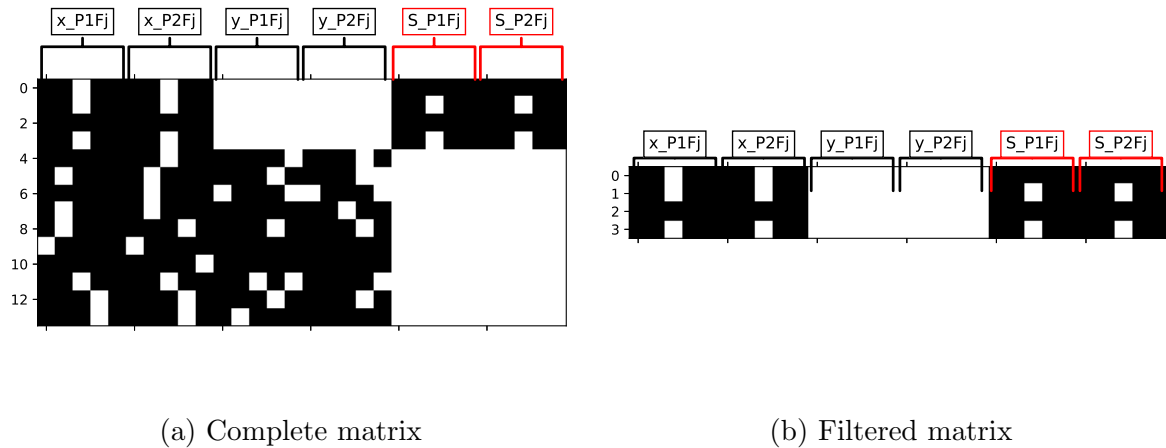


Figure 3.7: Spy matrix plots of the modes obtained for all output responses through PCA for coupon 1x5 (threshold 0.05)

From Fig. 3.7a, we filter only the modes able to describe the relation between inputs and outputs: therefore, we look for modes (in the rows) which have contributions from both input misalignments and output bearing forces. In particular, a specific mode (i.e. a specific row in the *spy* plot) is retained if there is at least one black pixel (i.e. a non-null term in the matrix W^T) in any column related to an output. The results of the application of this filtering on the matrix W^T (related to the H2H coupon 1x5) are depicted in Fig. 3.7b. From our analysis, we obtained that four modes were sufficient to describe the relation between the two groups. However, it should be noted that these first four components represent just 45% of the whole variance of the complete data matrix.

It is worth noticing that the threshold (and the corresponding black-white spy representation) is only used to determine the number of components which are actually needed. Once the selection of the modes is done, the modes themselves will be represented on the original coordinate space to understand the relations between inputs that impact the responses. These modes will be represented without applying any further threshold. The related components are depicted in Fig. 3.8.

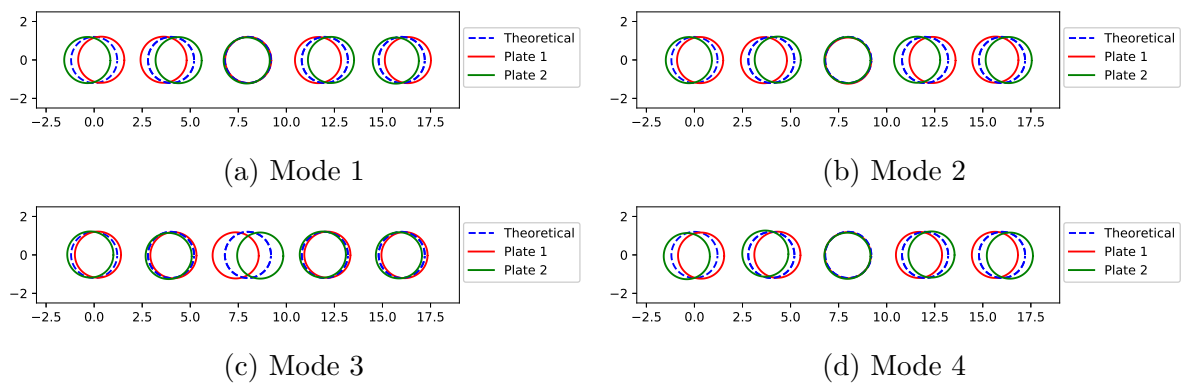


Figure 3.8: First four modes obtained through PCA for coupon 1x5

From the plots in Fig. 3.8, we can state that the only contributions to the output variability is due to the longitudinal deviations on both plates. Moreover, the modes

are symmetrical with respect to the central hole: this is explained by the symmetry of the coupon itself and the related free body diagram. It can be also observed that the deviation coordinates on the central hole only marginally interact with the other holes in the third mode. The lateral hole deviations interact with each other in all other modes: these can be considered as linear combinations of the single mode retrieved for the coupon 1x2 (see Fig. 3.5).

From a qualitative point of view the results of PCA are consistent with the physical phenomena intervening on the tested coupon 1x5. However, we need to check also the convergence of the algorithm itself: to this aim, we consider different trainings of the PCA model with progressively increasing sample sizes (always extracted without replacement from the original dataset with 900 points) and we compute the associated eigenvalues $\lambda_{(k)}$ and components $w_{(k)}$.

At this point, we can evaluate the evolution of the outcomes of the eigenvalues vector $\lambda = [\lambda_{(1)}, \dots, \lambda_{(h)}]$ and the component matrix $W = [w_{(1)}, \dots, w_{(h)}]$ as a function of the sample size. In particular, we define two errors:

$$\begin{aligned} Err_{\lambda} &= \frac{\|\lambda_i - \lambda_N\|_2}{\|\lambda_N\|_2} \\ Err_W &= \frac{\| |W_i| - |W_N| \|_2}{\|W_N\|_2} \end{aligned} \quad (3.1)$$

Where $\|\cdot\|_2$ indicates the euclidean L^2 norm, λ_i (respectively W_i) represents the eigenvalue vector λ (respectively the eigenvector matrix W) computed with a sample of size i . These are compared with the reference values, namely λ_N and W_N , obtained with the complete dataset of size $N = 900$. We remark that, being the sign of components $w_{(k)}$ arbitrary for PCA, the absolute values $|w_{(k)}|$ are considered. In Fig. 3.9, we plot the evolution of the errors Err_{λ} and Err_W (from Eq. 3.1), expressed in percentages.

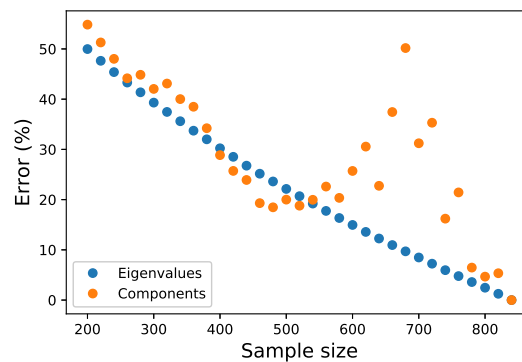


Figure 3.9: Convergence plot for the first four modes obtained through PCA for coupon 1x5

From the convergence plot in Fig. 3.9, one can notice that the eigenvalues of the modes converge quite well with the increase in the number of samples, but the components have a difficult convergence and present high variations also in the region between 650 and 750 points (which are relatively close to the size of the reference population with 900 samples).

Moreover, there is an unbalance in variances given to inputs and outputs, due to the relative numbers (20 inputs and 4 outputs). Therefore, the algorithm is capable of individuating some relations in the first components but which are not clear, as the main purpose of PCA is to explain the variance of the whole data. In practice, the algorithm seeks to explain the greatest possible amount of variance: however, due to the fact that most of the variance comes from the inputs (re-scaled in the standard space), the outcomes cannot be considered as conclusive.

The unbalance in the variance sources and the difficult convergence are in fact connected to each other. The variance unbalance causes parasite modes, leading to a slow and irregular convergence of principal components.

3.3.4.3 PLS regression between inputs and reduced outputs

In order to seek to alleviate the issues retrieved in the previous section, we repeat a similar analysis through PLS. In a first trial, we apply it to retrieve the link between the input geometrical misalignments and the bearing outputs reduced via PCA. The obtained components are depicted in Fig. 3.10. This time, it is possible to draw some conclusions on the patterns followed by the inputs to impact the outputs. The overall score is $R^2 = 0.97$. At a first glance, it is visible that all deviations are symmetrical for the first and the second plate, leading to the idea that relative displacements are sufficient to explain the outcomes of the system. On top of that, there is no effect of transversal misalignments: therefore, the only contribution is due to the relative longitudinal deviations.

Moreover, we can see that there is the combination of several couplings of mutual displacements between all holes. It is worth noting that increasing the number of components does not allow any further improvement in the R^2 score.

Looking more carefully at the modes, the contribution of every hole deviation is not exactly the same in every mode, making appear in the principal components first and second order contributions: from a graphical point of view this can be observed, for example, by comparing the effect on the first mode of the misalignments of the second hole (first order contribution) with the effect of the third hole (second order contribution). At a global level, we can recognize a symmetric pattern (around central hole) only for the third and the fourth components. However, the linear combination of all modes gives symmetrical patterns around the central hole, which can be observed on the illustration in Fig. 3.11 of the coefficient matrix \tilde{B} of the PLS surrogate model: these latter are very similar to the modes retrieved via PCA in Fig. 3.8. Once again, the symmetry around the central hole can be explained by the physical symmetry of the free-body diagram of the structure itself.

3.3.4.4 PLS regression between inputs and original outputs

In a second investigation, we apply the PLS directly on the inputs and original outputs, instead of the PCA outputs. The related modes, which are depicted in 3.12, are similar to the modes observed for PCA (see Fig. 3.8) and the graphical representation of the coefficient matrix obtained through PLS on reduced outputs 3.11. Therefore, we confirm here that it is possible to obtain an efficient modal description by applying the PLS procedure directly on the original sets of inputs and outputs, without passing through output reduction via PCA.

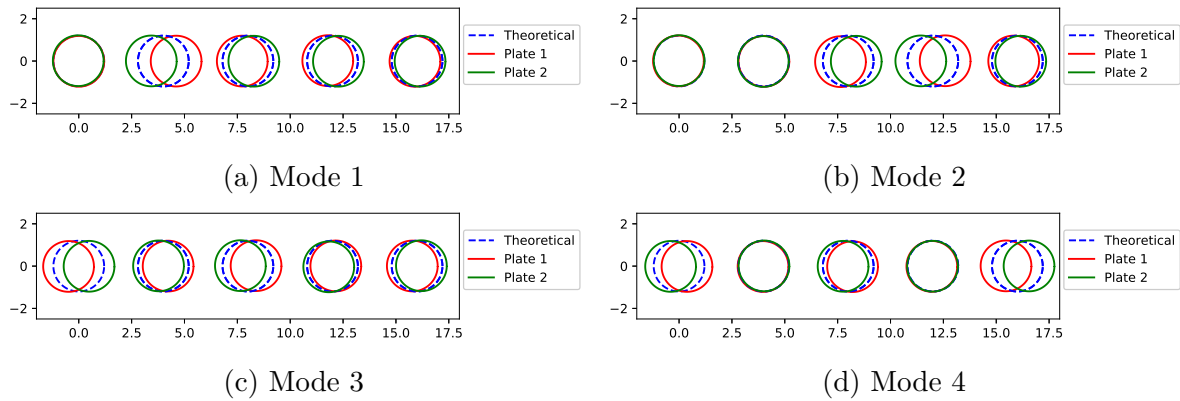


Figure 3.10: First four modes obtained through PLS on reduced outputs (from PCA) for coupon 1x5

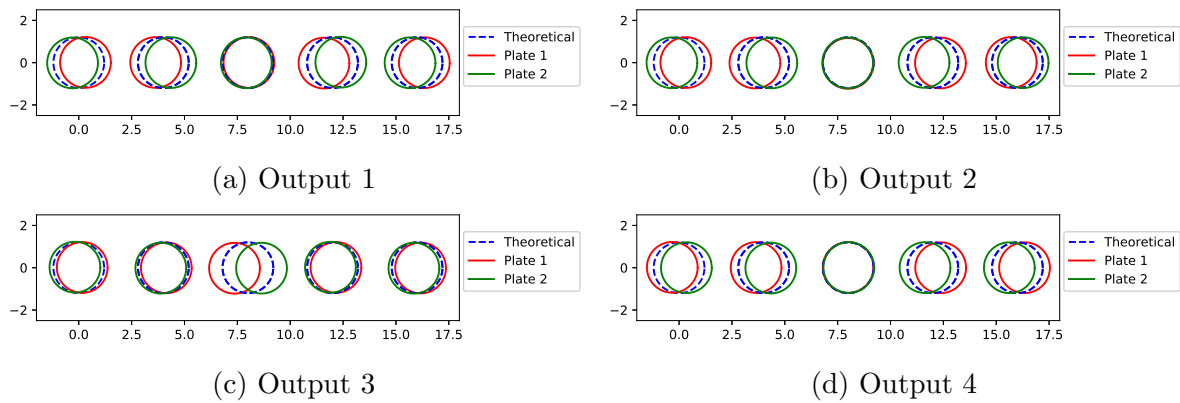


Figure 3.11: Graphical representation of coefficient matrix obtained through PLS on reduced outputs (from PCA) for coupon 1x5

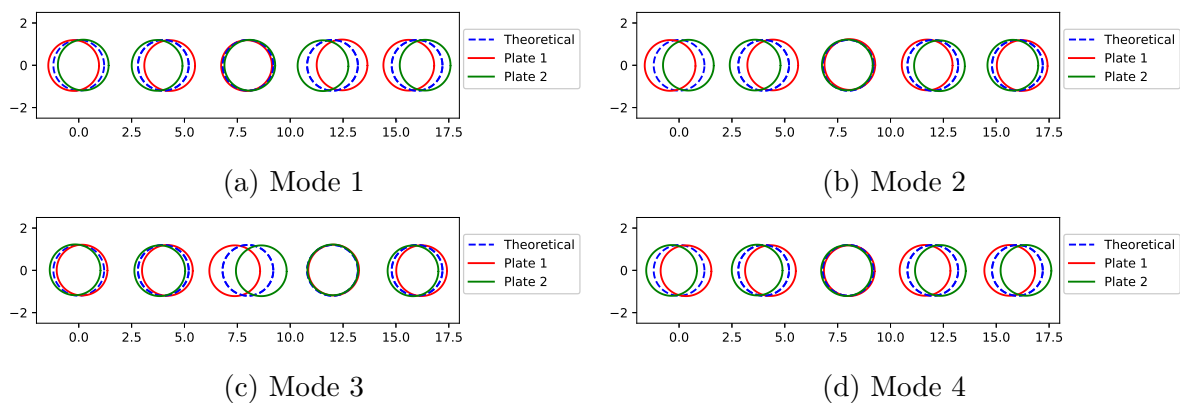


Figure 3.12: First four modes obtained through PLS for coupon 1x5

Focusing on the linear coefficients matrix \tilde{B} retrieved for this second application of PLS (reported in Fig. 3.13), it can be observed that the transferred bearing related to the i -th hole and the j -th plate is principally affected by the relative longitudinal misalignments of the same hole. A secondary effect is given by the relative longitudinal

misalignments of the adjacent holes. Moreover, the response on the same hole must be the same on both plates as the force equilibrium must be ensured at every location: the PLS surrogate model identifies the same relation between inputs and outputs, attenuating the noise in the finite element analyses.

At a global level, we may interpret the coefficients illustrated in Fig. 3.13 as linear combinations of the elementary mode retrieved on the coupon 1x2 (in Fig. 3.5): the modes can be interpreted as the collection of all combinations of couples of relative misalignments between the hole location where the bearing is measured (or better, computed) and other distinct hole locations (i.e. applying the elementary mode associated to the coupon 1x2 on the first and second hole, first and third hole, etc.); the coefficients of the linear combination will rely on the concept of the distance between each pair of holes. This explains why the most important effect on the bearing force measured at a specific hole location is given by the misalignment on the same hole location, while the relative magnitude effects of other holes decreases while increasing the distance. Moreover, for the bearing on second hole (see Fig. 3.13) the effect of the nearest hole locations, i.e. the first and the third hole, are not symmetrical as there are fewer holes on the left of the second hole (with respect to the right side), leading to higher effects due to the first hole. The same conclusion can be extended to the opposite case of the fourth hole. We will make use of this interpretation also on the coupon with bolting pattern 3x5 to explain the outcomes of the related PLS analysis.

Finally, in Fig. 3.14 the convergence plots on R^2 score and component matrix W_* (from Eq. 3.1) are illustrated, as function of the sample size. For both, we have a regular convergence with the increase of number of samples. Only one convergence plot is reported for the two applications of PLS, as results are very close. By comparing Fig. 3.14 with Fig. 3.9, we can state that we can rely more on PLS than PCA to find the patterns defining the relationship between inputs and outputs, with a given size of the DoE (i.e. with a given number of simulations of the complete model).

To sum-up, the results given for coupon 1x5 prove that the PLS procedure can be used directly on the original inputs and outputs to retrieve a linear relationship between them. Moreover, the effect of geometrical misalignments on the bearing load at every location can be equivalently described by introducing only the relative longitudinal (i.e. parallel to the direction of the applied load) misalignments coordinates. This transformation allows to reduce by 75% the number of inputs in the original problem.

3.3.5 Application on H2H: coupon 3x5

In this section we present results for the largest coupon assembly considered in this work, namely the bolting pattern 3x5, i.e. characterized by 5 rows of bolts in the longitudinal axis (parallel to the direction of the applied load) and 3 rows of bolts in the transversal axis (perpendicular to the direction of the applied load).

A DoE of 1000 simulations was used for this 3x5 coupon. The same difficulties concerning the applied load level that were encountered in the previous case were still found, and the same countermeasures as before were applied (the applied load level was tripled with respect to the load level retrieved in ISAMI).

From a qualitative point of view, only relative longitudinal misalignments were necessary to explain the impact on bearing response. However, the analysis did not give

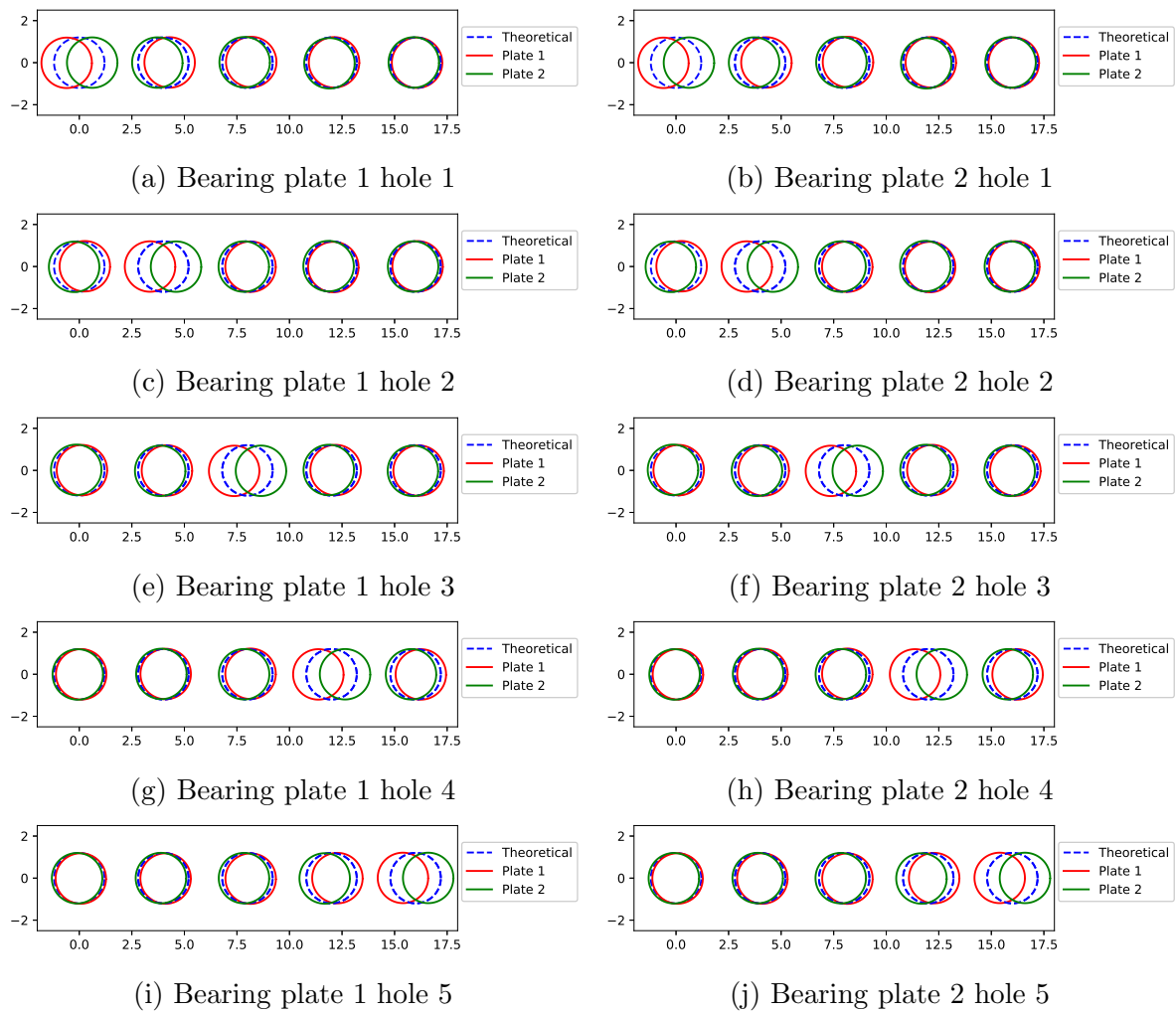


Figure 3.13: Graphical representation of coefficient matrix obtained through PLS for coupon 1x5

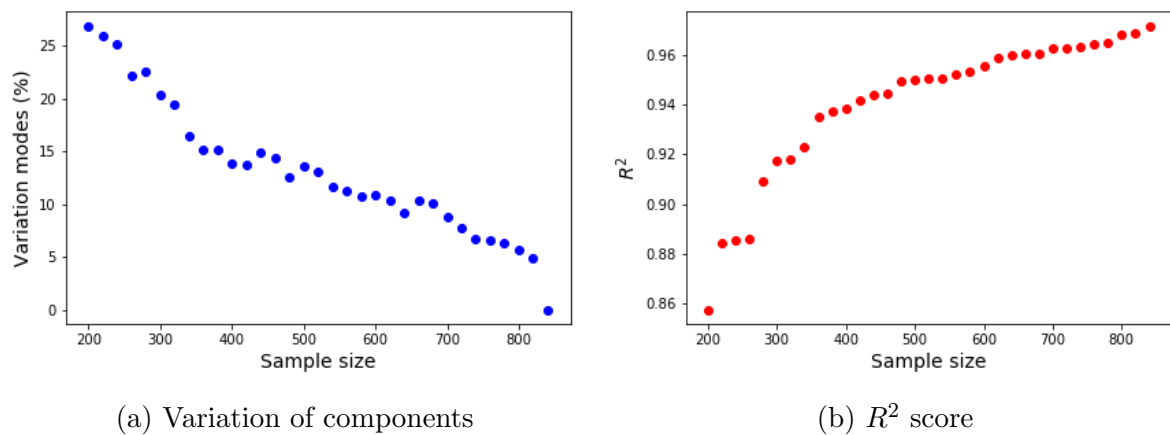


Figure 3.14: Convergence plots for the first four modes obtained through PLS for coupon 1x5

conclusive quantitative results when training all outputs in the same multi-output PLS surrogate model: we achieved a score $R^2 \approx 0.9$, but 14 components (out of 15 relative longitudinal misalignments) were necessary. Therefore, our conclusion is that the returns in terms of dimensionality reduction significantly diminish given the increasing computational cost for more complex bolting patterns. Still, the consideration of only adopting relative longitudinal misalignments is always valid on the coupons loaded with uni-axial longitudinal load and already allows to strongly reduce the input dimensionality.

Finally, we trained every output (bearing transmitted forces on every bolt location) separately and obtained 15 surrogate models. We noticed that for all outputs only one principal component was required to achieve a $R^2 \geq 0.99$: in particular, for such responses, the most important effect was given by the relative longitudinal misalignment at the same bolt location of the considered response, as happened for coupon 1x5 (confront Fig. 3.13), with secondary effects provided by the adjacent holes deviations. The graphical illustration of the coefficient matrix \tilde{B} are reported in Fig. 3.15.

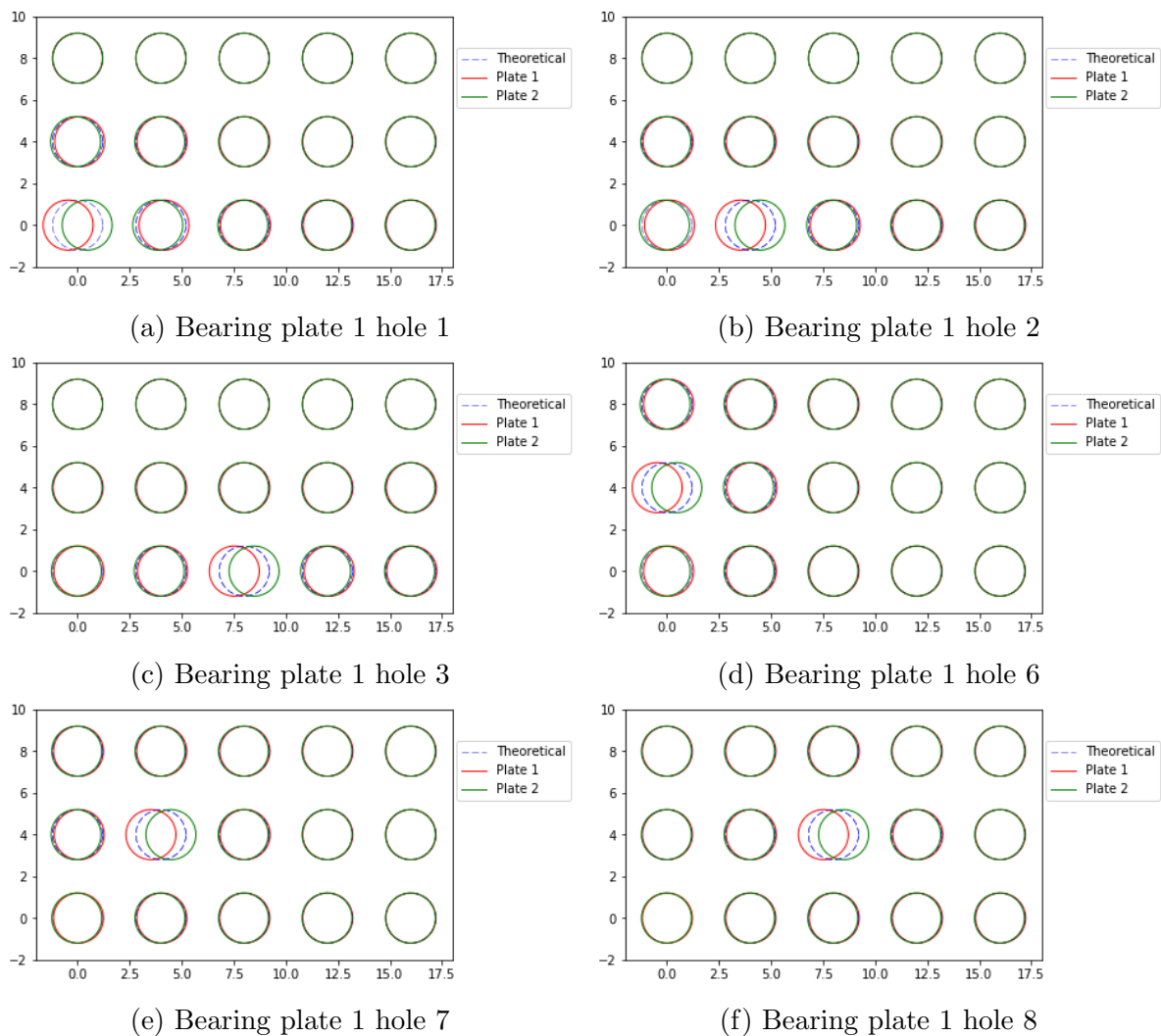


Figure 3.15: Graphical representation of coefficient matrix obtained through PLS for coupon 3x5

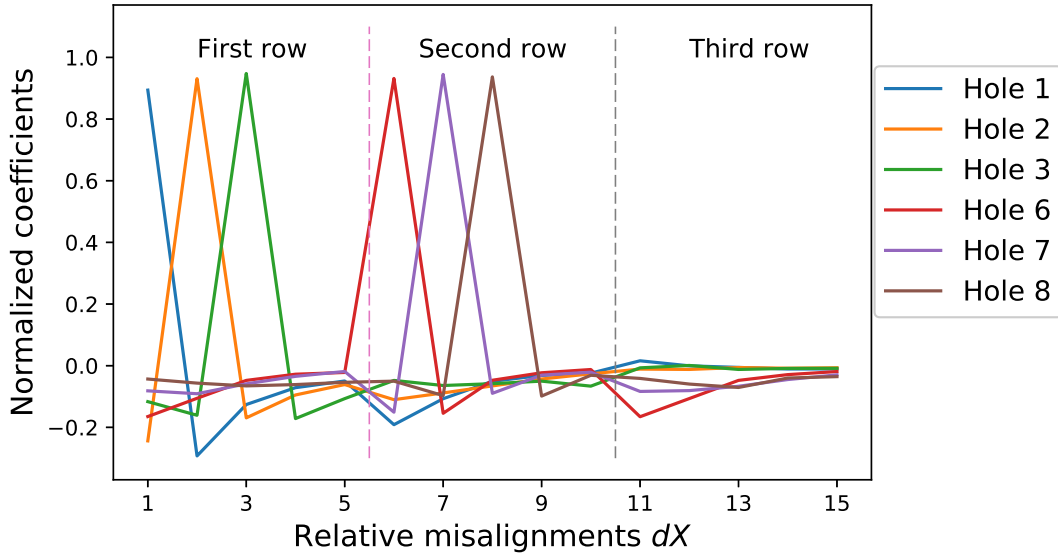


Figure 3.16: Coefficients of transferred bearing load forces retrieved through PLS expressed as function of the relative longitudinal misalignments on different bolt locations for coupon 3x5

At first sight, it could seem that the only relevant contribution to the bearing force transmission on the j -th hole is given by the relative longitudinal misalignments dX on the j -th hole itself (i.e. dX_j). However, the representation in Fig. 3.15 does not allow to appreciate the other contributions. In fact, we must think that the sum of all coefficients in the relation between bearing force and all dX_j must be zero. The same increase in the bearing force on the j -th hole is due to an early contact between the hole surface and the bolt on the j -th hole itself: but this can happen either if the j -th hole is drilled too much on the right (thus anticipating the contact on the same hole), but also if all other holes are drilled too much on the left (thus delaying the contact on the other holes). Therefore, we represent the coefficients of the matrix B of PLS surrogate model in Fig. 3.16: in particular, we re-interpret the input variables by considering the relative longitudinal misalignments dX_j associated to each hole (thus $j = 1, \dots, 15$). In the plot we also distinguish the three rows of the bolting pattern 3x5. We obtain an extension of the results retrieved for the coupon 1x5: the coefficients B (linking the bearing on the j -th hole and the misalignments) are then given by the linear combination of dX_j and of dX_k (with $k \neq j$, thus 14 couples overall), where the k -th coefficients are decreasing function of the distance between the hole locations j and k . As the dimension increases (with respect to the coupon 1x5), we will observe also an increase in the difference between the effects on the bearing on the j -th hole due to dX_j and dX_k (with $k \neq j$), as the term dX_j appears in all of the 14 couples (compared to 4 couples in the coupon 1x5). The effects of the k hole misalignment can be neglected when the j -th and the k -th hole locations are not adjacent. However, being the bolting pattern constituted by several rows, we have not only the effect of the adjacent holes on the same row (i.e. $k = j \pm 1$), but also on the adjacent holes on the same column (i.e. $k = j \pm 5$).

The PLS metamodells retrieved in this section will be used in the next chapter for statistical analyses.

In future works, further investigations are previewed to find a common thread linking all the obtained surrogate models. This can help to generalize the results for bolting patterns which are not explored in our analyses yet.

3.3.6 Implications on further statistical analyses

Up to this point, we observed that the only factor for load re-distribution in H2H applications are the relative longitudinal misalignments dX_j of each hole j . Now we raise the following question: *should we always neglect all transversal misalignments dY_j in all successive statistical analyses?*

To provide an answer, we support our reasoning through the illustrations in Fig. 3.17.

We consider a single hole, denoting with dX and dY respectively the relative longitudinal and relative transversal misalignments on this hole. Let us suppose that both dX and dY are initially described by uniform distributions on an interval $\pm\bar{R}$, where $2\bar{R}$ represents the total clearance of the hole (i.e. the difference between the diameter of the hole and the diameter of the bolt). We start by sampling dX and dY : in Fig. 3.17a, we represent the samples on the dX - dY plan, while in Fig. 3.17b we extract the marginal PDF of the dX samples.

Now, if we impose $dY = 0$, the samples related to the relative longitudinal variable dX would lie on a segment delimited by $\pm\bar{R}$, as in Fig. 3.17c: this would not affect the marginal distribution of the samples dX (as shown in Fig. 3.17d).

At this point, we consider a real constraint: we need to ensure that we are capable of inserting a bolt inside this hole. We can impose a *tolerance acceptance criterion* expressing this capability: this would lead to define a requirement on the hole misalignments, of the form $dX^2 + dY^2 \leq \bar{R}^2$. If we applied this constraint, together with imposing $dY = 0$, the results from Figs. 3.17c-d, would not be impacted: the samples dX would still be described by a uniform distribution on the interval $\pm\bar{R}$. In fact, the points in Fig. 3.17c already lie on a segment delimited by $\pm\bar{R}$, so none of these samples would be excluded from this population by the introduction of the upper-mentioned tolerance acceptance criterion.

If we do not impose $dY = 0$ but we add the tolerance acceptance criterion $dX^2 + dY^2 \leq \bar{R}^2$, the samples related to the relative deviations dX and dY will cover a circular area in the plane dX - dY of radius \bar{R} : this leads to exclude some samples with high absolute values of dX , as can be observed from Figs. 3.17e-f.

Consequently, the presence of non-zero samples dY allows, in combination with a tolerance acceptance criterion, to exclude a portion of the samples dX which exhibit the highest absolute values. From the PLS analysis, we saw that the output bearing forces are only driven by the dX : therefore, the most detrimental realizations would be exactly the ones characterized by the highest $|dX|$. As a final result, the variability of the transferred bearing loads would be reduced if we reduced the variability of the $|dX|$: and this is exactly what the introduction of the tolerance acceptance criterion can do, if there are also non-zeros dY samples. Therefore, if we aim at reducing the variability of the loads, it is in our best interest to take into account, in our upcoming statistical applications, also the presence of transversal misalignments.

We can thus say that, even if at a stress level they do not affect directly the bearing load transmission, the transversal misalignments should be considered for further

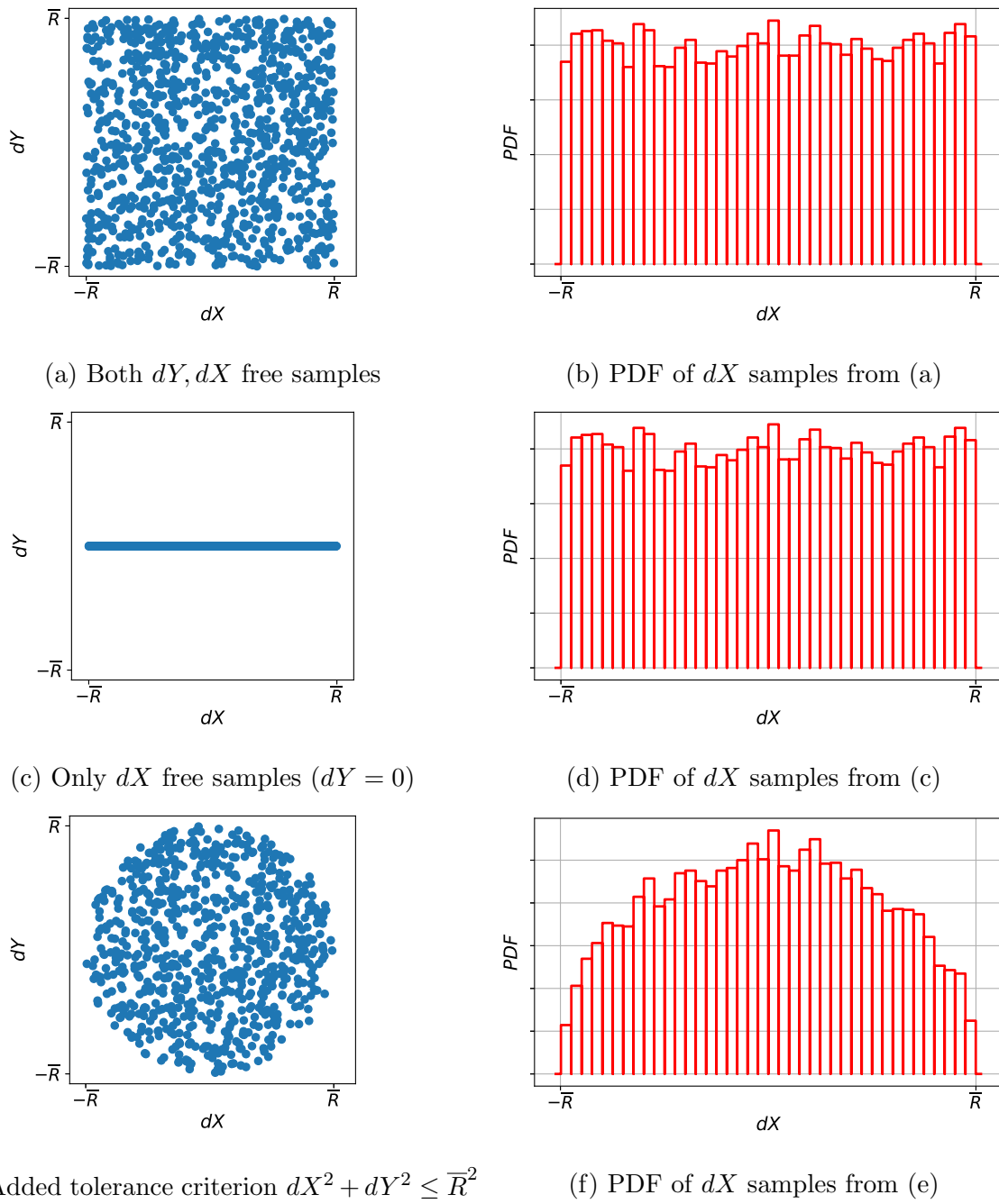


Figure 3.17: Illustration of the benefits of adding transversal misalignment samples in presence of a tolerance acceptance criterion

statistical studies when a coupling with tolerancing concepts is presented.

3.4 Screening

Screening procedures are often used to define a hierarchy in the effects of input variables on a given response, with the final goal of neglecting the inputs only marginally affecting

the output response [Campolongo et al., 2011, Montgomery, 2017].

Screening techniques are part of a larger framework, the sensitivity analysis [Brévault et al., 2013, Spagnol et al., 2019] [Iooss and Lemaître, 2015, Borgonovo and Plischke, 2016]. A general overview of the methods available in literature are depicted in Fig. 3.18 (from [Iooss and Lemaître, 2015]) and regrouped according to the number of model evaluations and the complexity of the model itself. In the sensitivity analysis framework, we find the screening and the variance decomposition techniques (the latter are not considered in this work).

A number of approaches used for screening come from 2^k *Factorial Designs* [Montgomery, 2017], based on the assumption of monotonicity of the output with respect to input variables and taking into account only the extreme values of inputs variabilities. Several evolutions, named *Fractional Factorial Designs* [Box and Hunter, 1961, Gunst and Mason, 2009], are based on additional simplifying assumptions on the possibility to *alias* (i.e. confuse the effects in the same quantity) different interaction terms: in RIII designs, the first-order interactions are aliased (i.e. resumed in the same equivalent quantity) with each other; in RIV designs, the first and second-order interaction terms are aliased; in RV, the second-order interactions are aliased with each other.

In this work, we focus on metamodel-based screening approaches. We make the assumption that in the region of interest the model is monotonic with respect to the input variables and there are first-order interactions we need to identify, while second-order interactions can be neglected.

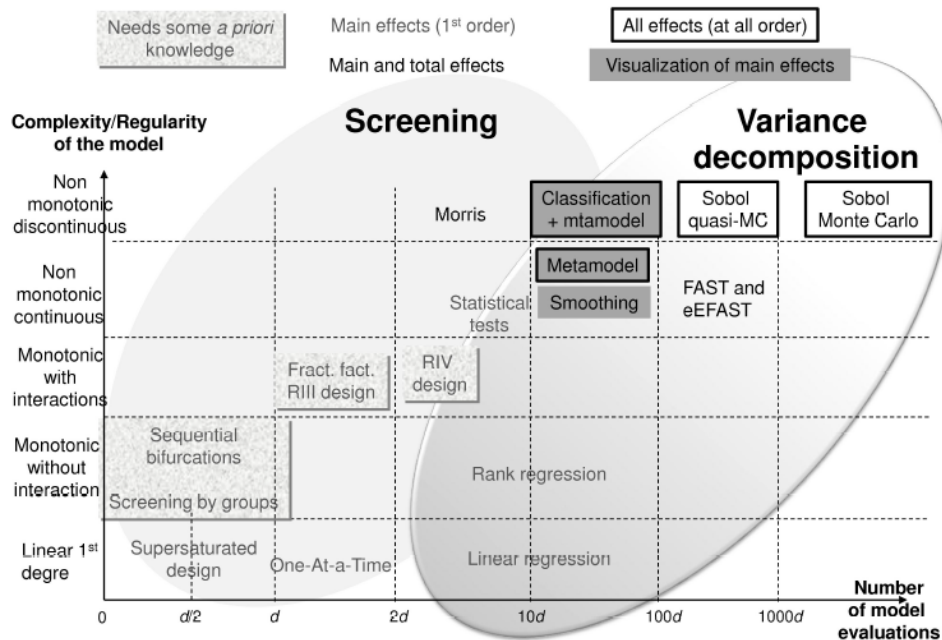


Figure 3.18: Graphical synthesis of sensitivity analysis methods (Source: [Iooss and Lemaître, 2015])

The input dimensionality reduction via screening typically has the following goals:

1. Delete inputs which only marginally affect the response;
2. Separate effects of inputs that can be superposed.

The first goal is addressed in Section 3.4.1 and the second in Section 3.4.2. The applications of both parts on two H2H coupons are reported in Sections 3.4.4 and 3.4.5.

3.4.1 Metamodel-based Screening

The main features characterizing this category of methods are highlighted in [Iooss and Lemaître, 2015]:

- the choice of a Design of Experiments (DoE), with the specific required qualities, like robustness, space filling property and low cost of construction;
- the choice of the surrogate model, affecting the minimum number of simulations required for training and the choice of a specific DoE as well;
- the validation of the surrogate model.

Several methods are available in the literature to create a Design of Experiments (DoE) to evaluate the response of a system [Ilzarbe et al., 2008, Durakovic, 2017]: from factorial designs, to robustness tests, to space-filling DoE [Viana, 2016]. We will focus on this latter, as it allows us to reduce the number of simulations of the virtual model to explore the full input domain. Among the different types of space-filling DoE, we choose an Hammersley DoE, which is provided by the Hyperstudy tool [Engineering, 2017].

After launching the analysis on the upper-mentioned DoE, we approximate the responses via a mixed effect linear model, the equation of which is given below:

$$y = a_0 + \sum_{i=1}^N a_i x_i + \sum_{j=1}^N \sum_{i=j+1}^N b_{ij} x_i x_j$$

Where the x represent the inputs, N the number of inputs, a_0 the intercept, a_i the linear effects of the input x_i and b_{ij} the mixed effect term measuring the effect of the interaction between x_i and x_j . The coefficients a_0, a_i, b_{ij} are computed via the least square method. Overall, $N(N+1)/2+1$ coefficients must be trained: several regularization techniques are available in the literature, such as Lasso, Ridge [Melkumova and Shatskikh, 2017] and elastic net [Zou and Hastie, 2005], among the others. It is worth noticing the importance of scaling the input data before the regression step, so that the relative dimensions (and absolute variabilities) do not affect the linear regression coefficients computation.

The scalability of this metamodel-based screening approach with respect to the original input dimensionality does not lie in the training of the surrogate model itself, but rather on the number of points in the DoE to explore the whole domain. Other techniques, like the screening by groups [Watson, 1961], could be preferred when the number of dimensions (and thus the required amount of simulations) makes classical space-filling exploration intractable.

The validation of the obtained surrogate model is done via cross-validation, distinguishing a training and a testing set. In particular, we choose a split between training and testing sets of 90/10.

The main purpose of this section is to eliminate all the inputs which have a minor impact on the output response. To do this, we scale all estimated coefficients with respect to the maximum absolute value (among all coefficients) and then we fix a threshold of 1%: all linear coefficients below this threshold will be neglected and approximated to 0.

At this point, we make use of a matrix representation for the filtered coefficients. We build a square matrix A of size N , indexed per row $i=1,\dots,N$ and per column $j=1,\dots,N$. Every term of this matrix will be defined as:

$$A_{ij} = \begin{cases} a_i & \text{if } i = j \\ b_{ij} & \text{if } i > j \\ b_{ji} & \text{if } i < j \end{cases} \quad (3.2)$$

Therefore, in the main diagonal we find the linear effects and out-of-diagonal terms will represent the interaction effects. In the i -th row we will find all coefficients related to the i -th input, and so for the columns. This matrix will be symmetric per definition, thus it is irrelevant whether we reason in terms of rows or columns. Once this matrix built, we delete every row/column where there are no relevant effects in the whole row/column (based on the 1% threshold).

A graphical representation through *spy* command can help identify the blanks in the matrix, as done previously for the PCA: in fact, relevant effects would be represented as black pixels, while neglectable effects in white (after relative scaling). We can easily visualize the null effects by observing the black/white pattern. If there is a row (respectively a column) which is completely white, we can state that the related variable has only a minor effect on the response itself.

3.4.2 Physics separation

In this part, we focus on separating the effects of input variables which are independent of each other. In practice, we seek groups of variables which interact with each other within the same group but do not exhibit interaction effects with other groups. This is an application of a clustering algorithm, i.e. the part of methods of machine learning aiming at identifying groups and patterns [García-Escudero et al., 2010, Saxena et al., 2017, Ghosal et al., 2020].

To properly identify groups of variables, we seek a block structure in the coefficient matrix retrieved in the previous section. To this purpose, we cluster at the same time rows and columns of the upper-mentioned matrix. The chosen method to perform this task on sparse matrices is the Spectral Co-Clustering [Dhillon, 2001, Von Luxburg, 2007, Govaert and Nadif, 2013]: this assumes the data matrix to have an intrinsic block-diagonal structure. The algorithm is based on singular value decomposition of the data matrix and clustering is then performed on both rows and columns on the transformed space. The number of clusters (i.e. the number of groups of variables) can be identified through the number of relevant non-null eigenvalues: this implies that the separation of the effect of variables can be done if and only if the number of non-null eigenvalues is greater or equal than 2. Further details on the algorithm can be retrieved in Section 3.4.3.

In order to work, the eigenvectors should never be null: this implies that before starting, all rows and columns with all zeros should be deleted before starting the procedure. Therefore, the physics separation process can be started only after having performed the screening part (described in previous section).

Thanks to this separation, different effects of variables can be studied in separated design of experiments, leading to the decomposition of the original problem into multiple

lower dimensional problems. When dealing with repeated statistical analyses, the outputs of non-interacting groups of variables can be sampled separately: this allows to re-use part of the samples (coming from a given group) if only the settings of the other groups are modified.

3.4.3 Spectral Co-clustering

Before starting the spectral co-clustering, an input data matrix A of size $N_X \times N_Y$ is preprocessed via the row sum diagonal matrix $R = R_i = \sum_j A_{ij}$ and the column sum diagonal matrix $C = C_j = \sum_i A_{ij}$ as follows:

$$A_n = R^{-1/2} A C^{-1/2}$$

The preprocessed matrix A_n is then decomposed through a Singular Value Decomposition (SVD):

$$A_n = U \Sigma V^T$$

From this, only the M non-negligible (non-null) eigenvalues in the diagonal matrix Σ and related couples of eigenvectors U, V are retained. This spectral decomposition (hence the "spectral" in the name) provides the partitions of rows (via the left singular vector U) and columns (via the left singular vector V). The partition information are reported on the following matrices:

$$Z_U = R^{-1/2} U \quad Z_V = C^{-1/2} V$$

Then the overall transformed matrix is obtained by stacking vertically the two matrices: $Z = [Z_U; Z_V]$. Here, the first N_X rows of the matrix Z are related to the row partitioning, while the remaining N_Y rows correspond to the column partitioning. The whole Z matrix constitutes the input data for the clustering procedure itself. Here K-Means algorithm is used: this divides the set of $N = N_X + N_Y$ samples Z into K disjoint clusters C_j , each described by the mean (or centroid) μ_j of the samples in each cluster. The objective is to minimize the inertia or "*within-cluster sum-of-squares criterion*", formalized as follows.

$$\sum_{i=0}^N \min_{j \in C} (||z_i - \mu_j||^2)$$

This criterion can be considered as a measure of how internally coherent clusters are. Clustering the whole Z matrix leads to identify clusters for both rows and columns at the same time (from here the appellative "co"-clustering). For a squared symmetric matrix where rows and columns have the same meaning, row- and column-clustering should lead to the same result.

In Fig. 3.19, a simple application on a block-diagonal matrix (with 8 blocks) is presented. It can be observed how the algorithm is particularly useful when the number of involved variables is large, and the re-ordering by hand would be way too challenging.

It is worth noticing that the original (non-shuffled) matrix and the re-ordered one are not exactly coincident, but the block structure is recovered: in fact, the algorithm re-arranges the matrix to identify a block structure, without taking into account the ordering inside the same cluster nor the ordering of the clusters themselves. In our

specific application of the algorithm to retrieve groups of variables interacting with each other (on the output response) but not interacting with variables from other groups, the ordering is not relevant.

Finally, we can generate a cluster plot, assigning a different color to each block of the matrix which is recognized by the co-cluster algorithm to belonging to the same cluster. This is done to graphically illustrate the different blocks: in the generic example depicted in Fig. 3.19, the distinction into eight blocks can be easily recognized.

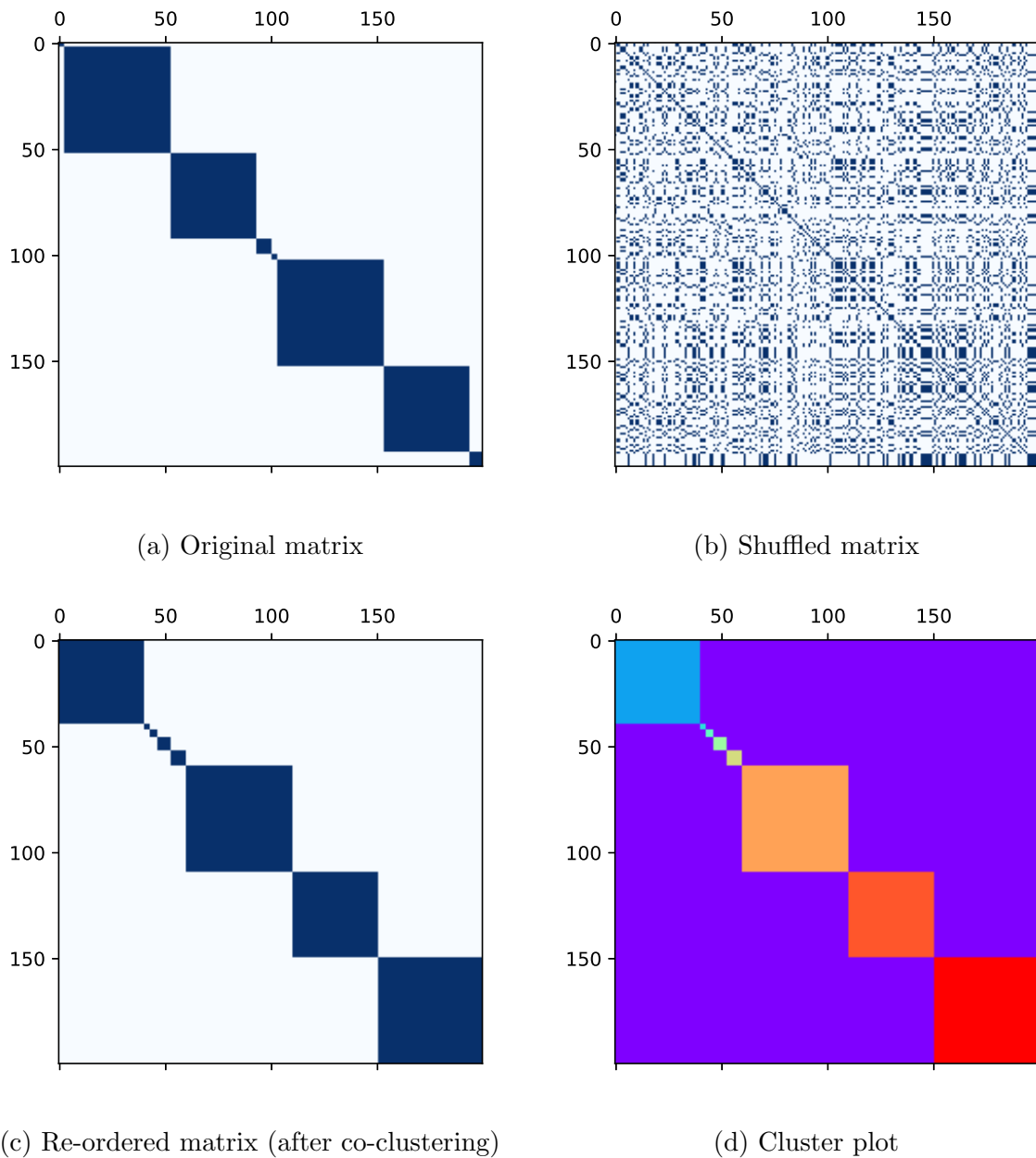


Figure 3.19: Example of physics separation for a 200-dimensional problem

3.4.4 Application to H2H: coupon 1x2

In this part, we investigate the effects of the Young Moduli of plates (E_{P1}, E_{P2} related to the two plates) and fasteners (E_{F1}, E_{F2} for the two fasteners), preload ratios (PLR_1, PLR_2 associated to the two plates) and misalignments. In particular, we considered that the preload ratios and friction coefficient between plates can be aliased (i.e. the individual effects considered as unique), as they both intervene to lower the amount of transmitted efforts via bearing. Regarding the geometrical inputs, we retain the conclusions drawn in the modal description analysis: we use the relative longitudinal misalignments, concentrating all variability on the second plate (hence retaining only X_{P2F1}, X_{P2F2} for the two fasteners locations). By applying the procedure described in Section 3.4.1, we investigated a DoE with 200 points and obtained a linear regression model with $R^2 = 0.989$ and the related spy matrix plot is illustrated in Fig. 3.20.

The results indicate that, apart from misalignments, the only significant variables intervening on the load transmission are the preload ratios of both bolts. The elastic properties of plates and fasteners can be neglected, as they have only a minor effect on the output response. This conclusion will be extended to further coupons. Moreover, on this application case, the physics separation procedure is not useful as no interaction terms are available in the global coefficient matrix.

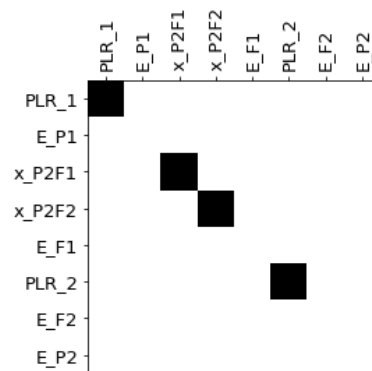


Figure 3.20: Screening spy matrix plot for H2H coupon 1x2

3.4.5 Application to H2H: coupon 1x5

In this part, we report an application to H2H on coupons with bolting pattern 1x5.

Here, we make some assumptions which come from all previous steps: from the modal description of coupon 1x5 itself, we consider only relative longitudinal deviations, the variability of which is concentrated on the holes of the second plate; from the screening on coupon 1x2, we only consider misalignments, friction coefficient (denoted with μ) and preload ratios, dropping all elastic properties (i.e. the Young Moduli of plates and fasteners). Moreover, to reduce the number of variables to treat and to guarantee convergence stability to the original model, the preload ratios have been considered as equal to the preload ratio on the first bolt (denoted with PLR).

We generated a mixed linear/interaction regression model, based on a DoE with 200 points, which gives a score $R^2 = 0.89$. In Fig. 3.21 it is reported the ordering process

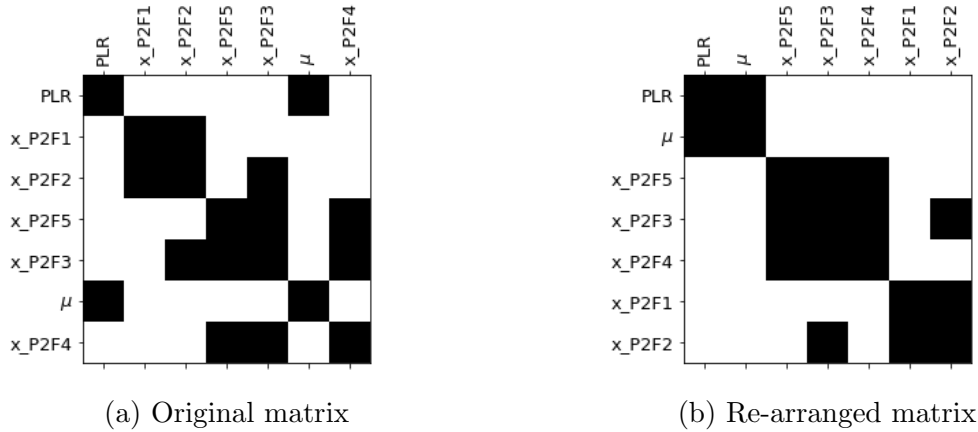


Figure 3.21: Example of physics separation on H2H coupon 1x5

allowed by the spectral co-clustering algorithm. In the obtained model, we may observe that the friction-related variables (i.e. μ , PLR) and the misalignments do not exhibit any interaction term: as a consequence, these two categories of variables can be clustered in two different groups and their effects are, therefore, cumulative (i.e. we can apply the principle of superposition of effects).

Note that all misalignments have interaction terms with the other misalignments associated to the adjacent hole locations (for example, x_{P2F2} with x_{P2F1} and x_{P2F3}). However, we may notice that the term x_{P2F3} exhibits an interaction with x_{P2F5} , but not with x_{P2F1} , which constitutes an approximation error of the surrogate model: given the fact that the tested system is symmetrical, it is expected that these interaction terms are the same. However, we will not use the surrogate model trained in this section for further statistical studies, but rather we retain the general conclusion that the effects of friction-related and geometry-related variables can be treated separately and then superposed.

At a global level, all input variables in the considered example are independent. If we add the conclusion on the separability of the effects of friction-related and geometry-related input variables, we can treat the two upper-mentioned clusters in distinct DoEs: the lower dimensionality of each generated input space can improve the efficiency of further explorations and/or the training of specific surrogate models.

These outcomes can be exploited also to reduce the computational burden induced by repeated statistical analyses, as the outputs of the cumulative effects (from the two separated clusters) can be sampled separately. For example, if we perform first a sampling-based statistical analysis and then we change only the parameters describing the friction domain (e.g. when evaluating several surface treatments options), we can still re-use the samples related to the effect of geometric inputs (i.e. the misalignments). The analogue is valid when changing only the statistical setting related to the misalignments.

3.5 Conclusion

In this chapter we carried out the input dimensionality reduction on the typical H2H coupon assemblies, with the purpose of simplifying the problem and thus reduce subse-

quent computational costs. To achieve this, we acted on the following three axes:

1. re-definition of the input variables: on H2H problems this is done via modal description (specifically via PLS) to re-define the input geometrical misalignments;
2. removal of secondary variables: this is performed on H2H via a screening procedure based on a linear/interaction metamodel, considering geometrical misalignments, elastic field material properties, friction between plates and bolt preload;
3. separation of the physics effect of input variables: this is done by re-grouping the inputs which interact with each other inside the same group, while not exhibiting interaction effects with variables from other groups.

In Table 3.2 an overview of the final number of input variables after dimensionality reduction is given for different bolting patterns. By comparing this with Table 3.1, a reduction of about 60% in the number of variables is achieved. The effects of the input dimensionality reduction are reported in the plot in Fig. 3.22 for different bolting patterns: the reduction of number of inputs is more effective when increasing the complexity of the bolting patterns. Moreover, as it was observed in the physics separation section, the geometrical misalignments and friction-related variables (friction coefficient between plates and bolt preload) can be treated in different input spaces. For linear materials, a further separation is automatically allowed between the response (e.g. the transferred bearing load) and the capacity (e.g. the material strength): this is not true when the elasto-plastic behavior of materials is introduced in the finite element model.

Random variable	Per bolt	Per plate	1x2	1x3	1x5	2x3	2x5	3x5
Misalignments	1		2	3	5	6	10	15
Friction coefficients		1/2	1	1	1	1	1	1
Preloads	1		2	3	5	6	10	15
Plate bearing strengths		1	2	2	2	2	2	2
Bolt shear strengths	1		2	3	5	6	10	15
Total	3	3/2	9	12	18	21	33	48

Table 3.2: Final list (after dimensionality reduction) of input variables on H2H problem for different bolting patterns

In the application of probabilistic frameworks, a number of dimensionally independent sampling methods are available in the literature for different purposes, as will be shown in the following chapters. The dimensionality reduction presented in this chapter is primarily intended as a support to simplify the interpretation of the results (especially for Chapters 4 and 7), driven by the modal description discussed above. Moreover, the screening analysis leads to a simplification in the case where multiple analyses must be performed: the deletion of elastic behavior material properties allows to avoid the repetition of multiple statistical analyses with different material choices; the separation between friction-related, material strength properties and misalignments allows to reuse the samples from previous analyses where only one part of the global setting is changed (e.g. when considering different surface treatments of parts, affecting the friction properties).

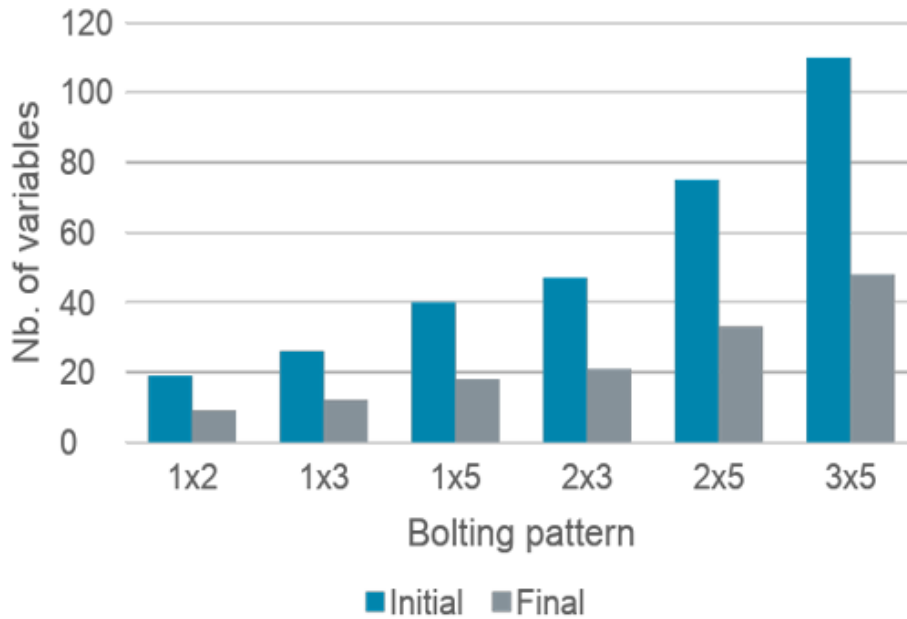


Figure 3.22: Effects of the dimensionality reduction on different bolting patterns

The decomposition of the input domain in multiple reduced-order spaces can also be exploited to improve the exploration features of a DoE and to train distinct surrogate models on each input space.

Focusing on the validity of the PLS surrogate models retrieved in this chapter for H2H coupons, we have clear linear relations between inputs and outputs with good R^2 score results. However, this was helped by the introduction of high load levels. Therefore, the quantitative regression results are consistent with high ratios of thickness over hole diameter (ratio t/d).

Regarding the variables screening, more advanced techniques based on global sensitivity analysis [Iooss and Lemaître, 2015], using for example Sobol indices [Saltelli, 2002, Lamboni et al., 2013, Borgonovo and Plischke, 2016, Bourinet, 2019], could be considered, especially when moving to higher bolting patterns.

Finally, for analyses assisted by machine learning techniques, the dimensionality reduction can be useful to support simple surrogate models generally affected by the curse of dimensionality, as will be shown in Chapter 6. Moreover, for H2H applications, this can help to overcome the validity limitation of PLS results for lower load levels, which will be consistent with low ratios t/d as well.

Chapter 4

Semi-probabilistic Approach for Aircraft Components Design

4.1 Introduction

This chapter focuses on a key-feature of the UQ&M general framework, specifically the choice of the decision criterion to implement in the static strength substantiation for large airplanes. As discussed in Chapter 2, the applications of probabilistic analyses on aeronautical engineering are strictly related to the constraints imposed by the certification requirements.

The classical approach used for sizing aeronautical structural components is based on the adoption of specific quantiles for material properties and specific scenarios for the load levels, which are defined in the current certification requirements (CS 25 for large aircrafts). For some design parameters, characterized by small variabilities and/or justified by engineering judgment, mean values are considered (e.g. thickness of plates). For others, the worst cases are retained: this category may include temperature scenarios, geometrical flaws, effects of impacts, stress induced by the manufacturing process, among others. We will refer to this methodology as *fixed-case scenario* approach, keeping in mind that the worst cases are only considered for a part of the design parameters, while for others values corresponding to low probability events are considered.

In the H2H framework the adoption of a literal *worst-case scenario* approach would make the application impossible. Indeed, the worst case would always be a single bolt supporting the totality of the applied load: this would imply safety factors equal to the number of bolts in the bolting pattern (which can reach values of several dozens!). A mitigation process based on a probabilistic framework becomes fundamental in this specific case. The objective is to determine representative deterministic quantities based on a probabilistic framework, i.e. integrating the variability of the input parameters affecting structural performances.

On the other hand, a *fully-probabilistic approach* would consider the whole variability of all input parameters used in the design phase, to deduce failure probabilities or, alternatively, reliability indexes. However, as explained in Chapter 2, the aeronautical certification requirements do not consider the concept of failure probability for static strength demonstration. Therefore, the adoption of this kind of *fully-probabilistic approaches* would not be compatible with current certification requirements.

Therefore, we aim at formalizing a framework able to take into account the variability of the random inputs (instead of considering the worst cases only), but also integrating this framework in the current European certification requirements and in the classical deterministic design process.

In this chapter, we will propose an extension of the definitions of the deterministic quantities prescribed by the CS 25 for load levels and material properties. The input variables will be distinguished according to the analogies, in terms of statistical variability, with these two base references (i.e. loads and material properties). The purpose of the proposed approach is to compute *deterministic* quantities to introduce in classical design process, based on a *probabilistic* framework: we will refer to our proposed framework with the name "*semi-probabilistic approach*". We call it "*semi-probabilistic*" since it does not aim to probabilistically model all input parameters that involve significant uncertainties, but only part of these, while for others deterministic (sometimes conservative) values are kept.

First, we introduce the main deterministic quantity of our applications - the *overload* - and define it from a mathematical and engineering point of view in Section 4.2. Then, a classification of the random variables to extend the current certification requirements is proposed in Section 4.3. The proposed framework is formalized in Section 4.4, where two different declinations of the semi-probabilistic approach are presented. The first declination, intended as a point quantile estimation problem, is used to define the *overloads* and is detailed in Section 4.5. The application of this first declination on the H2H problem is reported in Section 4.6. At the end of the chapter, some conclusions regarding the proposed approach and the results of H2H application are reported in Section 4.7. The second declination will be only introduced in Section 4.4, and it will be formalized, analyzed and further discussed in Chapter 7.

4.2 Definition of the OverLoad (*OL*)

In this section, we introduce the concept of the *overload*, which constitutes one of the main representative deterministic quantities for our applications of the proposed *semi-probabilistic framework*.

First of all, we associate to the *overloads* the meaning of deterministic correction coefficients which represent the *internal* redistribution of loads within a given structure, considering the variabilities affecting it: in particular, these factors are used to guarantee a certain margin on the computed *internal* loads in a given structure. The *overloads* are computed at specific scenarios of the applied (i.e. *external*) loads. Therefore, the determination of the *overloads* does not take into account the variability of the magnitude of the applied (i.e. *external*) loads.

But what are the *overloads* in practice? To answer to this question, we refer to the H2H example related to the coupon 1x2. In Chapter 1, we introduced this example to explain the industrial need of challenging the *worst case scenario* approach. In Chapter 3, we trained a PLS surrogate model to describe the effects of the misalignments on the redistribution of bearing forces in the coupon. In Fig. 4.1 we propose the comparison between the diagrams of the load redistributions (*Free Body Diagram*, FBD) related to the nominal configuration (i.e. fitted and perfectly aligned holes) and the worst H2H

configuration (i.e. with holes oversized and misligned in the worst condition, consistent with the PLS mode retrieved in Section 3.3.3), in order to physically and mathematically define the concept of *overload*. We suppose that there is no friction phenomenon, and we denote with F_{app} the applied force and with $S_{i,j}$ the internal bearing force acting on the j^{th} hole of the i^{th} plate, with $i = 1, 2$ and $j = 1, 2$: as a reminder, the equilibrium in each bolt leads (for two plates) to $S_{1,j} = S_{2,j}$ (for $j = 1, 2$) and the equilibrium of the plates $S_{1,1} + S_{1,2} = S_{2,1} + S_{2,2} = F_{app}$.

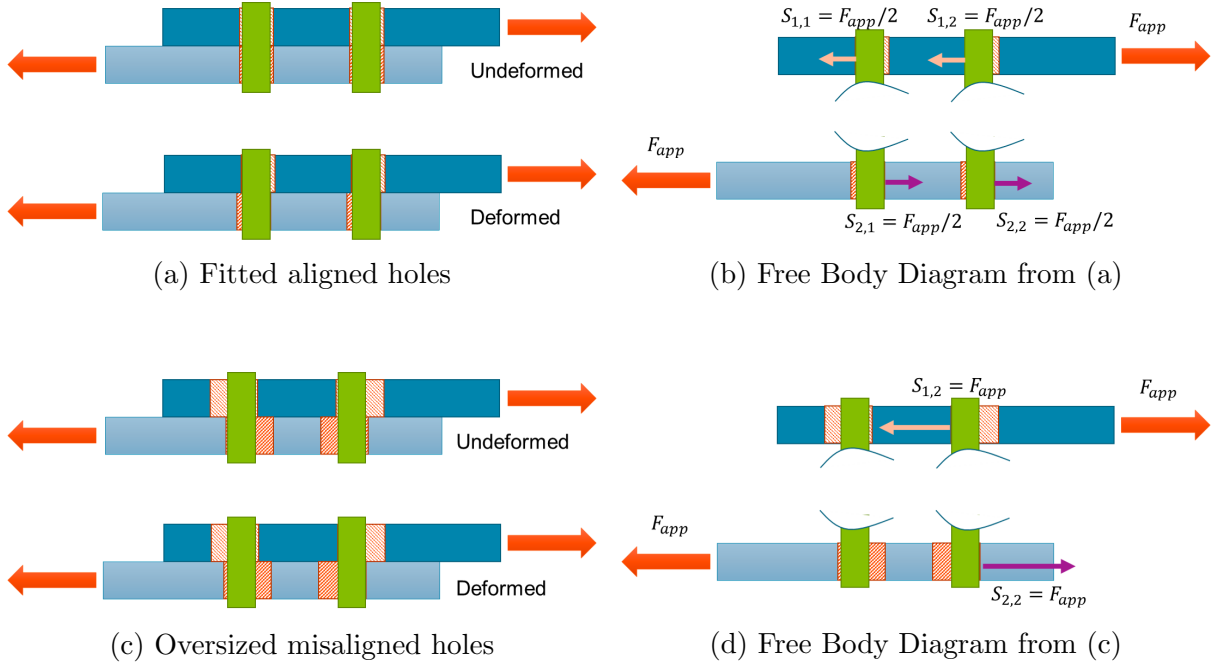


Figure 4.1: Effect of oversize and misalignments on H2H load transfer

In the nominal configuration (in Fig. 4.1a) both bolts are in contact with the holes of each plate. In the associated FBD (in Fig. 4.1b), the applied load F_{app} is equally redistributed among the hole locations: from the equilibrium conditions on bolts and plates, all $S_{i,j}$ are equal to $F_{app}/2$.

In the worst H2H configuration (in Fig. 4.1c), only the right bolt ($j = 2$) is in contact with the plate: the first bolt will not contribute to the load transfer (i.e. $S_{1,1} = S_{2,1} = 0$), while the second must carry the whole applied load F_{app} (i.e. $S_{1,2} = S_{2,2} = F_{app}$). With respect to the nominal configuration, the second bolt location carries a load amplified by a factor 2: the overload represents this amplification factor, thus $OL = 2$ in this case.

From an engineering perspective, we define the *overload* OL as the load concentration factor in the most critical location of a given structure (e.g. the right bolt in the H2H example in Fig. 4.1). The OL is therefore defined by four elements:

1. the *locations*: the load is redistributed differently in the distinct points of the structure, so that we need to check the load amplifications in all locations (e.g. all bolt locations in a bolted joint assembly);
2. the *reference*: the choice of the nominal configuration and the internal loads retrieved in this latter (e.g. the configuration with fitted aligned holes in H2H);

3. the *local internal loads*: the redistribution of the internal loads in each location, due to the variability of intrinsic properties (e.g. the bearing load transfer modification due to the misalignments in H2H);
4. the *extension of applicability*: the choice between assigning a local overload to each location (hence considering a different reference value for each location) or a unique value summarizing the behavior of the whole structure (e.g. the maximum local overload).

We apply now this generic definition to the H2H example, this time not restricted to a *worst-case scenario*. We denote with $S_{i,j,nom}$ the reference internal loads (at the j^{th} hole of the i^{th} plate) associated to the nominal configuration, with fitted and perfectly aligned holes (considered in the deterministic sizing of structures assembled with the classical procedure, i.e. without H2H). On the other side, we denote with $S_{i,j}$ the bearing load transferred (at the j^{th} hole of the i^{th} plate) in a given H2H configuration with given hole misalignments. We can define the *local* overloads as:

$$OL_{i,j} = \frac{S_{i,j}}{S_{i,j,nom}} \quad (4.1)$$

To define a global measure of the overload OL for the whole assembly, we may have two choices: (1) consider the maximum local $OL_{i,j}$; (2) compute the amplification of the maximum load $S_{i,j}$, among the i, j locations, with respect to the maximum internal load in the nominal configuration, leading to define a new reference value $S_{REF,nom} = \max_{i,j} S_{i,j,nom}$. These two choices lead to two different mathematical formulations of the OL , represented by the following equations:

$$OL = \max_{i,j} OL_{i,j} = \max_{i,j} \left(\frac{S_{i,j}}{S_{i,j,nom}} \right) \quad (4.2)$$

$$OL = \frac{\max_{i,j} S_{i,j}}{\max_{i,j} S_{i,j,nom}} = \frac{S}{S_{REF,nom}} \quad (4.3)$$

Where $S = \max_{i,j} S_{i,j}$ represents the maximum transferred load over the different locations i, j of the assembly where the H2H process is applied and $S_{REF,nom} = \max_{i,j} S_{i,j,nom}$ is the equivalent on the nominal configuration (i.e. with fitted and perfectly aligned holes). For a coupon 1x2, the two expressions in Eq. 4.2-4.3 are equivalent as the internal loads are redistributed equally in the different locations. However, for more complex bolting patterns, the bolts placed at extreme sides of the plates generally carry a higher amount of the total load, decreasing progressively when going towards more internal bolts. This makes a difference in the definitions of the global measure of the overload at assembly level provided in Eq. 4.2 and Eq. 4.3. In the following of the manuscript, we will adopt the formulation of the overloads in Eq. 4.3.

The definition of the overload can be extended to other examples, apart from H2H: one can think of structures with uncertain boundary conditions, randomly distributed cracks, among others. The choices of the four upper-mentioned ingredients to formalize the specific overloads would be done on a case-by-case basis.

We focus now on the practical use of the overloads in a deterministic structural design context. As explained in Section 2.5, this latter is based, in aeronautical context, on

the notion of *safety factors* for loads and *knock-down factors* for structural strength properties. The overloads act de facto as *safety factors*, but on the *internal loads*. The inverse of the OL can be re-interpreted as a *knock-down factor*, representing a reduction of the structural strength, instead of a load amplification (as do the OL). Now, when we determine a value of the overload $OL = \overline{OL}$, we will consider in deterministic design phase that the internal loads associated to the nominal configurations are amplified by a factor \overline{OL} (distinct factors is the local definition in Eq. 4.1 is retained): then, we adapt the sizing to these new values of the internal loads, by rescaling the critical dimensions (e.g. thickness of plates, diameters of bolts). In this process, the analysis is done only on the nominal configuration which is normally used in the classical deterministic sizing (e.g. the bolted joint assembly with fitted aligned holes, in H2H framework). Once the overloads are defined, they become mere multiplicative coefficients (i.e. equivalent to special safety factors), allowing to avoid a specific finite element simulation for the misaligned configuration.

Furthermore, we need to highlight the consequences of the overloads on the structural sizing criteria. We focus on the case of bolted joint assemblies, starting from a low ratio t/d , where t is the plate thickness and d the bolt diameter: in this case, the dominant failure mode is the *bearing* on the plates (cf. Section 3.2). Consequently, if the overload is $OL = \overline{OL}$, we must multiply by \overline{OL} the thickness t . But then, we would obtain a higher ratio t/d , which can make *bolt shear* the new most critical failure mode: therefore, we should also check if the sizing of the bolts can allow to resist to these internal loads updated with the overloads. Therefore, the consequences on the global weight can be somehow difficult to predict without a complete knowledge of all sizing criteria in the structure. In the following, we assume that the only sizing criterion is the bearing on the plates and thus we consider that only the weight of the plates will be affected by the overloads (in particular, linearly proportional to the obtained \overline{OL}). This is valid either for very low ratios t/d or for low overloads.

The main purpose of the proposed *semi-probabilistic framework* is to provide a statistical-based general process to define the deterministic quantities to be used in the deterministic sizing. In the H2H application, we challenge the *worst case scenario* approach (common practice in aeronautical industry), by defining an overload value to be used for the sizing that is statistically representative of the variability of the input parameters and in particular of hole misalignments. By computing these representative values of the overloads through the proposed *semi-probabilistic framework* we seek to reduce the potential over-conservatism inherent to the *worst case scenario*. Indeed, the reduction of the overloads can be interpreted as the improvement of the sizing assumptions adopted in structural design, thus leading to potential mass savings.

In the next sections, we formalize the proposed *semi-probabilistic approach*, by starting from the definition of the random inputs.

4.3 Classification of random inputs for aircraft components sizing

In this section we define and classify the input properties which may affect the structural performances. The distinction constitutes an extension of the current certification

requirements in aeronautical industry.

The approach which is currently adopted for airframe design is a *fixed-case scenario* approach, which is in line with the constraints introduced by regulations. We remind that the concept of "worst case" is restricted to a part of design parameters. Satisfying these constraints constitutes an essential requirement to be able to certify an airplane.

In particular, the Certification Specifications (namely CS 25 for large aircrafts) prescribe specific deterministic quantities for load levels and material properties to demonstrate the aircraft static strength. For the former, we retrieve the concept of the *limit loads*, which are the maximum load levels which may arrive once in an aircraft lifetime, hence linked to a probability of about $10^{-5}/FH$ (per Flight Hour FH). As regards the material properties, two quantile levels are prescribed according to the redundancy level of a given structure: for non-redundant structures, we have the A-values, which correspond to the deterministic quantity such that 99% of the population has better properties (with 95% confidence level); for redundant structures, we have B-values, which constitute the analogue concept linked to a probability of 90% instead (with 95% confidence level). These two last definitions, applicable to all material properties, imply that a given material has with 95% confidence a probability of 1% to exhibit worse performances than the upper-mentioned A-value, and a 10% probability to perform worse than the related B-value. These can be translated into specific percentiles, with two alternative options chosen according to whether the increase of the magnitude of a given quantity I improves or worsens the overall performances: if increasing the value of I improves performances, the A-value is defined as the 1st percentile of the quantity I and the B-value as the 10th percentile; on the other hand, if increasing I worsens the overall performances, the A-value will be defined as the 99th percentile and the B-value as the 90th percentile. In the following we refer to the former option as "*low-level quantiles*" and to the latter as "*high-level quantiles*".

Specific safety factors are applied on these deterministic quantities to take into account the uncertainty associated mainly to physical phenomena, lack of knowledge on structural behavior and modeling errors. For a number of complex phenomena, it is common practice to adopt either fixed scenarios defined by engineering judgment or the worst cases. However, the choice of the particular scenario is generally done on a case-by-case basis, thus lacking a general process.

In the classical sizing, the verification is often done by means of a reserve factor RF , defined as:

$$RF = \frac{R_{REF}}{S_{REF}}$$

Where R_{REF} and S_{REF} refer to the reference deterministic values associated to respectively strength R and stress S , related to the specific rules prescribed by the CS 25. The design is considered as acceptable if $RF \geq 1$. However, the assumptions posed by the classical design approach may lead to consider scenarios beyond what is reasonably needed.

On the other hand, *fully-probabilistic approaches* would consider the full variability of all input parameters, leading to the definition of a failure probability P_f . In the simple case with only two variables R and S , the P_f can be formalized as:

$$P_f = P[R < S]$$

Currently, fully-probabilistic approaches can not be integrated in aeronautical regulation as no acceptable failure probability threshold is available (only partial safety factors related to external loads and material properties are reported in CS).

An approach to address these issues was initially proposed in the work by [Kempeneers, 2018], aiming at integrating the UQ&M analysis in the deterministic context of aeronautical regulations requirements. In particular, a distinction is made according to the nature of variables:

1. *Environmental variables*: they are associated to a given instant of the aircraft's life, thus varying in time but affecting in the same way all the airplanes of the fleet;
2. *Intrinsic variables*: these vary among the different parts of an aircraft (and different aircrafts of each fleet), but do not vary during the aircraft's life.

Among environmental variables, we may find temperature, aerodynamic loads and flight conditions for example. In the second category of the intrinsic variables, we recognize material properties and geometric imperfections, among the others.

This distinction is done on the basis of the analogy in the metrics of variability between environmental variables and load levels (both varying during the aircraft's life) and between intrinsic variables and material properties (both varying among different parts of an aircraft). In this way, we can extend the probabilistic concepts and constraints prescribed in CS 25 (for loads and material properties) to all environmental and intrinsic variables. By making this assumption, we can link the two newly-introduced categories of variables to the classical quantiles levels prescribed in CS 25. This classification constitutes the starting point to formalize our proposed *semi-probabilistic approach*.

4.4 Semi-probabilistic approach: a double-declination formalization

In this section, we formalize, from a mathematical point of view, the proposed *semi-probabilistic approach*.

Based on the previous distinction regarding the nature of the variables affecting structural design, we can formulate a specific term to represent the probability of over-estimating the performances a given structure, by means of exceeding the deterministic values used in sizing: we will denominate this as *Probability of Exceedence (PoE)*. For a given performance index I (e.g. stress), we introduce a general *detrimental variable* K_I , such that a detrimental condition can be expressed as $K_I < 1$.

Within this perspective, a partial reliability analysis can be performed, considering separately the variability coming from environmental and intrinsic variables. The output will not be a failure probability (as in fully-probabilistic approach), but rather the probability that the nominal values used in deterministic sizing over-estimate the structural performances. The upper-mentioned *PoE* will denote this probability. The denomination "*semi-probabilistic approach*" is used here to formalize a comprehensive framework to define deterministic quantities (related to structural sizing) based on a probabilistic

framework, but different from the *fully-probabilistic approach* in that partial probabilities are calculated, instead of the overall probability of failure.

The detrimental variable K must be defined in such a way that the condition $K < 1$ implies that we are over-estimating the structural performances in the deterministic design process: this can happen, for example, either if we under-estimate the loadings applied to the given structure, or if we over-estimate the capability.

In particular, if a high value of the random performance index I can improve overall performances (e.g. if I represents material strength), the over-estimation can be translated into $I < I_{REF}$, where I_{REF} represents the conservative quantity associated to I and used in deterministic sizing. The detrimental variable will be expressed as:

$$K = \frac{I}{I_{REF}} \quad (4.4)$$

Otherwise, if a reduction of I can improve performances (e.g. if I represents loadings, stress, material density), the over-estimation of overall structural performances is given by $I > I_{REF}$, and the detrimental variable will be expressed as:

$$K = \frac{I_{REF}}{I} \quad (4.5)$$

The probability of exceedence PoE will be given, for a single output performance index, by:

$$PoE = P(K \leq 1) \quad (4.6)$$

Moreover, if multiple independent phenomena affect the same failure mode and their cumulative effect is multiplicative, the definition of the PoE can be extended to:

$$PoE = P\left(\prod_i K_i \leq 1\right) \quad (4.7)$$

A number of failure modes can be represented in the form provided in Eq. 4.7. A simple example is given by the statistical variability induced on stresses by load amplification (associated with intrinsic properties) S and strength (associated with intrinsic properties as well) R . In the proposed semi-probabilistic approach, the sizing verification would lead to the equation:

$$PoE = P(K_S K_R < 1) = P\left(\frac{S_{REF}}{S} \frac{R}{R_{REF}} < 1\right) = P\left(\frac{R}{S} < \frac{R_{REF}}{S_{REF}}\right) \quad (4.8)$$

In this example, the PoE in Eq. 4.8 can be interpreted as the probability of obtaining poorer performances (in terms of reserve factor) compared to the nominal case. The same mathematical formulation can be retrieved in all phenomena which are typically treated via product of separated safety factors. On the other hand, several failure modes, such as composite rupture criteria (e.g. the Tsai-Hill criterion), can not be interpreted as the multiplicative cumulative effect of the individual properties: for these cases, the PoE must be treated as in Eq. 4.6, with a single detrimental variable K taking into account the propagation of the uncertainty related to all input variables. In the following, we will work under the assumption of multiplicative effects and consider the Eq. 4.7 as the general formulation which includes also the special case we just exposed (in Eq. 4.8).

We define then the PoE limits \overline{PoE} , related to the nature of variables. In particular, we make an analogy between intrinsic variables and material properties. In CS 25.613, two quantiles for material properties are prescribed for redundant structures (B values) and non-redundant structures (A values). This distinction leads to a maximum allowed $\overline{PoE} = 0.1$ for redundant structures and $\overline{PoE} = 0.01$ for non-redundant structures. For environmental variables, we link the PoE limit to the probability of $\overline{PoE} = 10^{-5}/FH$ typically retained for limit loads. This different vision allows to accept a specific sizing if the PoE reflects the quantiles prescribed by regulations.

By denoting with \mathbf{X} the vector of input random variables affecting the detrimental variables K_i , the general constraint of the semi-probabilistic approach can be written as:

$$PoE(\mathbf{X}) \leq \overline{PoE} = \begin{cases} 0.1 & \text{if } \mathbf{X} \text{ intrinsic, redundant structure} \\ 0.01 & \text{if } \mathbf{X} \text{ intrinsic, non-redundant structure} \\ 10^{-5}/FH & \text{if } \mathbf{X} \text{ environmental} \end{cases} \quad (4.9)$$

In Fig. 4.2, the three different approaches are illustrated on a purely mathematical example, with a generic resistance (allowable or strength) in blue and a generic stress (or, more generally, response of the system) in red:

1. *Fixed-case scenario approach*: two quantiles related to strength and stress are computed and compared through a Reserve Factor (RF); for material properties A/B values are considered, while for loads a distinction is made between "Limit loads" (maximum load appearing only once in aircraft life) and "Ultimate Loads" (limit loads multiplied by a safety factor); for a number of complex phenomena affecting structural performances, the worst cases are retained, while for others engineering judgment is adopted.
2. *Fully-probabilistic approach*: all input variabilities are taken into account to determine the global failure probability (P_f).
3. *Semi-probabilistic approach*: the variability coming from intrinsic and environmental variables are considered separately (thus leading to a reduced variability, as depicted by the continuous lines in Fig. 4.2c) to compute the probability of exceeding the nominal values; this value is then compared to the limit \overline{PoE} .

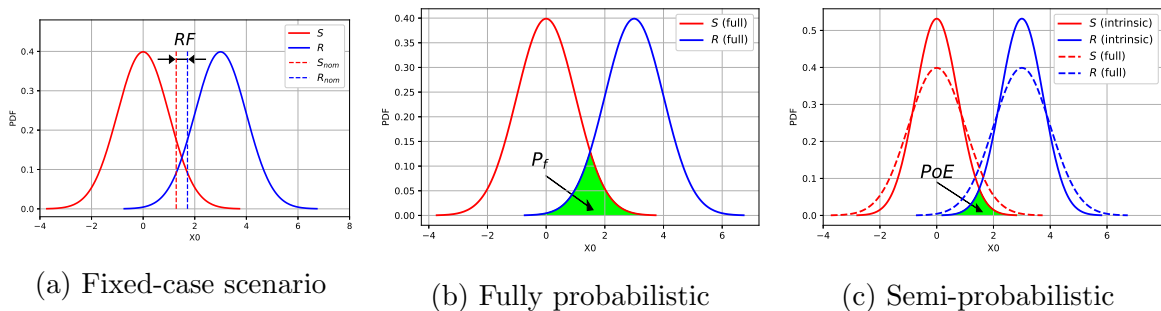


Figure 4.2: Schematic representation of three design approaches

This semi-probabilistic approach constitutes a proposal to extend the requirements defined in CS 25 for aircraft components certification. By guaranteeing the constraint in Eq. 4.9, we satisfy the semi-probabilistic decision criterion in our UQ&M framework.

A final remark should be done on the use of Eqs. 4.6-4.7 coupled with the constraint in Eq. 4.9. Two different directions can be given to the semi-probabilistic approach usage:

1. starting from fixed input distributions, it is possible to determine the new nominal values to adopt in deterministic sizing;
2. starting from fixed nominal structural performances request, it is possible to optimize the parameters of the controllable input distributions.

From a mathematical point of view, the former constitutes a quantile problem, while the latter would be treated as a reliability-based design optimization. The following of the chapter will focus on the quantile estimation problem and the application on H2H, using off-the-shelf methods. The second perspective will be pursued in Chapter 7, where the methodological outcomes of the present work (a sampling method presented in Chapter 5 and a machine learning assisted reliability estimation presented in Chapter 6) are collected and implemented in a framework allowing to optimize the parameters of the controllable input distributions.

4.5 Quantile Analysis

The quantile q_α of a response Y is generally defined by the inverse of the Cumulative Distribution Function (CDF) F_Y at a quantile level α :

$$F_Y(q_\alpha) = P[Y \leq q_\alpha] = \alpha \iff q_\alpha = F_Y^{-1}(\alpha) \quad (4.10)$$

When estimating the quantile q_α from sample data, we introduce an uncertainty linked to the sampling process. Therefore, we need to evaluate the accuracy and the confidence bounds related to the estimation, to ensure a certain robustness to the outcomes of the estimation itself.

We focus, in particular, on the estimation of the upper bound of a quantile. This problem can be written as:

$$\widehat{q_{Y,\alpha,\beta}} = \begin{cases} \arg \min_x (\widehat{F}_Y(x) > \alpha) \\ \text{s.t. } P[F_Y^{-1}(\alpha) \leq x] \geq \beta \end{cases} \quad (4.11)$$

Where $F_Y(x) = P[Y \leq x]$ is the true CDF of the output response Y , \widehat{F}_Y represents its empirical estimation, α is the targeted quantile level and β constitutes the confidence level associated to the estimation on the quantile itself. The constraint says that the probability of over-estimating the true α -quantile $q_\alpha = F_Y^{-1}(\alpha)$ should be greater than β .

In literature, a number of methods are available to solve the quantile estimation problem. Some of them are based purely on sampling methods, where the reference is given by the Monte Carlo method. Based on this method, the mean value of the estimation of q_α is estimated from a population of N samples of the variable Y as:

$$\widehat{q}_\alpha = Y_{[[N\alpha]+1]}$$

Where $Y_{[.]}$ represents the ordered sample (in ascending order) and $[N\alpha]$ is the integer part of $N\alpha$.

The other main quantity which is retained is the variance of the quantile estimate:

$$\sigma^2 \approx \frac{\alpha(1-\alpha)}{N \times g^2(\widehat{q}_\alpha)}$$

Where $g(\widehat{q}_\alpha)$ represents the Probability Density Function (PDF) of the output response itself at the estimated quantile \widehat{q}_α . Therefore, the minimum number of samples required to achieve convergence (i.e. reaching a targeted coefficient of variation) is not a priori known without access to the PDF of the response.

The mathematical problem formalized in Eq. 4.11 constitutes a *point quantile estimation* problem, involving the estimation of a single point $q_{Y,\alpha,\beta}$ from the random variable Y . Note that this should not be confused with the *conditional quantile regression* [Huang et al., 2017]: coming from econometrics [Koenker, 2017], this was based on the prediction of a target variable conditioned to a fixed point of an input (deterministic or random) x . However, in the quantile regression, the output also depends on other random uncontrolled inputs X . The interest of quantile regression would be to identify a conservative regression, guaranteeing a fixed probability of overestimating the output, given by the quantile level itself. We can consider the *point quantile estimation* as a *conditional quantile regression* on a single point of the input x .

Several variance-reduction techniques are available in the literature to increase the convergence rate of classical Monte Carlo: examples are given by stratified sampling [Samawi et al., 2019], conditional Monte Carlo [Nakayama, 2014], bootstrap [Brodin, 2006], importance sampling [Hu and Su, 2008, Egloff and Leippold, 2010, Morio, 2012], among others. A general resume of Monte Carlo-based approaches for point quantile estimation is given in the review [Dong and Nakayama, 2018].

Other works make use of machine learning techniques to reduce the computational burden of the point quantile estimation [Torossian et al., 2020]. This perspective is not pursued in the present work.

Particular attention is given in this chapter to Wilks' method [Wilks, 1941]. This can be considered as a minimal Monte Carlo approach, based on order statistics [David and Nagaraja, 2004], i.e. the part of statistics dealing with ordered samples. This technique is particularly interesting when seeking to identify the minimum number of samples able to build a confidence interval related to a given confidence level β .

In this section, the central focus is given to Wilks' method and the declination of the semi-probabilistic approach as a point quantile estimation problem.

4.5.1 Wilks' method

Wilks' method [Wilks, 1941] is commonly used in the context of robust quantile determination. The main interest of this method is given by the limited number of simulations required, which varies only as a function of the targeted quantile, the targeted confidence level and the hyper-parameter known as *order statistics rank* (which is a typical index in order statistics). In practice, in an ordered sample (sorted in ascending order) of N

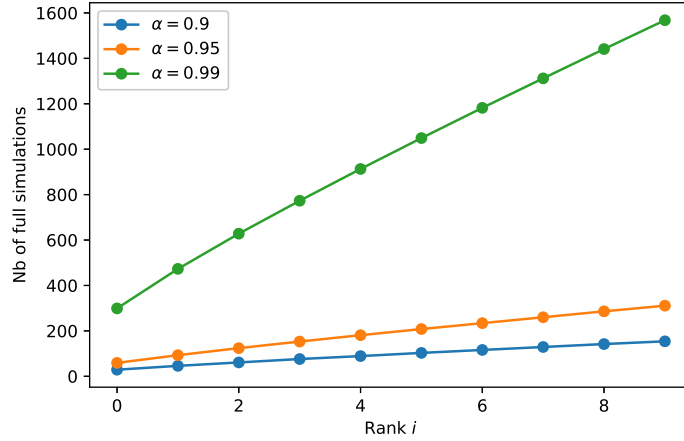


Figure 4.3: Minimum number of samples according to Wilks’ formula (confidence $\beta = 0.95$)

individuals, we define the i -th rank sample as the $(N - i)$ -th highest value: if the rank $i = 0$, we consider the highest value, with $i = 1$ the second and so on. Therefore, Wilks’ method does not require any information about the output distribution nor the dimension (thus neither the complexity) of the problem. The minimum number N of samples which are required by Wilks’ method to estimate a quantile q_α with confidence level β depending on the rank i , the quantile level α and the confidence level β will be given by Wilks’ formula:

$$N_{i,\alpha,\beta} = \min_N \left[\sum_{k=N-i}^N C_N^k \alpha^k (1 - \alpha)^{N-k} < 1 - \beta \right] \quad (4.12)$$

By using $N \geq N_{i,\alpha,\beta}$, we can ensure that the condition in Eq. 4.11 is automatically satisfied. From an engineering perspective, this result can be interpreted as the minimum number of samples required to guarantee that the i -th highest value is a conservative estimation of the quantile α with confidence level β . Therefore, the probability of underestimating the correct value of the targeted quantile cannot overcome $1 - \beta$. This method allows us to estimate an upper bound of quantiles. In Fig. 4.3, the evolution of the minimum N to compute three different quantile levels with fixed confidence level $\beta=0.95$ as a function of the rank is illustrated.

Finally, denoting with $Y_{[i]}$ the ordered sample (in ascending order), the estimation via Wilks’ method of the quantile $q_{Y,\alpha,\beta}$ related to the response Y , quantile level α and confidence level β is given by:

$$\widehat{q_{Y,\alpha,\beta}} = Y_{[N-i]} \quad \text{with } N \geq N_{i,\alpha,\beta} \quad (4.13)$$

The Wilks’ method is recognized as the main nonparametric procedure to determine material strength properties and design values in *Metallic Materials Properties Development and Standardization (MMPDS)* (specifically chapter 9.5.5.3). This is referenced in *AMC* related to CS 25.613, concerning material properties. In particular, the first rank ($i = 0$) related to A values ($\alpha = 0.99$, $\beta = 0.95$) is retained in *MMPDS*, leading to a

minimum number of samples equal to 299, obtained via the application of Wilks' formula in Eq. 4.12. Moreover, according to *MMPDS*, the B-values should be extracted from the same population (with 299 samples) used for A-values, thus considering the 22nd value (rank $i = 21$).

4.5.2 Declination for semi-probabilistic approach

In this subsection we explore the semi-probabilistic approach presented in Section 4.4 and re-interpret it as a quantile problem. The main purpose of this declination of the semi-probabilistic approach is the determination of *new* deterministic quantities, which resume the probabilistic nature of the structural performances: such values will be used in the deterministic sizing process.

In the H2H framework, the distinction between environmental and intrinsic variables is trivial as the only environmental variable is constituted by the applied loads and all other variables can be considered as intrinsic: therefore, for H2H applications we focus only on the intrinsic variable part, fixing the applied load as a scenario. This is justified by the fact that the application of H2H framework only affects the production of parts in aeronautical assemblies, without modifying the loading conditions.

Now, as the purpose of this first declination is the definition of *new* deterministic values resuming the probabilistic variability, we distinguish two cases: for the deterministic quantities which stem from *classical* sizing process, we adopt the suffix "*REF*"; for the *unknown* deterministic quantities we aim at determining in the proposed semi-probabilistic framework, we use the suffix "*det*". The formalization of the detrimental variables K_I will be therefore extended, according to whether the reference of the random performance I is known or not:

$$K_I = \begin{cases} \frac{I}{I_{REF}} & \text{if increasing } I \text{ improves performances, } I_{REF} \text{ known} \\ \frac{I}{I_{det}} & \text{if increasing } I \text{ improves performances, } I_{det} \text{ unknown} \\ \frac{I_{REF}}{I} & \text{if increasing } I \text{ worsens performances, } I_{REF} \text{ known} \\ \frac{I_{det}}{I} & \text{if increasing } I \text{ worsens performances, } I_{det} \text{ unknown} \end{cases}$$

The requirement in terms of *PoE* to be able to extend current certification requirements (CS 25 for large airplanes) will be defined as in Eq. 4.9, according to the distinction between intrinsic and environmental properties. For intrinsic properties, the *PoE* requirement will be defined by:

$$PoE = P\left(\prod_i K_i \leq 1\right) \leq 1 - \alpha \quad (4.14)$$

Where α represents the high-level quantile equivalent to A or B values (thus respectively 0.99 and 0.9).

In a number of structural applications, including the H2H framework, it is possible to use two key performance indexes, namely the allowables R and the response S of the structure. In the following, the response S will identify for H2H the highest transferred

load over the different bolt locations. In the case that both references associated to R and S are unknown, the associated detrimental variables will be formalized as:

$$K_r = \frac{R}{R_{det}} \quad \text{and} \quad K_s = \frac{S_{det}}{S}$$

In a first case, we do not consider the variability of the allowables R . If we do not want to consider any strength variability, K_s alone is sufficient to evaluate the variability of transmitted load on a given structure. Therefore, the PoE requirement can be simplified as follows:

$$PoE = P(S_{det} \leq S) = 1 - P(S \leq S_{det}) = 1 - F_S(S_{det}) \leq 1 - \alpha \quad (4.15)$$

The objective is actually to retrieve the unknown S_{det} which should be used in further design phases. This is equivalent to a quantile problem:

$$S_{det}^* = q_{S,\alpha,\beta} = \operatorname{argmin}_S (F_S(S_{det}) > \alpha) \quad (4.16)$$

Where $q_{S,\alpha,\beta}$ is the α -quantile with confidence level β of the output S , representing the transmitted load. This format is convenient in Wilks' framework as it provides robust upper bound precision for quantile levels $\alpha \geq 0.5$. Moreover, as it consists of a robust approximation with a given confidence level, the minimum confidence level requirements from certification regulations can be considered as well.

At this point, we can define the overload OL from a statistical perspective. As a reminder, this represents an amplification factor of the nominal applied load, acting de facto as a safety factor in the structural sizing. In the H2H framework, the overload OL is defined (see Eq.4.3) as the ratio between the load S transferred at the most critical bolt location (in a H2H realization) and the maximum transferred load $S_{REF,nom}$ in the nominal configuration (with fitted perfectly aligned holes). Therefore, the α -quantile related to the overload OL will be given by:

$$OL = \frac{q_{S,\alpha,\beta}}{S_{REF,nom}} \quad (4.17)$$

In a second case, we introduce the variability of the allowables as well. If we want to consider strength variability, we should adopt K_r as well. The PoE requirement can be re-written as:

$$PoE = P(K_r K_s \leq 1) = P(R S_{det} \leq S R_{det}) \quad (4.18)$$

We consider now two other auxiliary variable $H = S/R$ and $H_{det} = S_{det}/R_{det}$ to simplify the problem:

$$PoE = P(H_{det} \leq H) = 1 - P(H \leq H_{det}) = 1 - F_H(H_{det}) \leq 1 - \alpha \quad (4.19)$$

The solution of the quantile problem will be given by:

$$H_{det}^* = \left(\frac{S_{det}}{R_{det}} \right)^* = q_{H,\alpha,\beta} = \operatorname{argmin}_H (F_H(H_{det}) > \alpha) \quad (4.20)$$

At this point, we need to pass from this quantile to an overload OL , representing the ratio between the transferred load S_{det} and the reference $S_{REF,nom}$. Note also that the

solution of the quantile problem in Eq. 4.20 only provides a ratio between two unknown quantities S_{det} and R_{det} . Consequently, from a mathematical point of view, we need to fix one of them or define at least another relation between S_{det} and R_{det} . As the objective is to retrieve an overload OL , we choose to fix $R_{det} = R_{REF}$, where R_{REF} represents the $(1 - \alpha)$ -quantile of the allowable related to the specific failure mode considered (e.g. the A value, thus $\alpha = 0.99$, of the bearing strength). The solution of Eq. 4.20 will define a ratio S_{det}/R_{REF} . Therefore, to obtain the α -quantile related to the OL , we can just normalize this solution by introducing the reserve factor $RF_{REF} = R_{REF}/S_{REF,nom}$ associated to the sizing of the structure assembled without H2H (i.e. with fitted and perfectly aligned holes), leading to the expression:

$$OL = q_{H,\alpha,\beta} \times RF_{REF} \quad (4.21)$$

Note that these considerations can be extended to the cases with more than two performance indexes I and thus more than two detrimental variables K_I . The interpretation of the PoE requirement as a quantile problem leads to only one condition: therefore, if M unknown variables I_{det} are introduced in the PoE definition, we still need other $(M - 1)$ conditions to fully define all the unknowns. In this work, it is chosen to fix the remaining $(M - 1)$ unknown $I_{det} = I_{REF}$ (with I_{REF} the reference used in the classical design process), but other strategies can be implemented.

4.6 H2H application

In this section, we apply the quantile estimation process via Wilks' method to the H2H overload analysis problem. In the first subsection, the general setting is introduced, presenting the different effects which are considered. The following subsections will cover the actual implementations on three different coupons (characterized respectively by the bolting patterns 1x2, 1x5 and 3x5): the related computations are done with the PLS surrogate models described in Chapter 3. Specifically on the H2H coupon 1x2 we evaluated the effects of the mathematical framework, in order to draw some general conclusions concerning the suggested sizes of Wilks' approach for the overloads analysis.

4.6.1 General setting

Before starting the analysis one needs to define the statistical distributions of the considered input variables. These depend on several prior choices:

1. Decision criterion
2. Assembly process and associated stack chain
3. Individual distribution of a single variable
4. Tolerance acceptance criterion

In our context, the choice of the specific decision criterion intervenes in the inclusion of the variability of allowables and the dissociation between types of variables. Here we only consider intrinsic random variables.

The assembly process and the associated stack chain modify the meaning of the geometric input variables (i.e. the misalignments), while not interfering with other effects (allowables, preload ratios, material elastic properties). The stack chain consists in the succession of operations (defined in design phase) to manufacture the elementary parts and assemble the whole structure. In Fig. 4.4, we have a schematic representation of a stack chain: for simplicity, only longitudinal (along the applied force direction) deviations are reported, but the sketches are valid in two dimensions (longitudinal X and transversal Y) as well. In particular, each X_{ij} (respectively Y_{ij}) represents the deviation from the theoretical perfect coordinate X (respectively Y) of the j^{th} hole of the i^{th} plate, while X_G (respectively Y_G) represents the global relative translation of the second plate with respect to the first one. When several lines are prescribed by the specific bolting pattern, the ordering of the holes is done per longitudinal rows.

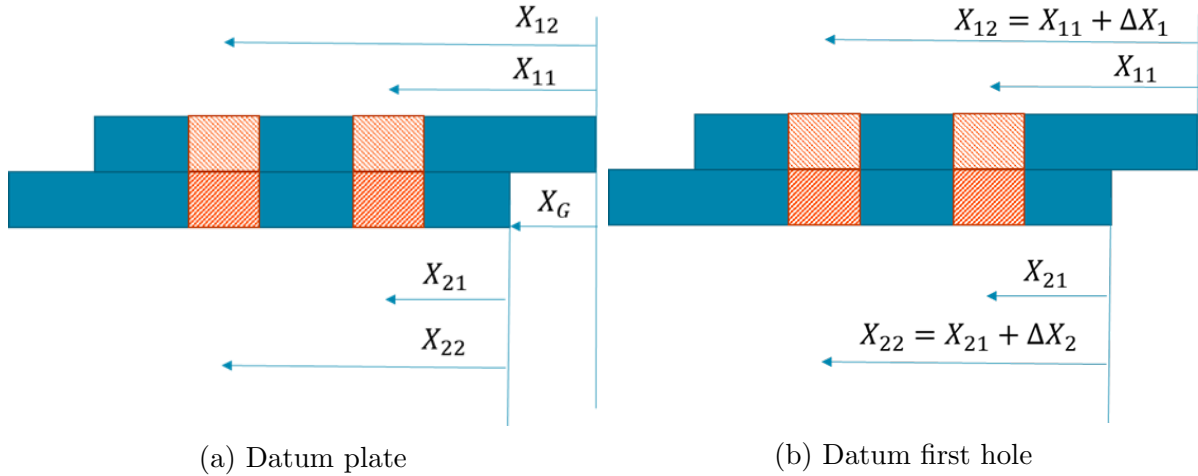


Figure 4.4: Schematic representation of stack chains associated with manufacturing processes

We adopt in the present work, six different alternatives, based on the upper-described scheme:

- *Stack chain 1* (datum plate, cf. Fig. 4.4a): all holes are drilled individually and the plates are perfectly placed before assembly routine (i.e. implying no global translation errors between the borders of two plates); in this case, we consider the nominal X_G and Y_G (which is a deterministic variable) and every X_{ij}, Y_{ij} is supposed to be a random variable, independent from the others.
- *Stack chain 2* (datum plate): all holes are drilled individually and the plates are placed with a random relative translation; in this case, all variables X_G, Y_G, X_{ij}, Y_{ij} are treated as independent random variables.
- *Stack chain 3* (ideal drilling grid): all holes in the same plate are drilled together with a perfect drilling grid and the plates are placed with a random relative translation in both directions; in this case, all X_G, Y_G, X_{i1}, Y_{i1} are considered as random variables, while all successive X_{ij}, Y_{ij} ($j > 1$) are linked to the first hole of each plate i through the relations $X_{ij} = X_{i1} + (j - 1)\Delta X$ and $Y_{ij} = Y_{i1} + (j - 1)\Delta Y$,

where ΔX and ΔY are deterministic quantities (exactly equal to the theoretical distance between two successive holes).

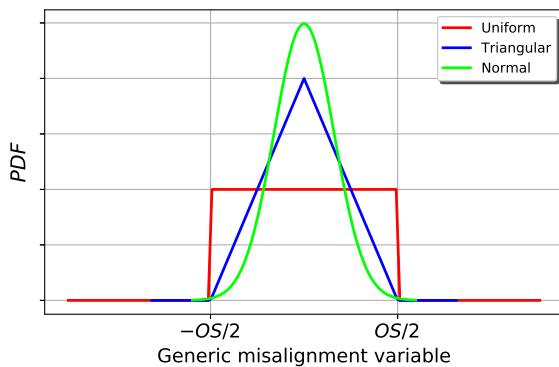
- *Stack chain 4* (datum first hole, cf. Fig. 4.4b): all holes are drilled using the first hole as a reference for all successive holes, while the global translation is not considered; the assembly is done without any specific referenced hole; all variables $X_{i1}, Y_{i1}, \Delta X_{ij}, \Delta Y_{ij}$ ($j > 1$) are treated as independent random variables.
- *Stack chain 5* (datum first hole): similar to stack chain 4, but with the assembly done with an expandable pin on the first reference hole. Therefore, we have that the variables X_{i1}, Y_{i1} are all deterministic and equals to zero.
- *Stack chain 6* (datum first hole): similar to stack chain 4, but the assembly is done with a reference pin. Therefore, the variability of the random variables X_{i1}, Y_{i1} is fixed at a minimum level, given by the sum of the nominal clearance and the tolerance on the pin diameter.

It is worth noticing that the first two stack chains arise from the same drilling process but they make different assumptions on the assembly process. Regarding the third alternative, it is an idealized perfect situation when the drilling grid is absolutely perfect.

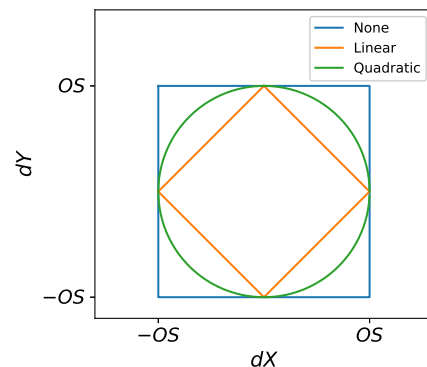
The last 3 stack chains constitute realistic compromises between the ideal perfect drilling grid and the intuitive (but conservative) first stack chain option.

As regards to the individual input distributions, we picked three options, defined via different PDF shapes spanning on a domain $\pm OS/2$ (where OS indicates the oversize). We list them in descending variability order (measured via the standard deviation σ):

1. *Uniform*: centered with bandwidth equal to the oversize ($\sigma = OS/\sqrt{12}$);
2. *Triangular*: centered with bandwidth equal to the oversize ($\sigma = OS/\sqrt{24}$);
3. *Normal*: centered with standard deviation $\sigma = OS/6$.



(a) Individual distributions



(b) Tolerance acceptance criteria

Figure 4.5: General setting options for OL analysis on H2H

It must be noted that the normal distribution which has been taken into account was specifically chosen to highlight this difference in terms of statistical dispersion. Actually,

the distribution itself can be characterized by a larger variance and truncated at a fixed limit (generally symmetrical for lower and upper bounds). Therefore, the comparison must be interpreted not in terms of pure PDF shape but as a particular case of reduced input variability. Moreover, it should be noted that the individual distributions are not arbitrarily chosen but they are strictly related to the manufacturing process itself: it is typical to consider uniform distributions when no measure on the manufacturing statistical dispersion is available and fitted normal (or truncated normal) distributions as data is available.

Finally, the tolerance acceptance criterion intervenes as a filter for input samples. In fact, one can define a criterion to restrict the input domain, related to the geometric input variables. We denote by dX_{ij} and dY_{ij} the relative misalignment related to the j^{th} hole between two successive plates $i, i + 1$. In the case of only two plates, we simplify the notation to dX_j and dY_j . In the present work, by denoting ρ the maximum allowed assembly tolerance requirement, two tolerance acceptance criteria are considered on any hole j :

- *Linear*: $|dX_j| + |dY_j| \leq \rho$
- *Quadratic*: $\sqrt{dX_j^2 + dY_j^2} \leq \rho$

Of course, the possibility not to include any tolerance acceptance criterion is considered as well. This is only fictive, as normally a minimum criterion to consider the assemblability of the plates should be considered: in particular, this minimal criterion would correspond to an enlarged quadratic criterion with a top-level requirement covering the maximum variability of the misalignments, plus the nominal clearance between hole and pin of every bolt.

The effect of the two tolerance acceptance criteria (plus none) on a single hole (thus two variables dX and dY) is illustrated in Fig. 4.5. The linear criterion is more conservative from a tolerance perspective as it accepts fewer combinations of points, restricting the input domain and thus, the variability of input variables.

The basic principle to compute overloads (*OLs*) consists in extracting a population of N points (given by Wilks' formula) to compute an α -level quantile at β confidence level. Every point implies a Finite Element Analysis (FEA) or a surrogate model evaluation. However, it is possible to use a surrogate model only if the precision is sufficiently high in the part of the domain leading to the highest responses and/or it is possible to evaluate the conservativeness of the metamodel itself.

In order to improve the accuracy of the estimations (i.e. reduce the variance of the estimated quantile $\widehat{q_{Y,\alpha,\beta}}$), we generally need to increase the order statistics rank in Wilks' approach, thus increasing the number of required samples. Another opportunity can be given by the bootstrap procedure, consisting in a random sampling with replacement: from a large population with M samples, sub-groups of $N < M$ samples are extracted to evaluate a specific quantity of interest (in our case, the overloads). Then a statistical analysis is done on the outcomes related to the different sub-groups, to determine, for example, mean and variance.

In H2H application, we use the bootstrap to exploit the fact that, for linear materials, transmitted loads and allowables are independent. In structural analysis context, the allowable generally does not require any numerical simulations, it is thus very cheap to

sample. The idea which is explored in this work is to enrich the database of allowables with a separated bootstrap procedure: in particular, for the stress part of the quantile definition (i.e. S) we consider N samples issued from the application of Wilks' formula; on the other hand, we introduce a larger number M of points, related to the strength part (i.e. R) of the quantile to determine. In every re-sampling, we extract a sub-group of N samples related to R , while considering the whole population of N samples related to S : the outcomes (in terms of the α -quantile estimated as in Eq. 4.13) issued from the re-sampled sub-groups are then used to estimate the mean. Looking at the definition of the two decision criteria described above, this bootstrap can only be applied when the strength variability is included in the analysis. Note that the independence assumption can only be verified for linear elastic material behavior, since for nonlinear elasto-plastic material law the stress-strain relation is modeled as a function of the yield stress.

In Wilks' framework, the probability of over-estimating the quantile itself is controlled by the confidence level, but the magnitude of the overestimation changes from one estimation to the other. Therefore, a statistical study over repeated analyses is needed if the intent is to compare the performances issued from specific industrial choices (e.g. using different stack chains).

Before diving into the numerical applications, we need to clarify the concept of *conservativeness* related to the computation of overloads OLs . The adjective *conservative* can be misleading when referring either to the estimation of the OL quantile or the design approach (i.e. the decision criterion): in the former case, being conservative implies a confidence of a fixed probability that the real quantity (for higher values are sought) is not under-estimated (e.g. considering the upper bound of the statistical estimation rather than the mean); for the latter, a higher level of conservativeness would be linked to the fact that the variability of part of phenomena affecting performance is not taken into account and unnecessary conservativeness is artificially added (e.g. considering only the worst case instead of the whole variability). Therefore, while conservative (or more precisely, robust) quantile estimations constitute an added value, excessive (over-)conservativeness in the design process can limit the potentials of the airframe performances.

4.6.2 Coupon 1x2

In this section, we focus on the determination of the overloads OLs for the H2H coupon with bolting pattern 1x2. We will start the analysis by studying the effects of the mathematical framework. In a second step, we are going to evaluate the consequences of several industrial choices on the OL .

4.6.2.1 Effect of mathematical framework

First, we seek to investigate the effects of several choices in the mathematical framework:

- Bootstrap procedure: this consists in enriching the database with more data coming from cheap samples (see details in previous section);
- Order statistics rank i : in the ordered response sample, this indicates which margin we take from the highest sample to determine the robust quantile through Wilks' method;

- Targeted quantile level α ;
- Decision criterion: a comparison between the inclusion or not of strength variability.

As a reminder, the features which significantly change the number of full stress analyses (FEA or via surrogate models) are the order statistics rank and the targeted quantile. In this section, we use the PLS surrogate model (related to the H2H coupon 1x2) obtained in Chapter 3. Regarding the setting parameters, we chose for this first section a triangular distribution for every hole deviation, associated with Stack chain 1 (implying all independent hole positions and perfect assembly process, i.e. without any added translation between plates).

Bootstrap is intended to enrich the database by adding cheap samples, coming from allowables of the bearing resistance of material: therefore it could only be applied to the semi-probabilistic decision criterion including strength variability. This is applied exclusively to the lowest quantile (90th percentile) and first four order statistics ranks. The related results are reported in Fig. 4.6 in the form of box-plots for different order statistics ranks: in the abscissa, we indicate by M the number of samples of the allowables and by N the number of samples of the stress, coming from full stress analysis simulations. Every box resumes the statistical results based on the repetition of the same procedure 1000 times. On the ordinate axis, we retrieve the estimated overloads.

We analyze three fundamental performances through these box-plots: (1) mean precision, represented by the mean level of error (orange line); (2) maximum over-estimation error, represented by the 99th percentile of the statistical samples represented by the upper bound of the boxes; (3) maximum under-estimation error, given by the positions of the 1st percentile of the boxes, with respect to the reference value (provided by Monte Carlo, $coV = 0.001$).

It can be observed that, compared to Wilks' method, no substantial improvement of the mean precision nor the maximum error of the solution is provided by the bootstrap procedure, even at very high enrichment ratios M/N . The low improvement provided by the bootstrap procedure can probably be explained to the low variability of allowables with respect to stress samples. We conclude that Wilks' method can give conservative results of quantile estimation in H2H applications with a limited number of samples.

We then use other box-plots to evaluate the effect of order statistics rank on the quantile estimation via Wilks' method. Results are shown in Fig. 4.7 for three levels of quantiles (90th, 95th and 99th percentiles) and the two decision criteria (i.e. the semi-probabilistic approach with or without strength variability). It can be observed that by increasing the order statistics rank, both mean and maximum error (of under- and over-estimation) can be reduced, without degrading the level of conservativeness (ensured by the theoretical Wilks' formula). We may notice, however, that beyond $i = 2$ the gains in accuracy are much less significant. The same considerations are valid for all three targeted quantile levels and both decision criteria.

From the computational burden point of view, it must be kept in mind, however, that increasing the rank i has significant effects on the sample size according to the targeted quantile level α , as depicted in Fig. 4.3. If for $\alpha = 0.9$ each unitary increase in i implies to add 30 samples, for $\alpha = 0.99$, an addition of 150 samples are necessary when passing from rank i to the successive one $i + 1$. Therefore, to establish a coherent criterion to estimate the quantile $q_{Y,\alpha,\beta}$ this effect must be taken into account and different ranks are

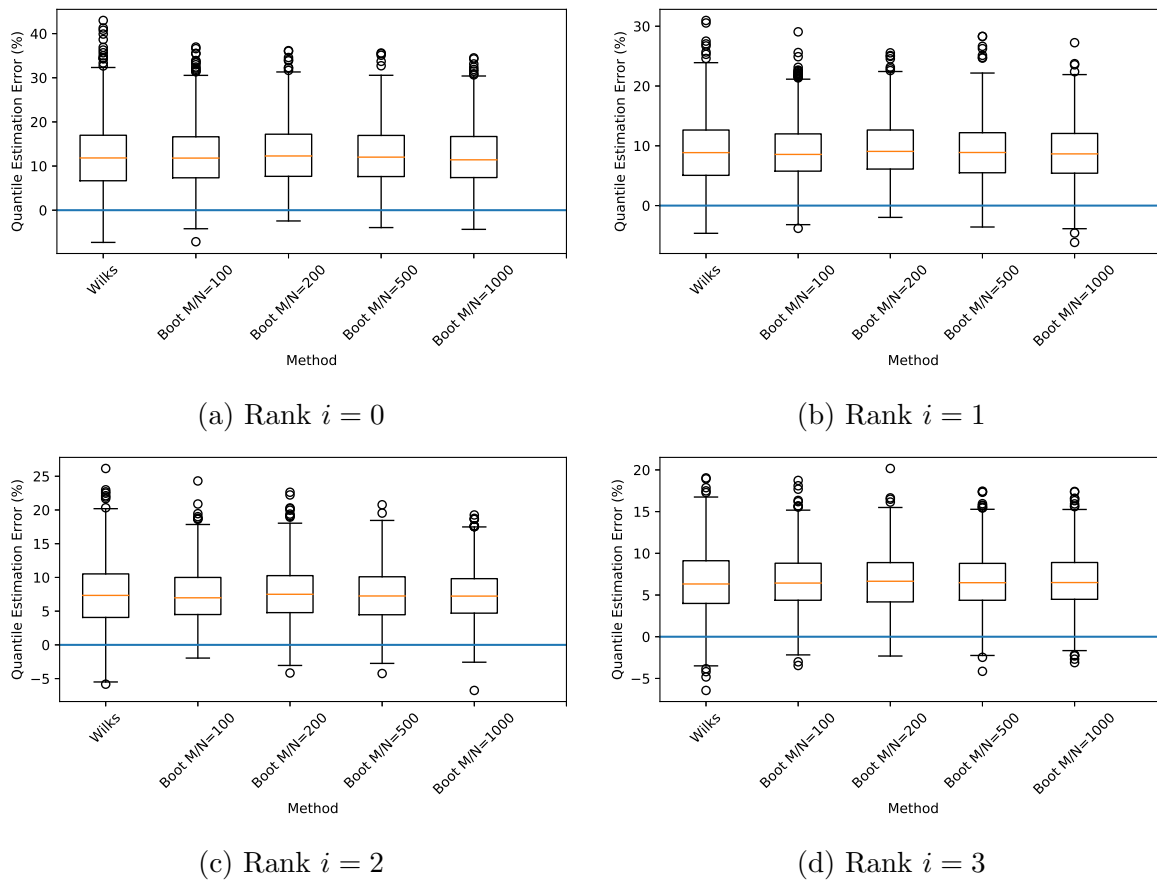
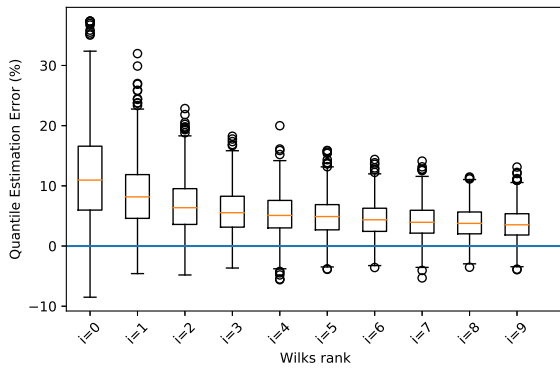


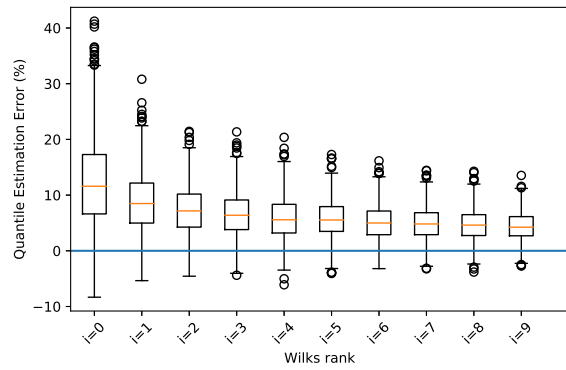
Figure 4.6: Comparison of performances for OL quantile estimation on the H2H 1x2 coupon (via semi-probabilistic approach) with Wilks and bootstrap enrichment for different ranks: values of OL quantile estimation ($\alpha = 0.9$)

suggested according to the category of structures retained: for redundant structures (i.e. prescribed B values, thus $\alpha = 0.9$, $\beta = 0.95$), a rank $i = 2$, corresponding to $N_{i,\alpha,\beta} = 61$, is suggested; for non-redundant structures (i.e. prescribed A values, thus $\alpha = 0.99$, $\beta = 0.95$), a rank $i = 0$, corresponding to $N_{i,\alpha,\beta} = 299$, is suggested. There can be cases where both quantile levels must be computed on the same category of structures: for those cases, we use 299 samples, considering the ranks $i = 0$ and $i = 21$ respectively for A and B values. This last consideration is in fact in line with the procedure suggested in *MMPDS*.

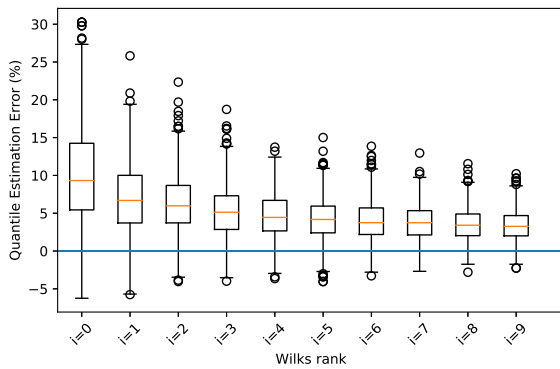
The comparison of performances between Wilks and Monte Carlo is reported in Fig. 4.8 for both decision criteria (i.e. both including or not the strength variability). We reported in abscissa the number of evaluations and on ordinates the relative errors of the quantile estimations with respect to the reference given by Monte Carlo. It can be observed that Wilks always guarantees a conservative estimation of quantiles, independently of the decision criterion, the rank or the quantile level. Relative errors are somewhat lower with the increase of targeted quantile level because of the intrinsically higher values involved. With the increase of order rank, more simulations are required and the mean error decreases. There are no differences in the relative errors of the quantiles estimated through semi-probabilistic approaches with and without strength variability.



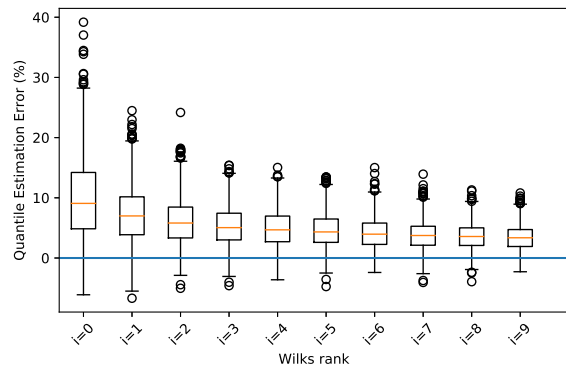
(a) $\alpha = 0.9$, no strength variability



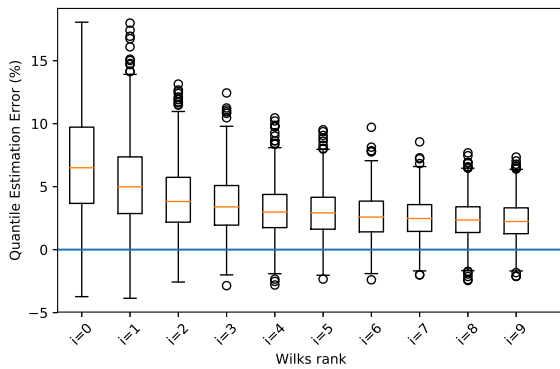
(b) $\alpha = 0.9$, with strength variability



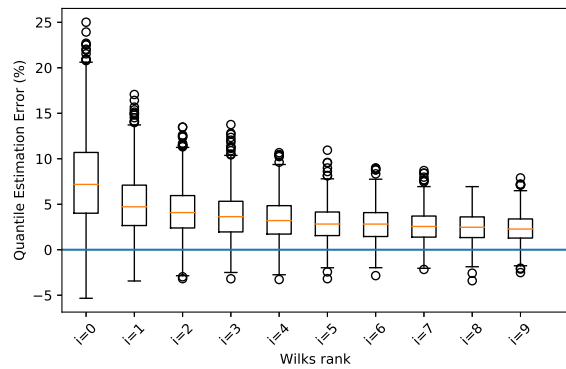
(c) $\alpha = 0.95$, no strength variability



(d) $\alpha = 0.95$, with strength variability



(e) $\alpha = 0.99$, no strength variability



(f) $\alpha = 0.99$, with strength variability

Figure 4.7: Box-plots of quantile estimations for two decision criteria and three quantile levels in function of Wilks' rank

To conclude the numerical investigation regarding several choices that can be made in the mathematical quantile estimation framework, we can say that, Wilks' approach provides the necessary tools for making a compromise between precision and computational burden to determine a quantile with fixed confidence level.

The convergence of the estimations as a function of the required sample sizes is reported in Fig. 4.9 for Wilks' method only. It can be observed, by comparing the curves related to the same α on the two decision criteria (i.e. with and without strength vari-

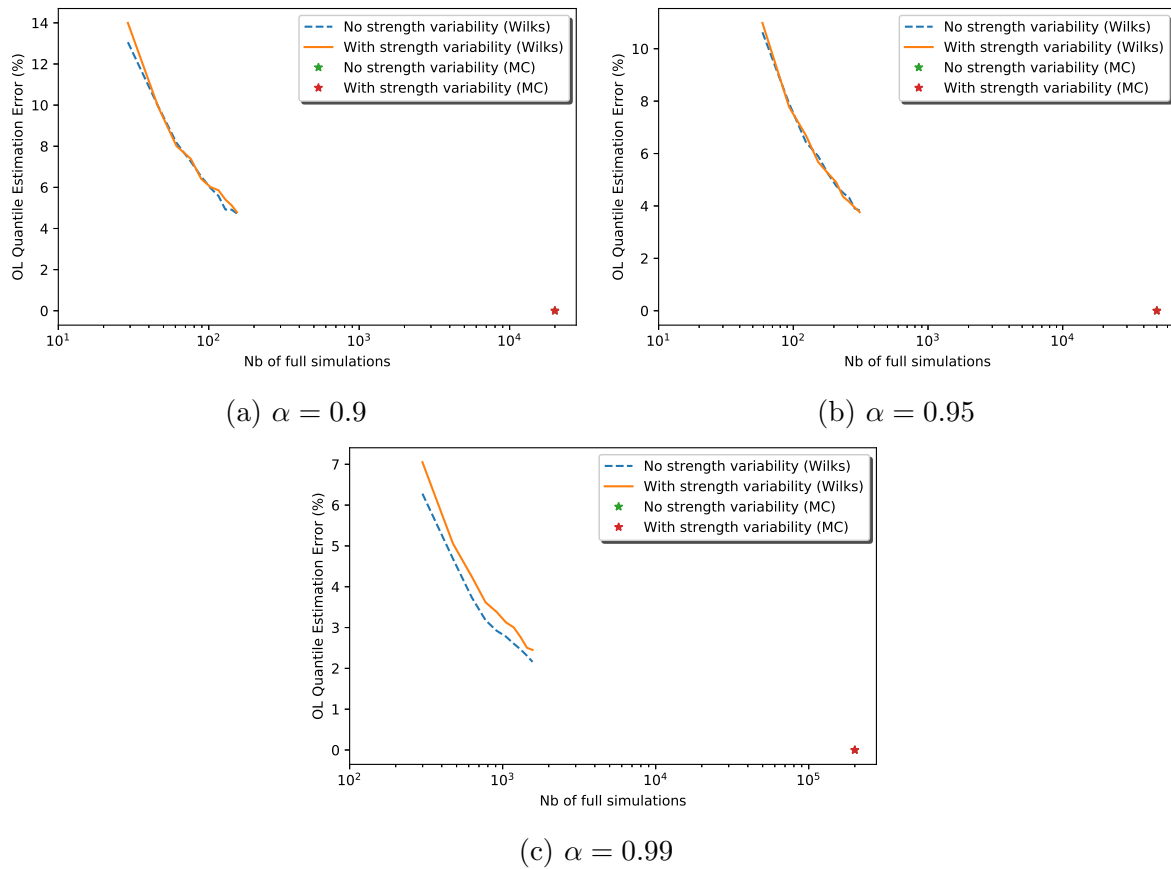


Figure 4.8: Comparison between Wilks and Monte Carlo estimations at three different quantile levels

ability), that the semi-probabilistic approach always offers improved design assumptions when it also considers strength (allowables) variability: in fact, when ignoring the whole variability of the strength, we need to introduce the nominal values R_{REF} which, being related to the quantile level α , prevent us from fully exploiting the potentials of airframe sizing. Observing more closely Fig. 4.9, the difference between the two decision criteria is constant no matter the level of precision guaranteed at the different order statistics ranks (implying different numbers of full stress analyses) and the different targeted quantile levels. Therefore, in the next section, several industrial choices affecting the overall performances are discussed on the 90th percentile level.

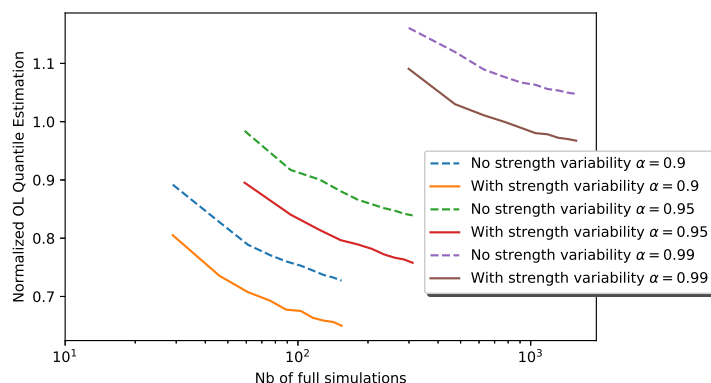


Figure 4.9: Convergence of quantile estimations for two decision criteria and three quantile levels as a function of the number of simulations

4.6.2.2 Effect of industrial choices

In this section the effects of prior industrial choices are investigated on the H2H coupon with bolting pattern 1x2. These industrial choices include:

- Decision criterion (including or not the strength variability);
- Input variables distributions (uniform, triangular and normal);
- Assembly process and associated stack chain;
- Tolerance acceptance criteria.

The effects of the definition of geometric input variability were presented in Section 4.6.1. As a reminder, the stack chain modifies the interpretation of the input variables, the individual distributions constitute the statistical description of such variables and the tolerance acceptance criteria can restrict (by filtering) the input domain.

At a general level, it must be noted that every misalignment generates an unbalance in transmitted loads: therefore, the maximum bearing load can only increase with respect to the nominal value, i.e. $OL \geq 1$. Therefore, a higher variability in inputs will certainly lead to higher variabilities in the outputs and thus higher quantiles, for a fixed quantile level α . This means that limiting the variability in inputs can improve (i.e. reduce) the overloads. Moreover, as in each location we cannot transfer more than the applied load, we will have a saturation on the overloads, specifically $OL \leq 2$ for coupon 1x2. Coupling both consideration, the support of the overload response will lie in the interval $1 \leq OL \leq 2$. The output distributions of the overloads are reported in Appendix A.

At first, we can analyze the effects of industrial specifications on 90th percentile of the output response (the maximum bearing overload) considering uniform distributions, reported in Fig. 4.10. Note that the overloads (reported on the ordinate axis) are normalized with respect to the largest value obtained in this analysis. The relative reduction of the total weight is directly proportional to the relative reduction of the loads considered in design phase, and, thus, directly proportional to the reduction of overloads OL : passing from normalized $OL = 1$ to normalized $OL = 0$ implies a weight reduction of about 40%. It can be observed a large reduction in terms of overloads for Stack Chain 3 with respect to the others, due to the fact that we block the main component (analyzed in the previous chapter): by imposing a constant distance between successive holes in the

same plate, we prevent the most detrimental configurations, based on the holes of the first plate spaced apart and the holes of the second plate approached (and vice versa).

Switching from Stack Chain 1 to Stack Chain 3 allows to reduce by almost 40% the total weight of the structure. However, we must keep in mind that the Stack Chain 3 implies the use of a drilling grid: this can be applied for relatively small structures (i.e. small H2H assemblies), but can become less affordable for larger structures. If, for example, we applied a drilling grid to the whole aircraft, this would imply to build a "negative" of the aircraft itself, which would not be affordable from an engineering (and costs) perspective.

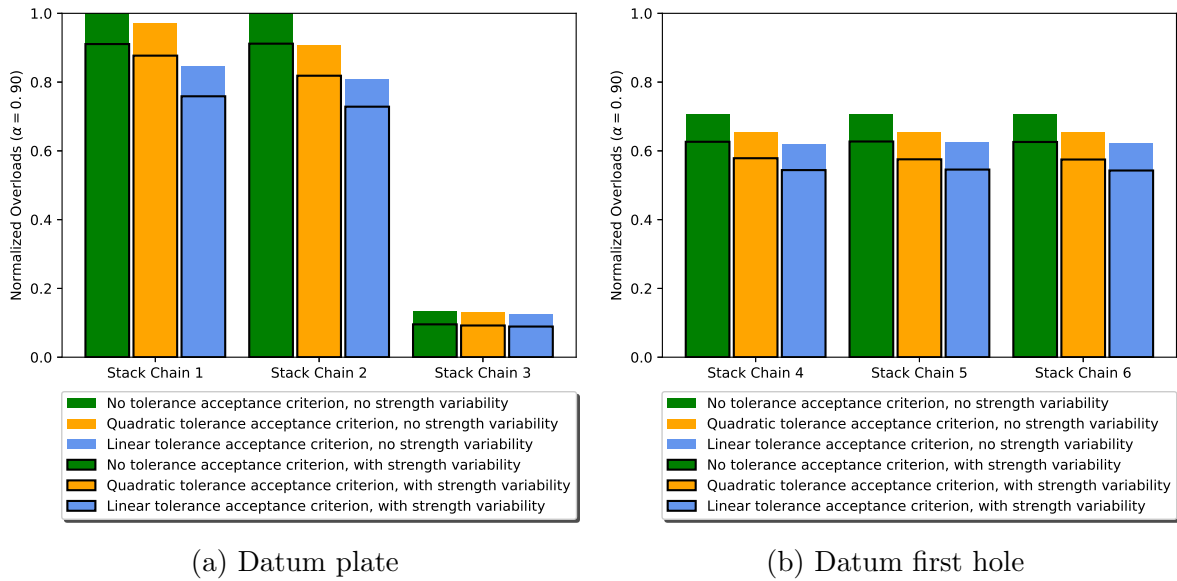


Figure 4.10: Coupon 1x2: Overload results for 90th percentile for different decision criteria, stack chains and tolerance acceptance criteria (input distribution: uniform)

All stack chains defined with datum first hole (i.e. 4, 5, 6) have similar behaviors: in fact, the only important contribution is given to the upper-mentioned main component; by introducing the same distributions on the distance between first and successive holes of the same plate, the results keep unchanged.

Comparing the stack chains defined with datum first hole (i.e. 4, 5, 6) to the ones with datum plate (i.e. 1, 2), we see a reduction in the overload. In fact, when assigning a specific distribution $X_j \sim U(-a, a)$ to every j hole on the plate i (for stack chains 1, 2), the relative distance between two holes on the same plate i will be characterized by a statistical distribution which is the convolution of the initial distributions, giving $dX_i \sim T(-2a, 0, 2a)$. On the other hand, for stack chains with datum first hole, the relative distance between holes is already an input random variable, to which we assigned from the very beginning the distribution $dX_i \sim U(-a, a)$. This leads to obtaining a larger and more dispersed PDF on the relative distance with datum plate compared to the one obtained with datum first hole.

At a general level, it is confirmed that including strength variability in the OL computation process can allow to define optimized deterministic values for the overload, independently from the other choices listed in this section.

Without any tolerance acceptance criterion, the stack chain 2 (which adds assembly errors with respect to the stack chain 1) takes into account a higher variability in misalignments between holes due to the added global translation of the second plate with respect to the first one: this could imply a slightly higher variability in outputs. However, Wilks' method does not allow to compare little differences between values, as the conservativeness is only available in probabilistic terms: strictly speaking, we know the probability of overestimating the quantiles (through the imposed confidence level) but not the magnitude of the overestimation itself. On the other hand, when including a tolerance acceptance criterion, more combinations are excluded in stack chain 2 than in stack chain 1, leading to the opposite effect of reducing the input variability and thus the overloads.

On top of that, it can be observed that the linear tolerance acceptance criterion offers at the same time a more conservative reduction of the input domain and lower overloads. Still, the effect is limited for the stack chain 3 (based on perfect drilling process and imperfect assembly routine).

In Fig. 4.11 and Fig. 4.12 we reported the results relative to, respectively, triangular and normal individual distributions of the input variables.

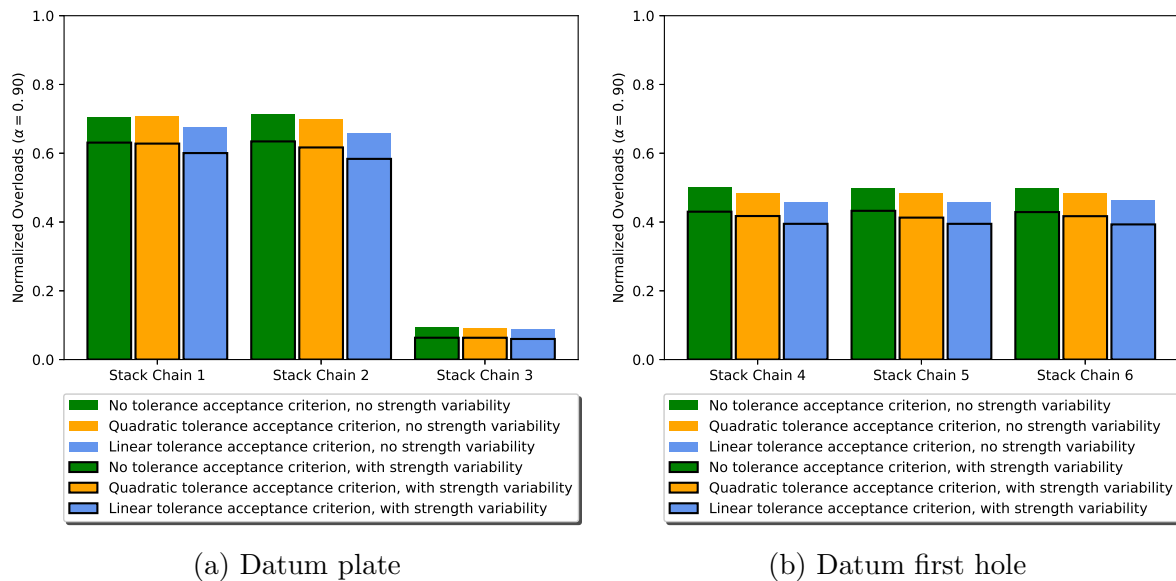


Figure 4.11: Coupon 1x2: Overload results for 90th percentile for different decision criteria, stack chains and tolerance acceptance criteria (input distribution: triangular)

The comparisons among different choices of individual distributions follow the same logic as the ones mentioned in the previous analysis. Reducing input variability (thus passing from uniform to triangular to normal distributions) can lower the overloads. On the other hand, reduced individual input variabilities attenuate the effects of the tolerance acceptance criteria. This is due to the fact that the PDF is reduced on the tails, reducing the amount of samples involved in the filtering induced by the tolerance acceptance criterion: therefore, switching formulation of tolerance acceptance criterion affects overloads results much less.

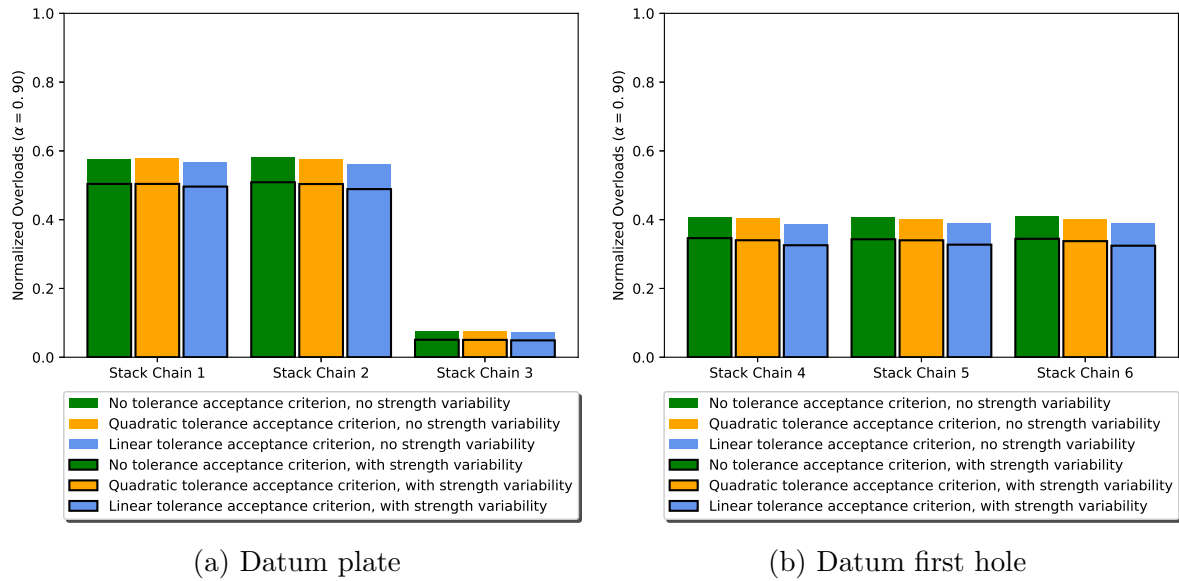


Figure 4.12: Coupon 1x2: Overload results for 90th percentile for different decision criteria, stack chains and tolerance acceptance criteria (input distribution: normal)

4.6.3 Coupon 1x5

We repeated the same procedure for a coupon with bolting pattern 1x5, using the PLS surrogate model constructed in the previous chapter (cf. Section 3.3.4.4).

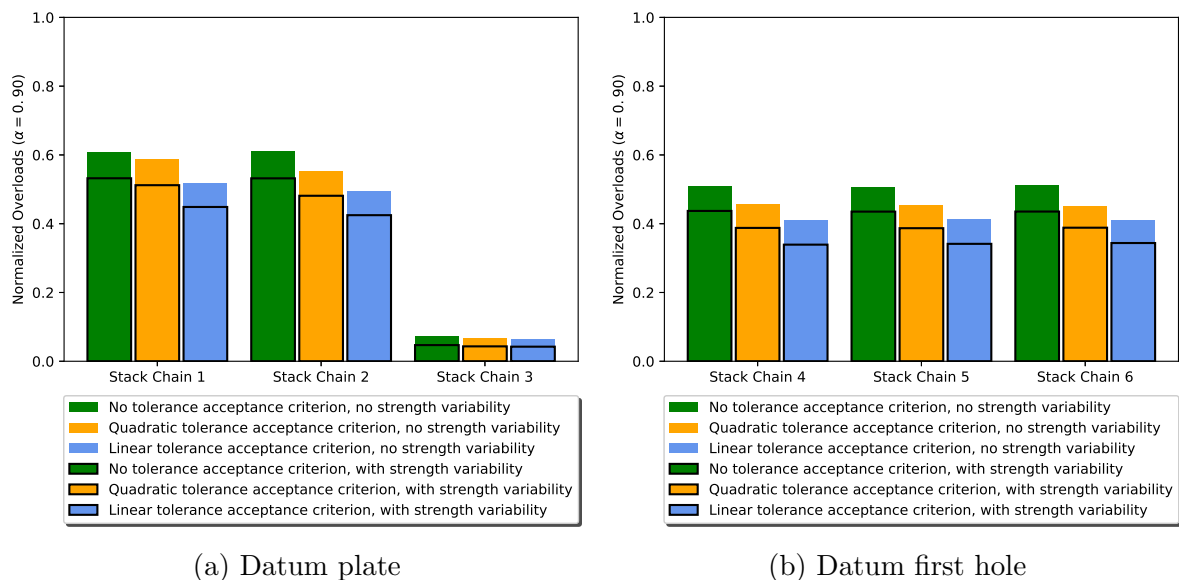


Figure 4.13: Coupon 1x5: Overload results for 90th percentile for different decision criteria, stack chains and tolerance acceptance criteria (input distribution: uniform)

Globally, similar conclusions can be drawn for the analysis on coupon 1x5. With respect to previous results, it can be observed from Fig. 4.13, 4.14 and 4.15:

- With respect to the coupon 1x2, overloads are generally reduced;

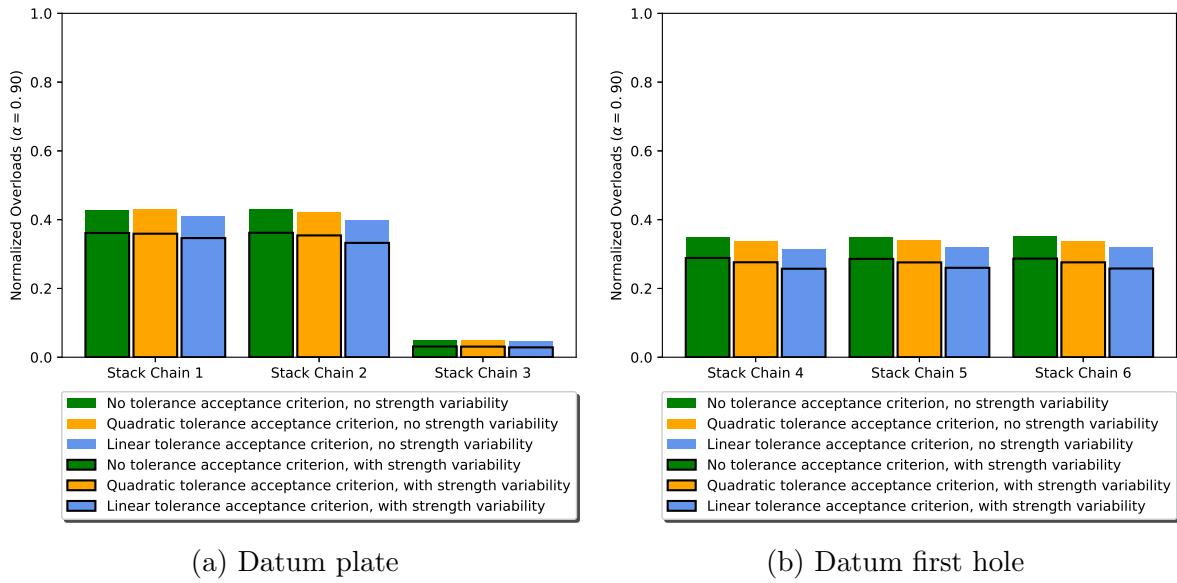


Figure 4.14: Coupon 1x5: Overload results for 90th percentile for different decision criteria, stack chains and tolerance acceptance criteria (input distribution: triangular)

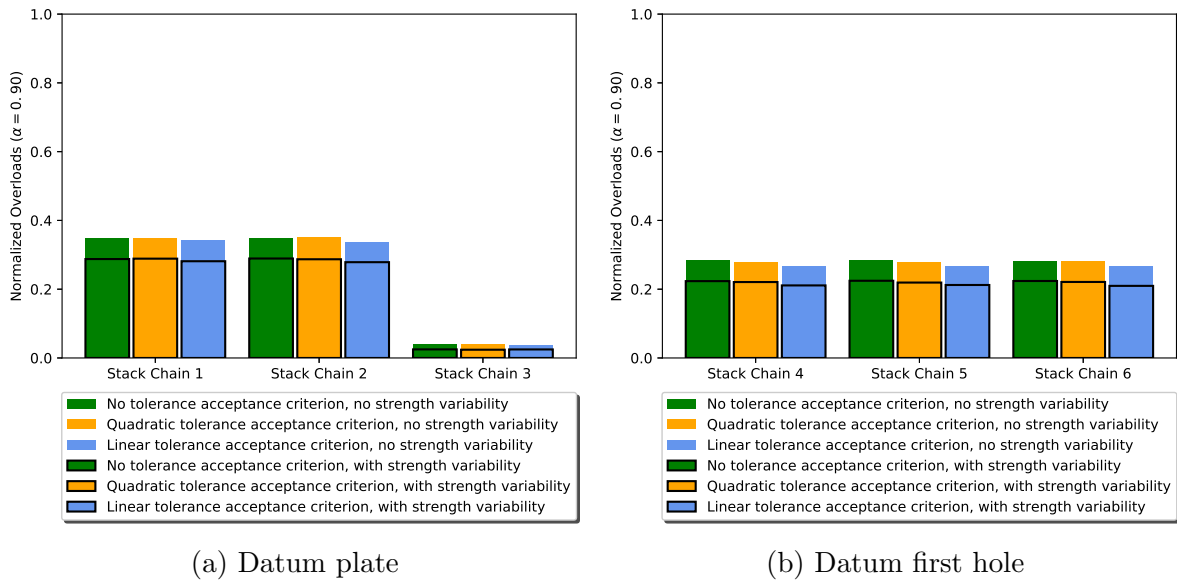


Figure 4.15: Coupon 1x5: Overload results for 90th percentile for different decision criteria, stack chains and tolerance acceptance criteria (input distribution: normal)

- Gains from stack chains with datum plate (1, 2) to datum first hole (4, 5, 6) are less evident, but still present;
- The same conclusions on the overall rank of effects of industrial choices on coupon 1x2 can be extended to coupon 1x5, except for the differences among entry distributions and the effects of stack chains, which are less evident.

The reduction in gains due to the input PDFs can be explained by the augmented input dimensionality. In fact, it is more difficult to access the most detrimental configura-

tions for the load redistribution. The same principle explains the reason for the decrease in the global level of overloads.

On the other hand, the augmented dimension attenuates the differences between the groups of stack chains with datum plate with respect to the ones with datum first hole. Considering two-by-two couples of holes on the same plate, it is more difficult to access the configurations on the tails distributions of relative two-by-two deviations.

Another explanation of the reduced effect of the choice of the stack chain must be sought in the modal description offered by the PLS surrogate model. Let us focus on the variables δX_j explaining the relative (i.e. considering the difference between the two plates) longitudinal misalignment on the j -th hole. On coupon 1x2 we had only one component, fundamentally given by $\delta X_2 - \delta X_1$, which was responsible for the variability of the bearing response on every location. For the H2H coupon 1x5, we have 4 components which consider different combinations of i, j for the expression $\delta X_i - \delta X_j$. Now, when we use the first hole as a datum (i.e. considering stack chains 4, 5, 6), we only reduce the variability of the difference $\delta X_j - \delta X_1$ (with $j > 1$), for the reasons exposed in the previous section. The problem is that this constitutes actually only a part of the complete list of modes: therefore, the final outcome will be an attenuation of the overload gains provided by the use of manufacturing processes based on datum first hole (i.e. stack chains 4, 5, 6).

4.6.4 Coupon 3x5

A similar analysis was conducted on coupon 3x5 as well, using the PLS surrogate model retrieved in the previous chapter (cf. Section 3.3.5) for the stress analyses. Related results are reported in Fig. 4.16, 4.17 and 4.18.

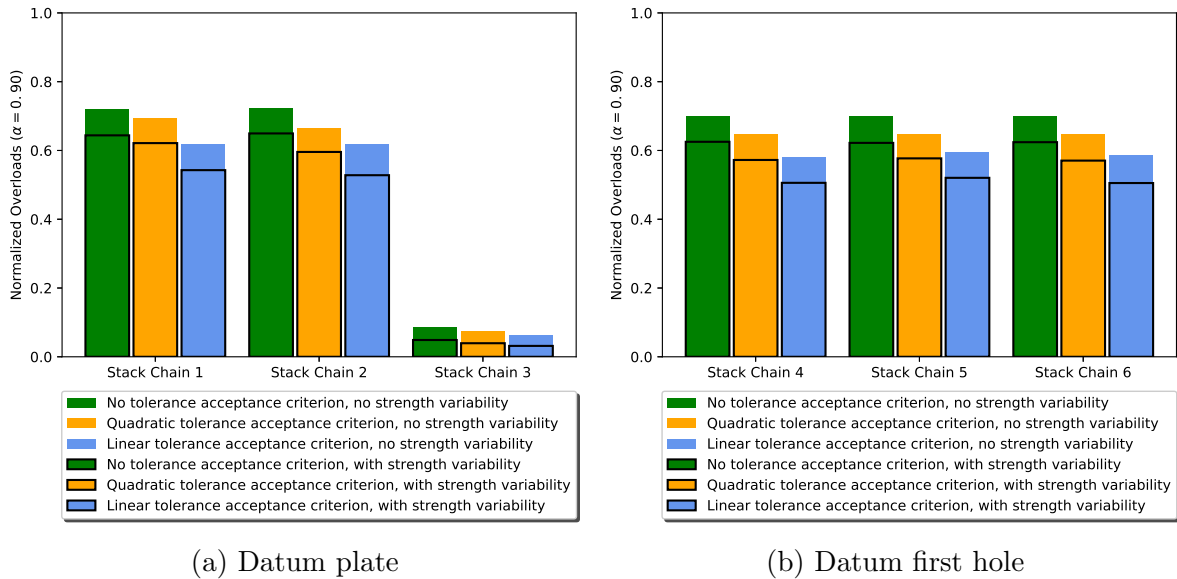


Figure 4.16: Coupon 3x5: Overload results for 90th percentile for different decision criteria, stack chains and tolerance acceptance criteria (input distribution: uniform)

With respect to the previous cases, we have:

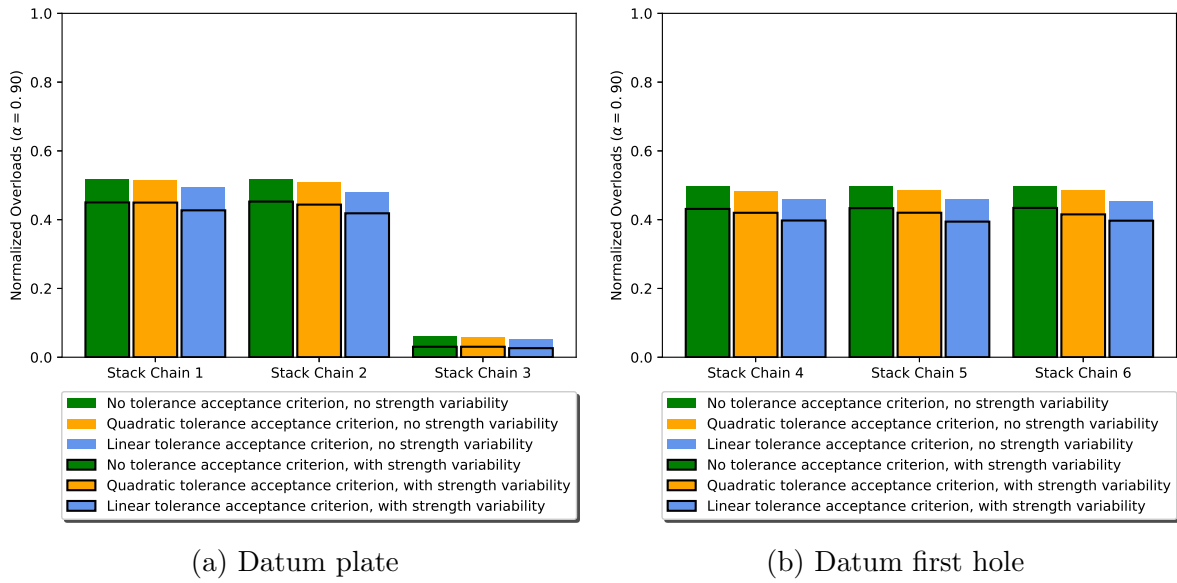


Figure 4.17: Coupon 3x5: Overload results for 90th percentile for different decision criteria, stack chains and tolerance acceptance criteria (input distribution: triangular)

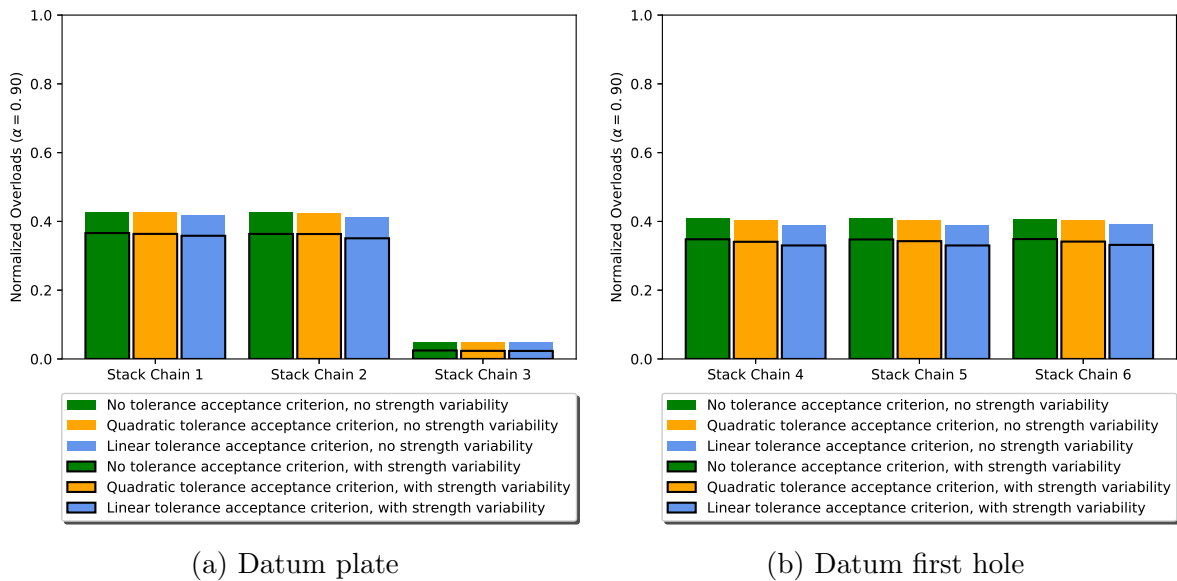


Figure 4.18: Coupon 3x5: Overload results for 90th percentile for different decision criteria, stack chains and tolerance acceptance criteria (input distribution: normal)

- The difference between groups of stack with different datums (1,2 vs 4,5,6) are much less evident than other cases;
- Overall overloads levels are higher compared to 1x5, but lower than 1x2;
- The effect of different input distributions is lower than 1x2 and higher than 1x5.

The general behavior of reduction of the effects of the choice of the stack chain which was observed on coupon 1x5 is still valid on the coupon 3x5. In fact, even more com-

ponents explain the general behavior of the bearing load re-distribution, reducing the impact of the choice of different datums in the manufacturing process.

On the other hand, to explain the difference between the results related to coupons 1x5 and 3x5, we may think at the latter as a series system of the former. Practically speaking, when disposing of multiple lines of bolts with bolting pattern 1x5, the event related to a threshold exceedence can happen with similar probability occurrence on the different lines. Therefore, the related quantiles of the output response of the system will be increased. Note, however, that this simplification from a system point of view is only qualitative and not numerically confirmed by the computations: in fact, in the nominal configuration with fitted and perfectly aligned holes (drilled with counter-drilling techniques), the loads transferred on the corners are higher than the ones on the edges, so that the upper-mentioned probability of exceeding a fixed threshold is not exactly the same in the three lines of bolts.

4.7 Conclusion

In this chapter we formalized a so called semi-probabilistic approach, capable to define new deterministic representative values to adopt in an aircraft design phase, supported by a probabilistic framework. This is coherent with the current certification requirements on the static strength demonstration from CS 25 (for large airplanes). The proposed semi-probabilistic approach can be used to define overloads (representing load concentration factors) from fixed input distributions, or to re-define the input tolerances to guarantee a target probability *PoE* of over-estimating the structural performances. The former direction was pursued in this chapter to define the overloads on H2H coupons via Wilks' method.

From the mathematical framework analysis, we observed that, for H2H applications, the statistical ranks and the inclusion of strength variability allows to define optimized deterministic values for the overload, while no improvement was observed using a bootstrap procedure. Generalizing this conclusion, we can state that including more contributions to the overall variability in the semi-probabilistic approach, can allow to further improve the associated deterministic values.

For further analyses on overload factors on H2H applications, we suggest to use for non-redundant structures the minimum rank $i = 0$ on the quantile level $\alpha = 0.99$, a minimum sample size of 299. This is in line with the prescriptions from *MMPDS*. On the other hand, if only redundant structures are to be analyzed (i.e. quantile level $\alpha = 0.9$), a rank $i = 2$ is sufficient, leading instead to a minimum population, according to Wilks' formula, with 61 samples.

Focusing on the effects of industrial choices on the numerical results of overloads, we observed that the manufacturing process and the associated stack chain is the main driver allowing to improve the structural performances of H2H application on aeronautical assemblies, through reduced overloads. In second place, the statistical distributions of individual features in the tolerance mapping can also significantly affect the performances. The tolerance acceptance criterion assumes only a marginal role in influencing the overload outcomes.

An important point is given by the variation of overload factors as a function of

the bolting pattern: they decrease when increasing the complexity of bolting patterns on longitudinal direction (going from 1x2 to 1x5) but, at the same time, they slightly increase when increasing the complexity on transversal direction (going from 1x5 to 3x5). However, this latter effect is much less significant than the former. Nevertheless we recall that all the conclusions related to the comparison between different bolting patterns must be confirmed by further numerical studies involving nonlinear material models.

The numerical results presented in this chapter are related to specific surrogate models trained in Chapter 3. Therefore, these are valid for high levels of applied load (which would be consistent with higher t/d), where the linear approximation via PLS is accurate. As it will be shown in Chapter 6, the PLS can be used to support other machine learning techniques, overcoming this difficulty. However, in this dissertation we will focus on this alternative use of PLS for estimating failure probabilities (or, specifically in our framework, PoE), leaving the application for quantile estimations as a perspective.

In the following chapters, we will analyze the second declination of the semi-probabilistic approach, to re-define the input tolerances guaranteeing a targeted PoE . Chapter 5 and 6 focus on proposing methods for the computational burden reduction when estimating a general failure probability: in Chapter 5 the attention is focused on the use of sampling methods, while Chapter 6 deals with the approximation of high dimensional problems via a Kriging-based surrogate model. Finally, in Chapter 7 the tolerance optimization problem is formalized and the methods developed in Chapter 5 and 6 are introduced in the optimization process.

Chapter 5

Sampling Methods for Reliability Analysis

5.1 Introduction

In the previous chapters, we highlighted the important role of uncertainties in engineering design and the impact they can have on final performances.

Uncertainties in input data can be analyzed in the general UQ&M framework (described in Section 1.2) to measure the impact on outputs, determine the most influential factors in output variability, accredit a model, verify the compliance of prerequisites imposed by legislation or select the best design [De Rocquigny et al., 2008] (cf. Section 2.1). Reliability analyses focus on ascertaining the failure risk associated to a specific engineering design [Larsson, 2015]. Over the past decades, the paradigms of this field have been progressively formalized [Pham, 2006, Rykov et al., 2010, Birolini, 2013, Trivedi and Bobbio, 2017]. Such concepts are applied in almost all knowledge fields, from medicine, finance [Rykov et al., 2010], engineering systems [Rausand and Høyland, 2003] to automotive, aerospace and ship industry [Nikolaidis et al., 2007]. In this work, particular attention is given to structural reliability applications [Lemaire, 2013, Pellissetti and Schuëller, 2006, Qiu et al., 2013, Gogu, 2021]. A state of the art of the applications of reliability in the civil and aeronautical domain was presented in Section 2.4.

In Chapter 4, we introduced the *semi-probabilistic approach*, constituting a framework to extend the current certification requirements for the static strength demonstration of large aircrafts. We classified the input properties according to the metric of variability and defined the probability *PoE* of under-estimating the structural performances in the deterministic design phase. Then, we formulated two declinations of this framework: the first, analyzed in Chapter 4, aims at identifying new deterministic values to use in classical deterministic design, by means of evaluating the effect of the uncertainty of the input parameters; the second aims at determining the largest input variabilities which can allow to satisfy a specific constraint on the *PoE*, defined from fixed requirements of the structural performances. The first declination constitutes, from a mathematical point of view, a quantile estimation problem. The second declination can be considered as a reliability-based design optimization problem. In this chapter (and in the following one), we focus on the methods to evaluate the reliability, proposing some enhancements to existing methodology.

To assess the reliability level of a designed structure, several metrics were introduced in the literature. Among, the most common is the index β_{HL} introduced by Hasofer and Lind [Hasofer and Lind, 1974], which is defined as the minimum euclidean distance (L^2 norm) between origin of a standard normal space and the Limit State Surface (LSS) representing a failure mode of the system. The point situated at distance β_{HL} is known as *design point* or *Most Probable Failure Point (MPFP)*.

Another important reliability performance metric is given by the failure probability P_f , which can be associated to the *PoE* of the proposed *semi-probabilistic approach*. As a reminder, the *PoE* does not constitute a probability of being in failure condition (as does the P_f), but represents the probability of over-estimating the structural performances by using deterministic quantities in the classical (deterministic) design phase. However, from a mathematical point of view, the methods which can be implemented to evaluate the P_f can be also used to compute the *PoE*.

The classical Monte Carlo (MC) simulation method is probably among the simplest and most popular sampling based simulation methods used in reliability applications [Hammersley, 2013, Bourinet, 2021] to determine P_f . Originally defined to compute general integrals, it simply consists in sampling data according to the input distributions and estimating the expectation through an arithmetic sum. This constitutes the reference for all successive approaches, because of its simplicity, intrinsic stability and independence from problem dimension and complexity of the system considered in the analysis.

On the other hand, MC presents a slow convergence rate, above all for rare events estimation. This led to the need for more agile methods, able to reduce the variance of the P_f estimation with the same number of samples.

Importance Sampling (IS), is a popular variance reduction technique [Tokdar and Kass, 2010], based on the concentration of the sampling in specific areas defined by a support distribution. While IS has been initially developed in the context of reliability several decades ago, it continues to be a very active topic with many recent developments seeking to further improve it [Papaioannou et al., 2019, Xiao et al., 2020b, Chaudhuri et al., 2020, Ling and Lu, 2021, Wang et al., 2021b, Zuniga et al., 2021, Jia and Wu, 2022], together with industrial applications, like [Gao et al., 2020, Misraji et al., 2020, Subramanian and Mahadevan, 2020], among others. One open problem is given by the most efficient construction of the support importance distribution of IS. Several advanced techniques, going by the name of Adaptive Importance Sampling, build this importance function during the simulations in an adaptive way [Richard and Zhang, 2007, Cappé et al., 2008, Müller et al., 2019, Zhang et al., 2022a]. This issue is not specifically considered in the present work, but needs to be kept in mind.

Another variance reduction technique, Separable Monte Carlo (SMC) [Smarslok, 2009, Smarslok et al., 2010] focuses on a particular category of limit state functions, where response and capacity (typically stress and strength in structural analysis) present no mutual dependence (or simply rely on distinct independent input variables). This assumption is common in structural engineering [Smarslok, 2009]. This consists in sampling stress and strength (or response and capacity, as denoted in [Smarslok et al., 2010]) separately and evaluate every possible combination of the two. Therefore, a larger database could be built with fewer simulations, while also allowing the construction of unbalanced datasets to exploit differences in computational burden of response and capacity (the latter is usually computationally inexpensive to sample).

Following the same idea, Importance Separable Monte Carlo (ImpSMC) was also proposed by Chaudhuri et al. [Chaudhuri and Haftka, 2013]. This is in fact a combination of IS and SMC, benefiting from the respective advantages of both approaches. In [Chaudhuri and Haftka, 2013], a failure probability estimator was presented, and the resulting variance reduction was illustrated empirically. Unfortunately, to date no closed form expression of the variance of the P_f estimated by ImpSMC is available. This shortcoming makes it difficult to optimally exploit the method in order to achieve maximum numerical efficiency gains. Thus, the objective of this chapter is to develop a closed form variance estimator of the P_f estimated by ImpSMC and to extensively analyze situations in which the ImpSMC procedure will be most useful.

In Section 5.2 a brief overview of MC, IS and SMC is provided. In Section 5.3, ImpSMC approach is presented and mathematically formalized. Two numerical examples, related to two structural reliability test cases, are presented in Section 5.4 to compare methods enunciated in Sections 5.2 and 5.3. Then, conclusions are summarized in Section 5.6. For the interested reader, empirical variance validation and further details of the variance estimator proof are reported in Appendix B.

5.2 Background on relevant sampling-based methods

The goal of this section is to present several approaches adopted to evaluate the failure probability of a system. We are going to use the following notation:

- X : random design variable;
- x : realization of X ;
- $g(X)$: Limit State Function (LSF), conventionally negative to indicate a failure state;
- $G(X) = 1_{g(X)<0}$: failure indicator.

The LSF is expressed in a way that it is negative when the system is in a failure condition. The hypersurface described by $g(X) = 0$ is often referred as Limit State Surface (LSS).

5.2.1 Monte Carlo (MC) Simulation

MC is usually considered as the reference for all sampling-based reliability approaches [Metropolis and Ulam, 1949]. In integral form, the failure probability can be expressed as follows:

$$P_f = \int_D G(x)f(x)dx \quad (5.1)$$

Here f represents the Probability Density Function (PDF) of the random variable X . Denoting by \widehat{P}_f an estimator of P_f , expectation, variance and coefficient of variation coV of this estimator are reported in the following equations:

$$E[\widehat{P}_f] \approx \frac{1}{N} \sum_{i=1}^N G(x_i) \quad \text{Var}(\widehat{P}_f) \approx \frac{E[\widehat{P}_f] - E[\widehat{P}_f]^2}{N} \quad \text{coV}(\widehat{P}_f) \approx \sqrt{\frac{1 - E[\widehat{P}_f]}{NE[\widehat{P}_f]}} \quad (5.2)$$

Generally, coV is the performance indicator adopted to indicate the precision of the estimation itself. It is easy to understand that MC is not affected by the curse of dimensionality of the problem. Moreover, it is stable and makes no assumption on the LSS itself. However, for rare event estimation, the convergence rate of coV follows $(P_f N)^{-1/2}$, leading to a very high number of simulations necessary to achieve an acceptable precision.

5.2.2 Importance Sampling (IS)

Importance Sampling is a well-known approach to estimate integrals with fewer data than MC. It stems from a very simple operation on the P_f integral:

$$P_f = \int_D G(x)f(x)dx = \int_D G(x)f(x)\frac{q(x)}{q(x)}dx = \int_D \left(G(x)\frac{f(x)}{q(x)}\right)q(x)dx \quad (5.3)$$

Here q represents a generic function, which must only respect the requirement of being equal to zero where $f(x) = 0$. In particular, in *IS* the function q is a PDF constituting the support importance function. Therefore, x realizations of the random variable X are sampled following the PDF q . In a compact notation, Eq. 5.3 can be rewritten as follows:

$$P_f = E_q[G(X)w(X)] \quad w(X) = \frac{f(X)}{q(X)} \quad X \sim q \quad (5.4)$$

The quantity w is often referred in the literature as *importance weight*. Expectation and variance of the corresponding P_f estimator are reported in the following equation:

$$E[\widehat{P}_f] \approx \frac{1}{N} \sum_{i=1}^N G(x_i)w(x_i) \quad \text{Var}(\widehat{P}_f) \approx \frac{1}{N} \sum_{i=1}^N [G(x_i)w(x_i) - E[\widehat{P}_f]]^2 \quad (5.5)$$

The reader can observe that the choice of q is not trivial and could even lead to non-converging situations. On the other hand, a good choice of q may significantly accelerate convergence rate compared to MC. An abundant literature on procedures to build an optimal q PDF is available to the interested reader [Karamchandani et al., 1989, Zhang, 1996, Au and Beck, 1999, Richard and Zhang, 2007, Cappé et al., 2008, Tokdar and Kass, 2010, Müller et al., 2019].

5.2.3 Separable Monte Carlo (SMC)

The Separable Monte Carlo (SMC) method, proposed by Smarslok et al. [Smarslok, 2009, Smarslok et al., 2010], was initially developed in a structural reliability context but it is generalizable to any reliability problem, under an independence assumption. In structural reliability, the method starts from the assumption that strength R and stress S rely on distinct independent variables. The key feature behind SMC is the possibility to sample separately R and S , and successively compare all combinations.

In this context the LSF is expressed as follows [Smarslok et al., 2010]:

$$g(X) = g(X_R, X_S) = R(X_R) - S(X_S) \quad (5.6)$$

Where X_R and X_S are partitions of the original design variable vector X affecting either capacity R or response S respectively. Random variables X_R and X_S are considered to be independent. Such an independence assumption is often verified in structural reliability but it can, of course, be verified in a large number of other applications. The failure indicator G is rewritten in compact notation as follows:

$$G(R, S) = 1_{R < S} = I(R < S) \quad (5.7)$$

Here we omit the fact that response and capacity are actually functions of original variable sets X_R and X_S (i.e. $R = R(X_R)$ and $S = S(X_S)$) in order not to overload the notation. Of course, input variables X_R and X_S are sampled according to their original distributions while R and S are computed as output. This does not affect neither results nor the proof. It is worth noticing that the expressions in Eqs. 5.6-5.7 are mere examples of separation between two blocks R and S : since the proof for the SMC procedure [Smarslok et al., 2010] does not require a particular choice on the expression of g , the validity is actually extended to any LSF defined by any operation linking two independent variables. Denoting by r and s realizations of respectively R and S , and by D_R and D_S their domains, failure probability can be expressed as:

$$P_f = \int_D G(r, s) f_{RS}(r, s) dr ds = \int_{D_S} f_S(s) \left(\int_{D_R} G(r, s) f_R(r) dr \right) ds \quad (5.8)$$

Using a compact notation, expectation will be given by:

$$P_f = E_S [E_R [\widetilde{F}_R(S)]] \quad \text{where } \widetilde{F}_R(S) = G(R, S) \quad (5.9)$$

The choice of the symbol $\widetilde{F}_R(S)$ is justified by the fact that its expectation with respect to the capacity variable is the conditional CDF F_R of the variable R at point S [Smarslok et al., 2010]. Failure probability estimation will therefore be given by [Smarslok et al., 2010]:

$$E [\widehat{P}_f] \approx \frac{1}{NM} \sum_{i=1}^N \sum_{j=1}^M G(r_j, s_i) \quad (5.10)$$

A variance estimator can be expressed as follows (proof available in [Smarslok, 2009]):

$$\begin{aligned} \text{Var}(\widehat{P}_f) &= \frac{1}{NM} P_f + \frac{M-1}{NM} E_S [E_R [\widetilde{F}_R(S)]^2] + \frac{N-1}{MN} E_S [E_R [\widetilde{F}(\min(S_1, S_2))]] \\ &\quad - \frac{N+M-1}{NM} P_f^2 \end{aligned} \quad (5.11)$$

The numerical quantities can be obtained through the following approximations:

$$\begin{aligned}
E_S \left[E_R \left[\widetilde{F}_R(S) \right]^2 \right] &\approx \frac{1}{N} \sum_{i=1}^N \left(\sum_{j=1}^M \frac{G(r_j, s_i)}{M} \right)^2 \\
E_S \left[E_R \left[\widetilde{F}_R(S_1), \widetilde{F}_R(S_2) \right] \right] &\approx \frac{2}{NM} \sum_{i=1}^{N/2} \sum_{j=1}^M (G(r_j, s_{2i-1})G(r_j, s_{2i}))
\end{aligned} \tag{5.12}$$

The term $G(r_j, s_{2i-1})G(r_j, s_{2i})$ was reported in the original work [Smarslok et al., 2010] as $G(r_j, \min(s_{2i-1}, s_{2i}))$, since the main focus was on LSF expressed as in Eq. 5.6. However, the proof of the analytical variance estimator is not affected by the choice of the shape of g (and thus G) function, but only requires a separation between two independent blocks R and S , thus we propose to use the more general notation in Eq. 5.12. A compact form is provided as well [Smarslok et al., 2010] to better understand the effect of number of samples of response and capacity:

$$Var(\widehat{P}_f) = \frac{1}{NM} \phi_1 + \frac{1}{N} \phi_2 + \frac{N-1}{NM} \xi_{12} \tag{5.13}$$

Where:

$$\begin{aligned}
\phi_1 &= P_f - E_S \left[E_R \left[\widetilde{F}_R(S) \right]^2 \right] \\
\phi_2 &= E_S \left[E_R \left[\widetilde{F}_R(S) \right]^2 \right] - P_f^2 \\
\xi_{12} &= E_S \left[E_R \left[\widetilde{F}_R(S_1) \widetilde{F}_R(S_2) \right] \right] - P_f^2
\end{aligned} \tag{5.14}$$

Separate sampling of R and S allows to create a larger database with fewer simulations of each. Moreover, when capacity and response simulations imply very different computational burdens (often sampling S is much more costly), one can use unbalanced datasets, reducing the overall computational efforts. On top of that, a significant variance reduction with respect to MC was shown in [Smarslok, 2009, Smarslok et al., 2010]. In particular, SMC proved to be increasingly beneficial when most of LSF variance came from capacity [Smarslok, 2009].

5.3 ImpSMC approach

This section provides a full description of the method known as *ImpSMC* (Importance Separable Monte Carlo), introduced by Chaudhuri [Chaudhuri and Haftka, 2013]. This method consists of a combination of the upper-mentioned *IS* and *SMC*, and it is the method for which we will seek to construct a variance estimator for its probability of failure estimate.

The description of the ImpSMC approach starts from the definition of the estimation of the failure probability P_f in Section 5.3.1. Then, we define the variance estimator in Section 5.3.2. From this, in Section 5.3.3 we propose an alternative version of the same variance estimator, discussing their equivalence in Section 5.3.4. Then, we discuss and prove the necessary conditions for the validity of the analytical variance estimator in Section 5.3.5, from a theoretical point of view. Finally, we highlight the potential of the variance estimator itself, underlining the effects on its practical implementation.

5.3.1 Probability of failure estimation

As for *SMC*, R and S are functions of original variable sets X_R and X_S . To improve readability, this dependence is omitted, while keeping in mind that the actual sampling is performed on X_R and X_S . These are sampled according to support functions (or importance distributions) respectively $q(X_R)$ et $h(X_S)$. In the following, response and capacity will be treated as the sampled variables and importance distributions will be denoted as $q(R)$ and $h(S)$, without this affecting results. Repeating the same processes used for *IS* and *SMC*, one obtains:

$$P_f = E_h \left[\frac{f_S(S)}{h(S)} E_q \left[\frac{G(R, S) f_R(R)}{q(R)} \mid S \right] \right] \quad (5.15)$$

In the following, a compact notation, consistent with [Smarslok et al., 2010], is adopted:

$$\begin{aligned} \widetilde{H}_R(S) &= \widetilde{H}(R, S) = \frac{f_S(S)}{h(S)} \frac{f_R(R)}{q(R)} G(R, S) \\ \widehat{H}_R(S) &= \frac{1}{M} \sum_{j=1}^M \widetilde{H}(R_j, S) \\ H(S) &= E_q[\widehat{H}_R(S)|S] = E_q[\widetilde{H}_R(S)|S] \\ \widehat{P}_f &= \frac{1}{N} \sum_{i=1}^N \widehat{H}_R(S_i) \\ P_f &= E_h [E_q[\widetilde{H}_R(S)|S]] = E_h[H(S)] = E[\widehat{P}_f] \end{aligned} \quad (5.16)$$

Here the subscript R implies a dependence of \widetilde{H} with respect to R variable and must not be confused with q and h representing the two importance functions used to sample R and S variables respectively. As for *SMC*, when estimating P_f based on samples according to Eq. 5.15, all possible combinations of R and S are compared to each other to verify a failure condition. We take this into account by introducing N independent identically distributed copies of S in our estimation. We make the distinction between the original variable \widetilde{H}_R and its estimation \widehat{H}_R via arithmetic mean.

The corresponding probability of failure estimator will be given by [Chaudhuri and Haftka, 2013]:

$$E[\widehat{P}_f] \approx \frac{1}{NM} \sum_{i=1}^N \sum_{j=1}^M G(r_j, s_i) \frac{f_R(r_j)}{q(r_j)} \frac{f_S(s_i)}{h(s_i)} \quad (5.17)$$

Where M represents the number of realizations of the capacity R .

5.3.2 Variance estimation on \widehat{P}_f

The novelty proposed in this chapter consists in the determination of an analytical variance estimator. In [Chaudhuri and Haftka, 2013], variance reduction was proved empirically, but no actual theoretical estimator of the associated variance was provided.

We focus on the definition of the analytical estimator of $Var(\widehat{P}_f)$, starting from Eq. 5.16. It is worth noticing that even though all S_i are independent, the terms $\widetilde{H}_R(S_i)$ are

not. Therefore, a correlation in datasets is present and a covariance term will appear in the variance of the sum over all terms defined by the copies of the variable S :

$$Var(\widehat{P}_f) = \frac{1}{N^2} \left(\sum_{i=1}^N Var[\widetilde{H}_R(S_i)] + 2 \sum_{i=1}^N \sum_{j=i+1}^N Cov[\widetilde{H}_R(S_i), \widetilde{H}_R(S_j)] \right)$$

Here, the variable R is unique and thus is not indexed in the sum (the notation $\widetilde{H}_R(S)$ clarifies the concept). Since all S_i and S_j are independent identically distributed random variables according to S , one may obtain:

$$Var(\widehat{P}_f) = \frac{1}{N} Var[\widetilde{H}_R(S)] + \frac{N-1}{N} Cov[\widetilde{H}_R(S_1), \widetilde{H}_R(S_2)] \quad (5.18)$$

It is important to underline the fact that all samples of R are combined with all samples of S . We do not simply assign M different samples to each of the N samples of S : this would lead to use NM samples of R , as in conditional expectation method, and the variance term of Eq. 5.18 would be sufficient. If we arrange the values of $\widetilde{H}(R_j, S_i)$ in a 2D matrix, this re-use of the same samples induces a correlation between the results in the same row (respectively column). Given the need for a covariance term describing such correlation, we start the proof from the covariance estimation at a fixed point (which will be necessary to easily compute both variance and covariance terms).

The determination of the variance estimator is then carried out according to the following steps:

1. covariance estimation at a fixed point of S_1, S_2 ;
2. decomposition of the variance term in Eq. 5.18 following to the total variance law and using the result from step 1;
3. decomposition of the covariance term in Eq. 5.18 from the total covariance law and using the result from step 1;
4. complete assembly of previous results to analytically express the variance estimator;
5. derive the sampling based expression of this variance estimator.

The first step aims at determining the covariance between two values of \widetilde{H}_R at two fixed points t_1 and t_2 . After several operations (detailed in Appendix B.1) one may obtain:

$$Cov_q[\widetilde{H}_R(t_1), \widetilde{H}_R(t_2)] = \frac{1}{M} (E_q[\widetilde{H}_R(t_1)\widetilde{H}_R(t_2)] - H(t_1)H(t_2)) \quad (5.19)$$

In the second step, the total variance law allows to write:

$$Var(\widetilde{H}_R(S)) = E_h[Var_q(\widetilde{H}_R(S)|S)] + Var_h[E_q(\widetilde{H}_R(S)|S)] \quad (5.20)$$

The first term can be treated as the conditional covariance of $\widetilde{H}_R(S)$ on itself:

$$\begin{aligned} E_h[Var_q(\widetilde{H}_R(S)|S)] &= E_h[Cov_q(\widetilde{H}_R(S)|S, \widetilde{H}_R(S)|S)] \\ &= \frac{1}{M} (E_h[E_q[\widetilde{H}_R^2(S)]] - E_h[H^2(S)]) \end{aligned} \quad (5.21)$$

Then the second term:

$$Var_h [E_q(\widetilde{H}_R(S)|S)] = E_h [E_q [\widetilde{H}_R(S)]^2] - E_h [E_q [\widetilde{H}_R(S)]]^2 = E_h [H^2(S)] - P_f^2 \quad (5.22)$$

Substituting Eq. 5.21 and 5.22 into 5.20:

$$Var(\widetilde{H}_R(S)) = \frac{1}{M} (E_h [E_q [\widetilde{H}_R^2(S)]] - E_h [H^2(S)]) + E_h [H^2(S)] - P_f^2 \quad (5.23)$$

To determine the covariance part in Eq. 5.18, one has to start from the total covariance theorem:

$$Cov(X_1, X_2) = E_Y [Cov_{X_1, X_2}(X_1, X_2|Y)] + Cov_Y [E_{X_1}(X_1|Y), E_{X_2}(X_2|Y)] \quad (5.24)$$

In this case, the different variables in Eq. 5.24 are given by the tern:

$$X_1 = \widetilde{H}_R(S_1), \quad X_2 = \widetilde{H}_R(S_2), \quad Y = (S_1, S_2)$$

The term Cov_Y in Eq. 5.24 can be neglected as S_1 and S_2 are, by definition, independent copies of S . The only remaining part is reported here:

$$Cov(\widetilde{H}_R(S_1), \widetilde{H}_R(S_2)) = E_{S_1, S_2} [Cov_{\widetilde{H}_R(S_1), \widetilde{H}_R(S_2)}(\widetilde{H}_R(S_1), \widetilde{H}_R(S_2)|S_1, S_2)]$$

This can be developed by using the fixed point covariance equation (see Eq. 5.19):

$$Cov_{\widetilde{H}_R(S_1), \widetilde{H}_R(S_2)}(\widetilde{H}_R(S_1), \widetilde{H}_R(S_2)|S_1, S_2) = \frac{1}{M} (E_q [\widetilde{H}_R(S_1)\widetilde{H}_R(S_2)] - H(S_1)H(S_2))$$

Passing to the expectation, it is worth noticing that, since $H(S_1)$ and $H(S_2)$ are independent (as they are functions of S_1 and S_2 which are independent by definition), we obtain:

$$E_h [H(S_1)H(S_2)] = E_h [H(S_1)] E_h [H(S_2)] = P_f^2$$

Therefore, one may obtain the following relation:

$$Cov(\widetilde{H}_R(S_1), \widetilde{H}_R(S_2)) = \frac{1}{M} (E_h [E_q [\widetilde{H}_R(S_1)\widetilde{H}_R(S_2)]] - P_f^2) \quad (5.25)$$

Now, joining together results from Eq. 5.23 and Eq. 5.25 and substituting in Eq. 5.18, the final analytical covariance estimator is obtained:

$$\begin{aligned} Var(\widehat{P}_f) &= \frac{1}{NM} E_h [E_q [\widetilde{H}_R^2(S)]] + \frac{M-1}{NM} E_h [H^2(S)] + \frac{N-1}{MN} E_h [E_q [\widetilde{H}_R(S_1)\widetilde{H}_R(S_2)]] \\ &\quad - \frac{N+M-1}{NM} P_f^2 \end{aligned} \quad (5.26)$$

Re-writing this expression in a more compact way, one may retrieve a relation formally analogue to Eq. 5.13:

$$\text{Var}(\widehat{P}_f) = \frac{1}{NM} \phi_1 + \frac{1}{N} \phi_2 + \frac{N-1}{NM} \xi_{12} \quad (5.27)$$

Where:

$$\begin{aligned} \phi_1 &= E_h [E_q [\widetilde{H}_R^2(S)]] - E_h [H^2(S)] \\ \phi_2 &= E_h [H^2(S)] - P_f^2 \\ \xi_{12} &= E_h [E_q [\widetilde{H}_R(S_1) \widetilde{H}_R(S_2)]] - P_f^2 \end{aligned} \quad (5.28)$$

The numerical estimation of the variance obtained in Eq. 5.27 thus needs the following ingredients:

$$\begin{aligned} \widetilde{T}_{j,i} &= G(R_j, S_i) \frac{f_R(r_j)}{q(r_j)} \frac{f_S(s_i)}{h(s_i)} \\ P_f &= E_h [E_q [\widetilde{H}_R(S)]] \approx \frac{1}{NM} \sum_{i=1}^N \sum_{j=1}^M \widetilde{T}_{j,i} \\ E_h [E_q [\widetilde{H}_R(S)^2]] &\approx \frac{1}{NM} \sum_{i=1}^N \sum_{j=1}^M \widetilde{T}_{j,i}^2 \\ E_h [H^2(S)] &= E_h [E_q [\widetilde{H}_R(S)]^2] \approx \frac{1}{N} \sum_{i=1}^N \left(\sum_{j=1}^M \frac{\widetilde{T}_{j,i}}{M} \right)^2 \\ E_h [E_q [\widetilde{H}_R(S_1), \widetilde{H}_R(S_2)]] &\approx \frac{2}{NM} \sum_{i=1}^{N/2} \sum_{j=1}^M (\widetilde{T}_{j,2i-1} \widetilde{T}_{j,2i}) \end{aligned} \quad (5.29)$$

A particular remark needs to be done to verify that from Eqs. 5.26 and 5.29 one can retrieve Eqs. 5.11 and 5.12. The two couples of systems of equations should constitute an identity when importance sampling distributions coincide with original PDFs, hence the ratios $\frac{f_S}{h}$ and $\frac{f_R}{q}$ are equal to one, while E_h and E_q correspond to E_S and E_R respectively. In this case, the term \widetilde{T} would be reduced to an indicator function, formally the same as \widetilde{F}_R : this implies that $\widetilde{T}^2 = \widetilde{T}$ and the first term in Eq. 5.26 is reduced to P_f . On the other hand, the cross product $\widetilde{T}_{j,2i-1} \widetilde{T}_{j,2i}$ could be expressed as the indicator function \widetilde{F}_R evaluated at the minimum between S_{2i-1} and S_{2i} (if we refer to the original work [Smarslok, 2009] focused on LSF defined as in Eq. 5.6). Thus, it is indeed possible to obtain Eq. 5.11 from Eq. 5.26.

In order to ensure the validity of this variance estimator, all parameters in Eq. 5.28 must be non-negative. It can be demonstrated that the analytical quantities always verify this condition (proof available in Appendix 5.3.5), but guaranteeing the same on the numerical estimators is more challenging. Another alternative formulation of the upper-mentioned variance estimator is introduced in next section, aimed at avoiding numerical issues that may appear in some cases.

5.3.3 Mirror formulation

Given the independence assumption between S and R , the separated estimators E_h and E_q can be switched. For the expectation, we obtain:

$$P_f = E_q \left[\frac{f_R(R)}{q(R)} E_h \left[\frac{G(R, S) f_S(S)}{h(S)} \mid R \right] \right] \quad (5.30)$$

A compact notation similar to Eq. 5.16 is adopted:

$$\begin{aligned} \widetilde{H}_S(R) &= \widetilde{H}(R, S) = \frac{f_S(S)}{h(S)} \frac{f_R(R)}{q(R)} G(R, S) \\ \widehat{H}_S(R) &= \frac{1}{N} \sum_{i=1}^N \widetilde{H}(R, S_i) \\ K(R) &= E_h[\widehat{H}_S(R)|R] = E_h[\widetilde{H}_S(R)|R] \\ \widehat{P}_f &= \frac{1}{M} \sum_{j=1}^M \widehat{H}_S(R_j) \\ P_f &= E_q [E_h[\widetilde{H}_S(R)|R]] = E_q[K(R)] = E[\widehat{P}_f] \end{aligned} \quad (5.31)$$

Then, the variance estimator becomes:

$$\begin{aligned} \text{Var}(\widehat{P}_f) &= \frac{1}{NM} E_q [E_h [\widetilde{H}_S^2(R)]] + \frac{N-1}{NM} E_q [K^2(R)] + \frac{M-1}{MN} E_q [E_h [\widetilde{H}_S(R_1) \widetilde{H}_S(R_2)]] \\ &\quad - \frac{N+M-1}{NM} P_f^2 \end{aligned} \quad (5.32)$$

In compact form, it becomes:

$$\text{Var}(\widehat{P}_f) = \frac{1}{NM} \phi_1 + \frac{1}{M} \phi_2 + \frac{M-1}{NM} \xi_{12} \quad (5.33)$$

Where:

$$\begin{aligned} \phi_1 &= E_q [E_h [\widetilde{H}_S^2(R)]] - E_q [K^2(R)] \\ \phi_2 &= E_q [K^2(R)] - P_f^2 \\ \xi_{12} &= E_q [E_h [\widetilde{H}_S(R_1) \widetilde{H}_S(R_2)]] - P_f^2 \end{aligned} \quad (5.34)$$

The numerical estimation thus needs the following ingredients

$$\begin{aligned}
\tilde{T}_{j,i} &= G(R_j, S_i) \frac{f_R(r_j) f_S(s_i)}{q(r_j) h(s_i)} \\
P_f &= E_q [E_h [\tilde{H}_S(R)]] \approx \frac{1}{NM} \sum_{i=1}^N \sum_{j=1}^M \tilde{T}_{j,i} \\
E_q [E_h [\tilde{H}_S(R)^2]] &\approx \frac{1}{NM} \sum_{i=1}^N \sum_{j=1}^M \tilde{T}_{j,i}^2 \\
E_q [K^2(R)] &= E_q [E_h [\tilde{H}_S(R)]^2] \approx \frac{1}{M} \sum_{j=1}^M \left(\sum_{i=1}^N \frac{\tilde{T}_{j,i}}{N} \right)^2 \\
E_q [E_h [\tilde{H}_S(R_1) \tilde{H}_S(R_2)]] &\approx \frac{2}{NM} \sum_{i=1}^N \sum_{j=1}^{M/2} (\tilde{T}_{2j-1,i} \tilde{T}_{2j,i})
\end{aligned} \tag{5.35}$$

The two formulations are analogue and lead to identical variance estimations (proof available in Section 5.3.4). To ensure the validity of this variance estimator, the parameters ϕ_1 , ϕ_2 and ξ_{12} must be non-negative. As stated before, it can be proved that this is always verified on the theoretical expressions (proof available in Section 5.3.5), but can represent a remarkable challenge regarding their numerical estimations.

In the following, the first estimator (enunciated in Eqs. 5.27-5.29) will be referred as *S-based formulation*, while the second (related to Eqs. 5.33-5.35) will be denoted as *R-based formulation*: the equivalence between these two formulations of the variance estimator will be discussed in the next section. The usefulness of having a mirror formalization is related to their numerical accuracy, as will be illustrated in Section 5.4.

5.3.4 On the equivalence of *S*-based and *R*-based variance estimator

In this section, some observations about the theoretical equivalence between the two upper-mentioned estimators of the variance of P_f estimation via ImpSMC approach. We start from the definition of ξ_{12}^S parameter related to *S*-based estimator.

$$\xi_{12}^S = E_h [E_q [\tilde{H}_R(S_1) \tilde{H}_R(S_2) | S_1, S_2]] - P_f^2$$

We start expressing the first term in integral form. We denote here with H_1 the domain of $h(S_1)$, H_2 the domain of $h(S_2)$, Q the domain of $q(r)$. The integral formulation will be given by:

$$\begin{aligned}
&E_h [E_q [\tilde{H}_R(S_1) \tilde{H}_R(S_2) | S_1, S_2]] = \\
&= \int_{H_1} h(s_1) \int_{H_2} h(s_2) \int_Q q(r) \frac{f_S(s_1) f_S(s_2) f_R^2(r)}{h(s_1) h(s_2) q^2(r)} G(r, s_1) G(r, s_2) dr ds_2 ds_1 \\
&= \int_{H_1} \int_{H_2} \int_Q \frac{1}{q(r)} f_S(s_1) f_S(s_2) f_R^2(r) G(r, s_1) G(r, s_2) dr ds_2 ds_1
\end{aligned}$$

In the following, a simplified notation will be used:

$$\begin{aligned} g_1(r, s_1) &= f_R(r) f_S(s_1) G(r, s_1) \\ g_2(r, s_2) &= f_R(r) f_S(s_2) G(r, s_2) \end{aligned}$$

Therefore, Eq. 5.3.4 will be reduced to:

$$\begin{aligned} E_h [E_q [\widetilde{H}_R(S_1) \widetilde{H}_R(S_2) | S_1, S_2]] &= \int_{H_1} \int_{H_2} \int_Q \frac{1}{q(r)} f_S(s_1) f_S(s_2) f_R^2(r) G(r, s_1) G(r, s_2) dr ds_2 ds_1 \\ &= \int_{H_1} \int_{H_2} \int_Q \frac{1}{q(r)} g_1(r, s_1) g_2(r, s_2) dr ds_2 ds_1 \end{aligned}$$

By considering that s_1 and s_2 are independent, we can split the integral as follows:

$$E_h [E_q [\widetilde{H}_R(S_1) \widetilde{H}_R(S_2) | S_1, S_2]] = \int_Q \frac{1}{q(r)} \left(\int_{H_1} g_1(r, s_1) ds_1 \right) \left(\int_{H_2} g_2(r, s_2) ds_2 \right) dr$$

The internal integrals on H_1 and H_2 will give the same result, leading to:

$$\begin{aligned} E_h [E_q [\widetilde{H}_R(S_1) \widetilde{H}_R(S_2) | S_1, S_2]] &= \int_Q \frac{1}{q(r)} \left(\int_H g_1(r, s) ds \right)^2 dr \\ &= \int_Q q(r) \left(\int_H h(s) \frac{f_R(r)}{q(r)} \frac{f_S(s)}{h(s)} G(r, s) ds \right)^2 dr \quad (5.36) \\ &= E_q [E_h [\widetilde{H}_S(R) | R]^2] \end{aligned}$$

Therefore, we can write:

$$\xi_{12}^S = \phi_2^R$$

Where the first term is referred to the ξ_{12} parameter of S -based estimator and the second to ϕ_2 of R -based estimator. We can extend this to the inverse relation:

$$E_q [E_h [\widetilde{H}_S(R_1) \widetilde{H}_S(R_2) | R_1, R_2]] = E_h [E_q [\widetilde{H}_R(S) | S]] \quad (5.37)$$

Thus, obtaining:

$$\xi_{12}^R = \phi_2^S$$

Till this point, the analogy between the asymptotic behaviors of both variance estimators was explained. With conclusions from Eqs. 5.36 and 5.37, we can re-write Eqs. 5.26 and 5.32:

$$\begin{aligned}
\text{Var}(P_f)^S &= \frac{1}{NM} E_h [E_q [\widetilde{H}_R^2(S)]] + \frac{M-1}{NM} E_h [E_q [\widetilde{H}_R(S)]^2] + \frac{N-1}{MN} E_h [E_q [\widetilde{H}_R(S_1)\widetilde{H}_R(S_2)]] \\
&\quad - \frac{N+M-1}{NM} P_f^2 \\
&= \frac{1}{NM} E_h [E_q [\widetilde{H}_R^2(S)]] + \frac{M-1}{NM} E_h [E_q [\widetilde{H}_R(S)]^2] + \frac{N-1}{MN} E_q [E_h [\widetilde{H}_S(R)]^2] \\
&\quad - \frac{N+M-1}{NM} P_f^2 \\
\text{Var}(P_f)^R &= \frac{1}{NM} E_q [E_h [\widetilde{H}_S^2(R)]] + \frac{N-1}{NM} E_q [E_h [\widetilde{H}_S(R)]^2] + \frac{M-1}{MN} E_q [E_h [\widetilde{H}_S(R_1)\widetilde{H}_S(R_2)]] \\
&\quad - \frac{N+M-1}{NM} P_f^2 \\
&= \frac{1}{NM} E_q [E_h [\widetilde{H}_S^2(R)]] + \frac{N-1}{NM} E_q [E_h [\widetilde{H}_S(R)]^2] + \frac{M-1}{MN} E_h [E_q [\widetilde{H}_R(S)]^2] \\
&\quad - \frac{N+M-1}{NM} P_f^2
\end{aligned}$$

Finally we can state that both estimators lead to the same variance of P_f estimation.

5.3.5 Necessary conditions for variance estimator validity

In this section, we define the conditions to ensure the validity of the proposed variance estimator of ImpSMC approach.

We start from defining an useful property of the main terms of the variance estimator described in 5.3.2, in particular in Eq. 5.29.

PROPERTY - Let ϕ_1 , ϕ_2 and ξ_{12} the parameters described in Eq. 5.29. The inequality:

$$\phi_1 + \phi_2 - \xi_{12} \geq 0 \quad (5.38)$$

Is always verified.

PROOF -

$$\phi_1 + \phi_2 - \xi_{12} = E_h [E_q [\widetilde{H}_R^2(S)]] - E_h [E_q [\widetilde{H}_R(S_1)\widetilde{H}_R(S_2)]] \quad (5.39)$$

Considering that $H(S_1)$ and $H(S_2)$ follow the same distribution, one can write:

$$E_h [E_q [\widetilde{H}_R^2(S_1)]] = E_h [E_q [\widetilde{H}_R^2(S)]] = E_h [E_q [\widetilde{H}_R^2(S_2)]]$$

Therefore, we can re-arrange the equation:

$$E_h [E_q [\widetilde{H}_R^2(S)]] = \frac{1}{2} (E_h [E_q [\widetilde{H}_R^2(S_1)]] + E_h [E_q [\widetilde{H}_R^2(S_2)]])$$

By introducing this latter in Eq. 5.39:

$$\begin{aligned}
\phi_1 + \phi_2 - \xi_{12} &= E_h \left[E_q \left[\frac{1}{2} \widetilde{H}_R^2(S_1) + \frac{1}{2} \widetilde{H}_R^2(S_1) - \widetilde{H}_R(S_1)\widetilde{H}_R(S_2) \right] \right] \\
&= \frac{1}{2} E_h \left[E_q \left[[\widetilde{H}_R(S_1) - \widetilde{H}_R(S_2)]^2 \right] \right] \geq 0
\end{aligned}$$



The previous property can be also extended to the R -based estimator.

It is mandatory to verify that variance of P_f estimation via ImpSMC approach does not increase by adding new samples. This can be verified thanks to gradient computation, with respect to N and M . As shown in Section 5.4, the extrapolation parameters ϕ_1 , ϕ_2 and ξ_{12} do not depend on N or M . Therefore, we obtain the following derivatives:

$$\begin{cases} \frac{\partial}{\partial N} [Var(\widehat{P}_f)] = -\frac{1}{N^2 M} \phi_1 - \frac{1}{N^2} \phi_2 + \frac{1}{N^2 M} \xi_{12} \\ \frac{\partial}{\partial M} [Var(\widehat{P}_f)] = -\frac{1}{NM^2} \phi_1 - \frac{N-1}{NM^2} \xi_{12} \end{cases}$$

In particular, both derivatives must always be non-positive. To achieve such condition:

$$\begin{cases} \phi_1 + M\phi_2 - \xi_{12} \geq 0 \\ \phi_1 + (N-1)\xi_{12} \geq 0 \end{cases} \quad (5.40)$$

Thanks to property in Eq. 5.38, condition in Eq. 5.40 can be reduced to:

$$\begin{cases} (M-1)\phi_2 \geq 0 \\ \phi_1 + (N-1)\xi_{12} \geq 0 \end{cases}$$

Finally, to ensure validity of the variance estimator in Eq. 5.27 for all values of N and M , one needs to verify that:

$$\begin{cases} \phi_1 \geq 0 \\ \phi_2 \geq 0 \\ \xi_{12} \geq 0 \end{cases} \quad (5.41)$$

It is possible to verify that the theoretical expressions of these parameters always satisfy the necessary conditions in Eq. 5.41. However, this can be more challenging in regards of their numerical estimators in Eq. 5.29. The same conclusion can be drawn for R -based estimator.

We are then able to enunciate and prove the following theorem.

THEOREM - *Let ϕ_1 , ϕ_2 and ξ_{12} the parameters described in Eq. 5.29. The necessary condition to make S -based variance estimator of P_f estimation via ImpSMC approach requires:*

$$\begin{cases} \phi_1 \geq 0 \\ \phi_2 \geq 0 \\ \xi_{12} \geq 0 \end{cases} \quad (5.42)$$

In particular, this condition is always verified.

5.3.5.1 First proof: $\phi_1 \geq 0$

$$\begin{aligned}\phi_1 &= E_h [E_q [\widetilde{H}_R^2(S)]] - E_h [E_q [\widetilde{H}_R(S)]^2] \\ &= E_h [E_q [\widetilde{H}_R^2(S)] - E_q [\widetilde{H}_R(S)]^2]\end{aligned}$$

We should now consider:

$$E_q [\widetilde{H}_R^2(S)] - E_q [\widetilde{H}_R(S)]^2 \geq 0$$

The expectation will verify the same relation, arriving to obtain then: $\phi_1 \geq 0$ ■

5.3.5.2 Second proof: $\phi_2 \geq 0$

This proof is similar to the previous one:

$$\begin{aligned}\phi_2 &= E_h [E_q [\widetilde{H}_R(S)|S]^2] - P_f^2 \\ &= E_h [E_q [\widetilde{H}_R(S)|S]^2] - E_h [E_q [\widetilde{H}_R(S)|S]]^2 \\ &= E_h [H^2(S)] - E_h [H(S)]^2 \geq 0\end{aligned}$$
■

5.3.5.3 Third proof: $\xi_{12} \geq 0$

Given that $\xi_{12}^S = \phi_2^R$, this is a straight-forward application of the previous proof on ϕ_2^R . ■

The mathematical framework of the analytical estimator of the variance associated to the estimation of the failure probability P_f via ImpSMC has been discussed. In the next section, we define the potential of this variance estimator and the advantages it brings on engineering applications.

5.3.6 Variance estimator potential

The closed form variance estimator of P_f estimated by ImpSMC makes it possible to completely exploit the ImpSMC approach, as it allows to:

- evaluate variability of P_f without having to reproduce the reliability analysis several times;
- stop sampling when a fixed accuracy target on P_f estimation is reached;
- preliminarily estimate the minimum number M of R samples (respectively N for S) necessary to achieve the accuracy goal;
- preview the number M_k of R (respectively N_k of S) samples needed to reach targeted variance \overline{Var} , given a fixed ratio $k = N/M$;

- a priori determine the ratio N/M between number of samples of S and R allowing to minimize global computational burden.

The first two advantages of such variance estimator are straight-forward. For preliminary evaluation purposes, it is possible to exploit outcomes in Eq. 5.27 (respectively Eq. 5.33) by determining all terms in Eq. 5.29 (respectively Eq. 5.35) with few simulations, say $N = M = 100$. Then, under the assumptions that those latter do not significantly change with an increase in number of samples nor with variation in ratio k , Eq. 5.27 (respectively Eq. 5.33) can be used to preview all the relations between precision and number of samples. This can be represented on a contour plot, graphically illustrating the levels of $coV(\widehat{P}_f)$ as a function of N and M , as done in [Smarslok, 2009, Smarslok et al., 2010] for SMC. Table 5.1 summarizes the main possible evaluations for both S and R -based formulations.

	<i>S</i>-based	<i>R</i>-based
$\min N$	ϕ_2/\overline{Var}	ξ_{12}/\overline{Var}
$\min M$	ξ_{12}/\overline{Var}	ϕ_2/\overline{Var}
N_k	$\frac{k\phi_2 + \xi_{12} + \sqrt{(k\phi_2 + \xi_{12})^2 - 4k\overline{Var}(\xi_{12} - \phi_1)}}{2k\overline{Var}}$	$\frac{\phi_2 + k\xi_{12} + \sqrt{(\phi_2 + k\xi_{12})^2 - 4k\overline{Var}(\xi_{12} - \phi_1)}}{2k\overline{Var}}$
$\arg \min_k N_k M_k$	ϕ_2/ξ_{12}	ξ_{12}/ϕ_2

Table 5.1: Main outcomes of variance estimator

A particular remark can be done about the ratio k allowing to minimize the product NM : this does not depend on the targeted \overline{Var} , but just relies on the nature of the model and input variabilities, namely through the terms ϕ_2 and ξ_{12} . Such ratio is not necessarily optimal in terms of computational costs as minimizing the product NM does not necessarily imply reducing the overall computational burden. In the following, we are referring to it as the *reference ratio*, individuating the ratio which is exactly mid-way between two asymptotic behaviors.

5.4 Numerical results

In this Section, two test cases are introduced to investigate the gain in terms of number of simulations needed to achieve a target coV , arbitrarily fixed (for the examples presented in this chapter) at 0.05. In particular, in the first application a comparative analysis between two *LSF* formulations is reported, while in the second use case we conducted a study on the effects of the ratio between variances due to response and capacity components and the effect of target P_f .

In both sections, the importance function is identified as a normal distribution centered at the *MPFP* in Gaussian standard space. The same *MPFP* is adopted for IS and ImpSMC: at the implementation level, distributions are separated in two blocks related to X_R and X_S for ImpSMC. *OpenTURNS* library is used to deal with *MPFP* determination, MC and IS algorithms. In-house codes were created to implement SMC and ImpSMC approaches.

5.4.1 Composite plate test case

As a first example, a cross-ply composite plate deflection problem was considered, which was also used in [Smarslok et al., 2010, Chaudhuri and Haftka, 2013]. We focus on maximum deflection, at the middle point of a simply supported squared cross-ply plate, characterized by a $[90, 45, -45]_{sym}$ laminate with lamina thickness of $125 \mu m$. This test case is illustrated in Fig. 5.1. We consider the loading condition to be a sinusoidally varying pressure, defined as:

$$q(x, y) = q_0 \sin\left(\frac{\pi x}{L}\right) \sin\left(\frac{\pi y}{L}\right)$$

Where q_0 represents the amplitude and L the length of each side of the square plate. The associated LSF can be expressed in the form of Eq. 5.6, as follows:

$$g(w_{all}, X_S) = w_{all} - w(X_S) \quad (5.43)$$

Where w_{all} is the R variable representing the allowable deflection here, X_S is the variable set intervening on deflection output w , defined as:

$$w = \frac{q_0 L^4}{D^*} \quad D^* = \pi^4 [D_{11} + 2(D_{12} + D_{66}) + D_{22}] \quad (5.44)$$

Here the terms D_{ij} represent the components of the bending stiffness matrix of the plate. Overall, 7 random variables (listed in Table 5.2) affect the LSF of Eq. 5.43.

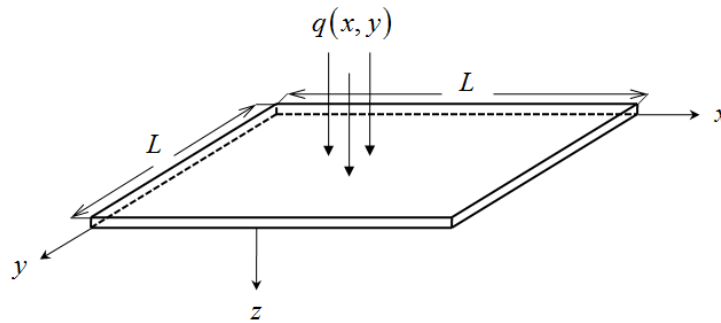


Figure 5.1: Cross-ply test case: illustration (Source: [Smarslok et al., 2010, Chaudhuri and Haftka, 2013])

Variable	Unit	Distribution	Mean	St. Deviation
E_1	Pa	Normal	1.5×10^{11}	7.5×10^9
E_2	Pa	Normal	9×10^9	4.5×10^8
G_{12}	Pa	Normal	4.6×10^9	2.3×10^8
ν_{12}		Normal	0.34	0.017
L	m	Normal	7.5×10^{-2}	1.5×10^{-3}
q_0	Pa	Normal	1.30×10^5	1.95×10^4
w_{all}	m	Log-Normal	8×10^{-3}	2.4×10^{-4}

Table 5.2: Cross-ply test case: random variables

This part of the analysis aims at evaluating the effect of the ratio between variances of capacity and response variables (respectively R and S). To this purpose, in analogy with works from [Smarslok, 2009, Smarslok et al., 2010], two different formulations of LSF are introduced:

$$R = w_{all} \quad S = \frac{q_0 L^4}{D^*} \quad (5.45a)$$

$$R = \frac{w_{all}}{q_0} \quad S = \frac{L^4}{D^*} \quad (5.45b)$$

In particular, the variable sets X_R and X_S are changed, providing a higher variance to capacity variable R (respectively lower variance to response S) according to Eq. 5.45a to Eq. 5.45b. To improve readability, in the following we will refer to Eq. 5.45a as *Low R-Variability Formulation* (LRVF) and to Eq. 5.45b as *High R-Variability Formulation* (HRVF). Outputs distributions are illustrated in Fig. 5.2 for *LRVF* and in Fig. 5.3 for *HRVF*. The upper-mentioned differences in terms of variability repartition between R and S are visible in the scales of these graphs. These differences are also summarized in Table 5.3.

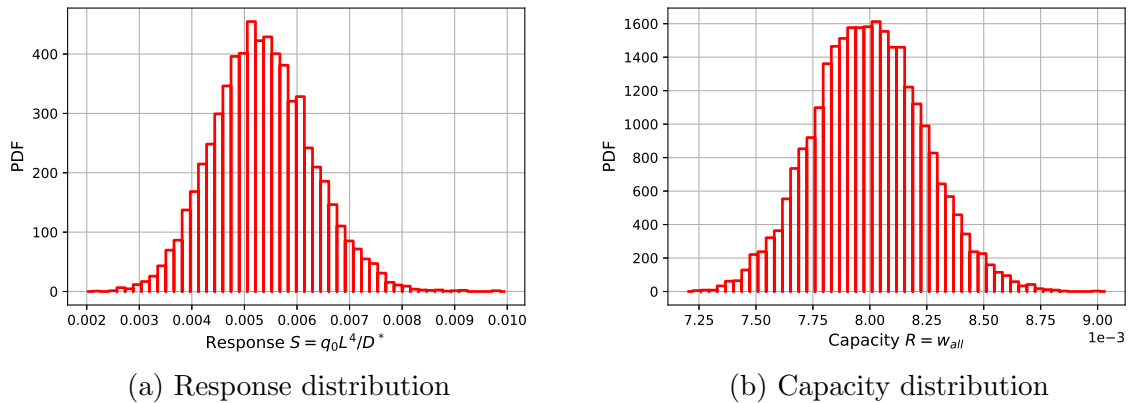


Figure 5.2: Composite plate test case: outputs distributions in *LRVF*

The analytical variance estimators described in Section 5.3 were empirically validated on both LSF formulations of this first test case. The empirical validation is carried out with 10^4 repeated ImpSMC analyses with $N = 10^3$ response samples and $M = 10^3, 10^4, 10^5$ capacity samples for each one. Error is measured as follows:

$$Err(P_f) = \frac{\sigma_{analytical}(P_f) - \sigma_{emp}(P_f)}{\sigma_{emp}(P_f)}$$

Where $\sigma_{analytical}$ is the standard deviation predicted by analytical estimators from Eqs. 5.27-5.29 (related to *S-based* formulation), and Eqs. 5.33-5.35 (related to *R-based* formulation) and σ_{emp} the empirical one estimated based on the 10^4 repetitions of ImpSMC.

Results are reported in form of box plots in Fig. 5.4: distinct boxes are depicted for the two variance estimators and the two LSF formulations. The different ratios M/N are summarized in the same box. It can be observed that errors are lower than 1%, thus validating both analytical variance estimators introduced in Section 5.3.

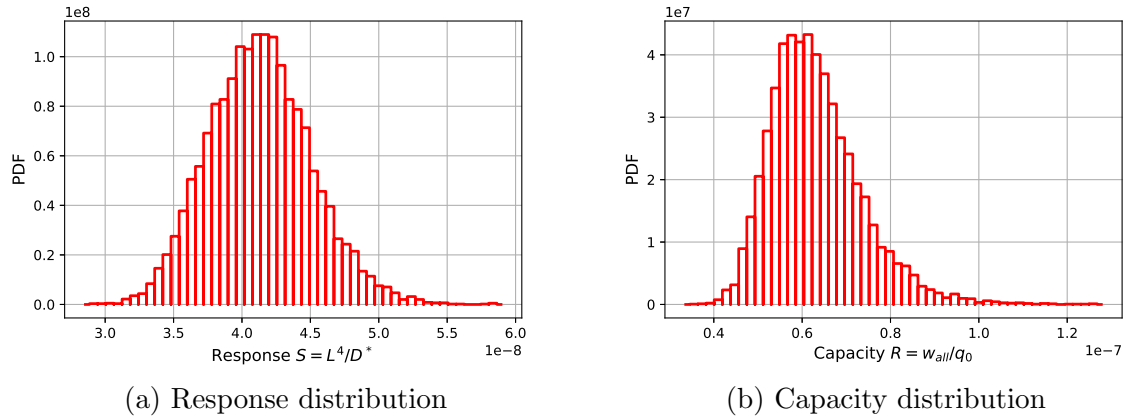


Figure 5.3: Composite plate test case: outputs distributions in *HRVF*

Parameter		LRVF	HRVF
Mean	\bar{R}	8.00×10^{-3}	6.31×10^{-8}
	\bar{S}	5.35×10^{-3}	4.13×10^{-8}
	R/S	1.50	1.53
Standard Deviation	$\sigma(R)$	2.41×10^{-4}	1.03×10^{-8}
	$\sigma(S)$	9.31×10^{-4}	3.73×10^{-9}
	$\sigma(R)/\sigma(S)$	0.259	2.76
Variance	$Var(R)$	5.79×10^{-8}	1.06×10^{-16}
	$Var(S)$	8.67×10^{-7}	1.39×10^{-17}
	$Var(R)/Var(S)$	0.067	7.63
Coefficient of Variation	$coV(R)$	0.030	0.163
	$coV(S)$	0.174	0.090
	$coV(R)/coV(S)$	0.172	1.81

Table 5.3: Composite plate test case: output statistical parameters for *LRVF* and *HRVF* formulations

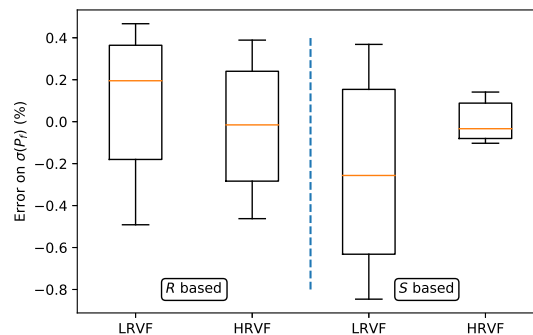


Figure 5.4: Composite plate test case: experimental validation of both variance estimators

Reliability simulation results are reported in Table 5.4 for *LRVF* and Table 5.5 for *HRVF*. The first three columns in both tables represent the mean of P_f estimations,

the mean and the standard deviation of required N to achieve $coV(\widehat{P}_f) = 0.05$. The successive ones report standard deviation and coefficient of variation of P_f estimation at fixed number N of S samples ($N = 100$ in 4th and 5th columns, $N = 1000$ in 6th and 7th columns). All values are obtained by repeating 100 times the reliability analyses.

For both formulations, ImpSMC outperforms MC, IS and SMC: both $\sigma(\widehat{P}_f)$ and N to reach $coV(\widehat{P}_f) = 0.05$ are noticeably reduced.

In the *LRVF* case, the introduction of a separate sampling process appears more efficient when IS concept is applied: this can be observed by comparing gains allowed by ImpSMC with respect to IS (N reduced by 52%) and gains of SMC with respect to MC (N reduced by 30%). Here the ratio M/N appears to present no substantial advantage for neither SMC nor ImpSMC approach.

Looking at the *HRVF* results, improvement ratios increase for both ImpSMC and SMC with respect to IS and MC respectively. Still, ImpSMC introduces gains with respect to IS which are superior to the ones ensured by the transition from MC to SMC. Moreover, in this case the ratio M/N has a significant influence on reducing both variance of failure probability and number of required samples. In particular, creating an unbalanced dataset with more R samples, can reduce the substantial number of S samples, which usually determine most of overall computational burden.

For both formulations, IS outperforms SMC and MC: therefore, in the following, IS approach will be used as a reference for comparison.

		Results at $coV(\widehat{P}_f) = 0.05$			Results at $N = 100$		Results at $N = 1000$	
		\widehat{P}_f	\overline{N}	$\sigma_N(\%)$	$\sigma(\widehat{P}_f)$	$coV(\widehat{P}_f)$	$\sigma(\widehat{P}_f)$	$coV(\widehat{P}_f)$
MC		6.23×10^{-3}	6.4×10^4	4.45	7.36×10^{-3}	1.18	2.17×10^{-3}	0.35
IS		6.22×10^{-3}	1159	5.18	1.02×10^{-3}	0.16	2.90×10^{-4}	0.047
SMC	M/N=1	6.20×10^{-3}	4.5×10^4	3.35	7.21×10^{-3}	1.16	2.05×10^{-3}	0.33
	M/N=10	6.20×10^{-3}	4.4×10^4	4.37	6.95×10^{-3}	1.12	2.00×10^{-3}	0.32
	M/N=100	6.20×10^{-3}	4.4×10^4	2.42	6.41×10^{-3}	1.03	1.92×10^{-3}	0.31
ImpSMC	M/N=1	6.26×10^{-3}	552	7.39	7.58×10^{-4}	0.121	2.31×10^{-4}	0.037
	M/N=10	6.24×10^{-3}	549	7.10	7.46×10^{-4}	0.120	2.30×10^{-4}	0.037
	M/N=100	6.23×10^{-3}	547	6.95	7.07×10^{-4}	0.113	2.30×10^{-4}	0.037

Table 5.4: Composite plate: main results for *LRVF* from Eq. 5.45a (values issued from 100 repetitions of each reliability algorithm)

		Results at $coV(\widehat{P}_f) = 0.05$			Results at $N = 100$		Results at $N = 1000$	
		\widehat{P}_f	\overline{N}	$\sigma_N(\%)$	$\sigma(\widehat{P}_f)$	$coV(\widehat{P}_f)$	$\sigma(\widehat{P}_f)$	$coV(\widehat{P}_f)$
MC		6.23×10^{-3}	6.4×10^4	4.45	7.36×10^{-3}	1.18	2.17×10^{-3}	0.35
IS		6.26×10^{-3}	1143	11.5	1.03×10^{-3}	0.16	2.90×10^{-4}	0.046
SMC	M/N=1	6.24×10^{-3}	1.4×10^4	5.09	2.68×10^{-3}	0.43	8.01×10^{-4}	0.13
	M/N=10	6.29×10^{-3}	4105	9.74	1.71×10^{-3}	0.27	6.20×10^{-4}	0.099
	M/N=100	6.22×10^{-3}	2985	20.2	1.47×10^{-3}	0.24	5.88×10^{-4}	0.095
ImpSMC	M/N=1	6.28×10^{-3}	178	35.7	3.11×10^{-4}	0.054	1.32×10^{-4}	0.021
	M/N=10	6.24×10^{-3}	59	30.5	2.37×10^{-4}	0.038	7.62×10^{-5}	0.012
	M/N=100	6.25×10^{-3}	51	23.5	2.35×10^{-4}	0.038	6.82×10^{-5}	0.011

Table 5.5: Composite plate: main results for *HRVF* from Eq. 5.45b (values issued from 100 repetitions of each reliability algorithm)

Exploiting the potentialities of the variance estimator at a higher level, it is possible

to trace the evolution of coV as a function of both N and M , thanks to the algorithm described in Section 5.3.6. The ingredients which must be computed are ϕ_1 , ϕ_2 and ξ_{12} . These are evaluated through the numerical estimators presented in Eqs. 5.28-5.29 (for S -based formulation) and Eqs. 5.34-5.35 (for R -based formulation). In this part, we aim to analyze both magnitude and precision of the estimation provided for each of the extrapolation parameters ϕ_1 , ϕ_2 and ξ_{12} . Numerical estimations are performed with 100 repetitions of the dataset containing $N = 100$ response (S) samples. Both LSF formulations and three different M/N ratios are investigated. Results of such estimations are summarized in Table 5.6 (R -based variance estimator is adopted).

Parameter	Sample size	LRVF		HRVF	
		Mean	St. Dev. (%)	Mean	St. Dev. (%)
ϕ_1	M/N=1	1.12×10^{-4}	3.50	9.96×10^{-5}	1.85
	M/N=10	1.12×10^{-4}	3.50	9.96×10^{-5}	0.66
	M/N=100	1.12×10^{-4}	3.54	9.96×10^{-5}	0.34
ϕ_2	M/N=1	2.63×10^{-7}	50.77	1.28×10^{-5}	6.64
	M/N=10	2.59×10^{-7}	49.62	1.28×10^{-5}	6.16
	M/N=100	2.60×10^{-7}	48.46	1.28×10^{-5}	6.13
ξ_{12}	M/N=1	5.32×10^{-5}	4.61	4.52×10^{-6}	44.78
	M/N=10	5.31×10^{-5}	3.69	4.50×10^{-6}	14.67
	M/N=100	5.31×10^{-5}	3.63	4.51×10^{-6}	6.44

Table 5.6: Composite plate test case: extrapolation parameters for two LSF formulations at different M/N sample ratios ($N = 100$, R -based variance estimator is adopted)

From such results, it is confirmed that the estimations of the extrapolation parameters ϕ_1 , ϕ_2 and ξ_{12} do not depend on the sample size. For a same LSF formulation, mean values are not affected by the ratio M/N . On the other hand, bigger dataset sizes can improve ξ_{12} estimation precision, as can be seen in Table 5.6. Increasing ratio M/N can be used as an efficient procedure to enlarge the database by only enriching the population of the cheapest variable, thus without a huge additional computational burden. Moreover, from Table 5.6 it may be observed that the LSF formulation itself can greatly affect the average values of ϕ_2 and ξ_{12} : the former is increased, while ξ_{12} mean value decreases when switching from $LRVF$ to $HRVF$.

Looking at ϕ_1 results, a negligible difference in average values is obtained in the upper-mentioned formulations. The precision improvement provided by $HRVF$ is thought to be circumstantial and just related to the adopted use case.

Estimations related to ϕ_2 seem poor in $LRVF$ case: however, being on average two orders of magnitude lower than the others, their effect is not relevant. This excessive error is mostly due to the low magnitude of the quantity itself. The same precision issue is also visible for ξ_{12} in $HRVF$, with the difference that here larger M/N ratios can reduce the related standard deviation.

Thanks to the upper-mentioned parameters, contour plots are extrapolated and reported in Fig. 5.5, where M number of R samples constitutes the abscissa, N number of S samples is the ordinate and the curves represents the ensemble of points allowing the same estimation precision, defined through the coefficient of variation $coV(\widehat{P}_f)$. In such graphs, it is visible that every iso- coV can be described as an hyperbole branch. As

shown in Section 5.3.6, all points minimizing the product NM are perfectly aligned in logarithmic axes, as the reference ratio does not depend on the targeted variance level. It is possible to recognize a vertical asymptote, identifying the minimum number M of R samples, and an horizontal one, related to minimum N . The reference ratio M/N described in Section 5.3.6 represents a transition between two asymptotic behaviors. Therefore, for ratios M/N higher than the reference one, precision will be defined essentially by N and adding further R samples would be ineffective. The opposite considerations can be done for ratios M/N lower than the reference one. The estimated value of such reference ratio M/N can be seen as a decision tool to state which component (namely R or S) mostly contributes to variance of \widehat{P}_f estimation: in particular, if this is higher than 1, one can expect to improve precision by adding more R samples, and conversely if it is lower than 1. A sampling strategy can thus be defined from this ratio to reduce the number of samples, but it needs to be coupled with information about the relative computational burdens of R and S to make a more rational choice to reduce the overall analysis cost.

The effect of *LSF* formulation can be extrapolated from the translation towards right-down of the contour plots when transitioning from *LRVF* to *HRVF*. This implies that the minimum number N of response samples can be reduced, while the minimum number M of capacity samples and the reference ratio M/N are increased. Such phenomenon can be explained by the higher (respectively lower) variability assigned to R (respectively S) component in *HRVF*. Associating results from Table 5.1, Table 5.6 and Fig. 5.5, it can be observed that for R -based variance estimator, ϕ_2 translates *coV* contour plot horizontally (towards right as it increases), ξ_{12} is responsible for vertical translation (towards up if it increases) and ϕ_1 has a minor effect on the contour shape. The roles of ϕ_2 and ξ_{12} are switched when S -based variance estimator is adopted instead. Moreover, on the same problem, same *LSF* formulation and same input distributions, the orders of magnitude of ϕ_2 and ξ_{12} are reversed as well.

At this point, we can propose a simple guideline in order to choose whether to use R - or S -based variance estimator. As stated in Section 5.3, all extrapolation parameters ϕ_1 , ϕ_2 and ξ_{12} must be non-negative to ensure the variance of P_f estimation to decrease as N . Looking at numerical estimators which are used to compute ϕ_2 , one can easily understand that there is no chance that the numerical approximation could lead to a negative value of ϕ_2 itself. Therefore, the main concern regards numerical estimation precision of ξ_{12} : given that the issue arises in problems with low-magnitude $\overline{\xi_{12}}$, one can switch from a variance estimator formulation to the other, according to the relative orders of magnitude of ϕ_2 and ξ_{12} . A more refined analysis on this topic is presented on the second test case and further discussed in next section.

Another aspect to take into account is the variance reduction - measured in terms of $coV(\widehat{P}_f)$ ratios - provided by ImpSMC with respect to IS, used as reference. Relative results are extrapolated from variance estimator, as done for the $coV(\widehat{P}_f)$ contour plots, and reported in Fig. 5.6. The simple introduction of a separated sampling approach on the same amount of data is given by the central abscissa point in every subplot (corresponding to $M/N = 1$): it can be seen that in any case, substantial gains are ensured by ImpSMC approach, without even altering the ratio M/N .

For *LRVF*, N number of S samples has a significant impact on variance reduction, while little effect is observed from M number of R samples. The gains illustrated herein are in line with the ones reported in Table 5.4. These stem directly from the $coV(\widehat{P}_f)$

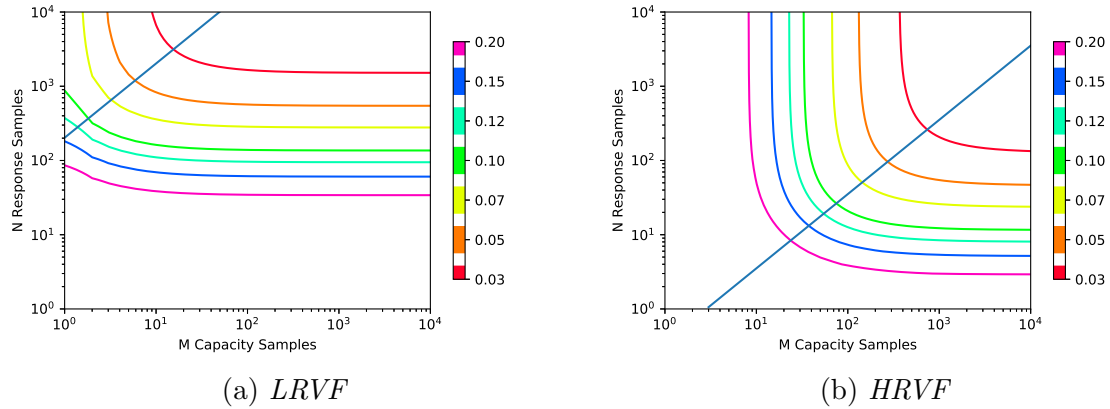


Figure 5.5: Composite plate test case: $coV(\widehat{P}_f)$ contour plots on two LSF formulations

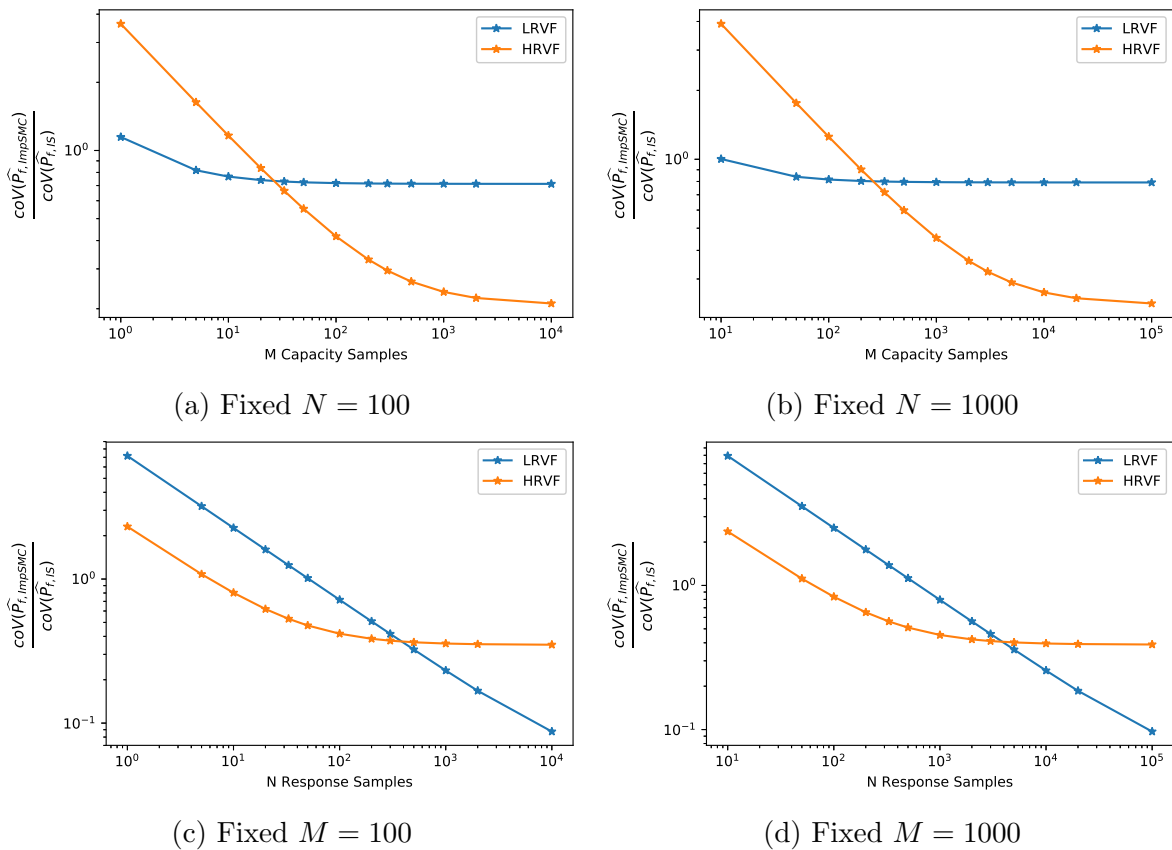


Figure 5.6: Composite plate test case: effect of LSF formulation on variance reduction of \widehat{P}_f estimation as a function of number of samples N of S and M of R

contour plot. In fact, as for $M > 10$, only horizontal lines are present in Fig. 5.5a, the only relevant effect is provided by N . Such conclusions are confirmed when switching from Fig. 5.6a to 5.6b or from 5.6c to 5.6d.

Focusing on *HRVF*, both N and M significantly affect precision. They both have a nonlinear effect on variability of P_f estimation for small sample sizes, reaching an asymp-

otic behavior for bigger sizes. These observations are direct consequences of the contour plot in Fig. 5.5b: compared to *LRVF*, contours of the *HRVF* are more balanced and almost symmetric with respect to the first bisector of the Cartesian plane (in logarithmic axes). However, considering the reference ratio $M/N \approx 3$ (individuated by the hyperbole branch bisector), a slightly superior influence by M is expected. This is confirmed in Fig. 5.6, where a delay in transition from nonlinear to asymptotic behavior of M with respect to N can be observed by comparing Figs. 5.6a and 5.6c (or alternatively Figs. 5.6b and 5.6d): this implies that the increase of M keeps affecting precision at higher samples sizes than N does. As for *LRVF*, no difference is encountered in terms of variance reduction (with respect to IS) when increasing the overall database size without altering the ratio M/N , as it appears when comparing Fig. 5.6a with 5.6b or 5.6c with 5.6d.

Again, the differences between ImpSMC performances in *LRVF* and *HRVF* directly come from the $\text{coV}(\widehat{P}_f)$ contour plots. Moreover, these do not depend on the size of the dataset itself but just on the adopted ratio M/N and *LSF* formulation. Variance reduction effects are directly reflected on the number of samples required to achieve a target precision.

5.4.2 Truss test case

In this section, we focus on a common benchmark problem, generally adopted as medium-complexity reliability example [Lee and Kwak, 2006, Blatman and Sudret, 2008, Blatman and Sudret, 2018, Lelievre, 2018], mainly due to a medium-large number of uncertain design variables. A 23-bar truss problem is considered (confront Fig. 5.7), for which the LSF is formulated here as:

$$g(V_{all}, X_S) = V_{all} - V_1(X_S) \quad (5.46)$$

Where X_S represents the whole set of variables affecting the deflection V_1 , computed through Finite Element Analysis (FEA). Maximum allowable deflection is denoted as V_{all} . Different Young's Modulus and cross section areas are assigned to each finite element, with different section statistical distributions for horizontal and oblique bars. Considering 23 elements, 6 load variables and one capacity variable (the allowed V_{all}), we have overall 53 variables (52 forming X_S and one forming X_R). We use mean $\bar{S} = \bar{V}_1 = 0.079$ and standard deviation $\sigma(S) = \sigma(V_1) = 6.47 \times 10^{-3}$ as references to analyze results from different configurations in following sections.

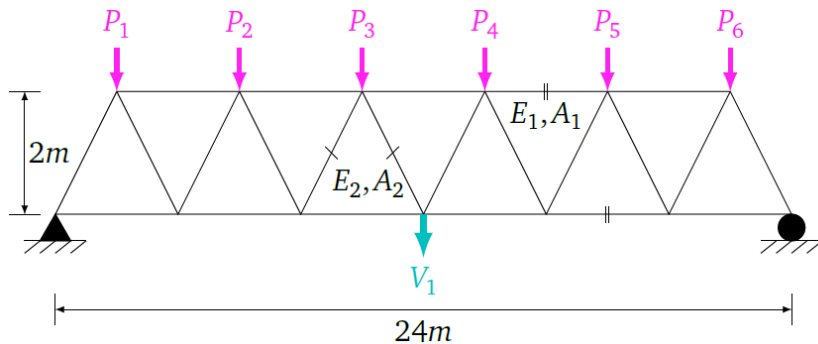


Figure 5.7: Truss test case: illustration (Source: [Lelievre, 2018])

Variable	Unit	Distribution	Mean	St. Deviation
E_1, E_2	GPa	Log-Normal	210	21
A_1	m^2	Log-Normal	2.0×10^{-3}	2.0×10^{-4}
A_2	m^2	Log-Normal	1.0×10^{-3}	1.0×10^{-4}
$P_1 - P_6$	N	Gumbel	5.0×10^4	7.5×10^3
V_{all}	m	Normal	0.115	0.01

Table 5.7: Truss test case: random variables

As done previously for the composite plate test case, several configurations of the truss example were used to experimentally validate the analytical variance estimators. The experimental validation is reported in Appendix B.2: in all configurations analyzed, the maximum error never exceeded 3%, while the mean value of errors was below 0.3%.

In Table 5.8, all main results related to different reliability estimators are provided, as done for the previous test case. Note that the mean, standard deviation and coV estimations of \widehat{P}_f and required N to achieve $coV(\widehat{P}_f) = 0.05$ come from statistical repetition of 100 reliability analysis: the analytical variance estimator was used to stop sampling when target $coV = 0.05$ was obtained. Several ratios between number of sample N of S and M of R were introduced for both SMC and ImpSMC approaches. It can be easily observed that this latter allows to reduce both variance at fixed number N of response samples and necessary amount of simulations to achieve a fixed coV , clearly outperforming MC, IS and SMC. Moreover, such gains can be even improved by increasing the ratio M/N , then reaching an asymptotic behavior at very high M/N ratios.

	Results at $coV(\widehat{P}_f) = 0.05$			Results at $N = 100$		Results at $N = 1000$	
	\widehat{P}_f	\bar{N}	σ_N (%)	$\sigma(\widehat{P}_f)$	$coV(\widehat{P}_f)$	$\sigma(\widehat{P}_f)$	$coV(\widehat{P}_f)$
MC	2.01×10^{-3}	2×10^5	5.46	4.21×10^{-3}	2.094	1.38×10^{-3}	0.687
IS	1.97×10^{-3}	1862	21.52	4.01×10^{-4}	0.204	1.32×10^{-4}	0.067
SMC	M/N = 1	3.51×10^4	7.82	2.13×10^{-3}	1.077	5.15×10^{-4}	0.261
	M/N = 10	1.33×10^4	14.05	1.17×10^{-3}	0.598	3.45×10^{-4}	0.176
	M/N = 100	1.07×10^4	21.25	1.11×10^{-3}	0.568	3.41×10^{-4}	0.174
ImpSMC	M/N = 1	190	41.79	1.47×10^{-4}	0.074	4.49×10^{-5}	0.023
	M/N = 10	135	39.01	1.26×10^{-4}	0.064	3.96×10^{-5}	0.020
	M/N = 100	130	33.66	1.23×10^{-4}	0.062	3.90×10^{-5}	0.019

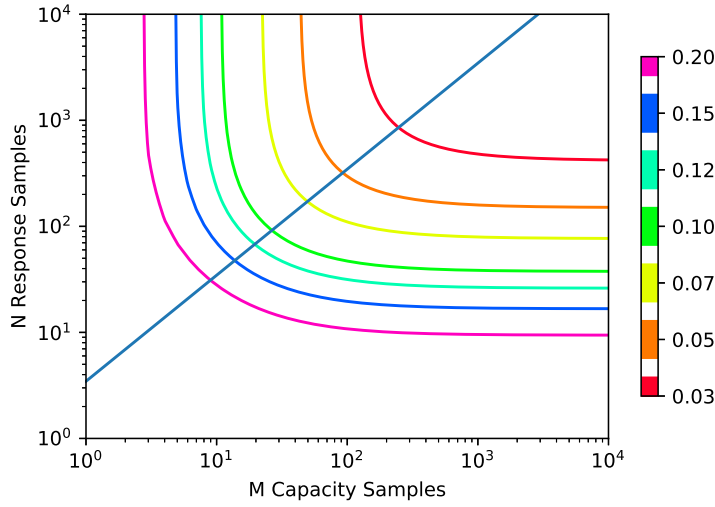
Table 5.8: Truss test case: main reliability results from different simulation algorithms (values issued from 100 repetitions of each reliability algorithm)

As done for the previous numerical example, the $coV(\widehat{P}_f)$ contour plot as a function of both N and M is plotted in Fig. 5.8, by using the algorithm described in Section 5.3.6.

In the next sections, we analyze the different effects which may drive the performances of the ImpSMC approach: the effects of the variation of the $\sigma(R)$ are discussed in Section 5.4.2.1; the effects of the failure probability target are analyzed in Section 5.4.2.2.

5.4.2.1 Effect of variation of $\sigma(R)$

Overall, 15 configurations are defined to take into account different variabilities of the capacity variable R . The correspondent means are calibrated to maintain the same failure probability target P_f of the nominal case. These are listed in Table 5.9 (ID=8

Figure 5.8: Truss nominal case: coV contour plot

corresponds to nominal case). In this Section, all statistical parameters of S are kept constant: mean $\bar{S} = \bar{V}_1 = 0.079$, standard deviation $\sigma(S) = \sigma(V_1) = 6.47 \times 10^{-3}$ and coefficient of variation $coV(S) = coV(V_1) = 0.082$. Reference results related to MC and IS are reported in Table 5.10.

ID	\bar{R}	$\sigma(R)$	$coV(R)$	\bar{R}/\bar{S}	$\sigma(R)/\sigma(S)$	$coV(R)/coV(S)$
1	0.1023	0.001	0.01	1.29	0.16	0.12
2	0.1024	0.0012	0.012	1.30	0.19	0.15
3	0.1026	0.0016	0.016	1.30	0.25	0.20
4	0.1028	0.002	0.019	1.30	0.30	0.23
5	0.1031	0.0025	0.024	1.31	0.38	0.29
6	0.1037	0.0033	0.032	1.31	0.51	0.39
7	0.1057	0.005	0.047	1.34	0.77	0.57
8*	0.115	0.01	0.087	1.46	1.55	1.06
9	0.1405	0.02	0.142	1.78	3.08	1.73
10	0.1685	0.03	0.178	2.13	4.64	2.17
11	0.196	0.04	0.204	2.48	6.18	2.49
12	0.225	0.05	0.222	2.85	7.72	2.71
13	0.253	0.06	0.237	3.20	9.27	2.89
14	0.31	0.08	0.258	3.92	12.36	3.15
15	0.368	0.10	0.272	4.66	15.46	3.32

Table 5.9: Truss test case: configurations for study on $\sigma(R)/\sigma(S)$ effect (fixed statistical parameters of S : mean $\bar{S} = \bar{V}_1 = 0.079$, standard deviation $\sigma(S) = \sigma(V_1) = 6.47 \times 10^{-3}$ and coefficient of variation $coV(S) = coV(V_1) = 0.082$)

A first evaluation can be done with respect to different evolutions shown in the coV contour plots, depicted in Fig. 5.9. The reader may observe a translation toward down-right of the contours as the ratio $\sigma(R)/\sigma(S)$ increases (Fig. 5.9b). This implies that the necessary number of needed M samples increases, while minimum N decreases. The reference ratio M/N will therefore increase. It is worth noticing that in this case, as

ID	$\sigma(R)/\sigma(S)$	MC			IS		
		\widehat{P}_f	\bar{N}	$\sigma_N/\bar{N}(\%)$	\widehat{P}_f	\bar{N}	$\sigma_N/\bar{N}(\%)$
1	0.1023	1.91×10^{-3}	2.10×10^5	5.23	1.91×10^{-3}	3351	37.8
2	0.1024	1.90×10^{-3}	2.11×10^5	4.45	1.95×10^{-3}	3289	49.2
3	0.10255	1.93×10^{-3}	2.08×10^5	4.72	1.88×10^{-3}	3154	31.7
4	0.10275	1.91×10^{-3}	2.10×10^5	4.73	1.97×10^{-3}	3376	38.2
5	0.1031	1.90×10^{-3}	2.11×10^5	5.00	1.88×10^{-3}	3309	73.2
6	0.1037	1.97×10^{-3}	2.03×10^5	5.06	1.91×10^{-3}	2927	29.6
7	0.1057	1.96×10^{-3}	2.04×10^5	4.77	1.98×10^{-3}	2643	31.0
8*	0.115	1.98×10^{-3}	2.03×10^5	5.27	2.08×10^{-3}	1868	20.7
9	0.1405	1.93×10^{-3}	2.08×10^5	4.37	1.98×10^{-3}	1399	16.0
10	0.1685	1.87×10^{-3}	2.14×10^5	5.17	1.87×10^{-3}	1353	5.2
11	0.196	2.02×10^{-3}	1.98×10^5	4.76	2.02×10^{-3}	1298	11.3
12	0.225	1.95×10^{-3}	2.05×10^5	5.43	1.94×10^{-3}	1317	5.1
13	0.253	2.02×10^{-3}	1.98×10^5	4.94	2.01×10^{-3}	1282	11.4
14	0.310	2.03×10^{-3}	1.97×10^5	5.21	2.16×10^{-3}	1275	15.2
15	0.368	2.00×10^{-3}	2.01×10^5	5.55	2.02×10^{-3}	1286	11.6

Table 5.10: Truss test case: reference results for study on $\sigma(R)/\sigma(S)$ effect (100 simulations considered, targeted $coV(\widehat{P}_f) = 0.05$)

$N > 10$, the dominant contributor to the P_f estimate precision will be M , as we are already very close to the vertical asymptote. Opposite conclusions are drawn if the ratio $\sigma(R)/\sigma(S)$ is reduced (Fig. 5.9a).

These findings will allow us to illustrate again the usefulness of disposing of two mirror formulations. Considering S -based estimator, the term ϕ_2 (defining the horizontal asymptote) increases while ξ_{12} (defining the vertical asymptote) decreases as the ratio $\sigma(R)/\sigma(S)$ decreases, arriving to the uncomfortable situation when ξ_{12} tends to 0. This is consistent with the upper-mentioned translational behavior of the coV contour plot. Numerical approximation errors could lead ξ_{12} to be negative, making the derivatives of $Var(\widehat{P}_f)$ with respect to N and M positive for very low ratios M/N , where ξ_{12} is the dominant term: this is unacceptable as it would imply that by adding new samples we may lose precision in P_f estimation. Conversely, for R -based estimator, evolutions of ϕ_2 and ξ_{12} are reversed: therefore, numerical instabilities can be found for very high ratios $\sigma(R)/\sigma(S)$, where ξ_{12} can be negative, thus leading to unacceptable extrapolations related to very high ratios M/N . In all cases considered in the present work, no evidence of analogue numerical issues related to the term ϕ_2 was found.

Based on these results we can thus define an empirical rule to choose the best-suited variance estimator formulation. In particular, extrapolations with S -based estimator are more precise than the ones provided by R -based when most of variance contribution comes from capacity R . On the other hand, when the response S exhibits a higher variability, extrapolations from R -based estimator are preferred. In the intermediate situation, when $\sigma(R) \approx \sigma(S)$, the two formulations are equivalent. Given the fact that the two contributions to the variance of LSF are not known a priori, this choice cannot be easily done. However, during a real reliability analysis, one may evaluate the ratio ξ_{12}/ϕ_2 with either S - or R -based estimator after a minimal amount of samples, then

switch to the other alternative if such ratio is too low (say < 1).

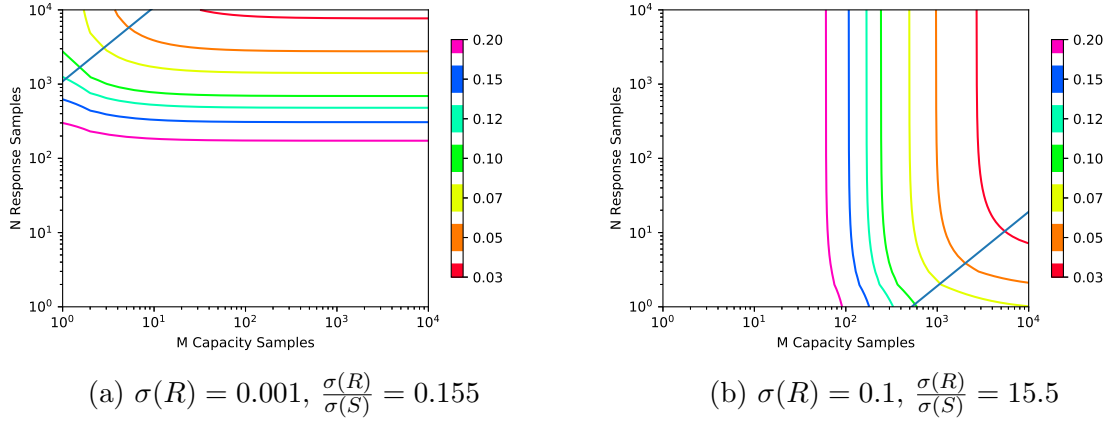


Figure 5.9: Truss test case: effect of $\sigma(R)/\sigma(S)$ on coV contour plot

Another aspect to consider is the variance reduction allowed by ImpSMC approach with respect to N and M . In the previous section it was already observed the potential variance reduction (compared to other reliability simulation-based algorithms) for a nominal case and with different N and M/N ratios. In Fig. 5.10 is reported a complete study over the effects of the ratio $\sigma(R)/\sigma(S)$. Results are consistent with previous conclusions from contour plots. All curves related to configurations with $\sigma(R) \ll \sigma(S)$ show a small sensitivity to variations of M , but a massive coV reduction can be achieved by increasing N . With the increase of the ratio $\sigma(R)/\sigma(S)$, impact of M over coV becomes more visible, while the influence of N is reduced. The turning point is given by $\sigma(R) \approx \sigma(S)$, where the effects of N and M are almost perfectly balanced. Then, for $\sigma(R) \gg \sigma(S)$, the only responsible for coV is the number M of R samples. Comparing ImpSMC and IS performances, the coV reduction factor is kept constant when multiplying the available computational budget: this is visible when passing from $N = 100$ (respectively $M = 100$) to $N = 1000$ (respectively $M = 1000$) we obtain almost identical graphs of coV_{ImpSMC}/coV_{IS} .

We would now like to make some comments regarding the computational cost gains. Thanks to the variance estimator, it is in fact also possible to preview the overall number of complete analysis without even needing to actually perform them. In Fig.5.12, the needed N and M to achieve $coV = 0.05$ are compared to the ones necessary for IS.

In particular, in Fig. 5.11, the minimum values of N and M are depicted. It is easy to verify that in presence of extreme values of the ratio $\sigma(R)/\sigma(S)$, ImpSMC becomes equivalent to IS: in fact, here we approach the limit condition where one of the two components (either R or S) becomes deterministic, making useless the separated sampling procedure. One might conclude that ImpSMC is more effective when the variabilities of the two variables are balanced. However, in most of structural applications, response sampling requires a fairly superior computational burden compared to capacity sampling, since the former usually involves evaluations through numerical simulations (e. g. evaluation of stress through a finite element analysis) while the latter usually implies only drawing from a distribution determined empirically (as in the case for failure strength): in such cases, ImpSMC method provides superior gains with high levels of $\sigma(R)/\sigma(S)$.

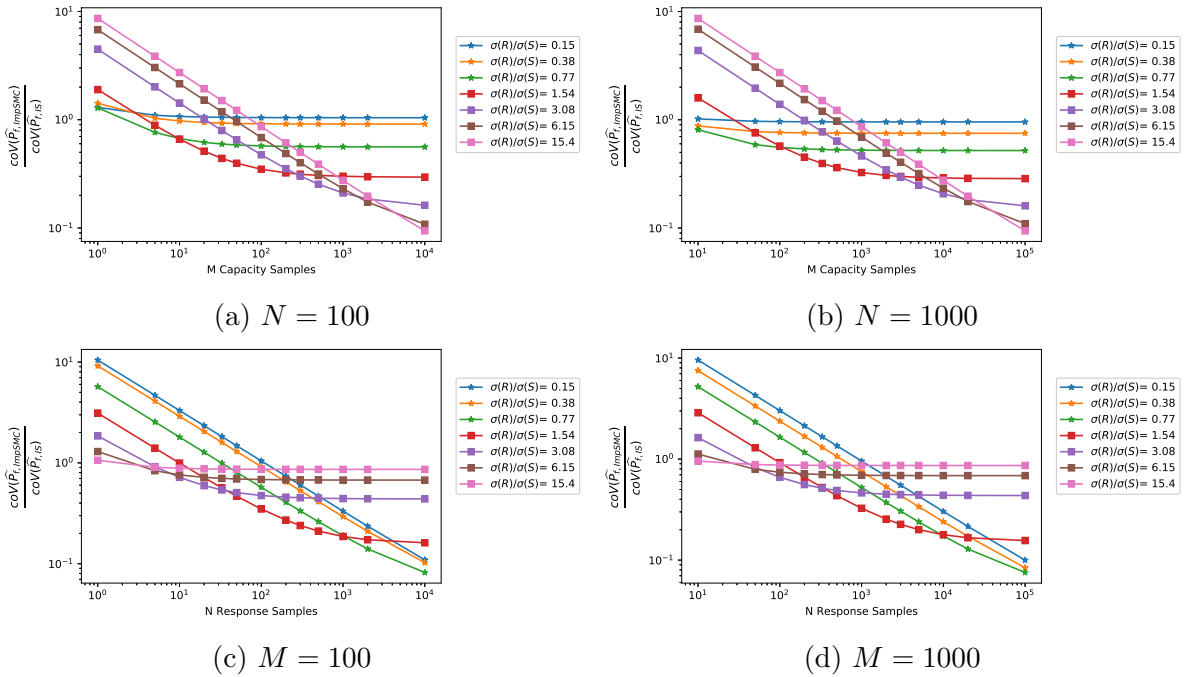


Figure 5.10: Truss test case: effect of $\sigma(R)/\sigma(S)$ on variance reduction in function of number of samples N of S and M of R (fixed $\sigma(S) = 6.47 \times 10^{-3}$)

In case of balanced variances the gains are somewhat lower than for high $\sigma(R)/\sigma(S)$ but they are still significant compared to IS.

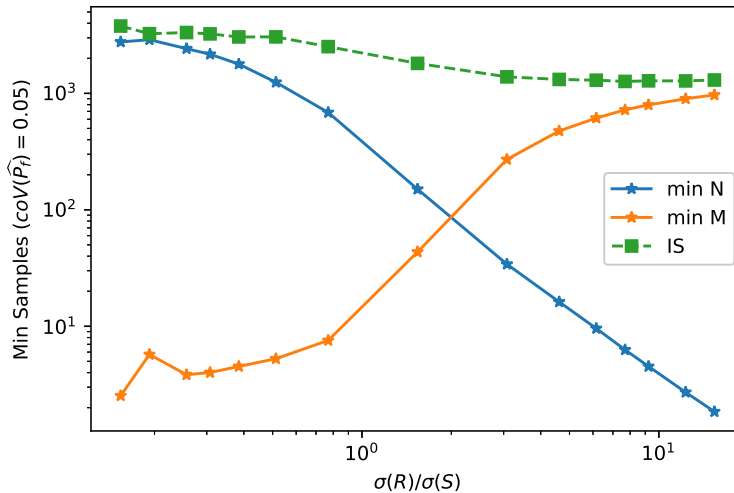


Figure 5.11: Minimum N and M to obtain $coV = 0.05$ in function of $\sigma(R)/\sigma(S)$

In Fig. 5.12, attention is focused on the balance of necessary N (as in this example, response sampling is computationally more expensive than capacity) to achieve a target $coV = 0.05$. This analysis allows to confirm what was previewed in previous sections. In fact, when $\sigma(R) < \sigma(S)$ the effect of M/N is not relevant, and ImpSMC approaches

IS when $\sigma(R) \ll \sigma(S)$. On the other hand, when $\sigma(R) \gg \sigma(S)$, low ratios M/N do not allow to fully exploit ImpSMC potentialities, as the necessary M increases. In this context, it is fundamental to increase the imposed ratio M/N to be able to decrease N (here considered as the only contributor to overall computational burden).

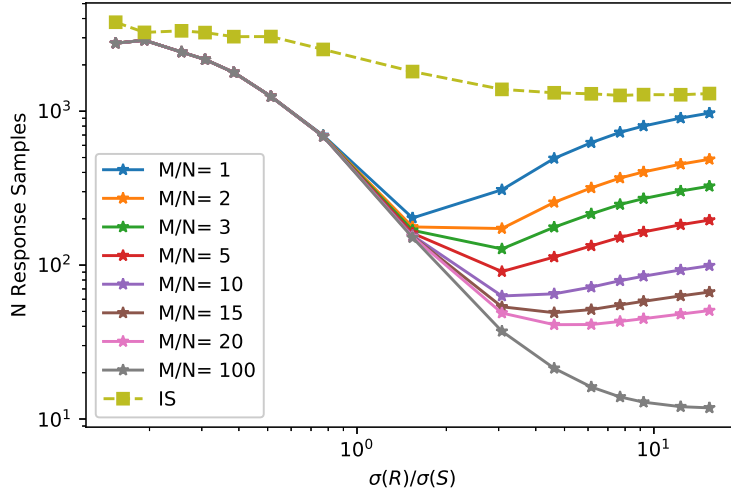


Figure 5.12: Truss test case: effect of $\sigma(R)/\sigma(S)$ on needed number of samples N of S and M of R to achieve $cov(P_f) = 0.05$ at given M/N ratios

5.4.2.2 Effect of failure probability target

Four additional configurations (listed in Table 5.11) are defined by different means of capacity variable, keeping the same nominal variance, in order to explore distinct failure probability targets P_f . The reference results for MC and IS simulations are reported in Table 5.11 (ID=3 represents the nominal configuration). In this Section, all statistical parameters of S are kept constant: mean $\bar{S} = \bar{V}_1 = 0.079$, standard deviation $\sigma(S) = \sigma(V_1) = 6.47 \times 10^{-3}$) and coefficient of variation $coV(S) = coV(V_1) = 0.082$.

ID	Strength R		MC			IS		
	\bar{V}_{all}	$\sigma(V_{all})$	\widehat{P}_f	\bar{N}	$\sigma_N/\bar{N}(\%)$	\widehat{P}_f	\bar{N}	$\sigma_N/\bar{N}(\%)$
1	0.095	0.01	9.52×10^{-2}	3825	5.59	9.82×10^{-2}	666	12.71
2	0.105	0.01	1.76×10^{-2}	22439	4.63	1.75×10^{-2}	1148	14.50
3*	0.115	0.01	1.99×10^{-3}	2.02×10^5	5.15	1.97×10^{-3}	1862	21.52
4	0.124	0.01	1.93×10^{-4}	2.08×10^6	4.84	2.01×10^{-4}	3023	37.02
5	0.132	0.01	1.99×10^{-5}	2.13×10^7	5.15	1.89×10^{-5}	4861	41.65

Table 5.11: Truss test case: configurations and reference results for study on P_f effect (100 simulations considered, targeted $coV(\widehat{P}_f) = 0.05$, fixed statistical parameters of S : mean $\bar{S} = \bar{V}_1 = 0.079$, standard deviation $\sigma(S) = \sigma(V_1) = 6.47 \times 10^{-3}$ and coefficient of variation $coV(S) = coV(V_1) = 0.082$)

As done for the previous study on the truss test case, we report in Fig. 5.13 two contour plots related to two extreme failure probability targets (reported in Table 5.11 as ID 1 and 5). A relatively small change can be observed: decreasing the capacity mean (thus increasing P_f) coV contour plot is translated to the down-right corner. Therefore, we are led to think that the ratio $\sigma(R)/\sigma(S)$ is not the only contributor affecting ImpSMC performances, as was suggested till this point. Also the ratio of means \bar{R}/\bar{S} apparently influences ImpSMC performances: the effect is opposite to the one observed for $\sigma(R)/\sigma(S)$: this suggests that actually the ratio $coV(R)/coV(S)$ could be considered instead to resume both effects.

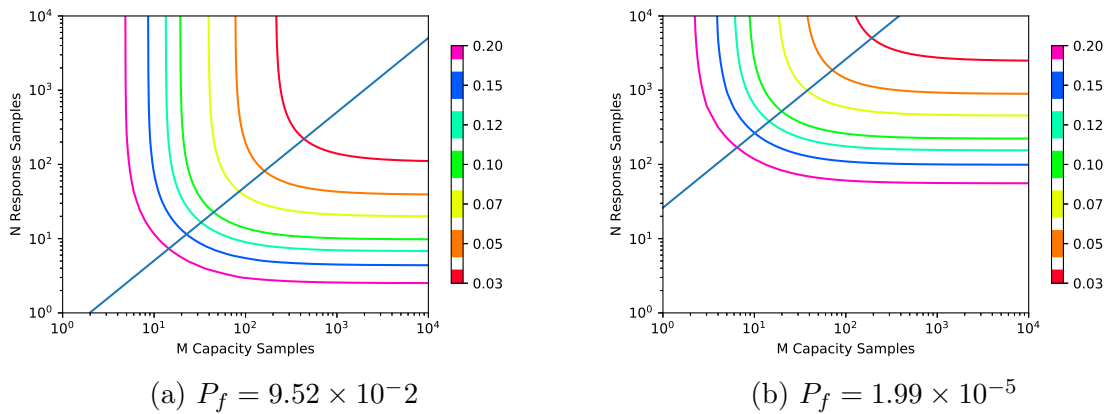


Figure 5.13: Truss test case: effect of P_f target on $coV(P_f)$ contour plot

From contour plots, same conclusions than before can be reported for variance reduction power of ImpSMC approach (depicted in Fig. 5.14). Here the effects are less visible when comparing Fig. 5.14 to Fig. 5.10. Since all coV contour plots are much closer one to the other, it is easy to verify that all curves do not significantly change and follow the same path as the nominal case. When multiplying the available computational budget (then passing from graphs of Fig. 5.14a to 5.14b or from 5.14c to 5.14d), the variance reduction provided by ImpSMC with respect to IS, is kept constant.

When dealing with the number of necessary samples (depicted in Fig. 5.15), the reader may observe that the minimum amounts of N and M follow the same evolution (but less accentuated) with increases in P_f target (i.e. when mean R is decreased) than the one previewed with augmentation of $\sigma(R)$. This confirms, once again, the hypothesis that the bisector (individuated by $argmin[N_k M_k]$) is somehow guided by the ratio $coV(R)/coV(S)$.

Finally, we focus on the needed amount N of response samples (illustrated in Fig. 5.16). We may notice that the ratio M/N can somewhat reduce the overall N for high levels of P_f . However, gains of ImpSMC with respect to IS, in terms of needed samples, are quite relevant and almost identical for all configurations considered in this section.

5.5 Discussion of results

From the analysis conducted in the two test cases some general conclusions can be drawn.

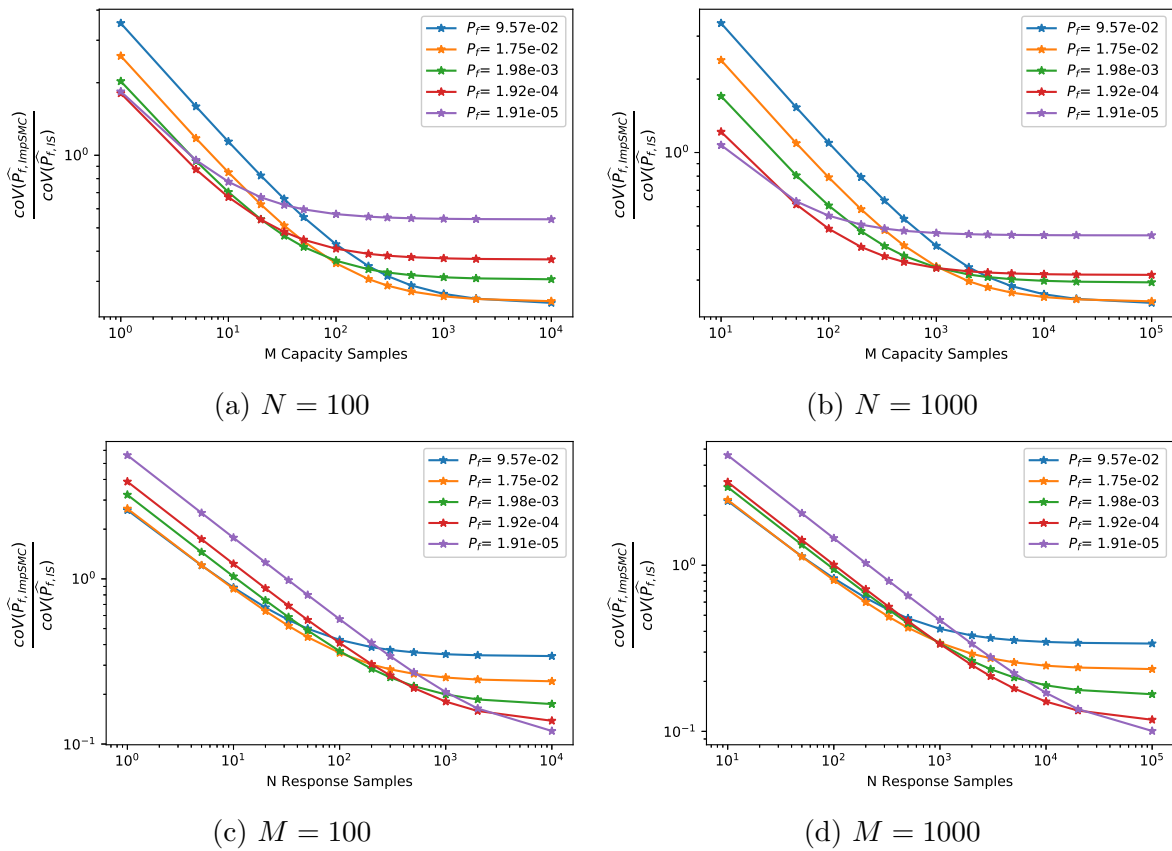


Figure 5.14: Truss test case: effect of P_f on variance reduction in function of number of samples N of S and M of R

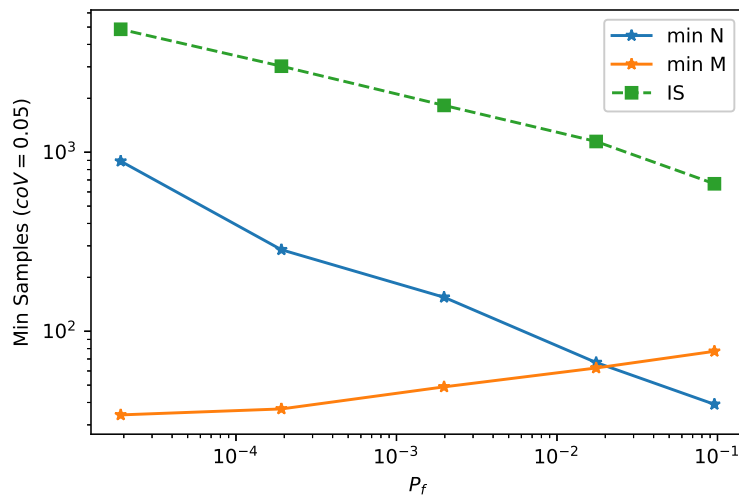


Figure 5.15: Minimum N and M to obtain $\text{coV} = 0.05$ in function of P_f target

First, the only assumption for the formalization of the ImpSMC approach relies on the possibility of separating LSF in two independent variables R and S : therefore, no further assumption on the shape of LSF nor the operation linking R and S is needed.

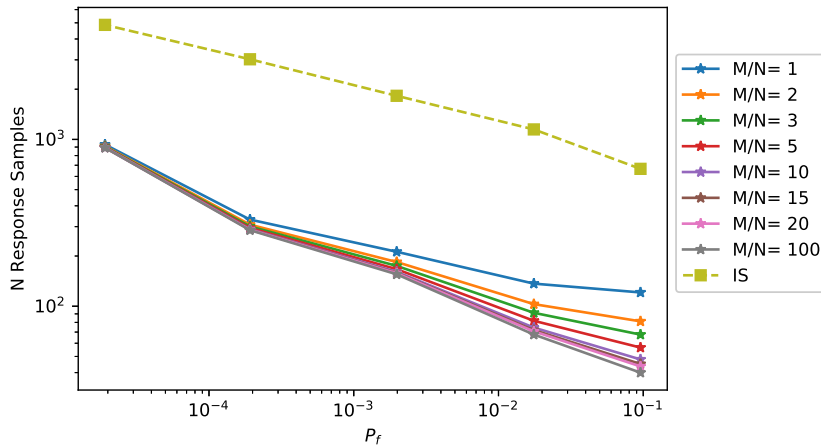


Figure 5.16: Truss test case: effect of P_f target on needed number of samples N of S and M of R to achieve $cov(P_f) = 0.05$ at given M/N ratios

In the examples considered in this chapter, two LSFs are described as difference between two components R (expressing the strength of a structure or more generally the capacity of a system) and S (expressing the stress on a structure or more generally the response of a system). But one is allowed to consider either sums, products or other operations: the only requirement is the clear distinction between two independent components. Moreover, even if only two displacement limit states are treated in the present work, the method can be applied to any kind of system where the response is compared to an allowable value, as long as the two can be considered as independent. In structural applications, one may think to static strength demonstration, frequency responses, among the others. Additionally, ImpSMC approach can be applied to any engineering field and extended to system reliability applications, aerodynamic studies, power engineering or even fields outside of engineering requiring the determination of a reliability, like pharmaceutical industry.

Looking at the two mirror formulations of the analytical variance estimator, it has been stated that the S -based formulation can lead to numerical estimation errors when $\sigma(R) \ll \sigma(S)$ for very low ratios M/N (between the number of R samples and number of S samples) and conversely for R -based. Actually, the maximum errors found in these examples on variance estimation never surpass 3%. Some relevant errors can be found only in an extrapolation phase and are restricted to zones of the $coV(\widehat{P}_f)$ contour plot which are not of practical interest, as they covers number of samples inferior to 10. On the other hand, disposing of two mirror formulations can give us the opportunity of reducing such errors in the related zones. The same opposite reasoning is valid for R -based variance estimator. The criterion to follow to establish which formulation better suites a given problem relies on the evaluation of the extrapolation parameters ϕ_1 , ϕ_2 , ξ_{12} (used to extrapolate the analytical variance prediction on P_f estimation), and in particular the ratio ϕ_2/ξ_{12} , which individuates the bisector of $coV(\widehat{P}_f)$ contour plot.

One possible reason for such errors can be found in the estimation of ξ_{12} term for both formulations. In fact, one should consider all possible combinations between two distinct values of S (in S -based formulation) or R (in R -based formulation). But here we consider only couples of consecutive values of the response of interest. This could be critical when the real value of ξ_{12} is very small, compared to ϕ_2 . It can be analytically

proven that all three terms (ϕ_1 , ϕ_2 and ξ_{12}) are always positive: therefore, we make the conjecture that the eventual errors come from numerical approximations.

From the study on the composite plate, it can be observed that slight changes in LSF formulation can lead to substantial gains. The key bias in transferring - whenever possible - variability on the computationally cheapest component (between response and capacity) can allow to reduce the needed amount of samples required to achieve a prescribed precision target, above all when making use of unbalanced datasets.

From both test cases, we observed that the efficiency of increasing ratio M/N is more relevant with high levels of the ratio $coV(R)/coV(S)$. This is valid for all situations where response sampling implies a fairly superior computational burden, compared to capacity sampling. This means that in such cases, if the variability of the capacity R is greater than that of response S , more capacity samples (M) can be very efficiently generated and allow to significantly decrease the variability of the P_f estimate. The reverse reasoning must be done in the opposite situation, where most of computational efforts comes from resistance model.

Finally, the ratio $coV(R)/coV(S)$ can justify the evolution of gains of ImpSMC over other approaches, but is not sufficient to explain the exact position of the bisector (in blue) in the $coV(\widehat{P}_f)$ contour plot. One would expect such plot to be perfectly symmetric around $N = M$ when the ratio $coV(R)/coV(S)$ gets near to 1: but for the nominal case this ratio is equal to 1.06 and correspondent bisector is situated at $M/N \approx 0.3$. Therefore, one cannot simply use information on $coV(R)/coV(S)$ to explain translations in the $coV(P_f)$ contour plot, making it necessary to actually evaluate ϕ_2 and ξ_{12} to draw conclusions on the contour plot itself. The reason probably lies in the asymmetric PDF of the response considered in the example, which cannot be described only through mean and standard deviation.

5.6 Conclusion

In this chapter, an analytical variance estimator related to ImpSMC approach is proposed and numerical studies are conducted on two test cases. This method can be used to estimate failure probability in reliability applications where it is possible to identify two separated independent components in the Limit State Function (LSF). Generally, we could think of response and capacity of a system. In structural applications, we refer respectively to stress and strength.

The basic idea of ImpSMC is to separately sample these two components and concentrate them around failure zones. Thanks to the variance estimator, it is possible to show without large number of simulations how such an approach outperforms other simulation methods like MC, IS and SMC. Variance of the P_f estimator is significantly reduced as well as the number of required samples to achieve a good precision target. Separate sampling allows also to deal with very unbalanced datasets, leading to even higher gains. Results show that ImpSMC approaches IS when all variability in LSF comes from the most expensive component. In all other cases, precision improvements with respect to IS are significant, above all in the opposite situation of variability mostly due to the cheapest component of LSF. Overall, gains of using ImpSMC instead of IS are not sensible to failure probability target. On the other hand, compared to MC, the added value of

ImpSMC grows significantly.

The two test cases presented in this chapter, despite their simplicity, allow to highlight the potential of disposing of a variance estimator for ImpSMC. In particular, the first use case shows that it is not an obligation to distinguish a stress and a strength component, but LSF can be re-adapted (if possible) to any form containing two separated independent terms. A key to increase gains in term of computational burden is to work towards unbalanced datasets and assigning (where possible) most of variability to the component which is cheaper to sample.

Focusing on the practical use of ImpSMC approach, the allowance of unbalanced datasets is of utmost importance. Generally, the response S of a system is often much more expensive to sample than the capacity R : for example, in structural applications, the response will be provided by finite element model simulations, while the capacity is often given by a random variable which is cheap to sample. Allowing unbalanced datasets, one can focus on maximizing the ratio between the number M of R samples and the number N of S samples to reduce the overall computational burden, while improving the precision of the estimation of the failure probability P_f .

In industrial engineering applications, such an analytical variance estimator can predict the precision of failure probability estimation and the required amount of simulations to achieve a good precision target without being forced to replicate empirically the entire procedure for a statistical analysis. Moreover, the bisector of the $coV(\widehat{P}_f)$ plot (which can be estimated from a low number of samples) may give an idea of a good ratio M/N between number of capacity and response samples to guarantee a good compromise between precision and computational burden. However, as this just minimizes the product NM , engineering judgment is needed to refine it: if sampling the response S is more expensive than sampling capacity R , this ratio can be multiplied - or divided, if the reverse consideration is valid - up to 10 (no more than this as an asymptotic behavior would be reached). The fact that this does not change according to the targeted precision of failure probability estimation, makes it possible to validate such ratio for a given problem and given input distributions. These advantages can be very convenient in real industrial applications, when minimizing the computational effort is of utmost relevance.

Further investigations on the phenomena determining the exact position of the reference ratio for unbalanced datasets could constitute an interesting topic for further research on this subject. Explicitly introducing computational costs associated to response and capacity sampling and minimizing overall computational burden would be another interesting future research work.

Moreover, coupling our method to Adaptive Importance Sampling algorithm could extend its application to any reliability problem with unknown importance function. On the other hand, the introduction of ImpSMC in machine learning techniques would make it possible to cheaply evaluate failure probability in real-life applications where response is so expensive to evaluate that it must be approximated by a surrogate model.

In the next chapters, we use SMC as a special case of ImpSMC to improve the performances of the classical Monte Carlo approach. In Chapter 6, SMC is introduced in an adaptive learning framework for reliability assessment applications, to further reduce the computational burden. In Chapter 7, it is used as the default sampling method for PoE estimations. The interest in H2H application is devoted to intrinsic variables only, in the semi-probabilistic framework described in Chapter 4: therefore the targeted quantile lev-

els correspond to the ones related to material properties in CS 25.613, thus characterized by $PoE = 0.1$ for redundant structures and $PoE = 0.01$ for non-redundant structures. In the semi-probabilistic framework, the application of ImpSMC becomes actually fundamental when dealing with environmental variables, linked to lower target probabilities (i.e. $PoE = 10^{-5}/FH$ per flight hour): this use of ImpSMC is left as a perspective.

Chapter 6

High-dimensional Adaptive Learning for Reliability Analysis

6.1 Introduction

In the previous chapters, we highlighted the interest of managing the uncertainties of input parameters in engineering design. We presented several applications of probabilistic frameworks in Chapter 2, focusing on aeronautical and civil engineering field. Among these, we introduced the concept of reliability analysis, which focuses on determining the failure probability associated to a specific design with non-deterministic input variables [Larsson, 2015]. In Chapter 4, we proposed a *semi-probabilistic approach* to integrate the uncertainties of the design parameters affecting the performances of aeronautical structures. Two declinations were presented: the first, formalized as a quantile estimation problem (analyzed in Chapter 4), aims at determining new deterministic quantities to integrate in the classical design process; the second declination, presented as a reliability-based design optimization problem (which will be formalized and investigated in Chapter 7), tries to optimize the input variabilities while limiting the probability that the real structure under-performs with respect to fixed structural requirements. In the previous and in the present chapter, we aim at developing methods to improve the compromise between accuracy and computational burden of the evaluation of a failure probability P_f , defined as the probability that a given system of exceeding nominal values (in the context of our work referred as Probability of Exceedance *PoE* [Kempeneers, 2018]) or leading to unsafe conditions.

Classical sampling-based approaches typically involve repeated sampling of input random variables to estimate a failure probability P_f . The Monte Carlo (MC) method [Hammersley, 2013], generally considered as reference, gives an estimate of P_f , associates a statistical characterization of the estimation itself and is not sensitive to problem input dimensionality. On the other hand, it exhibits a slow convergence rate, requiring a large number of simulations to achieve a given coefficient of variation on the P_f estimate, roughly proportional to $1/P_f$. As numerical models adopted in current industrial applications often imply huge computational burdens, classical MC can become of impractical use, above all for low P_f targets. Lots of research efforts have been done to reduce MC costs, following, in particular, three main paths: (1) modifying the sampling strategy to reduce the number of needed samples [Au and Beck, 2001, Tokdar and Kass, 2010]

to achieve a fixed targeted accuracy level; (2) replacing the full numerical model with a cheaper surrogate model [Alsina et al., 2018, Xu and Saleh, 2021]; (3) combining the first two approaches [Dubourg et al., 2011, Bourinet et al., 2011]. We already analyzed the first perspective in Chapter 5, introducing the ImpSMC approach and the analytical estimator of the variance of the P_f estimation. The second and the third perspective are pursued in the present chapter.

In the literature, multiple works pursued adaptive surrogate learning approaches, which iteratively enrich the database of the evaluations of the full model (which constitute the training set of the surrogate model) to progressively improve the approximation of the LSS and use it to sort a large MC population. Five key features fully define this category of algorithms: (1) the surrogate model choice; (2) the training set enrichment criterion; (3) the learning-phase stopping criterion; (4) the sampling strategy; (5) the overall procedure convergence criterion.

Among the most popular Machine Learning (ML) approaches adopted to reproduce an expensive model in reliability context [Alsina et al., 2018, Xu and Saleh, 2021], we find in literature Kriging [Lelievre, 2018, Zhang et al., 2019a, Wang and Shafieezadeh, 2019b, Chen et al., 2019, Xiao et al., 2020a, Jiang et al., 2020, Wang et al., 2022], Support Vector Machine (SVM) [Bourinet et al., 2011, Pan and Dias, 2017, Hariri-Ardebili and Pourkamali-Anaraki, 2019, Zhang et al., 2019b, Bourinet, 2021] and Neural Networks (NN) [Elhewy et al., 2006, Ferrero Bermejo et al., 2019, Xiang et al., 2020]. In particular Kriging, thanks to its inherent uncertainty structure, exhibits useful exploration features, making it particularly well suited for efficient adaptive reliability analyses assisted by ML. However - unlike MC, SVM and NN - Kriging suffers from the curse of dimensionality, making it challenging to deal with high input dimensionality. In the present article, we introduce an adaptive ML algorithm based on KPLS [Bouhleb et al., 2016b], which addresses this issue by using the Partial Least Square (PLS) method [Vinzi et al., 2010] to project the input space onto a lower-dimensional space.

Focusing on Kriging-based approaches, a number of training set enrichment criteria can be found in the literature, e.g. U [Echard et al., 2011], Expected Feasibility Function (EFF) [Bichon et al., 2008], $REIF$ [Zhang et al., 2019d] among the others. A first application of KPLS in a reliability assessment problem can be found in [Zuhal et al., 2021], which highlighted the gains in terms of computational burden provided by KPLS with respect to Ordinary Kriging. In our work, we propose a novel enrichment strategy using the KPLS model and the U and EFF criteria.

Inspired from [Menz et al., 2021], the proposed method introduces a two-phases algorithm, alternating between a learning phase and an MC population enrichment phase. The transition from one phase to the other (i.e. the learning stopping criterion) is based on the variance decomposition of two sources of uncertainty, namely the metamodel and the MC population. This is in contrast to traditional stopping criteria which usually compare the values of the learning function [Bichon et al., 2008, Echard et al., 2011, Zhang et al., 2019d] or the changes in P_f estimates at successive iterations [Gaspar et al., 2015, Schöbi et al., 2017, Lelievre, 2018, Wang and Shafieezadeh, 2019a] to sometimes arbitrary limits. In the proposed approach, the overall convergence criterion is based on the total variance which takes into account the errors stemming from both the surrogate model and the MC population, allowing to give a global measure of the uncertainty associated to the P_f estimate. Our method thus provides a sound basis for balancing the effect of surrogate model accuracy and the effect of the MC sampling density on the estimation

of the probability of failure in problems that have high-dimensional uncertain inputs.

In Section 6.2, the main elements of the mathematical framework are provided. Then, the novel approach is presented in Section 6.3. In Section 6.4 the performances of the proposed method are compared to other reference methods on four high-dimensional problems. We couple the Separable Monte Carlo sampling technique with the proposed variance-based framework in Section 6.5, comparing the performances on an academic test case and on the application to the Hole2Hole problem. A discussion on the obtained results is reported in Section 6.6. Finally, Section 6.7 provides some concluding remarks and perspectives for future work.

6.2 Mathematical Framework

In this section, the mathematical framework of the proposed approach is presented. As typical for surrogate modelling, the metamodel is trained on a limited set of points (named *training set* or *Design of Experiments* DoE) and the predictions are made in our case on a large dataset constituting the *samples population* used for reliability assessment.

We start in Section 6.2.1 with a reminder from Chapter 5 on Monte Carlo sampling method. We will introduce the machine learning techniques which constitutes the focus of the present work, in Section 6.2.2. A general overview of the adaptive learning techniques used for reliability estimations is reported in Section 6.2.3. The main principle on which the proposed algorithm is based will be presented in Section 6.2.4.

6.2.1 Monte Carlo (MC) Simulation

As a reminder from Section 5.2, MC is usually considered as the reference for all sampling-based reliability approaches [Hammersley, 2013]. In integral form, the expectation of the failure probability P_f can be presented as follows:

$$P_f = \int_D I[g(x) < 0] f(x) dx \quad (6.1)$$

Where I is an indicator function, g represents the Limit State Function (LSF) and f is the Probability Density Function (PDF) of the random variable X . Denoting by \widehat{P}_f an estimator of P_f , expectation and variance of this estimator can be computed through the following equations:

$$\widehat{P}_f = \frac{1}{N} \sum_{i=1}^N I[g(X_i) < 0] \quad \text{Var}(\widehat{P}_f) = \frac{\widehat{P}_f - \widehat{P}_f^2}{N} \quad (6.2)$$

The coefficient of variation of the P_f estimation is often used as stopping criterion for reliability analyses.

6.2.2 Kriging - Partial Least Square (KPLS)

The Kriging - Partial Least Square (KPLS) method was firstly introduced in [Bouhlef et al., 2016b]. This is based on the union of two separated approaches: Kriging and Partial Least Square.

The main purpose is to extend Kriging advantages to high-dimensional problems. In the present work, KPLS is used to approximate a computationally expensive model M :

$$\begin{aligned} M : B &\rightarrow Y \\ \mathbf{x} &\mapsto g(\mathbf{x}) \end{aligned} \quad (6.3)$$

Where $B \subset \mathbb{R}^d$ denotes the domain of the input variable \mathbf{x} , with d representing the original dimension.

6.2.2.1 Kriging

Kriging is a well-known method to approximate a black-box function, which perfectly interpolates training data and provides a proper error structure of the prediction itself. This feature makes the approach attractive in an adaptive learning context: in fact, the training dataset can be enriched in a rational way, by selecting the best-suited evaluation points in the domain, and thus leading to more and more accurate prediction models across iterations. On the other hand, Kriging's performances worsen for high input dimensionality.

Suppose we have a training set of n points defined by the coordinates:

$$\mathbf{x}^{(i)} = [\mathbf{x}_1^{(i)}, \dots, \mathbf{x}_d^{(i)}] \quad y^{(i)} = M(\mathbf{x}^{(i)}) \quad \forall i = 1, \dots, n \quad (6.4)$$

In the following, we will denote by \mathbf{X} the matrix $[\mathbf{x}^{(1)t}, \dots, \mathbf{x}^{(n)t}]^t$ and by \mathbf{y} the column array $[y^{(1)}, \dots, y^{(n)}]^t$. Kriging offers a prediction $\hat{y}(\mathbf{x})$ of the supposedly expensive model $y = M(\mathbf{x})$, considered as a realization of the stochastic process:

$$Y(\mathbf{x}) = \sum_{j=1}^m \beta_j f_j(\mathbf{x}) + Z(\mathbf{x})$$

Where β_j are unknown coefficients to train, f_j are known basis functions and Z is a Gaussian process defined as $Z \sim \mathcal{N}(0, k)$, where k represents a stationary covariance function, referred as covariance kernel. The kernel k can be written as:

$$k(\mathbf{x}, \mathbf{x}') = \sigma^2 r(\mathbf{x}, \mathbf{x}') = \sigma^2 r_{\mathbf{xx}'}, \quad \forall \mathbf{x}, \mathbf{x}' \in B$$

With σ^2 representing the process variance and $r_{\mathbf{xx}'}$ the correlation function between points \mathbf{x} and \mathbf{x}' . The correlation function $r_{\mathbf{xx}'}$ is fully defined by a set of hyper-parameters $\boldsymbol{\theta}$. In the present work, the isotropic Gaussian kernel function is considered:

$$r(\mathbf{x}, \mathbf{x}') = \prod_{i=1}^d \exp(-\theta_i (\mathbf{x}_i - \mathbf{x}'_i)^2) \quad \text{with } \theta_i \in \mathbb{R}^+ \quad (6.5)$$

From this, we may define the vector $\mathbf{r}_{\mathbf{xx}} = [r_{\mathbf{xx}^{(1)}}, \dots, r_{\mathbf{xx}^{(n)}}]$ and the matrix $\mathbf{R} = [\mathbf{r}_{\mathbf{x}^{(1)}\mathbf{x}}, \dots, \mathbf{r}_{\mathbf{x}^{(n)}\mathbf{x}}]$.

The best linear unbiased estimator of the quantity $y(\mathbf{x})$ will be:

$$\hat{y}(\mathbf{x}) = \mathbf{f}(\mathbf{x})^t \hat{\boldsymbol{\beta}} + \mathbf{r}_{\mathbf{xx}}^t \mathbf{R}^{-1} (\mathbf{y} - \mathbf{F} \hat{\boldsymbol{\beta}}) \quad (6.6)$$

Where $\mathbf{F} = [\mathbf{f}(\mathbf{x}^{(1)}), \dots, \mathbf{f}(\mathbf{x}^{(n)})]^t$ and $\mathbf{f}(\mathbf{x}) = [f_1(\mathbf{x}), \dots, f_m(\mathbf{x})]^t$. The Kriging model provides a proper error structure of the prediction itself as well, given by estimation of the variance, defined as follows:

$$s^2(\mathbf{x}) = \hat{\sigma}^2 (1 - \mathbf{r}_{\mathbf{x}\mathbf{x}}^t \mathbf{R}^{-1} \mathbf{r}_{\mathbf{x}\mathbf{x}}) \quad (6.7)$$

The parameters $\boldsymbol{\beta}$ and σ^2 can be estimated via least squares method, leading to the expressions:

$$\begin{aligned} \hat{\boldsymbol{\beta}} &= (\mathbf{F}^t \mathbf{R}^{-1} \mathbf{F})^{-1} \mathbf{F}^t \mathbf{R}^{-1} \mathbf{y} \\ \hat{\sigma}^2 &= \frac{1}{n} (\mathbf{y} - \mathbf{F} \hat{\boldsymbol{\beta}})^t \mathbf{R}^{-1} (\mathbf{y} - \mathbf{F} \hat{\boldsymbol{\beta}}) \end{aligned} \quad (6.8)$$

The most challenging part in Kriging training is given by the estimation of the hyper-parameters $\boldsymbol{\theta}$. These are generally determined by Maximum Likelihood (ML), which aims at maximizing the expression:

$$\log\text{-ML}(\boldsymbol{\theta}) = -\frac{1}{2} \left[n \ln(2\pi\sigma^2) + \ln(\det \mathbf{R}(\boldsymbol{\theta})) + \frac{1}{\sigma^2} (\mathbf{y} - \mathbf{F} \hat{\boldsymbol{\beta}})^t \mathbf{R}^{-1} (\mathbf{y} - \mathbf{F} \hat{\boldsymbol{\beta}}) \right] \quad (6.9)$$

By introducing the expressions of the estimations of β and σ^2 from Eq. 6.8 into 6.9, the only dependence from $\boldsymbol{\theta}$ lies in the matrix \mathbf{R} (which is omitted in the following to improve readability), obtaining the contracted ML:

$$\log\text{-ML}(\boldsymbol{\theta}) = -\frac{1}{2} \left[n \ln \left(\frac{1}{n} \mathbf{C}^t \mathbf{R} \mathbf{C} \right) + \ln(\det \mathbf{R}) \right] \quad (6.10)$$

Where

$$\mathbf{C} = \mathbf{y} - \mathbf{F} (\mathbf{F}^t \mathbf{R}^{-1} \mathbf{F})^{-1} \mathbf{F}^t \mathbf{R}^{-1} \mathbf{y}$$

For high dimensional inputs and large number of samples in the training set, maximizing Eq. 6.10 can be computationally expensive, as it implies a wider domain search for the optimization procedure and requires multiple inversions of the matrix \mathbf{R} , of size $n \times n$, to evaluate the objective function (log-ML).

The challenge of extending Kriging advantages for high-dimensional problems is achieved, in the KPLS approach, via the Partial Least Square regression. This will be the main subject of the next section.

6.2.2.2 Partial Least Square

The most common methods currently adopted to reduce dimensionality of a complex dataset are Principal Components Analysis (PCA) and Partial Least Square (PLS), already discussed in Chapter 3 and recalled here for the sake of completeness. The respective algorithms are quite similar but the nature is different: the former constitutes an unsupervised approach, used to describe the general behavior of data; the latter is a supervised method which identifies a linear relationship between inputs and outputs. To extend Kriging usage to high-dimensional problems, PLS is adopted to reduce the number of inputs involved in the hyper-parameters training by projecting them on a reduced-order space. This is achieved by the introduction of virtual variables, called

principal components, which are linear combinations of the original input variables. The number of components (or modes) h are defined a priori, before initializing the regression procedure.

Starting from $\mathbf{X}^{(0)} = \mathbf{X}$ and $\mathbf{y}^{(0)} = \mathbf{y}$, the principal directions $\mathbf{w}^{(l)}$ ($l = 1, \dots, h$) are sequentially determined by maximizing the squared covariance between projected inputs and outputs:

$$\mathbf{w}^{(l)} = \arg \max_{\mathbf{w}} \mathbf{w}^t (\mathbf{X}^{(l-1)})^t \mathbf{y}^{(l-1)} (\mathbf{y}^{(l-1)})^t \mathbf{X}^{(l-1)} \mathbf{w} \quad (6.11)$$

The successive terms of $\mathbf{X}^{(l)}$ and $\mathbf{y}^{(l)}$ (for $l = 1, \dots, h$) are computed as the residual matrix from the local regression of $\mathbf{X}^{(l-1)}$ and $\mathbf{y}^{(l-1)}$ respectively:

$$\begin{aligned} \mathbf{X}^{(l)} &= \mathbf{X}^{(l-1)} - \mathbf{t}^{(l)} \mathbf{p}^{(l)} \\ \mathbf{y}^{(l)} &= \mathbf{y}^{(l-1)} - c_l \mathbf{t}^{(l)} \end{aligned} \quad (6.12)$$

Where $\mathbf{p}^{(l)}$ is the regression vector of the local regression of \mathbf{X} onto $\mathbf{t}^{(l)}$ and c_l represents the regression coefficient of the local regression of \mathbf{y} onto $\mathbf{t}^{(l)}$. The principal components $\mathbf{t}^{(l)}$ can be obtained for $l = 1, \dots, h$ as follows:

$$\mathbf{t}^{(l)} = \mathbf{X}^{(l-1)} \mathbf{w}^{(l)} = \mathbf{X} \mathbf{w}_*^{(l)} \quad (6.13)$$

Where $\mathbf{w}_*^{(l)}$ constitute the columns of the matrix \mathbf{W}_* , determined by [Manne, 1987b]:

$$\mathbf{W}_* = \mathbf{W} (\mathbf{P}^t \mathbf{W})$$

Where $\mathbf{W} = [\mathbf{w}^{(1)}, \dots, \mathbf{w}^{(h)}]$ and $\mathbf{P} = [\mathbf{p}^{(1)t}, \dots, \mathbf{p}^{(h)t}]$.

PLS is used inside KPLS to define a linear projection of input onto a reduced-order space, so to reduce the number of hyper-parameters to optimize to construct the Kriging model.

6.2.2.3 KPLS

KPLS method was proved to extend the use of Kriging technique by exploiting the dimensionality reduction offered by PLS [Bouhleb et al., 2016b]. As stated before, this allows to reduce the number of hyper-parameters θ that need to be evaluated to train Kriging model [Bouhleb et al., 2016b].

In particular, the method is based on a linear transformation of the input variables:

$$\begin{aligned} F : B &\rightarrow B' \\ \mathbf{x} &\mapsto [\alpha_1 \mathbf{x}_1, \dots, \alpha_d \mathbf{x}_d]^t \end{aligned}$$

With $\alpha_1, \dots, \alpha_d \in \mathbb{R}$ and $B' \subset \mathbb{R}^d$. Of all possible linear mappings, the coefficients α_i are chosen from PLS decomposition results, generating h linear functions F_l ($l = 1, \dots, h$), defined as [Bouhleb et al., 2016b]:

$$\begin{aligned} F_l : B &\rightarrow B' \\ \mathbf{x} &\mapsto [\mathbf{w}_{*1}^{(l)} \mathbf{x}_1, \dots, \mathbf{w}_{*d}^{(l)} \mathbf{x}_d]^t \end{aligned} \quad (6.14)$$

This relation is the same for all $l = 1, \dots, h$. In [Bouhlef et al., 2016b], the new covariance kernel is defined as the tensor product of all stationary kernels $k_l : B \times B \rightarrow \mathbb{R}$:

$$k(\mathbf{x}, \mathbf{x}') = \prod_{l=1}^h k_l(F_l(\mathbf{x}), F_l(\mathbf{x}')) \quad (6.15)$$

If the chosen k_l is a Gaussian kernel, then the following kernel function will be obtained for KPLS:

$$k(\mathbf{x}, \mathbf{x}') = \sigma^2 \prod_{l=1}^h \prod_{i=1}^d \exp \left[-\theta_l \left(\mathbf{w}_{*i}^{(l)} \mathbf{x}_i - \mathbf{w}_{*i}^{(l)} \mathbf{x}'_i \right)^2 \right] \quad \forall \theta_l \in \mathbb{R}^+ \quad (6.16)$$

The proof of the equivalence between Kriging and KPLS kernels is available in [Bouhlef et al., 2016b]. It is possible to observe, by comparing Eq. 6.5 and Eq. 6.16, that for $h \ll d$ fewer hyper-parameters θ must be determined in order to train the Kriging-based metamodel. In terms of computational burden, this step constitutes the most challenging part of the whole training: therefore, KPLS construction tends to be more advantageous compared to Kriging. This feature makes KPLS very well-suited to manage problems with high number of input variables.

Note also that all results recalled in the previous section are still valid for KPLS, with the only difference lying in the covariance kernel definition, as in Eq. 6.16 rather than Eq. 6.5.

On the other hand, a lower precision may be expected with respect to Ordinary Kriging, due to the reduced flexibility conferred to the surrogate model. However, it should be noted that the PLS dimensionality reduction is not directly applied as an input transformation (with consequent loss of information) but rather as a regularization technique for the Kriging model training. Work in [Bouhlef et al., 2016a] presented an improved version of KPLS, called KPLSK, where a new Kriging model is trained by using KPLS hyper-parameters as starting points. However, in this chapter we show that a satisfying accuracy of the approximation of the LSF can be reached with KPLS in an adaptive learning framework.

The KPLS is used in the present work to approximate the LSF g . By denoting the approximation via KPLS of g with \hat{g} , we can estimate the failure probability P_f by applying the MC method on the samples of $\hat{g}(\mathbf{X})$:

$$\widehat{P}_f = \frac{1}{N} \sum_{i=1}^N I[\hat{g}(\mathbf{X}_i) < 0] \quad (6.17)$$

The KPLS is trained on a given *training set*, which is built iteratively in *adaptive learning* frameworks. In the next section, we report an overview of the kriging-based adaptive learning approaches used for reliability assessment.

6.2.3 Kriging-based adaptive learning techniques for reliability

In this section, we present an overview of the main features defining the adaptive learning techniques used to estimate a failure probability P_f in time consuming numerical models. In particular, the attention is focused on the Kriging-based approaches.

The general idea of adaptive learning techniques is to iteratively enrich the training dataset to progressively improve the approximation of the limit state function (LSF) g , especially around the limit state surface (LSS) which defines the border between failure and non-failure regions (i.e. around $g = 0$). Overall, five main general features characterize the adaptive learning approaches:

- *choice of the surrogate model*: in the literature, the use of Kriging, SVM and NN are common for reliability problems; focusing on Kriging, we also need to define the kernel formulation.
- *training set enrichment criterion*: this constitutes the choice of the mathematical expression to identify the best candidate point to enrich the training set (or DoE) [Echard et al., 2011, Bichon et al., 2008, Zhang et al., 2019d]; moreover, it includes the choice of how we select such point, based on optimization process [Bichon et al., 2008] or enumeration over a given sample population [Echard et al., 2011].
- *learning-phase stopping criterion*: this establishes the criterion to stop the enrichment of the training set, often based either on the values of the enrichment function [Echard et al., 2011, Lelièvre et al., 2018] or the convergence of the estimated P_f [Gaspar et al., 2015, Schöbi et al., 2017].
- *sampling strategy*: this constitutes the choice of how to sample the inputs for the predictions of the surrogate model, in order to estimate the P_f . This feature includes also the choice of whether progressively increasing the sample size [Echard et al., 2011] or using a fixed large sample population from the beginning of the process [Zuhal et al., 2021].
- *overall convergence criterion*: this constitutes the choice of when to stop the overall procedure, typically based either on the uncertainty of the estimation of the failure probability P_f [Bichon et al., 2008, Echard et al., 2011], the convergence of the estimated P_f [Gaspar et al., 2015, Schöbi et al., 2017], or the number of points added to the training set [Zuhal et al., 2021].

The final outcome of the adaptive learning approaches provides an *estimation* of the failure probability P_f . Therefore, we need to evaluate the associated uncertainty. In the upper-mentioned references, the uncertainty is associated to the variance of the P_f estimate due to the application of sampling techniques on the Kriging-based approximation of the LSF. In particular, the contribution to the overall variance due to the surrogate model is not generally taken into account (especially in the learning-phase stopping criterion, the sampling strategy and overall stopping criterion). In the next section, we present a method to evaluate the variance associated to the estimation of P_f , considering all sources of uncertainty.

6.2.4 Variance decomposition

As for many sampling-based reliability methods, \widehat{P}_f is a numerical estimate of the probability of failure. It is fundamental to take into account the uncertainty involved in its estimation and it can in particular serve as a convergence measure. Generally, a reliability

analysis is stopped when a targeted level of accuracy of \widehat{P}_f is reached, which is usually measured through the coefficient of variation of the P_f estimation. Following the work in [Menz et al., 2021], we decompose the total variance of \widehat{P}_f according to the sources of uncertainty affecting it:

$$V_{TOT} = V_X + V_G + V_{GX} \quad (6.18)$$

Where V_X represents the contribution to total variance due to Monte Carlo (MC) population, V_G constitutes the amount of variance due to the KPLS surrogate model and V_{GX} is the covariance term (between MC and KPLS). Moreover, as done in [Menz et al., 2021], we suppose that V_{GX} can be neglected: this is justified by the fact that the number of training points of the surrogate model (i.e. the number of simulations of the full model) is typically much lower than the number of samples in the MC population.

The contribution V_X can be determined by adopting the mean trajectory of KPLS (see Eq. 6.6) to approximate the LSF. In particular, the random variable $Y = I(\widehat{y}(\mathbf{X}))$ is a Bernoulli random variable $\mathcal{B}(p(\mathbf{X}))$ with parameter $p(\mathbf{X}) = \Phi\left(-\frac{\widehat{y}(\mathbf{X})}{s(\mathbf{X})}\right)$. The variance V_X will be therefore defined as:

$$V_X = \frac{1}{N(N-1)} \sum_{i=1}^N \left(p(\mathbf{X}_i) - \frac{1}{N} \sum_{j=1}^N p(\mathbf{X}_j) \right)^2 \quad (6.19)$$

In the case without any uncertainty due to the MC population, the variance term V_G , due to KPLS, could be analytically computed from the samples Y_i of the Bernoulli random variable $Y = I(\widehat{y}(\mathbf{X}))$:

$$V_G = Var_G [\widehat{P}_f(\mathcal{G})] = Var_G \left[\frac{1}{N} \sum_{i=1}^N Y_i \right] = \frac{1}{N^2} \sum_{i=1}^N \left(Var [Y_i] + \sum_{j \neq i} Cov [Y_i, Y_j] \right) \quad (6.20)$$

With:

$$Var [Y_i] = p(\mathbf{X}_i) (1 - p(\mathbf{X}_i)) \quad (6.21)$$

$$Cov [Y_i, Y_j] = \Phi_{2,\mathbf{C}}(0, 0) - p(\mathbf{X}_i)p(\mathbf{X}_j) \quad (6.22)$$

Where $\Phi_{2,\mathbf{C}}$ represents the cumulative distribution function of the 2-dimensional Gaussian variable of mean $(\widehat{y}(\mathbf{X}_i), \widehat{y}(\mathbf{X}_j))$ and covariance matrix \mathbf{C} evaluated at the points \mathbf{X}_i and \mathbf{X}_j . The contribution of the covariance term in Eq. 6.22 can imply a large computational effort on an MC population. The work in [El Haj and Soubra, 2021] adopts these expressions to propose an exploration criterion based on the contributions in Eq. 6.20 of a restricted number of samples. However, if the objective is to compute the variance V_G due to KPLS, such an approach to reduce the computational burden is not possible.

To compute the variance term V_G , due to KPLS, we adopt in this work the methodology introduced in [Menz et al., 2021]. In particular, V_G can be evaluated as the variance of the P_f estimation on a fixed number n_t of random trajectories G_i induced by the KPLS model. Denoting by $\widehat{P}_f(\mathcal{G}_i)$ the estimation of P_f via the application of the i^{th} trajectory

realization of the KPLS model on the MC population, the term V_G can be computed [Menz et al., 2021] as:

$$V_G = \frac{1}{n_t - 1} \sum_{i=1}^{n_t} \left(\widehat{P}_f(\mathcal{G}_i) - \frac{1}{n_t} \sum_{j=1}^{n_t} \widehat{P}_f(\mathcal{G}_j) \right)^2 \quad (6.23)$$

For sake of clarity, we add in the following the index n to refer to all quantities related to the metamodel conditioned to the training set (\mathbf{X}, \mathbf{y}) . Generally, to generate n_t trajectories \mathcal{G}_n on N points $\tilde{\mathbf{x}}$, the following expression can be used:

$$\mathcal{G}_n(\tilde{\mathbf{x}}) = \widehat{\mathbf{y}}_n(\tilde{\mathbf{x}}) + \mathbf{L}_n \xi \quad (6.24)$$

Where $\widehat{\mathbf{y}}_n$ constitutes the prediction provided by the Kriging-based surrogate model, $\mathbf{L}_n \in \mathbb{R}^N$ represents the Cholesky decomposition matrix of the covariance matrix $\mathbf{C}_n(\tilde{\mathbf{x}}) = (k_n(\mathbf{x}_i, \mathbf{x}_j))_{i,j}$ of size $N \times N$ and $\xi \sim \mathcal{N}(\mathbf{0}_N, \mathbf{I}_{N,N})$. Unfortunately, the covariance matrix \mathbf{C}_n can be ill-conditioned, as variance drops to zero at points nearby the training dataset X . Moreover, given the high number N of MC points to simulate, the overall computational effort can rapidly become intractable. The importance of the last problem significantly grows for lower probability estimations, as the size of MC is inverse proportional to the square of P_f . The first issue is addressed by simulating a non-conditioned Gaussian Process, while the second is managed by Karhunen-Loeve expansion. In the following, the two methods adopted in the present work to overcome these difficulties are briefly illustrated. The implementations of both approaches are similar to the analogues for Kriging models [Menz et al., 2021], as all Kriging results can be extended to KPLS as well.

6.2.4.1 Ill-conditioned covariance matrix

To solve the issue related to the ill-conditioning of the covariance matrix, we approximate, following [Menz et al., 2021], the initial KPLS model via a non-conditioned Gaussian process. We denote by \mathcal{G}_n the initial Gaussian process, conditioned to the training set (\mathbf{X}, \mathbf{y}) , described by the covariance kernel k_n defined by the hyper-parameters $\boldsymbol{\theta}_n$ and σ_n . We introduce a centered Gaussian process $\tilde{\mathcal{G}}$ defined by the same kernel k_n of \mathcal{G}_n :

$$\tilde{\mathcal{G}}(\mathbf{x}) \sim \mathcal{N}(0, k_n(\mathbf{x}, \mathbf{x}')) \quad (6.25)$$

Then, the parameter $\tilde{\beta}$ related to $\tilde{\mathcal{G}}$ is estimated as in Eq. 6.8, but conditioned on the new training points $(\mathbf{X}, \tilde{\mathcal{G}}(\mathbf{X}))$:

$$\tilde{\beta} = (\mathbf{F}^t \mathbf{R}^{-1} \mathbf{F})^{-1} \mathbf{F}^t \mathbf{R}^{-1} \tilde{\mathcal{G}}(\mathbf{X}) \quad (6.26)$$

Thanks to this, the mean \tilde{y} of the unconditioned Gaussian process $\tilde{\mathcal{G}}$ can be predicted:

$$\tilde{y}(\mathbf{x}) = \mathbf{f}(\mathbf{x})^t \tilde{\beta} + \mathbf{r}_{\mathbf{x}\mathbf{X}}^t \mathbf{R}^{-1} (\tilde{\mathcal{G}}(\mathbf{X}) - \mathbf{F} \tilde{\beta}) \quad (6.27)$$

Finally, introducing $\widehat{\mathbf{y}}_n$ from Eq. 6.6, we can approximate the original Gaussian process \mathcal{G}_n through the non-conditioned analogue Gaussian process $\tilde{\mathcal{G}}_n$, by correcting the mean of $\tilde{\mathcal{G}}$:

$$\tilde{\mathcal{G}}_n(\mathbf{x}) = \hat{y}_n(\mathbf{x}) - \tilde{y}(\mathbf{x}) + \tilde{\mathcal{G}}(\mathbf{x}) \quad (6.28)$$

This follows the same statistic properties of the original \mathcal{G}_n and does not exhibit zero variance near the points of the training set \mathbf{X} . Therefore, it can be used to simulate trajectories and without any ill-conditioned covariance matrix.

6.2.4.2 Simulate large amounts of data

The second key-problem related to the simulation of trajectories refers to the huge amount of data to generate. Even if disposing of a well-conditioned covariance matrix, the Cholesky decomposition can imply a huge computational effort that could become intractable with very high number N of points (namely all samples in MC population) to simulate. To this purpose, the Karhunen-Loeve (KL) expansion, based on the spectral decomposition of the covariance kernel, is adopted. In particular, the KL expansion of a Gaussian Process $\mathcal{G} \sim GP(\mu(\cdot), k(\cdot, \cdot))$ can be written as:

$$\mathcal{G}(\mathbf{x}, \omega) = \mu(\mathbf{x}) + \sum_{i=1}^{\infty} \sqrt{\lambda_i} \phi_i(\mathbf{x}) \xi_i(\omega) \quad (6.29)$$

Where λ_i are the eigenvalues of the kernel $k(\cdot, \cdot)$, $\phi_i : B \rightarrow \mathbb{R}$ constitutes the related eigenfunctions, and ξ_i represent mutually independent centered normal random variables. After sorting the eigenvalues in decreasing order, the expression in Eq. 6.29 can be truncated at the M -th term, leading to:

$$\mathcal{G}(\mathbf{x}, \omega) \approx \mu(\mathbf{x}) + \sum_{i=1}^M \sqrt{\lambda_i} \phi_i(\mathbf{x}) \xi_i(\omega) \quad (6.30)$$

Determining all λ_i and ϕ_i implies solving the integral equations (for $i = 1, \dots, M$):

$$\lambda_i \phi_i(\mathbf{x}) = \int_B k(\mathbf{x}, \mathbf{x}') \phi_i(\mathbf{x}') d\mathbf{x}' \quad (6.31)$$

Here, the eigenvalues and the eigenvectors are estimated via the Nystrom method on N_q integration points:

$$\widehat{\lambda}_i \widehat{\phi}_i(\mathbf{x}) = \sum_{j=1}^{N_q} k(\mathbf{x}, \mathbf{x}_j) \widehat{\phi}_i(\mathbf{x}_j) w_j \quad (6.32)$$

Denoting with \mathbf{C}_q the covariance matrix computed at integration points (thus of size $N_q \times N_q$), the weight matrix $\mathbf{W}_q = \text{Diag}(w_1, \dots, w_{N_q})$ and the eigenfunction vector $\widehat{\Phi}_i = [\widehat{\phi}_i(\mathbf{x}_1), \dots, \widehat{\phi}_i(\mathbf{x}_{N_q})]$, the Eq. 6.32 can be written in matrix form:

$$\mathbf{C}_q \mathbf{W}_q \widehat{\Phi}_i = \widehat{\lambda}_i \widehat{\Phi}_i \quad (6.33)$$

By introducing the base change induced by $\mathbf{W}_q^{1/2}$ (which is symmetrical), we can simplify the eigenvalue problem:

$$\mathbf{B}_q \widehat{\Phi}_i^* = \widehat{\lambda}_i \widehat{\Phi}_i^* \quad (6.34)$$

Where $\mathbf{B}_q = \mathbf{W}_q^{1/2} \mathbf{C}_q \mathbf{W}_q^{1/2}$ and $\widehat{\Phi}_i^* = \mathbf{W}_q^{-1/2} \widehat{\Phi}_i$. Once the eigenvalue problem in Eq. 6.34 to determine $\widehat{\lambda}_i$ and all related elements $\widehat{\phi}_{i,j}^*$ of the vector $\widehat{\Phi}_i^*$, the eigenfunctions can be approximated by:

$$\widehat{\phi}_i(\mathbf{x}) = \frac{1}{\widehat{\lambda}_i} \sum_{j=1}^{N_q} \sqrt{w_j} \widehat{\phi}_{i,j}^* k(\mathbf{x}, \mathbf{x}_j) \quad \forall i = 1, \dots, M \quad (6.35)$$

The Gaussian process can be finally approximated by introducing the results of Eq. 6.35 into Eq. 6.30, leading to the expression:

$$\mathcal{G}(\mathbf{x}, \omega) \approx \mu(\mathbf{x}) + \sum_{i=1}^M \frac{\xi_i(\omega)}{\sqrt{\widehat{\lambda}_i}} \sum_{j=1}^{N_q} \sqrt{w_j} \widehat{\phi}_{i,j}^* k(\mathbf{x}, \mathbf{x}_j) \quad (6.36)$$

In the context of this work, the integration point are randomly generated from a uniform distribution covering the whole input domain B . The associated weights w_j are all equal to $w_j = |B|/N_q = w$ for $j = 1, \dots, N_q$, where $|B| = \int_B d\mathbf{x}$. The KL expansion is used to approximate the non-conditioned Gaussian process defined in Eq. 6.25. The quantities in Eq. 6.26-6.27 are computed with:

$$\tilde{\mathcal{G}}(\mathbf{X}) \approx \sum_{i=1}^M \frac{\xi_i}{\sqrt{\widehat{\lambda}_i}} \sum_{j=1}^{N_q} \sqrt{w_j} \widehat{\phi}_{i,j}^* k(\mathbf{X}, \mathbf{x}_j) \quad (6.37)$$

For further details on the application of these methods on adaptive Kriging, the reader is referred to [Menz et al., 2021]. As stated before, once the kernel is modified as in Eq. 6.16, the extension to KPLS is straight-forward.

6.3 Adaptive Variance-based Kriging Partial Least Square (Vb-KPLS)

In this section, we describe the proposed method. In the first subsection, the criterion allowing to select the most promising input points is presented. Secondly, the stopping criteria of the learning phase are provided. In the last subsection, we describe the overall proposed algorithm.

6.3.1 Exploration criteria

As for all adaptive learning frameworks, a fundamental ingredient is given by the criterion to select the best-suited point to enrich the training set. In the present work, we will consider two exploration criteria: the *Expected Feasibility Function* (EFF) [Bichon et al., 2008] and the U enrichment function [Echard et al., 2011]. In the different examples, we will use one or the other on a case-by-case basis.

The *EFF* can be expressed in an analytical closed-form expression:

$$\begin{aligned}
 EFF(\mathbf{x}) = & \hat{y}(\mathbf{x}) \left[2\Phi \left(-\frac{\hat{y}(\mathbf{x})}{s(\mathbf{x})} \right) - \Phi \left(-\frac{\epsilon(\mathbf{x}) + \hat{y}(\mathbf{x})}{s(\mathbf{x})} \right) - \Phi \left(\frac{\epsilon(\mathbf{x}) - \hat{y}(\mathbf{x})}{s(\mathbf{x})} \right) \right] \\
 & - s(\mathbf{x}) \left[2\phi \left(-\frac{\hat{y}(\mathbf{x})}{s(\mathbf{x})} \right) - \phi \left(-\frac{\epsilon(\mathbf{x}) + \hat{y}(\mathbf{x})}{s(\mathbf{x})} \right) - \phi \left(\frac{\epsilon(\mathbf{x}) - \hat{y}(\mathbf{x})}{s(\mathbf{x})} \right) \right] \\
 & + \epsilon(\mathbf{x}) \left[\Phi \left(\frac{\epsilon(\mathbf{x}) - \hat{y}(\mathbf{x})}{s(\mathbf{x})} \right) - \Phi \left(-\frac{\epsilon(\mathbf{x}) + \hat{y}(\mathbf{x})}{s(\mathbf{x})} \right) \right]
 \end{aligned} \tag{6.38}$$

Where Φ and ϕ are respectively the cumulative distribution function and the probability density function of a Standard Normal distribution. Typically the function ϵ represents a band around LSS in which exploration is privileged and is fixed to $\epsilon(\mathbf{x}) = 2s(\mathbf{x})$. The best-suited point to enrich the training set is the point maximizing the EFF criterion.

This criterion makes it possible to make a compromise between improving the approximation around the already known limit state surface portions and discovering unexplored failure regions. In the present work, this criterion is adapted to KPLS model and implemented after modification of the covariance kernel. This constitute the default enrichment criterion in our framework.

The U function [Echard et al., 2011, Zuhail et al., 2021] is the second retained enrichment criterion. Unlike EFF , this must be minimized and can be written as:

$$U(\mathbf{x}) = \frac{|\hat{y}(\mathbf{x})|}{s(\mathbf{x})} \tag{6.39}$$

This is related to the misclassification error probability of the Kriging-based surrogate model on the point \mathbf{x} .

As a final remark, to individuate the best-suited new point to enrich the DoE, we select the MC candidate sample maximizing the EFF (respectively minimizing the U) criterion (as in [Echard et al., 2011, Zuhail et al., 2021]), instead of solving an actual optimization problem (as done in [Bichon et al., 2008]).

6.3.2 Stopping criteria

After a certain number of Kriging enrichments, we need to decide when to stop the enrichment phase. All stopping criteria are evaluated by enumeration on a given MC population. It should be noted that, as the final P_f is not a priori known, the required number of MC samples is not known either. To this extent, once a learning phase is stopped we enrich the MC population if a sufficient level of global accuracy, measured in terms of coV of the P_f estimate, is yet not reached: the targeted variance level, denoted as \bar{V} , is defined by the desired target \overline{coV} and the estimation \widehat{P}_f at a given iteration. This implies that the final variance target \bar{V} will evolve across iterations, as the P_f estimate is updated iteratively.

In this work, two classical learning stopping criteria related to measure of the upper-mentioned enrichment functions are adopted as references for the comparison with our approach:

- U stopping criterion [Echard et al., 2011], referring to the maximum classification error probability over the given MC population:

$$\min_{\mathbf{x}} U(\mathbf{x}) \geq 2 \tag{6.40}$$

- *EFF* stopping criterion [Bichon et al., 2008], constituting an index of the possibility to extract further information from the current MC population to improve the description of the LSS:

$$\max_{\mathbf{x}} EFF(\mathbf{x}) \leq 0.001 \quad (6.41)$$

When *U* or *EFF* stopping criterion is adopted in existing approaches in the literature, the computation of $coV(\widehat{P}_f)$ takes into account only the variance accounting for the limited MC population. This is however only one of the sources of variance in the P_f estimate, the other source being that accounting for the prediction uncertainty of the Kriging surrogate model. Not explicitly accounting for those two sources of variance may lead to numerical inefficiencies.

Our proposed method is based on the upper-mentioned variance decomposition, from which the name *Variance-based* (*Vb*). It addresses the need to take into account both sources of uncertainty affecting the estimation of the failure probability P_f . In particular, two Variance-based (*Vb*) variants, which are distinguished by the learning phase stopping criterion, are presented:

- Local Variance-based stopping criterion (*LVb*) [Menz et al., 2021], identifies the most important source of uncertainty and stops learning phase when most of variance comes from MC sampling and not from the surrogate model:

$$V_G \leq V_X \quad (6.42)$$

- Global Variance-based stopping criterion (*GVb*), comparing the variance due to the surrogate model to a global variance target \bar{V} :

$$V_G \leq \bar{V}/2 \quad (6.43)$$

The main objective of these proposed stopping criteria is to balance the two sources of uncertainty in the machine learning assisted reliability algorithm, namely the MC population and the KPLS model. Conversely to the reference *U* and *EFF* based stopping criteria, for *LVb* and *GVb*, the overall algorithm is stopped when the total variance (thus including the contributions from MC and KPLS) is lower than a global target \bar{V} .

The *LVb* criterion can be interpreted as a local measure of the variance balance as it compares the uncertainties of MC and KPLS at a given iteration. This allows to compare when the variance due to the Kriging surrogate model is lower than the one due to the limited MC samples and thus decide to enrich the MC population instead of continuing enriching the surrogate model. On the other hand, *GVb* can be seen as a comparison between the variance V_G due to the KPLS model and the global variance target \bar{V} : as the overall algorithm is stopped when a global measure of variance is achieved, the right term is divided by a factor 2 to guarantee, at the last iteration, that the sum of V_X and V_G is lower than the target \bar{V} and the contribution of KPLS is lower than the one corresponding to the MC population. Therefore, the two variants of variance-based stopping criterion have the same meaning at the last iteration, but the evolution all across the intermediate iterations will be different.

Algorithm 1: Variance-based proposed algorithm

Input: distributions, DoE, MC initialization

repeat

$learn, MCenrich \leftarrow False$

 KPLS \leftarrow training on DoE

$P_f \leftarrow$ prediction on MC via KPLS

$V_G, V_X \leftarrow$ sensitivity analysis

if not Vb stopping criterion then

$learn \leftarrow True$

else if $V_G + V_X > \bar{V}$ then

$MCenrich \leftarrow True$

else

$\bar{P}_f, V_{TOT} \leftarrow$ bootstrap analysis

if $V_{TOT} > \bar{V}$ then

if not Vb stopping criterion then

$learn \leftarrow True$

else

$MCenrich \leftarrow True$

if learn then

 add point to DoE $\leftarrow \max EFF(X_{MC})$

else if MCenrich then

 enrich MC population

until $learn \vee MCenrich$;

Output: \bar{P}_f, V_{TOT}

6.3.3 Proposed Variance-based (*Vb*) algorithm

The proposed algorithm is illustrated in Figure 6.1 and in Algorithm 1.

In our approach, we consider a fully variance-based adaptive learning process, specifically suited for reliability assessment problems. The variance decomposition and, thus, the distinction between the two sources of uncertainty of the P_f estimate (i.e. the KPLS model and the MC population), is taken into account in the whole algorithm. The MC population and the surrogate model training set are gradually enriched, based on the variance decomposition results. The overall procedure is stopped as well when the total variance V_{TOT} from both sources reaches an acceptable level, determined by a target $co\bar{V}$ of the P_f estimate itself. The overall stopping criterion will be then formalized as:

$$V_{TOT} \leq \bar{V} = \overline{coV} \widehat{P}_f^2 \quad (6.44)$$

Thanks to the *Vb* approach, we are able to provide a sufficiently accurate estimation of the failure probability, together with a global measure of the total variance. Moreover, the balance between the variance levels stemming from the different sources of uncertainty allows to improve the efficiency of the overall learning algorithm, leading to a reduction in the number of evaluations of a computationally expensive numerical model.

To enrich the DoE ("*Enrich DoE*" box in the flowchart of Fig. 6.1), we select a point from the MC population according to a learning criterion, typically *EFF* or *U* criterion.

A fundamental aspect of the presented approach is the principle of enriching not only

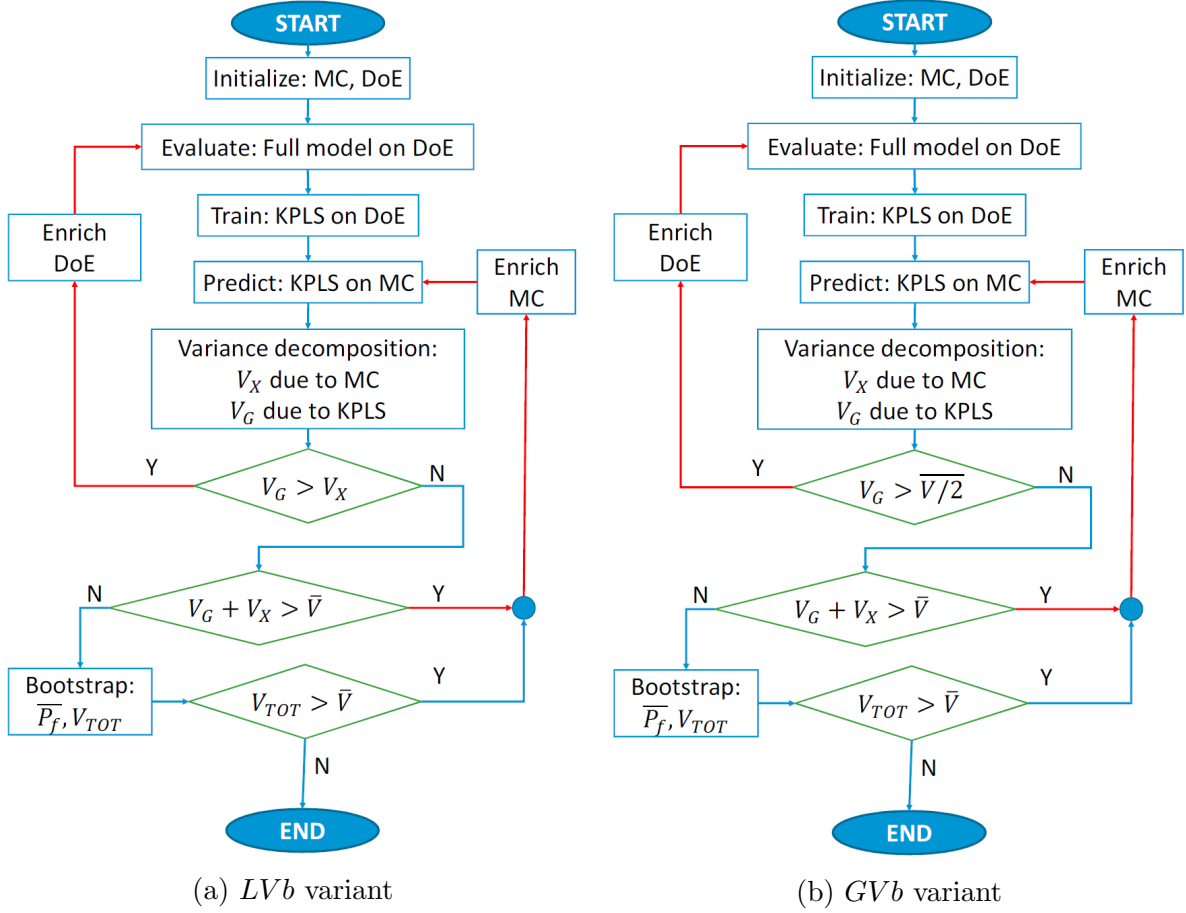


Figure 6.1: Proposed algorithm flowchart

the training set, via new simulations of the complete model, but also the MC population itself. This becomes necessary when a balance between variances of different sources is sought: in fact, introducing from the very beginning a very large MC population (oversized with respect to the targeted \overline{coV} and the magnitude of P_f) would imply an excessive accuracy requirement to the metamodel, thus deteriorating the overall efficiency of the algorithm. The MC population is then initialized with N samples and it is enriched in specific steps ("Enrich MC" box in the flowchart of Fig. 6.1) adding P new samples. The implementation of the MC sampling and enriching is implemented in this work with the Python library OpenTURNS [Baudin et al., 2016].

It is important to underline the introduction of an additional bootstrap analysis at the last step to also verify the assumption we made on the possibility to neglect the covariance term V_{GX} in Eq. 6.18.

The adoption of KPLS as surrogate model makes the algorithm scalable for reliability problems with black-box functions with high number of inputs.

6.4 Numerical results

In this section, four reliability problems with high number of uncertain inputs are presented. We implemented four methods for the comparative study: two reference approaches stem from *AK-MCS+U* [Echard et al., 2011] and *AK-MCS+EFF* [Bichon et al., 2008], where the Kriging model is substituted with KPLS; the other two cover the two variants *GVb* and *LVb* of the presented *Vb* framework. These are named, for readability, after the corresponding learning stopping criteria, respectively *U*, *EFF*, *LVb* and *GVb*.

The results are compared in terms of the accuracy of the P_f final estimate, the number of enrichments of the training set, the final ratios between the variance terms V_G and V_X and the number of failed simulations N_{fail} (exhibiting a relative error above 15%). These are issued from the statistical analysis over 11 repetitions of every algorithm.

The comparison also covers different numbers of PLS components adopted in the KPLS kernel definition: coherently with [Bouhlef et al., 2016b], we name these by $KPLSi$ where i is the number of PLS components.

6.4.1 40-dimensional linear problem

The first numerical example involves a linear LSF, given by the expression:

$$g(\mathbf{X}) = (m + 3\sigma\sqrt{m}) - \sum_{i=1}^m X_i \quad (6.45)$$

In particular, we adopt $m = 40$ (40-dimensional problem) and $\sigma = 0.2$. Note that in the next subsection we will also consider $m = 100$. The variables X_i follow a log-normal distribution with unitary mean and standard deviation equals to σ . The initial DoE contains 20 points and the enrichment criterion adopted for *Vb* framework is the *EFF* function. The MC population is initialized with $N = 10000$ points, while other $P = 10000$ samples are added in each MC enrichment step.

The numerical results, grouped per learning algorithm and number of PLS components in the KPLS kernel definition, are reported in Table 6.1.

All approaches considered in this study lead to a correct estimation of failure probability P_f , as can be observed in Table 6.1. The variabilities of the P_f estimations are in line with the analysis of the predicted variance, consistent with the imposed limit of $coV = 5\%$. As anticipated in previous sections, both *Vb* variants lead to higher ratios $\overline{V_G/V_X}$ with respect to *U* and *EFF*, as the focus is to balance the sources of uncertainties.

Focusing on the number of DoE updates, it can be observed that for any number of PLS components, the *Vb* approaches (both variants *LVb* and *GVb*) clearly outperform both *U* and *EFF*.

Comparing the results at different number of PLS components, we may observe that both *EFF* and *U* approaches exhibit a minimum number of DoE updates for $KPLS_2$, increasing when more components are added. For *LVb* and *GVb* a more regular behavior is observed, with a number of DoE updates essentially decreasing with the increase in the complexity of the KPLS kernel definition. The gains tend to stabilize for the highest numbers of components considered herein.

We analyze in this section the evolution of the variance decomposition across iterations, issued from the application of different approaches on this first numerical example.

Method	N. components	N. DoE updates	P_f	$\overline{V_G/V_X}$	N_{fail}
U	KPLS1	134 (18.9%)	1.99e-03 (4.28%)	2.37e-02	0
	KPLS2	61.9 (8.25%)	1.99e-03 (4.84%)	<1e-15	1
	KPLS3	71.4 (7.87%)	1.98e-03 (5.83%)	<1e-15	0
	KPLS4	93.2 (10.5%)	1.99e-03 (5.28%)	<1e-15	0
EFF	KPLS1	157 (21.2%)	2.00e-03 (4.63%)	<1e-15	0
	KPLS2	61.9 (9.69%)	1.98e-03 (5.98%)	<1e-15	0
	KPLS3	78.1 (11.4%)	1.98e-03 (5.88%)	<1e-15	0
	KPLS4	99.3 (10.6%)	1.96e-03 (5.34%)	1.06e-07	0
LVb	KPLS1	55.5 (19.3%)	1.95e-03 (2.61%)	3.56e-01	0
	KPLS2	39.0 (13.8%)	1.98e-03 (5.01%)	2.49e-01	0
	KPLS3	34.7 (8.46%)	2.00e-03 (3.57%)	2.76e-01	0
	KPLS4	32.2 (7.13%)	1.96e-03 (2.45%)	4.77e-01	0
GVb	KPLS1	58.2 (15.0%)	1.98e-03 (4.38%)	1.96e-01	0
	KPLS2	36.6 (11.0%)	2.01e-03 (4.90%)	2.38e-02	0
	KPLS3	36.9 (9.80%)	1.97e-03 (4.06%)	1.54e-01	0
	KPLS4	36.9 (8.70%)	1.98e-03 (4.10%)	1.23e-01	0

Table 6.1: Main results for 40-dimensional linear problem (reference MC: $P_f = 2.00 \times 10^{-3}$). Note that the number in parentheses provide the coV of the values provided in the respective cells.

This allows to illustrate the interest of explicitly considering the variance decomposition in the adaptive learning approach. These conclusions are analogue for all the test cases studied in this chapter.

In Fig. 6.2, we report in the same plot the curves related to V_X (i.e. the variance due to the MC population), V_G (i.e. the variance due to KPLS), V_{TOT} (i.e. the total variance) and the moving variance target \overline{V} (defined by a fixed target on coV and the P_f estimate at a given iteration). For *GVb* case, we also report the curve related to the evolution of $\overline{V}/2$ to highlight the alternation between learning and MC enrichment phases.

In general, the term V_X stems from the evolution of the estimation of P_f with varying size of the MC population: in particular, it is expected to increase when new failure regions are discovered (i.e. the estimated P_f increases) or decrease when the size of the MC population increases. Moreover, V_X can slightly be affected by updates in the approximation of the LSS, as it would impact the P_f estimate. The variance target \overline{V} is deduced from the imposed \overline{coV} and is only affected by the updates of the estimations of P_f : in early stages, when few region are known, this can go beyond the machine precision; later on, this evolves as a quadratic function of P_f , reaching several plateaus corresponding to stagnations of the failure probability estimations.

The variance V_G due to the KPLS model generally decreases when new points are added to enrich the training set. However, this is not a general rule as the function used to select a new exploration point (either *U* or *EFF* learning function) makes no reference to the effect of the variance induced by the candidate points: therefore, the term V_G can, in some cases, increase with new enrichments, above all in the initial phase.

A different effect on variance decomposition stems from the enrichments of the MC population. In early stages of the algorithm, increasing the MC sample size can lead to

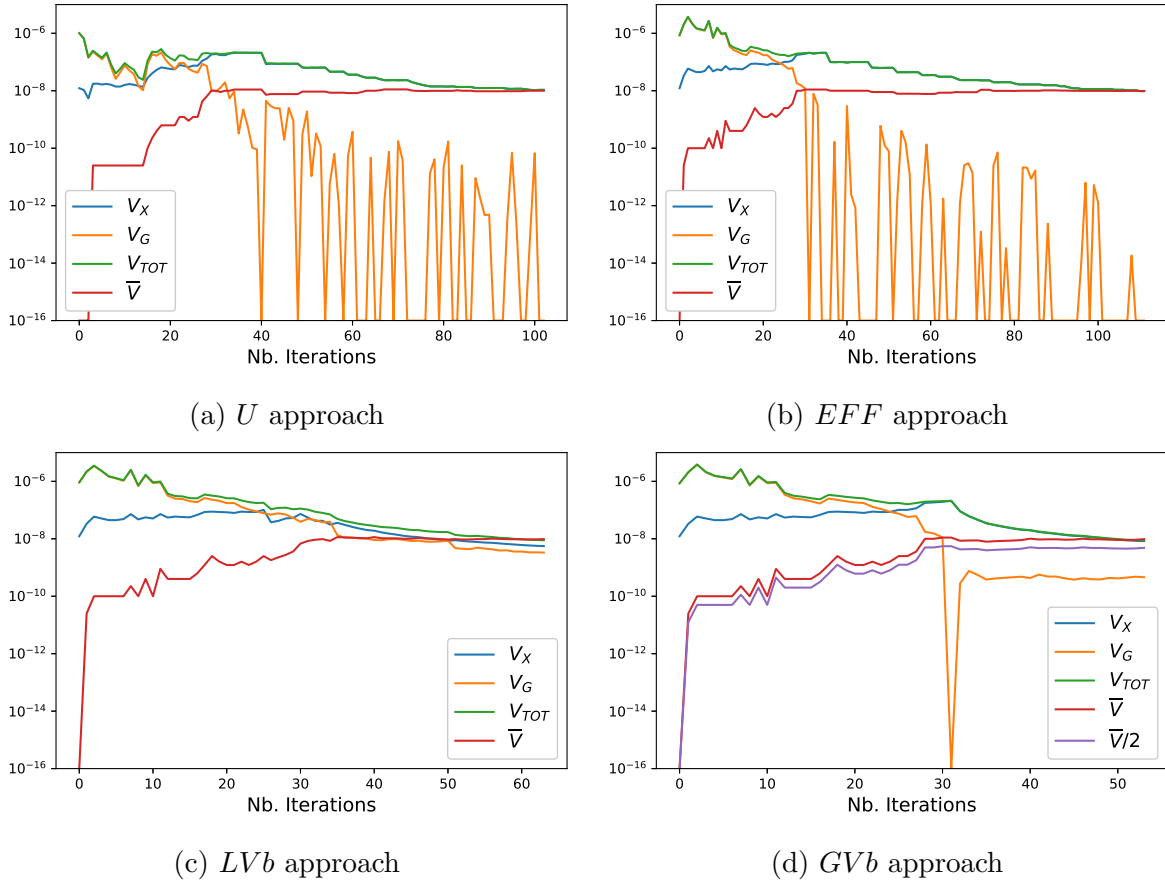


Figure 6.2: 40-dimensional linear problem: variance decomposition results across iterations with different adaptive approaches (4 components in KPLS setting)

no difference or even increase the variability of the P_f estimated via different trajectories of the KPLS model: in fact in initial stages the surrogate model is not mature yet and the MC population is relatively small; as a consequence, adding MC samples may lead to large variations of the predicted P_f , so that the behavior of V_G is unpredictable.

It can be observed from Fig. 6.2a-b, that the classical approaches based solely on U and EFF lead to very unbalanced variance sources, with most of uncertainty stems from the MC population. For the EFF approach, the term V_G can even reach values which are comparable to the machine precision.

On the other hand, both variants LVb and GVb of the presented Vb approach can allow to balance the sources of variance V_X and V_G . The former continuously compares the two terms at every iteration, leading globally to a stair-like evolution for both V_X and V_G : therefore, learning and MC enrichment phases alternates until the end of the algorithm and both V_X and V_G converge to roughly $\bar{V}/2$: this alternation is visible in Fig.6.2c through the intersections between the curves of V_X and V_G . This continuous balance of these two sources of uncertainty generally leads to improved efficiency of the variance based approaches for a given accuracy target (in terms of coV) on the final probability of failure.

For the GVb variant, the updates of the DoE continue until a satisfying level of variability (compared to a global target) in P_f estimates from different realizations of KPLS

is achieved (i.e. until $V_G < \bar{V}/2$): in this case, the Kriging learning phase generally covers a large portion of the first iterations, until the Vb stopping criterion is satisfied, while the MC enrichment phase covers the final stages of the algorithm. As a consequence, the alternation between the two phases - which is typical for the LVb variant - is reduced: this can be observed in Fig.6.2d on the intersections between the curves of V_G and $\bar{V}/2$. The evolution depicted in Fig. 6.2d constitutes an extreme example, as at a iteration 31 the term V_G reaches the machine precision and the two phases are totally decoupled; in certain cases, the alternation between the learning and MC enrichment is more continuous, but the initial learning phase lasts for more iterations than the analogue analysis conducted with the LVb variant. Moreover, as the level of V_G should just be lower than the global target, the convergence of V_X and V_G to exactly $\bar{V}/2$ is not guaranteed, making V_G slightly lower than the former.

Overall, the GVb variant of the Vb approach proposed herein provides a more conservative criterion than LVb in the early stages of the algorithm, where the MC population is still relatively small (and thus $V_X > \bar{V}/2$). However, this does not necessarily imply a reduction in the overall efficiency of the algorithm, measured in terms of the total number of evaluations of the full computationally expensive model. The evolutions of the variance decomposition across iterations reported in Fig. 6.2 generally present the same features, with very few differences between the results coming from different reliability problems and different numbers of PLS components adopted in the KPLS framework.

6.4.2 100-dimensional linear problem

In this second test case, we propose the same LSF defined in Eq. 6.45, but considering a 100-dimensional problem (hence $m = 100$) with an initial DoE of 50 points. The MC population is initialized with $N = 10000$ points, while other $P = 10000$ samples are added in each MC enrichment step. The other parameters, enrichment criterion and probability distribution functions are unchanged.

The numerical results related to the 100-dimensional linear problem are reported in Table 6.2, grouped per learning algorithm and number of PLS components in the KPLS kernel definition.

The obtained estimations of P_f are acceptable on all algorithms. The conclusions on P_f variability and the ratio \bar{V}_G/\bar{V}_X are analogue to the ones drawn for the previous example. Analogue conclusions can be drawn also on the variation of performances with respect to the number of PLS components in KPLS kernel definition.

Looking at the efficiency of both Vb variants, the overall number of full simulations required to estimate P_f is again lower than EFF and U applications.

The gains of our approach with respect to EFF in terms of full model simulations vary in a range between 1.5 (for KPLS2) and 2.8 (for KPLS4). When comparing U and Vb variants, the gain is slightly reduced but still evident, with a range between 1.4 (for KPLS2) and 2.5 (for KPLS4).

Note that on these first two application examples the LSF was linear. Higher efficiency of the variance based framework is expected on the non-linear problems and this will be investigated in the next two applications.

Adaptive method	N. components	N. DoE updates	P_f	$\overline{V_G}/\overline{V_X}$	N_{fail}
U	KPLS1	271 (10.5%)	1.68e-03 (4.48%)	<1e-15	0
	KPLS2	123 (6.48%)	1.70e-03 (4.31%)	<1e-15	0
	KPLS3	143 (9.99%)	1.70e-03 (4.49%)	<1e-15	0
	KPLS4	183 (8.72%)	1.66e-03 (4.51%)	<1e-15	0
EFF	KPLS1	312.7 (14.05%)	1.66e-03 (3.43%)	<1e-15	0
	KPLS2	128.9 (8.13%)	1.66e-03 (3.53%)	<1e-15	0
	KPLS3	160.0 (12.19%)	1.66e-03 (3.50%)	<1e-15	0
	KPLS4	202.5 (10.21%)	1.65e-03 (3.86%)	<1e-15	0
LVb	KPLS1	139.8 (9.68%)	1.65e-03 (2.34%)	1.87e-02	0
	KPLS2	84.64 (7.69%)	1.65e-03 (4.50%)	4.24e-01	0
	KPLS3	74.7 (2.81%)	1.63e-03 (4.89%)	5.41e-01	0
	KPLS4	71.9 (4.67%)	1.65e-03 (5.26%)	4.29e-01	0
GVb	KPLS1	153.2 (7.10%)	1.65e-03 (5.21%)	2.31e-02	0
	KPLS2	87.2 (7.66%)	1.65e-03 (4.05%)	1.45e-01	0
	KPLS3	72.5 (4.31%)	1.66e-03 (4.03%)	1.62e-01	0
	KPLS4	71.9 (7.45%)	1.66e-03 (4.48%)	2.03e-01	0

Table 6.2: Main results for 100-dimensional linear problem (reference MC: $P_f = 1.66 \times 10^{-3}$). Note that the number in parentheses provide the *coV* of the values provided in the respective cells.

6.4.3 53-dimensional truss example

In this section, we re-propose the truss example used in Chapter 5. A 23-bar truss problem is considered (confront Fig. 6.3), for which the LSF is formulated here as:

$$g(V_{all}, X_S) = V_{all} - V_1(X_S) \quad (6.46)$$

Where X_S represents the whole set of variables affecting the deflection V_1 , computed through Finite Element Analysis (FEA). The maximum allowable deflection is denoted as V_{all} . Different Young's Modulus and section areas are assigned to each finite element, with different section statistical distributions for horizontal and oblique bars. Considering 23 elements, 6 load variables and the allowable deflection V_{all} , overall 53 input variables are introduced. The initial DoE dataset contains 30 points and the enrichment criterion adopted for *Vb* framework is the *EFF* function. The MC population is initialized with $N = 10000$ points, while other $P = 10000$ samples are added in each MC enrichment step.

Variable	Unit	Distribution	Mean	St. Deviation
E_1, E_2	<i>GPa</i>	Log-Normal	210	21
A_1	m^2	Log-Normal	2.0×10^{-3}	2.0×10^{-4}
A_2	m^2	Log-Normal	1.0×10^{-3}	1.0×10^{-4}
$P_1 - P_6$	<i>N</i>	Gumbel	5.0×10^4	7.5×10^3
V_{all}	<i>m</i>	Normal	0.115	0.01

Table 6.3: Truss test case: random variables

All numerical results related to this example are reported in Table 6.4. Compared to the outcomes of the previous two test cases, the number of required simulations are less

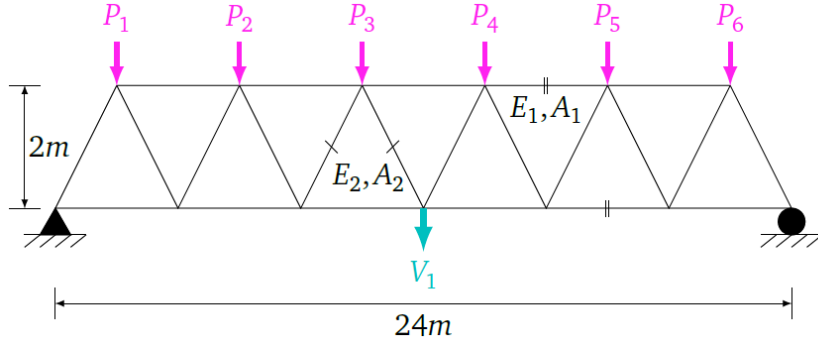


Figure 6.3: Truss test case: illustration (Source: [Lelievre, 2018])

clear cut for different numbers of PLS components in the KPLS kernel definition. Moreover, the U approach, conversely to the previous outcomes, proves to be less performing than all other approaches, being outperformed also by the EFF approach.

Both variants of Vb framework provide good estimations of the P_f value, gaining a factor 2 in terms of efficiency with respect to EFF and about 6 compared to the U approach.

At a general level, the regularity of the behavior of different approaches with increasing number of PLS components is observed for EFF and Vb approaches, providing a decreasing number of training points when increasing the complexity of the KPLS kernel.

Adaptive method	N. components	N. DoE updates	P_f	$\overline{V_G/V_X}$	N_{fail}
U	KPLS1	344 (3.58%)	1.98e-03 (4.29%)	<1e-15	1
	KPLS2	310 (7.86%)	1.99e-03 (5.13%)	<1e-15	0
	KPLS3	304 (7.78%)	1.99e-03 (5.16%)	<1e-15	0
	KPLS4	323 (4.08%)	1.98e-03 (5.18%)	<1e-15	0
EFF	KPLS1	125.8 (14.1%)	2.05e-03 (5.88%)	1.07e-01	0
	KPLS2	122.9 (16.9%)	1.99e-03 (4.56%)	8.00e-02	0
	KPLS3	121.1 (12.2%)	1.97 (4.31%)	7.63e-02	0
	KPLS4	116.0 (18.8%)	2.05e-03 (4.58%)	7.81e-02	0
LVb	KPLS1	63.43 (20.6%)	1.98e-03 (4.29%)	7.85e-01	0
	KPLS2	57.94 (22.6%)	2.03e-03 (3.01%)	8.70e-01	0
	KPLS3	47.48 (24.2%)	1.98e-03 (3.64%)	8.73e-01	0
	KPLS4	50.65 (19.9%)	2.05e-03 (3.65%)	8.92e-01	0
GVb	KPLS1	64.4 (15.36%)	1.98e-03 (4.29%)	5.71e-01	0
	KPLS2	54.5 (12.0%)	1.98e-03 (2.52%)	5.74e-01	0
	KPLS3	59.5 (10.3%)	1.98e-03 (5.72%)	6.78e-01	0
	KPLS4	51.1 (14.6%)	2.01e-03 (5.32%)	6.53e-01	0

Table 6.4: Main results for 53-dimensional truss problem (reference MC: $P_f = 2.00 \times 10^{-3}$). Note that the number in parentheses provide the coV of the values provided in the respective cells.

6.4.4 53-dimensional heat conduction problem

The last test case involves a heat conduction problem introduced in [Konakli and Sudret, 2016] and analyzed in a KPLS-based framework in [Zuhal et al., 2021]. The computational do-

main is the square $D = (-0.5, 0.5)m \times (-0.5, 0.5)m$. The partial differential equation (PDE) that describes the temperature field $T(z)$, ($z \in D$):

$$-\nabla \cdot (\kappa(z)\nabla(T(z))) = QI_A(z)$$

Where $\kappa(z)$ is the variable diffusion coefficient, $Q = 2KW/m^3$, A is the square region $A = (0.2, 0.3)m \times (0.2, 0.3)m$ where the heat source is applied and I_A represents the indicator function, equals to 1 if $z \in A$ and 0 otherwise. The boundary conditions are defined as $T = 0$ on the top and $\nabla T \cdot n = 0$ on the other boundaries. The output is defined as the mean temperature on the region $B = (-0.3, -0.2)m \times (-0.3, -0.2)m$. The domain definition is illustrated in Fig. 6.4a.

We define the term $\kappa(z)$ as in [Konakli and Sudret, 2016, Zuhail et al., 2021], as a lognormal random field $\kappa(z) = \exp[a + bg(z)]$ with $g(z)$ representing a standard Gaussian random field with autocorrelation function $\rho(z, z') = \exp[-(z - z')^2/l^2]$ and correlation length $l = 0.2 m$. The parameters a, b are set so that mean and standard deviation of κ equal respectively $\mu_\kappa = 1 Wm/^\circ C$ and $\sigma_\kappa = 0.3 Wm/^\circ C$. The discretization of $g(z)$ is performed via the Expansion Optimal Linear Estimation (EOLE):

$$g(z) = \sum_{i=1}^M \frac{\xi_i}{\sqrt{l_i}} \phi_i^T \mathbf{C}_{z\zeta}(z)$$

Where ξ_i are standard normal variables, $\mathbf{C}_{z\zeta}$ is a vector with elements $\mathbf{C}_{z\zeta}^{(k)} = \rho(z, \zeta_k) \forall k = 1, \dots, p$, while l_i and ϕ_i represent respectively the eigenvalues and the associated eigenvectors of the i^{th} mode. As done in [Konakli and Sudret, 2016], we use an EOLE grid with element width equals to $0.1 m$, thus $p = 121$ points overall. We retain only the first 53 modes, as their cumulative sum is greater than 99% of the sum of all eigenvalues [Zuhail et al., 2021]. The problem is therefore 53-dimensional.

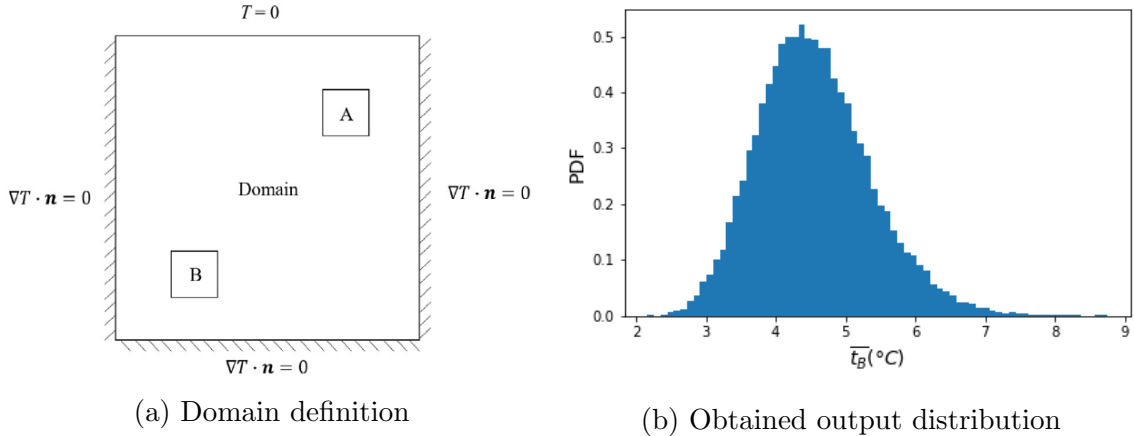


Figure 6.4: Heat conduction problem: domain definition and output sample distribution

The heat conduction simulations are performed on an in-house explicit code with a domain discretized via 100×100 elements. We extracted the mean temperature \bar{t}_B of the sub-domain B on a MC population of 20000 samples. The distribution, reported in Fig. 6.4b, is very close to the one presented in [Konakli and Sudret, 2016]. We used this population to calibrate the target temperature on a target P_f around 5%. In particular,

we defined the limit temperature at $6^\circ C$, corresponding to a $P_f = 4,75 \times 10^{-2}$. This result is slightly different from the one in [Zuhal et al., 2021], which reported $P(\bar{t}_B > 3^\circ C) = 4.1 \times 10^{-2}$, most likely due to the different numerical solvers used.

The LSF therefore is defined as:

$$g(X) = 6 - \bar{t}_B$$

The analyses are carried out with 30 starting points in the initial DoE and the enrichment criterion adopted for Vb framework is the U function. The MC population is initialized with $N = 10000$ points, while other $P = 1000$ samples are added in each MC enrichment step.

Numerical results are reported in Table 6.5. Note that we excluded the EFF approach, as it was observed to be very far from convergence until iteration 300. On the other hand, the higher P_f target of this test case would make the stopping criterion related to GVb unsuited all alone: in fact, the MC population can be easily oversized with $P_f \geq 10^{-2}$, leading to possible scenarios where both V_X, V_G are lower than half of the target, but with $V_X > V_G$. As the main purpose of the Vb framework is to balance the sources of uncertainties, in the GVb variant we couple the stopping criteria of GVb variant (see Eq. 6.43) with the one of LVb (see Eq. 6.42), for relatively high P_f targets.

Method	N. components	N. DoE updates	P_f	$\overline{V_G/V_X}$	N_{fail}
U	KPLS1	331.2 (8.09%)	4.79e-02 (5.21%)	3.54e-02	1
	KPLS2	279 (7.46%)	4.75e-02 (3.87%)	4.05e-02	0
	KPLS3	282.5 (7.67%)	4.72e-02 (4.19%)	4.45e-02	0
	KPLS4	273.2 (7.56%)	4.73e-02 (4.53%)	4.66e-02	0
LVb	KPLS1	62.8 (14.6%)	4.69e-02 (4.33%)	9.10e-01	0
	KPLS2	60.8 (8.67%)	4.75e-02 (3.78%)	9.41e-01	0
	KPLS3	57.6 (11.2%)	4.78e-02 (4.42%)	9.66e-01	0
	KPLS4	57.0 (11.5%)	4.76e-02 (4.49%)	9.71e-01	0
GVb	KPLS1	69.5 (12.2%)	4.74e-02 (2.77%)	8.96e-01	0
	KPLS2	67.2 (17.6%)	4.74e-02 (3.43%)	9.20e-01	0
	KPLS3	63.5 (6.35%)	4.73e-02 (2.65%)	9.09e-01	0
	KPLS4	58.7 (9.58%)	4.72e-02 (3.94%)	9.40e-01	0

Table 6.5: Main results for 53-dimensional heat conduction problem (reference MC: $P_f = 4.75 \times 10^{-2}$). Note that the number in parentheses provide the coV of the values provided in the respective cells.

From results in Table 6.5, we may observe a reduction of the number of DoE updates of a factor close to 4.7 when passing from U to GVb and up to 5.5 when considering LVb . The progression of the efficiencies with respect to the number of components in KPLS kernel definition can be observed via the continuous decrease in the number of DoE updates for all algorithms. However, for U , there is a large improvement in performances from KPLS1 to KPLS2, while for Vb the evolution of the gains is much smoother. Overall, the highest gains of Vb framework are related to the KPLS1 implementation.

In this test case, the stopping criterion related to the U approach proved to be over-conservative, as visible in the results of the ratio $\overline{V_G/V_X}$. The only failed simulation on

$U + KPLS1$ led to a ratio $\overline{V_G/V_X} \approx 46$: this can suggest that such ratio can be a reliable index of accuracy of the final estimation, confirming the findings of the truss test case.

When comparing the Vb variants, the obtained accuracies are similar, but the computational effort implied by LVb is slightly lower than the one linked to GVb .

6.5 Improvement with SMC

In this section we propose an improvement of the Vb -KPLS algorithm, linked to the introduction of Separable Monte Carlo (SMC) sampling method. As a reminder, the main principle of SMC is to sample separately two independent blocks R and S (representing respectively strength and stress in structural problems) and then couple each combination of each sample R_j and S_i of the populations of R (of size M) and S (of size N). The result is an augmented population of size NM , where the M samples of R are replicated N times (for each sample of S), and the N samples of S are replicated M times (for each sample of R). However, if we posed $N = M$, due to the fact that the samples are replicated, the SMC population with N^2 samples combinations will lead to an accuracy which is higher than the one obtained with N MC samples, but also lower than the one we would obtain with a MC population with N^2 elements.

In the application of SMC to the KPLS surrogate model approximating the LSF g as \hat{g} , we could denote the estimation of the failure probability P_f via the simultaneous application of KPLS and SMC as:

$$\widehat{P}_{f,SMC} = \frac{1}{NM} \sum_{i=1}^N \sum_{j=1}^M \widehat{G}(r_j, s_i) \quad (6.47)$$

Where $\widehat{G} = I(\hat{g} < 0)$ is the indicator function associated to the approximation (via KPLS) \hat{g} of g , and r_j (respectively s_i) represent sampled realizations of the random variable R (respectively S). In the following, we use the compact notation $g_{ij} = r_j - s_i$.

Now, we focus on the integration of SMC in the variance decomposition. As a reminder, the analytical estimator of the variance associated to the P_f estimate via SMC can be expressed as:

$$\begin{aligned} Var(\widehat{P}_{f,SMC}) &= \frac{1}{NM} P_f + \frac{M-1}{NM} E_S \left[E_R \left[\widetilde{F}_R(S) \right]^2 \right] \\ &+ \frac{N-1}{MN} E_S \left[E_R \left[\widetilde{F}(\min(S_1, S_2)) \right] \right] - \frac{N+M-1}{NM} P_f^2 \end{aligned} \quad (6.48)$$

The analytical quantities in Eq. 6.48 can be obtained through the following numerical approximations:

$$\begin{aligned} E_S \left[E_R \left[\widetilde{F}_R(S) \right]^2 \right] &\approx \frac{1}{N} \sum_{i=1}^N \left(\sum_{j=1}^M \frac{G(r_j, s_i)}{M} \right)^2 \\ E_S \left[E_R \left[\widetilde{F}_R(S_1), \widetilde{F}_R(S_2) \right] \right] &\approx \frac{2}{NM} \sum_{i=1}^{N/2} \sum_{j=1}^M (G(r_j, s_{2i-1}) G(r_j, s_{2i})) \end{aligned} \quad (6.49)$$

From Eqs. 6.48-6.49, it can be observed that we need to separate the contributions from R and S . In the applications presented in this work, we actually know the contribution of R and the analytical relation between the LSF g , R and S . In particular, we will pose LSFs of the simple form:

$$g = R - S \quad (6.50)$$

Therefore, in these cases, we might re-extract the approximation (via KPLS) \widehat{S}_i of S_i from the approximation \widehat{g}_{ij} of the LSF g and the realization R_j , from the expression $\widehat{S}_i = R_j - \widehat{g}_{ij}$. Note that if we have a bijective relation between g , R and S it is possible to re-extract the contribution of S from the known R and the approximation of g . Otherwise, if the contribution of R is known and the relation (between g , R and S) is also known but is not bijective, it would be convenient to approximate via KPLS the response S instead of the LSF g .

In this work we choose the first option, thus approximating via the KPLS surrogate model the LSF g of the full model: we will then obtain the approximation \widehat{g} of the limit state function, training the KPLS model on the available DoE. To incorporate the SMC sampling method in the estimation of the failure probability P_f assisted by KPLS, we will proceed as follows:

1. *MC prediction step*: we predict the outcomes $\widehat{g}_i = \widehat{g}(\mathbf{X}_i)$ on the full MC population;
2. *response reconstruction step*: we obtain the approximated outcomes $\widehat{S}_i = R_i - \widehat{g}_i$;
3. *capacity re-sampling step*: as the SMC allows unbalanced datasets with different number M of samples of R and N samples of S , we can optionally add more samples of R ;
4. *SMC prediction step*: we retrieve the augmented SMC population of the LSF samples $\widehat{g}_{ij} = R_j - \widehat{S}_i$.

To highlight the different way of sampling the LSF, we formalize the estimation of the P_f via the application of KPLS and SMC as:

$$\widehat{P}_{f,SMC} = \frac{1}{NM} \sum_{i=1}^N \sum_{j=1}^M \widehat{G}(R_j, \widehat{S}_i) \quad (6.51)$$

Where $\widehat{G} = I(\widehat{g} < 0)$ represents the indicator function applied on the approximated LSF \widehat{g} . Note that the roles of R and S in this process can be reversed if sampling R is more expensive than sampling S .

Then, we can also formalize the contribution V_X of the variance, due to the SMC population, via the expression:

$$\begin{aligned} V_X^{SMC} = Var(\widehat{P}_{f,SMC}) &= \frac{1}{NM} P_f + \frac{M-1}{NM} E_S \left[E_R \left[\widehat{F}_R(\widehat{S}) \right]^2 \right] \\ &+ \frac{N-1}{MN} E_S \left[E_R \left[\widehat{F}(\min(\widehat{S}_1, \widehat{S}_2)) \right] \right] - \frac{N+M-1}{NM} P_f^2 \end{aligned} \quad (6.52)$$

Then, by denoting with $\widehat{P}_f(\mathcal{G}_i)$ the estimation of P_f via the application of the i^{th} trajectory realization of the KPLS model \mathcal{G} on the SMC population, the term V_G can be computed [Menz et al., 2021] as:

$$V_G^{SMC} = \frac{1}{n_t - 1} \sum_{i=1}^{n_t} \left(\widehat{P}_{f,SMC}(\mathcal{G}_i) - \frac{1}{n_t} \sum_{j=1}^{n_t} \widehat{P}_{f,SMC}(\mathcal{G}_j) \right)^2 \quad (6.53)$$

Note that each estimation $\widehat{P}_{f,SMC}(\mathcal{G}_i)$ associated to the i -th trajectory requires to build a matrix $N \times M$, leading to overall a complexity of the V_G estimation of the order $n_t NM$ (as there are n_t matrices $N \times M$ to be built). The analogue estimation through MC sampling implies only n_t vectors of size N , thus overall complexity $n_t N$. As reminded before in this section, if we imposed $N = M$, with SMC we would obtain an augmented population of N^2 samples with a lower accuracy than the one expected from a MC population with N^2 samples. Now the number N of samples of S required by SMC will be significantly reduced but the reduction will not be as large as \sqrt{N} . Therefore, the coupling between Vb-KPLS and SMC implies a computational cost associated to the estimation of the variance V_G due to the KPLS model which is higher than the cost associated to the V_G estimation in Vb-KPLS coupled with MC sampling. Consequently, we limit the application of Vb-KPLS + SMC to relatively high failure probability target, generally $P_f \geq 10^{-2}$, where the number of MC samples is known to be relatively small.

Given the relatively high P_f targets, we couple the stopping criteria associated to the *LVb* and the *GVb* variants. In fact, using the *GVb* alone can ensure that $V_G < \overline{V}/2$: however, with the relatively high P_f the added samples can largely reduce the V_X , leading perhaps to situations where $V_X \leq V_G$, i.e. where most of the uncertainty comes from the surrogate model. This effect was highlighted already in the application of Vb-KPLS on the heat conduction problem (in Section 6.4.4). For the application of Vb-KPLS + SMC, we systematically couple *LVb* and *GVb*, as the targeted failure probabilities will always be higher than 10^{-2} . We will refer to the coupled framework simply as *Vb*. With respect to the algorithm presented in Section 6.3, the main difference is given by the learning stopping criterion, which will be formalized as:

$$V_G^{SMC} \leq \min \left(V_X^{SMC}, \frac{\overline{V}}{2} \right)$$

When we apply the SMC principle to the enrichment functions U and EFF , we augment the original MC dataset by considering all the combinations of the samples generated separately of the blocks R and S . The identification of the next point to enrich the DoE will be therefore done on this augmented dataset: the U exploration criterion will seek the SMC sample minimizing the U function, while the EFF will look for the SMC sample maximizing the EFF function.

In the next sections, we apply the coupling between Vb-KPLS and SMC depicted in this section on two numerical examples.

6.5.1 Application to the truss example

In this section we re-propose the example related to the 53-dimensional truss from Section 6.4.3. We modify the settings of the problem by proposing two different values of the

mean \bar{R} of the random strength R : in the first setting, we consider $\bar{R} = 0.105$ (reference $P_f = 1.76 \times 10^{-2}$ estimated via MC), while in the second we fix $\bar{R} = 0.105$ (reference $P_f = 9.70 \times 10^{-2}$ estimated via MC). The initial DoE contains 20 points. In the initial (S)MC population we have 5000 points and 1000 new samples are added in each (S)MC enrichment step. For the SMC we consider the same number of samples for S and R components. We use for this section KPLS surrogate models with 4 PLS components in the kernel definition. In the proposed Vb-KPLS framework, we choose the *EFF* enrichment function as exploration criterion to select the new points to add to the DoE.

The numerical results for these two different settings are reported respectively in Table 6.6 and Table 6.7, differentiating the results according to the method (U , *EFF* or Vb) and the sampling technique (MC or SMC).

Method	Sampling	N. DoE updates	P_f	$\overline{V_G/V_X}$	N_{fail}
U	MC	257 (5.11%)	1.75e-02 (3.06%)	<1e-15	1
	SMC	140 (6.87%)	1.84e-02 (4.67%)	<1e-15	0
EFF	MC	106 (4.74%)	1.83e-02 (4.87%)	6.83e-02	0
	SMC	87.2 (3.91%)	1.76e-02 (5.30%)	3.02e-02	0
Vb	MC	47.0 (6.35%)	1.82e-02 (5.11%)	9.64e-01	0
	SMC	22.7 (8.41%)	1.77e-02 (4.20%)	9.81e-01	0

Table 6.6: Main results for 53-dimensional truss problem with $\bar{R} = 0.105$ (reference MC: $P_f = 1.76 \times 10^{-2}$). Note that the number in parentheses provide the *coV* of the values provided in the respective cells.

Method	Sampling	N. DoE updates	P_f	$\overline{V_G/V_X}$	N_{fail}
U	MC	201 (6.75%)	9.61e-02 (3.62%)	<1e-15	0
	SMC	150 (6.68%)	9.84e-02 (4.31%)	<1e-15	0
EFF	MC	109 (6.23%)	9.81e-02 (4.02%)	1.10e-01	0
	SMC	58.6 (3.19%)	9.82e-02 (2.69%)	5.47e-02	0
Vb	MC	27.0 (10.23%)	9.69e-02 (4.28%)	9.80e-01	0
	SMC	20.7 (6.85%)	9.63e-01 (4.53%)	9.41e-01	0

Table 6.7: Main results for 53-dimensional truss problem with $\bar{R} = 0.095$ (reference MC: $P_f = 9.70 \times 10^{-2}$). Note that the number in parentheses provide the *coV* of the values provided in the respective cells.

Consistently with the results shown in the previous sections, the U method provides good estimations of the P_f but leads to the highest number of evaluations of the full model. The result is an excessive reduction of the variance V_G due to the metamodel. Fewer simulations are required for *EFF* approach, without significant detriment to the accuracy of the P_f estimations.

The proposed Vb framework allows to reduce the number of simulations of the full model required to achieve a good accuracy target. When coupling the Vb framework with MC, compared to *EFF*, we have a reduction of number of DoE updates of a factor 2.3 in the first example and 4 in the second. When introducing SMC, these gains become

respectively 4 and 3, so that we cannot give a general rule on the gains even for the same problems. In the comparison between Vb and U approach, these gains are further enhanced, leading to reductions of the number of required simulations of factors up to 7.5 (in the second test case). Moreover, we manage to balance the sources of uncertainty, i.e. the contributions to the overall variance of the P_f estimate, namely the V_G due to the KPLS and V_X due to the sampled population: all ratios V_G/V_X are close to the unit, for both MC and SMC sampling techniques.

Globally, the introduction of the SMC allows to reduce the number of required simulations of the complete model in all tested approaches. This reduction can reach a value of around 2, as shown in the Vb application in the first example (cf. Table 6.6).

6.5.2 Application to Hole2Hole

In this section, we apply the Vb -KPLS framework to three H2H coupons we already analyzed in Chapters 3 and 4, namely characterized by bolting patterns 1x2, 1x5 and 3x5. We consider here the effects of the misalignments (affecting the transferred bearing loads S_k on each hole k) and the material strength (defined by the random variable R). All coupons analyzed in this section are characterized by the same (low) ratio between plate thickness and hole diameter: therefore, the associated failure mode is the bearing of the plate.

We define the LSF of the Hole2Hole example from the definition of the *semi-probabilistic framework* introduced in the Chapter 4. The adaptive Vb -KPLS procedure (coupled with SMC) is used to train a surrogate model approximating the limit state functions G_k associated to the transferred bearing loads S_k on each hole location k . The obtained KPLS models will be later used in the second declination of the *semi-probabilistic framework*, which will be formalized and applied in Chapter 7.

Now, we remind that the general scope of the *semi-probabilistic approach* is to control the probability PoE that the real structure under-performs with respect to the reference performance quantities used in the deterministic design. For more in depth explanations the reader is referred to Section 4.4. For each performance index, we introduce one detrimental variable K_i which tells us whether we overcome or not the prescribed limits:

$$K_i \begin{cases} \leq 1 & \text{worse than in deterministic design} \\ > 1 & \text{better than in deterministic design} \end{cases} \quad (6.54)$$

In presence of multiple effects which affect in multiplicative way the same failure mode, the conditions $K_i \leq 1$ are replaced by $\prod_i K_i \leq 1$:

$$\prod_i K_i \begin{cases} \leq 1 & \text{worse than in deterministic design} \\ > 1 & \text{better than in deterministic design} \end{cases} \quad (6.55)$$

In the H2H example, we define two detrimental variables, K_R and K_S :

$$K_R = \frac{R}{R_{REF}} \quad K_{S,k} = \frac{S_{REF}}{S_k} \quad (6.56)$$

Where R represents the bearing material strength (of the plate), S_k the transferred load on the k -th hole location, R_{REF} (respectively S_{REF}) the reference value of R (respec-

tively of S_k) used in deterministic design. Note that a distinct K_S is defined for each hole k . In principle, we should consider, for an assembly of two plates with bolting pattern $N_X \times N_Y$, overall $2N_X N_Y$ loads S_k : however, given the load equilibrium at bolt level, we only consider the loads on the first plate, thus $H = N_X N_Y$ loads overall. Furthermore, we define the reference value of transferred loads S_{REF} from the nominal load $S_{REF,nom}$ on the nominal misalignment configuration (i.e. with fitted and perfectly aligned holes), and the overload OL :

$$S_{REF} = S_{REF,nom} \times OL \quad (6.57)$$

The LSF associated to the exceedance of the transferred bearing load S_k on a single hole location k will be formalized by introducing Eqs. 6.56-6.57 in Eq. 6.55:

$$G_k = K_R K_{S,k} - 1 = \frac{R}{R_{REF}} \frac{S_{REF,nom}}{S_k} OL - 1 \begin{cases} \leq 0 & \text{worse than in deterministic design} \\ > 0 & \text{better than in deterministic design} \end{cases} \quad (6.58)$$

The probability that the deterministic quantities used in the deterministic sizing actually over-estimate the real structural performances given the considered variabilities (in terms of stress S_k and strength R) will be defined as *individual Probability of Exceedance* PoE_k , and is formalized as follows:

$$PoE_k = P[G_k \leq 0] = P\left[\frac{R}{R_{REF}} \frac{S_{REF,nom}}{S_k} OL \leq 1\right] \quad (6.59)$$

We apply the Vb-KPLS + SMC framework to train the limit state functions G_k and estimate the individual PoE_k : this means that we train a different KPLS surrogate model for each k failure mode (associated to each k bolt location). All kernels of the KPLS surrogate models are defined from 4 PLS components (i.e. KPLS4 are used). The variance decomposition is done at k failure mode level: from a mathematical point of view, we aim at determining the different sources of uncertainties (in terms of variance) of the estimation of each PoE_k . We define therefore the total variance $V_{TOT,k}$ associated to the estimation of each PoE_k . We will then distinguish, for each k failure mode, the variance component $V_{X,k}^{SMC}$ (representing the variance due to the SMC population) and the $V_{G,k}^{SMC}$ (representing the variance due to the KPLS model approximating the LSF G_k). The learning stopping criterion associated to each KPLS surrogate model will be defined as:

$$V_{G,k} < \min\left(\frac{\bar{V}}{2}, V_{X,k}\right)$$

The global structure performs worse than expected in deterministic design (using R_{REF} , $S_{REF,nom}$ and OL) if in *at least one* hole location k (out of overall $H = N_X \times N_Y$ hole locations) we have $G_k \leq 0$. The probability that this happens will be defined as the (global) *Probability of Exceedance* PoE and formalized as:

$$PoE = P\left[\min_{k=1,\dots,H} G_k \leq 0\right] = P\left[\min_{k=1,\dots,H} \left(\frac{R}{R_{REF}} \frac{S_{REF,nom}}{S_k} OL\right) \leq 1\right] \quad (6.60)$$

To simplify this calculation, we implemented the estimation of the global PoE as a final step, after the convergence of all the adaptive learning processes (based on Vb-KPLS + SMC algorithm) associated to the different individual LSFs G_k : therefore, we do not include the "min" directly in the definition of the full model to be approximated via KPLS, as it would induce large nonlinearities. We use the KPLS surrogate models to reproduce the samples of the limit state functions G_k , and the minimum will be extracted numerically from the obtained samples.

Regarding the inputs of the responses S_k , we use all the geometrical hole misalignments, both in longitudinal and transverse direction: in order to ensure feasible assemblies (i.e. with all bolts fitting inside the holes), we filter the samples (and thus the candidate points to enrich the DoE) by considering only the misalignments realizations that lead to a relative distance between two superposed hole centers in the two plates which is lower than the oversize. Only for the coupon characterized by bolting pattern 3x5 we also introduce, for comparison, a different setting, considering only relative longitudinal misalignments (reducing by a factor 4 the number of geometrical inputs affecting S_k).

The input misalignments are all described by normal variables with zero mean and standard deviation equal to 1/6 of the maximum oversize: the samples are then filtered to ensure that all bolts fit inside the holes. Then, by assuming that the bearing material resistance does not change in the different locations, the strength R is described by a single random variable.

In order to exploit the parallel computing power, we add multiple points at each DoE enrichment step. In particular, we select the points maximizing the EFF enrichment criterion on each LSF where the associated KPLS model does not satisfy the learning stopping criteria in the Vb framework (i.e. $V_{G,k} \leq \min(V_{X,k}, \bar{V}/2)$). But then, the information coming from each finite element analysis are shared among all surrogate models. For example, if the KPLS metamodel associated to the mode $k = 1$ satisfies the stopping learning criterion, but the one related to $k = 2$ does not, we only consider the best candidate for DoE enrichment associated to the latter, hence determining via finite element analysis the bearing load S_2 (associated to the mode $k = 2$, i.e. to the hole $k = 2$): however, as the finite element analysis will give both S_1 and S_2 , we do not waste this information and assign the calculated S_1 to the training set of the $KPLS$ associated to $k = 1$.

In all the presented applications, we start from SMC populations with $N = M = 5000$ samples and we add 1000 further samples in each (S)MC enrichment step. The Vb-KPLS + SMC algorithm is stopped when we reach $coV \leq 5\%$ on all the estimations of PoE_k of all distinct LSFs. We consider four scenarios of the overloads OL : starting from a fixed initial DoE, we firstly apply the Vb-KPLS + SMC framework on the lowest OL scenario; then, for the successive OL scenario, we initiate the DoE by using the final DoE obtained in the previous scenario; then we repeat this procedure until we reach the highest OL scenario.

We report the numerical results in Table 6.8, specifying the H2H coupon (distinguished according to the bolting patterns), the number of inputs (misalignments and material strength), the OL scenarios (normalized with respect to the maximum OL retrieved in Chapter 4), the number of points in the initial DoE, the number of updates of the DoE in each application, the overall probability PoE and the average $\overline{V_{G,k}/V_{X,k}}$ (over all applications of Vb-KPLS + SMC algorithm on all k limit states in the same coupon).

Coupon	N. Inputs	OL (normalized)	N DoE (start)	N DoE (updates)	PoE	$\overline{V_{G,k}}/\overline{V_{X,k}}$
1x2	9	0.05	9	5	0.66	0.368
		0.1	14	0	0.5	0.321
		0.15	14	0	0.36	0.24
		0.2	14	0	0.25	0.217
1x5	21	0.05	20	46	0.41	0.789
		0.1	66	0	0.34	0.786
		0.15	66	0	0.27	0.78
		0.2	66	0	0.21	0.779
3x5 (*)	16	0.05	20	61	0.64	0.832
		0.1	81	0	0.58	0.85
		0.15	81	2	0.51	0.822
		0.2	83	4	0.44	0.821
3x5	61	0.05	30	99	0.62	0.863
		0.1	129	0	0.56	0.861
		0.15	129	0	0.48	0.866
		0.2	129	0	0.41	0.863

Table 6.8: Application of Vb-KPLS+SMC on H2H coupons (*: only relative longitudinal misalignments are considered)

First of all, we may notice that the average $V_{G,k}/V_{X,k}$ are all lower than 1. For the simplest coupon with bolting pattern 1x2, this is due to the fact that the last DoE enrichment step allows to significantly reduce the variance due to the KPLS, given the simplicity of the problem treated herein. On the other coupons, the reason lies in the fact that before completing the whole procedure we need to control the $V_{G,k}$ of all k limit states: therefore, some of the KPLS metamodells will reach convergence before the others. We remind that the information of each finite element analyses are shared on all training sets, even if part of them already converged: adding new samples to these latter leads to further reduce the variance $V_{G,k}$ (due to the surrogate model), thus decreasing the final ratio $V_{G,k}/V_{X,k}$.

Looking at the number of DoE enrichments, we notice that for all coupons where we consider both longitudinal and transversal misalignments, the DoE obtained for the lowest OL scenario are sufficient to achieve a good accuracy also for the higher levels of OL . Overall, the number of simulations required to achieve the targeted accuracy increases with the complexity of the bolting pattern, i.e. going from 1x2 to 1x5 to 3x5. It is also worth noting that using only the relative longitudinal misalignments in the coupon 3x5 can reduce the number of required simulations: however, the DoE trained on the lowest OL scenario is not sufficient to guarantee the same accuracy on the superior OL scenarios (thus other points are required in the progression towards the highest OL scenario values).

Focusing on the probability PoE , we have higher values at the lowest OL , and the PoE progressively decreases when going towards higher overload scenarios OL . This is due to the fact that by increasing the OL , we indirectly increase the reference value S_{REF} associated to the responses S_k in the assembly: consequently, if we keep the same input distributions (in the same coupon) we are systematically increasing (i.e. we multiply by a fixed factor) the random detrimental variable $K_{S,k}$, thus decreasing the probability PoE . We notice that this effect is progressively less evident when the complexity of the H2H coupon increases. This is explained by the fact that increasing the number

of failure modes (i.e. the bearing LSFs associated to each bolt location), we flatten the distribution of the maximum of the outputs S_k , leading to smaller differences of the global PoE between distinct scenarios of the imposed overload OL .

Finally, if we compare the number of samples required by the Vb-KPLS + SMC framework with the population sizes we used to determine the PLS components in Chapter 3 (200 for 1x2, 900 for 1x5 and 1000 for 3x5), we may notice a significant reduction. Moreover, we did not need to triplicate the load level issued from ISAMI computations to achieve a good accuracy of the approximation of the model. Overall, the proposed Vb approach allows to minimize the number of samples required to have a good estimation of the response of the model: this is achieved by focusing on the zones of interest, in the neighbor of the limit state surface determining the border between critical (where the deterministic quantities used in design phase over-estimate the structural performances) and non-critical regions.

6.6 Discussion of results

In this Section we analyze the obtained numerical results at a global level.

In all test cases, the presented framework provided accurate estimations of failure probabilities, while this was not the case for the U or EFF based approaches. The GVb variant can be slightly more conservative than the LVB variant at the first stages of the algorithm, involving more learning steps and less MC enrichment phases. However, on final stages, both converge with similar behavior.

Focusing on the performances of the algorithms in terms of number of simulations of the original model, we found that on average both variants of our proposed Vb algorithm - coupled with MC sampling - allow to perform significantly better than the classical approaches tested in this chapter, depending on the test case and used parameters. The differences between performances of both proposed approaches are not significant on the examples presented in this work. In all the investigated cases we found that the proposed approaches led to a reduction in the number of required simulations compared to both the EFF and U approach. Furthermore, we observed that these gains increased when increasing the complexity of the LSFs, for which adaptive learning approaches are most relevant, where the number of required simulations can be reduced by up to a factor 7.5. The introduction of Separable Monte Carlo (SMC) sampling method in Vb-KPLS framework allows to further reduce by half (with respect to the analogue Vb-KPLS with MC sampling) the number of simulations of the full model required to achieve the same accuracy targets on the considered applications.

Note also that the algorithm presented in this work aims at reducing the arbitrary choices over the hyper-parameters of the classical stopping criteria. We implement a rational framework dealing with the distinction of the different sources of uncertainties. The proposed method constitutes therefore a good compromise between accuracy and computational burden, providing also an overall measure of the global uncertainty of the resulting P_f estimation, while taking into account the main sources of uncertainty: the uncertainty due to the surrogate model, and the uncertainty due to limited (S)MC samples.

Another consideration should be made on the scalability of the proposed method, in

terms of number of inputs and failure probability target. From an input dimensionality point of view, the extension of Kriging advantages to high number of input variables is allowed by the introduction of KPLS, which depending on the complexity of the problem, can deal with input dimensionality reduction of the order of 10^2 or more. On the other hand, when focusing on lower orders of magnitude of P_f (roughly below 10^{-4}), the number of data to reproduce could make the presented approach intractable as it is. This effect is evident also at $P_f \approx 10^{-3}$ when the *Vb* framework is coupled with SMC. Variance-reduction sampling techniques (Importance Sampling for example) should replace the classical MC method to reduce the number of samples required to achieve a satisfying level of overall variance of P_f estimate.

In the application on the H2H problem, we dealt with multiple limit state functions by iteratively training separated KPLS models, each associated to the LSF describing the exceedance of the transferred bearing load S_k on the corresponding k hole location. However, we took into account all LSFs, independently from the magnitude of the probabilities PoE_k . Further works may investigate the integration of a framework to prioritize the refinement of the LSFs which most affect the global PoE , hence neglecting the least informative LSFs (leading to lower PoE_k) in the adaptive training process.

Finally, the proposed algorithm can still be customized and improved in different features: the choice of the learning function, the possibility to including an active learning procedure capable to determine the optimal number of PLS components in KPLS kernel definition, the reproduction of multiple trajectories of the Gaussian Process, and finally the sampling method.

6.7 Conclusion

In this chapter we presented a variance-based algorithm to estimate, with the aid of machine learning, the failure probability in reliability problems with high number of input variables. In particular, a KPLS surrogate model was used to approximate the limit state function: this allowed to extend the advantages of Kriging to high-dimensional problems via the Partial Least Square transformation. A new framework, combining KPLS with a variance-based adaptive enrichment approach was then proposed. Four test cases were analyzed to evaluate the accuracy and computational burden, measured via the number of needed simulations of the full model.

The numerical examples showed that our variance-based approach could lead to good accuracy over the final estimation of the failure probability. Compared to other reference methods, the proposed approach allowed to reduce by up to a factor 7.5 the number of added simulations. This gain increases when increasing the complexity of the problem (i.e. the limit state function) and when introducing the Separable Monte Carlo sampling method.

Two variants of the presented algorithm (namely *LVb* and *GVb*) were introduced and discussed: while generally giving similar performances, the latter allowed to improve the convergence of the algorithm. These variants are coupled together for high failure probability targets, to improve the compromise between accuracy and computational burden.

We applied this framework to the main industrial test case of this manuscript, namely

the Hole2Hole project, where the main interest of the proposed method lies. The formulation of the associated reliability problem stems from the *semi-probabilistic framework* we proposed in Chapter 4: this is based on the probability PoE that the deterministic quantities used in the classical (deterministic) design process over-estimate the performances of the real structures. In particular, the estimation of the PoE is part of the second declination of the proposed *semi-probabilistic framework*: this addresses the challenge of optimizing the input variability, such as to satisfy specific structural requirements, defined from a (semi-)probabilistic perspective. The Vb-KPLS+SMC framework allowed to minimize the computational burden required to achieve a target accuracy of the estimation of the PoE , by means of reducing the number of required simulations of the full finite elements models.

From a methodological perspective, several ingredients of the proposed variance-based framework could be customized. One of the most important improvements would be given by the definition of different sampling techniques, other than the classical Monte Carlo and Separable Monte Carlo used in this chapter, to allow the scalability of the algorithm to very low failure probability target (below 10^{-4}). In this context, the introduction of adaptive Importance Sampling techniques can support this challenge, focusing also on the scalability of these latter for real engineering problems with high number of inputs.

Moreover, different analytical approximations of the contribution of the variance induced by the KPLS surrogate model can help to reduce the computational burden associated to its estimation. Different decomposition techniques, other than the KL expansion used in this chapter, can be introduced in the proposed framework. With the same objective in mind, embedded implementations exploiting parallel computing can be beneficial to reduce the computational time of the variance estimation, above all when dealing with SMC or ImpSMC sampling approaches.

Furthermore, the key concept of the proposed method, consisting in equilibrating the uncertainty associated to the surrogate model and the sampled population, can be extended to other machine learning techniques.

In the global picture of the whole manuscript, the previous and the present chapter dealt with the estimation of the probability of trespassing a given threshold, focusing more on structural reliability applications. The methods provided in Chapters 5 and 6 constitute two main ingredients to evaluate the reliability constraints in a Reliability-Based Design Optimization (RBDO) framework. The final step in this work will assemble all the pieces (collected in the previous chapters) in a comprehensive codesign RBDO framework, in order to establish a translator for the compromises between tolerancing, manufacturing and stress analysis.

Chapter 7

Codesign Framework for Aircraft Assembly Design

7.1 Introduction

In the previous chapters we evaluated how the variability of input parameters can affect the overall structural performances of a given assembly. In particular, in Chapter 4, we introduced a semi-probabilistic approach to evaluate the propagation of uncertainties of input parameters on the structural outcomes.

In this chapter, particular attention is given to the control of the variability of geometrical features of individual components in the manufacturing and assembly processes. The bounds of the variability of geometric inputs are generally described by the definition of specific *tolerances*. This chapter seeks to provide some answers to the questions:

- ” *Can we conceive a general probabilistic framework able to extend current certification requirements and which can be easily integrated in the classical deterministic structural design?*”
- ” *Which input variabilities can guarantee a specific structural performance (in probabilistic terms)?*”

The tolerancing activities, concerning the definitions of tolerances, are collocated in a general framework internally known as *Geometric Dimensioning and Tolerancing* (GD&T). A common distinction is done between geometric and dimensional tolerancing: the former is related to the limitations in terms of shape (e.g. flatness) and position (e.g. inclination, parallelism, localization) of the geometric features (e.g. planes, hole centers), with respect to specific references, called *datums*; the latter, dimensional tolerancing, concerns the limitations in the size of features of elementary parts. The geometric tolerancing, referred to as *Geometrical Product Specifications* (GPS), is regulated via specific standards reported in ISO 1101, [iso, 2006], ISO 14405 [iso, 2010], ISO 5459 [iso, 2011b], ISO 17450 [iso, 2011a], EN 9100 [Hinsch, 2020].

In an aircraft, different assembly levels can be distinguished: in a top-down decomposition, we generally recognize the aircraft level, the section, the work-package, the assembly and the elementary parts. In Fig. 7.1 we illustrate an example of the partition from the aircraft, to the fuselage (section level), to a frame (work-package level), to the

assembly of plates (assembly level), to an individual plate (elementary part level). Each level must be designed to satisfy specific requirements from the superior level (generally referred as *top-level requirements*), coming from a variety of considerations on the process, kinematic, structural or aerodynamic constraints. The top-down definition of tolerances requirements is often referred as *tolerance cascade*. On the other hand, the *tolerance allocation* problem refers to the re-distribution of tolerances on different contributors at the same level in the cascade.

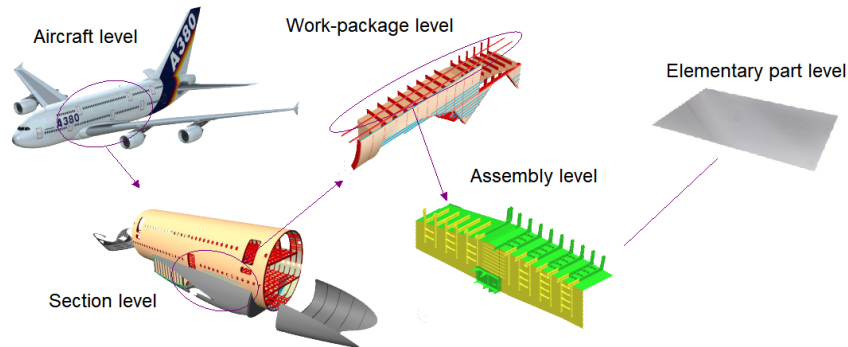


Figure 7.1: Assembly levels in aircrafts (Source [Diet, 2021])

In the literature, the tolerancing analysis constitutes a very active research field. A recent review of methods and applications is available in [Hallmann et al., 2020], where approximately 300 papers are analyzed. The efforts of the research community are mainly focused on the propagation of uncertainties due to geometric imperfections [Wang et al., 2006, Dantan and Qureshi, 2009, Mansuy et al., 2011, Beaucaire et al., 2013, Morse et al., 2018] or tolerance allocation [Kim et al., 1999, Qureshi et al., 2010, Geetha et al., 2013, Andolfatto et al., 2015, Zong and Mao, 2015, Wang et al., 2019b]. Recent works involve applications in aeronautical industry as well [Jing et al., 2020, Miah et al., 2021, Han and Ouyang, 2021, Diet, 2021]. Most of the studies available in the literature are based on a statistical framework [Hallmann et al., 2020].

A number of definitions of tolerance costs have been defined during the years, leading to a variety of objectives pursued in the studies available in literature. The final goals may include product degradation and time value of money [Chou and Chang, 2001], quality verification costs [Moroni et al., 2011], economic and ecological sustainability [Hoffenson et al., 2013], scheduling management [Geetha et al., 2015], risk of delivering non-compliant assemblies [Diet, 2021], selection of machining techniques [Hallmann et al., 2022], among others. In general practice, the formalization of a single objective function in a tolerance optimization problem can be troublesome, because of the different sources of costs. In Fig. 7.2, an example of conflict of costs [Cheikh and McGoldrick, 1988] is illustrated: with the increase on tolerances of elementary features, we may decrease the manufacturing cost, as the quality demand in this first step is reduced; on the other hand, at assembly level we may need to intervene to adjust the geometrical global outcomes to a fixed top-level requirement. When taking into account different sources of cost, multi-objective optimization problems can be formalized [Hallmann et al., 2020].

In the context of the optimization of the tolerance allocation, a single representative objective can be defined when having a specific model for the financial impact of each

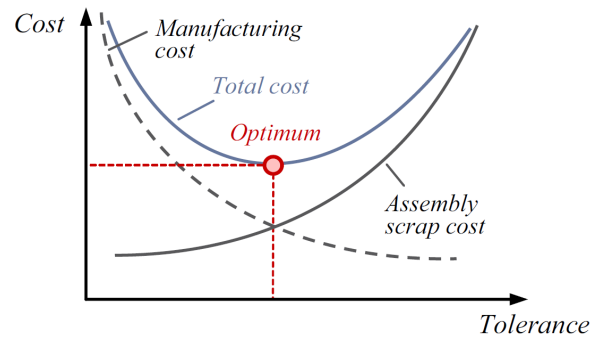


Figure 7.2: Example of conflict of costs in tolerance allocation (Source [Cheikh and McGoldrick, 1988])

source [Cheikh and McGoldrick, 1988, Bhachu et al., 2015]. However, it is common to aggregate all objectives in a weighted sum [Hallmann et al., 2020].

Focusing on the coupling between tolerances and the uncertainty propagation on structural performances, some examples are available in the literature [Dahlström and Lindkvist, 2007, Le Riche et al., , Guo et al., 2016, Govindarajalu et al., 2012, Gouyou et al., 2018, Askri et al., 2018, Beaurepaire et al., 2018]. In the aeronautical industry, the activities of tolerancing and stress design are generally treated separately. The interface between these two domains is generally provided by the definition of some top-level requirements by structural team, often (choices are defined on a case-by-case basis) following a *worst-case scenario* strategy. Separating stress and tolerancing activities generally simplifies the way of working, but it can also lead to assumptions which are more conservative than the ones which are realistically needed.

In Chapter 4 we proposed a semi-probabilistic approach in line with current certification requirements for large aircrafts (namely CS 25 in Europe), while taking into account the variability of the input parameters involved in design and sizing process. The main purpose of the work presented in this chapter is to propose a comprehensive codesign framework to deal with tolerance-cost optimization and comply with stress aeronautical certification requirements within this semi-probabilistic framework. Compared to Chapter 4, a different declination of the semi-probabilistic approach is considered in this chapter: in particular, the formulation is transposed into a reliability constraint.

In this work we focus on the coupling between tolerance-cost optimization and the semi-probabilistic approach, to conceive a codesign perspective involving manufacturing, tolerancing and stress analysis. The goal is to redefine at the same time the top-level requirements and the tolerances at elements level, in order to make a compromise between different sources of out-of-quality costs coming from different steps of the assembly process, while guaranteeing the static stress requirements redefined in the semi-probabilistic framework. As this latter is formulated as a reliability constraint, the optimization problem is therefore a multi-objective reliability based optimization. The numerical methods introduced in Chapters 5-6 are used to evaluate the semi-probabilistic constraint, declined in form of reliability problem.

In Section 7.2 we provide a brief overview of the adopted problems formulation. Then, we define, formalize and discuss the proposed semi-probabilistic codesign framework in Section 7.3. In Section 7.4 we report the application on two representative use cases,

related to the problem of built-in stresses induced by the fastener installation in assemblies due to the presence of initial gaps. The application of the proposed framework on the H2H problem is detailed and discussed in Section 7.5. An extensive discussion of the obtained results and the interpretation of some consequences is reported in Section 7.6. Finally, in Section 7.7 we delineate the overall conclusions of the proposed framework and way-forwards for future extensions and further applications.

7.2 Formulations background

In this section we report a brief overview of the adopted formulations for Reliability-Based Design Optimization (*RBDO*) and multi-objective optimization. In the following, we restrict, without loss of generality, to the case of minimization problems.

7.2.1 Reliability-Based Design Optimization

A generic formulation for a deterministic optimization problem under inequality and bound constraints is provided in Eq. 7.1 below:

$$\begin{aligned} \min_{\mathbf{x}} \quad & f(\mathbf{x}) \\ \text{s.t.} \quad & g_j(\mathbf{x}) \leq 0 \quad j = 1, \dots, N_g \\ & x_{LB,i} \leq x_i \leq x_{UB,i} \quad i = 1, \dots, N \end{aligned} \quad (7.1)$$

Where $\mathbf{x} = [x_1, \dots, x_N]$ is the vector of N *decision* or *design variables*, f is the objective (or cost) function, g_j represents the j -th inequality constraint (N_g constraints overall) and the last line constitutes bounds constraints (linked to the search domain of the design variables). In particular, for classical deterministic optimization, all f, g_j are deterministic.

The transition from deterministic to Reliability-Based Design Optimization (RBDO) is typically done by formulating all or some of the constraints g_j in probabilistic terms [Enevoldsen and Sørensen, 1994, Paiva et al., 2014]. We introduce other random variables \mathbf{r} , which are not included among design variables. Note however that, in some applications, the statistical description of \mathbf{r} can be affected by the design variables \mathbf{x} . Considering a deterministic objective and the introduction of reliability constraints we can express the RBDO problem as follows:

$$\begin{aligned} \min_{\mathbf{x}} \quad & f(\mathbf{x}) \\ \text{s.t.} \quad & g_j^{RC}(\mathbf{x}, \mathbf{r}) \leq 0 \quad j = 1, \dots, N_R \\ & g_j^D(\mathbf{x}) \leq 0 \quad j = 1, \dots, N_D \\ & x_{LB,i} \leq x_i \leq x_{UB,i} \quad i = 1, \dots, N \end{aligned} \quad (7.2)$$

Where the constraints are distinguished into N_R *reliability constraints* g_j^{RC} and N_D *design constraints* (which are deterministic) g_j^D . Note that the random variables \mathbf{r} will only intervene on the g_j^{RC} . The reliability constraints g_j^{RC} can be expressed in terms of failure probability P_f or alternatively in terms of reliability index, such as the Hasofer-Lindt index β_{HL} [Hasofer and Lind, 1974]. These must be kept within certain limits:

considering the probability of failure P_f , we seek to impose an upper acceptable bound \overline{P}_f (i.e. in the form $P_f \leq \overline{P}_f$); otherwise, for reliability indexes, we may need the opposite (e.g. for the Hasofer-Lindt reliability index $\beta_{HL} \geq \overline{\beta}$). For the former case, we would have:

$$g_j^{RC} = P[g_j(\mathbf{x}, \mathbf{r}) \geq 0] - \overline{P}_f$$

Moreover, we can have problems where certain random design parameters \mathbf{r} affect the reliability constraints or the objective function f , but they are not included among design variables. Such cases would require the introduction of a probabilistic metric on the objective function (such as expected value or a robustness metric) thus further complexifying the problem formulation. Here in this work we will only consider RBDO problems according to Eq. 7.2, thus without probabilistic functions.

A survey of the methods available in literature to solve RBDO problems can be found in [Moustapha and Sudret, 2019], with a particular focus on RBDO approaches assisted by surrogate models [Dubourg et al., 2011]. According to [Moustapha and Sudret, 2019], a number of current approaches follow a framework based on the decomposition of the modules devoted to the metamodel training, reliability analysis and optimization process. In this work we propose a strategy based on the use of KPLS surrogate models (trained prior to optimization via the algorithm described in Chapter 6), coupled with *Separable Monte Carlo* (SMC) sampling for the reliability analysis.

7.2.2 Multi-objective optimization

The general formulation of a multi-objective optimization (specifically minimization) problem can be formalized as follows [Jaimes et al., 2009]:

$$\begin{aligned} \min_{\mathbf{x}} \quad & \mathbf{f} = [f_1(\mathbf{x}), \dots, f_k(\mathbf{x})] \\ \text{s.t.} \quad & \mathbf{x} \in \mathcal{X} \end{aligned} \tag{7.3}$$

Where $\mathbf{x} = [x_1, \dots, x_N]$ represents the vector of the N design variables, \mathcal{X} represents the feasible set (implicitly determined by a set of equality and inequality constraints) and the vector function $\mathbf{f} : \mathbb{R}^N \rightarrow \mathbb{R}^k$ is defined by a set of k scalar objective functions $f_i : \mathbb{R}^N \rightarrow \mathbb{R}$.

In the case $k = 1$, we retrieve a single-objective optimization problem. We say that a candidate $\mathbf{x}^{(1)}$ dominates (in a weak sense) another $\mathbf{x}^{(2)}$ according to the (single-)objective f , if:

$$f(\mathbf{x}^{(1)}) \leq f(\mathbf{x}^{(2)})$$

Conversely to single-objective optimization problems, the solution of a multi-objective optimization is not unique. In fact, as multiple criteria are established to define a hierarchy of candidate solutions, a further mathematical formalization of the concept of dominance is required. We say that a vector $\mathbf{z}^{(1)} = [f_1(\mathbf{x}^{(1)}), \dots, f_k(\mathbf{x}^{(1)})]$ Pareto dominates $\mathbf{z}^{(2)} = [f_1(\mathbf{x}^{(2)}), \dots, f_k(\mathbf{x}^{(2)})]$ if and only if:

$$\forall i \in \{1, \dots, k\} \quad z_i^{(1)} \leq z_i^{(2)}$$

and

$$\exists i \in \{1, \dots, k\} \quad z_i^{(1)} < z_i^{(2)}$$

We define the *Pareto front* as the set of non-dominated vectors.

An abundant literature is available on the methods to solve multi-objective optimization problems [Jaimes et al., 2009, Emmerich and Deutz, 2018, Rao, 2019]. The upper-mentioned weighted sum is one of the scalarization techniques available in the literature to simplify a multi-objective problem by transforming it into a single-objective one [Rao, 2019], i.e. to convert the vector \mathbf{f} into a scalar.

Another common technique is the *constraint method*, which transforms the multi-objective optimization into a constrained single-objective optimization with several constraints on the cost functions excluded from the objective vector. For a bi-objective optimization, this formulation leads to:

$$\left\{ \begin{array}{l} \min_{\mathbf{x}} \quad \mathbf{f} = [f_1(\mathbf{x}), f_2(\mathbf{x})] \\ \text{s.t.} \quad \mathbf{x} \in \mathcal{X} \end{array} \right\} \iff \left\{ \begin{array}{l} \min_{\mathbf{x}} \quad f_1(\mathbf{x}) \\ \text{s.t.} \quad \mathbf{x} \in \mathcal{X} \\ f_2(\mathbf{x}) \leq \bar{f}_2 \end{array} \right. \quad (7.4)$$

Different scenarios for the constraint \bar{f}_2 are generally imposed to build the Pareto front. The concept can be extended to multi-optimization problems with more than two objectives.

Other categories of methods are also available in the literature to deal with multi-objective optimization problems [Jaimes et al., 2009, Emmerich and Deutz, 2018]. Evolutionary algorithms are very popular in the context of multi-objective optimization [Emmerich and Deutz, 2018]: they generally use concepts from the natural evolution (e.g. selection, mutation and recombination) to steer a population of individuals (which constitute a set of candidates) towards Pareto optimal or near-optimal solutions. In particular, among the most common methods of this category, we find the Non-dominated Sorting Genetic Algorithm II (*NSGA-II*) [Deb et al., 2002], which is often used to benchmark new multi-objective evolutionary algorithms [Jaimes et al., 2009].

Recent works in the field of multi-objective optimization focus on the introduction of machine learning techniques to approximate computationally expensive numerical models (used to evaluate the objectives and/or the constraints) [Allmendinger et al., 2017, Qu et al., 2021]. In particular, large efforts are done to develop the Bayesian multi-objective optimization framework [Greenhill et al., 2020], based on the principle of approximating the objectives and constraints functions via adaptive Kriging-based surrogate models. A number of works available in the literature focus on the definition of adaptive learning frameworks to progressively enrich the training set, while making a compromise between accuracy and computational burden [Keane, 2006, Knowles, 2006, Gaudrie et al., 2020].

According to the method adopted to solve the problem, we may retrieve in the sets of solutions some *weak Pareto points* which are actually Pareto dominated by other points. In the example with two objectives, this can be translated via the relations $f_1(x_1) < f_1(x_2)$ and $f_2(x_1) = f_2(x_2)$ (or vice versa), implying that x_2 does not actually belong to the Pareto front, but is a weak Pareto point. This can arise from the application of the constraint method or genetic algorithms, retrieving points where the difference between

cost functions is comparable with the numerical precision of the machine approximation. Therefore, further analysis of the obtained solutions is generally required before exploiting the results.

7.3 Semi-probabilistic codesign framework

In Chapter 4, we introduced the semi-probabilistic framework to integrate the uncertainties of input properties inside the sizing of a given structure. The whole framework was based on the concept of the *Probability of Exceedence (PoE)*, defined as the probability that the nominal values adopted in classical deterministic sizing lead to overestimating the structural performances of a given assembly. The general purpose of the semi-probabilistic approach is to extend the current certification requirements for large aircrafts in CS 25, in order to collocate them in a more general statistical framework. Two declinations of the semi-probabilistic framework were enunciated in Chapter 4:

1. we fix the variability of the input properties to define new nominal values to use in deterministic sizing, consistent with a fixed *PoE*;
2. we fix the nominal values of some of the structural input properties used in deterministic sizing, in order to tune the input variabilities that lead to an acceptable level of *PoE*.

The first declination was pursued in Chapter 4 in the context of the overload analysis. As a reminder, we defined the overloads, for the H2H example, as the local amplification factors of the transferred loads: in particular, the overloads constitute the ratio between the maximum transferred load on a given realization of an H2H assembly (i.e. a bolted joint assembly with oversized and misaligned holes) and the nominal configuration (i.e. with perfectly fitted aligned holes). The first declination was used in Chapter 4 to obtain, from given distributions of the input misalignments, specific quantiles of the overloads on several H2H coupons. These quantiles are then integrated in the deterministic sizing process as additional safety factors on the nominal loads: the goal is to automatically take into account the misalignments variability in H2H framework, without being forced to perform a statistical analysis every time we size a new structure.

In this section, we formalize the second declination of the semi-probabilistic framework, which constitutes, from a mathematical point of view, an optimization problem. In particular, the goal is to optimize the parameters of the input distributions of controllable input variables, while satisfying the structural safety requirements imposed by the semi-probabilistic approach, in terms of the probability *PoE*.

The proposed *codesign framework* focuses on a tolerance optimization problem based on the risk of delivering geometrically non-compliant structures, as in [Diet, 2021]. We will build the optimization problem progressively in this section. The explanation of each piece of the puzzle will be supported by concrete examples related to the application on the H2H framework.

We start by presenting, in Section 7.3.1, the main random variables which may intervene in the proposed framework. Then we introduce in Section 7.3.2 the optimization design variables, together with the links with the upper-mentioned random variables.

The cost functions of the optimization problem are introduced and described in Section 7.3.3. The link with the semi-probabilistic global framework of Chapter 4 is described in Section 7.3.4, where we will formalize the *PoE* constraint in this second declination. In Section 7.3.5, we analyze the sensitivities of the costs and the *PoE* with respect to the design variables. Then, we formalize the problem from a mathematical point of view in Section 7.3.6, introducing two different variants. In Section 7.3.7 we introduce some preliminary analyses to perform prior to the resolution, in order to ascertain the added value of the semi-probabilistic constraint. Finally, the numerical tools implemented and adopted for the problem resolution are detailed in Section 7.3.8.

Two additional formulations of the same framework, derived from the main two variants introduced in Section 7.3.6, are presented in Appendix C.1.

7.3.1 Definition of main random variables

In this section we will introduce the main random variables which intervene in the proposed codesign framework. From the semi-probabilistic approach we presented in Chapter 4, we recall the same distinction between random variables, based on the metrics of variability:

- *intrinsic properties*: these include all the random variables which may vary within different aircrafts of a fleet but do not evolve during the aircraft's life (e.g. material properties, geometric imperfections);
- *environmental properties*: all random variables that vary during the aircraft's life but with no variation on the statistical description from one aircraft to another in the same fleet (e.g. aerodynamic loads).

In the rest of the chapter we will focus on the former category. In particular, we aim at redefining the variability of the geometric features, which can be included among intrinsic properties.

An illustration of the geometric features used in H2H problem is proposed in Fig. 7.3. One single hole is considered for explanation purpose.

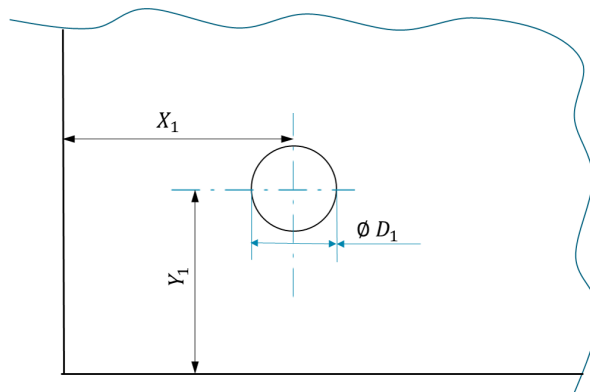


Figure 7.3: Illustration of geometrical features for H2H problem (one hole considered)

We start from the distinction between *geometrical* and *dimensional* features: the former considers all distances between plans, holes and solid extrusions; the latter category

describes the sizes of holes and solid edges, in terms of respectively diameter and linear length. In the illustration in Fig. 7.3, X_1 and Y_1 represent the coordinates of the position of the hole center and are *geometrical* features, while the hole diameter D_1 is a *dimensional* feature: note that X_1 , Y_1 and D_1 are not deterministic quantities, but constitute in fact random variables. In this chapter we will focus on *geometrical* features, but the proposed framework can be extended also to *dimensional* features.

To each of the defined *geometrical* features, we need to associate *nominal values* and *tolerance bounds*. In this codesign framework, we will not intervene on the nominal values. We are mainly interested in optimizing the variabilities of the geometrical features, which are dictated by the tolerance bounds. According to the possibility to change the tolerance bounds, we distinguish two main vectors of input random variables:

- **X**: the vector of the input random variables related to the geometrical features on which we can intervene by proposing new tolerance bounds;
- **Z**: the vector of input random variables including the geometrical features whose tolerance plans are already defined and can not be modified. We also include in **Z** all non-geometrical intrinsic random properties, which are not related to any tolerance plan.

At a general level, when we fix the variability of a given random variable affecting structural performances, we will include it in the vector **Z**. In the H2H applications, we focus on the effects on structural performances due to the holes geometrical misalignments and the material strength R : this latter will always be included in the vector **Z**. The collocation of the misalignments variables inside one of the two vectors **X** and **Z** will change in H2H applications according to the different stack chains, i.e. according to whether we block the variability of one specific misalignment coordinate. Further details will be given in Section 7.5.

During the optimization, we will iteratively propose new tolerance bounds, which will affect the variability of the random variable **X**. Therefore, we need to define a starting point for **X**, which we denote as \mathbf{X}_{orig} : this constitutes the vector of random variables described by an original tolerance plan (and thus an original statistical distribution, consistent with the availability of measurement data) which we want to modify. If no original tolerance plan or no data are available, as in H2H example, the vector \mathbf{X}_{orig} will constitute a random variable described by the distribution with the largest variability previewed for the specific features.

Moreover, we need to define the geometrical features at assembly level: these will be linked to the component features **X**, through a *tolerance model*. In the literature, the tolerance model is often denoted with $Y(\mathbf{X})$ [Diet et al., 2020]: however, to avoid confusion with the transversal misalignments of H2H applications, we will denote the tolerance model with $\rho(\mathbf{X})$. In the H2H example, these top level geometric features can be related to the relative misalignments distance of the corresponding holes from two plates. Therefore, we can define a tolerance model related to the first hole of the assembly as:

$$\rho(\mathbf{X}) = \sqrt{(X_{11} - X_{12})^2 + (Y_{11} - Y_{12})^2} : \quad (7.5)$$

Where X_{ij} (respectively Y_{ij}) represents the longitudinal (respectively transversal) misalignment of the j -th hole of the i -th plate.

In the following, we suppose that \mathbf{Z} and \mathbf{X} are independent and the distributions of the vectors \mathbf{X}_{orig} and \mathbf{X} are unimodal.

7.3.2 Definition of design variables

In this section we define the design variables which will be included in the optimization formulation of the proposed codesign framework. We start by distinguishing the tolerance requirements involved at elementary and at assembly levels. We introduce, therefore, two different variables:

- \mathbf{v} : the vector of the *tolerance bounds* (or *tolerance plans*) related to an elementary part;
- v_{assy} : the *top-level requirement* related to the whole assembly.

The vector of tolerance bounds \mathbf{v} will define the limits of the variability of the features included in the vector \mathbf{X} : we will therefore associate each component v_i of the vector \mathbf{v} to the geometrical feature X_i in the vector \mathbf{X} . This relation will be denoted as $\mathbf{X}(\mathbf{v})$. Note that for the sake of simplicity the dependence on \mathbf{v} will be sometimes omitted.

To explain the association of tolerance bounds v_i to features X_i , we make use of the example from Fig. 7.3 related to the definition of the position of one single hole on a plate in H2H applications. As anticipated in the previous section, we will associate to the geometrical features X_1, Y_1 both nominal values (respectively TX_1, TY_1 , within rectangular boxes) and tolerance bounds. Two different definitions of positioning tolerances are illustrated in Fig. 7.4. The positioning tolerances are denoted with the symbol \oplus , the shape of the tolerance interval (only if circular, denoted with \emptyset), the width of the tolerance interval (defined by the tolerance bounds v_i) and referenced to a system of *datums* (in this case, the system $A/B/C$).

In both cases, we associate three datums A, B, C as reference for the manufacturing and control of the holes positions. Then in the first case (see Fig. 7.4a), we apply a circular tolerance limit, denoted via the diameter $\emptyset 2v_1$: the result (depicted in Fig. 7.4b) is the generation of a circular tolerance zone (in blue) which defines the bounds for the realizations of the center of the hole. In the second case, in Fig. 7.4c, we apply two tolerance bounds in horizontal v_{X1} and vertical v_{Y1} directions, leading to the generation of a rectangular tolerance region (in Fig. 7.4d) to define the bounds of the hole center realizations. Furthermore, supposing a perfect shape of the hole, it is possible to define the bounds for the realizations of the holes, plotted as blue dotted lines.

In the classical statistical approach to tolerancing, the geometrical features affecting the assembly are supposed to follow a Gaussian statistical distribution $\mathcal{N}(\mu, \sigma^2)$ truncated on an interval of bandwidth 6σ and centered on the nominal value: in this way, the tolerance bounds are interpreted as an allowed maximum deviation from the nominal values of $\pm 3\sigma$ (thus $v_i = 3\sigma_i$). Within this perspective, the tolerance plans induce a specific distribution on each geometric input. As also underlined in [Diet, 2021], the normal assumption can not be verified until measurement data are available, specifically in the production phase.

In the aeronautical context, uniform distributions are generally assumed at initial design phases (when data are not available yet) while specific distributions (generally normal) are fitted on the measurement data related to each contributor in the assembly.

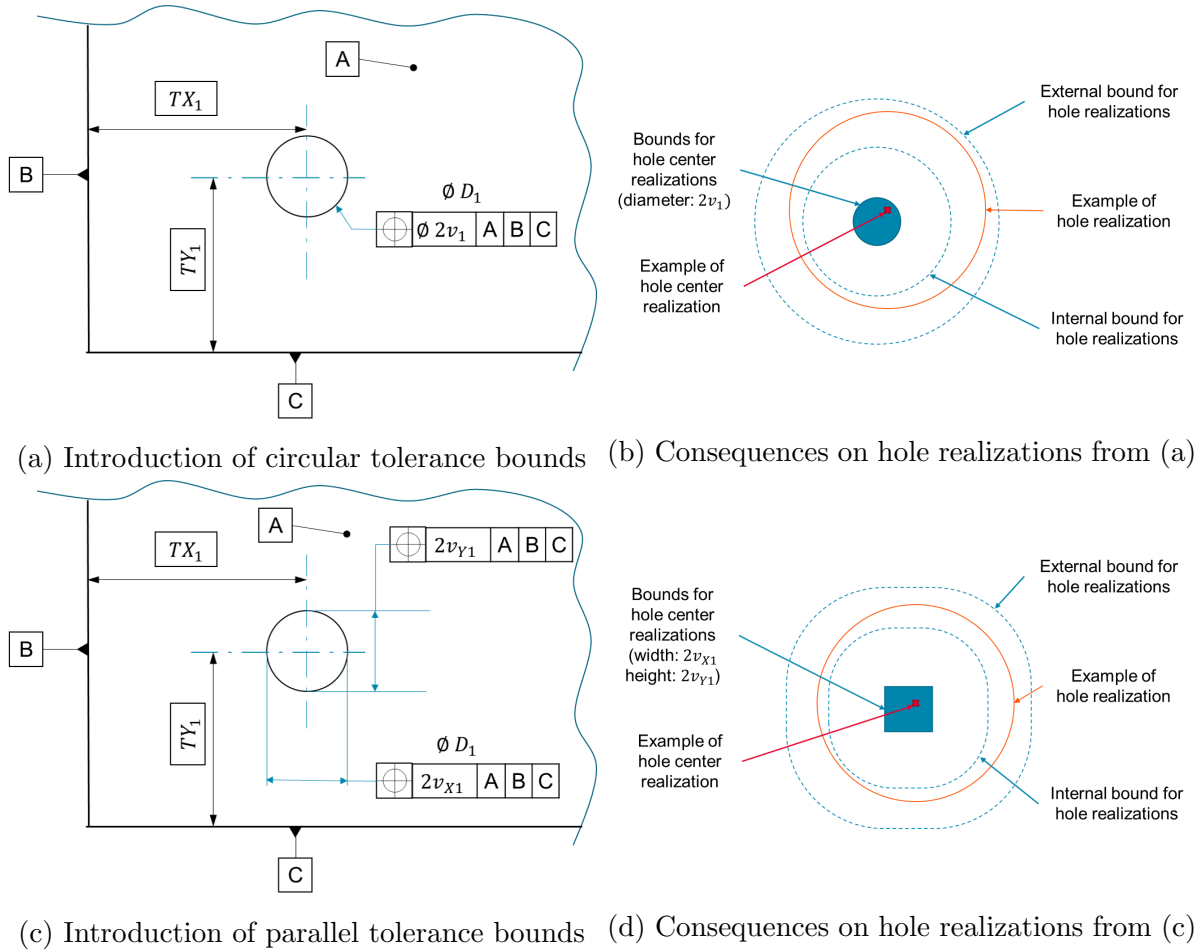


Figure 7.4: Illustration of the association of tolerance bounds \mathbf{v} to H2H geometrical features at component level (one hole considered)

We focus now on the top-level requirement v_{assy} . This is a limit threshold that must be satisfied by the tolerance model $\rho(\mathbf{X})$. The relation between ρ and v_{assy} is generally referred to as *tolerance acceptance criterion* and aims at identifying whether an assembly can be considered as conform: this can represent a physical obstacle preventing the assembly itself or a limit to determine whether it is necessary to intervene to adjust the assembly. An example of the former case, related to H2H application, is depicted in Fig. 7.5, where we need to distinguish the assemblies which allow the bolt to fit inside the holes of two plates from the ones which physically prevent it. For the latter case, we will introduce in Section 7.4 an example of assemblies with gaps: in this case, it will be necessary to measure the gap and compare it to a virtual value of v_{assy} to decide whether the assembly is conform (i.e. if it is acceptable as is) or it is necessary to implement some specific corrective measures.

In general, the *tolerance acceptance criterion* can be formalized as the following condition:

$$|\rho(\mathbf{X}(\mathbf{v}))| \leq v_{assy} \tag{7.6}$$

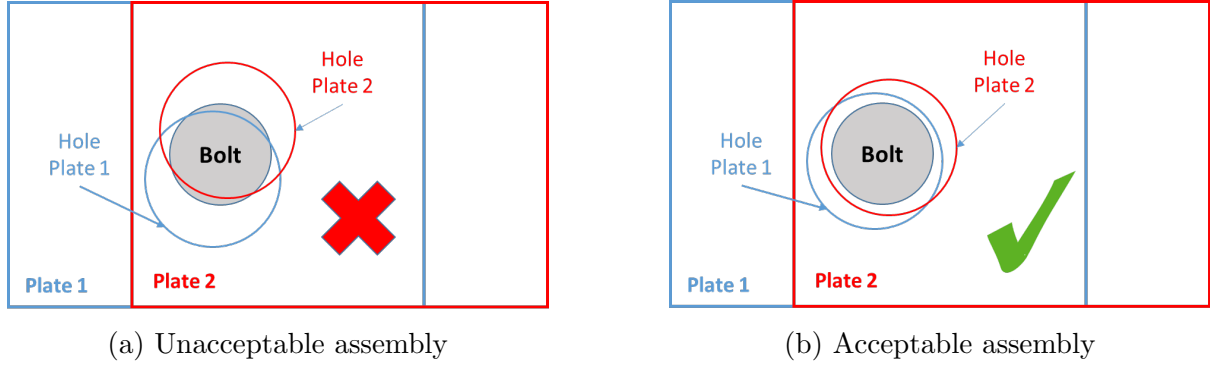


Figure 7.5: Capability to distinguish acceptable from unacceptable assemblies which must be ensured by the *tolerance acceptance criterion*, in presence of a physical obstacle: two H2H examples with a limited oversize

In the H2H example, we can use the formulation of ρ from Eq. 7.5, which represents the euclidean distance between two center holes (of two superposed plates) associated to the same bolt. The v_{assy} can be interpreted as either a physical obstacle which prevents the assembly itself (thus identifying half of the oversize, as in Fig. 7.5), or as a quality threshold to measure and verify at assembly level.

At this point, once we defined the random variables and the tolerance bounds (at component and assembly level), we can introduce the cost functions of the codesign framework optimization problem.

7.3.3 Definition of main costs

In our proposed framework, the tolerance allocation is focused on the minimization of non-quality costs, as done in [Diet, 2021]. These are strictly related to the risks of delivering non-conform elementary parts or assemblies. Therefore, we will distinguish the two main sources of non-quality costs: elementary parts (referred also as elements or components) and assemblies.

We first define a cost related to the N geometrical features of all structural elements:

$$c_1 = \sum_{i=1}^N m_i P[|X_{orig,i}| > v_i] \quad (7.7)$$

Where $X_{orig,i}$ and v_i are the components of the vectors \mathbf{X}_{orig} and \mathbf{v} , and m_i represent weighting factors related to the contributors $i = 1, \dots, N$.

The weighting factors represent the relative importance of the costs of the production of different features. For example, in H2H applications, we can have parts with different manufacturing complexity or simply coming from different manufacturers. Therefore, adopting the same tolerance bounds for the corresponding features of different parts (e.g. the first hole in the bolting pattern) can have different financial impacts on the different parts: consequently, we need to prioritize the definition of the tolerance bounds related to the most expensive contributors. In the definition of the cost c_1 , we would adopt higher weighting factors m_i for the features i with the highest priority in the relaxation of the tolerance bounds v_i .

The elements-related cost c_1 can be interpreted as the risk of having non-compliant elements with a new tolerance plan \mathbf{v} (starting from the original distributions $X_{orig,i}$) or either the cost of improving the precision of the manufacturing process itself (at elementary level). Note that the cost formulation in Eq. 7.7 can be directly applied to symmetrical tolerance plans v_i (i.e. obtaining intervals with extremes of the form $\pm v_i$): otherwise, if two different terms $v_{L,i}, v_{U,i}$ related to lower and upper bounds of the tolerance intervals are defined, one should decompose the i -th contribution in two components sharing the same $X_{orig,i}$. The definition of c_1 would become, in this case:

$$c_1 = \sum_{i=1}^N m_i (P[X_{orig,i} < v_{L,i}] + P[X_{orig,i} > v_{U,i}]) \quad (7.8)$$

The definition of asymmetric tolerance limits can be preferred when either the means of the original distributions $X_{orig,i}$ are not zero or the associated effects on the structural performances of the geometrical features X_i are not symmetrical. In the context of this dissertation, we assume that all distributions $X_{orig,i}$ are centered (i.e. have zero mean) and tolerance bounds are symmetric.

In all cases, a cost $c_1 = 0$ indicates that all features X_i follow the same distributions of $X_{orig,i}$. On the opposite extreme, $c_1 = 1$ represents a situation where all X_i are deterministic, linked to all $v_i = 0$.

The cost related to the assembly can be formalized for a given top-level requirement v_{assy} and according to a tolerance model $\rho(\mathbf{X})$ linking the elementary tolerances to the top-level geometric features:

$$c_2 = P[|\rho(\mathbf{X}(\mathbf{v}))| > v_{assy}] \quad (7.9)$$

The assembly-related cost c_2 can be interpreted as the probability of having non-compliant assemblies, but can also be viewed as the frequency of intervention on already existing structures, in order to make them compliant. This latter imply delays and repair costs. Note that this cost does not involve the original distribution \mathbf{X}_{orig} , as it is assumed that the tolerance guidelines can modify the overall outcomes of the production chains: this is the main reason which allows to switch from \mathbf{X}_{orig} to \mathbf{X} .

In Fig. 7.6, we illustrate the steps from the definitions of tolerance bounds until the verification at assembly level.

The process starts from an available distribution of each geometrical feature $X_{orig,i}$. From this, we define new tolerance bounds $\pm v_i$. The cost c_1 represents the amount of components which would be considered as non-conform according to the limits $\pm v_i$ if the distributions $X_{orig,i}$ were not modified. Alternatively, c_1 can be viewed as an index of the required improvement of the precision in the manufacturing process of the components.

Once the new tolerance bounds are defined, these are implemented in production, leading to different distributions of $X_i(v_i)$: from the Gaussian assumption, the X_i would be defined as normal variables with zero mean and standard deviation $\sigma_i = v_i/3$, truncated at $\pm v_i$.

In a third step, the assembly is built from the manufactured components. We describe the top-level geometric features from the output of the tolerance model ρ . The cost c_2 represents the amount of assemblies which are not conform with respect to the top-level requirement v_{assy} . The non-conform assemblies (i.e. the regions highlighted in purple

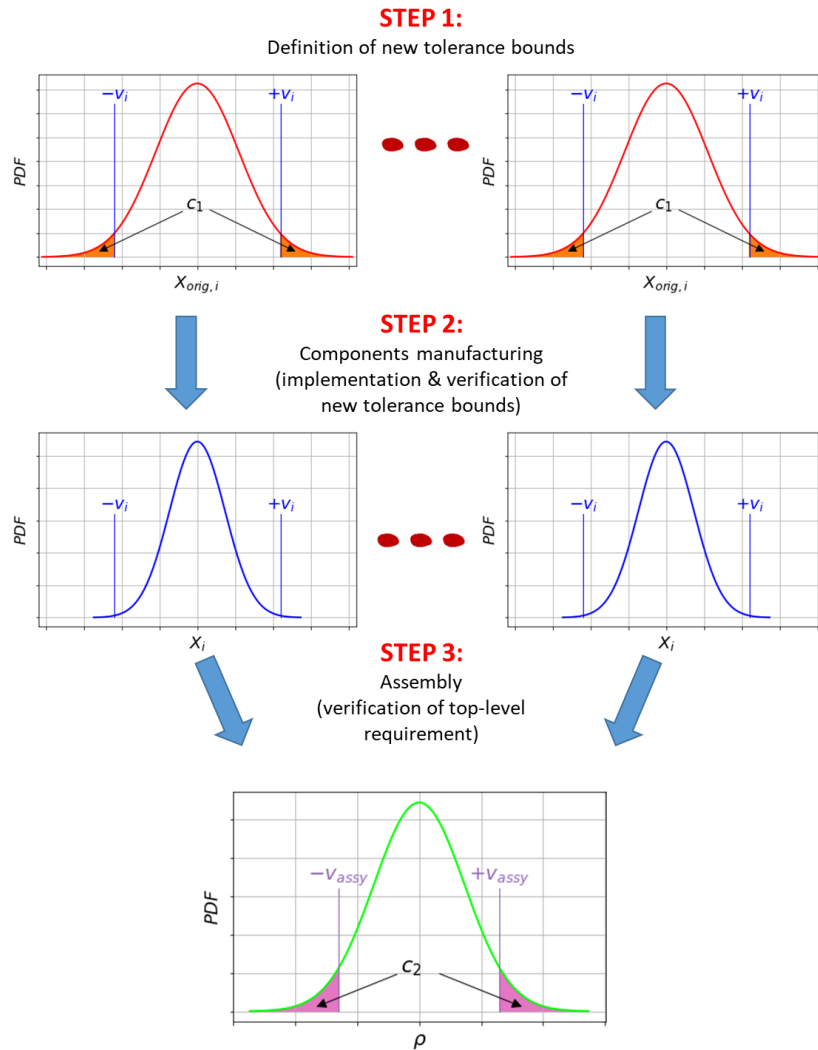


Figure 7.6: Illustration of the steps followed in the implementation of the tolerance plans

in Fig. 7.6) will be adjusted via specific corrective interventions: these may include sealant, shimming (in presence of gaps), counter-drilling parts (in H2H applications), among others.

The parallelism between mathematical quantities and the industrial process, described in the flowchart in Fig. 7.6, can be better understood by following the steps we would follow in the assembly process of H2H framework:

1. Start from an existing tolerance plan or available data, to fit the initial distributions of the component-related geometrical features $X_{orig,i}$;
2. Define new tolerance bounds v_i for each geometrical feature of each component: the amount of samples $X_{orig,i}$ non-conform with the tolerance bounds v_i (i.e. $|X_{orig,i}| > v_i$) will define the cost c_1 . This latter represents also the amount of effort which is needed in the manufacturing phase to actually implement new component-related tolerance bounds v_i ;
3. Manufacture the pre-drilled parts, following the component-related tolerance bounds v_i : the toleranced features X_i associated to v_i will reproduce new distributions

- $X_i \sim \mathcal{N}(0, \sigma_i^2)$, with $\sigma_i = v_i/3$;
4. Put together the parts, then measure the relative misalignments on the different bolts location: these will constitute the outputs of the tolerance model $\rho(\mathbf{X}(\mathbf{v}))$;
 5. Verify whether the assembly is conform, meaning to verify, in the specific case of H2H, if all the bolts fit inside the holes: the determination of the capability or not to assemble the parts is reproduced by the *tolerance acceptance criterion*, (i.e. $|\rho| \leq v_{assy}$), and the rate of non conform assemblies will define the cost c_2 .

We need to highlight the probabilistic modeling of the effect of the corrective interventions (done when the *tolerance acceptance criterion* is not satisfied, i.e. $|\rho| \geq v_{assy}$), represented in Fig. 7.7. If we know the effect on the structural performances of the corrective interventions (left branch of Fig. 7.7), we may keep the same distributions of the tolerance model output ρ , but considering that the structural performances will be affected by the interventions in the region $|\rho| \geq v_{assy}$ (purple region of the left branch of Fig. 7.7). Otherwise, if we do not know precisely the effect of the corrective interventions (right branch of Fig. 7.7), we make the conservative assumption that, after the interventions, there are only conform realizations of the tolerance model output, with $|\rho| \leq v_{assy}$ (thus, truncating the distribution of ρ): this assumption is conservative if the interventions are able to restore the nominal geometric features of the assembly. We can apply this assumption also to the cases where assemblies are just thrown away (rare) or where the tolerance activities actually manage to never trespassing the limit imposed by the top-level requirement v_{assy} . In any case, the top-level requirement v_{assy} represents the truncation level of the conform realizations of the output ρ of the tolerance model.

Following the flowchart in Fig. 7.6, we can re-interpret the role of the design variables under a different perspective, based on the statistical description of the outcomes of the tolerance model ρ : the tolerance bounds \mathbf{v} determine the variance of the output ρ ; on the other hand, the top-level requirement v_{assy} represents the truncation level of the distribution of the conform realizations of ρ . This perspective allows us to relax the definition of the design variable \mathbf{v} , which can also be used directly to identify the tolerance bounds of the output of the tolerance model ρ prior to the corrective interventions. As a reminder, under the Gaussian assumption, the definition of tolerance bounds induces a specific statistical distribution. Therefore, this alternative perspective does not dig inside the tolerance allocation among the different components, but will lead to define only the optimal parameters of the distribution of the output of the tolerance model. In Section 7.4, we will adopt this different perspective on two examples related to the stress induced by the closure of gaps during fastener installations.

In the work of [Diet, 2021], the tolerance optimization problem considered also another cost, c_3 representing the cost associated to a change in the tolerance plans. This is not considered in our framework. Excluding this cost and introducing bounds constraints related to the distinct components of the vector \mathbf{v} , the tolerance allocation problem can be formalized [Diet, 2021] as follows:

$$\begin{aligned} \min_{\mathbf{v}} \quad & c_1(\mathbf{v}), c_2(\mathbf{v}; v_{assy}) \\ \text{s.t.} \quad & v_{LB,i} \leq v_i \leq v_{UB,i} \quad \forall i = 1, \dots, N \end{aligned} \tag{7.10}$$

This formulation is retained in the following as our reference, under the name "current practice". Note that in Eq. 7.10, the top-level requirement v_{assy} is not a design variable,

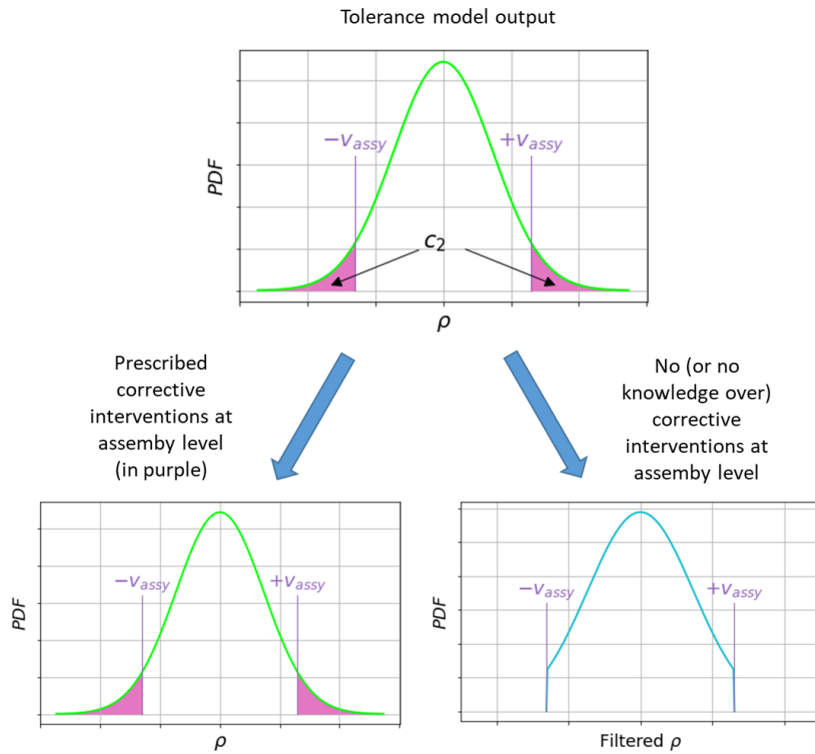


Figure 7.7: Possible outcomes of the application of the top-level requirement check on the distribution of the tolerance model output

but an input scenario provided to the tolerance team to take into account functionality and structural constraints, often defined (for some *geometrical* features) on a worst-case scenario basis.

7.3.4 Introduction of semi-probabilistic constraints

In the following sections, we will modify the tolerance optimization from *current practice*, in order to take into account the effects of the variability of the geometric features on the structural performances. The main constraint of the treated problem is defined by the satisfaction of stress requirements within the semi-probabilistic framework described in Chapter 4. As a reminder, this constitutes an extension of the current certification requirements for the static strength demonstration of large airplanes (i.e. CS 25), based on the modeling of part of the sizing input variables (thus *semi-probabilistic framework*).

First, we need to formulate the semi-probabilistic approach for tolerance costs optimization problem. In particular, we focus on problems with intrinsic variables only, as the geometrical flaws in specific components may vary among different aircrafts of the same fleet but can be considered as constant during the whole aircraft life. This does not imply that the approach is valid only when there is no variability in environmental properties, but rather the assessments for the effects of distinct category of variables are treated in separated analysis.

In Chapter 4, we introduced the concept of the Probability of Exceedence PoE , starting from the definition of the detrimental variables K_j . In general, the detrimental vari-

ables K_j represent a ratio between actual realizations of random structural performances I_j and the related deterministic value $I_{REF,j}$ used in deterministic sizing. As a reminder, the detrimental variables K_j are formalized as:

$$K_j = \begin{cases} \frac{I_j}{I_{REF,j}} & \text{if high } I_j \text{ improve performances} \\ \frac{I_{REF,j}}{I_j} & \text{if low } I_j \text{ improve performances} \end{cases} \quad (7.11)$$

In the first case, we can provide the example of the material resistance. For the second, we may think of the load amplification factors (e.g. the bearing load redistribution in H2H applications, due to the hole misalignments).

The detrimental variables K_j may depend on the input geometric variables \mathbf{X} - directly linked to the tolerance plans \mathbf{v} - and the random variables \mathbf{Z} - not affected by \mathbf{v} . Moreover, distinct scenarios can be imposed by fixing the sizing $I_{REF,j}$ at different values. In the following, we will denote this chain of dependencies of K_j as:

$$K_j = K_j(\mathbf{X}(\mathbf{v}), \mathbf{Z}; I_{REF,j}) \quad (7.12)$$

Here we separate with the symbol ";" the random variables $\mathbf{X}(\mathbf{v})$ and \mathbf{Z} from the scenarios $I_{REF,j}$.

The condition $K_j < 1$ implies that the actual realization of a given structural performance is worse than the one previewed in deterministic sizing: we denote this as *detrimental condition*. Then, if M independent phenomena affect the same failure mode and their cumulative effect is multiplicative, the *detrimental condition* can be generalized into:

$$\prod_j^M K_j \leq 1 \quad (7.13)$$

The *detrimental condition* in Eq. 7.13 can be re-conducted to the classical definition of a *limit state function* G which can be formalized, for the semi-probabilistic framework, as:

$$G = \prod_j^M K_j - 1 \begin{cases} \leq 0 & \text{exceedance} \\ > 0 & \text{no exceedance} \end{cases} \quad (7.14)$$

We need to remark that trespassing the limit $G = 0$ does not imply the *failure* of a given realization of structural performances, but only the fact that the given realization under-performs with respect to what is previewed by the nominal values $I_{REF,j}$ used in deterministic sizing, which are usually determined conservatively.

The *PoE* is therefore defined as the probability that the combined effects of M performance indexes lead to worse structural performances than the ones considered in deterministic sizing:

$$PoE = P\left(\prod_j^M K_j \leq 1\right) = P(G \leq 0) \quad (7.15)$$

In the H2H example we essentially deal with material strength R and bearing forces S . We denote with R_{REF} and $S_{REF,nom}$ the nominal quantities typically retained for

deterministic sizing of classical counter-drilled bolted joint assemblies, i.e. with perfectly fitted aligned holes. When passing to the H2H context, every misalignment leads to unbalanced load transfer: therefore, in deterministic sizing phase, we need to consider an amplified nominal load, given by multiplying $S_{REF,nom}$ with an *overload* OL (strictly greater than unity). Therefore, we may define for the H2H case two detrimental variables:

$$K_R = \frac{R}{R_{REF}} \quad K_S = \frac{S_{REF}}{S} = \frac{S_{REF,nom}OL}{S}$$

The PoE can be formalized in H2H case as:

$$PoE = P\left(\frac{R}{R_{REF}} \frac{S_{REF,nom}OL}{S} \leq 1\right) \quad (7.16)$$

Alternatively, a limit state function G can be used:

$$PoE = P(G \leq 0) \quad \text{with} \quad G = \frac{R}{R_{REF}} \frac{S_{REF,nom}OL}{S} - 1 \quad (7.17)$$

Now we link the PoE to the design variables introduced in Section 7.3.2: the component-related tolerance bounds \mathbf{v} and the top-level requirement v_{assy} . If we did not consider the effect of the top-level requirement v_{assy} on the PoE , this latter could be formalized by introducing the Eq. 7.12 into Eq. 7.15:

$$PoE(\mathbf{v}) = P\left[\prod_j^M K_j(\mathbf{X}(\mathbf{v}), \mathbf{Z}; I_{REF,j}) \leq 1\right] \quad (7.18)$$

At first sight, in the Eq. 7.18, it might seem that there are multiple scenarios given by the different combinations of the nominal performance indexes $I_{REF,j}$. However, we remind that the $I_{REF,j}$ are aggregated via products and ratios (cf. Eqs. 7.11-7.13): therefore, there is only one degree of freedom for the choices of the scenario. Looking at the H2H example, in Eq. 7.16 the only degree of freedom is the cumulated quantity $S_{REF,nom}OL/R_{REF}$: now, if we doubled both R_{REF} and OL , the resulting PoE would be the same (without altering the other quantities). For this reason, in the following, we will refer to only one degree of freedom for the sizing scenarios: when dealing with the effects of gaps in Section 7.4, we will talk of *sizing gaps* scenarios; for the H2H applications, we will only refer to the *imposed overload limits* OL . To keep trace of the scenarios imposed on the PoE definition and the fact that there is only one degree of freedom for the nominal structural performances, we introduce the notation:

$$PoE(\mathbf{v}; I_{REF}) = P\left[\prod_j^M K_j(\mathbf{X}(\mathbf{v}), \mathbf{Z}; I_{REF,j}) \leq 1\right] \quad (7.19)$$

Where I_{REF} represents the global scenario degree of freedom, taking into account the products and ratios of all $I_{REF,j}$. We separate through the symbol ";" the design variables \mathbf{v} from the scenario I_{REF} .

The relation in Eq. 7.19, however, can be directly applied only if we do not preview any correction at assembly level (or at least, no intervention affecting the structural performances, but only kinematic functionalities). This case is not of interest for the proposed framework.

Therefore, we need to add the effect of the top-level requirement v_{assy} . In a first trial, we can consider only the realizations of the vector $\mathbf{X}(\mathbf{v})$ which satisfy the top-level requirement v_{assy} : this filtering would be a realistic assumption if the non-conform (with respect to top-level requirement) structural parts were just thrown away, but can be a conservative assumption if the interventions in the assembly line are able to restore (or even improve) the nominal performances of the assembly, but the exact consequence of the adjustments is not known. The expression of PoE will be therefore declined for the codesign framework as follows:

$$PoE(\mathbf{v}, v_{assy}; I_{REF}) = P \left[\prod_j^M K_j(\mathbf{X}(\mathbf{v}), \mathbf{Z}; I_{REF,j}) \leq 1 \mid |\rho(\mathbf{X}(\mathbf{v}))| < v_{assy} \right] \quad (7.20)$$

In the example of H2H applications, we can think at the assemblies where it is not possible to insert a bolt inside a hole. If we can demonstrate that the prescribed interventions (e.g. re-drilling) allow to restore the nominal conditions (i.e. $\prod K_j \geq 1$), the fact of filtering only the conform assemblies (i.e. the assemblies where all bolts fit inside each hole location without any correction) will lead to over-estimate the PoE .

A second option, however, can arise from the implementation of adjustments which lead to relevant known consequences on the structural performances. In this case, the detrimental variables K_j will directly depend on the top-level requirement v_{assy} , while no top-level truncation is applied. Therefore, the expression of the PoE related to this second option is given by:

$$PoE(\mathbf{v}, v_{assy}; I_{REF}) = P \left[\prod_j^M K_j(\mathbf{X}(\mathbf{v}), v_{assy}, \mathbf{Z}; I_{REF,j}) \leq 1 \right] \quad (7.21)$$

In this formalization, the expression of each K_j will be formalized per cases, each defined according to whether the top-level requirement is encountered or not (for a specific realization of the random variable \mathbf{X}). In the H2H example, this would need to identify a specific corrective intervention at assembly level (for bolts not fitting inside the holes) and evaluate the associated effects on the structural performances. This option better reflects the reality of the process. However, this requires also the knowledge of the consequences of the interventions at assembly level: we will investigate in Section 7.4 the actual added value of this knowledge, by comparing two test cases, related to the effect of the stresses induced by the closure of gaps, with and without the knowledge of the effects of the interventions on the non-conform assemblies.

Finally, we can define the *semi-probabilistic constraint* for the proposed codesign framework. Consistently with the extension of CS 25.613 introduced in Chapter 4, we formulate the following condition, related to intrinsic properties:

$$PoE(\mathbf{v}, v_{assy}; I_{REF}) \leq \overline{PoE} = \begin{cases} 0.1 & \text{for redundant structure} \\ 0.01 & \text{for non-redundant structure} \end{cases} \quad (7.22)$$

The expression in Eq. 7.22 constitutes the *semi-probabilistic constraint* of the proposed framework and is valid for both formulations of the PoE in Eqs. 7.20-7.21.

The explicit consideration of the *semi-probabilistic constraint* will make the tolerance optimization problem *reliability-based*. Before formulating the complete optimization problem, we will qualitatively evaluate the sensitivities of the main quantities described in the last two sections (namely the costs c_1 and c_2 , and the probability PoE) with respect to the design variables.

7.3.5 Sensitivities of the main quantities

In this section we analyze the sensitivities of the component-related cost c_1 , the assembly-related cost c_2 and the probability PoE . In particular, we will focus on their sensitivities with respect to the design variables introduced in Section 7.3.2, namely the component tolerance bounds \mathbf{v} and the top-level requirement v_{assy} .

The two costs, c_1 from Eq. 7.7 and c_2 from Eq. 7.9, exhibit opposite sensitivities with respect to the tolerance bounds \mathbf{v} : while the former decreases with larger tolerance bounds, the latter increases. This can be explained by collocating the two costs in the right chronological and tolerance cascade order (cf. flowchart in Fig. 7.6): if larger variabilities (thus larger \mathbf{v}) are allowed in manufacturing steps, the required precision (the cost of which is measured via c_1) is reduced, but more interventions (measured via c_2) are required to adjust the product in the assembly line to align to the same top-level requirement. Moreover, we underline the fact that the top-level requirement v_{assy} only affects the assembly-related cost c_2 , with c_2 decreasing with an increase of the value of v_{assy} .

We focus now on the sensitivities of the PoE with respect to the input variables v_i , constituting the components of the vector \mathbf{v} . We will distinguish, in the following, the features X_i which affect one or more factors K_j from the others X_i which have no effect on any factor K_j : we will denote the first category by the name of *active features* and the second by *passive features*. The tolerance variables v_i related to the features X_i will be, on their turn, referred respectively as *active tolerance variables* and *passive tolerance variables*.

In order to draw some general conclusions, we start from the example of the H2H problem: for the sake of simplicity, instead of considering the elementary features X_{ij}, Y_{ij} (representing the longitudinal and transversal misalignments of the j -th hole of the i -th plate), we will focus on the relative misalignments (between two plates) on the j bolt locations in longitudinal $dX_j = X_{1j} - X_{2j}$ and transversal direction $dY_j = Y_{1j} - Y_{2j}$. In Chapter 3, the dimensionality reduction allowed us to deduce that the dX_j are the only responsible for the bearing redistribution across the different bolt locations. Therefore, we can collocate the dX_j in the category of *active features* and the dY_j among *passive features*.

Let us focus on the effect of the tolerance acceptance criterion from Eqs. 7.5-7.6 on the sampled population of misalignments for the first bolt location (i.e. $j = 1$), illustrated in Fig. 7.8. Now, we start by considering only the variability on the dX_1 while imposing $dY_1 = 0$: the tolerance acceptance criteria does not lead to any filtering effect on the input variability on dX_1 , as all points would lie on a segment (cf. Fig. 7.8). When introducing the variability on dY_1 , we force the tolerance acceptance criterion to filter a part of the most detrimental samples (the main responsible for the variation of the PoE), situated in the extreme regions with high $|dX_1|$. This effect helps to explain why increasing the

passive tolerance variables can reduce the *PoE*.

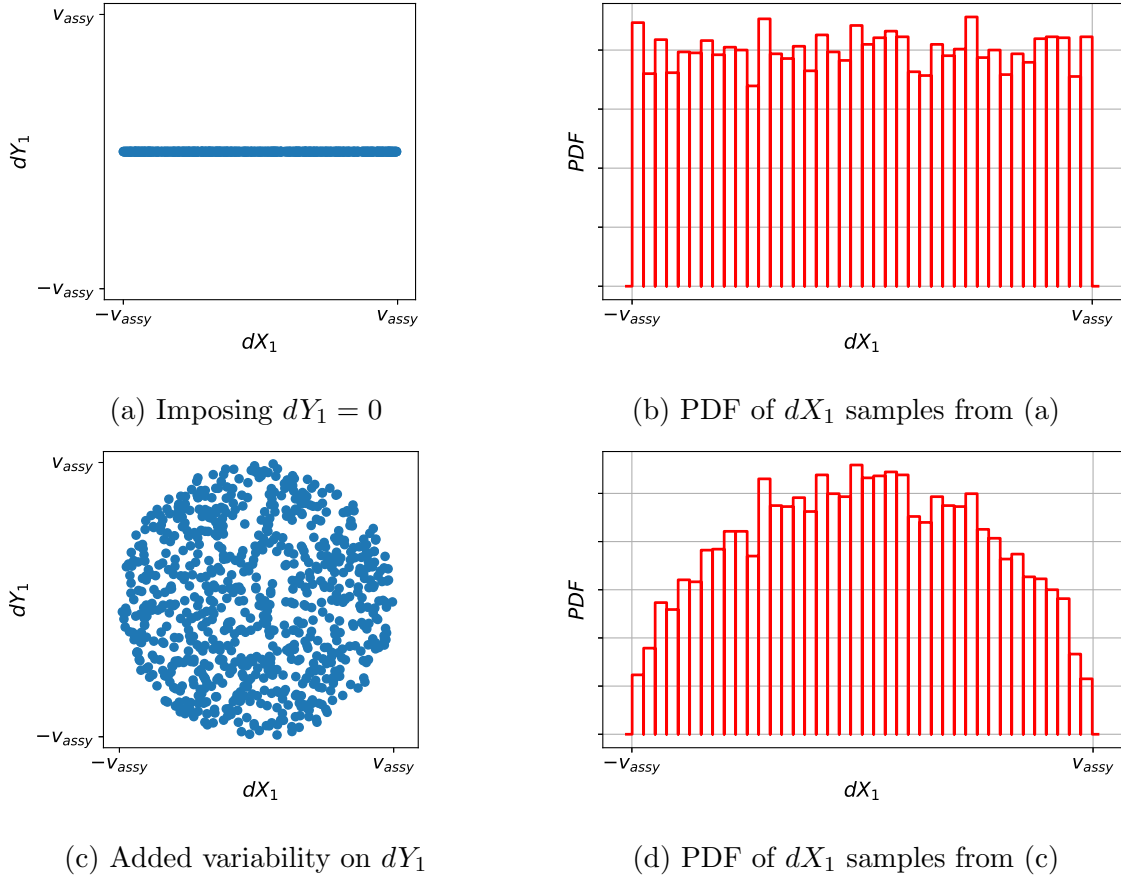


Figure 7.8: Illustration of the benefits of adding transversal misalignment samples in presence of a tolerance acceptance criterion $\sqrt{dX_1^2 + dY_1^2} \leq v_{assy}$

From a more general perspective, when we increase the variability of input *active features* X_i via the related *active tolerance variable* v_i , we tend to increase also the variability of the random variables K_j . On the other hand, the variation of the variability of *passive features* X_i does not directly affect the K_j . However, the variability of the output of the tolerance model may be impacted: therefore, a larger portion of the population of \mathbf{X} will exceed the top-level requirement and more samples related to critical values of the *active features* will be subject to the interventions at assembly level. As a final result, the *PoE* will decrease either if the tolerance acceptance criterion simply induces a restriction of the sample population (as in Eq. 7.20), either if the impact is measured via a modification of the law of K_j (as in Eq. 7.21).

However, we remark that this distinction can only be easily evaluated and verified if the effect of the features X_i on K_j is linear and no interaction effect with other features is relevant. Otherwise, the sensitivity of the quantity *PoE* would require more evolved sensitivity analysis methods.

On the other hand, the quantity *PoE* will increase when increasing v_{assy} , provided that the interventions at assembly level actually affect the structural performances.

7.3.6 Problem statement

In this section, we formalize the codesign framework from a mathematical point of view. The global objective is to allocate geometrical tolerance features to minimize all out-of-tolerance costs, while satisfying stress requirements in the proposed semi-probabilistic framework.

The first step consists in defining the design variables: we always retain the tolerance bounds \mathbf{v} as main design variables. Moreover, we can include the top-level requirement v_{assy} either as a scenario for different optimization problems or as an additional design variable. In the following, we refer to the former option as "codesign framework with fixed top-level requirement" and to the latter as "codesign framework with smart top-level requirement re-definition" or alternatively "full codesign framework".

The objective function definition constitutes the second step in the formalization. The goal is to reduce both elementary part-related out-of-tolerance risk c_1 (cf. Eq. 7.7) and assembly-related out-of-tolerance risk c_2 (cf. Eq. 7.9). Therefore the optimization problem will be bi-objective and will not lead to single optima points but rather Pareto fronts, thus catalogs of solutions satisfying the set of constraints.

A third step consists in defining the bounds constraints. A wise choice of the domain restriction on \mathbf{v} could be given by the imposition of the smallest tolerance actually measurable as lower bound and the largest tolerances provided by the proposal distribution of \mathbf{X}_{orig} as upper bounds. An analogue reasoning can be followed to specify the lower bound of v_{assy} (when it is included as design variable) as the lowest value actually measurable with the available means.

Finally, we can formalize the codesign optimization problem by including the constraint provided by the semi-probabilistic approach. To improve readability, we omit in the notation the dependences of the PoE on the random variables \mathbf{Z} not affected by the components-related tolerance bounds \mathbf{v} . Moreover, we use the symbol ";" to separate the design variables from the imposed scenarios.

The variant of the proposed approach entitled "codesign framework with fixed top-level requirement" is mathematically formalized as:

$$\begin{aligned}
 \min_{\mathbf{v}} \quad & c_1(\mathbf{v}), c_2(\mathbf{v}; v_{assy}) \\
 \text{s.t.} \quad & PoE(\mathbf{v}; v_{assy}, I_{REF}) \leq \overline{PoE} \\
 & v_{LB,i} \leq v_i \leq v_{UB_i} \quad \forall i = 1, \dots, N
 \end{aligned} \tag{7.23}$$

Where the last line includes the bounds constraints for all the N components of the tolerance bounds vector \mathbf{v} to include in the tolerance plan.

On the other hand, the variant we named "codesign framework with smart top-level requirement re-definition" or "full codesign framework", includes v_{assy} among design variables and can be formalized as follows:

$$\begin{aligned}
 \min_{\mathbf{v}, v_{assy}} \quad & c_1(\mathbf{v}), c_2(\mathbf{v}, v_{assy}) \\
 \text{s.t.} \quad & PoE(\mathbf{v}, v_{assy}; I_{REF}) \leq \overline{PoE} \\
 & v_{LB,i} \leq v_i \leq v_{UB_i} \quad \forall i = 1, \dots, N \\
 & v_{assy, LB} \leq v_{assy} \leq v_{assy, UB}
 \end{aligned} \tag{7.24}$$

Both formulations in Eq. 7.23 and Eq. 7.24 constitute, from a mathematical point of view, two multi-objective reliability-based design optimization problems.

The choice between one variant and the other may be forced by the choice of the previewed interventions at assembly level, affecting consequently the effects of the top-level requirement v_{assy} : in particular, if the previewed interventions can only take place, in practice, at few specific scenarios of v_{assy} (e.g. solid shimming), it may not be worth it to define the continuous variation of the allowed values of v_{assy} in the Pareto front. In these cases, the variant "codesign framework with fixed top-level requirement" should be preferred.

7.3.7 Preliminary analysis

Before addressing the resolution of the optimization problem itself, let us highlight the added value of the introduction of the semi-probabilistic constraint in the codesign framework. In this section, we focus on the cases where the interventions (with respect to the top-level requirement v_{assy}) affect the structural performances, hence we focus on the situations where the relations between the PoE and the inputs \mathbf{v} , v_{assy} can be described by Eqs. 7.20-7.21.

We fix the ideas by considering the variations of the PoE with respect to the input vector \mathbf{v} . Let us take into account the considerations from Section 7.3.4 on the distinction between *active* and *passive tolerance variables*: for the former, the PoE increases when increasing the v_i ; for the latter, PoE decreases. We remind that this clear distinction can be ascertained only if the effect of the related feature X_i is linear, without exhibiting any interaction effect with other features.

We consider only the values of the PoE at the extremes denoted by the bounds constraints, namely $v_{LB,i}$ and $v_{UB,i}$. We denote by \underline{v}_i the bound of v_i leading to the minimum PoE : for *active features* we will have $\underline{v}_i = v_{LB,i}$, while for *passive features* $\underline{v}_i = v_{UB,i}$. We repeat this process for all components v_i , composing the vector $\underline{\mathbf{v}} = [\underline{v}_1, \dots, \underline{v}_N]$, which can be seen as a worst-case design choice for the tolerances v_i .

Now, if the relation $PoE(\underline{\mathbf{v}}, v_{assy, LB}) \geq \overline{PoE}$ were true, this would imply that no candidate solution could satisfy the semi-probabilistic constraint. This is due to the fact that the defined bounds constraints are not compatible with the set of the imposed nominal structural requirements $I_{REF,j}$. Therefore, we may have two choices: either we consider different machining procedures (if any available) to modify the bounds on the design variables, either we accept the compromise on less restrictive $I_{REF,j}$ (i.e. a less convenient structural sizing), moving away from worst-case design choices of v_i .

An example of too restrictive structural requirements can be given by the overloads OL on the H2H problem, representing the load amplification factor which must be considered in deterministic sizing. Now, as all deviations from the nominal configuration (with perfectly fitted aligned holes) lead to an unbalance in transferred loads, there will always be a location where there is a higher transfer of loads with respect to its nominal value. In Chapter 4, we computed the B-quantiles of OL on different coupons, when having as input the distributions of the input geometrical features. We showed that we have always the relation $OL > 1$, as for any location which absorbs lower loads (with respect to what the same location would transfer in the nominal configuration), there is another one which will have to carry that part of load: if we imposed an overload limit $OL = 1$,

no feasible solution would exist as, by definition, the overloads OL will always be strictly greater than unity.

On the other side, we denote by \bar{v}_i the bound of v_i leading to the maximum PoE (intended in the comparison between the results of the PoE on $v_{LB,i}$ and $v_{UB,i}$): for *active features* we will have $\bar{v}_i = v_{UB,i}$, while for *passive features* $\bar{v}_i = v_{LB,i}$. The opposite reasoning will be valid if for the vector $\bar{\mathbf{v}} = [\bar{v}_1, \dots, \bar{v}_N]$, we obtain a correspondent $PoE(\bar{\mathbf{v}}, v_{assy,UB}) \leq \overline{PoE}$. In this case, the semi-probabilistic constraint is redundant and will not be active: therefore, in this case the constraint itself can be omitted and the nature of the problem will be purely geometrical. This kind of situations can happen if the prescribed structural requirements $I_{REF,j}$ are too conservative (from the point of view of structural performances) and all possible solutions of the unconstrained tolerance optimization problem automatically guarantee to respect the PoE constraint.

Coming back to the case of H2H, if we imposed an overload limit $OL = 3$ in a coupon 1x2, every possible combination of tolerances would guarantee to satisfy this constraint. In the nominal configuration (with perfectly fitted aligned holes), each bolt would carry a load equal to half of the applied load. In the worst case, a single bolt will have to carry, at most, the totality of the applied load, corresponding to the double (i.e. $OL = 2$) of the load he would transfer on a nominal configuration. Therefore, imposing $OL = 3$ would be unnecessary and the tolerance optimization would boil down to a geometrical problem. However, this physical reasoning does not always work well to define reasonable nominal values of the structural performances (in terms of imposed overload limits OL). For the H2H coupon with bolting pattern 1x5, we would be led to think that, in order to activate the PoE constraint, it would be sufficient to just impose an overload limit $OL < 5$ (ignoring the fact that, in the nominal configuration, the transferred bearing loads are not actually uniformly redistributed among the different bolts). But if we look back at the overload results in Chapter 4, we notice that the B-values were lower than the ones retrieved for the coupon 1x2, hence $OL < 2$. Therefore, a more appropriate preliminary analysis, like the one we presented in this section, should be generally performed prior to the resolution of the optimization itself.

The upper-mentioned preliminary analysis can be done on a complete 2^k factorial DoE or, alternatively, on a filling-space DoE, to obtain an approximate behavior of the PoE in the search domain of the design variables, defined by the bounds constraints.

The purpose of this preliminary analysis is, therefore, to identify the limits of the semi-probabilistic constraints. This can be resumed in the concept of determining if the upper-mentioned constraint gives an actual added value (i.e. if it is not automatically satisfied by all geometrical solutions) and/or if the constraint itself is too stringent (i.e. if no solution can satisfy it).

7.3.8 Numerical tools

In this section, we describe the numerical tools used in the computation of the different quantities involved in the optimization problem and its solving.

Concerning the mathematical tools used to compute the objectives appearing in the optimization problems in Eqs. 7.23-7.24, we adopt classical Monte Carlo simulations [Hammersley, 2013] to compute the cost c_2 , while c_1 can be analytically evaluated through the cumulative distribution functions of the vector \mathbf{X}_{orig} .

The computation of the PoE is assisted, when needed (e.g. for H2H applications) in order to reduce computational burden, by the Vb-KPLS algorithm, coupled with Separable Monte Carlo (SMC, [Smarslok et al., 2010]) sampling introduced in Chapter 6. The adaptive training algorithm (described in Chapter 6) is done prior to optimization, on the largest domain of all input variables, hence covering the full variability of \mathbf{X}_{orig} and the vector of random variables \mathbf{Z} not affected by the tolerance bounds \mathbf{v} . Moreover, different simulations of Vb-KPLS+SMC algorithm are performed for distinct levels of the nominal performances in the semi-probabilistic PoE formulation. During the evaluation of the PoE , we never come back to the training phase again. Note that the training of the KPLS model is done, actually, before the preliminary analysis presented in the previous section: if the condition $PoE < \overline{PoE}$ is verified on the largest domain, the constraint will not be added to the optimization problem, as it will not be active.

In all test cases, as default sampling method we use the SMC technique [Smarslok et al., 2010]. As was shown in Chapter 5 on ImpSMC, separable sampling methods can reduce the variance of the failure probability (PoE in our case) with respect to the analogue classical approaches: the SMC is treated as a particular case of ImpSMC, where the importance functions are the same than the original input probability distribution functions. When the separability assumption is not verified, the alternative is the Monte Carlo method. The use of importance sampling (and analogue separable version) are not necessary on the examples reported in this chapter, as the main focus is given to intrinsic properties in the variable distinction of the semi-probabilistic framework, hence leading to constraints $\overline{PoE} = 0.01/0.1$. Note that Importance Sampling and ImpSMC would however be advantageous if smaller $PoEs$ would be sought, such as when considering environmental variables.

In terms of the optimization itself, the Non-dominated Sorting Genetic Algorithm II (NSGA-II) [Deb et al., 2002] is used to deal with the constrained and bounded bi-objective optimization. A part of the post-processing of results is done at fixed levels \overline{c}_2 of the cost c_2 : this reproduces the interpretation of the results issued from the constraint method, i.e. converting the bi-objective optimization of c_1, c_2 into the single-objective optimization of c_1 while constraining $c_2 \leq \overline{c}_2$. The interpretation of \overline{c}_2 is, in this framework, an expandable budget on the cost c_2 : therefore, we will refer to this quantity as *budget*. However, we remark that the set of solutions is retrieved with NSGA-II and this analysis is posterior to the optimization itself.

From an implementation perspective, we use the python library OPENTURNS [Baudin et al., 2017] to generate the samples distributions and the package PYMOO [Blank and Deb, 2020] to solve the optimization problem.

Next sections will present the results obtained on two applications: the first focuses on the phenomenon of the built-in stress, i.e. the stress induced by closing the gaps in a given assembly; the second application concerns the Hole2Hole example.

7.4 Applications on built-in stresses

In this section we apply the codesign framework on the problem of the built-in stress due to gaps in aeronautical assemblies. These are the stresses which can be induced by the manufacturing process, when closing a gap in an assembly. A representation of this

phenomenon is depicted in Fig. 7.9.

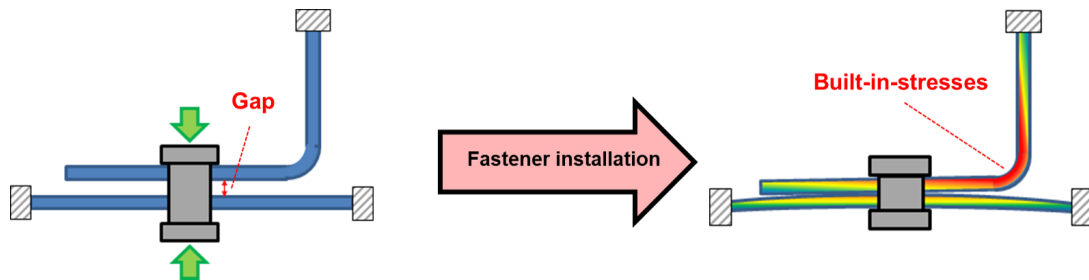


Figure 7.9: Built-in stress arising from gaps closure in fastener installation [Kempeneers, 2018]

The classical manufacturing procedure involves a quality control on gaps. In theory, when the gap between two components is higher than a certain limit (indicated by the top-level requirement v_{assy}), the assembly is considered non conform.

The gaps in aeronautical assembly can rise from three categories of errors, managed by specific tolerances: translation, orientation and flatness. These are listed in increasing order of importance of the effects on the structural performances, measured in terms of induced built-in stress. However, in this study we consider very tight tolerance intervals on the flatness (compared to positioning and orientation), so that the variability of the flatness defects can be considered to be sufficiently small such as not to have an impact on the global outcome.

Two different applications of built-in stresses are analyzed in the following: the wing root joint, in Section 7.4.1, and the joint between spar and cover (or skin) in an aircraft wing, in Section 7.4.2. In Fig. 7.10 we report an illustration of the wing structure from [Venkatesan et al., 2021]. This can allow the reader to localize the junctions which are going to be tested in the following sections.

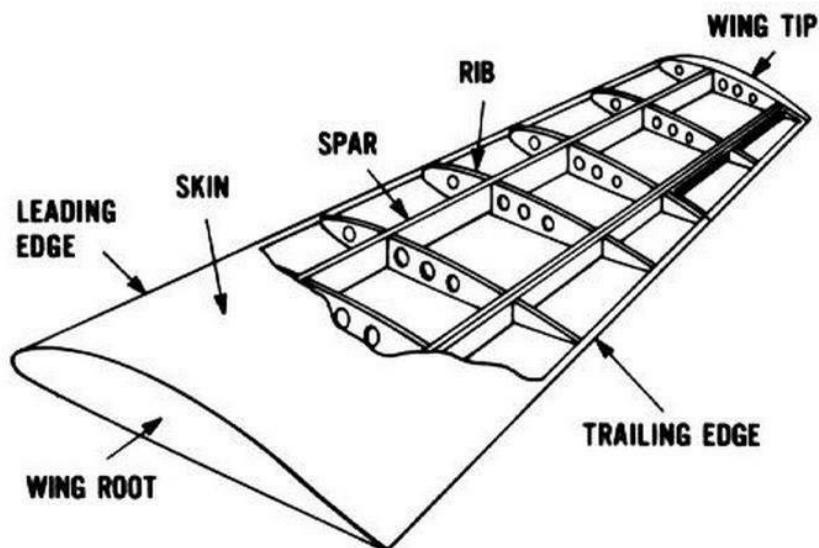


Figure 7.10: Illustration of wing components (Source: [Venkatesan et al., 2021])

7.4.1 Built-in stress examples: wing root joint

In this section we present an application of the proposed codesign framework to the tolerance-cost optimization of a fictitious wing root joint, i.e. the junction between the wing and the fuselage. In Fig. 7.11a, we provide a simplified sketch of the upper corner of the junction of the wing root. The connection is ensured via a cruciform structure, fixed to the fuselage on one side and to the wing on the other. In the following, we will focus our attention on the junction between the cruciform and the wing upper skin, considering the profiles of both parts to be perfectly planar.

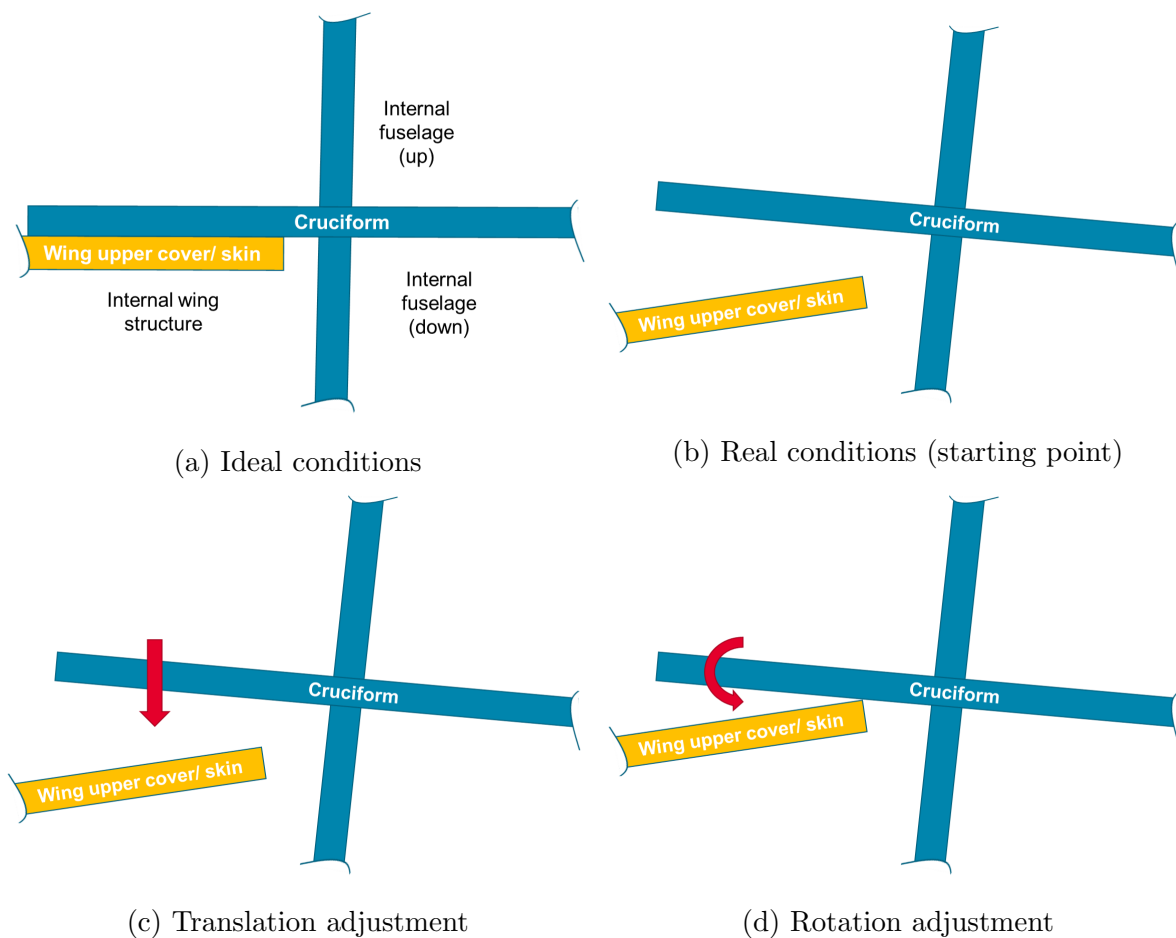


Figure 7.11: Gap closure on wing root joint (fastener between wing cover and cruciform not represented)

In Fig. 7.11a, the ideal positioning of both parts is reported. However, in real conditions, gaps may appear between the skin and the cruciform, leading to configurations as in Fig. 7.11b. In this case, two adjustments must be done: the first is a translation to impose the contact at one extreme (see Fig. 7.11c); the second is a rotation to close the gap on the other extreme (see Fig. 7.11d). These adjustments may give rise to built-in stresses. For large structures, it is possible to assume that the stresses induced by the translation can be neglected, compared to rotational adjustments. Then, we focus on the sizing of this section of the wing root joint, considering the isolated effect of the rotational component of gaps on the built-in stresses.

We introduced here the generalities of the problem of built-in stress on the wing root joint. In the following subsections, we will present the application of the codesign framework on the same example. In Section 7.4.1.1 we will introduce all the ingredients to properly formalize the mathematical problem. Next, we will present the results related to the applications of different tolerance optimization formulations on the wing root joint example: in particular, we discuss the results related to the application of the *current practice* in Section 7.4.1.2, the *codesign framework with fixed top-level requirement* in Section 7.4.1.3 and the *codesign framework with smart top-level requirement re-definition* in Section 7.4.1.4.

7.4.1.1 Mathematical formulation

In this section we define the full optimization problem from a mathematical point of view. We will start from the definition of the geometrical features at components and assembly level.

In Fig. 7.12, we report the reference systems used for evaluating the entity of the gaps. We start from the global system (see Fig. 7.12a): here the gaps are measured at the endpoints of the segment identifying the superposition of the two parts, using as reference a theoretical virtual plane (represented as a dotted green line in Fig. 7.12a). The components of the gaps are determined separately for the cruciform and the wing upper skin on the two endpoints. At the left extreme we obtain the components XA' and XA'' (related to respectively cruciform and wing), and on the right the equivalent XB' and XB'' . The quantities XA' , XA'' , XB' , XB'' constitute the geometrical features at component level, which can be described by tolerances on the parallelism error between the virtual plane and each of the two surfaces (i.e. a tolerance bound on the wing cover and another on the cruciform). However, the definition of the parallelism tolerance of each component goes beyond the scope of the present work.

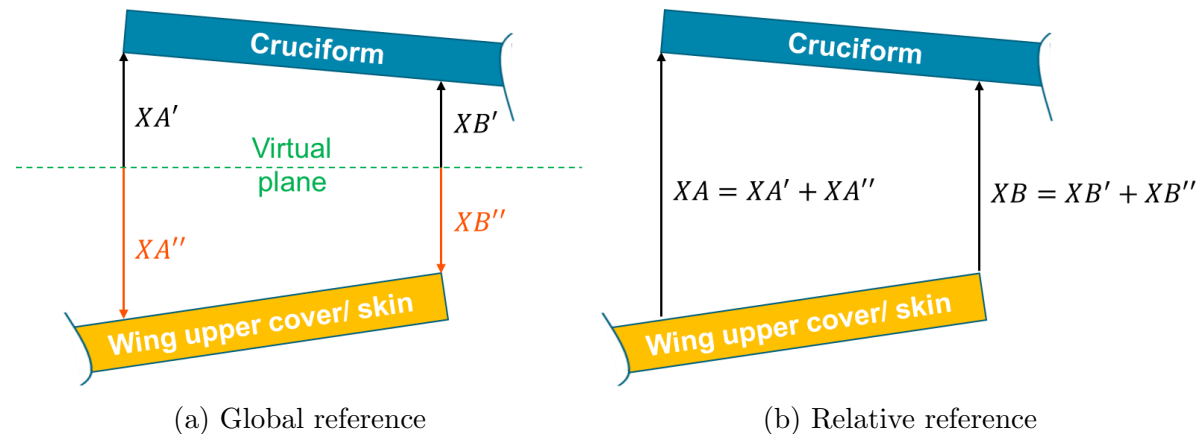


Figure 7.12: Representation of reference systems on wing root joint example (the arrows directions indicate the positive sign of the different geometrical features)

Now, in order to define the gaps, it is equivalent to switch to a reference system based on one of the components (the wing is picked in Fig. 7.12b), leading to the definition of only two relative distances $XA = XA' + XA''$ and $XB = XB' + XB''$. This system is consistent with the measurement data of the gaps from real structures. The random

variable defining the rotational component of the gap will be denoted as G and formalized as:

$$G = XA - XB = XA' + XA'' - XB' - XB'' \quad (7.25)$$

The tolerance model ρ , linking the component-level to the assembly-level geometrical features, gives in output the gap G itself:

$$\rho(XA', XA'', XB', XB'') = G = XA - XB = XA' + XA'' - XB' - XB'' \quad (7.26)$$

We assume here that all the component features XA', XA'', XB', XB'' are defined by the same tolerance bounds $v_{A'} = v_{A''} = v_{B'} = v_{B''} = v_{el}$: under the Gaussian assumption, this leads to generate four independent normal variables following the distribution $\mathcal{N}(0, \sigma_{el}^2)$ with $\sigma_{el} = v_{el}/3$.

We define also a random variable, related to the components features and characterized by the largest variability as $X_{orig} \sim N(0, 0.056^2)$ (in common for all features XA', XA'', XB', XB''). The component-related cost c_1 , representing the precision required in manufacturing steps for the component level features XA', XA'', XB', XB'' (4 overall), will be formalized as:

$$c_1(v_{el}) = \frac{1}{4} \sum_{i=1}^4 P(|X_{orig}| \geq v_{el}) = P(|X_{orig}| \geq v_{el}) \quad (7.27)$$

As anticipated in Section 7.3.3, we will not intervene here on the tolerance allocation between different components XA', XA'', XB', XB'' : for the purpose of this section, we will only follow the assumption that all these 4 component features share the same value v_{el} for their associated tolerance bounds, but the v_{el} will not be directly considered as the design variable. Instead, we will focus on the application of the codesign framework to identify the best parameters of the statistical distribution of the gap G . Therefore, we define the design variable $\mathbf{v} = v_g$ as the tolerance bound of the gap G : under the Gaussian assumption and supposing a zero mean gap, the tolerance bound v_g defines a normal distribution $G \sim \mathcal{N}(0, \sigma_g^2)$, with $\sigma_g = v_g/3$. In the following we will denote the random variable described by this distribution as $G(v_g)$.

We can relate the σ_g and v_g to σ_{el} and v_{el} , by considering the sum of the four independent normal variables intervening in the relation in Eq. 7.25:

$$\sigma_g = 2\sigma_{el} = 0.112 \quad v_g = 2v_{el} \quad (7.28)$$

Consequently, we can define a formulation of the cost c_1 equivalent to Eq. 7.27 and expressed as function of the design variable v_g :

$$c_1(\mathbf{v}) = c_1(v_g) = P(|G_{orig}| \geq v_g) \quad (7.29)$$

Where $G_{orig} \sim N(0, \sigma_g^2) = N(0, 0.112^2)$ (stemming from Eq. 7.28) represents the gap random variable with the largest variability.

The distribution of $G(v_g)$ will be filtered after the verification of the top-level requirement v_{assy} . The tolerance acceptance criterion at assembly level will only compare the absolute value of the realizations g of the gap $G(v_g)$ (which already constitutes the output

of the tolerance model) with the v_{assy} . The effect of the filtering induced by the top-level requirement v_{assy} is measured via the assembly-related non-quality cost c_2 , which represents the percentage of non-conform assemblies and can be formalized as follows:

$$c_2(\mathbf{v}, v_{assy}) = P[|G(v_g)| > v_{assy}] \quad (7.30)$$

Now we need to formalize the *PoE* for the wing root joint example. We define, at first the detrimental variable K_G due to the built-in stress induced by the fastener installation in presence of the gap G (which, we remind, constitutes only the rotational component of the gap). In particular, we suppose that the effects of G on the built-in stress S are symmetrical (i.e. G and $-G$ lead to the same result), and the stress S is linearly related to $|G|$:

$$S = k_1|G| + k_2$$

Where k_1 indicates the effect the rotational component G of the gap, while k_2 contains the effect of the translational component of the gap (considered as constant and neglectable with respect to the effect of the rotational component). The nominal stress, used in deterministic sizing will be:

$$S_{REF} = k_1 G_{REF} + k_2$$

Where G_{REF} represents the (positive) nominal value of the gap used for deterministic sizing. In particular, higher values of G_{REF} imply more constraining sizing which result into weight increases. The relation between the design variable v_g and the detrimental variable K_G can be therefore defined as:

$$K_G(v_g) = \frac{S_{REF}}{S(G(v_g))} = \frac{BG_{REF} + 1}{B|G(v_g)| + 1} \quad (7.31)$$

Where $B = k_1/k_2 = 100$ is a constant factor, arbitrarily fixed for explanatory purpose. The sizing gap G_{REF} will constitute our degree of freedom for the scenarios (denoted with I_{REF} in Section 7.3.4) on the structural requirements.

Furthermore, we consider also the variability of the strength, via the introduction of the detrimental variable K_R :

$$K_R = \frac{R}{R_{REF}} \quad (7.32)$$

From the definitions in Eq. 7.31 and Eq. 7.32, the effects of load amplification due to gaps and strength are cumulative in a multiplicative way, so the *PoE* can be determined from the definition of the detrimental variables in the form of Eq. 7.15.

The top-level requirement v_{assy} acts, in this case, as a filter of the gap realizations and thus affect structural performances. The *PoE* will also be affected by the filtering from v_{assy} , leading to a declination of the *PoE* as in Eq. 7.20:

$$PoE(\mathbf{v}, v_{assy}; I_{REF}) = PoE(v_g, v_{assy}; G_{REF}) = P \left[K_G(G(v_g)) K_R \leq 1 \mid |G(v_g)| \leq v_{assy} \right] \quad (7.33)$$

If not differently specified, we impose on the semi-probabilistic constraint, by default, the limit $\overline{PoE} = 0.01$ and the 1st percentile of R as R_{nom} in the K_R definition. As a reminder, the PoE constraint is not included in *current practice*, but the outcomes are analyzed post optimization.

Before introducing the results of the different formulations of the tolerance optimization problem, we need to highlight what we are looking for. The only random variables - which are introduced in the wing root joint example - are the strength R and the gap G . This latter constitutes the output of the tolerance model, and its statistical distribution is a centered normal distribution described by the tolerance bound v_g (which leads to the standard deviation σ_g of G via the relation $\sigma_g = v_g/3$). In a successive step, the top-level requirement v_{assy} truncates this distribution at $\pm v_{assy}$, via the tolerance acceptance criterion (i.e. $|G| \leq v_{assy}$). In practice, we are going to optimize (using the costs c_1 and c_2 as ranking criteria) the parameters of the distribution of G after the filtering induced by the tolerance acceptance criterion. Note that we can do this also *without* the knowledge of the tolerance model itself, as we work directly with its output (in this case the gap G). Within this perspective, we can keep the tolerance allocation (among the individual components) to the internal activities of the tolerance team: as a result, from the proposed semi-probabilistic codesign framework, they will receive as inputs the most favorable feasible combinations of standard deviation (induced by the tolerance bound v_g) and top-level requirement v_{assy} which satisfy the semi-probabilistic stress constraint. This separation of activities can be more suitable for design processes, like the wing root joint example, which are well established in the culture of the aeronautical industry.

In the following sections, we present the results related to the applications of different tolerance optimization formulations on the wing root joint example. In particular, we discuss the results related to the application of the *current practice* in Section 7.4.1.2, the *codesign framework with fixed top-level requirement* in Section 7.4.1.3 and the *codesign framework with smart top-level requirement re-definition* in Section 7.4.1.4.

7.4.1.2 Results for *current practice*

In this section, we report the results related to the application of *current practice* on the wing root joint example. The optimization problem can be formalized as:

$$\begin{aligned} \min_{v_g} \quad & c_1(v_g), c_2(v_g; v_{assy}) \\ \text{s.t.} \quad & 0.05 \leq v_g \leq 0.35 \end{aligned} \tag{7.34}$$

As a reminder, the top-level requirement v_{assy} is defined in such a way that no excessive built-in stresses can ever appear. Therefore, it is defined here on a *worst-case scenario* basis and equal to the sizing gap, thus $v_{assy} = G_{REF}$: this means that all possible realizations of the gap going beyond G_{REF} (which would lead to excessive built-in stresses) are automatically filtered through the verification of the top-level requirement v_{assy} (i.e. when $G \geq v_{assy}$). Therefore, there is no chance that detrimental configurations (i.e. $G \geq G_{REF}$) could appear. For this reason, no semi-probabilistic constraint is applied, as the stress constraint is already taken into account by the assumption $v_{assy} = G_{REF}$. The results are depicted in Fig. 7.13.

In the Pareto front (see Fig. 7.13a) the results related to different scenarios of the sizing gap G_{REF} are reported, representing the sets of optimal solutions in terms of

the two objective functions c_1 (on the abscissa axis) and c_2 (on the ordinate axis). We may notice that the shape is convex and the extreme points of both costs c_1 and c_2 can be reduced when increasing the sizing gap. In fact, by considering higher values for the nominal G_{REF} , we generate a heavier structure, capable to support higher built-in stresses: as a consequence, as the top-level requirement is always strictly equal to the sizing gap G_{REF} , we leave more freedom to the tolerance optimization.

Another parallel analysis is needed to evaluate the results in terms of the optimal design variable v_g as a function of the $v_{assy} = G_{REF}$, reported in Fig. 7.13b. Despite v_g being the dependent variable in this representation, it is reported on the abscissa axis to reflect the same sensitivity as in the Pareto front: going from left to right, we move towards higher v_g , which imply a reduction in c_1 and an increase in c_2 .

We may observe on Fig. 7.13b that, for all levels of the sizing gap G_{REF} , we can reach the highest allowed values of v_g . By comparing the corresponding region (on the right) of the Pareto front, we retrieve progressively reduced maximum costs c_2 . In fact, this is not due to the sizing gap G_{REF} itself, but more to the top-level requirement v_{assy} linked by identity to G_{REF} : by increasing v_{assy} we may reduce the cost c_2 , while maintaining the same v_g . This explains the reduction of the maximum value of the cost c_2 on the Pareto front with progressively higher sizing gaps.

On the opposite side, we may notice that the minimum extreme values of v_g in Fig. 7.13b increase when increasing the sizing G_{REF} , thus attenuating the maximum cost c_1 on the Pareto front. From Fig. 7.13a it is visible that for these points we get the extreme condition $c_2 = 0$: the convergence towards zero c_2 is accelerated (i.e. it arrives for higher v_g) when we increase v_{assy} . This explains the reduction of the maximum value of the cost c_1 on the Pareto front with progressively higher sizing gaps.

On a further analysis we report the effects of optimal c_2 (treated as an a priori fixed budget) on the optimal v_g . To extract these results, we interpolate the evolution of the optimal v_g as a function of the related optimal cost c_2 for different scenarios of G_{REF} (and corresponding v_{assy}), as reported in Fig. 7.13c. The outcomes of this interpolation are then exploited to evaluate the effects of the sizing gap G_{REF} on the tolerance results. This constitutes the actual interface between tolerance and structural fields, illustrated for the wing root joint example in Fig. 7.13d. The points are extracted at fixed points of interest \bar{c}_2 of the optimal cost c_2 : we indicate with the same color the points extracted at the same values of \bar{c}_2 . This latter may be regarded as a budget on the cost c_2 which we are allowed to spend: this would be equivalent to treating the multi-objective optimization via the constraint method, i.e. solving the single-objective minimization of c_1 , while constraining $c_2 \leq \bar{c}_2$.

Focusing on the behavior of the optimal v_g in the iso- c_2 results plot (in Fig. 7.13d), we notice a slight increase with respect to the sizing nominal gap G_{REF} . In this specific framework coming from *current practice*, the variation is not driven directly by the *structural* requirement, but rather by the associated *geometrical* top-level requirement v_{assy} . As a consequence of the sensitivities highlighted in Section 7.3.2, c_2 increases with an increase of v_g and a decrease of v_{assy} : therefore, to reach the same level of c_2 , an increase of v_{assy} leads to the possibility to increment the corresponding v_g . Now, as in *current practice* we make the assumption $v_{assy} = G_{REF}$, the final evolution of the optimal v_g as a function of G_{REF} will be monotonic and increasing for fixed levels \bar{c}_2 of the cost c_2 .

In Fig. 7.14 we report the post-optimization evaluations of the *PoE* for different

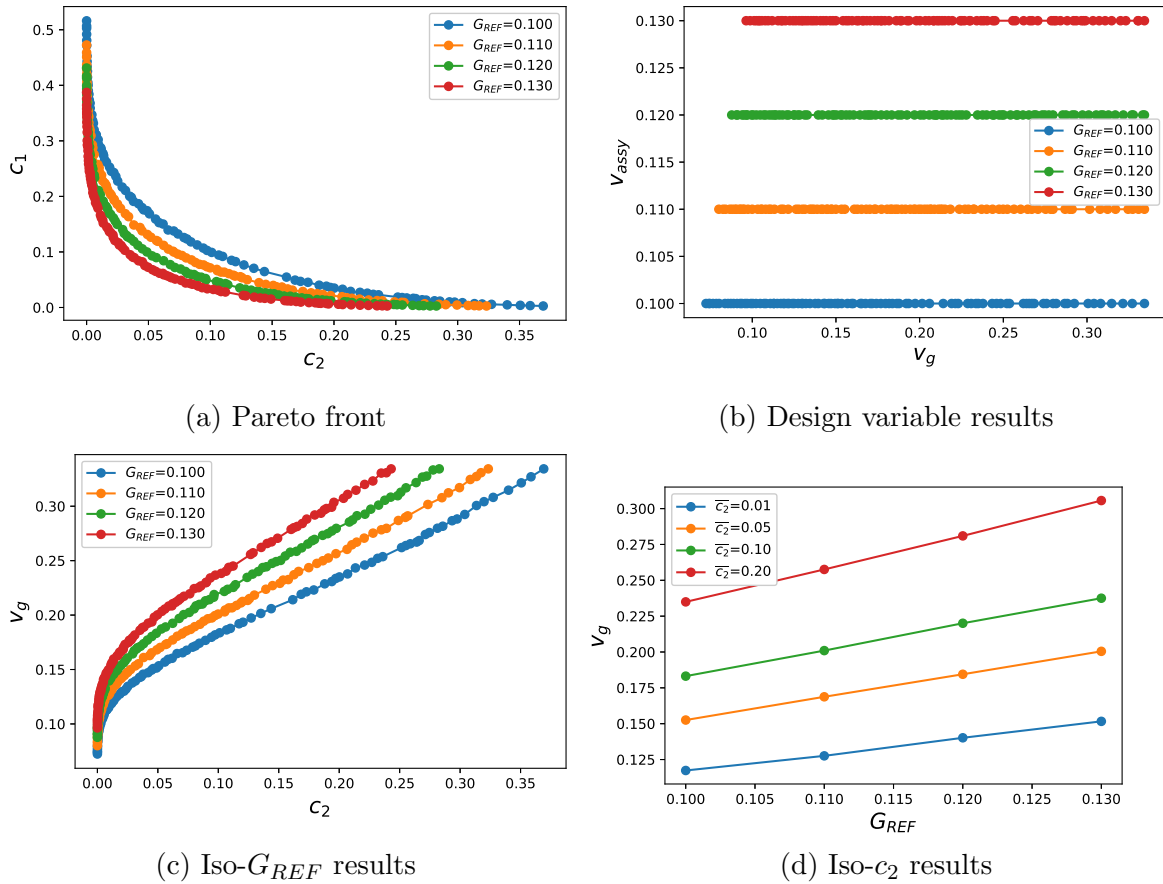


Figure 7.13: Wing root joint example: results of optimization with *current practice*

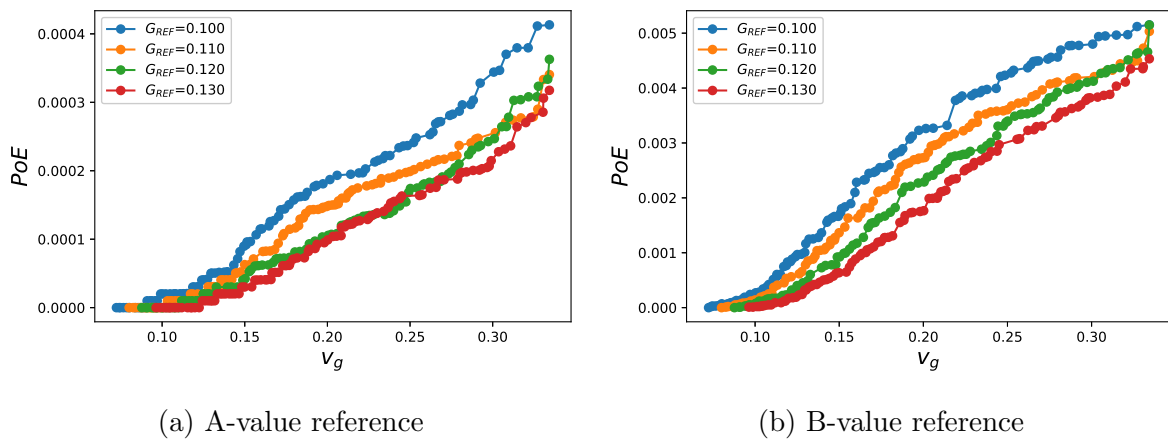


Figure 7.14: Wing root joint example: PoE results post-optimization with *current practice* for two reference quantiles on strength R

settings of G_{REF} and depicted as functions of the optimal v_g . We may confirm that the PoE actually increases by increasing v_g (as increasing the input variability leads to higher amounts of detrimental realizations) or decreasing G_{REF} (as it becomes easier for the structure the overcome a lower threshold on the built-in stress). Note that in the examples retained here, the maximum PoE is lower than the respective references

($\overline{PoE} = 0.01$ in Fig. 7.14a and $\overline{PoE} = 0.1$ in Fig. 7.14b): this implies that by setting $v_{assy} = G_{REF}$ for the sake of conservativeness, the semi-probabilistic constraint would not be active. This also highlights the space left for improvement, by reducing this over-conservativeness as we will investigate in the following two subsections.

In order to graphically illustrate the comparison between different formulations, we represent the optimized tolerance intervals on the variables XA and XB (cf. Fig. 7.12b). An example of illustration of the tolerance plan is depicted in Fig. 7.15. Note that the re-allocation on the components XA and XB , together with the definition of the tolerance plans, is traditionally part of the internal activities of the tolerance teams: here we propose a simplistic re-allocation, based on the assumption that the tolerances associated to XA and XB are the same. As a reminder, the design variable of the wing root joint problem is the definition of the tolerance bound v_g of the gap G , which constitutes the output of the tolerance model: this allows to maintain separated the internal activities of tolerance and stress design teams. The following analysis is proposed to illustrate what *would be* the impact of the proposed codesign framework (in the next sections) on the tolerance plans.

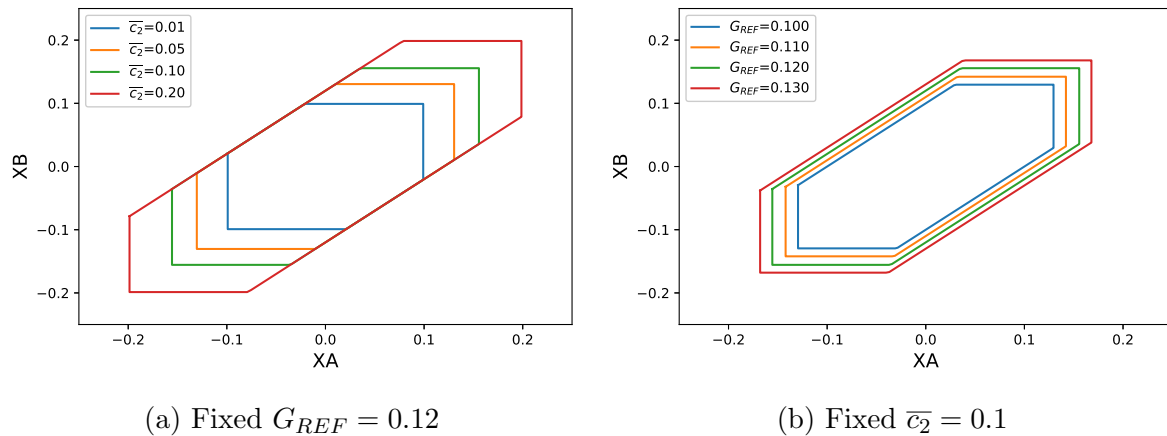


Figure 7.15: Wing root joint example: representation of results from optimization with *current practice* at fixed sizing gap G_{REF} and budget $\overline{c_2}$

The resulting tolerance plot related to each individual combination of the variables v_g and v_{assy} is an hexagon enclosed by: two vertical segments defining the lower and upper bounds of XA , two horizontal segments defining the lower and upper bounds of XB and two oblique segments defining the limits imposed by the top-level requirement $|G(v_g)| = |XA - XB| < v_{assy}$. According to the obtained tolerance plan, all configurations of XA and XB inside this hexagon will be considered as acceptable. We are considering here a symmetrical acceptance criterion to verify the alignment with top-level requirement, given by the absolute value of the gap G : this implies that the oblique segments will be symmetric with respect to the first bisector.

The main interest is to enlarge this hexagon via an increase of either the top-level requirement (to augment the distance between the oblique segments) or the tolerance bounds on the elements XA (to increase the distance between the vertical segments) and XB (on the horizontal segments). As in the explanatory applications introduced in the following we only consider the distribution of the random gap $G \sim \mathcal{N}(0, \sigma_g^2)$

with $\sigma_g = v_g/3$, the re-allocation on XA and XB is simplified by associating the same distribution to both of them. From the definition of the gaps $G = XA - XB$, we can re-allocate the standard deviations $\sigma_{XA} = \sigma_{XB} = \sigma_g/\sqrt{2}$ and the tolerance bounds $v_{XA} = v_{XB} = v_g/\sqrt{2}$. In the hexagonal tolerance plot, this assumption implies that the vertical and the horizontal segments are placed at the same distance from respectively the ordinate and the abscissa axes.

In Fig. 7.15 we represent the effects of the variations of the sizing gap G_{REF} and of the budget \bar{c}_2 on the upper-mentioned hexagonal diagrams.

As stated before, when fixing the sizing G_{REF} , an increase of \bar{c}_2 allows to increment the optimal v_g , as depicted in Fig. 7.15a. Since in the *current practice* $v_{assy} = G_{REF}$, the oblique segments are not moved. At the same time, the horizontal (related to XB margins) and vertical (related to XA margins) segments are generally furthered from the origin, led by the increase of v_{XA} and v_{XB} . Moreover, in the special case of equal re-allocation between XA and XB tolerances, the translations are done with the same distance on horizontal and vertical axes.

In parallel, when fixing the budget \bar{c}_2 on the cost c_2 , an increase of the sizing G_{REF} induces an augmentation in the optimal v_g . In the tolerance hexagonal diagram, this causes an increase of the distances between all segments of the contour, as illustrated in Fig. 7.15b: the oblique segments are furthered from the origin as a consequence of the increase of $v_{assy} = G_{REF}$; the vertical and horizontal borders, led respectively by v_{XA} and v_{XB} , are moved outwards because of the increase of v_g .

The results presented in this section constitute a baseline to understand, evaluate and compare against the outcomes of our codesign framework, which are exposed in the next sections.

7.4.1.3 Results for codesign framework with fixed top-level requirement

In this section we analyze the application of the *codesign framework with fixed top-level requirement* on the example of the wing root joint. The optimization problem is formulated in Eq. 7.23. In this setting of the proposed framework, we dissociate the sizing G_{REF} from the top-level requirement v_{assy} , fixing this latter as an input scenario, prior to the optimization. As can be intuited from the previous section, the interest lies in the scenarios with $v_{assy} > G_{REF}$, to be able to enlarge the tolerance domain. The only design variable in this variant of our proposed framework is given by the tolerance level of the gap v_g . The complete problem can be formulated as:

$$\begin{aligned} \min_{v_g} \quad & c_1(v_g), c_2(v_g; v_{assy}) \\ \text{s.t.} \quad & PoE(v_g; v_{assy}, G_{REF}) \leq 0.01 \\ & 0.05 \leq v_g \leq 0.35 \end{aligned} \tag{7.35}$$

Where the quantities c_1, c_2 and PoE are computed respectively via Eqs. 7.29, 7.30 and 7.33. The main results are illustrated in Fig. 7.16 for two values of the nominal sizing gap G_{REF} : in particular we report the Pareto front, the optimal design variables and the PoE outcomes.

The Pareto fronts related to $G_{REF} = 0.1$ is depicted in Fig. 7.16a for different scenarios of the top-level requirement v_{assy} . First of all, the results related to $v_{assy} \leq$

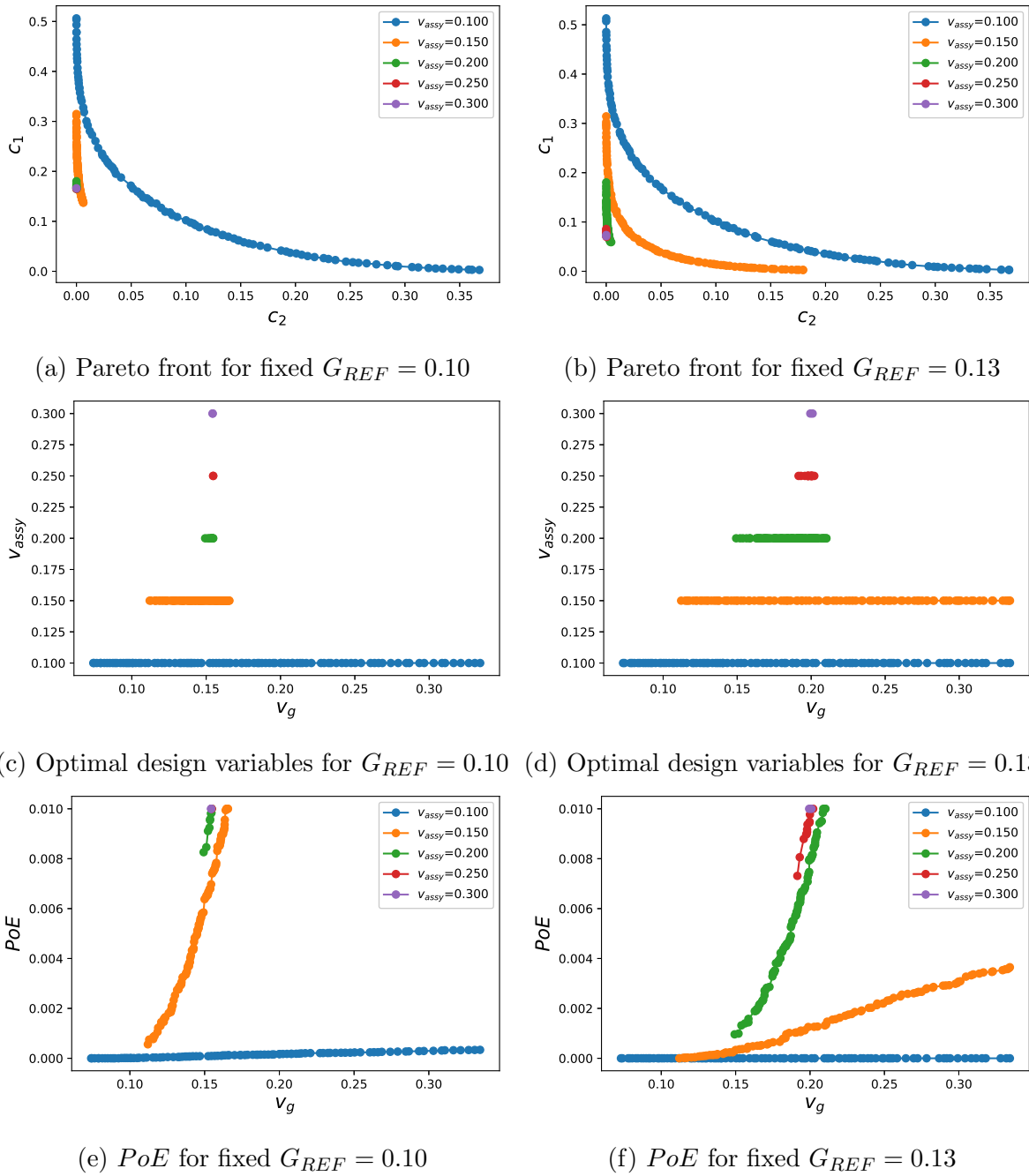


Figure 7.16: Wing root joint example: representation of results from optimization with codesign framework at fixed top-level requirement v_{assy} and sizing gap G_{REF}

G_{REF} (specifically in this analysis $v_{assy} = 0.1$) are unchanged with respect to the outcomes from the previous section, as the PoE constraint is not active. On the other hand, the other Pareto fronts in the same pictures appear as cut from below on the c_1 axis. To explain this phenomenon, we should focus on the right side of the plots in Figs. 7.16a-7.16c-7.16e. The reason behind this phenomenon can be understood by starting from the evolution of the PoE with respect to the design variable v_g in Fig. 7.16e. All curves are monotonic and increasing with respect to v_g , as expected. But for the same v_g , if

we increase v_{assy} , we accept more gap realizations (which pass the quality check as the requirement becomes less restrictive) which are in fact detrimental for the structural performances, thus increasing the PoE . The direct result is that we reach the saturation point $PoE = \overline{PoE}$ for lower and lower values of v_g as we increase v_{assy} . This is reflected on the set of acceptable solutions (depicted in Fig. 7.16c for $G_{REF} = 0.1$), where the upper bound of v_g is progressively pushed towards left. This latter leads finally to cutting from below the Pareto fronts and preventing better minimizations of the cost c_1 .

The conclusions drawn up to this point in this section could seem counter-intuitive, as we would be brought to think that by allowing a larger (more relaxed) top-level requirement, we could help the tolerance optimization and allow larger tolerance intervals. This intuitive reasoning could only work if the PoE constraint on the structural performances is not active (or not imposed at all, as done in *current practice*).

Focusing then on the left side of the plots in Figs. 7.16a-7.16c-7.16e, we can draw the same conclusions than the ones from the previous section, concerning the evolution of the lower bounds of the optimal v_g : the limit $c_2 = 0$ can be attained progressively sooner (i.e. for larger v_g) as we increase v_{assy} . Combining the conclusions from upper and lower bounds, we expect (and it is confirmed in Fig. 7.16c) a progressive reduction of the interval of optimal solutions v_g with the increase of the top-level requirement. A particular extreme case can be found on the set of solutions related to $v_{assy} = 0.3$: here the Pareto front is constituted by a single point, thus the conclusions about the upper bounds dominate (as the upper limits are ruled by the PoE constraint).

At this point, we can compare the results from Figs. 7.16a-7.16c-7.16e, related to $G_{REF} = 0.1$ with the ones in Figs. 7.16b-7.16d-7.16f, related to $G_{REF} = 0.13$. Previewing a more conservative (i.e. higher) G_{REF} , the probability of exceeding the nominal structural requirement decreases, with the same tolerance settings. Therefore, the PoE curves are lowered, the saturation point $PoE = \overline{PoE}$ is delayed to higher v_g , the upper bounds of the optimal solutions v_g are pushed towards right and the cut of the Pareto front is attenuated.

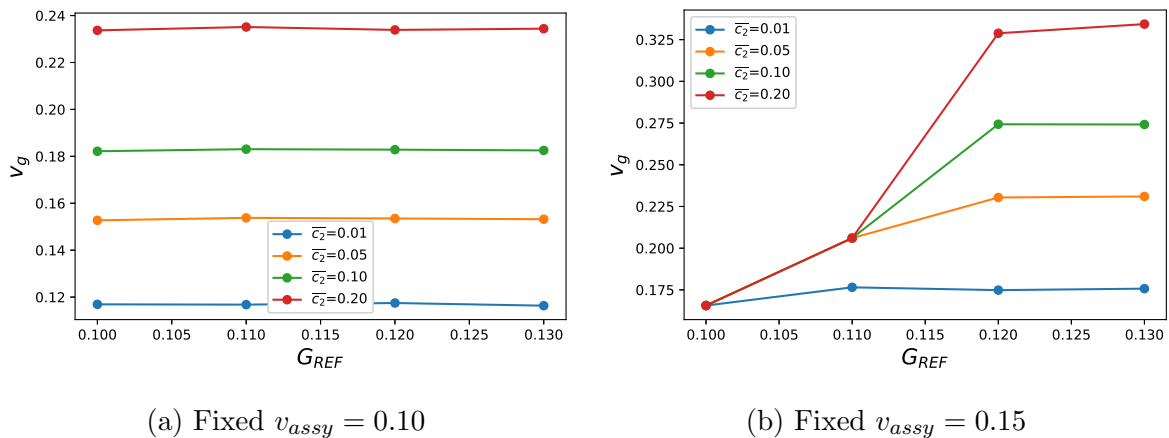


Figure 7.17: Wing root joint example: evolution of results from optimization with code-sign framework with respect to the sizing gap G_{REF} for two top-level requirements v_{assy}

At this point, we re-extract the results in a similar way as done in the previous section. We report in Fig. 7.17 the evolutions of the optimal v_g as function of the nominal sizing

gap G_{REF} , for two different scenarios of v_{assy} and regrouping the points extracted at the same levels of the budget \bar{c}_2 .

In the first case, for $v_{assy} = 0.1$ (in Fig. 7.17a), we do not observe any variation of v_g with respect to G_{REF} . Here the PoE constraint is not active: therefore, we would expect the same evolution of the curves as for the case with *current practice*. However, in our codesign framework we dissociate the notions of the geometrical top-level requirement v_{assy} from the sizing gap G_{REF} . If the v_{assy} is fixed, the relation between v_g and c_2 is bijective (as long as v_g is a scalar): therefore, for the same fixed budget \bar{c}_2 of c_2 , we have a unique solution in terms of v_g , independently from the prescribed sizing gap. Then, by increasing the budget \bar{c}_2 , we may increase the value of v_g .

On the other hand, for $v_{assy} = 0.15$, we need to explain the results depicted in Fig. 7.17b by starting from some considerations on the PoE and the budget \bar{c}_2 . The PoE constraint acts by limiting the sets of available solutions v_g on low sizing gaps G_{REF} . This means that even when allowing a high budget \bar{c}_2 , we can not use all of it, as the Pareto front is cut beforehand (as shown in Figg. 7.16a-b). Therefore, as we reach the saturation point on the structural constraint $PoE = \overline{PoE}$ progressively later (i.e. higher v_g) when increasing G_{REF} , the plots of v_g as a function of G_{REF} tend to increase for low G_{REF} and then stabilize for high G_{REF} , when maintaining the same budget \bar{c}_2 . Switching from one curve to the other in Fig. 7.17b, when increasing the \bar{c}_2 , the saturation point is delayed towards higher G_{REF} . The extreme case is given by $\bar{c}_2 = 0.01$: here we are situated in fact in the left regions of the Pareto fronts, which are not affected by the PoE constraint.

Specifically for the *codesign framework with fixed top-level requirement*, we can interpret the results of the evolution of v_g as a function of G_{REF} from another perspective: we can fix the budget \bar{c}_2 and reproduce the evolution for different scenarios of v_{assy} , as reported in Fig. 7.18. Coherently with the results described above, for $v_{assy} = 0.1$, the PoE constraint is never active, making the problem purely geometric and no variations can be appreciated with variable G_{REF} . For $v_{assy} = 0.15$ and low $\bar{c}_2 = 0.01$ the PoE constraint is not active, leading to a constant value of v_g with variations of G_{REF} . On the other hand, for $v_{assy} = 0.15$ and $\bar{c}_2 = 0.1$, we reach the saturation point $PoE = \overline{PoE}$ for configurations $c_2 < 0.1$, preventing further reductions of c_1 (and thus increases of v_g): this phenomenon is enhanced for low G_{REF} . If we further increase v_{assy} the saturation point (and the consequent cut in the Pareto front) arrives for lower and lower values of v_g : for $v_{assy} \geq 0.25$ the evolutions are the same for the two retained \bar{c}_2 scenarios, as the Pareto front is cut at $c_2 < 0.01$ for all imposed G_{REF} . Moreover, we confirm the observations drawn on the link between the optimal v_g and v_{assy} scenarios: the application of the semi-probabilistic constraint disrupts the intuitive consideration that higher top-level geometrical requirements can systematically help to enlarge the tolerance bounds at component level.

7.4.1.4 Results for full codesign framework (with smart top-level requirement re-definition)

In this section, we apply the full codesign framework to the wing root joint example. As a reminder, we introduce among the design variables the gap tolerance limit v_g and the top-level requirement v_{assy} . The problem statement is formalized as in Eq. 7.24:

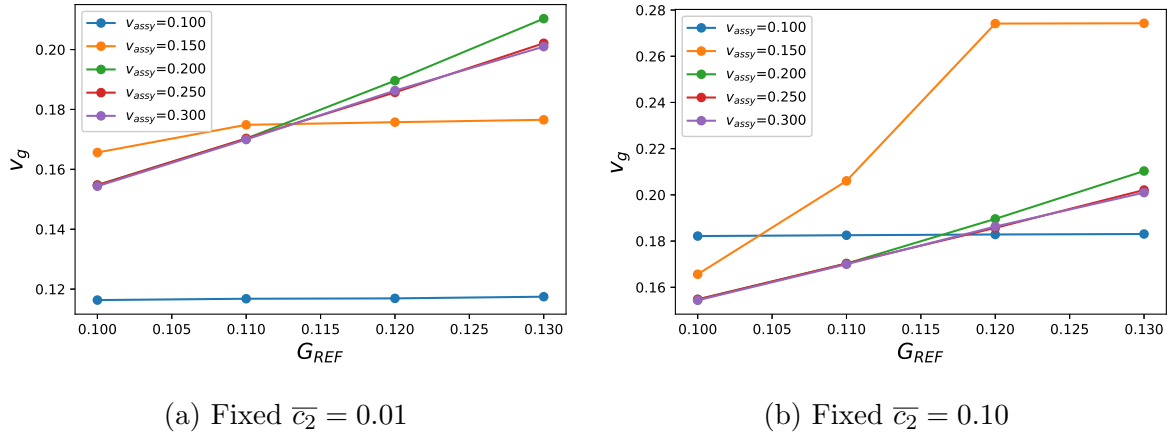


Figure 7.18: Wing root joint example: evolution of results from optimization with code-sign framework with respect to the sizing gap G_{REF} for two fixed budgets \bar{c}_2

$$\begin{aligned}
 \min_{v_g} \quad & c_1(v_g), c_2(v_g, v_{assy}) \\
 \text{s.t.} \quad & PoE(v_g, v_{assy}; G_{REF}) \leq 0.01 \\
 & 0.05 \leq v_g \leq 0.35 \\
 & 0.1 \leq v_{assy} \leq 0.7
 \end{aligned} \tag{7.36}$$

The optimization results are reported in Fig. 7.19 for different settings of G_{REF} : in particular, we report the Pareto front, the optimal design variables and the extraction of the optimal v_g and v_{assy} for fixed scenarios of the sizing gap G_{REF} and the budget \bar{c}_2 on the cost c_2 .

From the Pareto front in Fig. 7.19a, we may observe that there is no cut similar to the one seen in the previous subsection, and for both costs we can asymptotically reach the limit to zero cost. With respect to the results depicted in Section 7.4.1.2 related to the application of *current practice*, both costs can be significantly reduced.

Focusing on the plot of the optimal design variables in Fig. 7.19b, we obtain a decreasing evolution of the optimal v_{assy} with respect to the optimal v_g , and vice versa. Two asymptotic behaviors can be retrieved: the vertical one indicates the minimum v_g below which it is not relevant to consider a specific v_{assy} to ensure the structural semi-probabilistic constraint; the horizontal asymptote constitutes the analogue for v_{assy} . Since the vector of the design variables is 2-dimensional, the set of solutions corresponds to the boundary induced by the PoE constraint: therefore, the semi-probabilistic constraint will always be active for all optimal points. When increasing the prescribed G_{REF} , this boundary can be moved towards higher (thus more convenient) v_g and v_{assy} . The described evolution of the link between optimal v_g and v_{assy} and the translation with variations of G_{REF} are consistent with the conclusions drawn in the previous section.

A specific remark should be done on the optimal points situated on the vertical asymptote. All these points exhibit $c_2 \approx 0$, with differences which are below the machine precision: consequently, their exact positions (in ordinate axis, i.e. v_{assy}) can not be determined via an optimization algorithm where v_{assy} itself is a design variable. However, we can retain the asymptotic behavior and the upper bound $v_{assy,UB}$. Moreover, we

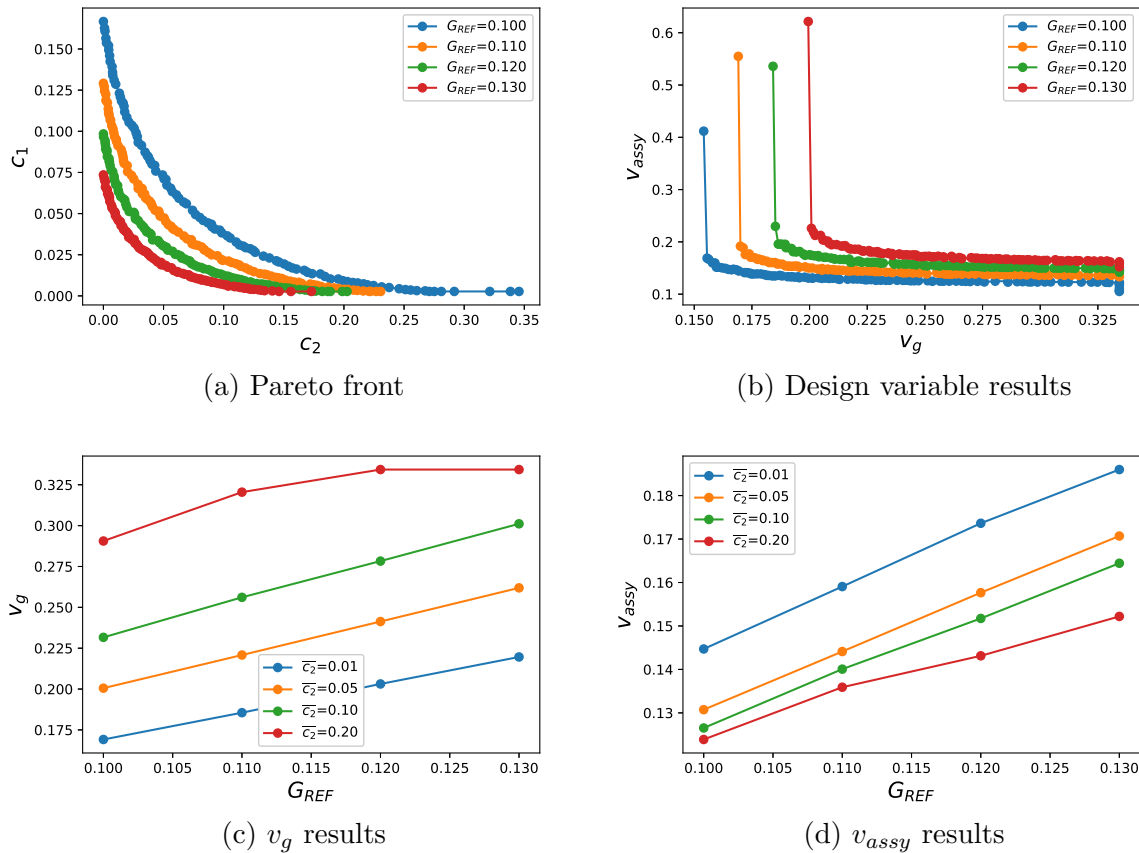


Figure 7.19: Wing root joint example: results of optimization with *full codesign framework*

remind that the upper bound should be determined to prevent any structural disruption which would be too severe to be tolerated for both design and operations, independently from the probability of occurrence.

From the evolutions of v_g and v_{assy} as functions of G_{REF} depicted in Fig. 7.19c-d, it can be observed that for a fixed budget c_2 we can enlarge the tolerance plans (in terms of both v_g and v_{assy}) by increasing G_{REF} . This is a direct consequence of the upper-mentioned translation of the boundary with variations of G_{REF} . Moreover, when increasing the budget \bar{c}_2 we can increase v_g , at the cost of a reduction of the correspondent v_{assy} , as a consequence of the sensitivities of the cost c_2 with respect to the design variables. Note that for the highest $\bar{c}_2 = 0.20$ we reach a constant value of v_g : this saturation is not due to a specific point with $PoE = \overline{PoE}$ (as for the whole sets of solutions the PoE constraint is always active), but rather because we simply reach the upper bound of v_g defined in our bounds constraints in Eq. 7.24.

We may analyze, at this point, the obtained results also on the hexagonal plot on the plane XA/XB described in Section 7.4.1.2. The outcomes of this analysis are reported in Fig. 7.20, for fixed levels of \bar{c}_2 and G_{REF} . As a reminder, the dimensions XA and XB constitute the coordinates of the endpoints of the perfectly straight segment illustrated in Fig. 7.12b, from which the gap random variable G is obtained as a difference between the two. The horizontal and the vertical segments of the boundary are defined by v_g ,

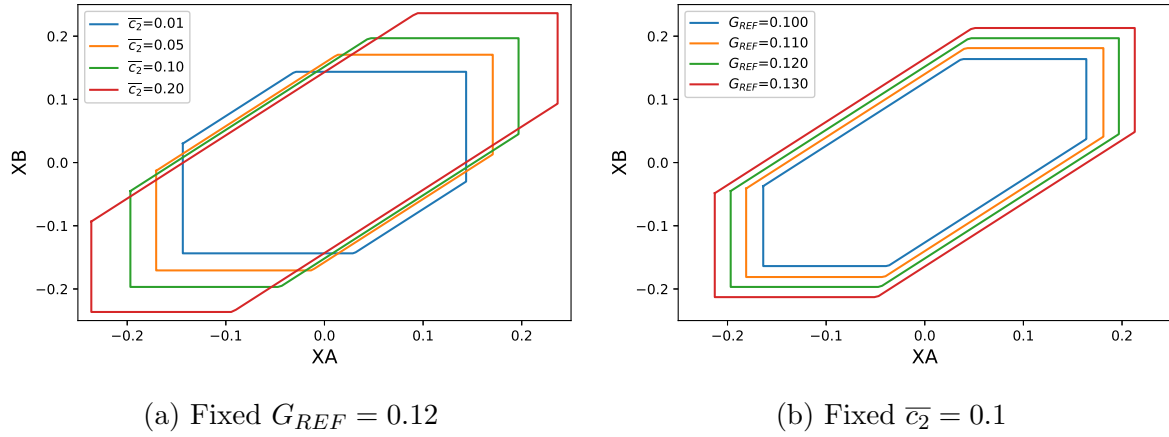


Figure 7.20: Wing root joint example: representation of results from optimization with full codesign framework at fixed \bar{c}_2 and sizing gap G_{REF}

while the top-level requirement v_{assy} defines the distance between the oblique segments.

When fixing the sizing gap, we obtain progressively larger hexagonal plots by increasing \bar{c}_2 . Conversely to what happens for *current practice*, the top-level requirement v_{assy} is not equal to G_{REF} and thus v_g is not the only design variable which evolves in the Pareto front: therefore, the variations of the tolerance plot are not restricted to the horizontal and vertical segments, but also to the oblique ones. However, considering the boundaries induced by the *PoE* constraint on v_g and v_{assy} and the sensitivities of c_2 , if \bar{c}_2 increases, then v_g will increase but v_{assy} decreases. Overall, increasing \bar{c}_2 leads to push outwards the horizontal and vertical segments while pulling inwards the oblique ones. The variation on these latter reaches an asymptotic behavior for high \bar{c}_2 .

On the other hand the evolution of the hexagonal plot at fixed \bar{c}_2 for different scenarios G_{REF} is the same that can be retrieved for *current practice*. All segments of the boundary plot are pushed outwards when increasing the G_{REF} . However, the explanation is not the same: for *current practice*, we simply have $v_{assy} = G_{REF}$ fixing the oblique segments; for the full codesign framework, the evolution of v_{assy} is a consequence of the translation (due to G_{REF}) of the boundary induced in the design variable domain by the *PoE* constraint.

Finally, we compare the outcomes of tolerance optimization results issued from different formulations of the semi-probabilistic constraint. In particular, we compare the effect of the inclusion of the strength variability in the *PoE* formulation and the limit \overline{PoE} . We report in Fig. 7.21 the results related to five formulations, denoted by:

- "No R (A-value)": no variability in R considered and $\overline{PoE} = 0.01$, leading to the constraint $PoE = P[K_G < 1] \leq 0.01$;
- "No R (B-value)": no variability in R considered and $\overline{PoE} = 0.1$, leading to the constraint $PoE = P[K_G < 1] \leq 0.1$;
- "With R (A-value)" (default option): variability in R explicitly considered and $\overline{PoE} = 0.01$, leading to the constraint $PoE = P[K_G K_R < 1] \leq 0.01$;
- "With R (B-value)": variability in R explicitly considered and $\overline{PoE} = 0.1$, leading to the constraint $PoE = P[K_G K_R < 1] \leq 0.1$;
- "Current": *current practice*, hence no *PoE* constraint.

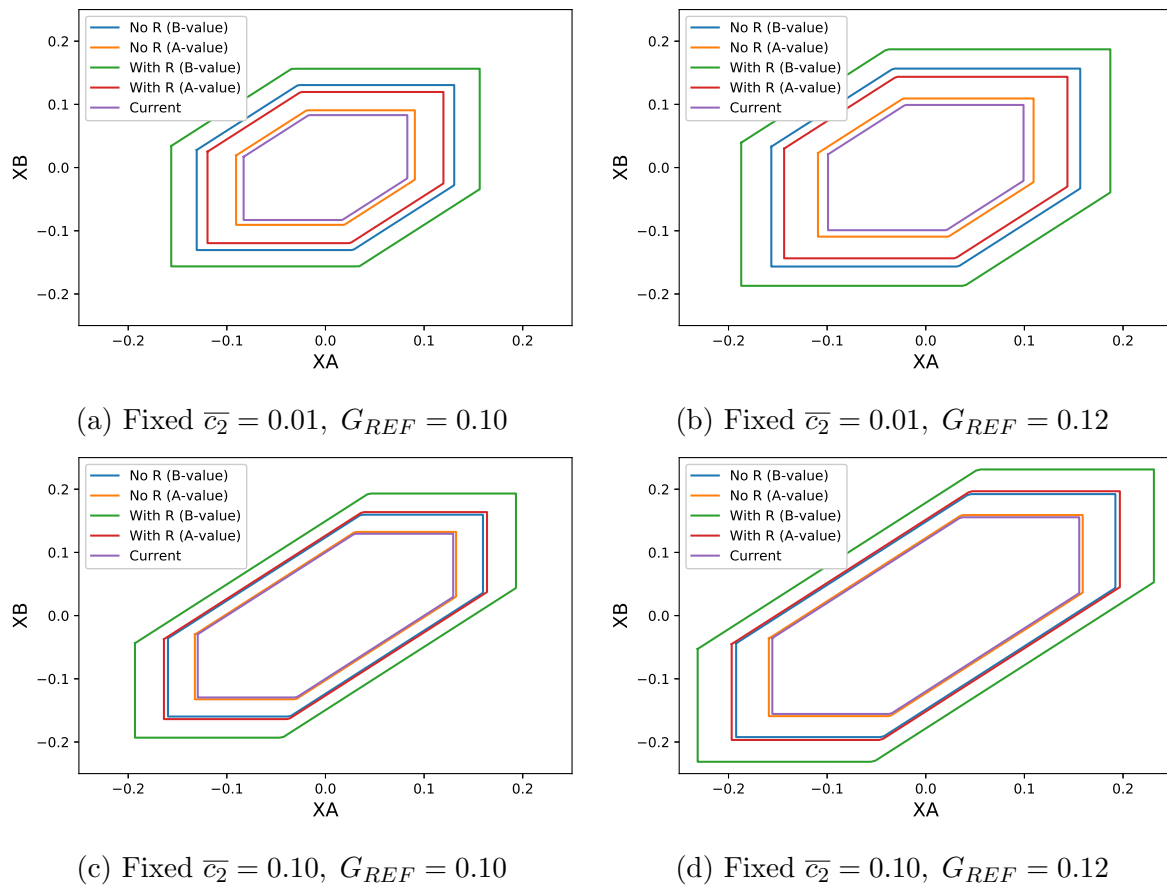


Figure 7.21: Wing root joint example: comparison of optimization results with different formulations of the *full codesign framework* and *current practice*

We extracted the results for two levels of \bar{c}_2 and two levels of G_{REF} . It can be observed that the first option, without R variability and $\overline{PoE} = 0.01$ leads to approximately the same results as the *current practice*. All other formulations of the *PoE* constraint lead to major gains in the extension of the hexagonal plot. The consideration of R variability proves to reduce the (over-)conservativeness of the analogue formulations for both fixed quantile levels. For high \bar{c}_2 we can also observe that the boundary plot related to the option "With R (A-value)" are larger than the ones related to the option "No R (B-value)": therefore, this implies that explicitly considering the variability of the strength R can be more convenient than increasing the quantile level.

From the hexagonal plots results, we can finally draw the conclusion that, for any of the formulations of the *PoE* constraint analyzed in this section, the proposed full codesign framework allows to significantly enlarge the tolerance domains.

Finally, from the formulation of the *full codesign framework*, we can derive all other formalizations. The results are consistent when passing from one formulation to the other.

7.4.2 Built-in stress results: spar2cover

In this second test case, we focus on an analogue example on the junction between spar and cover skin in a wing airframe. In Fig. 7.22, we illustrate the junction, together with the reference system and the adjustment to close the gap.

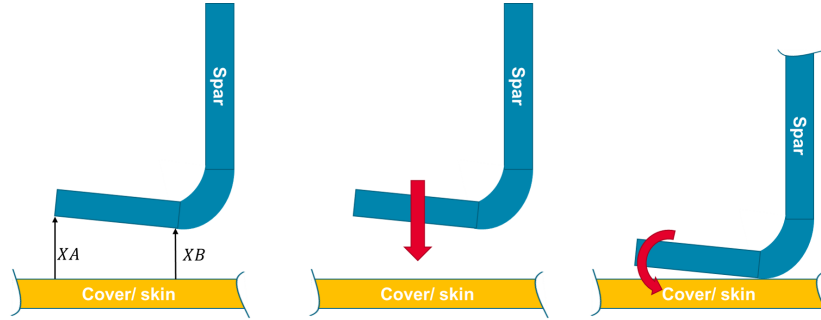


Figure 7.22: Illustration of the spar2cover junction test case

As for the wing root joint example, we will focus on the rotational component of the gap, which will be defined as $G = XA - XB$. All statistical parameters intervening in the definition of the costs c_1 and c_2 are unchanged from the previous test case. In particular, we keep the same definition of the design variables v_g (defining the tolerance bounds of G) and v_{assy} (i.e. the top-level requirement), the same formulation of the tolerance model (giving in output the gap G itself) and the same starting distribution $G_{orig} \sim \mathcal{N}(0, 0.112^2)$. The mathematical formulation of the costs are equivalent to the ones provided for the wing root joint example in Eq. 7.29, related to c_1 , and Eq. 7.30, for the c_2 . Moreover, we pose the same assumptions on the symmetry of the effect of the gap G on the stress S (i.e. $S(G) = S(-G)$) and the same linear relation between S and $|G|$:

$$S = k_1|G| + k_2$$

this would lead to consider the same definition of detrimental variable K_G . However, with respect to the previous use case, we introduce for the *spar2cover* junction the possibility to intervene on the assembly through a shimming procedure: this consists in inserting a non-structural element to fill the gap, which can be liquid (as in Fig. 7.23) or solid.

The choice on the application of shimming or not is based on the comparison between the realization g of the random gap $G(v_g)$ and the top-level requirement v_{assy} : in particular the shimming is applied if $|g| > v_{assy}$. The cost c_2 reproduces here the shimming frequency, related to a given combination of the variables v_g and v_{assy} . Therefore, the interest in reducing c_2 in this example is given by the cost of shimming procedure and the consequent delays in the assembly line.

The shimming procedure is here supposed to completely prevent the residual built-in stresses, thus restoring the condition to the one with $g = 0$. The effects of gaps on the stress S will be then differentiated according to the outcomes of the quality check at assembly level for a given realization g of the random gap $G(v_g)$:

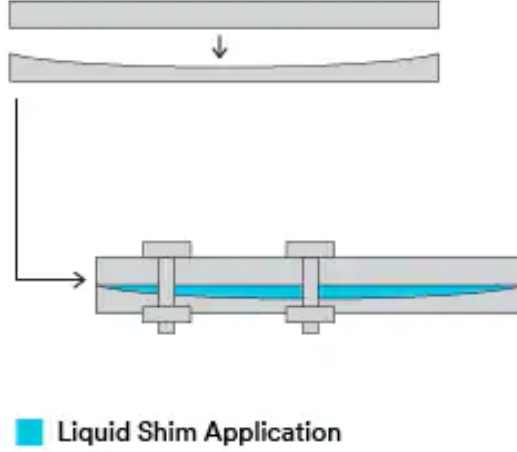


Figure 7.23: Example of liquid shim application

$$S(g, v_{assy}) = \begin{cases} k_1|g| + k_2 & |g| \leq v_{assy} \\ k_2 & |g| > v_{assy} \end{cases} \quad (7.37)$$

Introducing the same concept of sizing gap G_{REF} , we obtain the expression of the detrimental variable K_G :

$$K_G(g, v_{assy}; G_{REF}) = \frac{S(G_{REF})}{S(g, v_{assy})} = \begin{cases} \frac{BG_{REF}+1}{B|g|+1} & |g| \leq v_{assy} \\ BG_{REF} + 1 & |g| > v_{assy} \end{cases} \quad (7.38)$$

Where $B = k_1/k_2 = 100$ is the same constant factor used in the wing root joint example and G_{REF} constitutes the scenario degree of freedom (denoted as I_{REF} in Section 7.3.4). In the second line of Eq. 7.38 we have introduced the effect of the shimming procedure, which is supposed to restore the stress condition to the zero gap configuration (i.e. $g = 0$). The PoE will be affected by v_{assy} via the direct intervention on the expression of K_G from Eq. 7.38, leading to a formulation derived from Eq. 7.21:

$$PoE(\mathbf{v}, v_{assy}; I_{REF}) = PoE(v_g, v_{assy}; G_{REF}) = P [K_G(G(v_g), v_{assy}; G_{REF}) K_R \leq 1] \quad (7.39)$$

We use this example to evaluate the consequences of the knowledge of the effects of specific interventions at assembly level. Therefore, all problem parameters and specific scenarios from the previous application are retained, to better highlight the differences. We focus, in particular, on the results issued from the *full codesign framework* formulation:

$$\begin{aligned}
& \min_{v_g} c_1(v_g), c_2(v_g, v_{assy}) \\
& \text{s.t. } PoE(v_g, v_{assy}; G_{REF}) \leq 0.01 \\
& \quad 0.05 \leq v_g \leq 0.35 \\
& \quad 0.1 \leq v_{assy} \leq 0.7
\end{aligned} \tag{7.40}$$

The optimization results are reported in Fig. 7.24 for different settings of G_{REF} : as for the root joint example, we report the Pareto front, the optimal design variables and the extraction of the optimal v_g and v_{assy} for fixed scenarios of the sizing gap G_{REF} and the budget \bar{c}_2 on the cost c_2 .

All results are very close to the ones related to the previous test case (cf. Fig. 7.19). Only marginal differences can be observed for the extraction of the optimal v_g, v_{assy} at high $\bar{c}_2 > 0.10$: both v_g, v_{assy} are increased by around 3% in the case of *spar2cover*, where the interventions are allowed at assembly level and their effect on the structural performance is known. In fact, the knowledge of the effects of the interventions on structural performances can affect the PoE only if the amount of interventions is sufficiently high. As the cost c_2 constitutes a measure of the shimming frequency, the differences can be noticed only for high values of \bar{c}_2 .

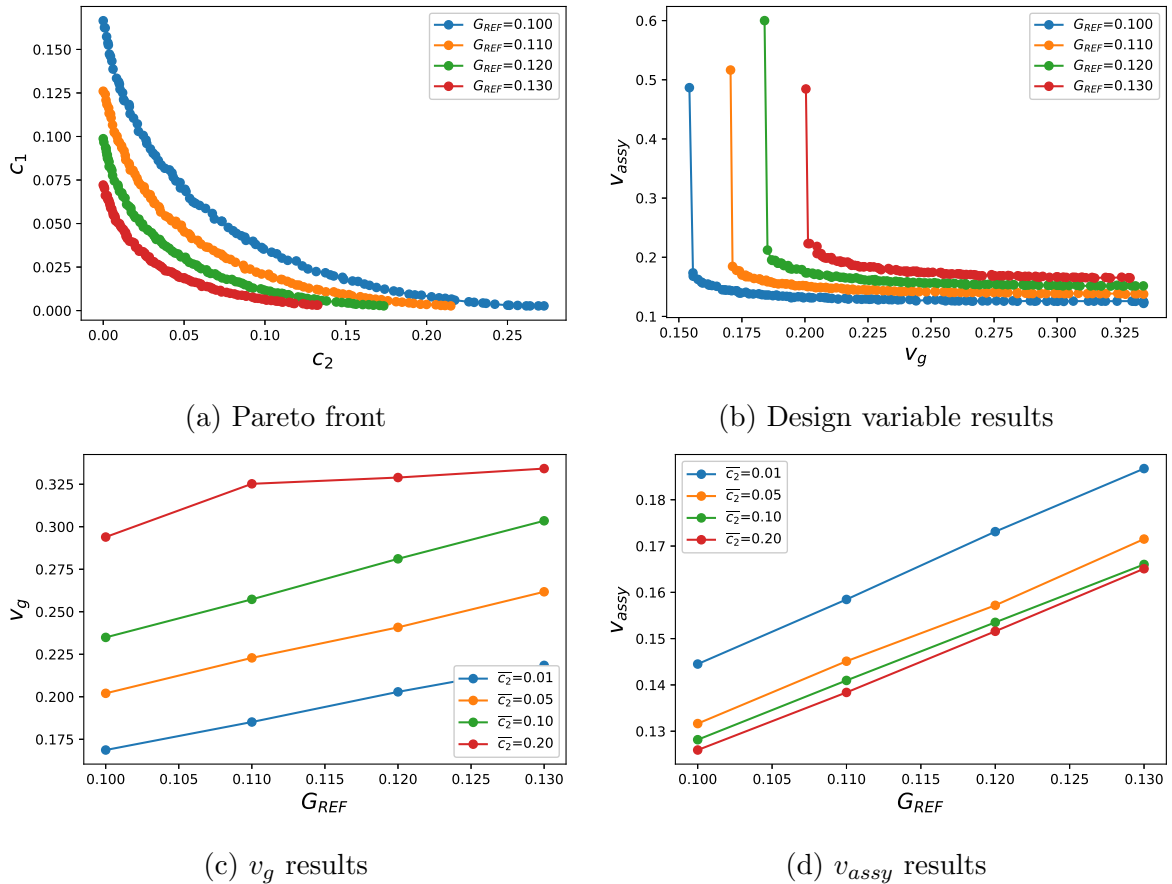


Figure 7.24: Spar2cover example: results of optimization with full codesign framework

7.5 Applications on H2H

In this section, we apply the *full codesign framework* to the H2H problem. In particular, we will focus on the three coupons already analyzed in Chapter 4, i.e. the Single Lap Shear bolted joints with bolting patterns 1x2, 1x5 and 3x5.

In Fig. 7.25, we report the same schematic representation of the stack chains which were presented in Chapter 4, but integrated with the concepts of geometric tolerances. For simplicity, only longitudinal (along the applied force direction) deviations are reported, but the scheme is valid in two dimensions (longitudinal X and transversal Y) as well. In both Fig. 7.25a-b, we introduce a first *datum A* on the upper face of the each plate. Then in the first case, which we call *datum plate*, we associate a secondary datum B to the left border of the plate (cf. Fig. 7.25a). In the case denoted by *datum first hole*, we associate the secondary datum B to the center axis of the first hole of the bolting pattern (cf. Fig. 7.25b).

We define two types of tolerance bounds at component level:

- v_X : when using *datum plate*, this refers to the tolerance (equal for X and Y direction) of all position of the hole centers (in a given plate), with respect to the reference given by the left border of the same plate; when using *datum first hole*, it becomes the tolerance bound associated to the distance between the center of the first hole and the left border of the plate.
- $v_{\Delta X}$: only defined for *datum first hole*, where it represents the tolerance bound (equal for X and Y direction) associated to the distance from the first hole (of a given plate) of all successive holes (in the same plate).

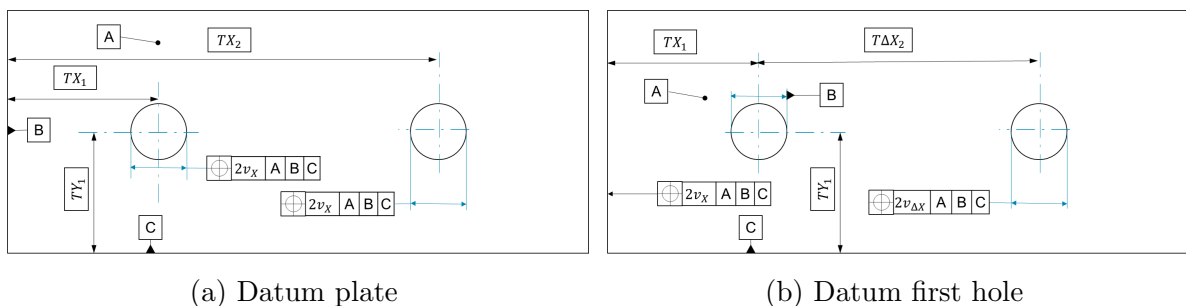


Figure 7.25: Schematic representation of stack chains associated with manufacturing processes

We adopt in the present application of the *full codesign framework*, four different alternative stack chains, based on the upper-described scheme:

- Stack chain 1 (datum plate): all holes are drilled individually and the plates are perfectly aligned before assembly routine. In this case, every X_{ij}, Y_{ij} is supposed to be a random variable, independent from the others.
- Stack chain 4 (datum first hole): all holes are drilled using the first hole as a reference for all successive holes. The assembly is done by aligning the plates. In this case, all variables $X_{i1}, Y_{i1}, \Delta X_{ij}, \Delta Y_{ij}$ ($j > 1$) are treated as independent random variables.

- Stack chain 5 (datum first hole): similar to stack chain 4, but with the assembly done with an expandable pin on the first reference hole. Therefore, we have that the positions of the first hole center of each plate are all deterministic (i.e. $v_X = 0$). In this case, every $\Delta X_{ij}, \Delta Y_{ij}$ ($j > 1$) is a random variable, independent from the others, while X_{i1} and Y_{i1} are deterministic, i.e. $X_{i1} = Y_{i1} = 0$.
- Stack chain 6 (datum first hole): similar to stack chain 4, but the assembly is done with a reference pin. Therefore, the tolerance bound v_X is fixed at a minimum level $v_X = v_{LB}$, given by the sum of the nominal clearance and the tolerance on the pin diameter. In this case, all variables $X_{i1}, Y_{i1}, \Delta X_{ij}, \Delta Y_{ij}$ ($j > 1$) are treated as independent random variables, but the variabilities of X_{i1} and Y_{i1} are fixed.

The tolerance bounds design variables (at component level) $v_X, v_{\Delta X}$ will be collected in the vector \mathbf{v} . The definition of the tolerance bound design vector \mathbf{v} (at component level) will differ according to the stack chain (SC):

$$\begin{aligned}
 \text{Stack Chain 1: } \mathbf{v} &= v_X \\
 \text{Stack Chain 4: } \mathbf{v} &= [v_X, v_{\Delta X}] \\
 \text{Stack Chain 5/6: } \mathbf{v} &= v_{\Delta X}
 \end{aligned} \tag{7.41}$$

We associate to all components of the vector \mathbf{v} the same bounds constraint v_{LB}, v_{UB} to define the search domain of the optimization problem. In the applications presented in this chapter, we do not truncate the distribution of the geometrical features X_i associated to the v_i : therefore, the components v_i will only induce a normal distribution (to describe the associated random variable X_i) with zero mean and standard deviation $\sigma_i = v_i/3$.

Then, we introduce also the top-level requirement v_{assy} among design variables. When associated to the appropriate *tolerance model*, we obtain the *tolerance acceptance criterion*. This latter should be able to filter only the assembly configurations where it is possible to fit the bolts inside the holes. Therefore, the top-level requirement v_{assy} can be associated to half of the oversize (which, we remind, constitutes an increase of the hole *diameter* to allow the assembly process in presence of misaligned holes). Before defining the *tolerance model*, we introduce the main notations and the sampling process associated to the different stack chains.

We report the main notations used in the example of application of the *full codesign perspective* on the H2H problem, in Table 7.1 and Table 7.2, respectively for stack chain 1 (SC1) and stack chains 4/5/6 (SC4/SC5/SC6). We indicate with H the number of holes in each plate with bolting pattern $N_X \times N_Y$ (i.e. N_X holes in longitudinal direction and N_Y holes in transversal direction, in each plate), leading to $H = N_X N_Y$. The indexes j and i represent respectively the hole location in each plate (i.e. $j = 1, \dots, H$) and the plate itself (i.e. $i = 1, 2$). We denote with X_{ij} (respectively Y_{ij}) the deviation from the theoretical perfect coordinate TX (respectively TY) of the j -th hole of the i -th plate.

For the bearing $S_{i,j}$, we evaluate the transferred load only at the j -th hole location of the first plate, because of the forces equilibrium at bolt level (i.e. $S_{1,j} = S_{2,j}$): therefore, we simplify the notation to S_j . In the following, we illustrate step-by-step the different definitions provided in Tables 7.1-7.2.

First of all, we analyze the sampling of the misalignment configurations of the two classes of stack chains:

- For stack chain 1, all X_{ij}, Y_{ij} are sampled following the distributions issued from

Notation	Global Definition	Declination for SC1
v_X	Tolerance bound design variable (at component level)	Equal for all holes
$v_{\Delta X}$	Tolerance bound design variable (at component level)	-
\mathbf{v}	Tolerance bound design vector (at component level)	$\mathbf{v} = v_X$
v_{LB}, v_{UB}	Bounds constraints of design variables (at component level)	$v_{LB} \leq v_X \leq v_{UB}$
v_{assy}	Top-level requirement design variable (at assembly level)	Equal for all holes
$v_{assy,LB}$ $v_{assy,UB}$	Bounds constraints of design variables (at assembly level)	$v_{assy,LB} \leq v_{assy} \leq v_{assy,UB}$
X_{ij}	Longitudinal misalignment (j -th hole of i -th plate)	Variability induced by v_X $X_{ij} \sim \mathcal{N}(0, \sigma^2)$ (with $\sigma = v_X/3$)
Y_{ij}	Transversal misalignment (j -th hole of i -th plate)	Variability induced by v_X $Y_{ij} \sim \mathcal{N}(0, \sigma^2)$ (with $\sigma = v_X/3$)
\mathbf{X}	Misalignment vector (impacted by tolerance bounds \mathbf{v})	$\mathbf{X}(\mathbf{v}) = [X_{11}, \dots, X_{1H}, X_{21}, \dots, X_{2H}, Y_{11}, \dots, Y_{1H}, Y_{21}, \dots, Y_{2H}]$
ΔX_{ij}	Deviation from nominal distance between j -th and first hole of i -th plate	$\Delta X_{ij} = X_{ij} - X_{i1}$
ΔY_{ij}	Deviation from nominal distance between j -th and first hole of i -th plate	$\Delta Y_{ij} = Y_{ij} - Y_{i1}$
dX_j	Relative longitudinal misalignment at the j -th hole location	$dX_j(\mathbf{v}) = X_{1j}(\mathbf{v}) - X_{2j}(\mathbf{v})$
dY_j	Relative transversal misalignment at the j -th hole location	$dY_j(\mathbf{v}) = Y_{1j}(\mathbf{v}) - Y_{2j}(\mathbf{v})$
ρ_j	Output of linear tolerance model at the j -th hole location	$\rho_j(\mathbf{v}) = dX_j(\mathbf{v}) + dY_j(\mathbf{v}) $
S_j	Random Bearing load (at j -th hole location)	$S_j = S_j(\mathbf{X}(\mathbf{v}))$
$S_{REF,nom}$	Nominal bearing load	Fixed, based on fitted aligned configuration
R	Bearing material strength	Random variable (not affected by v_i)
R_{REF}	Nominal material strength	\overline{PoE} -level quantile of R (A or B basis value)
OL	Imposed overload limit	Scenario
PoE	Probability that the structure underperforms wrt deterministic sizing conditions	From Eq. 7.48
\overline{PoE}	Constraint for PoE	Scenario
X_{orig}	Original distribution with the largest variability of component level tolerance bounds	Variability induced by v_{UB} $X_{orig} \sim \mathcal{N}(0, \sigma^2)$ (with $\sigma = v_{UB}/3$)
c_1	Out-of-quality cost: required precision improvement (at component level)	$c_1(\mathbf{v}) = P(X_{orig} \geq v_X)$
c_2	Out-of-quality cost: at least one corrective intervention (at assembly level)	$c_2(\mathbf{v}, v_{assy}) = P(\max_j \rho_j(\mathbf{v}) \geq v_{assy})$

Table 7.1: Notations and definitions used for the applications of the *full codesign framework* on H2H problem, with Stack Chain 1 (*datum plate*)

the tolerance bound design variable v_X (i.e. $X_{ij} \sim Y_{ij} \sim \mathcal{N}(0, \sigma^2)$ with $\sigma = v_X/3$): the $\Delta X_{ij}, \Delta Y_{ij}$ (representing the differences of misalignments between the first and the successive - i.e. $j = 2, \dots, H$ - holes of the i -th plate) can be also computed, but constitute only the consequences of the sampling of X_{ij}, Y_{ij} .

- For the stack chains with *datum first hole* (i.e. SC4, SC5, SC6), we sample the X_{i1}, Y_{i1} (related to the first hole of each plate) according to the distributions induced

Notation	Global Definition	Declination for SC4/SC5/SC6
v_X	Tolerance bound design variable (at component level)	Associated to the first hole of each plate SC4: free v_X / SC5: $v_X = 0$ / SC6: $v_X = v_{LB}$
$v_{\Delta X}$	Tolerance bound design variable (at component level)	Associated to successive holes of each plate (equal for all holes in the bolting pattern)
\mathbf{v}	Tolerance bound design vector (at component level)	SC4: $\mathbf{v} = [v_X, v_{\Delta X}]$ SC5/SC6: $\mathbf{v} = v_{\Delta X}$
v_{LB}, v_{UB}	Bounds constraints of design variables (at component level)	$v_{LB} \leq v_X \leq v_{UB}$ (only for SC4) $v_{LB} \leq v_{\Delta X} \leq v_{UB}$ (for SC4/SC5/SC6)
v_{assy}	Top-level requirement design variable (at assembly level)	Equal for all holes
$v_{assy, LB}$ $v_{assy, UB}$	Bounds constraints of design variables (at assembly level)	$v_{assy, LB} \leq v_{assy} \leq v_{assy, UB}$
X_{i1}	Longitudinal misalignment (first hole of i -th plate)	Variability induced by v_X $X_{i1} \sim \mathcal{N}(0, \sigma^2)$ (with $\sigma = v_X/3$)
Y_{i1}	Transversal misalignment (first hole of i -th plate)	Variability induced by v_X $Y_{i1} \sim \mathcal{N}(0, \sigma^2)$ (with $\sigma = v_X/3$)
ΔX_{ij}	Deviation from nominal distance between j -th and first hole of i -th plate	Variability induced by $v_{\Delta X}$ $\Delta X_{ij} \sim \mathcal{N}(0, \sigma^2)$ (with $\sigma = v_{\Delta X}/3$)
ΔY_{ij}	Deviation from nominal distance between j -th and first hole of i -th plate	Variability induced by $v_{\Delta X}$ $\Delta Y_{ij} \sim \mathcal{N}(0, \sigma^2)$ (with $\sigma = v_{\Delta X}/3$)
X_{ij}	Longitudinal misalignment (j -th hole of i -th plate)	$X_{ij}(\mathbf{v}) = X_{i1}(v_X) + \Delta X_{ij}(v_{\Delta X})$ ($j > 1$)
Y_{ij}	Transversal misalignment (j -th hole of i -th plate)	$Y_{ij}(\mathbf{v}) = Y_{i1}(v_X) + \Delta Y_{ij}(v_{\Delta X})$ ($j > 1$)
\mathbf{X}	Misalignment vector (impacted by tolerance bounds \mathbf{v})	$\mathbf{X}(\mathbf{v}) = [X_{11}, \dots, X_{1H}, X_{21}, \dots, X_{2H}, Y_{11}, \dots, Y_{1H}, Y_{21}, \dots, Y_{2H}]$
dX_j	Relative longitudinal misalignment at the j -th hole location	$dX_j(\mathbf{v}) = X_{1j}(\mathbf{v}) - X_{2j}(\mathbf{v})$
dY_j	Relative transversal misalignment at the j -th hole location	$dY_j(\mathbf{v}) = Y_{1j}(\mathbf{v}) - Y_{2j}(\mathbf{v})$
ρ_j	Output of linear tolerance model at the j -th hole location	$\rho_j(\mathbf{v}) = dX_j(\mathbf{v}) + dY_j(\mathbf{v}) $
S_j	Random bearing load (at j -th hole location)	$S_j = S_j(\mathbf{X}(\mathbf{v}))$
$S_{REF, nom}$	Nominal bearing load	Fixed, based on fitted aligned configuration
R	Bearing material strength	Random variable (not affected by v_i)
R_{REF}	Nominal material strength	PoE -level quantile of R (A or B basis value)
OL	Imposed overload limit	Scenario
PoE	Probability that the structure underperforms wrt deterministic sizing conditions	From Eq. 7.48
$Po\bar{E}$	Constraint for PoE	Scenario
X_{orig}	Original distribution with the largest variability of component level tolerance bounds	Variability induced by v_{UB} $X_{orig} \sim \mathcal{N}(0, \sigma^2)$ (with $\sigma = v_{UB}/3$)
c_1	Out-of-quality cost: required precision improvement (at component level)	SC4: $c_1(\mathbf{v}) = \frac{1}{2} [P(X_{orig} \geq v_X) + P(X_{orig} \geq v_{\Delta X})]$ SC5/SC6: $c_1(\mathbf{v}) = P(X_{orig} \geq v_{\Delta X})$
c_2	Out-of-quality cost: at least one corrective intervention (at assembly level)	$c_2(\mathbf{v}, v_{assy}) = P(\max_j \rho_j(\mathbf{v}) \geq v_{assy})$

Table 7.2: Notations and definitions used for the applications of the *full codesign framework* on H2H problem, with Stack Chain 4, 5, 6 (*datum first hole*)

by v_X (i.e. $X_{i1} \sim Y_{i1} \sim \mathcal{N}(0, \sigma^2)$ with $\sigma = v_X/3$), and the $\Delta X_{ij}, \Delta Y_{ij}$ ($j = 2, \dots, H$) according to the distributions induced by $v_{\Delta X}$ (i.e. $\Delta X_{ij} \sim \Delta Y_{ij} \sim \mathcal{N}(0, \sigma^2)$ with $\sigma = v_{\Delta X}/3$). The other X_{ij}, Y_{ij} (with $j = 2, \dots, H$) are then computed from $X_{i1}, Y_{i1}, \Delta X_{i1}, \Delta Y_{i1}$.

We assume in the following that all distributions \mathbf{X}_{orig} are centered normal with

standard deviation equal to $1/6$ of the maximum oversize OS : this latter constitutes the maximum width of the tolerance interval $\pm v$ in the search domain, thus leading to the definition of the upper bound constraint on all the components v_i of the vector \mathbf{v} , denoted as $v_{UL} = OS/2$. In the applications presented in this chapter, we will consider only one random variable X_{orig} , common to all geometrical features. In the optimization problem, we associate the same design variable v_X to all random features X_{ij}, Y_{ij} in the Stack chain 1 and to the position of the first hole related to the Stack chains 4, 5 and 6. On the other hand, we associate the same tolerance bound design variable $v_{\Delta X}$ to all random features $\Delta X_{ij}, \Delta Y_{ij}$ (for $j > 1$) related to Stack chains 4, 5 and 6.

We focus now on the out-of-quality costs c_1, c_2 . The former can be computed prior to sampling, as it requires (cf. Eq. 7.7) only the distribution of the random variable X_{orig} , the tolerance bounds at component level \mathbf{v} and the weighting factors m_i to ponderate the contributions of the different features (here we suppose uniform weights). We can formalize the definitions of the cost c_1 , differentiated per stack chain:

$$\begin{aligned} \text{Stack Chain 1: } c_1(\mathbf{v}) &= P(|X_{orig}| \geq v_X) \\ \text{Stack Chain 4: } c_1(\mathbf{v}) &= \frac{1}{2} [P(|X_{orig}| \geq v_X) + P(|X_{orig}| \geq v_{\Delta X})] \\ \text{Stack Chain 5/6: } c_1(\mathbf{v}) &= P(|X_{orig}| \geq v_{\Delta X}) \end{aligned} \quad (7.42)$$

The cost c_2 represents the probability of needing *at least one* correction intervention at assembly level, to restore the assembly-related geometric features. In order to evaluate this, we need to a priori evaluate the outputs of the tolerance model ρ_j for each bolt location and compare them to the top-level requirement v_{assy} : as a reminder, the association between ρ_j and v_{assy} constitutes the *tolerance acceptance criterion*. The idea of the *tolerance acceptance criterion* in H2H context is to select the assembly configurations where it is possible, without any correction measure, to fit the bolts inside the holes (cf. illustration in Fig. 7.5). Therefore, in principle, we need to use a tolerance model ρ_j measuring the euclidean distance between two hole centers at the j -th bolt location. We can therefore formalize the ρ_j as a function of the misalignments X_{ij}, Y_{ij} , which are realizations depending on the tolerance bound vector (at component level) \mathbf{v} :

$$\rho_j(\mathbf{v}) = \sqrt{(X_{1j}(\mathbf{v}) - X_{2j}(\mathbf{v}))^2 + (Y_{1j}(\mathbf{v}) - Y_{2j}(\mathbf{v}))^2} \quad \forall j \in \{1, \dots, H\} \quad (7.43)$$

Each tolerance model output is computed at each of the H hole location (H representing the number of bolts in the assembly). Switching to a more compact notation, we will have:

$$\rho_j(\mathbf{v}) = \sqrt{dX_j(\mathbf{v})^2 + dY_j(\mathbf{v})^2} \quad \forall j \in \{1, \dots, H\} \quad (7.44)$$

Where $dX_j(\mathbf{v}) = X_{1j}(\mathbf{v}) - X_{2j}(\mathbf{v})$ and $dY_j(\mathbf{v}) = Y_{1j}(\mathbf{v}) - Y_{2j}(\mathbf{v})$ represent the relative misalignments between two plates on the j -th bolt location (respectively in longitudinal and transversal direction). However, the linear approximation of the tolerance model is common in tolerancing activities [Diet, 2021]. In the H2H application example, we use the linear tolerance model:

$$\rho_j(\mathbf{v}) = |dX_j(\mathbf{v})| + |dY_j(\mathbf{v})| \quad \forall j \in \{1, \dots, H\} \quad (7.45)$$

The *tolerance acceptance criterion* will be given by the association of the tolerance model to the top-level requirement v_{assy} . As the assembly-related cost c_2 represents the probability of needing *at least one* correction intervention at assembly level, it will be defined by the max over all ρ_j , so that we have:

$$c_2(\mathbf{v}, v_{assy}) = P \left[\max_{j \in \{1, \dots, H\}} (\rho_j(\mathbf{v})) > v_{assy} \right] \quad (7.46)$$

We remind that the main interest in the H2H application is the reduction of interventions during the assembly line routine, to simplify the process and reduce the lead time: therefore, we will focus in the results section to cases related to low c_2 , specifically $c_2 \leq 0.1$. Considering the conclusions issued from the examples on built-in stresses applications (cf. Section 7.4), we can omit the description of the specific corrective intervention at assembly level: in fact, as shown in Section 7.4.2, the precise effects of these corrections restoring the assembly-related geometrical features are not relevant in the *full codesign framework* for low c_2 . This allows us to use the formulation of the *PoE* from Eq. 7.20.

To formalize the *PoE*, we start from the definition of the limit state function G_k at each of the k bolt locations, which can be formalized as:

$$G_k(\mathbf{X}; OL) = \frac{S_k(\mathbf{X})R_{REF}}{S_{REF,nom}R} - OL \begin{cases} \geq 0 & \text{exceedance} \\ < 0 & \text{no exceedance} \end{cases} \quad (7.47)$$

Where S_k represents the bearing force transferred at the k -th bolt location (H overall), R the bearing strength (common value in the whole plate), $S_{REF,nom}$, R_{REF} are the respective nominal values (related to the nominal configuration, i.e. fitted perfectly aligned holes) and OL is the imposed overload limit scenario (denoted as I_{nom} in Eq. 7.20). As a reminder, this represents the load amplification factor which must be considered in the deterministic sizing process to compensate the uncertainties linked to the actual structural performances, i.e. acting de facto as a *safety factor* (described in Chapter 2).

In the applications presented in this chapter, we will further challenge the overloads retrieved from the computations in Chapter 4: in particular, we fix four scenarios for the imposed (normalized) overload limits $OL = 0.05, 0.10, 0.15, 0.20$. We consider a different limit state for each bolt location. We used the formulation in Eq. 7.47 also in Chapter 6, as an application of the adaptive Vb-KPLS+SMC algorithm. We use the trained models from Chapter 6 to compute the G_k .

Introducing the limit state function from Eq. 7.47 in the definition of the *PoE* in Eq. 7.20, we can formalize the *PoE* as follows:

$$PoE(\mathbf{v}, v_{assy}; OL) = P \left[\max_{k \in \{1, \dots, H\}} G_k(\mathbf{X}(\mathbf{v}); OL) \geq 0 \mid \max_{j \in \{1, \dots, H\}} (\rho_j(\mathbf{v}, v_{assy})) \leq v_{assy} \right] \quad (7.48)$$

In particular, the conform assembly configurations are filtered by means of excluding all assemblies realizations where *at least one* output feature ρ_j is not conform with respect to the top-level requirement v_{assy} ; then the limit state function is evaluated for *all* hole locations in the retained assembly sample population. The goal of the constraint $PoE \leq \overline{PoE}$ is to limit the probability that the structural performances are worse than the

one previewed in the deterministic sizing process (i.e. using $R_{REF}, S_{REF,nom}, OL$) when adopting the tolerances \mathbf{v}, v_{assy} . In other terms, the $(1 - \overline{PoE})$ quantile of the overload issued from the propagation of misalignments variability must be lower than the imposed OL . Thanks to this constraint, we can ensure that if in deterministic sizing we use the overload OL , we have a probability that the real structure under-performs the penalized condition (i.e. that the real reserve factor is below $R_{REF}/S_{REF,nom}/OL$) lower than \overline{PoE} . Putting together the mathematical elements in Eqs. 7.42, 7.46 and 7.48, we formalize the application of the *full codesign framework* on the H2H problem:

$$\begin{aligned}
 \min_{\mathbf{v}, v_{assy}} \quad & c_1(\mathbf{v}), c_2(\mathbf{v}, v_{assy}) \\
 \text{s.t.} \quad & PoE(\mathbf{v}, v_{assy}; OL) \leq \overline{PoE} \\
 & v_{LB} \leq v_X, v_{\Delta X} \leq v_{UB} \\
 & v_{assy, LB} \leq v_{assy} \leq v_{assy, UB}
 \end{aligned} \tag{7.49}$$

Where the definition of the vector \mathbf{v} comes from the distinction on the different stack chains in Eq. 7.41. The surrogate models stemming from the analysis in Chapter 6 are used for the computations of the PoE . We remind that we trained a distinct surrogate model per output: in practice, we compute each term between brackets separately and then we evaluate the maximum. We impose the limit $PoE \leq \overline{PoE} = 0.1$, referring to the assumption of redundant structures (i.e. related to the use of B values according to the proposed extension of CS 25.613).

In the following, we report the results related to the three coupons with bolting patterns 1x2 (in Section 7.5.1), 1x5 (in Section 7.5.2) and 3x5 (in Section 7.5.3). The complete study is reported on the simple coupon 1x2, to illustrate the process and the justification of specific phenomena affecting the overall outcomes. Only the final results in terms of the evolutions of the optimal tolerance variables are reported for the other coupons. The related Pareto fronts and additional results are reported in the Appendix. All values of tolerance variables are normalized with respect to the related upper bounds.

7.5.1 H2H: coupon 1x2

In this section we analyze the results related to the application of the *full codesign framework* on the H2H coupon with bolting pattern 1x2. A complete study is done to explain the global outcomes of the codesign framework: this includes the study of the Pareto front in Section 7.5.1.1, the evaluation of the optimal tolerance variables at component level in Section 7.5.1.2, and the optimal top-level requirement in Section 7.5.1.3.

7.5.1.1 Study of the Pareto front

The optimal Pareto fronts resulting from the application of the *full codesign framework* on the H2H coupon 1x2 are reported in Fig. 7.26. A filtering is done to retrieve only the solutions with $c_2 > 0$ (strict inequality retained). At a general level, we may notice that for all stack chains an increase in the prescribed overload limit OL can lead to translate the Pareto front towards lower costs c_1, c_2 .

Focusing on stack chain 1, for the lowest $OL = 0.05$ we have a concave shape of the Pareto front. At low c_2 (thus high c_1) we have the smallest v_X . Going towards higher c_2

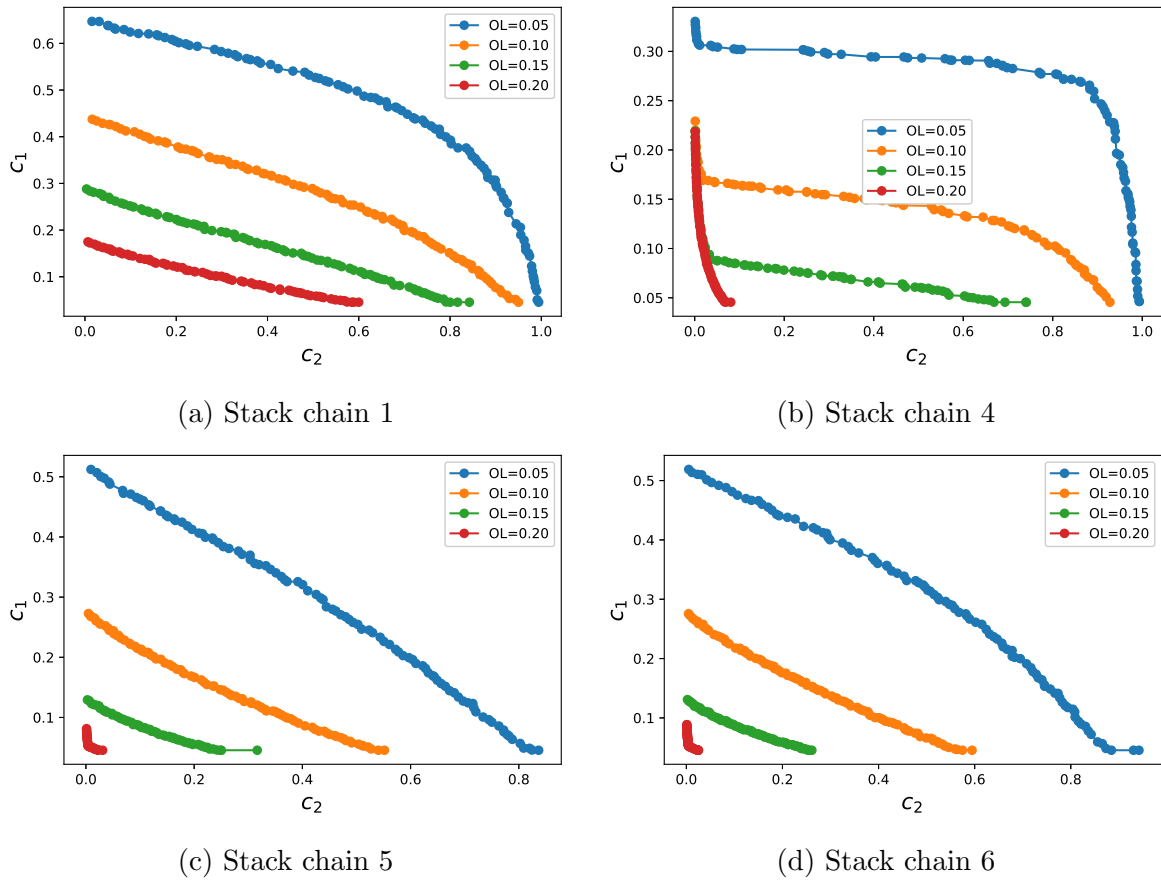


Figure 7.26: H2H coupon 1x2: obtained Pareto fronts for different overload limits OL , regrouped per stack chain

we are able to decrease the c_1 , hence increasing the v_X . However, to guarantee the same PoE constraint, we have to balance the increased v_X with lower v_{assy} . Note that c_1 is only affected by v_i , while in parallel both the increase in v_i and the decrease in v_{assy} lead to higher c_2 : consequently, the slope is low at the beginning, meaning that we have to penalize a lot the cost c_2 in order to slightly improve the cost c_1 .

Let us think again at v_X as the main actor in the variance of the output of the tolerance model (giving the dX_j, dY_j at every bolt location) and v_{assy} as the truncation level of the distribution: at a certain point, around $c_2 \approx 0.8$, we reach configurations where the top-level requirement v_{assy} is so low and the elementary tolerance bound v_X so high that the distribution of the filtered X can look like a uniform distribution where the bounds are given by $\pm v_{assy}$; increasing even more v_X we have only marginal effects on the relative misalignments affecting structural performances, so that we are allowed to increase it at a faster rate, and consequently accelerate the descent of the cost c_1 . The global outcome will be a steep fall in the cost c_1 in the zone of the highest c_2 . This result may not be relevant for H2H problem in itself as we want to focus on low c_2 : in fact, the interest of the project is to pre-drill the parts to assemble in order to minimize operations (and disruptions) in the assembly line. However, this phenomenon can be fundamental when applied to other use cases where the major interest is to demonstrate the effects of specific repair interventions.

A similar behavior can be observed for the results at $OL = 0.05$ for stack chains 5 and 6, and at $OL = 1.1$ for stack chain 1. By increasing the imposed OL level, the whole Pareto fronts are translated towards lower (thus better) costs and the final steep descent at high c_2 values is no longer visible. In fact, we can reach the upper bounds of the components tolerance bounds v_i for higher levels of the top-level geometrical acceptance criterion v_{assy} (which, we remind, lowers when progressing from left to right in the Pareto front).

A particular evolution is obtained with stack chain 4, reported in Fig. 7.26b. We remind that this stack chain receives the contributions from v_X (which is here a *passive tolerance variable*) and $v_{\Delta X}$ (which is an *active tolerance variable*, cf. Section 7.3.4). Conversely to what happens on the other stack chains, the leftmost portion of each Pareto front (related to the different OL) is convex. In order to explain this difference we need to zoom on the optimization results corresponding to this region.

The plots of the outcomes of PoE , c_1 , v_X and $v_{\Delta X}$ are reported in Fig. 7.27 as a function of the obtained cost c_2 . This is chosen to be able to compare the different overload limits and retrieve the reason behind the particular shape of the Pareto front. We start from the highest imposed overload limit $OL = 1.2$: looking at the PoE evolution, we notice that the semi-probabilistic stress constraint is active only from $c_2 \approx 0.07$. Therefore, we can state that for lower c_2 the problem is purely geometric and leads to equilibrated tolerance configurations with $v_X \approx v_{\Delta X}$ (they have the same influence factors on the costs c_1 and c_2). The Pareto front will be convex as it follows the nature of the geometrical unconstrained problem (i.e. with PoE constraint not active), for all levels of imposed overload limits OL .

Now, we would expect for the other curves, related to lower OL , that the imposition of the constraint would lead to a sudden change of slope and a corner point between unconstrained and constrained portion of the Pareto front. However, the change of slope is gradual. We will explain this by gradually lowering the overload level.

When decreasing the imposed OL to $OL = 0.15$, we reach the saturation of the constraint $PoE = \overline{PoE}$ for lower values of $v_{\Delta X}$, which correspond to lower costs c_2 (confront Fig. 7.27a and 7.27d). Going from left to right in Fig. 7.27d, we see that the increase in $v_{\Delta X}$ is tending towards saturation (with a slope which is still positive but almost flat). However, the variable v_X can still increase, generating a bifurcation between red (related to $OL = 1.2$) and green curves (related to $OL = 0.15$): therefore, we retrieve a transition zone where v_X increases and c_1 decreases. But then, around $c_2 \approx 0.03$, v_X reaches its upper bound: from here, we have a constant slope in the Pareto front, corresponding to the new balance between $v_{\Delta X}$ and v_{assy} (not included in this plot).

To sum up, the bifurcation between the unconstrained and the constrained problem is given by the point of saturation of the *active tolerance variable* $v_{\Delta X}$. The transition region between the unconstrained problem and the beginning of the portion of the Pareto front with constant slope is given by the progressive saturation of the *passive tolerance variable* v_X . If we further decrease the imposed OL , the activation of the PoE constraint, the consequent saturation of the variable $v_{\Delta X}$ and the successive point of saturation of v_X will be anticipated to lower levels of c_2 , translating the transition zone of the Pareto front towards left.

Coming back to the complete evolutions of the Pareto fronts related to the stack chain 4 (in Fig. 7.26b), the rightmost regions (i.e. for $0.8 \leq c_2 \leq 1$) are characterized by a

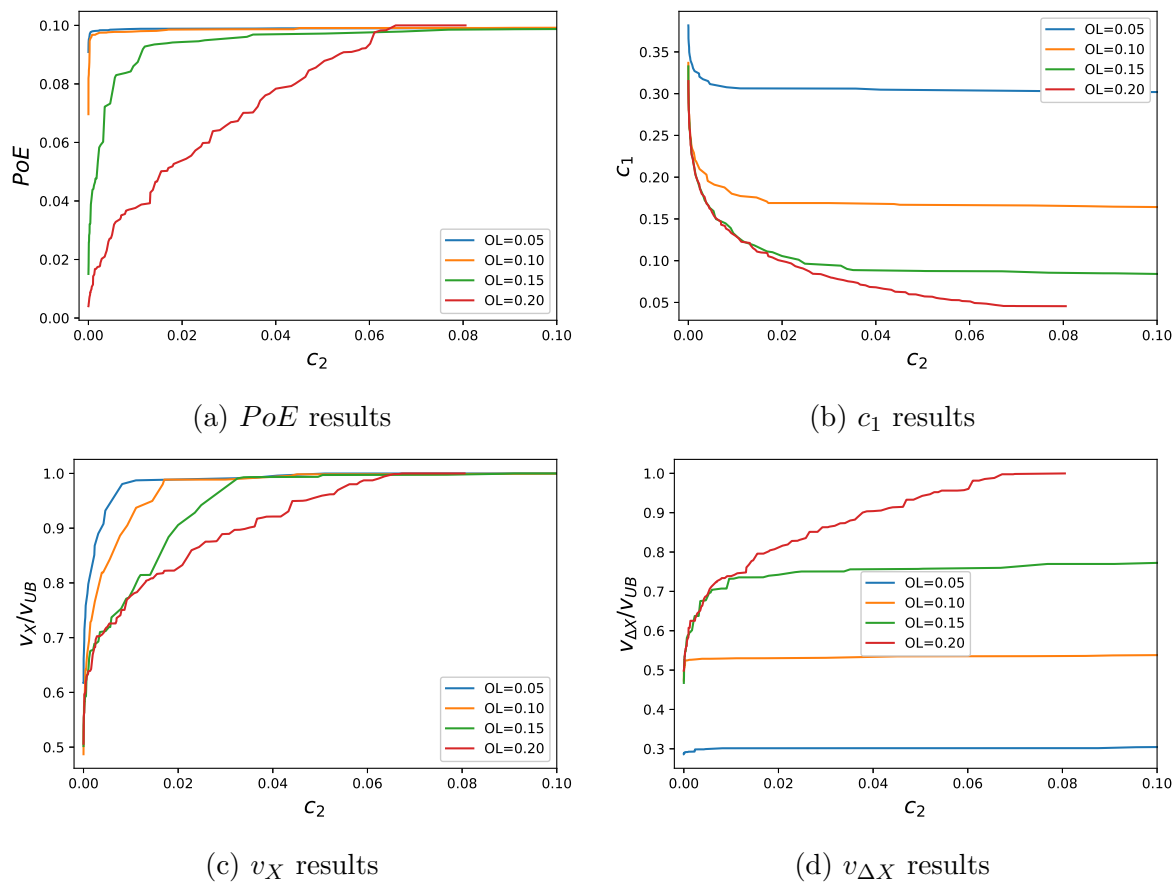


Figure 7.27: H2H coupon 1x2: zoom on optimization results for stack chain 4, as a function of cost c_2

step descent of the component-cost c_1 , when we consider overload limits $OL = 0.05$ and $OL = 0.10$. The reason behind this behavior is analogue to what happens for the other stack chains: in the flat portions of the Pareto fronts, the top-level requirement v_{assy} keeps decreasing to allow the component-related tolerance bound $v_{\Delta X}$ to increase. At about $c_2 \approx 0.8$, v_{assy} reaches values which are small enough to make the truncated distributions of the misalignments (after filtering all misalignment samples greater than v_{assy}) close to uniform distributions: with these conditions, $v_{\Delta X}$ can increase at a faster rate, as most detrimental configuration of misalignments are filtered and the upper-mentioned truncated distribution is not affected. However, for actual H2H applications, this region related to high c_2 is not of interest, as it would imply to correct in the assembly line most of the assemblies, thus hampering the main purpose of H2H itself to simplify the assembly routine.

Finally, comparing stack chain 4 with other stack chains we notice that the slopes of the Pareto fronts are reduced, above all for lower imposed OL levels. The root cause of this phenomenon will be clarified in the next sections.

7.5.1.2 Study of the optimal tolerance variables v_i

In this section we analyze the outcomes of the optimal tolerance design variables obtained from the application of the *full codesign framework* on the H2H coupon 1x2. The results related to the evolution of the optimal v_i (representing the components of the elementary tolerance bounds vector \mathbf{v}) are illustrated in Fig. 7.28 as a function of the imposed overload level OL . Each plot constitutes a collection of snapshots at fixed budgets \bar{c}_2 for the cost c_2 . All components related to the different stack chains are reported in the same plots: the legends report stack chains SC_j , where j is the identification number of a specific stack chain. Within brackets we indicate the suffix i of the component v_i of the vector \mathbf{v} : in particular, (X) represents the component v_X associated to the stack chains 1 and 4, while (ΔX) stands for the component $v_{\Delta X}$ for the stack chains 4, 5 and 6. The same naming is used in all following plots in this chapter. We will abbreviate *Stack Chain* j by SC_j also in the body of the text. This representation helps us to compare different stack chains while imposing the same constraint on PoE (by imposing the same overload limit OL) and the same expendable budget on c_2 .

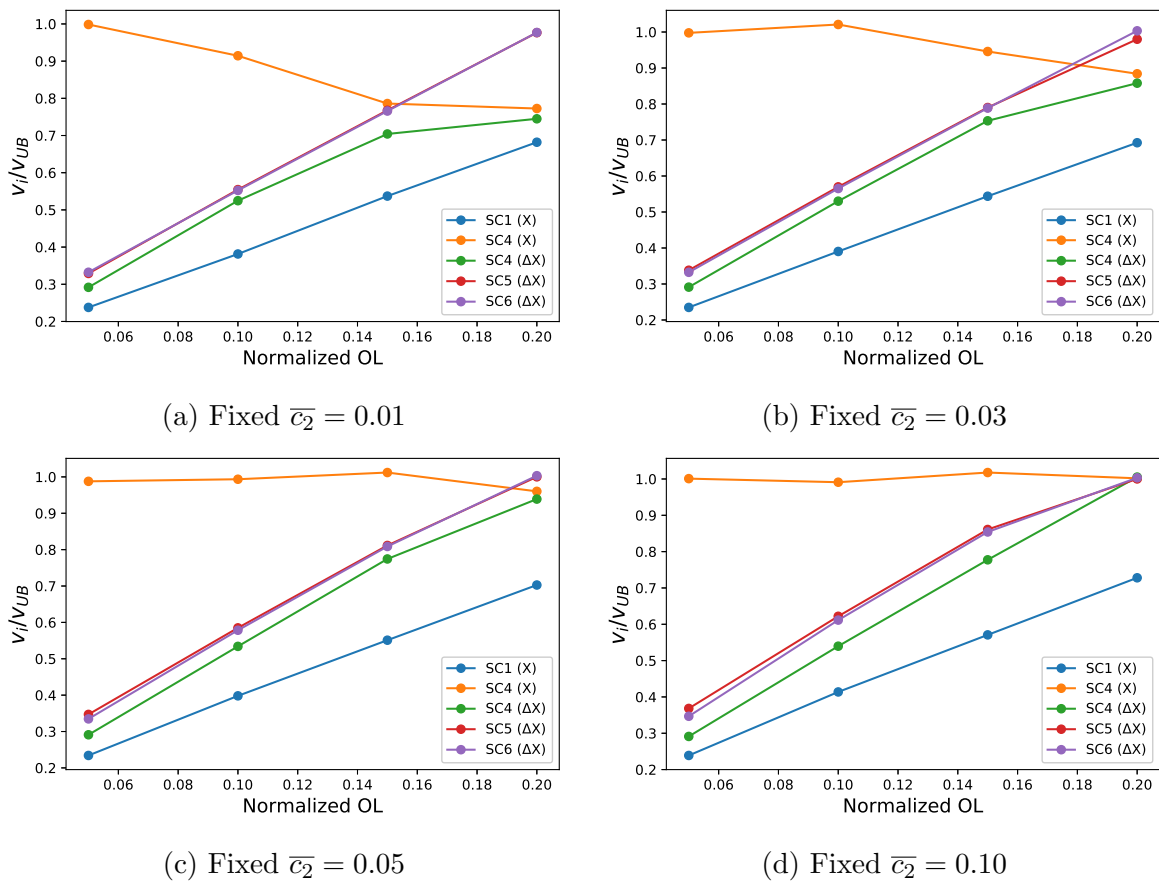


Figure 7.28: H2H coupon 1x2: optimal v_i with full codesign framework on different stack chains at fixed budgets \bar{c}_2

From Fig. 7.28 it is possible to observe positive and almost linear evolutions of the component v_X for the SC1 and of the component $v_{\Delta X}$ of SC5 and SC6. This can be explained by the fact that, consistently with previous results on built-in stress examples,

higher overload values (i.e. less performing structures) imply lower PoE , thus allowing larger tolerance bounds. The linearity is maintained for all levels of \bar{c}_2 , except for the maximum $\bar{c}_2 = 0.1$, where both $v_{\Delta X}$ (from SC5 and SC6) reach the upper bound related to the v_i .

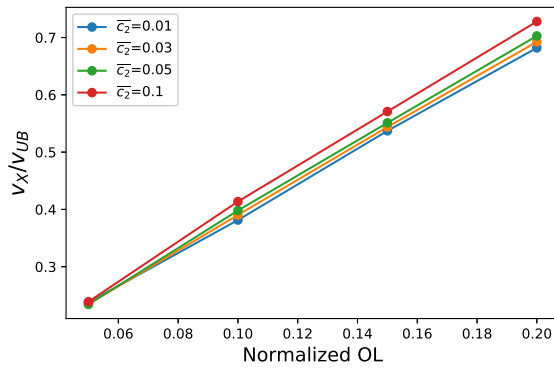
Note that the behaviors of SC5 and SC6 can be superposed: the only difference, given by an added variability on the features X_{i1}, Y_{i1} of SC6 (limited to the clearance of the reference pin), is not determinant for the tolerance optimization problem. Therefore, the specific treatment at assembly level on the reference hole might appear not to affect the overall performances. However, this is true only for small values of the variability of the first hole. This last observation can be better understood by looking at the different behavior (with respect to SC5/SC6) of the evolution curves of $v_{\Delta X}$ related to the SC4.

The difference between SC1 and SC5/SC6 follows the same logic we outlined in Chapter 4. In fact, the variability of the structural performances is caused by the variability of the difference between the relative longitudinal misalignments of the two bolt locations. When adopting SC5/SC6 we directly intervene on this difference via the component $v_{\Delta X}$, while for SC1 such difference will be given by the convolution of the individual features. Therefore, the tolerance results are less convenient for SC1, consistently with the outcomes for overload analysis in Chapter 4.

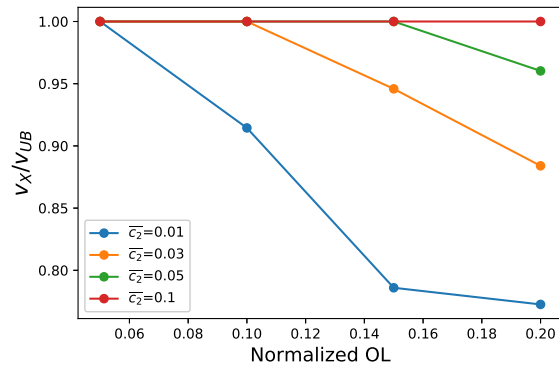
At this point we explain the outcomes of the SC4 from another perspective. Following the overload results from Chapter 4, we would expect the same behavior from SC4, SC5 and SC6. However, in this second declination of the semi-probabilistic approach, we need to optimize the out-of-quality costs c_1 and c_2 . The results will be therefore slightly different. Referring to the PLS mode related to coupon 1x2 in Chapter 3, the main principal coordinate responsible for the bearing load redistribution is given by the difference between relative longitudinal misalignments, hence by features only linked to the $v_{\Delta X}$. Therefore, according to the distinction we proposed in Section 7.3.4, we can class the component $v_{\Delta X}$ as *active tolerance variable* and v_X as *passive tolerance variable*. These intervene on the PoE in opposite directions, with $v_{\Delta X}$ increasing it and v_X decreasing it. Therefore, the former will follow the same evolution as a function of the overload limit than the one observed for the other features related to the other stack chains.

On the other hand, the component v_X of SC4 will decrease when increasing the imposed overload limit OL , for a fixed budget \bar{c}_2 . When increasing the overload limit OL , we relax the PoE constraint, giving more room for improvements to $v_{\Delta X}$. Let us remind that the original distributions are the same centered normal (standard deviation given by 1/6 of maximum oversize): from the point of view of the minimization of c_1 alone, it is more convenient to increase the smallest tolerances (where the PDF of X_{orig} is higher) and decrease the largest ones (where the PDF of X_{orig} is lower); from the point of view of c_2 , to reach the same amount \bar{c}_2 , if $v_{\Delta X}$ is increased, then the component v_X must be decreased. Therefore, when having the possibility (i.e. for increasing levels of imposed overload limit OL), the optimization process tend to equilibrate the different tolerance bandwidths. This considerations are valid for all levels of the budget \bar{c}_2 .

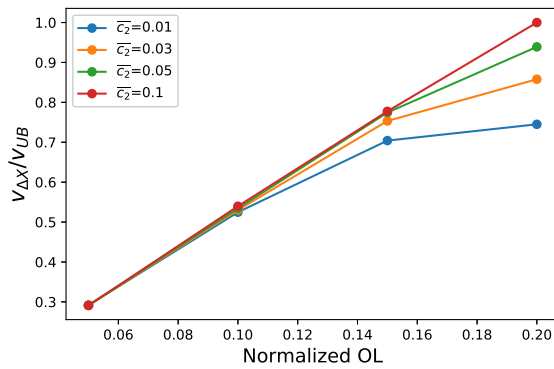
In all configurations, we retrieve that the optimal $v_X, v_{\Delta X}$ related to SC4 are both higher than the v_X from SC1. Compared to SC5/SC6, the $v_{\Delta X}$ is lower for the SC4: this is due to the fact that to maintain the same level of c_2 , we have to consider also the interaction with v_X , which would lead to increase c_2 . In the end, it is possible for SC4 to exhibit the same values of $v_{\Delta X}$, but only for a higher level of the budget \bar{c}_2 .



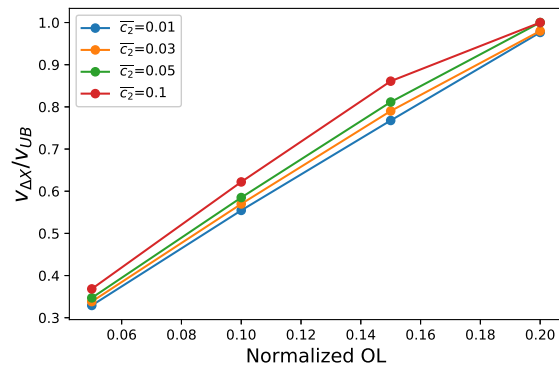
(a) Stack chain 1 $v_i = v_X$



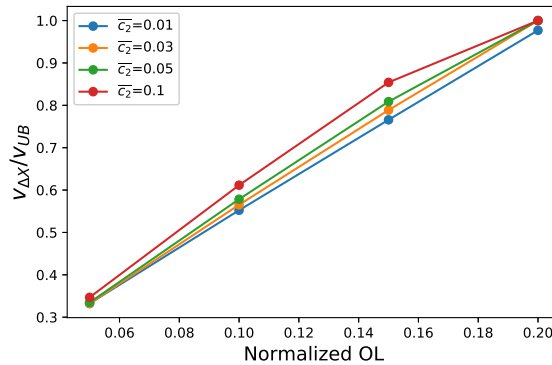
(b) Stack chain 4 $v_i = v_X$



(c) Stack chain 4 $v_i = v_{\Delta X}$



(d) Stack chain 5 $v_i = v_{\Delta X}$



(e) Stack chain 6 $v_i = v_{\Delta X}$

Figure 7.29: H2H coupon 1x2: optimal v_i with full codesign framework on different budgets \bar{c}_2 regrouped per stack chain

Another perspective to analyze the evolution of the tolerance design variables v_i as a function of budget \bar{c}_2 and overload limits is given in the representations of Fig. 7.29. Here the evolutions are grouped per feature, to isolate the effect of the budget \bar{c}_2 on the same stack chain and associate feature. We may observe from Fig. 7.29 that for SC1, SC5 and SC6 we have similar variations of the evolutions of optimal v_i (specifically v_X for SC1, $v_{\Delta X}$ for SC5/SC6) for different values of \bar{c}_2 : by increasing the budget \bar{c}_2 , we may slightly increase the width of the tolerance plans induced by v_i . In particular, the effect is smaller

at low OL (where not much room for enlargements of the tolerance plans is given), while increasing effects are visible for higher overload limits OL . For SC5 and SC6, we have a saturation point related to the maximum OL , as we reach the upper bound of $v_{\Delta X}$.

On SC4, we observe that the evolution v_X with respect to the overload limit OL (reported in Fig. 7.29b) is more affected by the budget \bar{c}_2 at low levels of this latter, while the effect attenuates for higher \bar{c}_2 . The descending curves of v_X stick to the upper bound $v_{i,UL}$ for progressively higher overload levels when increasing \bar{c}_2 : the final outcome is a wider range of choices for the v_X at higher overloads.

On the other hand, we have a similar response in terms of range of choices for $v_{\Delta X}$ (confront Fig. 7.29c): the asymptotic behavior is a straight line corresponding to $\bar{c}_2 = 0.1$; for low OL , almost no differences can be found, while as the OL increases the effect of lowering \bar{c}_2 is more evident (lower c_2 imply lower $v_{\Delta X}$). At $OL = 1.2$ the constraint on the budget c_2 makes the problem mostly geometrical and the PoE constraint is not active at this point.

7.5.1.3 Study of the optimal top-level requirement v_{assy}

The results related to the evolutions of the optimal top-level requirement v_{assy} are illustrated as a function of the imposed overload limits OL in Fig. 7.30 - regrouped per iso-budget \bar{c}_2 - and in Fig. 7.31 - regrouped per stack chain. As for the analysis of the optimal tolerance variables v_i , the first representation can help the comparison between different stack chains, while the second is useful to explain the compromise at different budgets on c_2 for the same stack chain.

At a global level, from both representations we may observe that the top-level requirement v_{assy} can increase when we impose higher (thus less restrictive) overload limits OL . In fact, as the structural requirements are less constraining, the boundary of feasible tolerance domain can be enlarged. This is allowed for all stack chains. These results are in line with the ones observed on the built-in stress applications.

From Fig. 7.30, it is possible to observe that for any level of \bar{c}_2 the top-level requirement is higher (thus more convenient) for SC4, thanks to the introduction of the *passive tolerance variable* v_X . In fact, the optimization mainly acts on the filtered distribution of the variable $dX_1 - dX_2$ (i.e. the difference between relative longitudinal misalignments) to guarantee $PoE \leq \overline{PoE}$: this is done via the simultaneous modifications of $v_{\Delta X}$ (to affect the variance of the component level distribution of dX_1 and dX_2) and v_{assy} (to affect the truncation level in terms of top-level geometric conformity dX_1, dX_2). Being in presence of a *passive tolerance variable*, to maintain the same \bar{c}_2 , the top-level requirement can be higher.

Second best in terms of stringency of the top-level requirement v_{assy} , we retrieve SC5/SC6, the behaviors of which can be superposed (in analogy with the outcomes on the v_i). With respect to SC4, the component of the *passive tolerance variable* v_X is here reduced to zero for SC5 and a fixed smaller tolerance related to the clearance of a reference pin in SC6. As a consequence, the beneficial effect of the *passive tolerance variable* is reduced and the top-level requirement must decrease with respect to SC4.

The lowest allowed top-level requirements are found on SC1. This is a consequence of the lower v_i values found in the previous section.

We focus now on the effects of the budget \bar{c}_2 on each v_{assy} related to the different

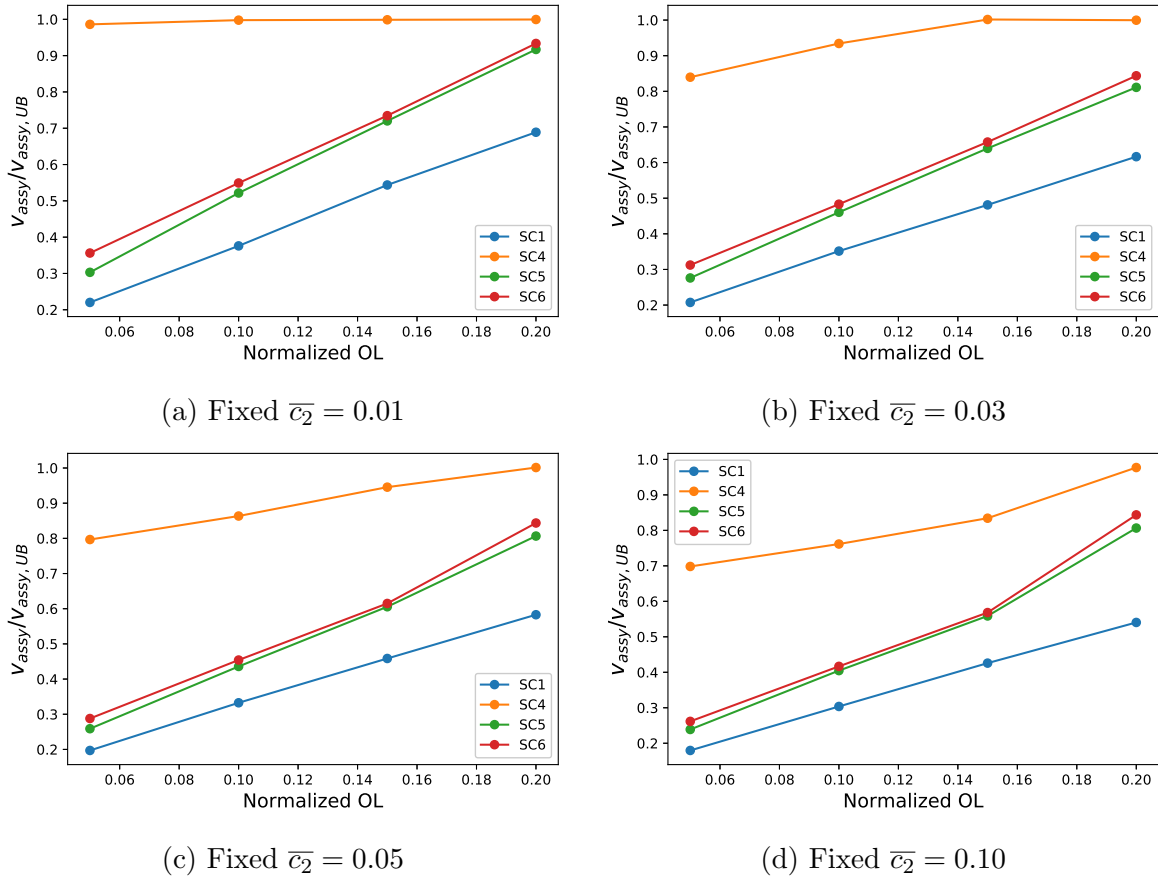
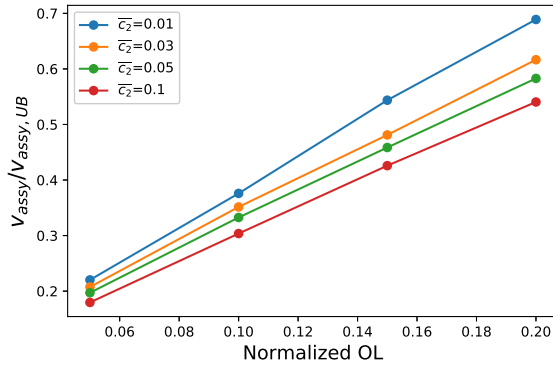


Figure 7.30: H2H coupon 1x2: optimal v_{assy} with full codesign framework on different stack chains at fixed budgets \bar{c}_2

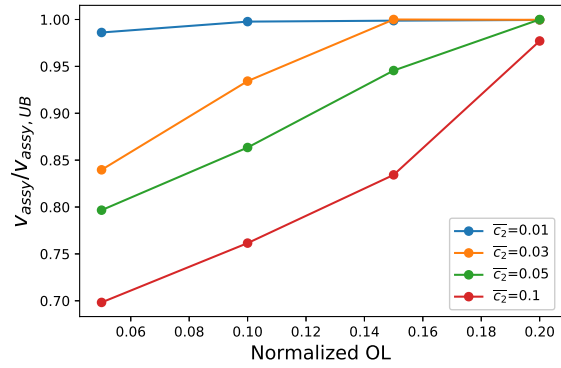
stack chains, illustrated in Fig. 7.31. As for the built-in stress results, the levels of v_{assy} decrease in general, when increasing the budget \bar{c}_2 to allow further reduction in the cost c_1 . When increasing v_i (to reduce c_1), a consequent reduction in v_{assy} is required to guarantee $PoE \leq \overline{PoE}$. By comparing Fig. 7.31 with Fig. 7.29, we may notice that the variation is more relevant on v_{assy} : this is in line with the slopes of the Pareto fronts in Fig. 7.26, where in the compromise between c_1 and c_2 , higher variations are demanded to the latter to decrease the former.

In the same comparison, we can find also configurations where there is no variation (over \bar{c}_2) on the v_i , while v_{assy} keeps decreasing when increasing \bar{c}_2 . An example is visible on the results related to SC4 (cf. Fig. 7.29b for v_X , Fig. 7.29c for $v_{\Delta X}$ and Fig. 7.31b for v_{assy}) while imposing $OL = 0.05$: these solutions are in fact only numerical. These are reflected in the horizontal portions of the Pareto front in Fig. 7.26, constituting in fact *weak Pareto points*.

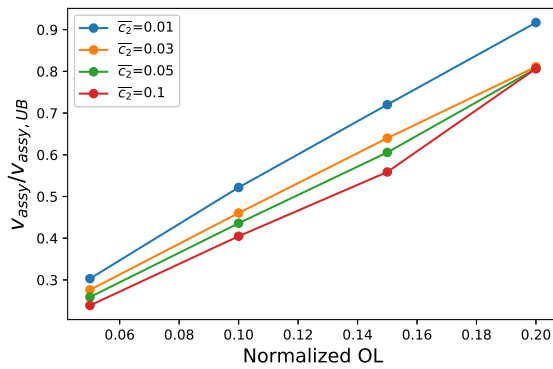
Comparing the effects of \bar{c}_2 on the optimal v_{assy} of the different stack chains, we may notice that the most sensible is SC4. This is due to the fact that the actual filtering must be done on the *active tolerance feature* (the variance of which is regulated by $v_{\Delta X}$). The reasoning follows the logic of expending the whole budget \bar{c}_2 : in presence of a larger variability on the *passive features*, to increase of the same amount the filtering effect of samples of *active features* than SC5 (i.e. to obtain the same variations on c_2), the filter



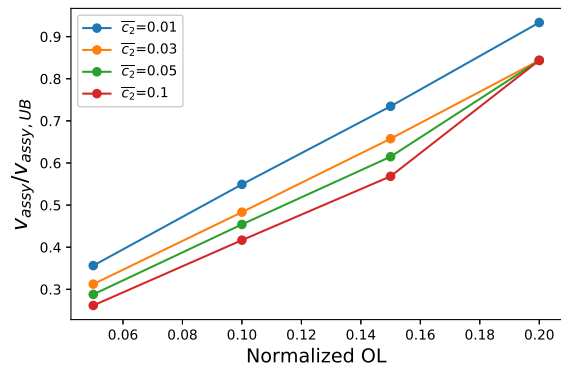
(a) Stack chain 1



(b) Stack chain 4



(c) Stack chain 5



(d) Stack chain 6

Figure 7.31: H2H coupon 1x2: optimal v_{assy} with full codesign framework on different budgets \bar{c}_2 regrouped per stack chain

width induced by v_{assy} must decrease more.

7.5.2 H2H: coupon 1x5

In this section we analyze the results related to the applications of the *full codesign framework* to the H2H coupon with bolting pattern 1x5. We associate to the misalignment features of different holes the same tolerances: this means that v_X represents the tolerances related to all features measured with datum plate, while $v_{\Delta X}$ corresponds to the tolerance bounds of the features evaluated with datum first hole. Declining these definitions per stack chain, the design variable v_X represents the tolerances of all holes in SC1, while for SC4/SC5/SC6 it only represents the tolerance associated to the position of the first hole. On the other hand, $v_{\Delta X}$ - which is defined only for SC4, SC5 and SC6 - describes the tolerance bounds of the position of each j -th hole (with $j > 1$) with respect to the position of the first hole. As a reminder, the tolerance variable v_X is fixed at zero for SC5 (as this is based on assembly procedure with expandable pin) and fixed equal to the clearance of a reference pin for SC6.

The Pareto fronts related to the applications of the *full codesign framework* on the H2H coupon with bolting pattern 1x5 are reported in Fig. 7.32, regrouped per stack chain. Different Pareto fronts are reported in the same plot for different imposed overload limits

OL.

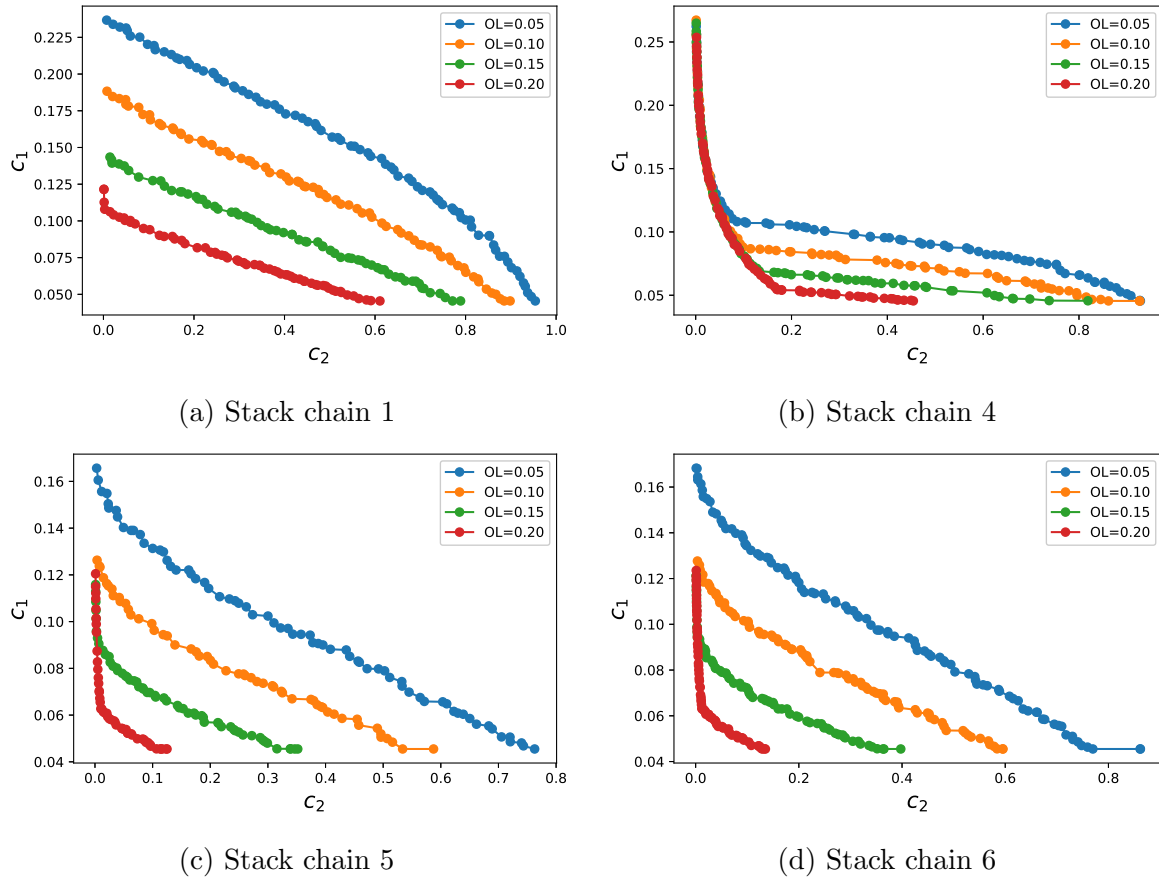


Figure 7.32: H2H coupon 1x5: obtained Pareto fronts for different overloads OL , regrouped per stack chain

With respect to the analogue Pareto fronts retrieved for the coupon 1x2 in Section 7.5.1.1, some differences may be highlighted:

- For the same budget \bar{c}_2 of the assembly-related cost c_2 , the costs c_1 are generally lower: this implies that the tolerance allocation is easier for the coupon 1x2, leading to higher values of the tolerance bounds v_i at component level. This is consistent with the overload results retrieved in Chapter 4.
- The differences between distinct imposed overload limits OL are less evident, compared to what was observed for the coupon 1x2. In particular, the Pareto fronts related to different values of OL are closer to each other. On one hand this implies that the tolerancing part will be less sensitive to the structural requirements. On the other hand, this also implies that lower changes in tolerance plans can affect more easily the structural performances, in probabilistic terms.
- Relatively to the results issued from the stack chain 4, the activation of the PoE constraint is delayed towards higher levels of the cost c_2 : this is visible on the prolongation of the leftest region which follows the response of the unconstrained

multi-objective optimization problem (i.e. the correspondent purely geometrical problem).

At this point, we report the evolutions of the optimal v_i, v_{assy} as functions of the imposed overload limits OL . We regroup the plots per fixed budgets \bar{c}_2 , displaying the outcomes of different stack chains in the same plot. In particular, we illustrate the evolutions of v_i in Fig. 7.33 and v_{assy} in Fig. 7.34. The analogue evolutions, regrouped per feature v_i and per top-level requirement v_{assy} of each stack chain, are reported in Appendix C.2.1.

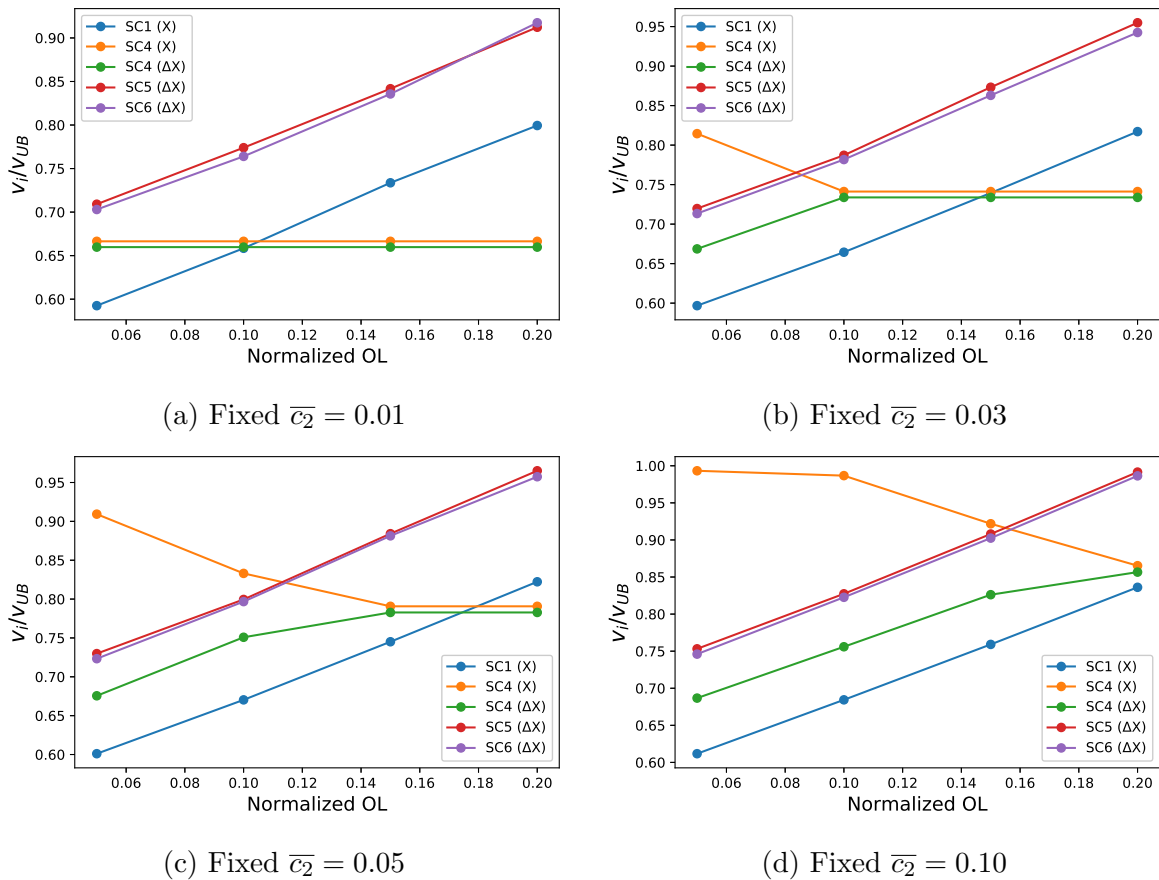


Figure 7.33: H2H coupon 1x5: optimal v_i with full codesign framework on different stack chains at fixed budgets \bar{c}_2

The outcomes of the optimization related to the tolerance variables v_i (reported in Fig. 7.33) show some analogies with the results obtained for the coupon 1x2. The optimal v_i of SC5/SC6 (the behavior of which can be superposed) and SC1 generally increase with both imposed overload limits OL and budget \bar{c}_2 . The gains of SC5/SC6 with respect to SC1 are reduced, compared to what happens on coupon 1x2, from 40% to 20% on average: as stated for the overload quantile analysis in Chapter 4, this is due to the fact that SC5/SC6 only acts on limiting the differences between the misalignment of the first and the successive holes; however, while for coupon 1x2 this component constitutes the only contribution to the variability of the bearing loads, for the coupon 1x5 there are

other contributions given by other combinations of hole misalignments (between distinct bolt locations).

Consistently with the outcomes of the Pareto fronts, we retrieve lower differences between optimal values of the different features at minimum and maximum imposed overload limits OL , compared to the results related to the coupon 1x2. This phenomenon is tightly linked to the Pareto fronts which are closer to each other for the coupon 1x5.

A particular behavior is retrieved on the evolutions of v_i related to SC4. For the highest budget $\bar{c}_2 = 0.1$, we retrieve an evolution similar to the one observed for the coupon 1x2 and the same considerations are still valid to explain the increase of $v_{\Delta X}$ coupled with the decrease of v_X : when increasing OL we allow the *active tolerance variable* $v_{\Delta X}$ to increase; as the same original distributions on $X_{orig,i}$ are used and uniform weighting factors are introduced in the formulation of c_1 , the optimization (from the perspective of c_1) tends to equilibrate the different tolerances, leading to progressively decrease v_X .

Now, we need to explain the evolution of the optimal v_X and $v_{\Delta X}$ associated to the Stack chain 4 on all budgets \bar{c}_2 . We start from the point related to $OL = 1.2$ and $\bar{c}_2 = 0.1$ in Fig. 7.33d: in this point the constraint $PoE \leq \overline{PoE}$ is not active, making the nature of the problem only geometrical and allowing the two values of v_X and $v_{\Delta X}$ to be equal. On the other imposed overload limits OL , the semi-probabilistic constraint on PoE is active, when associated to a budget $\bar{c}_2 = 0.1$. When passing to $\bar{c}_2 = 0.05$ (in Fig. 7.33c), the PoE constraint is inactive also for a lower imposed overload limit $OL = 0.15$: this is due to the fact that a constraint on the cost $c_2 \leq \bar{c}_2$ (following the logic of *constraint method* to solve the multi-objective optimization) becomes more stringent than imposing $PoE \leq \overline{PoE} = 0.1$. This effect continues for lower values of the \bar{c}_2 , leading to two curves of v_X and $v_{\Delta X}$ which can be progressively superposed when going from $\bar{c}_2 = 0.1$ to $\bar{c}_2 = 0.01$. For the lowest budget $\bar{c}_2 = 0.01$, the tolerance problem becomes purely geometrical for all imposed overload limits OL . Note that if the nature of the problem is geometrical, no variation is expected in the evolutions as functions of the overload level (as the PoE constraint is not active), and the plot reaches an horizontal asymptote: in the particular case of $\bar{c}_2 = 0.01$, this asymptote is reached already for imposed overload limits $OL < 0.05$.

The effects of the inactivation of the PoE constraint on the stack chain 4 are overall more evident on the coupon 1x5, compared to the coupon 1x2. This is consistent with the prolongation of the leftest region (i.e. for low c_2) of the Pareto front (comparing Fig. 7.26b and Fig. 7.32b), which in the 1x5 coupon follows the response of the unconstrained problem until higher levels of c_2 .

Moreover, for the configurations where the PoE constraint is not active, the tolerance variables of SC4 become lower than the one related to SC1. In fact, the simulated virtual constraint $c_2 \leq \bar{c}_2$ is more stringent for SC4 as two sources of geometrical variability exist, namely $v_X, v_{\Delta X}$. Therefore, the total variability must be split in two parts (equal if uniform weighting factors are adopted, as in our case, for the cost c_1).

We focus now on the results related to the optimal top-level requirement v_{assy} , depicted in Fig. 7.34. The same considerations on the reduction of the gain between SC5/SC6 and SC1 are also valid in the comparison of the outcomes of v_{assy} related to coupons 1x2 and 1x5. On the other hand, SC4 is less sensitive to variations in v_{assy} , which sticks to the upper bound.

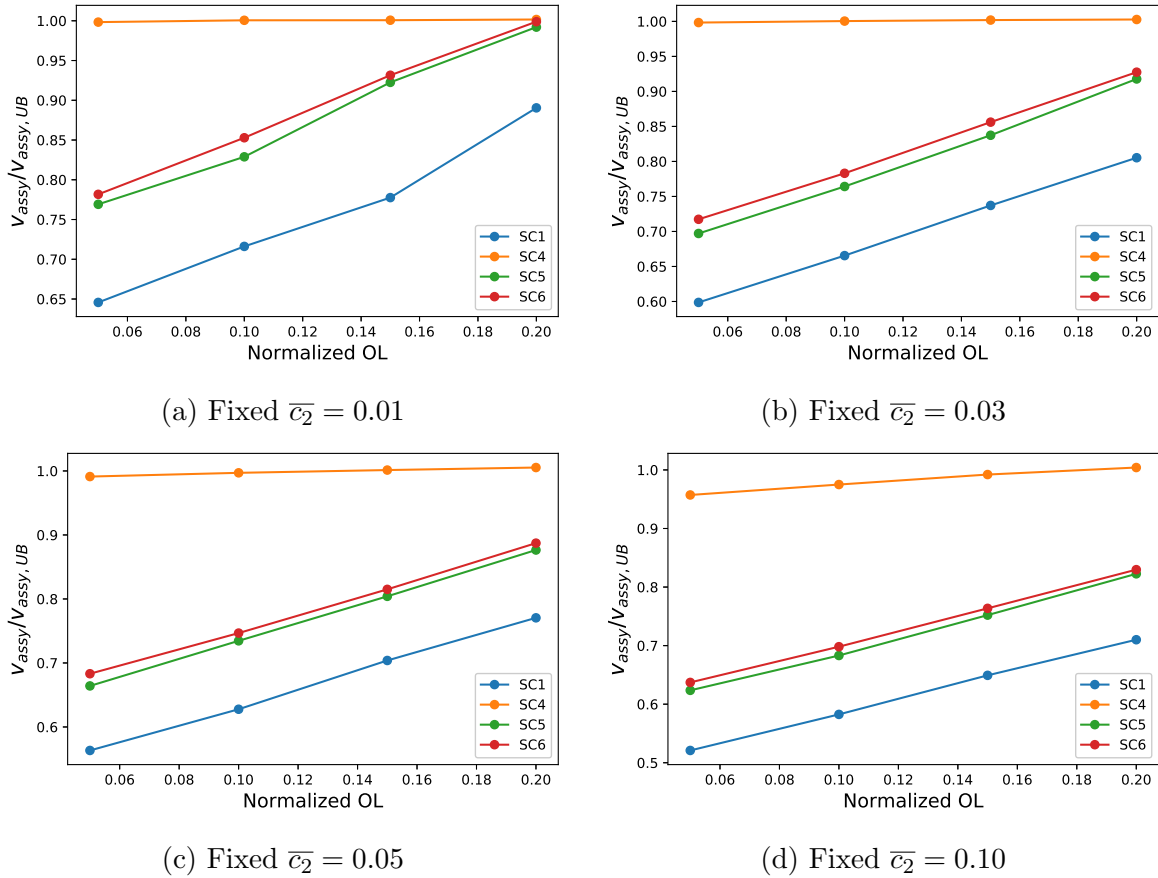


Figure 7.34: H2H coupon 1x5: optimal v_{assy} with full codesign framework on different stack chains at fixed budgets \bar{c}_2

At a global level, the tolerance variables are higher than the analogue optimal values retrieved for the coupon 1x2. This is consistent with the findings from Chapter 4 on the overload analysis. The increased dimension allows here to reduce the probability of detrimental regions, i.e. the parts of the input domain leading to the highest overloads.

7.5.3 H2H: coupon 3x5

In this section we analyze the results related to the application of the *full codesign framework* to the H2H coupon with bolting pattern 3x5. As for the previous coupons, we associate the same tolerance bounds v_X to all the component-related geometrical features which are referenced on a datum plate and the same $v_{\Delta X}$ to the analogues which are referenced on a datum corresponding to the center of the first hole.

We report in Fig. 7.35 the Pareto fronts issued from the resolution of the multi-objective optimization problem. The results are in half-way between the analogue Pareto fronts related to the coupons 1x2 and 1x5, consistently with the results retrieved in Chapter 4 concerning the overload analysis.

By comparing the Pareto fronts issued from the application of the *full codesign framework* of coupons 1x2, 1x5 and 3x5, we may highlight a ranking:

- the values of the component-related costs c_1 of all Pareto fronts of the coupon 3x5

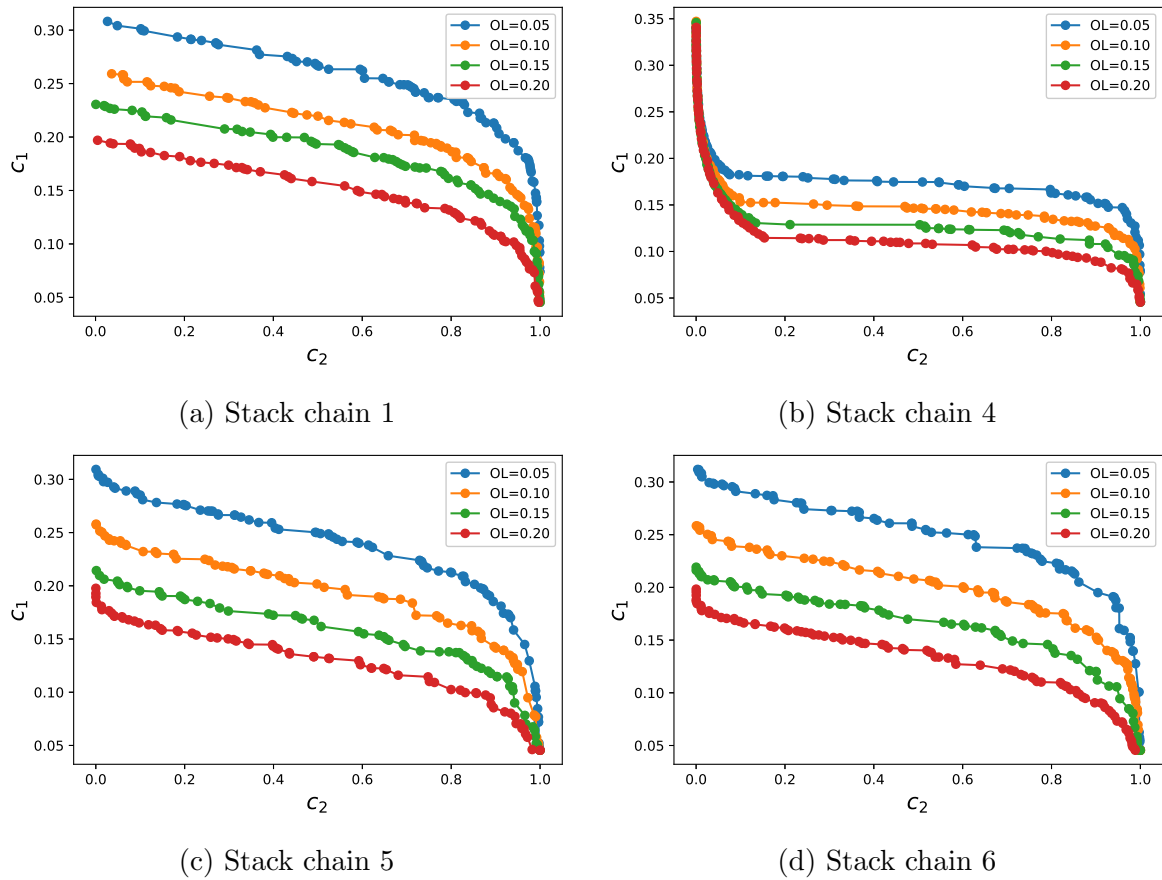


Figure 7.35: H2H coupon 3x5: obtained Pareto fronts for different overloads OL , regrouped per stack chain

are lower than the analogue of the coupon 1x2 and higher than the ones from the 1x5;

- the size of the unconstrained region (i.e. where the PoE constraint is inactive) of the Pareto front related to the stack chain 4 of coupon 3x5 is lower (i.e. it is stopped at lower levels of c_2) than the one of the coupon 1x5 and higher than 1x2;
- the distances between different Pareto fronts (associated to the same stack chains and different imposed overload limits OL) are reduced with respect to the analogue Pareto fronts of coupon 1x2, but increased with respect to the analogue in coupon 1x5.

As for the coupon 1x5, we report here the evolutions of the optimal v_i, v_{assy} as functions of the imposed overload OL . We regroup the plots per fixed budgets \bar{c}_2 , displaying the outcomes of different stack chains in the same plot. In particular, we illustrate the evolutions of v_i in Fig. 7.36 and v_{assy} in Fig. 7.37. The analogue evolutions regrouped per feature v_i and per top-level requirement v_{assy} of each stack chain are reported in Appendix C.2.2.

The global behavior of the optimal v_i confirm the findings from the previous coupons. Close results of $v_{\Delta X}$ are retrieved for SC5 and SC6. Both exhibit better $v_{\Delta X}$ than the

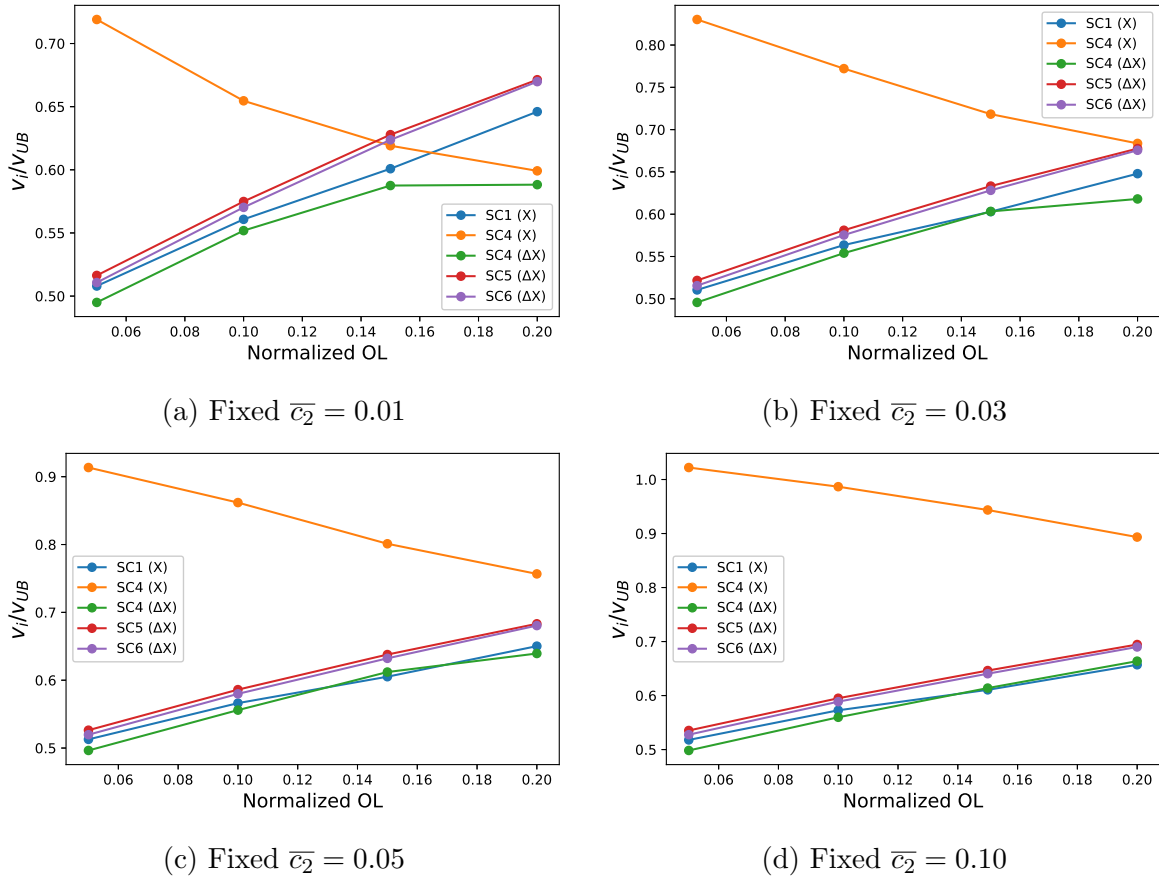


Figure 7.36: H2H coupon 3x5: optimal v_i with full codesign framework on different stack chains at fixed budgets \bar{c}_2

v_X related to SC1 and the $v_{\Delta X}$ from SC4. The evolutions of the features $v_X, v_{\Delta X}$ related to SC4 are consistent with the ones retrieved for the other coupons.

Two differences arise however in the comparison with the tolerance optimizations of the previous coupons. At a global level, the tolerance variables are higher than the ones retrieved on coupon 1x2 but lower than the analogue for the coupon 1x5: as stated in Chapter 4, this coupon can be seen, in the framework of system reliability as a series system of three blocks of the coupon 1x5, so that the probability of overcoming fixed threshold (i.e. the imposed overload limits OL) becomes higher, making the structural semi-probabilistic constraint more restrictive.

On the other hand, the differences between SC1 and the other stack chains become less evident. This is a continuation of the same phenomenon observed for coupon 1x5: blocking the difference of misalignments between the first and all other holes (in a one-by-one relation), only reduces one portion of the modes retrieved for the coupon 3x5. The consequence of this effect is more evident in the comparison between coupons 3x5 and 1x2, rather than what can be observed by comparing coupons 1x5 and 1x2.

Focusing on the results related to the optimal top-level requirement v_{assy} in Fig. 7.37, we retrieve similarities with the results observed on other coupons. For the SC4, the v_{assy} sticks to the upper bound for all levels of \bar{c}_2 . The SC1 still exhibits lower values than SC5 and SC6, even if the differences are less relevant than for the previous cases.

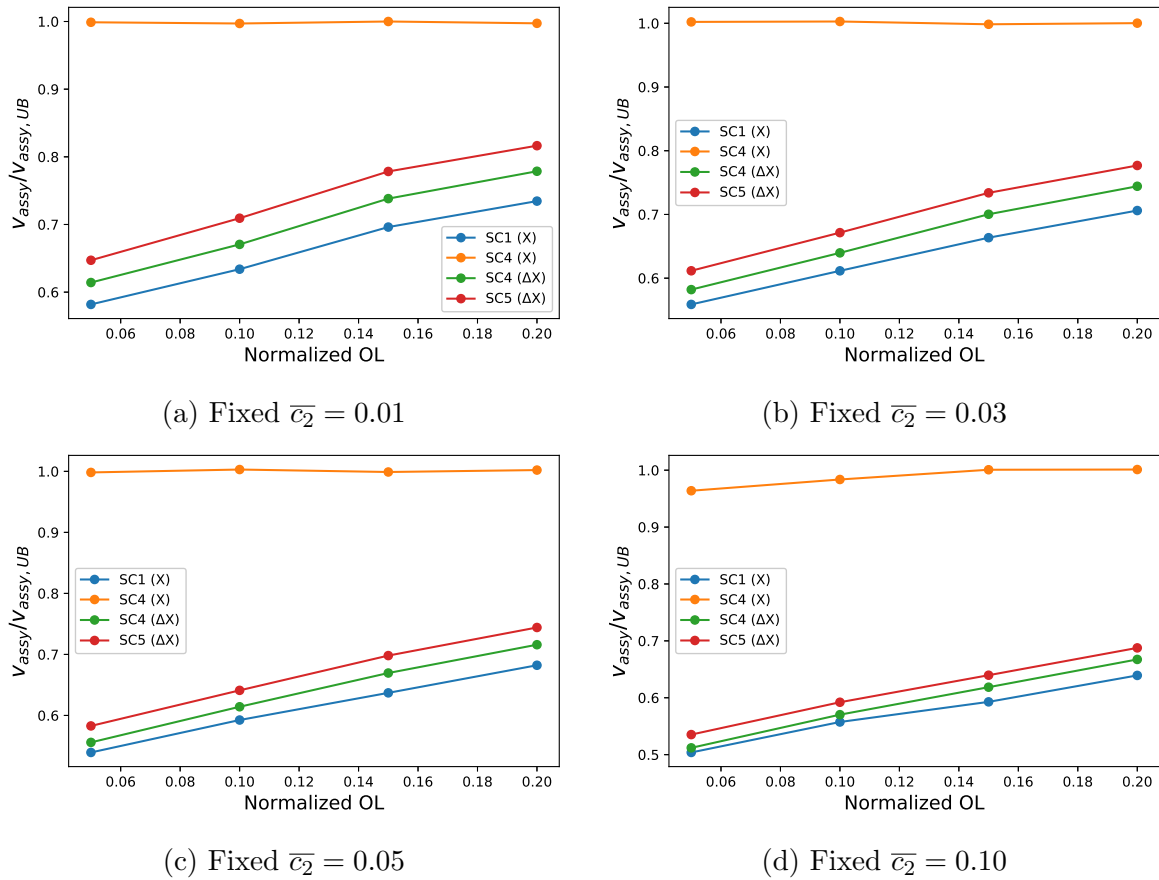


Figure 7.37: H2H coupon 3x5: optimal v_{assy} with full codesign framework on different stack chains at fixed budgets \bar{c}_2

One main difference is given by the distance which we retrieved between SC5 and SC6 (in the other coupons their behaviors could be superposed for both $v_{\Delta X}$ and v_{assy}): here the added variability from the SC6 on the first hole (linked to the clearance of the first hole), induces a larger variability on the output of the tolerance model; however, this is reflected only on the outcomes of c_2 (which becomes higher for SC6, while maintaining the same $v_{\Delta X}$), without affecting neither the PoE nor the cost c_1 . Therefore, the Pareto front is shifted on the right and we retrieve higher v_{assy} on SC6, but similar values of $v_{\Delta X}$, given the slope of the Pareto front (which is lower than unity in the c_2, c_1 axis plan). This effect was also present on other coupons but is amplified for this large coupon.

7.6 Discussion of results

In this section, a critical analysis of the obtained results of the proposed codesign framework is reported.

The two main variants of this framework have been analyzed on a built-in stress use case, namely the wing root joint, to which we associated a simple analytical limit state equation to evaluate the effects of gaps on structural performances. In the considered application of the *current practice*, the top-level requirement is imposed equal to the

worst-case scenario in terms of structural sizing gap. The first variant of the proposed framework, named *codesign framework with fixed top-level requirement*, allows to dissociate the sizing gap (the structural nominal input) from the top-level requirement, defined per different scenarios. The *full codesign framework* allows a deeper exploration of the potential of relaxing the tolerance plans, by introducing the top-level requirement among the design variables.

The effects of both variants of the framework can be seen in the relaxation of the tolerance plans, which imply less stringent quality demand on the different structural elements and associated costs reduction.

Another use case, involving the gaps between spar and cover skin, has been introduced to evaluate the relevance of the knowledge of the effects of the correction interventions at assembly level. We showed in fact that the knowledge of the precise outcomes is not relevant in the context of our proposed framework, as long as two assumptions are verified: (1) we focus on solutions with low intervention rate c_2 ; (2) we can ensure that the interventions are able to restore the performances to nominal levels or, at least, to better configurations than the threshold (in this case the sizing gap) considered in the semi-probabilistic constraint.

The application of the *full codesign framework* on three different H2H coupons (with bolting patterns 1x2, 1x5 and 3x5) allowed the comparison between different stack chains, reflecting the way of defining the tolerances at elementary level. The results showed that these may affect the tolerance optimization problem, in terms of both the elements-related tolerances v_i and the top-level requirement v_{assy} . The ranking of the results related to the stack chains was proved to be the same on all configurations: in particular, the use of a reference datum placed on the center of first hole allows to enlarge the tolerance plans more than if only a datum on the plate border is used. However, the relative gains can change according to the chosen bolting pattern. The overall results are consistent with the findings from the overload analysis in Chapter 4.

One way-forward in H2H activities is given by the generalization of the obtained results to bolting patterns not included in our analyses. Since we had different results for the different coupons, we will need to explore the challenge of extending the results of the proposed codesign framework to adapt them to different structures not included in our benchmark. This is an important step to allow the generalization of the coupons results to the real aeronautical structures.

The formulation of the optimization problem can be further customized to take into account the different impacts of the contributors in a given assembly. However, if the input feature(s) X_i of the defined problem are actually the output(s) of another tolerance model (as in the example of the built-in stresses due to gaps), the tolerance allocation can be included in the internal activities of the tolerance team. In this case, the codesign framework would lead to the redefinition of guidelines on the output of the tolerance model (in terms of variance and truncation level), to give as input to the tolerance team.

At a general level, the proposed codesign framework leads to conclusions which might sometimes seem as counter-intuitive. In fact, it was shown that higher top-level requirements do not necessarily allow easier exploitation of the tolerance definition at elementary level. This is essentially due to the explicit consideration of the semi-probabilistic constraint.

At this point, we need to underline several important aspects regarding the application

of the proposed framework from an engineering perspective.

A first remark should be done concerning the impact on the current way of working of the proposed *codesign framework*. On one hand, this consists of a tolerance allocation problem with structural constraints and can be considered as a monolithic block involving:

- the measurement data from manufacturing in production phase;
- the stack chains associated to the manufacturing process itself;
- the tolerance model explaining the relationship between the toleranced features at components level and the geometrical global features of the whole assembly;
- the stress model highlighting the effects of all the geometrical features of the assembly (at component and assembly level) and the structural response, incorporated in a semi-probabilistic framework.

For new applications, like the H2H, this approach can prove beneficial, as the established ways of working may evolve. On the other hand, for established design processes with separated fields of actions between tolerancing and structural sizing (e.g. the wing root joint and the junction between spar and cover), switching to a monolithic block could be considered as overly intrusive. To solve this issue, we proposed an alternative implementation, based on the concept of using the proposed *codesign framework* to redefine the inputs to the tolerance teams in the form of constraints on the variance and the truncation level of the output of the tolerance model: in this way, we can relax the tolerance plans (thanks to the introduction of the semi-probabilistic framework), without digging into the features of the tolerance model itself. The result would be a more rational management of uncertainties, without intersecting the activities of stress and tolerance teams, which would remain being treated separately. Note, however, that the use of a semi-probabilistic approach and the definition of a constraint on the variance of the outputs of the tolerance model are two main novel concepts of the framework proposed in this chapter.

Secondly, we should be able to guarantee the instrumental capability to achieve a tolerance goal and to check the quality of the global assembly: both constraints can be addressed in the optimization problem definition by imposing realistic lower bounds on all design variables, i.e. both on tolerance bounds \mathbf{v} and on top-level requirement v_{assy} (as scenario for the first variant and as design variable in the *full codesign framework*). In the post-processing step, it could be necessary to round the results to the closest feasible discrete values. If the largest optimal tolerances are too tight for the internal capability, the stress requirements should be relaxed, by means of considering more conservative nominal values in deterministic sizing (e.g. increasing the imposed overload limit in H2H) to compensate the effects of the consequent increase of geometrical variability. From an implementation perspective, the proposed *codesign framework* can be considered as a support to analyze the feasibility of a new design principle for aircraft components.

Moreover, the whole codesign framework is based on specific assumptions on the knowledge of the actual probability distribution of the geometric features. If data is available, the distributions can be fitted relatively accurately. Otherwise, we can introduce the least informative statistical distribution, which is the uniform distribution. However, it must be proved that this constitutes a conservative assumption. If this can not be proven, the proposed codesign framework must be delayed to a phase where production data for the geometric features are already available.

Finally, we should take into account the actual monetary costs related to the change of tolerance plans and the implementation of the obtained results, with a particular attention to the volume-variable costs. In fact, the proposed *codesign framework* may lead to relax significantly the tolerance plans, perhaps allowing to switch to different machining techniques which imply reduced cost per component: if the new machines have to be bought, their cost must be compensated by the savings on the volume production (i.e. the number of produced pieces must be sufficiently high to justify the expenses on the machine itself). This discussion goes beyond the scope of the proposed approach and the monetary costs are not considered in the presented applications of the proposed codesign process: however, this must be kept in mind for the posterior decision making. As stated before, the optimization itself gives several catalogs of available non-dominated solutions, thus needing further discussion over the compromise between different sources of costs.

7.7 Conclusion

In this chapter we conceived a codesign perspective involving manufacturing, tolerancing and stress analysis. The goal was to redefine at the same time the top-level requirements and the tolerances at elements level, in order to make a compromise between different sources of out-of-quality costs coming from different steps of the assembly process, while guaranteeing the static stress requirements redefined in the semi-probabilistic framework. The problem is therefore considered as a multi-objective reliability based optimization problem. Its goal is to determine sets of solutions which constitute a compromise between these sources of out-of-quality costs. The compromise is done via the identification of tolerance variables v_i , affecting the variability of structural elements, and the top-level requirement v_{assy} , filtering the variability of the geometrical outcomes of the global assembly.

The proposed framework is applied on different industrial use cases to highlight the potential in terms of the relaxation of both top-level requirements and element tolerances.

The results related to the different applications show that it is possible to significantly reduce the overall tolerance costs and comply with specific stress requirements. The cost reductions with respect to the current practices are paid with an increase of the risk of overestimating the actual structural performances in deterministic sizing. Such risk is kept under control thanks to the semi-probabilistic constraint on the probability of under-performing relative to the traditional A/B basis sizing.

Moreover, we should note that, in current practice, the only input provided to tolerance team is given by a constraint on the top-level requirement, often based on a worst-case scenario basis. The use of a semi-probabilistic approach itself and the definition of a constraint on the variance of the inputs (and/or the outputs) of the tolerance model are two main novel concepts of the framework proposed in this chapter.

The introduction of a statistical framework allows to challenge the worst-case scenario approach. Moreover, managing the tolerances and the associated uncertainties on the geometrical features also leads to further reduce the overloads from the original values computed in Chapter 4.

Further research on new formulations of the on-quality costs can enrich and further

customize the proposed codesign framework. Moreover, we could consider for future investigations also other sources of cost, including the choice of specific machining techniques, specific corrective interventions at assembly level and the cost associated to the change of tolerance plan. Future works may also investigate new applications on other examples of interest for aeronautical industry.

Bibliography

- [iso, 2006] (ISO 1101:2006). Geometrical product specifications (gps) - geometrical tolerancing: tolerances of form, orientation, location and run-out.
- [iso, 2010] (ISO 14405:2010). Geometrical product specifications (gps) - dimensional tolerancing.
- [iso, 2011a] (ISO 17450:2011a). Geometrical product specifications (gps) - general concepts.
- [iso, 2011b] (ISO 5459:2011b). Geometrical product specifications (gps) - geometrical tolerancing: datums and datum systems.
- [Abdi and Williams, 2010] Abdi, H. and Williams, L. J. (2010). Principal component analysis. *Wiley interdisciplinary reviews: computational statistics*, 2(4):433–459.
- [Abirami et al., 2019] Abirami, T., Loganaganandan, M., Murali, G., Fediuk, R., Sreekrishna, R. V., Vignesh, T., Januppriya, G., and Karthikeyan, K. (2019). Experimental research on impact response of novel steel fibrous concretes under falling mass impact. *Construction and Building Materials*, 222:447–457.
- [Acar et al., 2007] Acar, E., Kale, A., and Haftka, R. (2007). Comparing effectiveness of measures that improve aircraft structural safety. *Journal of Aerospace Engineering*, 20(3):186–199.
- [Airoldi and Cacchione, 2006] Airoldi, A. and Cacchione, B. (2006). Modelling of impact forces and pressures in lagrangian bird strike analyses. *International Journal of Impact Engineering*, 32(10):1651–1677.
- [Alam et al., 2021] Alam, Z., Sun, L., Zhang, C., Su, Z., and Samali, B. (2021). Experimental and numerical investigation on the complex behaviour of the localised seismic response in a multi-storey plan-asymmetric structure. *Structure and infrastructure engineering*, 17(1):86–102.
- [Alfano et al., 2006] Alfano, G., Chiancarella, C., Cirillo, E., Fato, I., and Martellotta, F. (2006). Long-term performance of chemical damp-proof courses: twelve years of laboratory testing. *Building and Environment*, 41(8):1060–1069.
- [Alfredo and Wilson, 1975] Alfredo, H.-S. A. and Wilson, H. (1975). Probability concepts in engineering planning and design. *John Wiley and Sons*.

- [Allen and Maute, 2005] Allen, M. and Maute, K. (2005). Reliability-based shape optimization of structures undergoing fluid–structure interaction phenomena. *Computer Methods in Applied Mechanics and Engineering*, 194(30-33):3472–3495.
- [Allmendinger et al., 2017] Allmendinger, R., Emmerich, M. T., Hakanen, J., Jin, Y., and Rigoni, E. (2017). Surrogate-assisted multicriteria optimization: Complexities, prospective solutions, and business case. *Journal of Multi-Criteria Decision Analysis*, 24(1-2):5–24.
- [Alsina et al., 2018] Alsina, E. F., Chica, M., Trawiński, K., and Regattieri, A. (2018). On the use of machine learning methods to predict component reliability from data-driven industrial case studies. *The International Journal of Advanced Manufacturing Technology*, 94(5):2419–2433.
- [Andolfatto et al., 2014] Andolfatto, L., Thiébaud, F., Lartigue, C., and Douilly, M. (2014). Quality-and cost-driven assembly technique selection and geometrical tolerance allocation for mechanical structure assembly. *Journal of Manufacturing Systems*, 33(1):103–115.
- [Apra et al., 2008] Apra, M., D’Amore, M., Gigliotti, K., Sarto, M. S., and Volpi, V. (2008). Lightning indirect effects certification of a transport aircraft by numerical simulation. *IEEE Transactions on Electromagnetic Compatibility*, 50(3):513–523.
- [Askri et al., 2018] Askri, R., Bois, C., Wargnier, H., and Gayton, N. (2018). Tolerance synthesis of fastened metal-composite joints based on probabilistic and worst-case approaches. *Computer-Aided Design*, 100:39–51.
- [Au and Beck, 1999] Au, S.-K. and Beck, J. L. (1999). A new adaptive importance sampling scheme for reliability calculations. *Structural safety*, 21(2):135–158.
- [Au and Beck, 2001] Au, S.-K. and Beck, J. L. (2001). Estimation of small failure probabilities in high dimensions by subset simulation. *Probabilistic engineering mechanics*, 16(4):263–277.
- [Bado and Casas, 2021] Bado, M. F. and Casas, J. R. (2021). A review of recent distributed optical fiber sensors applications for civil engineering structural health monitoring. *Sensors*, 21(5):1818.
- [Bair et al., 2006] Bair, E., Hastie, T., Paul, D., and Tibshirani, R. (2006). Prediction by supervised principal components. *Journal of the American Statistical Association*, 101(473):119–137.
- [Baldomir et al., 2013] Baldomir, A., Kusano, I., Hernandez, S., and Jurado, J. (2013). A reliability study for the messina bridge with respect to flutter phenomena considering uncertainties in experimental and numerical data. *Computers & Structures*, 128:91–100.
- [Bashor and Kareem, 2007] Bashor, R. and Kareem, A. (2007). Probabilistic performance evaluation of buildings: an occupant comfort perspective. In *Proceedings of the 12th international conference on wind engineering*, pages 1–6.

- [Baudin et al., 2016] Baudin, M., Dutfoy, A., Iooss, B., and Popelin, A.-L. (2016). *Open-TURNS: An Industrial Software for Uncertainty Quantification in Simulation*, pages 1–38. Springer International Publishing, Cham.
- [Baudin et al., 2017] Baudin, M., Dutfoy, A., Iooss, B., and Popelin, A.-L. (2017). Open-turns: An industrial software for uncertainty quantification in simulation. In *Handbook of uncertainty quantification*, pages 2001–2038. Springer.
- [Beaucaire et al., 2013] Beaucaire, P., Gayton, N., Duc, E., and Dantan, J.-Y. (2013). Statistical tolerance analysis of over-constrained mechanisms with gaps using system reliability methods. *Computer-Aided Design*, 45(12):1547–1555.
- [Beaurepaire et al., 2018] Beaurepaire, P., Mattrand, C., Gayton, N., and Dantan, J.-Y. (2018). Tolerance analysis of a deformable component using the probabilistic approach and kriging-based surrogate models. *ASCE-ASME Journal of Risk and Uncertainty in Engineering Systems, Part A: Civil Engineering*, 4(3):04018028.
- [Beck and Souza Jr, 2010] Beck, A. T. and Souza Jr, A. C. d. (2010). A first attempt towards reliability-based calibration of brazilian structural design codes. *Journal of the Brazilian Society of Mechanical Sciences and Engineering*, 32(2):119–127.
- [Belkhelfa and Boukraa, 2020] Belkhelfa, F.-Z. and Boukraa, S. (2020). Damage prediction and test validation of bird impacts on aircraft leading edge’s structures. *International Journal of Crashworthiness*, pages 1–18.
- [Benitez et al., 2020] Benitez, J., Henseler, J., Castillo, A., and Schuberth, F. (2020). How to perform and report an impactful analysis using partial least squares: Guidelines for confirmatory and explanatory is research. *Information & Management*, 57(2):103168.
- [Bernardini et al., 2012] Bernardini, E., Spence, S. M., and Giofrè, M. (2012). Effects of the aerodynamic uncertainties in hffb loading schemes on the response of tall buildings with coupled dynamic modes. *Engineering Structures*, 42:329–341.
- [Bhachu et al., 2015] Bhachu, K., Haftka, R., Waycaster, G., Kim, N., and Hurst, C. (2015). Probabilistic manufacturing tolerance optimization of damage-tolerant aircraft structures using measured data. *Journal of Aircraft*, 52(5):1412–1421.
- [Bichon et al., 2008] Bichon, B. J., Eldred, M. S., Swiler, L. P., Mahadevan, S., and McFarland, J. M. (2008). Efficient global reliability analysis for nonlinear implicit performance functions. *AIAA journal*, 46(10):2459–2468.
- [Birolini, 2013] Birolini, A. (2013). *Reliability engineering: theory and practice*. Springer Science & Business Media.
- [Blank and Deb, 2020] Blank, J. and Deb, K. (2020). Pymoo: Multi-objective optimization in python. *IEEE Access*, 8:89497–89509.
- [Blatman and Sudret, 2008] Blatman, G. and Sudret, B. (2008). Sparse polynomial chaos expansions and adaptive stochastic finite elements using a regression approach. *Comptes Rendus Mécanique*, 336(6):518–523.

- [Blatman and Sudret, 2011] Blatman, G. and Sudret, B. (2011). Adaptive sparse polynomial chaos expansion based on least angle regression. *Journal of computational Physics*, 230(6):2345–2367.
- [Bojórquez et al., 2021] Bojórquez, J., Ponce, S., Ruiz, S. E., Bojórquez, E., Reyes-Salazar, A., Barraza, M., Chávez, R., Valenzuela, F., Leyva, H., and Baca, V. (2021). Structural reliability of reinforced concrete buildings under earthquakes and corrosion effects. *Engineering Structures*, 237:112161.
- [Borgonovo and Plischke, 2016] Borgonovo, E. and Plischke, E. (2016). Sensitivity analysis: A review of recent advances. *European Journal of Operational Research*, 248(3):869–887.
- [Boudaud et al., 2015] Boudaud, C., Humbert, J., Baroth, J., Hameury, S., and Daudeville, L. (2015). Joints and wood shear walls modelling ii: Experimental tests and fe models under seismic loading. *Engineering Structures*, 101:743–749.
- [Bouhlef et al., 2016a] Bouhlef, M. A., Bartoli, N., Otsmane, A., and Morlier, J. (2016a). An improved approach for estimating the hyperparameters of the kriging model for high-dimensional problems through the partial least squares method. *Mathematical Problems in Engineering*, 2016.
- [Bouhlef et al., 2016b] Bouhlef, M. A., Bartoli, N., Otsmane, A., and Morlier, J. (2016b). Improving kriging surrogates of high-dimensional design models by partial least squares dimension reduction. *Structural and Multidisciplinary Optimization*, 53(5):935–952.
- [Bourinet, 2019] Bourinet, J.-M. (2019). An adaptive sampling method for global sensitivity analysis based on least-squares support vector regression. *Reliability Engineering & System Safety*, 183:323–340.
- [Bourinet, 2021] Bourinet, J.-M. (2021). Rare-event probability estimation. *Mechanical Engineering in Uncertainties From Classical Approaches to Some Recent Developments*, page 145.
- [Bourinet et al., 2011] Bourinet, J. M., Deheeger, F., and Lemaire, M. (2011). Assessing small failure probabilities by combined subset simulation and Support Vector Machines. *Structural Safety*, 33(6):343–353.
- [Box and Hunter, 1961] Box, G. E. and Hunter, J. S. (1961). The 2^kp fractional factorial designs. *Technometrics*, 3(3):311–351.
- [Brévault et al., 2013] Brévault, L., Balesdent, M., Bérend, N., and Le Riche, R. (2013). Comparison of different global sensitivity analysis methods for aerospace vehicle optimal design. In *10th World Congress on Structural and Multidisciplinary Optimization, WCSMO-10*.
- [Bristow and Irving, 2007] Bristow, J. W. and Irving, P. (2007). Safety factors in civil aircraft design requirements. *Engineering Failure Analysis*, 14(3):459–470.

- [Bro and Smilde, 2014] Bro, R. and Smilde, A. K. (2014). Principal component analysis. *Analytical methods*, 6(9):2812–2831.
- [Brodin, 2006] Brodin, E. (2006). On quantile estimation by bootstrap. *Computational statistics & data analysis*, 50(6):1398–1406.
- [Burgan et al., 2000] Burgan, B., Baddoo, N., and Gilsenan, K. (2000). Structural design of stainless steel members—comparison between eurocode 3, part 1.4 and test results. *Journal of Constructional Steel Research*, 54(1):51–73.
- [Cai and Lin, 1998] Cai, G. and Lin, Y. (1998). Reliability of nonlinear structural frame under seismic excitation. *Journal of engineering mechanics*, 124(8):852–856.
- [Campolongo et al., 2011] Campolongo, F., Saltelli, A., and Cariboni, J. (2011). From screening to quantitative sensitivity analysis. a unified approach. *Computer physics communications*, 182(4):978–988.
- [Cantero et al., 2019] Cantero, D., McGetrick, P., Kim, C.-W., and O'Brien, E. (2019). Experimental monitoring of bridge frequency evolution during the passage of vehicles with different suspension properties. *Engineering Structures*, 187:209–219.
- [Cappé et al., 2008] Cappé, O., Douc, R., Guillin, A., Marin, J.-M., and Robert, C. P. (2008). Adaptive importance sampling in general mixture classes. *Statistics and Computing*, 18(4):447–459.
- [Caracoglia, 2014] Caracoglia, L. (2014). A stochastic model for examining along-wind loading uncertainty and intervention costs due to wind-induced damage on tall buildings. *Engineering Structures*, 78:121–132.
- [Cascini et al., 2014] Cascini, L., Portioli, F., and Landolfo, R. (2014). Probabilistic time variant assessment of thin-walled steel members under atmospheric corrosion attack. *Journal of Civil Engineering and Management*, 20(3):404–414.
- [Chaudhuri and Haftka, 2013] Chaudhuri, A. and Haftka, R. T. (2013). Separable monte carlo combined with importance sampling for variance reduction. *International Journal of Reliability and Safety*, 7(3):201–215.
- [Chaudhuri et al., 2020] Chaudhuri, A., Kramer, B., and Willcox, K. E. (2020). Information Reuse for Importance Sampling in Reliability-Based Design Optimization. *Reliability Engineering & System Safety*, 201:106853.
- [Cheikh and McGoldrick, 1988] Cheikh, A. and McGoldrick, P. F. (1988). The influence of cost, function and process capability on tolerance. *International Journal of Quality & Reliability Management*.
- [Chen et al., 2019] Chen, W., Xu, C., Shi, Y., Ma, J., and Lu, S. (2019). A hybrid Kriging-based reliability method for small failure probabilities. *Reliability Engineering & System Safety*, 189:31–41.

- [Choi et al., 2021] Choi, C. H., Lee, D. J., Jo, J. H., Bae, S. H., Lee, M. J., and Lee, J. H. (2021). Reliability analysis on fatigue strength for certification of aircraft composite structures. *Journal of Aerospace System Engineering*, 15(2):16–25.
- [Chou and Chang, 2001] Chou, C.-Y. and Chang, C.-L. (2001). Minimum-loss assembly tolerance allocation by considering product degradation and time value of money. *The International Journal of Advanced Manufacturing Technology*, 17(2):139–146.
- [Cruse et al., 1988] Cruse, T., Burnside, O., Wu, Y.-T., Polch, E., and Dias, J. (1988). Probabilistic structural analysis methods for select space propulsion system structural components (psam). *Computers & Structures*, 29(5):891–901.
- [Dahlström and Lindkvist, 2007] Dahlström, S. and Lindkvist, L. (2007). Variation simulation of sheet metal assemblies using the method of influence coefficients with contact modeling.
- [Daniels, 1996] Daniels, J. N. (1996). A method for landing gear modeling and simulation with experimental validation.
- [Dantan and Qureshi, 2009] Dantan, J.-Y. and Qureshi, A.-J. (2009). Worst-case and statistical tolerance analysis based on quantified constraint satisfaction problems and monte carlo simulation. *Computer-Aided Design*, 41(1):1–12.
- [Davenport, 1983] Davenport, A. (1983). On the assessment of the reliability of wind loading on low buildings. *Journal of Wind Engineering and Industrial Aerodynamics*, 11(1-3):21–37.
- [David and Nagaraja, 2004] David, H. A. and Nagaraja, H. N. (2004). *Order statistics*. John Wiley & Sons.
- [De Rocquigny et al., 2008] De Rocquigny, E., Devictor, N., Tarantola, S., Lefebvre, Y., Prot, N., Castaings, W., Mangeant, F., Schwob, C., Lavin, R., Masse, J.-R., Limbourg, P., Kanning, W., and Gelder, P. (2008). Uncertainty in industrial practice: A guide to quantitative uncertainty management.
- [Deb et al., 2002] Deb, K., Pratap, A., Agarwal, S., and Meyarivan, T. (2002). A fast and elitist multiobjective genetic algorithm: Nsga-ii. *IEEE transactions on evolutionary computation*, 6(2):182–197.
- [Degenhardt et al., 2010] Degenhardt, R., Kling, A., Bethge, A., Orf, J., Kärger, L., Zimmermann, R., Rohwer, K., and Calvi, A. (2010). Investigations on imperfection sensitivity and deduction of improved knock-down factors for unstiffened cfrp cylindrical shells. *Composite Structures*, 92(8):1939–1946.
- [Dhillon, 2001] Dhillon, I. S. (2001). Co-clustering documents and words using bipartite spectral graph partitioning. In *Proceedings of the seventh ACM SIGKDD international conference on Knowledge discovery and data mining*, pages 269–274.
- [Diet, 2021] Diet, A. (2021). *An end-to-end approach of statistical tolerancing under industrial constraints: Contribution to the design/industrial virtual twin*. PhD thesis, IMT-Institut de Mathématiques de Toulouse UMR5219.

- [Diet et al., 2020] Diet, A., Couellan, N., Gendre, X., Martin, J., and Navarro, J.-P. (2020). A statistical approach for tolerancing from design stage to measurements analysis. *Procedia CIRP*, 92:33–38.
- [Dong et al., 2021] Dong, F., Shi, F., Wang, L., Wei, Y., and Zheng, K. (2021). Probabilistic assessment approach of the aerostatic instability of long-span symmetry cable-stayed bridges. *Symmetry*, 13(12):2413.
- [Dong and Nakayama, 2018] Dong, H. and Nakayama, M. K. (2018). A tutorial on quantile estimation via monte carlo. In *International Conference on Monte Carlo and Quasi-Monte Carlo Methods in Scientific Computing*, pages 3–30. Springer.
- [Dubourg et al., 2011] Dubourg, V., Sudret, B., and Bourinet, J.-M. (2011). Reliability-based design optimization using kriging surrogates and subset simulation. *Structural and Multidisciplinary Optimization*, 44:673–690.
- [Durakovic, 2017] Durakovic, B. (2017). Design of experiments application, concepts, examples: State of the art. *Periodicals of Engineering and Natural Sciences (PEN)*, 5(3).
- [Dymiotis, 2002] Dymiotis, C. (2002). Reliability based code calibration for earthquake-resistant design. In *Proceedings of JCSS Workshop on Reliability Based Code Calibration*.
- [Easa, 2009] Easa, C. (2009). Certification specifications for large aeroplanes, cs 25.
- [Echard et al., 2011] Echard, B., Gayton, N., and Lemaire, M. (2011). Ak-mcs: an active learning reliability method combining kriging and monte carlo simulation. *Structural Safety*, 33(2):145–154.
- [Egloff and Leippold, 2010] Egloff, D. and Leippold, M. (2010). Quantile estimation with adaptive importance sampling. *The Annals of Statistics*, 38(2):1244–1278.
- [El Haj and Soubra, 2021] El Haj, A.-K. and Soubra, A.-H. (2021). Improved active learning probabilistic approach for the computation of failure probability. *Structural Safety*, 88:102011.
- [Elhewy et al., 2006] Elhewy, A. H., Mesbahi, E., and Pu, Y. (2006). Reliability analysis of structures using neural network method. *Probabilistic Engineering Mechanics*, 21(1):44–53.
- [Elishakoff and Chamis, 2001] Elishakoff, I. and Chamis, C. C. (2001). Interrelation between safety factors and reliability.
- [Ellingwood and Rosowsky, 1991] Ellingwood, B. and Rosowsky, D. (1991). Duration of load effects in lrfd for wood construction. *Journal of Structural Engineering*, 117(2):584–599.
- [Ellingwood, 1997] Ellingwood, B. R. (1997). Probability-based lrfd for engineered wood construction. *Structural Safety*, 19(1):53–65.

- [Ellingwood and Lee, 2016] Ellingwood, B. R. and Lee, J. Y. (2016). Life cycle performance goals for civil infrastructure: intergenerational risk-informed decisions. *Structure and Infrastructure Engineering*, 12(7):822–829.
- [Emmerich and Deutz, 2018] Emmerich, M. and Deutz, A. H. (2018). A tutorial on multiobjective optimization: fundamentals and evolutionary methods. *Natural computing*, 17(3):585–609.
- [Enevoldsen and Sørensen, 1994] Enevoldsen, I. and Sørensen, J. D. (1994). Reliability-based optimization in structural engineering. *Structural safety*, 15(3):169–196.
- [Engineering, 2017] Engineering, A. (2017). *Hyperstudy 2017 Software Documentation*.
- [Enrico et al., 2019] Enrico, Z., Mengfei, F., Zhiguo, Z., and Rui, K. (2019). Application of reliability technologies in civil aviation: Lessons learnt and perspectives. *Chinese Journal of Aeronautics*, 32(1):143–158.
- [Esposito et al., 2014] Esposito, M., Barile, M., De Fenza, A., Di Leo, R., and Lecce, L. (2014). Multi-body model validation of a landing gear system for a general aviation aircraft. *Aerotecnica Missili & Spazio*, 93(3):101–108.
- [Esteva and Villaverde, 1973] Esteva, L. and Villaverde, R. (1973). Seismic risk, design spectra and structural reliability. In *Proceedings of Fifth World Conference on Earthquake Engineering*, volume 2, pages 2586–2596.
- [Faber, 2000] Faber, M. (2000). Reliability based assessment of existing structures. *Progress in Structural Engineering and Materials*, 2(2):247–253.
- [Faber and Sørensen, 2003] Faber, M. and Sørensen, J. D. (2003). Reliability-based code calibration: The jcsc approach. In *9th International Conference on Applications of Statistics and Probability in Civil Engineering*, pages 927–935. Millpress.
- [Faber and Sørensen, 2002] Faber, M. H. and Sørensen, J. D. (2002). Reliability based code calibration. *The Joint Committee on Structural Safety, Zurich, Switzerland*.
- [Faber et al., 2000] Faber, M. H., Val, D. V., and Stewart, M. G. (2000). Proof load testing for bridge assessment and upgrading. *Engineering structures*, 22(12):1677–1689.
- [Ferrero Bermejo et al., 2019] Ferrero Bermejo, J., Gomez Fernandez, J. F., Olivenca Polo, F., and Crespo Márquez, A. (2019). A review of the use of artificial neural network models for energy and reliability prediction. a study of the solar pv, hydraulic and wind energy sources. *Applied Sciences*, 9(9):1844.
- [Folz and Foschi, 1989] Folz, B. and Foschi, R. O. (1989). Reliability-based design of wood structural systems. *Journal of Structural Engineering*, 115(7):1666–1680.
- [Frangopol, 2011] Frangopol, D. M. (2011). Life-cycle performance, management, and optimisation of structural systems under uncertainty: accomplishments and challenges 1. *Structure and infrastructure Engineering*, 7(6):389–413.

- [Frangopol and Kim, 2019] Frangopol, D. M. and Kim, S. (2019). *Life-cycle of structures under uncertainty: Emphasis on fatigue-sensitive civil and marine structures*. CRC Press.
- [Frangopol and Kim, 2022] Frangopol, D. M. and Kim, S. (2022). *Bridge safety, maintenance and management in a life-cycle context*. CRC Press.
- [Frangopol and Maute, 2003] Frangopol, D. M. and Maute, K. (2003). Life-cycle reliability-based optimization of civil and aerospace structures. *Computers & Structures*, 81(7):397–410.
- [Frangopol et al., 2019] Frangopol, D. M., Yang, D. Y., Lantsoght, E. O., and Steenbergen, R. D. (2019). Reliability-based analysis and life-cycle management of load tests. *Load Testing of Bridges*, pages 265–296.
- [Fu et al., 2020] Fu, B., Zhao, J., Li, B., Yao, J., Teifouet, A. R. M., Sun, L., and Wang, Z. (2020). Fatigue reliability analysis of wind turbine tower under random wind load. *Structural Safety*, 87:101982.
- [Fujino et al., 2019] Fujino, Y., Siringoringo, D. M., Ikeda, Y., Nagayama, T., and Mizutani, T. (2019). Research and implementations of structural monitoring for bridges and buildings in japan. *Engineering*, 5(6):1093–1119.
- [Gao et al., 2020] Gao, H., Wang, A., Zio, E., and Bai, G. (2020). An integrated reliability approach with improved importance sampling for low-cycle fatigue damage prediction of turbine disks. *Reliability Engineering & System Safety*, 199:106819.
- [García-Escudero et al., 2010] García-Escudero, L. A., Gordaliza, A., Matrán, C., and Mayo-Iscar, A. (2010). A review of robust clustering methods. *Advances in Data Analysis and Classification*, 4:89–109.
- [Gary and Riskalla, 1997] Gary, P. and Riskalla, M. (1997). Development of probabilistic design methodology for composite structures. Technical report, VOUGHT AIRCRAFT CO DALLAS TX.
- [Gaspar et al., 2015] Gaspar, B., Teixeira, A. P., and Soares, C. G. (2015). A study on a stopping criterion for active refinement algorithms in kriging surrogate models. *Safety and reliability of complex engineered systems*, pages 1219–1227.
- [Gaudrie et al., 2020] Gaudrie, D., Le Riche, R., Picheny, V., Enaux, B., and Herbert, V. (2020). Targeting solutions in bayesian multi-objective optimization: sequential and batch versions. *Annals of Mathematics and Artificial Intelligence*, 88:187–212.
- [Ge et al., 2000] Ge, Y., Xiang, H., and Tanaka, H. (2000). Application of a reliability analysis model to bridge flutter under extreme winds. *Journal of Wind Engineering and Industrial Aerodynamics*, 86(2-3):155–167.
- [Geetha et al., 2013] Geetha, K., Ravindran, D., Kumar, M. S., and Islam, M. N. (2013). Multi-objective optimization for optimum tolerance synthesis with process and machine selection using a genetic algorithm. *The International Journal of Advanced Manufacturing Technology*, 67(9):2439–2457.

- [Geetha et al., 2015] Geetha, K., Ravindran, D., Kumar, M. S., and Islam, M. N. (2015). Concurrent tolerance allocation and scheduling for complex assemblies. *Robotics and Computer-Integrated Manufacturing*, 35:84–95.
- [Ghiocel and Wang, 2005] Ghiocel, D. and Wang, L. (2005). Computational advances in reliability assessment of aircraft structures under corrosion-fatigue damage. In *46th AIAA/ASME/ASCE/AHS/ASC Structures, Structural Dynamics and Materials Conference*, page 2148.
- [Ghiocel and Tuegel, 2004] Ghiocel, D. M. and Tuegel, E. J. (2004). Reliability assessment of aircraft structure joints under corrosion-fatigue damage. In *Engineering Design Reliability Handbook*, pages 667–726. CRC Press.
- [Ghobarah and EL-ATTAR, 1998] Ghobarah, A. and EL-ATTAR, M. (1998). Seismic reliability assessment of existing reinforced concrete buildings. *Journal of Earthquake Engineering - J EARTHQU ENG*, 2:569–592.
- [Ghosal et al., 2020] Ghosal, A., Nandy, A., Das, A. K., Goswami, S., and Panday, M. (2020). A short review on different clustering techniques and their applications. *Emerging Technology in Modelling and Graphics: Proceedings of IEM Graph 2018*, pages 69–83.
- [Ghosn and Moses, 1986] Ghosn, M. and Moses, F. (1986). Reliability calibration of bridge design code. *Journal of Structural Engineering*, 112(4):745–763.
- [Gibbons et al.,] Gibbons, M., Galsworthy, J., Chatten, M., and Kala, S. Wind load prediction on tall buildings in a stochastic framework. In *Structures Congress 2017*, pages 24–33.
- [Gogu, 2021] Gogu, C. (2021). *Mechanical Engineering under Uncertainties: From Classical Approaches to Some Recent Developments*. ISTE-Wiley.
- [Gouyou et al., 2018] Gouyou, D., Ledoux, Y., Teissandier, D., and Delos, V. (2018). Tolerance analysis of overconstrained and flexible assemblies by polytopes and finite element computations: application to a flange. *Research in Engineering Design*, 29(1):55–66.
- [Govaert and Nadif, 2013] Govaert, G. and Nadif, M. (2013). *Co-clustering: models, algorithms and applications*. John Wiley & Sons.
- [Govindarajalu et al., 2012] Govindarajalu, J., Karuppan, S., and Manoharan, T. (2012). Tolerance design of mechanical assembly using nsga ii and finite element analysis. *Journal of mechanical science and technology*, 26(10):3261–3268.
- [Gransden and Alderliesten, 2017] Gransden, D. I. and Alderliesten, R. (2017). Development of a finite element model for comparing metal and composite fuselage section drop testing. *International journal of crashworthiness*, 22(4):401–414.
- [Greenhill et al., 2020] Greenhill, S., Rana, S., Gupta, S., Vellanki, P., and Venkatesh, S. (2020). Bayesian optimization for adaptive experimental design: A review. *IEEE access*, 8:13937–13948.

- [Grihon, 2018] Grihon, S. (2018). Structure sizing optimization capabilities at airbus. In *Advances in Structural and Multidisciplinary Optimization: Proceedings of the 12th World Congress of Structural and Multidisciplinary Optimization (WCSMO12) 12*, pages 719–737. Springer.
- [Grihon et al., 2009] Grihon, S., Krog, L., and Bassir, D. (2009). Numerical optimization applied to structure sizing at airbus: a multi-step process. *International Journal for Simulation and Multidisciplinary Design Optimization*, 3(4):432–442.
- [Guerra-Santin and Tweed, 2015] Guerra-Santin, O. and Tweed, C. A. (2015). In-use monitoring of buildings: An overview of data collection methods. *Energy and Buildings*, 93:189–207.
- [Guida et al., 2008] Guida, M., Marulo, F., Meo, M., Riccio, M., and Russo, S. (2008). Evaluation and validation of multi-physics fe methods to simulate bird strike on a wing leading edge. In *Proceedings of ECCM*, volume 13.
- [Gulvanessian and Holický, 2002] Gulvanessian, H. and Holický, M. (2002). Reliability based calibration of eurocodes considering a steel member. In *JCSS Workshop on Reliability Based Calibration*.
- [Gunst and Mason, 2009] Gunst, R. F. and Mason, R. L. (2009). Fractional factorial design. *Wiley Interdisciplinary Reviews: Computational Statistics*, 1(2):234–244.
- [Guo et al., 2016] Guo, J., Li, B., Liu, Z., Hong, J., and Wu, X. (2016). Integration of geometric variation and part deformation into variation propagation of 3-d assemblies. *International Journal of Production Research*, 54(19):5708–5721.
- [Guo et al., 2019] Guo, Y., Hu, X., and Lv, J. (2019). Experimental study on the resistance of basalt fibre-reinforced concrete to chloride penetration. *Construction and Building Materials*, 223:142–155.
- [Hall and Tsai, 1989] Hall, W. B. and Tsai, M. (1989). Load testing, structural reliability and test evaluation. *Structural safety*, 6(2-4):285–302.
- [Hallmann et al., 2020] Hallmann, M., Schleich, B., and Wartzack, S. (2020). From tolerance allocation to tolerance-cost optimization: A comprehensive literature review. *The International Journal of Advanced Manufacturing Technology*, 107(11):4859–4912.
- [Hallmann et al., 2022] Hallmann, M., Schleich, B., and Wartzack, S. (2022). Process and machine selection in sampling-based tolerance-cost optimisation for dimensional tolerancing. *International Journal of Production Research*, 60(17):5201–5216.
- [Hammersley, 2013] Hammersley, J. (2013). *Monte carlo methods*. Springer Science & Business Media.
- [Han and Ouyang, 2021] Han, M. and Ouyang, L. (2021). Robust functional response-based metamodel optimization considering both location and dispersion effects for aeronautical airfoil designs. *Structural and Multidisciplinary Optimization*, 64(3):1545–1565.

- [Hariri-Ardebili and Pourkamali-Anaraki, 2018] Hariri-Ardebili, M. A. and Pourkamali-Anaraki, F. (2018). Support vector machine based reliability analysis of concrete dams. *Soil Dynamics and Earthquake Engineering*, 104:276–295.
- [Hasofer and Lind, 1974] Hasofer, A. M. and Lind, N. C. (1974). Exact and invariant second-moment code format. *Journal of the Engineering Mechanics division*, 100(1):111–121.
- [Heimbs, 2011] Heimbs, S. (2011). Bird strike simulations on composite aircraft structures. In *SIMULIA Customer Conference, Barcelona*, pages 73–86.
- [Heng et al., 2019] Heng, P., Le Gac, B., Keo, P., Somja, H., and Palas, F. (2019). Reliability-based analysis for thermal break system under low-cycle climatic fatigue loads. *Journal of Structural Engineering*, 145(3):04019003.
- [Hinsch, 2020] Hinsch, M. (2020). The process of en 9100 certification. In *Guideline for EN 9100: 2018*, pages 149–164. Springer.
- [Hoffenson et al., 2013] Hoffenson, S., Dagman, A., and Söderberg, R. (2013). Tolerance specification optimization for economic and ecological sustainability. In *Smart Product Engineering*, pages 865–874. Springer.
- [Hu and Su, 2008] Hu, J. and Su, Z. (2008). Bootstrap quantile estimation via importance resampling. *Computational statistics & data analysis*, 52(12):5136–5142.
- [Huang and Lin, 2005] Huang, C. and Lin, K. (2005). A method for reliability assessment of aircraft structures subject to accidental damage. In *46th AIAA/ASME/ASCE/AHS/ASC Structures, Structural Dynamics and Materials Conference*, page 1830.
- [Huang et al., 2020] Huang, H., Huang, M., Zhang, W., Pospisil, S., and Wu, T. (2020). Experimental investigation on rehabilitation of corroded rc columns with bsp and hpf under combined loadings. *Journal of Structural Engineering*, 146(8):04020157.
- [Huang et al., 2015] Huang, Q., Gardoni, P., and Hurlbaeus, S. (2015). Adaptive reliability analysis of reinforced concrete bridges subject to seismic loading using nondestructive testing. *ASCE-ASME Journal of Risk and Uncertainty in Engineering Systems, Part A: Civil Engineering*, 1(4):04015014.
- [Huang et al., 2017] Huang, Q., Zhang, H., Chen, J., and He, M. (2017). Quantile regression models and their applications: A review. *Journal of Biometrics & Biostatistics*, 8(3):1–6.
- [Huang et al., 2012] Huang, W., Wang, T.-J., Garbatov, Y., and Soares, C. G. (2012). Fatigue reliability assessment of riveted lap joint of aircraft structures. *International Journal of Fatigue*, 43:54–61.
- [Iervolino et al., 2018] Iervolino, I., Spillatura, A., and Bazzurro, P. (2018). Seismic reliability of code-conforming italian buildings. *Journal of Earthquake Engineering*, 22(sup2):5–27.

- [Ignatovich and Bouraou, 2013] Ignatovich, S. and Bouraou, N. (2013). The reliability of detecting cracks during nondestructive testing of aircraft components. *Russian journal of nondestructive testing*, 49(5):294–300.
- [Ilzarbe et al., 2008] Ilzarbe, L., Álvarez, M. J., Viles, E., and Tanco, M. (2008). Practical applications of design of experiments in the field of engineering: a bibliographical review. *Quality and Reliability Engineering International*, 24(4):417–428.
- [Iooss and Lemaître, 2015] Iooss, B. and Lemaître, P. (2015). A review on global sensitivity analysis methods. *Uncertainty management in simulation-optimization of complex systems*, pages 101–122.
- [Jackson and Fasanella, 2005] Jackson, K. E. and Fasanella, E. L. (2005). Crash simulation of a vertical drop test of a commuter-class aircraft. *International Journal of Crashworthiness*, 10(2):173–182.
- [Jaimes et al., 2009] Jaimes, A. L., Martinez, S. Z., Coello, C. A. C., et al. (2009). An introduction to multiobjective optimization techniques. *Optimization in Polymer Processing*, pages 29–57.
- [Jalayer et al., 2011] Jalayer, F., Asprone, D., Prota, A., and Manfredi, G. (2011). A decision support system for post-earthquake reliability assessment of structures subjected to aftershocks: an application to l’aquila earthquake, 2009. *Bulletin of Earthquake Engineering*, 9(4):997–1014.
- [Jalayer et al., 2010] Jalayer, F., Iervolino, I., and Manfredi, G. (2010). Structural modeling uncertainties and their influence on seismic assessment of existing rc structures. *Structural safety*, 32(3):220–228.
- [Jia and Wu, 2022] Jia, D.-W. and Wu, Z.-Y. (2022). An importance sampling reliability method combining Kriging and Gaussian Mixture Model through ring subregion strategy for multiple failure modes. *Structural and Multidisciplinary Optimization*, 65(2):61.
- [Jia et al., 2020] Jia, Y., Yang, Y., Liu, G., Gao, Y., Yang, T., and Hu, D. (2020). Reliability assessment of flexural fatigue failure of asphalt mixture: A new perspective. *Construction and Building Materials*, 257:119553.
- [Jiang et al., 2020] Jiang, C., Qiu, H., Gao, L., Wang, D., Yang, Z., and Chen, L. (2020). Real-time estimation error-guided active learning kriging method for time-dependent reliability analysis. *Applied Mathematical Modelling*, 77:82–98.
- [Jin et al., 1999] Jin, W., Ruan, L., Hu, Y., and HONG, Q.-s. (1999). Structural reliability assessment of buildings under typhoon calamity. *Journal of Natural Disasters*, 8:105–112.
- [Jing et al., 2020] Jing, T., Tian, X., Liu, X., Hu, H., Zhang, M., and Li, B. (2020). A multiple alternative processes-based cost-tolerance optimal model for aircraft assembly. *The International Journal of Advanced Manufacturing Technology*, 107(1):667–677.

- [Jolliffe, 1982] Jolliffe, I. T. (1982). A note on the use of principal components in regression. *Journal of the Royal Statistical Society Series C: Applied Statistics*, 31(3):300–303.
- [Jolliffe, 2002] Jolliffe, I. T. (2002). *Principal Components Analysis*. Springer New York, NY.
- [Kappas, 2002] Kappas, J. (2002). Review of risk and reliability methods for aircraft gas turbine engines. Technical report, DEFENCE SCIENCE AND TECHNOLOGY ORGANISATION VICTORIA (AUSTRALIA).
- [Karamchandani et al., 1989] Karamchandani, A., Bjerager, P., and Cornell, C. (1989). Adaptive importance sampling. In *Structural Safety and Reliability*, pages 855–862. ASCE.
- [Keane, 2006] Keane, A. J. (2006). Statistical improvement criteria for use in multiobjective design optimization. *AIAA journal*, 44(4):879–891.
- [Keller et al., 2008] Keller, T., Haas, C., and Vallée, T. (2008). Structural concept, design, and experimental verification of a glass fiber-reinforced polymer sandwich roof structure. *Journal of composites for construction*, 12(4):454–468.
- [Kempeneers, 2018] Kempeneers, M. (2018). Towards airframe static stress requirements improvement using probabilistic analyses. In *13th World Congress on Computational Mechanics (WCCM XIII)*, page 164, NY City, US.
- [Kermanidis et al., 2005] Kermanidis, T., Labeas, G., Sunaric, M., and Ubels, L. (2005). Development and validation of a novel bird strike resistant composite leading edge structure. *Applied Composite Materials*, 12(6):327–353.
- [Keye, 2011] Keye, S. (2011). Fluid-structure coupled analysis of a transport aircraft and flight-test validation. *Journal of aircraft*, 48(2):381–390.
- [Kim et al., 1999] Kim, C.-B., Pulat, P. S., Foote, B. L., and Lee, D. H. (1999). Least cost tolerance allocation and bicriteria extension. *International Journal of Computer Integrated Manufacturing*, 12(5):418–426.
- [Knowles, 2006] Knowles, J. (2006). Parego: A hybrid algorithm with on-line landscape approximation for expensive multiobjective optimization problems. *IEEE Transactions on Evolutionary Computation*, 10(1):50–66.
- [Koenker, 2017] Koenker, R. (2017). Quantile regression: 40 years on. *Annual review of economics*, 9:155–176.
- [Kolathayar et al., 2018] Kolathayar, S., Anupa, S., and Prakash, E. L. (2018). Development of earthquake readiness index tool to assess individual earthquake preparedness level. In *Urbanization Challenges in Emerging Economies: Resilience and Sustainability of Infrastructure*, pages 149–155. American Society of Civil Engineers Reston, VA.

- [Konakli and Sudret, 2016] Konakli, K. and Sudret, B. (2016). Reliability analysis of high-dimensional models using low-rank tensor approximations. *Probabilistic Engineering Mechanics*, 46:18–36.
- [Krejsa, 2013] Krejsa, M. (2013). Probabilistic reliability assessment of steel structures exposed to fatigue. In *Proceedings of Conference ESREL*, pages 2671–2679.
- [Kumar et al., 2020] Kumar, V., Kartik, K., and Iqbal, M. A. (2020). Experimental and numerical investigation of reinforced concrete slabs under blast loading. *Engineering Structures*, 206:110125.
- [Kusano et al., 2014] Kusano, I., Baldomir, A., Jurado, J. Á., and Hernández, S. (2014). Reliability based design optimization of long-span bridges considering flutter. *Journal of Wind Engineering and Industrial Aerodynamics*, 135:149–162.
- [Lam et al., 2003] Lam, F., Abayakoon, S., Svensson, S., and Gyamfi, C. (2003). Influence of proof loading on the reliability of members. *Holz als Roh-und Werkstoff*, 61(6):432–438.
- [Lamboni et al., 2013] Lamboni, M., Iooss, B., Popelin, A.-L., and Gamboa, F. (2013). Derivative-based global sensitivity measures: General links with sobol indices and numerical tests. *Mathematics and Computers in Simulation*, 87:45–54.
- [Lantsoght et al., 2017] Lantsoght, E. O., van der Veen, C., de Boer, A., and Hordijk, D. A. (2017). State-of-the-art on load testing of concrete bridges. *Engineering Structures*, 150:231–241.
- [Lantsoght et al., 2018] Lantsoght, E. O. L., Koekkoek, R. T., Hordijk, D., and de Boer, A. (2018). Towards standardisation of proof load testing: pilot test on viaduct zijlweg. *Structure and Infrastructure Engineering*, 14(3):365–380.
- [Larsen and Raju, 2016] Larsen, C. E. and Raju, I. S. (2016). Moving aerospace structural design practice to a load and resistance factor approach. In *57th AIAA/ASCE/AHS/ASC Structures, Structural Dynamics, and Materials Conference*, page 0230.
- [Larsson, 2015] Larsson, O. (2015). Reliability analysis. *Lecture notes, Lund University*.
- [Lavoie et al., 2007] Lavoie, M., Gakwaya, A., Ensan, M. N., and Zimcik, D. (2007). Validation of available approaches for numerical bird strike modeling tools. *International Review of Mechanical Engineering*, 1(4):380–389.
- [Le Riche et al.,] Le Riche, R., Picheny, V., Meyer, A., Kim, N.-H., and Ginsbourger, D. Gears design with shape uncertainties using controlled monte carlo simulations and kriging. In *50th AIAA/ASME/ASCE/AHS/ASC Structures, Structural Dynamics, and Materials Conference 17th AIAA/ASME/AHS Adaptive Structures Conference 11th AIAA No*, page 2257.
- [Leander, 2018] Leander, J. (2018). Reliability evaluation of the eurocode model for fatigue assessment of steel bridges. *Journal of constructional steel research*, 141:1–8.

- [Leander et al., 2014] Leander, J., Norlin, B., and Karoumi, R. (2014). Reliability-based calibration of fatigue safety factors for existing steel bridges. *Journal of bridge engineering*, 20(10):04014107.
- [Lee and Kwak, 2006] Lee, S. H. and Kwak, B. M. (2006). Response surface augmented moment method for efficient reliability analysis. *Structural safety*, 28(3):261–272.
- [Lelievre, 2018] Lelievre, N. (2018). *Développement des méthodes AK pour l'analyse de fiabilité. Focus sur les événements rares et la grande dimension*. PhD thesis, Université Clermont Auvergne.
- [Lelièvre et al., 2018] Lelièvre, N., Beaurepaire, P., Mattrand, C., and Gayton, N. (2018). Ak-mcsi: A kriging-based method to deal with small failure probabilities and time-consuming models. *Structural Safety*, 73:1–11.
- [Lemaire, 2013] Lemaire, M. (2013). *Structural reliability*. John Wiley & Sons.
- [Li et al., 2020] Li, C., Sun, L., Xu, Z., Wu, X., Liang, T., and Shi, W. (2020). Experimental investigation and error analysis of high precision fbg displacement sensor for structural health monitoring. *International Journal of Structural Stability and Dynamics*, 20(06):2040011.
- [Li et al., 2021] Li, L., Chakik, M., and Prakash, R. (2021). A review of corrosion in aircraft structures and graphene-based sensors for advanced corrosion monitoring. *Sensors*, 21(9):2908.
- [Lin et al., 2018] Lin, L., Luo, B., and Zhong, S. (2018). Multi-objective decision-making model based on cbm for an aircraft fleet with reliability constraint. *International Journal of Production Research*, 56(14):4831–4848.
- [Lin and Nowak, 1984] Lin, T. S. and Nowak, A. S. (1984). Proof loading and structural reliability. *Reliability Engineering*, 8(2):85–100.
- [Lincoln, 1985] Lincoln, J. W. (1985). Risk assessment of an aging military aircraft. *Journal of aircraft*, 22(8):687–691.
- [Lind, 1971] Lind, N. C. (1971). Consistent partial safety factors. *Journal of the Structural Division*, 97(6):1651–1669.
- [Ling and Lu, 2021] Ling, C. and Lu, Z. (2021). Compound kriging-based importance sampling for reliability analysis of systems with multiple failure modes. *Engineering Optimization*, pages 1–25.
- [Long and Narciso, 1999] Long, M. and Narciso, J. (1999). Probabilistic design methodology for composite aircraft structures. Technical report, NORTHROP GRUMMAN CORP DALLAS TX COMMERCIAL AIRCRAFT DIV.
- [Luo and Grandhi, 1997] Luo, X. and Grandhi, R. V. (1997). Astros for reliability-based multidisciplinary structural analysis and optimization. *Computers & structures*, 62(4):737–745.

- [Luo et al., 2021] Luo, Y., Zheng, H., Zhang, H., and Liu, Y. (2021). Fatigue reliability evaluation of aging prestressed concrete bridge accounting for stochastic traffic loading and resistance degradation. *Advances in Structural Engineering*, 24(13):3021–3029.
- [Madsen et al., 2010] Madsen, H. A., Larsen, G. C., Larsen, T. J., Troldborg, N., and Mikkelsen, R. (2010). Calibration and validation of the dynamic wake meandering model for implementation in an aeroelastic code. *Journal of Solar Energy Engineering*, 132(4).
- [Madsen et al., 2006] Madsen, H. O., Krenk, S., and Lind, N. C. (2006). *Methods of structural safety*. Courier Corporation.
- [Malecot et al., 2019] Malecot, Y., Zingg, L., Briffaut, M., and Baroth, J. (2019). Influence of free water on concrete triaxial behavior: The effect of porosity. *Cement and Concrete Research*, 120:207–216.
- [Manco et al., 2021] Manco, P., Caterino, M., Macchiaroli, R., Rinaldi, M., and Fera, M. (2021). Aircraft maintenance: Structural health monitoring influence on costs and practices. In *Macromolecular Symposia*, volume 396, page 2000302. Wiley Online Library.
- [Mangalgi, 2019] Mangalgi, P. D. (2019). Corrosion issues in structural health monitoring of aircraft. *ISSS Journal of Micro and Smart Systems*, 8(1):49–78.
- [Mangurian, 1957] Mangurian, G. N. (1957). The aircraft structural factor of safety. Technical report, ADVISORY GROUP FOR AERONAUTICAL RESEARCH AND DEVELOPMENT PARIS (FRANCE).
- [Manne, 1987a] Manne, R. (1987a). Analysis of two partial-least-squares algorithms for multivariate calibration. *Chemometrics and Intelligent Laboratory Systems*, 2(1-3):187–197.
- [Manne, 1987b] Manne, R. (1987b). Analysis of two partial-least-squares algorithms for multivariate calibration. *Chemometrics and Intelligent Laboratory Systems*, 2(1):187–197. Proceedings of the Multivariate Statistical Workshop for Geologists and Geochemists.
- [Manohar and Gupta, 2003] Manohar, C. and Gupta, S. (2003). Modeling and evaluation of structural reliability: Current status and future directions. *Research reviews in structural engineering, Golden Jubilee Publications of Department of Civil Engineering, Indian Institute of Science, Bangalore*.
- [Mansuy et al., 2011] Mansuy, M., Giordano, M., and Hernandez, P. (2011). A new calculation method for the worst case tolerance analysis and synthesis in stack-type assemblies. *Computer-Aided Design*, 43(9):1118–1125.
- [Mase, 2018] Mase, L. Z. (2018). Reliability study of spectral acceleration designs against earthquakes in bengkulu city, indonesia. *International Journal of Technology*, 9(5).

- [Mehmood et al., 2012] Mehmood, T., Liland, K. H., Snipen, L., and Sæbø, S. (2012). A review of variable selection methods in partial least squares regression. *Chemometrics and intelligent laboratory systems*, 118:62–69.
- [Melchers, 2005] Melchers, R. E. (2005). The effect of corrosion on the structural reliability of steel offshore structures. *Corrosion science*, 47(10):2391–2410.
- [Melkumova and Shatskikh, 2017] Melkumova, L. and Shatskikh, S. Y. (2017). Comparing ridge and lasso estimators for data analysis. *Procedia engineering*, 201:746–755.
- [Menz et al., 2021] Menz, M., Dubreuil, S., Morio, J., Gogu, C., Bartoli, N., and Chiron, M. (2021). Variance based sensitivity analysis for monte carlo and importance sampling reliability assessment with gaussian processes. *Structural Safety*, 93:102116.
- [Metropolis and Ulam, 1949] Metropolis, N. and Ulam, S. (1949). The monte carlo method. *Journal of the American statistical association*, 44(247):335–341.
- [Meyer et al., 2008] Meyer, M., Flourens, F., Rouquette, J. A., and Delnevo, A. (2008). Modeling of lightning indirect effects in cfrp aircraft. In *2008 International Symposium on Electromagnetic Compatibility-EMC Europe*, pages 1–5. IEEE.
- [Miah et al., 2021] Miah, M. H., Zhang, J., and Chand, D. S. (2021). Knowledge creation and application of optimal tolerance distribution method for aircraft product assembly. *Aircraft Engineering and Aerospace Technology*.
- [Mishra et al., 2013] Mishra, S. K., Roy, B. K., and Chakraborty, S. (2013). Reliability-based-design-optimization of base isolated buildings considering stochastic system parameters subjected to random earthquakes. *International Journal of Mechanical Sciences*, 75:123–133.
- [Misraji et al., 2020] Misraji, M. A., Valdebenito, M. A., Jensen, H. A., and Mayorga, C. F. (2020). Application of directional importance sampling for estimation of first excursion probabilities of linear structural systems subject to stochastic gaussian loading. *Mechanical Systems and Signal Processing*, 139:106621.
- [Mokhtari and Melchers, 2020] Mokhtari, M. and Melchers, R. E. (2020). Reliability of the conventional approach for stress/fatigue analysis of pitting corroded pipelines—development of a safer approach. *Structural Safety*, 85:101943.
- [Molent and Haddad, 2020] Molent, L. and Haddad, A. (2020). A critical review of available composite damage growth test data under fatigue loading and implications for aircraft sustainment. *Composite Structures*, 232:111568.
- [Montgomery, 2017] Montgomery, D. C. (2017). *Design and analysis of experiments*. John wiley & sons.
- [Morio, 2012] Morio, J. (2012). Extreme quantile estimation with nonparametric adaptive importance sampling. *Simulation Modelling Practice and Theory*, 27:76–89.
- [Moroni et al., 2011] Moroni, G., Petrò, S., and Tolio, T. (2011). Early cost estimation for tolerance verification. *CIRP annals*, 60(1):195–198.

- [Morse et al., 2018] Morse, E., Dantan, J.-Y., Anwer, N., Söderberg, R., Moroni, G., Qureshi, A., Jiang, X., and Mathieu, L. (2018). Tolerancing: Managing uncertainty from conceptual design to final product. *CIRP Annals*, 67(2):695–717.
- [Moustapha and Sudret, 2019] Moustapha, M. and Sudret, B. (2019). Surrogate-assisted reliability-based design optimization: a survey and a unified modular framework. *Structural and Multidisciplinary Optimization*, 60(5):2157–2176.
- [Müller et al., 2019] Müller, T., McWilliams, B., Rousselle, F., Gross, M., and Novák, J. (2019). Neural importance sampling. *ACM Transactions on Graphics (TOG)*, 38(5):1–19.
- [Muot et al., 2020] Muot, N., Strub, T., Roissé, D., Girard, C., Monferran, P., Guiffaut, C., Terrade, F., Fustin, F., and Tristant, F. (2020). Numerical evaluation of the lightning currents flowing through aircrafts fasteners—comparison and cross-validation of methods. In *2020 International Symposium on Electromagnetic Compatibility-EMC EUROPE*, pages 1–8. IEEE.
- [Nadim et al., 2015] Nadim, F., Choi, Y.-J., Lacasse, S., and Liu, Z. (2015). Calibration of partial safety factors for offshore foundation design. *International Journal of Reliability and Safety*, 9(1):51–69.
- [Nadolski et al., 2019] Nadolski, V., Rózsás, Á., and Sýkora, M. (2019). Calibrating partial factors—methodology, input data and case study of steel structures. *Periodica Polytechnica Civil Engineering*, 63(1):222–242.
- [Nakayama, 2014] Nakayama, M. K. (2014). Quantile estimation when applying conditional monte carlo. In *2014 4th International Conference On Simulation And Modeling Methodologies, Technologies And Applications (SIMULTECH)*, pages 280–285. IEEE.
- [Neal and Vangel, 1990] Neal, D. M. and Vangel, M. G. (1990). Statistically based material properties. a military handbook-17 perspective. Technical report, ARMY LAB COMMAND WATERTOWN MA MATERIAL TECHNOLOGY LAB.
- [Nguyen and Nguyen, 2020] Nguyen, T.-H. and Nguyen, D.-D. (2020). Reliability assessment of steel-concrete composite beams considering metal corrosion effects. *Advances in Civil Engineering*, 2020.
- [Nikolaidis et al., 2007] Nikolaidis, E., Ghiocel, D. M., and Singhal, S. (2007). *Engineering design reliability applications: for the aerospace, automotive and ship industries*. CRC Press.
- [Oehling and Barry, 2019] Oehling, J. and Barry, D. J. (2019). Using machine learning methods in airline flight data monitoring to generate new operational safety knowledge from existing data. *Safety science*, 114:89–104.
- [Olaszek et al., 2016] Olaszek, P., Casas, J., and Świt, G. (2016). Some relevant experiences from proof load testing of concrete bridges. In *Life-Cycle of Engineering Systems*, pages 1092–1099. CRC Press.

- [Orlando et al., 2018] Orlando, S., Marulo, F., Guida, M., and Timbrato, F. (2018). Bird strike assessment for a composite wing flap. *International journal of crashworthiness*, 23(2):219–235.
- [Ostachowicz et al., 2019] Ostachowicz, W., Soman, R., and Malinowski, P. (2019). Optimization of sensor placement for structural health monitoring: A review. *Structural Health Monitoring*, 18(3):963–988.
- [Othman et al., 2019] Othman, M. F., Silva, G. H., Cabral, P. H., Prado, A. P., Pirrera, A., and Cooper, J. E. (2019). A robust and reliability-based aeroelastic tailoring framework for composite aircraft wings. *Composite Structures*, 208:101–113.
- [Paiva et al., 2014] Paiva, R. M., Crawford, C., and Suleman, A. (2014). Robust and reliability-based design optimization framework for wing design. *AIAA journal*, 52(4):711–724.
- [Pan and Dias, 2017] Pan, Q. and Dias, D. (2017). An efficient reliability method combining adaptive support vector machine and monte carlo simulation. *Structural Safety*, 67:85–95.
- [Papadimitriou et al., 2001] Papadimitriou, C., Beck, J. L., and Katafygiotis, L. S. (2001). Updating robust reliability using structural test data. *Probabilistic engineering mechanics*, 16(2):103–113.
- [Papaioannou et al., 2019] Papaioannou, I., Geyer, S., and Straub, D. (2019). Improved cross entropy-based importance sampling with a flexible mixture model. *Reliability Engineering & System Safety*, 191:106564.
- [Park et al., 2000] Park, G., Cudney, H. H., and Inman, D. J. (2000). Impedance-based health monitoring of civil structural components. *Journal of infrastructure systems*, 6(4):153–160.
- [Pellisetti and Schuëller, 2006] Pellisetti, M. and Schuëller, G. (2006). On general purpose software in structural reliability—an overview. *Structural Safety*, 28(1-2):3–16.
- [Perfetto et al., 2018] Perfetto, D., De Luca, A., Lamanna, G., Chiariello, A., Di Caprio, F., Di Palma, L., and Caputo, F. (2018). Drop test simulation and validation of a full composite fuselage section of a regional aircraft. *Procedia Structural Integrity*, 12:380–391.
- [Pham, 2006] Pham, H. (2006). *Handbook of reliability engineering*. Springer Science & Business Media.
- [Pourzeynali and Datta, 2002] Pourzeynali, S. and Datta, T. (2002). Reliability analysis of suspension bridges against flutter. *Journal of Sound and Vibration*, 254(1):143–162.
- [Pourzeynali and Datta, 2005] Pourzeynali, S. and Datta, T. (2005). Reliability analysis of suspension bridges against fatigue failure from the gusting of wind. *Journal of Bridge Engineering*, 10(3):262–271.

- [Pourzeynali and Hosseinneshad, 2009] Pourzeynali, S. and Hosseinneshad, A. (2009). Reliability analysis of bridge structures for earthquake excitations.
- [Pradlwarter et al., 2005] Pradlwarter, H., Pellissetti, M., Schenk, C., Schueller, G., Kreis, A., Fransen, S., Calvi, A., and Klein, M. (2005). Realistic and efficient reliability estimation for aerospace structures. *Computer Methods in Applied Mechanics and Engineering*, 194(12-16):1597–1617.
- [Qiu et al., 2013] Qiu, Z., Huang, R., Wang, X., and Qi, W. (2013). Structural reliability analysis and reliability-based design optimization: Recent advances. *Science China Physics, Mechanics and Astronomy*, 56(9):1611–1618.
- [Qu et al., 2021] Qu, Q., Ma, Z., Clausen, A., and Jørgensen, B. N. (2021). A comprehensive review of machine learning in multi-objective optimization. In *2021 IEEE 4th International Conference on Big Data and Artificial Intelligence (BD AI)*, pages 7–14. IEEE.
- [Qu and Haftka, 2004] Qu, X. and Haftka, R. (2004). Reliability-based design optimization using probabilistic sufficiency factor. *Structural and Multidisciplinary Optimization*, 27(5):314–325.
- [Qureshi et al., 2010] Qureshi, A. J., Dantan, J.-Y., Bruyère, J., and Bigot, R. (2010). Tolerance analysis based on quantified constraint satisfaction problems. *Product Life-cycle Management: Geometric Variations*, pages 125–144.
- [Rackwitz and Flessler, 1978] Rackwitz, R. and Flessler, B. (1978). Structural reliability under combined random load sequences. *Computers & structures*, 9(5):489–494.
- [Rackwitz and Schrupp, 1985] Rackwitz, R. and Schrupp, K. (1985). Quality control, proof testing and structural reliability. *Structural Safety*, 2(3):239–244.
- [Rao, 2019] Rao, S. S. (2019). *Engineering optimization: theory and practice*. John Wiley & Sons.
- [Rausand and Høyland, 2003] Rausand, M. and Høyland, A. (2003). *System reliability theory: models, statistical methods, and applications*, volume 396. John Wiley & Sons.
- [Remennikov and Kaewunruen, 2020] Remennikov, A. and Kaewunruen, S. (2020). Impact resistance of reinforced concrete columns: experimental studies and design considerations. In *Progress in mechanics of structures and materials*, pages 817–823. CRC Press.
- [Richard and Zhang, 2007] Richard, J.-F. and Zhang, W. (2007). Efficient high-dimensional importance sampling. *Journal of Econometrics*, 141(2):1385–1411.
- [Riggio and Dilmaghani, 2020] Riggio, M. and Dilmaghani, M. (2020). Structural health monitoring of timber buildings: A literature survey. *Building Research & Information*, 48(8):817–837.
- [Rojiani and Wen, 1981] Rojiani, K. and Wen, Y.-K. (1981). Reliability of steel buildings under winds. *Journal of the Structural Division*, 107(1):203–221.

- [Rouchon, 1990] Rouchon, J. (1990). Certification of large airplane composite structures. In *ICAS Congress Proceedings*, volume 2, pages 1439–1447.
- [Rykov et al., 2010] Rykov, V. V., Balakrishnan, N., and Nikulin, M. S. (2010). *Mathematical and Statistical Models and Methods in Reliability: Applications to Medicine, Finance, and Quality Control*. Springer Science & Business Media.
- [Saltelli, 2002] Saltelli, A. (2002). Making best use of model evaluations to compute sensitivity indices. *Computer physics communications*, 145(2):280–297.
- [Samawi et al., 2019] Samawi, H., Chatterjee, A., Yin, J., and Rochani, H. (2019). On quantiles estimation based on different stratified sampling with optimal allocation. *Communications in Statistics-Theory and Methods*, 48(6):1529–1544.
- [Saxena et al., 2017] Saxena, A., Prasad, M., Gupta, A., Bharill, N., Patel, O. P., Tiwari, A., Er, M. J., Ding, W., and Lin, C.-T. (2017). A review of clustering techniques and developments. *Neurocomputing*, 267:664–681.
- [Schillo et al., 2017] Schillo, C., Kriegesmann, B., and Krause, D. (2017). Reliability based calibration of safety factors for unstiffened cylindrical composite shells. *Composite Structures*, 168:798–812.
- [Schöbi et al., 2017] Schöbi, R., Sudret, B., and Marelli, S. (2017). Rare event estimation using polynomial-chaos kriging. *ASCE-ASME Journal of Risk and Uncertainty in Engineering Systems, Part A: Civil Engineering*, 3(2):D4016002.
- [Shan et al., 2020] Shan, J., Zhang, H., Shi, W., and Lu, X. (2020). Health monitoring and field-testing of high-rise buildings: A review. *Structural Concrete*, 21(4):1272–1285.
- [Shao et al., 2022] Shao, Z., Zhang, C., Li, Y., Shen, H., Zhang, D., Yu, X., and Zhang, Y. (2022). A review of non-destructive evaluation (nde) techniques for residual stress profiling of metallic components in aircraft engines. *Aerospace*, 9(10):534.
- [Shittu et al., 2020] Shittu, A. A., Mehmanparast, A., Shafiee, M., Kolios, A., Hart, P., and Pilario, K. (2020). Structural reliability assessment of offshore wind turbine support structures subjected to pitting corrosion-fatigue: A damage tolerance modelling approach. *Wind Energy*, 23(11):2004–2026.
- [Smarslok, 2009] Smarslok, B. P. (2009). Measuring, using, and reducing experimental and computational uncertainty in reliability analysis of composite laminates. *Ph. D. Thesis*.
- [Smarslok et al., 2010] Smarslok, B. P., Haftka, R. T., Carraro, L., and Ginsbourger, D. (2010). Improving accuracy of failure probability estimates with separable monte carlo. *International Journal of Reliability and Safety*, 4(4):393–414.
- [Snyder et al., 2013] Snyder, M. R., Kang, H. S., Brownell, C. J., and Burks, J. S. (2013). Validation of ship air wake simulations and investigation of ship air wake impact on rotary wing aircraft. *Naval Engineers Journal*, 125(1):49–50.

- [Song et al., 2006] Song, G., Ma, N., and Li, H.-N. (2006). Applications of shape memory alloys in civil structures. *Engineering structures*, 28(9):1266–1274.
- [Song et al., 2017] Song, G., Wang, C., and Wang, B. (2017). Structural health monitoring (shm) of civil structures.
- [Song et al., 2021] Song, L.-K., Bai, G.-C., Li, X.-Q., and Wen, J. (2021). A unified fatigue reliability-based design optimization framework for aircraft turbine disk. *International Journal of Fatigue*, 152:106422.
- [Sørensen, 2002] Sørensen, J. D. (2002). Calibration of partial safety factors in danish structural codes. In *JCSS Workshop on Reliability Based Code Calibration*, volume 21, page 2002. Citeseer.
- [Sørensen et al., 2001] Sørensen, J. D., Hansen, J., and Nielsen, T. A. (2001). Partial safety factors and target reliability level in danish structural codes. In *IABSE International Conference on Safety, Risk and Reliability*, pages 179–184. International Association for Bridge and Structural Engineering.
- [Sørensen et al., 1994] Sørensen, J. D., Kroon, I. B., and Faber, M. H. (1994). Optimal reliability-based code calibration. *Structural Safety*, 15(3):197–208.
- [Sørensen et al., 2005] Sørensen, J. D., Svensson, S., and Stang, B. D. (2005). Reliability-based calibration of load duration factors for timber structures. *Structural Safety*, 27(2):153–169.
- [Spagnol et al., 2019] Spagnol, A., Riche, R. L., and Veiga, S. D. (2019). Global sensitivity analysis for optimization with variable selection. *SIAM/ASA Journal on uncertainty quantification*, 7(2):417–443.
- [Spence and Giofrè, 2012] Spence, S. M. and Giofrè, M. (2012). Large scale reliability-based design optimization of wind excited tall buildings. *Probabilistic Engineering Mechanics*, 28:206–215.
- [Su and Jin, 2019] Su, C.-Q. and Jin, J.-J. (2019). Frequency reliability sensitivity analysis of aircraft tension joints. In *2019 International Conference on Quality, Reliability, Risk, Maintenance, and Safety Engineering (QR2MSE)*, pages 625–630. IEEE.
- [Subramanian and Mahadevan, 2022] Subramanian, A. and Mahadevan, S. (2022). Importance sampling for probabilistic prognosis of sector-wide flight separation safety. *Reliability Engineering & System Safety*, 222:108410.
- [Sundararajan, 2012] Sundararajan, C. R. (2012). *Probabilistic structural mechanics handbook: theory and industrial applications*. Springer Science & Business Media.
- [Thoft-Christensen and Baker, 1982] Thoft-Christensen, P. and Baker, M. J. (1982). Extended level 2 methods. In *Structural Reliability Theory and Its Applications*, pages 95–111. Springer.

- [Thoft-Christensen et al., 1998] Thoft-Christensen, P. et al. (1998). *Industrial application of structural Reliability Theory*. Institutet for Bygningsteknik, Aalborg Universitet.
- [Thoft-Christensen and Murotsu, 2012] Thoft-Christensen, P. and Murotsu, Y. (2012). *Application of structural systems reliability theory*. Springer Science & Business Media.
- [Tokdar and Kass, 2010] Tokdar, S. T. and Kass, R. E. (2010). Importance sampling: a review. *Wiley Interdisciplinary Reviews: Computational Statistics*, 2(1):54–60.
- [Tong, 2001] Tong, Y. C. (2001). Literature review on aircraft structural risk and reliability analysis. Technical report, DEFENCE SCIENCE AND TECHNOLOGY ORGANISATION MELBOURNE (AUSTRALIA).
- [Torossian et al., 2020] Torossian, L., Picheny, V., Faivre, R., and Garivier, A. (2020). A review on quantile regression for stochastic computer experiments. *Reliability Engineering & System Safety*, 201:106858.
- [Towsyfyan et al., 2020] Towsyfyan, H., Biguri, A., Boardman, R., and Blumensath, T. (2020). Successes and challenges in non-destructive testing of aircraft composite structures. *Chinese Journal of Aeronautics*, 33(3):771–791.
- [Trezos and Thomos, 2002] Trezos, C. and Thomos, G. (2002). Reliability based calibration of the greek seismic code.
- [Trivedi and Bobbio, 2017] Trivedi, K. S. and Bobbio, A. (2017). *Reliability and availability engineering: modeling, analysis, and applications*. Cambridge University Press.
- [Tuken et al., 2017] Tuken, A., Dahesh, M. A., and Siddiqui, N. A. (2017). Reliability assessment of rc shear wall-frame buildings subjected to seismic loading. *Computers and Concrete, An International Journal*, 20(6):719–729.
- [Ushakov et al., 2002] Ushakov, A., Stewart, A., Mishulin, I., and Pankov, A. (2002). Probabilistic design of damage tolerant composite aircraft structures. Technical report, TSAGI ZHUKOVSKY (RUSSIA).
- [Val, 2007] Val, D. V. (2007). Deterioration of strength of rc beams due to corrosion and its influence on beam reliability. *Journal of Structural Engineering*, 133(9):1297–1306.
- [Val and Stewart, 2002] Val, D. V. and Stewart, M. G. (2002). Safety factors for assessment of existing structures. *Journal of Structural Engineering*, 128(2):258–265.
- [Vavruš et al., 2019] Vavruš, M., Bujňák, J., and Koteš, P. (2019). Experimental verification of real behavior of bridge structures using proof-load tests. *Pollack Periodica*, 14(1):75–84.
- [Venkatesan et al., 2021] Venkatesan, S., Beemkumar, N., Jayaprabakar, J., and Kadiresh, P. (2021). Modelling and analysis of aircraft wing with and without winglet. *International Journal of Ambient Energy*, 42(4):363–373.

- [Venter and Scotti, 2012] Venter, G. and Scotti, S. J. (2012). Accounting for proof test data in a reliability-based design optimization framework. *AIAA journal*, 50(10):2159–2167.
- [Viana, 2016] Viana, F. A. (2016). A tutorial on latin hypercube design of experiments. *Quality and reliability engineering international*, 32(5):1975–1985.
- [Vidal et al., 2016] Vidal, R., Ma, Y., and Sastry, S. S. (2016). *Principal component analysis*. Springer.
- [Vinzi et al., 2010] Vinzi, V. E., Chin, W. W., Henseler, J., Wang, H., et al. (2010). *Handbook of partial least squares*, volume 201. Springer.
- [Von Luxburg, 2007] Von Luxburg, U. (2007). A tutorial on spectral clustering. *Statistics and computing*, 17(4):395–416.
- [Vrouwenvelder and Siemes, 1987] Vrouwenvelder, A. and Siemes, A. (1987). Probabilistic calibration procedure for the derivation of partial safety factors for the netherlands building codes. *HERON*, 32 (4), 1987.
- [Wang et al., 2021a] Wang, C., Beer, M., and Ayyub, B. M. (2021a). Time-dependent reliability of aging structures: Overview of assessment methods. *ASCE-ASME Journal of Risk and Uncertainty in Engineering Systems, Part A: Civil Engineering*, 7(4):03121003–03121003.
- [Wang et al., 2006] Wang, H., Pramanik, N., Roy, U., Sudarsan, R., Sriram, R. D., and Lyons, K. W. (2006). A scheme for mapping tolerance specifications to generalized deviation space for use in tolerance synthesis and analysis. *IEEE transactions on automation science and engineering*, 3(1):81–91.
- [Wang et al., 2021b] Wang, J., Gao, X., and Sun, Z. (2021b). An importance sampling framework for time-variant reliability analysis involving stochastic processes. *Sustainability*, 13(14):7776.
- [Wang et al., 2022] Wang, J., Xu, G., Li, Y., and Kareem, A. (2022). AKSE: A novel adaptive Kriging method combining sampling region scheme and error-based stopping criterion for structural reliability analysis. *Reliability Engineering & System Safety*, 219:108214.
- [Wang and Liu, 2020] Wang, L. and Liu, Y. (2020). A novel method of distributed dynamic load identification for aircraft structure considering multi-source uncertainties. *Structural and Multidisciplinary Optimization*, 61(5):1929–1952.
- [Wang et al., 2003] Wang, X., Kruger, U., and Lennox, B. (2003). Recursive partial least squares algorithms for monitoring complex industrial processes. *Control Engineering Practice*, 11(6):613–632.
- [Wang et al., 2019a] Wang, X., Shi, Q., Fan, W., Wang, R., and Wang, L. (2019a). Comparison of the reliability-based and safety factor methods for structural design. *Applied Mathematical Modelling*, 72:68–84.

- [Wang et al., 2013] Wang, X., Wang, L., and Qiu, Z. (2013). Safety estimation of structural systems via interval analysis. *Chinese Journal of Aeronautics*, 26(3):614–623.
- [Wang et al., 2019b] Wang, Y., Li, L., Hartman, N. W., and Sutherland, J. W. (2019b). Allocation of assembly tolerances to minimize costs. *CIRP Annals*, 68(1):13–16.
- [Wang and Shafieezadeh, 2019a] Wang, Z. and Shafieezadeh, A. (2019a). Esc: an efficient error-based stopping criterion for kriging-based reliability analysis methods. *Structural and Multidisciplinary Optimization*, 59(5):1621–1637.
- [Wang and Shafieezadeh, 2019b] Wang, Z. and Shafieezadeh, A. (2019b). REAK: Reliability analysis through Error rate-based Adaptive Kriging. *Reliability Engineering & System Safety*, 182:33–45.
- [Wansaseub et al., 2020] Wansaseub, K., Slesongsom, S., Panagant, N., Pholdee, N., and Bureerat, S. (2020). Surrogate-assisted reliability optimisation of an aircraft wing with static and dynamic aeroelastic constraints. *International Journal of Aeronautical and Space Sciences*, 21(3):723–732.
- [Watson, 1961] Watson, G. (1961). A study of the group screening method. *Technometrics*, 3(3):371–388.
- [Whittaker and Besuner, 1969] Whittaker, I. C. and Besuner, P. M. (1969). A reliability analysis approach to fatigue life variability of aircraft structures. Technical report, BOEING COMMERCIAL AIRPLANE CO RENTON WA.
- [Wiggenraad et al., 2001] Wiggenraad, J., Michielsen, A., Santoro, D., Lepage, F., Kindervater, C., Beltran, F., and Al-Khalil, M. (2001). Finite element methodologies development to simulate the behaviour of composite fuselage structure and correlation with drop test. *Air & Space Europe*, 3(3-4):228–233.
- [Wilks, 1941] Wilks, S. S. (1941). Determination of sample sizes for setting tolerance limits. *The Annals of Mathematical Statistics*, 12(1):91–96.
- [Woch, 2014] Woch, M. (2014). Risk analysis of the point on aging aircraft structure. In *European Safety and Reliability Conference ESREL, 2014 Conference*, pages 14–18.
- [Wu et al., 2011] Wu, J., Shiao, M., and Seneviratne, W. (2011). Strength-conditioned importance sampling method for aircraft structural reliability analysis. In *52nd AIAA/ASME/ASCE/AHS/ASC Structures, Structural Dynamics and Materials Conference 19th AIAA/ASME/AHS Adaptive Structures Conference 13t*, page 2039.
- [Xiang et al., 2020] Xiang, Z., Chen, J., Bao, Y., and Li, H. (2020). An active learning method combining deep neural network and weighted sampling for structural reliability analysis. *Mechanical Systems and Signal Processing*, 140:106684.
- [Xiao et al., 2020a] Xiao, M., Zhang, J., and Gao, L. (2020a). A system active learning kriging method for system reliability-based design optimization with a multiple response model. *Reliability Engineering & System Safety*, 199:106935.

- [Xiao et al., 2020b] Xiao, S., Oladyshkin, S., and Nowak, W. (2020b). Reliability analysis with stratified importance sampling based on adaptive Kriging. *Reliability Engineering & System Safety*, 197:106852.
- [Xin et al., 2021] Xin, J., Akiyama, M., Frangopol, D. M., Zhang, M., Pei, J., and Zhang, J. (2021). Reliability-based life-cycle cost design of asphalt pavement using artificial neural networks. *Structure and Infrastructure Engineering*, 17(6):872–886.
- [Xu et al., 2022] Xu, J., Zhao, T., Wu, J., and Diao, B. (2022). Experimental study and reliability assessment of fatigue loaded reinforced concrete beams combined with chloride exposure. *Construction and Building Materials*, 322:126480.
- [Xu and Saleh, 2021] Xu, Z. and Saleh, J. H. (2021). Machine learning for reliability engineering and safety applications: Review of current status and future opportunities. *Reliability Engineering & System Safety*, 211:107530.
- [Yang et al., 2008] Yang, Y., Lim, Y. Y., and Soh, C. K. (2008). Practical issues related to the application of the electromechanical impedance technique in the structural health monitoring of civil structures: I. experiment. *Smart Materials and Structures*, 17(3):035008.
- [Yoo and Yoon, 2015] Yoo, D.-Y. and Yoon, Y.-S. (2015). Structural performance of ultra-high-performance concrete beams with different steel fibers. *Engineering Structures*, 102:409–423.
- [Yoon et al., 2014] Yoon, G. L., Kim, S. B., Kwon, O. S., and Yoo, M. S. (2014). Partial safety factor of offshore wind turbine pile foundation in west-south mainland sea. *Journal of the Korean Society of Civil Engineers*, 34(5):1489–1504.
- [Zang et al., 2002] Zang, T. A., Hensch, M. J., Hilburger, M. W., Kenny, S. P., Luckring, J. M., Maghami, P., Padula, S. L., and Stroud, W. J. (2002). Needs and opportunities for uncertainty-based multidisciplinary design methods for aerospace vehicles.
- [Zhang et al., 2010] Zhang, J., Bao, R., Zhang, X., and Fei, B. (2010). A probabilistic estimation method of multiple site damage occurrence for aircraft structures. *Procedia Engineering*, 2(1):1115–1124.
- [Zhang et al., 2019a] Zhang, J., Xiao, M., and Gao, L. (2019a). An active learning reliability method combining Kriging constructed with exploration and exploitation of failure region and subset simulation. *Reliability Engineering & System Safety*, 188:90–102.
- [Zhang et al., 2019b] Zhang, J., Xiao, M., Gao, L., and Chu, S. (2019b). Probability and interval hybrid reliability analysis based on adaptive local approximation of projection outlines using support vector machine. *Computer-Aided Civil and Infrastructure Engineering*, 34(11):991–1009.
- [Zhang et al., 2008] Zhang, L.-l., Li, J., and Peng, Y. (2008). Dynamic response and reliability analysis of tall buildings subject to wind loading. *Journal of Wind Engineering and Industrial Aerodynamics*, 96(1):25–40.

- [Zhang et al., 2019c] Zhang, M., Song, H., Lim, S., Akiyama, M., and Frangopol, D. M. (2019c). Reliability estimation of corroded rc structures based on spatial variability using experimental evidence, probabilistic analysis and finite element method. *Engineering Structures*, 192:30–52.
- [Zhang, 1996] Zhang, P. (1996). Nonparametric importance sampling. *Journal of the American Statistical Association*, 91(435):1245–1253.
- [Zhang et al., 2022a] Zhang, X., Lu, Z., and Cheng, K. (2022a). Cross-entropy-based directional importance sampling with von Mises-Fisher mixture model for reliability analysis. *Reliability Engineering & System Safety*, 220:108306.
- [Zhang et al., 2019d] Zhang, X., Wang, L., and Sørensen, J. D. (2019d). Reif: a novel active-learning function toward adaptive kriging surrogate models for structural reliability analysis. *Reliability Engineering & System Safety*, 185:440–454.
- [Zhang et al., 2022b] Zhang, Y., Wang, B., Ning, Y., Xue, H., and Lei, X. (2022b). Study on health monitoring and fatigue life prediction of aircraft structures. *Materials*, 15(23):8606.
- [Zhou et al., 2020] Zhou, D., Zhuang, X., Zuo, H., Wang, H., and Yan, H. (2020). Deep learning-based approach for civil aircraft hazard identification and prediction. *IEEE Access*, 8:103665–103683.
- [Zhou and Young, 2005] Zhou, F. and Young, B. (2005). Tests of cold-formed stainless steel tubular flexural members. *Thin-walled structures*, 43(9):1325–1337.
- [Zingg et al., 2016] Zingg, L., Briffaut, M., Baroth, J., and Malecot, Y. (2016). Influence of cement matrix porosity on the triaxial behaviour of concrete. *Cement and concrete research*, 80:52–59.
- [Zong and Mao, 2015] Zong, Y. and Mao, J. (2015). Tolerance optimization design based on the manufacturing-costs of assembly quality. *Procedia Cirp*, 27:324–329.
- [Zou and Hastie, 2005] Zou, H. and Hastie, T. (2005). Regularization and variable selection via the elastic net. *Journal of the royal statistical society: series B (statistical methodology)*, 67(2):301–320.
- [Zuhal et al., 2021] Zuhal, L. R., Faza, G. A., Palar, P. S., and Liem, R. P. (2021). On dimensionality reduction via partial least squares for kriging-based reliability analysis with active learning. *Reliability Engineering & System Safety*, page 107848.
- [Zuniga et al., 2021] Zuniga, M. M., Murangira, A., and Perdrizet, T. (2021). Structural reliability assessment through surrogate based importance sampling with dimension reduction. *Reliability Engineering & System Safety*, 207:107289.

Appendices

Appendix A

Overload output distributions for H2H: coupon 1x2

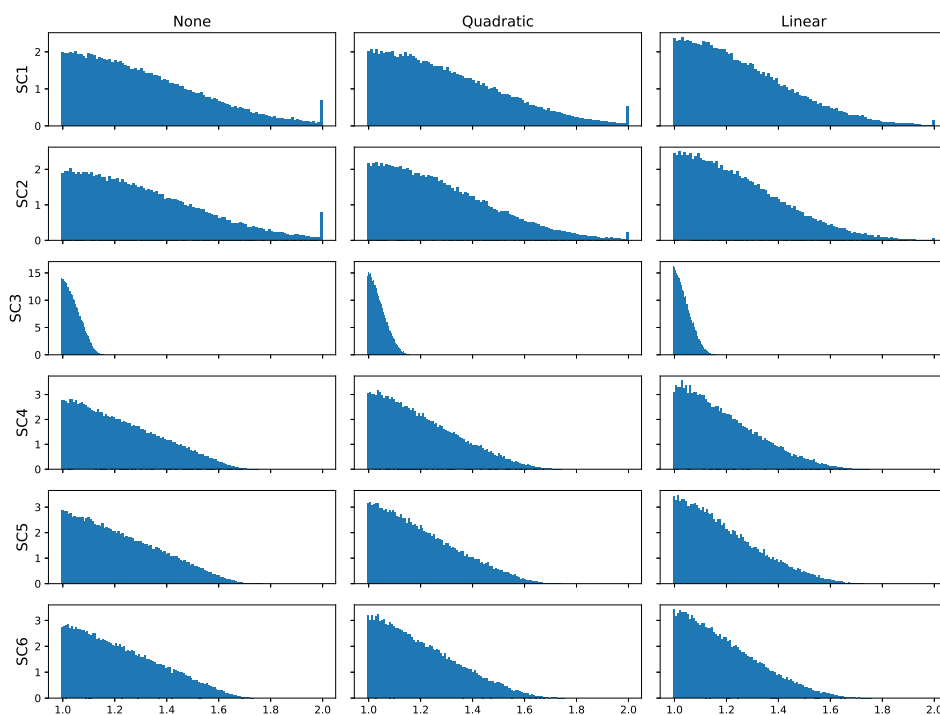


Figure A.1: Overload output PDFs for different stack chains and tolerance acceptance criteria (individual distribution: uniform)

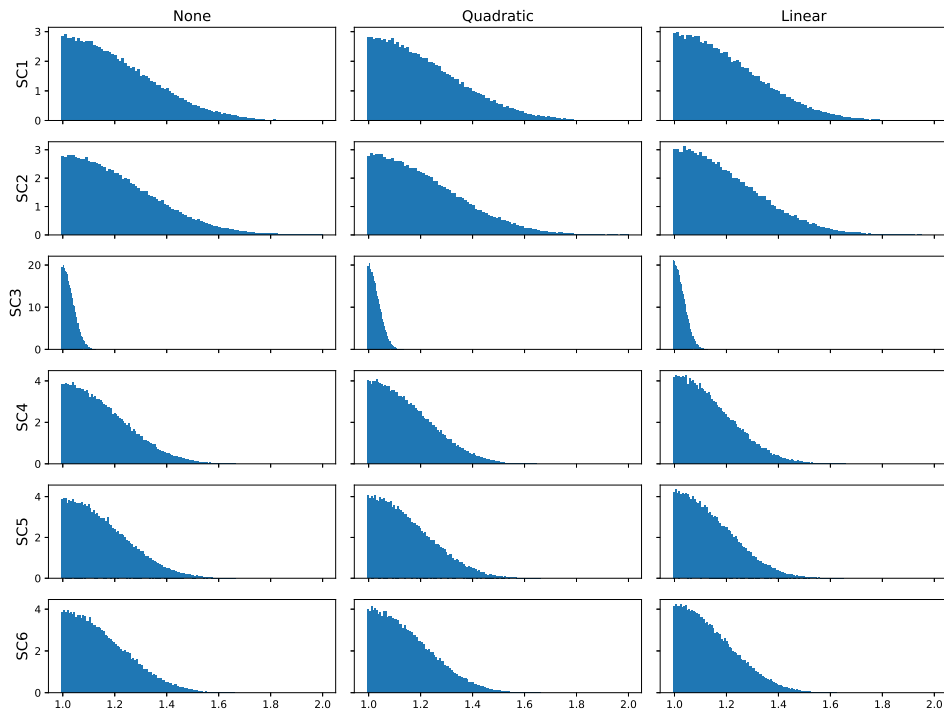


Figure A.2: Overload output PDFs for different stack chains and tolerance acceptance criteria (individual distribution: triangular)

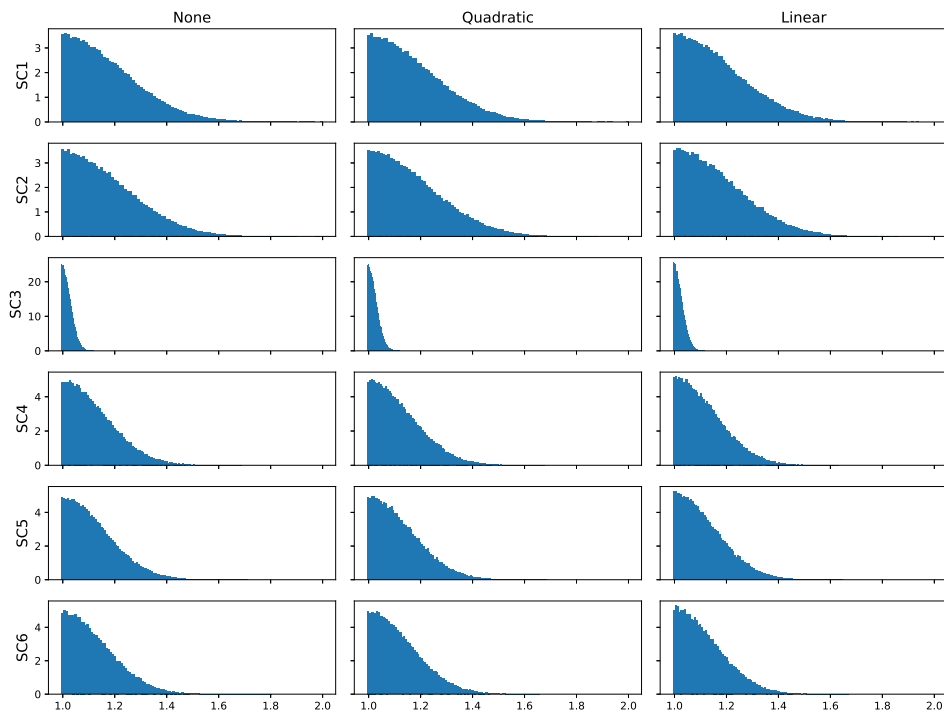


Figure A.3: Overload output PDFs for different stack chains and tolerance acceptance criteria (individual distribution: normal)

Appendix B

Additional material on ImpSMC

B.1 Proof of Eq. 5.19

For a fixed point $S = t$:

$$E_q[\widetilde{H}_R(t)] = H(t) \quad (\text{B.1})$$

We re-write the term $\widetilde{H}_R(t)$ as the arithmetic mean over M independent identically distributed variables R_j :

$$\widetilde{H}_R(t) = \frac{1}{M} \sum_{i=1}^M \frac{f_S(t)G(R_j, t)f_R(R_j)}{h(t)q(R_j)} \quad (\text{B.2})$$

This procedure is the same adopted to determine SMC variance estimator in [Smarslok, 2009]. The fixed-point covariance related to variable R sampled through q importance function will be given by:

$$Cov_q[\widetilde{H}_R(t_1), \widetilde{H}_R(t_2)] = \frac{1}{M^2} \sum_{j=1}^M \sum_{k=1}^M E_q[u_j v_k] \quad (\text{B.3})$$

Where:

$$\begin{aligned} u_j &= \frac{f_S(t_1)G(R_j, t_1)f_R(R_j)}{h(t_1)q(R_j)} - H(t_1) \\ v_k &= \frac{f_S(t_2)G(R_k, t_2)f_R(R_k)}{h(t_2)q(R_k)} - H(t_2) \end{aligned} \quad (\text{B.4})$$

These latter are centered. Then, for all $j \neq k$, u_j and v_k are independent, leading to:

$$E[u_j v_k] = E[u_j]E[v_k] = 0 \quad \forall j \neq k \quad (\text{B.5})$$

Joining Eq. B.3 and B.5 one may obtain:

$$Cov_q[\widetilde{H}_R(t_1), \widetilde{H}_R(t_2)] = \frac{1}{M^2} \sum_{j=1}^M E_q[u_j v_j] \quad (\text{B.6})$$

Keeping the j indexes implicit inside \widetilde{H}_R , we can develop every term:

$$\begin{aligned} u_j v_j &= [\widetilde{H}_R(t_1) - H(t_1)] [\widetilde{H}_R(t_2) - H(t_2)] \\ &= \widetilde{H}_R(t_1)\widetilde{H}_R(t_2) + H(t_1)H(t_2) - \widetilde{H}_R(t_1)H(t_2) - H(t_1)\widetilde{H}_R(t_2) \end{aligned} \quad (\text{B.7})$$

Passing to the expectation:

$$\begin{aligned} E_q[u_j v_j] &= E_q [\widetilde{H}_R(t_1)\widetilde{H}_R(t_2)] + H(t_1)H(t_2) - H(t_1)H(t_2) - H(t_1)H(t_2) \\ &= E_q [\widetilde{H}_R(t_1)\widetilde{H}_R(t_2)] - H(t_1)H(t_2) \end{aligned} \quad (\text{B.8})$$

Finally, involving again Eq. B.6 we obtain the result shown in Eq.5.19:

$$\begin{aligned} Cov_q [\widetilde{H}_R(t_1), \widetilde{H}_R(t_2)] &= \frac{1}{M^2} \sum_{j=1}^M (E_q [\widetilde{H}_R(t_1)\widetilde{H}_R(t_2)] - H(t_1)H(t_2)) \\ &= \frac{1}{M^2} M (E_q [\widetilde{H}_R(t_1)\widetilde{H}_R(t_2)] - H(t_1)H(t_2)) \\ &= \frac{1}{M} (E_q [\widetilde{H}_R(t_1)\widetilde{H}_R(t_2)] - H(t_1)H(t_2)) \end{aligned} \quad (\text{B.9})$$

B.2 Experimental variance validation on truss test case

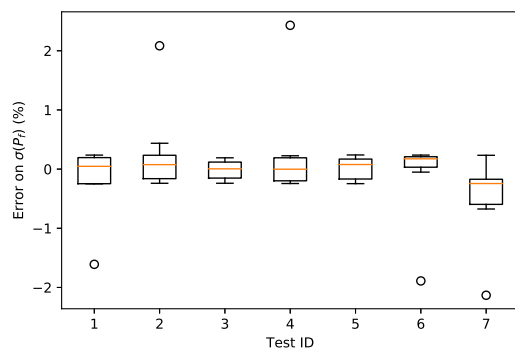
Every statistical treatment reported in the following graphs are issued of 10^4 repeated ImpSMC analyses with $N = 10^3$ response samples and $M = 10^3, 10^4, 10^5$ capacity samples for each one. This is intended to validate experimentally the variance estimators enunciated in Section 5.3 on truss test case.

Results are reported in form of box plots: distinct boxes are depicted for the two variance estimators and the configurations detailed in Table B.1. The different ratios M/N are resumed in the same box.

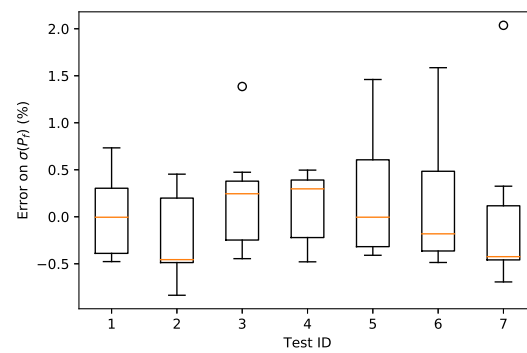
ID	Strength R	
	\overline{V}_{all}	$\sigma(\overline{V}_{all})$
1	0.095	0.01
2	0.132	0.01
3	0.1023	0.001
4	0.1057	0.005
5	0.115	0.01
6	0.225	0.05
7	0.368	0.1

Table B.1: Truss test case: configurations used for validation purpose

B.2. EXPERIMENTAL VARIANCE VALIDATION ON TRUSS TEST CASE **B01**



(a) R -based estimator



(b) S -based estimator

Figure B.1: Truss test case: experimental validation of both variance estimators

Appendix C

Additional material on codesign tolerance optimization

C.1 Additional formulations of codesign framework

In this section, we define other two formulations of the codesign framework, which can be derived by the principal variants presented in Section 7.3.6.

First of all, we can have problems where all input variabilities are defined (i.e. all fixed \mathbf{v}) and on which we can not intervene. As the only remaining design variable is the top-level requirement v_{assy} , we cannot insert the cost c_1 in the optimization problem statement. The mathematical formulation will become:

$$\begin{aligned} \min_{v_{assy}} \quad & c_2(v_{assy}; \mathbf{v}) \\ \text{s.t.} \quad & PoE(v_{assy}; \mathbf{v}, I_{nom}) \leq \overline{PoE} \\ & v_{assy, LB} \leq v_{assy} \leq v_{assy, UB} \end{aligned} \quad (\text{C.1})$$

The problem in Eq. C.1 will be a single-objective optimization problem, in the cases with a single top-level requirement related to a tolerance model with a single output. Otherwise, if multiple outputs are issued from the tolerance model and/or multiple top-level requirements are defined, the problem can become multi-objective, with a cost $c_{2,i}$ associated to each term $v_{assy,i}$.

Moreover, another possibility may be given by a restriction of the *codesign framework with fixed top-level requirement*. If the goal of the application of the framework is to focus exclusively on the definition of the constraint of the maximum variance of the output of the tolerance model $\rho(\mathbf{X}(\mathbf{v}))$, it is not necessary to evaluate the compromise between c_1 and c_2 : in this case, we may optimize either one of the costs, thus implying, according to the sensitivities detailed in Section 7.3.5, to either minimize c_1 or maximize c_2 . As an analytical solution is always available on the computation of c_1 , we can re-formulate the optimization problem as follows:

$$\begin{aligned} \min_{\mathbf{v}} \quad & c_1(\mathbf{v}) \\ \text{s.t.} \quad & PoE(\mathbf{v}; v_{assy}, I_{nom}) \leq \overline{PoE} \\ & v_{LB,i} \leq v_i \leq v_{UB,i} \quad \forall i = 1, \dots, N \end{aligned} \quad (\text{C.2})$$

As for the problem in Eq. C.1, this can be treated either as a single- or multi-objective optimization problem: in the first case, we will consider the weighted sum of all contributors, as in Eq. 7.7; otherwise, we can consider a separated component-related out-of-quality cost $c_{1,i}$ associated to each i component.

C.2 Additional results on H2H applications

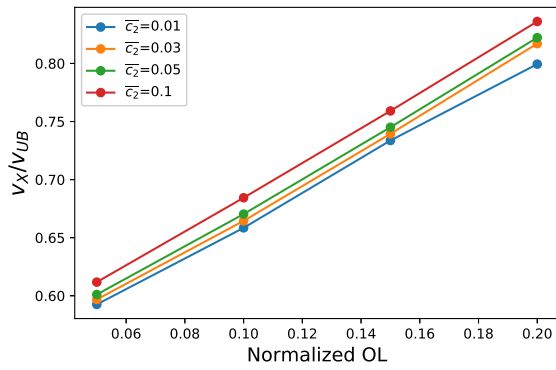
In this section we report the additional results of the application of the *full codesign framework* to the H2H coupons with bolting patterns 1x5 (in Section C.2.1) and 3x5 (in Section C.2.2). These include the evolutions of the component-related tolerance bounds v_i and the top-level requirement v_{assy} as functions of the imposed overload limits OL at different budgets \bar{c}_2 of the assembly-related cost c_2 , regrouped per stack chain.

C.2.1 Coupon 1x5

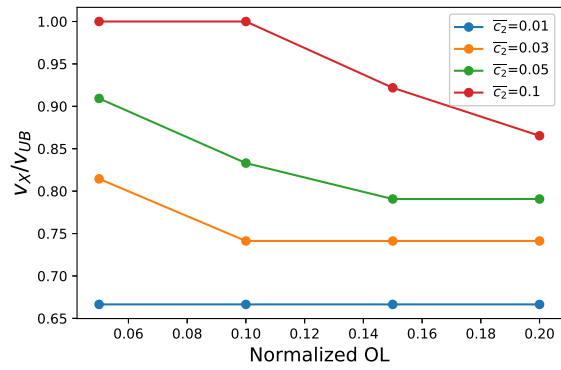
In this section we report the same optimization results from Section 7.5.2, related to the application of the *full codesign framework* on the H2H coupon with bolting pattern 1x5. However, this time we re-group the evolution curves of the optimal design variables (as a function of the imposed overload limit OL) per feature associated to each stack chain.

We report in Fig. C.1 the evolution of the component-related tolerance variables v_i . It is possible to observe, with this representation, the effect of the budget \bar{c}_2 of the assembly-related cost c_2 . All evolution curves confirm the findings of the H2H coupon 1x2 (cf. Section 7.5.1.2), i.e. a reduction of the optimal component-related tolerance bounds with an increase of the budget c_2 .

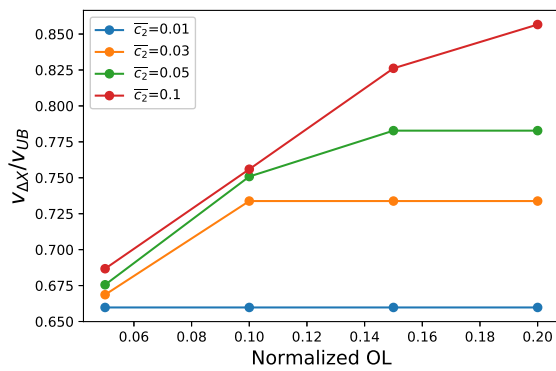
Focusing on the stack chain 4, we can observe the opposite evolutions of the component-related tolerance bounds v_X and $v_{\Delta X}$ as functions of the imposed overload limits OL . For low budgets $\bar{c}_2 = 0.01$, the problem is purely geometrical, as the *PoE* constraint is not active and $v_X \approx v_{\Delta X}$. When increasing the budget to $\bar{c}_2 = 0.03$, the *PoE* constraint becomes active for $OL \leq 1.1$, leading the $v_{\Delta X}$ of stack chain 4 to mimic the evolutions of the $v_{\Delta X}$ of the other stack chains. For higher imposed overload limits OL , the *PoE* constraint keeps being inactive as it is less stringent than the constraint $c_2 \leq \bar{c}_2 = 0.3$. This transition from active to inactive *PoE* constraint progressively moves towards higher OL when increasing the budget \bar{c}_2 . Finally, the evolution of v_X related to the stack chain 4 adapts to the evolutions of the associated $v_{\Delta X}$, confirming the findings in Section 7.5.2.



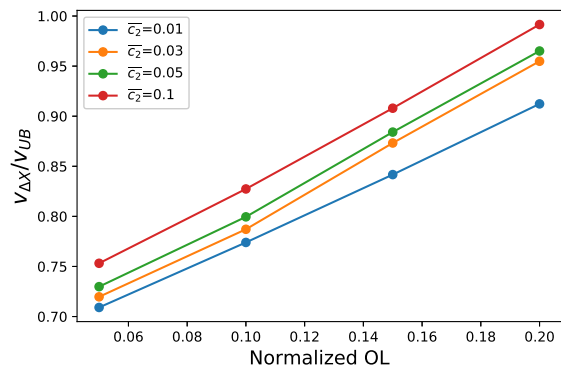
(a) Stack chain 1 $v_i = v_X$



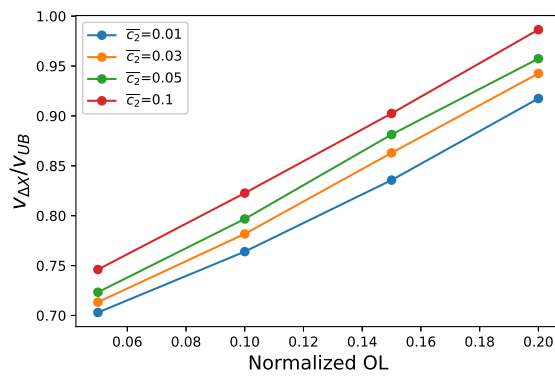
(b) Stack chain 4 $v_i = v_X$



(c) Stack chain 4 $v_i = v_{\Delta X}$



(d) Stack chain 5 $v_i = v_{\Delta X}$



(e) Stack chain 6 $v_i = v_{\Delta X}$

Figure C.1: H2H coupon 1x5: optimal v_i with full codesign framework on different budgets \bar{c}_2 regrouped per stack chain

The same representation is used for the optimal top-level requirement v_{assy} associated to each stack chain in Fig. C.2. The effect of \bar{c}_2 is opposite to what was retrieved for the component-related design variables: for the same imposed overload limit OL , we can increase the optimal top-level requirement v_{assy} by increasing the budget \bar{c}_2 . This confirms the findings from the application of the *full codesign framework* on the H2H coupon 1x2 (cf. Section 7.5.1.3).

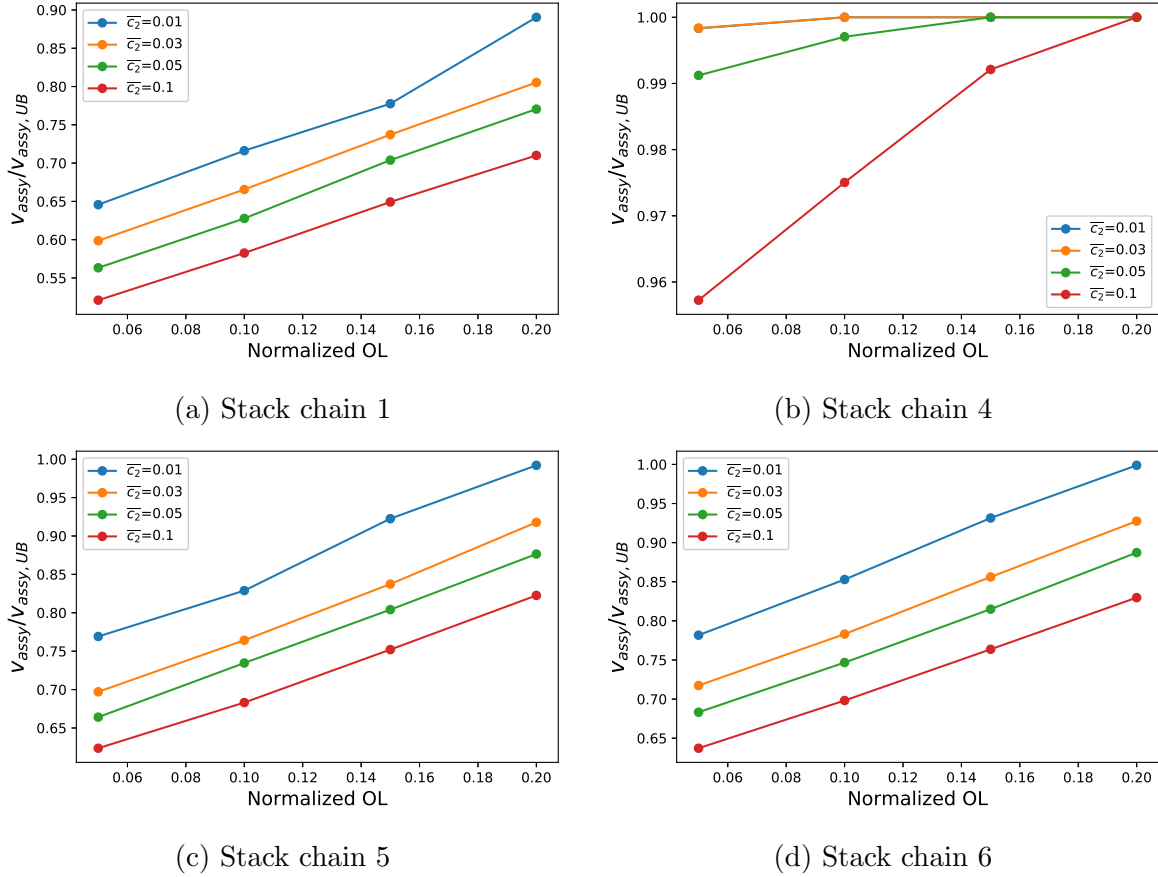
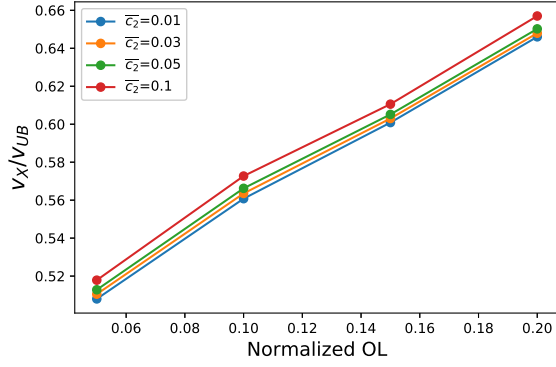


Figure C.2: H2H coupon 1x5: optimal v_{assy} with full codesign framework on different budgets \bar{c}_2 regrouped per stack chain

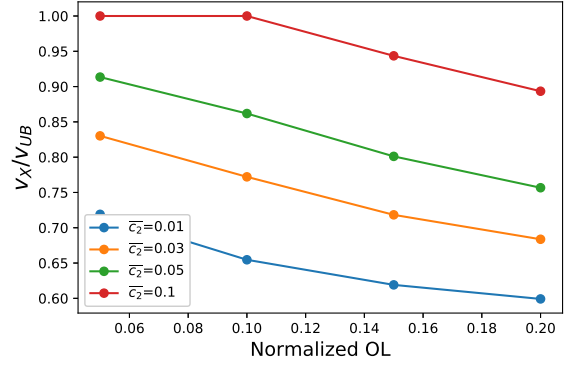
C.2.2 Coupon 3x5

In this section we report the same optimization results from Section 7.5.3, related to the application of the *full codesign framework* on the H2H coupon with bolting pattern 3x5. However, this time we re-group the evolution curves of the optimal design variables (as function of the imposed overload limit OL) per feature associated to each stack chain.

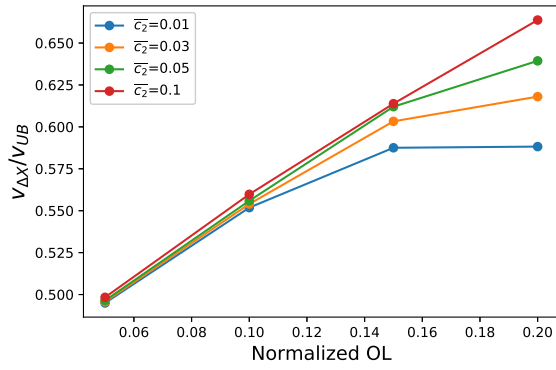
We report in Fig. C.3 the evolutions of the optimal component-related tolerance bounds v_i , and in Fig. C.4 the analogue evolutions related to the top-level requirement v_{assy} . All results confirm the previous findings on the effect of the budget \bar{c}_2 of the assembly-related cost c_2 : for a fixed imposed overload limit OL , by increasing \bar{c}_2 , we decrease the v_i and increase the v_{assy} .



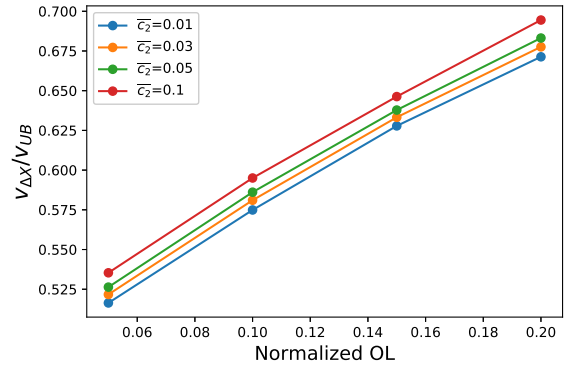
(a) Stack chain 1 $v_i = v_X$



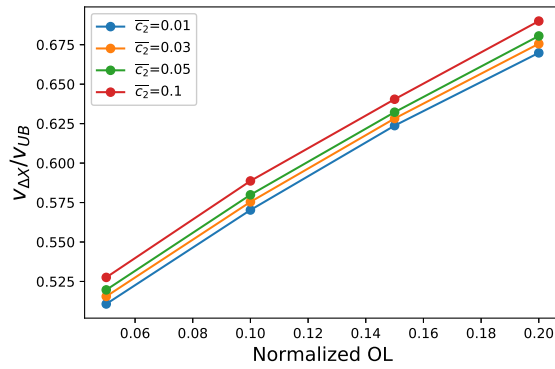
(b) Stack chain 4 $v_i = v_X$



(c) Stack chain 4 $v_i = v_{\Delta X}$

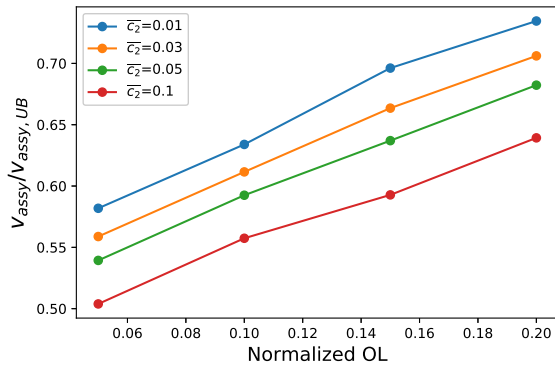


(d) Stack chain 5 $v_i = v_{\Delta X}$

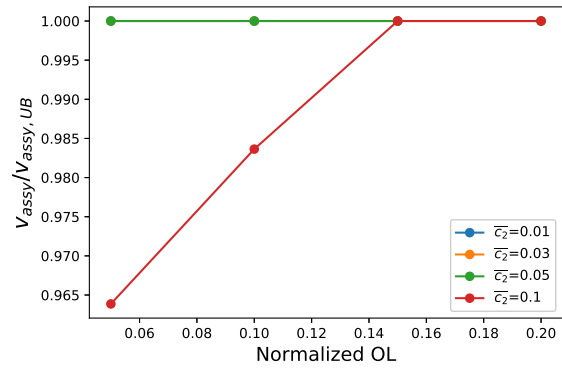


(e) Stack chain 6 $v_i = v_{\Delta X}$

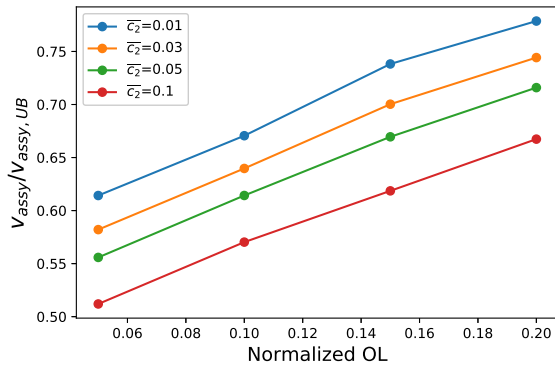
Figure C.3: H2H coupon 3x5: optimal v_i with full codesign framework on different budgets \bar{c}_2 regrouped per stack chain



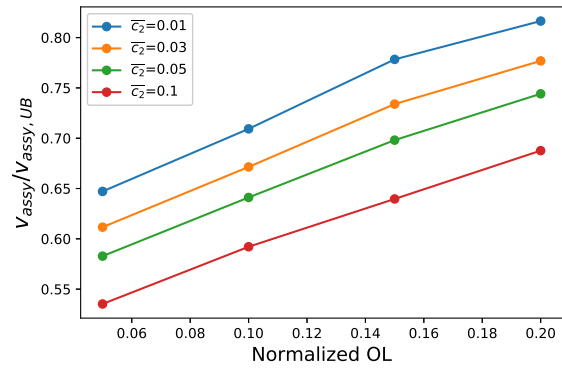
(a) Stack chain 1



(b) Stack chain 4



(c) Stack chain 5



(d) Stack chain 6

Figure C.4: H2H coupon 3x5: optimal v_{assy} with full codesign framework on different budgets \bar{c}_2 regrouped per stack chain